



TECHNICAL REPORT 0-6953-1
TXDOT PROJECT NUMBER 0-6953

3D Strut-and-Tie Modeling for Design of Drilled Shaft Footings

Yousun Yi
Hyunsu Kim
Ryan A. Boehm
Zachary D. Webb
Jongkwon Choi
Hwa-Ching Wang
Juan Murcia-Delso
Trevor D. Hrynyk
Oguzhan Bayrak

October 2021
Published March 2022

<https://library.ctr.utexas.edu/ctr-publications/0-6953-1.pdf>



TECHNICAL REPORT DOCUMENTATION PAGE

1. Report No. FHWA/TX-21/0-6953-1		2. Government Accession No.		3. Recipient's Catalog No.	
4. Title and Subtitle 3D Strut-and-Tie Modeling for Design of Drilled Shaft Footings				5. Report Date Submitted: Oct 2021 Published: Mar 2022	
				6. Performing Organization Code CTR	
7. Author(s) Yousun Yi, Hyunsu Kim, Ryan A. Boehm, Zachary D. Webb, Jongkwon Choi, Hwa-Ching Wang, Juan Murcia-Delso, Trevor D. Hrynyk, Oguzhan Bayrak				8. Performing Organization Report No. 0-6953-1	
9. Performing Organization Name and Address Center for Transportation Research The University of Texas at Austin 3925 W. Braker Lane, 4th Floor Austin, TX 78759				10. Work Unit No.	
				11. Contract or Grant No. 0-6953	
12. Sponsoring Agency Name and Address Texas Department of Transportation Research and Technology Implementation Division 125 E. 11th Street Austin, TX 78701				13. Type of Report and Period Covered Technical Report September 2017 – August 2021	
				14. Sponsoring Agency Code	
15. Supplementary Notes Project performed in cooperation with the Texas Department of Transportation and the Federal Highway Administration. Study Title: Strut-and-Tie Modeling and Design of Drilled Shaft Footings					
16. Abstract A comprehensive study was conducted to characterize the structural response and develop design guidelines for drilled shaft footings. The study included large-scale testing and numerical analyses of footing specimens subjected to various loading conditions. A database of 35 drilled shaft footings constructed in Texas by TxDOT was established and analyzed for designing test specimens. A total of 19 large-scale specimens were designed and tested to study various design parameters and loading scenarios including vertical compression and uniaxial bending. A series of numerical analyses employing experimentally-verified models were also performed to account for the effect of additional design parameters that could not be covered in the experimental program. Based on the data and insights obtained from the experimental and numerical studies, 3D strut-and-tie modeling guidelines for drilled shaft footings are proposed by refining current provisions for 2D strut-and-tie models in AASHTO LRFD (2020). The new guidelines include the definition of the 3D nodal geometry at bearing faces, refinements for strength modification factors, critical section definitions for development of horizontal and vertical ties, and recommendations for bottom mat reinforcement configuration. Project findings have indicated that the proposed recommendations improve the accuracy of the ultimate strength predictions for a database including drilled shaft footing tests from the literature and the current study, without generating unconservative or overly conservative predictions. This represents an improvement of the accuracy achieved using the recommendations of TxDOT Project 5-5253-01. Lastly, a design example of a drilled shaft footing subjected to various loading scenarios is provided.					
17. Key Words Drilled Shaft Footings, Strut-and-Tie Modeling, Strength, Serviceability			18. Distribution Statement No restrictions. This document is available to the public through the National Technical Information Service, Alexandria, Virginia 22312, https://www.ntis.gov/ .		
19. Security Classif. (of this report) Unclassified		20. Security Classif. (of this page) Unclassified		21. No. of Pages 494	22. Price



**THE UNIVERSITY OF TEXAS AT AUSTIN
CENTER FOR TRANSPORTATION RESEARCH**

3D Strut-and-Tie Modeling for Design of Drilled Shaft Footings

Yousun Yi
Hyunsu Kim
Ryan A. Boehm
Zachary D. Webb
Jongkwon Choi
Hwa-Ching Wang
Juan Murcia-Delso
Trevor D. Hrynyk
Oguzhan Bayrak

CTR Technical Report:	0-6953-R1
Report Date:	Submitted: July 2021
Project:	0-6953
Project Title:	Strut-and-Tie Modeling and Design of Drilled Shaft Footings
Sponsoring Agency:	Texas Department of Transportation
Performing Agency:	Center for Transportation Research at The University of Texas at Austin

Project performed in cooperation with the Texas Department of Transportation and the Federal Highway Administration.

Disclaimers

Author's Disclaimer: The contents of this report reflect the views of the authors, who are responsible for the facts and the accuracy of the data presented herein. The contents do not necessarily reflect the official view or policies of the Federal Highway Administration or the Texas Department of Transportation (TxDOT). This report does not constitute a standard, specification, or regulation.

Patent Disclaimer: There was no invention or discovery conceived or first actually reduced to practice in the course of or under this contract, including any art, method, process, machine manufacture, design or composition of matter, or any new useful improvement thereof, or any variety of plant, which is or may be patentable under the patent laws of the United States of America or any foreign country.

Engineering Disclaimer

NOT INTENDED FOR CONSTRUCTION, BIDDING, OR PERMIT PURPOSES.

Project Engineer: Oguzhan Bayrak

Professional Engineer License State and Number: Texas No. 106598

P.E. Designation: Research Supervisor

Acknowledgments

The authors express deep appreciation to the Texas Department of Transportation (TxDOT) for providing the funds and supports to conduct this research study. The contributions of the project manager Joanne Steele (RTI Division) and other members of TxDOT, including Jamie Farris, Sara Watts, Seth Cole, and Victoria McCammon (Bridge Division), facilitated great improvements to the outcomes of this project.

Table of Contents

Chapter 1. Introduction	1
1.1. Background	1
1.2. Project Objective and Scope	2
1.3. Organization.....	3
Chapter 2. Literature Review	4
2.1. Overview	4
2.2. Current STM Specifications	4
2.2.1. Nodal Strength Comparison.....	14
2.2.2. Strut Strength Comparison.....	14
2.2.3. Crack Control Reinforcement Comparison.....	15
2.3. Previous Research Review.....	15
2.3.1. Previous Research on Uniform Compressions in Drilled Shafts	16
2.3.2. Previous Research on Non-uniform compression in Drilled Shafts	32
2.3.3. Previous Research on Compression and Tension in Drilled Shafts	33
2.3.4. Previous Research on Finite Element Analysis of Drilled Shaft Footings	36
2.4. Summary and Discussion.....	39
Chapter 3. Design Parameter Review	41
3.1. Overview	41
3.2. TxDOT Drilled Shaft Footing Database	41
3.3. Geometric Parameters	43
3.3.1. Span-to-depth Ratio	43
3.3.2. Footing Dimension.....	43
3.3.3. Column Dimension	44
3.3.4. Drilled Shaft Diameter	45
3.3.5. Footing-to-shaft Edge Distance	46
3.4. Reinforcing Details	47
3.4.1. Bottom Mat Reinforcement	47
3.4.2. Top Mat Reinforcement	52
3.4.3. Side Face Reinforcement	53
3.4.4. Column Reinforcement.....	55

3.4.5. Shaft Reinforcement	56
3.5. Summary and Discussion.....	59
Chapter 4. Experimental Program – Phase I: Uniform Compression in Drilled Shafts.....	61
4.1. Overview	61
4.2. Experimental Program	61
4.2.1. Test Variables	61
4.2.2. Specimen Design	66
4.2.3. Materials	71
4.2.4. Testing Setup	76
4.2.5. Fabrication of Specimens.....	80
4.2.6. Instrumentation	86
4.2.7. Test Procedure	89
4.3. Experimental Results and Discussion.....	89
4.3.1. Summary of Experimental Results	89
4.3.2. Series I: Bottom Mat Reinforcement Details.....	94
4.3.3. Series II: Strut Inclination.....	102
4.3.4. Series III: Shaft Diameter	106
4.3.5. Series IV: Side Face Reinforcement Ratio	110
4.3.6. Series V: Footing Size	115
4.4. Summary and Discussion.....	119
Chapter 5. Experimental Program – Phase II: Non-uniform Compression in Drilled Shafts	121
5.1. Overview.....	121
5.2. Experimental Program	121
5.2.1. Test Variable	121
5.2.2. Specimen Design	124
5.2.3. Materials	126
5.2.4. Testing Setup	129
5.2.5. Fabrication of Specimens.....	130
5.2.6. Instrumentation	133
5.2.7. Test Procedure	136
5.3. Experimental Results and Discussion.....	136
5.3.1. Overview.....	136
5.3.2. Series VI: Anchorage Type of Column Reinforcement.....	138

5.3.3. Critical Section of Column Reinforcement.....	155
5.3.4. Summary and Discussion.....	155
Chapter 6. Experimental Program – Phase III: Compression and Tension in Drilled Shafts	157
6.1. Overview	157
6.2. Experimental Program	157
6.2.1. Equivalent Loading Condition	157
6.2.2. Test Variable	159
6.2.3. Specimen Design	160
6.2.4. Materials	164
6.2.5. Testing Setup	166
6.2.6. Fabrication of Specimens.....	169
6.2.7. Instrumentation	169
6.2.8. Test Procedure	174
6.3. Experimental Results and Discussion.....	174
6.3.1. Overview.....	174
6.3.2. Series VII: Anchorage Type of Drilled Shaft Reinforcement	175
6.3.3. Critical Section of Drilled Shaft Reinforcement.....	185
6.3.4. Summary and Discussion.....	187
Chapter 7. Finite Element Modeling.....	189
7.1. Introduction.....	189
7.2. Preliminary FE Model Assessment.....	189
7.2.1. Footing Research Database for the FE Validation.....	190
7.2.2. Finite Element Model	193
7.2.3. Results and Discussion	194
7.3. Phase I Testing: Uniform Compression in Shafts.....	197
7.3.1. Finite Element Model	197
7.3.2. Results and Validation with Experimental Data.....	200
7.3.3. Numerical Parametric Study.....	207
7.3.4. Summary and Discussion.....	220
7.4. Phase II Testing: Non-uniform Compression in Shafts.....	221
7.4.1. Finite Element Model	221
7.4.2. Results and Validation with Experimental Data.....	224
7.4.3. Numerical Parametric Study	227
7.4.4. Summary and Discussion.....	236

7.5. Phase III Testing: Tension-Compression in Shafts.....	237
7.5.1. Finite Element Model	237
7.5.2. Results and Validation with Experimental Data	242
7.5.3. Numerical Parametric Study	243
Chapter 8. Development of Strut-and-Tie Modeling Guidelines.....	249
8.1. Overview	249
8.2. Current STM Provision for Drilled Shaft Footings	249
8.2.1. AASHTO LRFD (2020) and Williams et al. (2012).....	251
8.2.2. Evaluation of Current STM Provision	260
8.3. Proposal of 3D STM Guidelines for Drilled Shaft Footings	269
8.3.1. Proposal of 3D STM	269
8.3.2. Assessment of Proposed 3D STM	283
8.4. Design Example	289
8.4.1. Overview	289
8.4.2. Design Task	289
8.4.3. Design Calculations: Load Case I.....	295
8.4.4. Design Calculations: Load Case II.....	307
8.4.5. Design Calculations: Load Case III	321
8.4.6. Design Calculations: Load Case IV	335
8.4.7. Design Calculations: Load Case V	349
8.4.8. Reinforcement Layout	361
8.5. Summary and Discussion.....	365
Chapter 9. Summary and Conclusions.....	367
9.1. Summary	367
9.2. Concluding Remarks.....	369
References	371
Appendix A. Proposed Modifications of AASHTO LRFD	376
Appendix B. Footing Research Database	386
Appendix C. TxDOT Footing Database	396
Appendix D. Drawings of Specimens.....	400
Appendix E. Material Test Results	425
Appendix F. Test Results: Phase I	427
Appendix G. 3D STM Predictions (Williams et al., 2012).....	453
Appendix H. 3D STM Predictions (Present Study)	458

List of Tables

Table 2.1 Nodal strength comparison for each specification.....	5
Table 2.2 Variables referenced in Table 2.1	8
Table 2.3 Strut strength comparison for each specification.....	9
Table 2.4 Variables referenced in Table 2.3	10
Table 2.5 Crack control reinforcement comparison for each specification	11
Table 2.6 Variables referenced in Table 2.5	13
Table 2.7 Summary of previously proposed methodologies	28
Table 2.8 Variables referenced in Table 2.7	31
Table 3.1 Details of banding configuration in TxDOT drilled shaft footing database	51
Table 3.2 Summary of TxDOT plan database (Geometry).....	59
Table 3.3 Summary of TxDOT plan database (Reinforcement).....	59
Table 4.1 Test matrix of Phase I testing	63
Table 4.2 Summary of dimensions of specimens	67
Table 4.3 Summary of details of reinforcement	69
Table 4.4 Concrete mixture design	72
Table 4.5 Measured Strengths of Cylinders.....	74
Table 4.6 Mechanical properties of bottom mat reinforcement.....	75
Table 4.7 Summary of experimental results	93
Table 4.8 Test results: Series I.....	94
Table 4.9 Summary of visual observations in Series I testing	95
Table 4.10 Summary of the serviceability condition: Series I.....	100
Table 4.11 Summary of constructability issues: Series I.....	100
Table 4.12 Comparison table for determining bottom mat reinforcing detail	101
Table 4.13 Test results: Series II.....	102
Table 4.14 Test results: Series III	106
Table 4.15 Test results: Series IV	110
Table 4.16 Test results: Series V	115

Table 5.1 Test matrix: Phase II.....	123
Table 5.2 Comparison between column reinforcement embedment lengths of TxDOT drilled shaft footing database and Phase II specimens	126
Table 5.3 Concrete mix design for Phase II specimens	126
Table 5.4 Measured strengths of cylinders: Phase II	127
Table 5.5 Mechanical properties of reinforcement: Phase II.....	128
Table 5.6 Summary of experimental results: Phase II	139
Table 6.1 Test matrix: Phase III.....	160
Table 6.2 Comparison between drilled shaft reinforcement embedment lengths of TxDOT drilled shaft footing database and Phase III specimens	163
Table 6.3 Measured strengths of cylinders: Phase III.....	165
Table 6.4 Mechanical properties of reinforcing bars: Phase III.....	166
Table 6.5 Summary of experimental results: Phase III.....	176
Table 7.1 Summary of FE Validation Database	192
Table 7.2 Summary of sensitivity analysis	195
Table 7.3 Summary of measured and computed ultimate capacities of FE Validation Database	197
Table 7.4 Summary of measured and computed ultimate capacities.....	201
Table 7.5 Analysis matrix of the numerical parametric study (Phase I).....	212
Table 7.6 Analysis matrix of the numerical parametric study (Phase II)	228
Table 7.7 Analysis matrix of the numerical parametric study (Phase III)	245
Table 8.1 Number of tests from previous research and this study.....	261
Table 8.2 Filtering criteria used for the footing research database.....	262
Table 8.3 Summary of predicted ultimate capacities based on current 3D STM provision.....	266
Table 8.4 Statistical data of predicted ultimate capacities.....	284
Table 8.5 Controlling failure mechanism by 3D STM	285
Table 8.6 Summary of statistics of SR.....	288
Table B1. Details of Test Specimens: Blevot & Frémy (1967).....	386
Table B2. Details of Test Specimens: Clarke (1973)	387
Table B3. Details of Test Specimens: Sabnis & Gogate (1984).....	387
Table B4. Details of Test Specimens: Adebar et al. (1990).....	388

Table B5. Details of Test Specimens: Suzuki et al. (1998)	389
Table B6. Details of Test Specimens: Suzuki et al. (1999)	390
Table B7. Details of Test Specimens: Suzuki et al. (2000)	391
Table B8. Details of Test Specimens: Suzuki and Otsuki (2002).....	392
Table B9. Details of Test Specimens in <i>Evaluation Database</i>	393
Table C1. Geometric Properties.....	396
Table C2. Reinforcing Details	398
Table E1. Mechanical properties of bottom mat reinforcement	425
Table E2. Mechanical properties of side face reinforcement	426
Table G1. Summary of 3D STM Predictions based on the recommendation by Williams et al. (2012).....	455
Table H1. Summary of 3D STM Predictions based on the proposal by present study.....	461

List of Figures

Figure 1.1 Congested reinforcement cage (footing construction at US-281 and Loop 1604 interchange).....	2
Figure 2.1 Assumed geometries of bottom node (left) and top node (right) (Klein, 2002)	16
Figure 2.2 Assumed 3D nodal geometry (Mitchell et al., 2004)	17
Figure 2.3 Typical specimen (Blevot and Frémy, 1967)	18
Figure 2.4 Beam-type shear failure (left) and punching shear failure (right) (Clarke, 1973).....	19
Figure 2.5 Anchorage details (Clarke, 1973).....	19
Figure 2.6 Test specimens (Adebar et al., 1990)	21
Figure 2.7 Comparison of experimental strengths and code predictions (Adebar et al., 1990).....	22
Figure 2.8 Three different reinforcement layouts adopted for test specimens (Miguel-Tortola et al., 2018)	23
Figure 2.9 Drilled shaft footing designed by sectional design method (left) and STM (right) (Klein, 2002)	32
Figure 2.10 Strut-and-tie model resulting in tension at column section (left) and suggested anchorage detail of column reinforcement (right) (Williams et al., 2012).....	33
Figure 2.11 Strut-and-tie model resulting tension at drilled shafts (Widianto and Bayrak, 2011)	34
Figure 2.12 Reinforcement details based on sectional design method (left) and STM (right) (Widianto and Bayrak, 2011).....	35
Figure 2.13 Strut-and-tie model (left) and suggested anchorage detail of drilled shaft reinforcement (right) (Williams et al., 2012).....	35
Figure 2.14 Finite element mesh for one-quarter of drilled shaft footing with slab-type reinforcement layout (Sam and Iyer, 1995).....	37
Figure 2.15 Drilled shaft footing design example (top) and topology from RESO (bottom) (Leu et al., 2006)	38
Figure 2.16 Basic grid element (left) and dimensioned shape of 3D grid strut-and-tie model for drilled shaft footing example of ACI SP-273 (right) (Yun et al., 2018)	39
Figure 3.1 Footing locations	42
Figure 3.2 Yearly distribution of selected footing plans.....	42
Figure 3.3 Span-to-depth ratio distribution of collected footing plans.....	43

Figure 3.4 Footing dimensions of collected footing plans.....	44
Figure 3.5 Column dimension of collected footing plans.....	45
Figure 3.6 Drilled shaft diameters of collected footing plans.....	46
Figure 3.7 Footing-to-shaft edge distances of collected footing plans	47
Figure 3.8 Average bottom mat reinforcement ratios of collected footing plans	48
Figure 3.9 Average bottom mat reinforcement ratio by year.....	49
Figure 3.10 Relationship between strut inclination and bottom mat reinforcement ratio	49
Figure 3.11 Grid configuration (left) and banding configuration (right) used in drilled shaft footings	50
Figure 3.12 Anchorage using straight bars (left) and using hooked bars (right).....	52
Figure 3.13 Average top mat reinforcement ratios of collected footing plans	52
Figure 3.14 Average longitudinal side face reinforcement ratios of collected footing plans	54
Figure 3.15 Typical transverse face reinforcement (left) and hooked bottom reinforcement used in Fort Worth (right).....	55
Figure 3.16 Average transverse face reinforcement ratios of collected footing plans	55
Figure 3.17 Two types of dowel bars coming from columns in the TxDOT Drilled shaft footing database	56
Figure 3.18 Ratio of provided to required lengths of dowel bars coming from shafts.....	58
Figure 3.19 Details of hooked dowel bars spliced to dowel bars coming from shafts.....	58
Figure 4.1 Generalized 3D strut-and-tie model for drilled shaft footings subjected to compression loading	62
Figure 4.2 Definition of the bandwidth.....	64
Figure 4.3 Geometry of a footing specimen	66
Figure 4.4 Bottom mat reinforcement configuration and anchorage of specimens in Series I.....	68
Figure 4.5 Drawings of reinforcing details (II-7)	70
Figure 4.6 Historical scaled testing of footings relative to actual TxDOT example	71

Figure 4.7 Concrete cylinders (left) and dog-bone direct tension specimens (right).....	72
Figure 4.8 Concrete cylinder tests	73
Figure 4.9 Reinforcement sample test	75
Figure 4.10 Structural test setup	76
Figure 4.11 General test configuration for Phase I testing	77
Figure 4.12 Layout of supports.....	78
Figure 4.13 Support fixtures	79
Figure 4.14 Roller frame.....	79
Figure 4.15 Loading frame	80
Figure 4.16 Spreader beam	80
Figure 4.17 Procedure of specimen fabrication	81
Figure 4.18 Typical rebar cage of Phase I testing.....	82
Figure 4.19 Assembled formwork prior to concrete placement	82
Figure 4.20 Aerial view of casting and testing area on the elevated slab at FSEL.....	84
Figure 4.21 The section of the bottom soffit formwork for V-13.....	84
Figure 4.22 The process of removing the bottom soffit for V-13.....	85
Figure 4.23 Moving reinforcement cage of V-13	85
Figure 4.24 Travelling of V-13 to test area.....	86
Figure 4.25 V-13 after setting up the loading test	86
Figure 4.26 Instrumentation map of II-7.....	87
Figure 4.27 ERSG attached on reinforcement to measure strains	87
Figure 4.28 Load cells in the support fixtures	88
Figure 4.29 Linear potentiometers to measure displacements on the bottom surface	88
Figure 4.30 Crack mapping at predefined loading stages.....	89
Figure 4.31 Dimension used for normalization of load and deflection	91
Figure 4.32 Details of the damage observed in Specimen I-1 after failure	95
Figure 4.33 Load-deflection responses of specimens: Series I.....	97
Figure 4.34 Strain distribution in bottom mat reinforcement at the ultimate load: Series I.....	98
Figure 4.35 Crack patterns on the bottom face under serviceability load	99
Figure 4.36 Crack maps: Series II.....	102

Figure 4.37 Typical cracking and damage pattern.....	103
Figure 4.38 Load-deflection responses of specimens: Series II	104
Figure 4.39 Strain distribution in bottom mat reinforcement at the ultimate load: Series II	105
Figure 4.40 Relationship between normalized ultimate loads and strut inclinations	106
Figure 4.41 Post-failure conditions near the failed drilled shaft.....	107
Figure 4.42 Post-failure conditions on top surface of III-9	107
Figure 4.43 Load-deflection responses of specimens: Series III	108
Figure 4.44 Strain distribution in bottom mat reinforcement at ultimate load: Series III	109
Figure 4.45 Relationship between normalized ultimate loads and shaft diameters and shaft area	110
Figure 4.46 Comparison of post-failure conditions on the side faces between specimens: Series IV	111
Figure 4.47 Post-failure conditions: IV-10	111
Figure 4.48 Comparison of post-failure conditions on the bottom face between specimens: Series IV	112
Figure 4.49 Load-deflection responses of specimens: Series IV	113
Figure 4.50 Strain distribution in bottom mat reinforcement at ultimate load: Series IV	114
Figure 4.51 Crack map of V-12	116
Figure 4.52 Post-failure conditions: V-13	116
Figure 4.53 Load-deflection response of specimens: Series V.....	117
Figure 4.54 Strain distribution in bottom mat reinforcement at ultimate load: Series V	118
Figure 4.55 Relationship between normalized ultimate loads and footing height.....	118
Figure 5.1 3D strut-and-tie model for drilled shaft footing where shafts are in non-uniform compression (isometric view: left / side views: right)	122
Figure 5.2 Dimension of specimen: Phase II	122
Figure 5.3 Typical hook orientation in a beam-column joint (left) and hook orientations planned for Phase II testing (right).....	123
Figure 5.4 Embedment lengths of TxDOT drilled shaft footing database and Phase II specimens	125
Figure 5.5 Eccentric loading test setup for Phase II testing.....	129

Figure 5.6 General test configuration for Phase II testing	130
Figure 5.7 Top mat reinforcement and column reinforcement	131
Figure 5.8 Procedure of column corbel fabrication	132
Figure 5.9 Lenton Terminators for headed bars.....	133
Figure 5.10 Linear potentiometers to measure relative displacement of column corbel	134
Figure 5.11 Polished longitudinal rib (left) and minimized protection area (right).....	134
Figure 5.12 Instrumentation map of Phase II specimens (VI-ST, VI-HD, VI-HKO)	135
Figure 5.13 Average bond stress acting between two adjacent strain measurement locations	138
Figure 5.14 Post-failure conditions of VI-ST	140
Figure 5.15 Post-failure condition of VI-HD.....	142
Figure 5.16 Post-failure condition of VI-HKO and VI-HKI	143
Figure 5.17 Cut sections of Phase II specimens	144
Figure 5.18 Internal cracks formed entire with of specimen (VI-ST)	145
Figure 5.19 Load-deflection responses of specimens: Phase II.....	146
Figure 5.20 Strain distribution in bottom mat reinforcement at ultimate load: Phase II.....	148
Figure 5.21 Stress profiles of column reinforcement.....	150
Figure 5.22 Bond stress profiles of column reinforcement.....	153
Figure 5.23 Compression field formed by diagonal struts and proposed critical section of column reinforcement.....	155
Figure 6.1 Comparison of 3D strut-and-tie models under original and equivalent loading scenario of Phase III testing.....	158
Figure 6.2 Dimension of specimen: Phase III.....	160
Figure 6.3 Reinforcing bar cage before cast concrete (left) and reinforcement detail to resist post-tensioning force (right)	161
Figure 6.4 Definition of pseudo-embedment length of drilled shaft reinforcement in a TxDOT footing plan	162
Figure 6.5 Pseudo-embedment lengths and drilled shaft reinforcement amount of TxDOT drilled shaft footing database	163
Figure 6.6 Bleeding occurred in batch #3 (left) and surface of the specimen after curing (right)	164

Figure 6.7 Coring work (left) and position of coring on the north face of the specimen (right).....	165
Figure 6.8 Test setup for planned equivalent loading of Phase III testing	167
Figure 6.9 Detail of connection between drilled shaft reinforcement and adopter plate	168
Figure 6.10 Mock-up test plan (left) and fracture of reinforcement after mock-up test (right).....	168
Figure 6.11 Type of anchorage detail for drilled shaft reinforcement.....	169
Figure 6.12 Instrumentation map of Phase III specimens.....	170
Figure 6.13 Welded hooked reinforcement to measure drilled shaft reinforcement slip.....	172
Figure 6.14 Instrumentation map of linear potentiometers for VII-TD-HD.....	173
Figure 6.15 Crack map of Phase III specimens after testing	178
Figure 6.16 Overall behavior of Phase III tests	180
Figure 6.17 Measured slips at anchorage ends of drilled shaft reinforcement	181
Figure 6.18 Stress profiles of drilled shaft reinforcement	182
Figure 6.19 Bond stress profiles of drilled shaft reinforcement	184
Figure 6.20 Assumed compression field and proposed critical section of drilled shaft reinforcement (equivalent Phase III loading condition)	186
Figure 6.21 Assumed compression field and proposed critical sections of column and drilled shaft reinforcement (original Phase III loading condition)	187
Figure 7.1 Dimension and details of test specimens (Suzuki et al. 1998)	190
Figure 7.2 Dimension and details of test specimens (Suzuki and Otsuki, 2002).....	191
Figure 7.3 Sample FE model of FE Validation Database (Suzuki and Otsuki, 2002).....	193
Figure 7.4 Two types of mesh size for mesh sensitivity analysis (BPB-35-25).....	194
Figure 7.5 Load-deflection responses of test specimens and FE models with 1 in. and 2 in. mesh size: Banded layout.....	195
Figure 7.6 Load-deflection responses of test specimens and FE models with 1 in. and 2 in. mesh size: Grid layout.....	196
Figure 7.7 FE mesh example for Phase I testing (II-7).....	199
Figure 7.8 Example of truss elements for reinforcement in FE models for Phase I testing.....	199

Figure 7.9 Example of boundary and loading conditions in FE models for Phase I testing.....	200
Figure 7.10 Comparison of measured and computed load-deflection plots	202
Figure 7.11 Experimentally measured versus computed post-failure crack patterns in IV-10.....	204
Figure 7.12 Experimentally measured versus computed post-failure crack patterns in II-5	205
Figure 7.13 Experimentally measured versus computed post-failure crack patterns in III-8.....	206
Figure 7.14 Experimentally measured versus computed post-failure crack patterns in II-7	207
Figure 7.15 Dimension (left) and reinforcing details (right) of the baseline model for numerical parametric study	209
Figure 7.16 Details of the FE model for numerical parametric study	209
Figure 7.17 Types of traverse side face reinforcement.....	211
Figure 7.18 Load-deflection plot (left) and plot of ultimate load versus aspect ratio of footing (right): Series ARF.....	214
Figure 7.19 Load-deflection plot (left) and plot of ultimate load versus aspect ratio of column (right): Series ARC.....	215
Figure 7.20 Load-deflection plot (left) and plot of ultimate load versus concrete compressive strength (right): Series CS	215
Figure 7.21 Load-deflection plot (left) and plot of ultimate load versus bottom mat reinforcement ratio (right): Series BM.....	216
Figure 7.22 Load-deflection plot (left) and plot of ultimate load versus top mat reinforcement ratio (right): Series TM.....	216
Figure 7.23 Load-deflection plot (left) and plot of peak load versus side face reinforcement ratio (right): Series SF.....	217
Figure 7.24 Load-deflection plot: Series SFT.....	218
Figure 7.25 Load-deflection plot (left) and plot of ultimate load versus strut inclination (right): Series SI.....	218
Figure 7.26 Load-deflection plot (left) and plot of ultimate load versus shaft diameter (right): Series SD.....	219
Figure 7.27 Load-deflection plot (left) and plot of ultimate load versus footing height (right): Series FH.....	219
Figure 7.28 FE mesh for Phase II testing.....	221
Figure 7.29 Truss elements for reinforcement in FE models for Phase II testing	222

Figure 7.30 Link element.....	223
Figure 7.31 Modeling strategy for anchorage types tested in Phase II.....	224
Figure 7.32 Boundary and loading conditions in FE models for Phase II testing	224
Figure 7.33 FE model validation with stress profiles (Phase II).....	225
Figure 7.34 Stress profiles of FE models (COL Series – Phase II)	230
Figure 7.35 Behavior of COL-2R modeled with hooked anchorage (COL-2R(HK))	232
Figure 7.36 Assumed critical section compared with required development lengths (COL Series – Phase II).....	233
Figure 7.37 Stress profiles of FE models (Series DSP – Phase II).....	234
Figure 7.38 Stress profiles of FE models with critical sections (Series DSP – Phase II).....	235
Figure 7.39 Stress profiles of FE models (DSD Series – Phase II)	235
Figure 7.40 FE mesh for Phase III testing (Equivalent loading condition)	238
Figure 7.41 Truss elements for reinforcement in FE models for Phase III testing (Equivalent loading condition)	239
Figure 7.42 Boundary and loading conditions in FE models for Phase III testing (Equivalent loading condition)	239
Figure 7.43 FE mesh for Phase III testing (Original loading condition)	240
Figure 7.44 Truss elements for reinforcement in the typical footing specimen (Original loading condition).....	241
Figure 7.45 Boundary and loading conditions in FE models for Phase III testing (Original loading condition)	241
Figure 7.46 FE model validation with stress profiles (Phase III – Equivalent & Original).....	243
Figure 7.47 Stress profiles of FE models (Series DSR – Phase III)	246
Figure 7.48 Assumed critical section compared with required development lengths (Series DSR – Phase III).....	247
Figure 7.49 Stress profiles of FE models (Series DSP – Phase III).....	247
Figure 7.50 Conservativeness of the proposed critical section of the drilled shaft reinforcement.....	248
Figure 8.1 Typical 3D strut-and-tie models for loading cases.....	252
Figure 8.2 Available development length of tie reinforcement	258
Figure 8.3 Histograms of attributes of the footing specimens in the evaluation database (N=60).....	263

Figure 8.4 Distribution of ultimate capacity ratios for the evaluation database	264
Figure 8.5 Comparison of experimental and predicted ultimate capacities	265
Figure 8.6 Comparison of experimental and predicted ultimate capacities controlled by bearing strength at node above drilled shafts	267
Figure 8.7 Flow chart to determine forces and position of struts and ties on the column section.....	271
Figure 8.8 3D Strut-and-tie model of drilled shaft footings under uniform compressive loading.....	273
Figure 8.9 The sectional views to define 3D nodal geometry (Phase I).....	274
Figure 8.10 Detail of 3D nodal geometries in drilled shaft footings (Phase I)	274
Figure 8.11 The sectional views to define 3D nodal geometry (Phase II).....	275
Figure 8.12 Detail of 3D nodal geometries in drilled shaft footings (Phase II).....	275
Figure 8.13 The sectional views to define 3D nodal geometry (Phase III)	276
Figure 8.14 Detail of 3D nodal geometries in drilled shaft footings (Phase III).....	276
Figure 8.15 Determination of notional area (AASHTO LRFD, 2020).....	277
Figure 8.16 Force system in a drilled shaft footing (Clarke, 1973).....	278
Figure 8.17 Proposed available length for anchorage of bottom mat reinforcement in drilled shaft footings	280
Figure 8.18 Proposed available length for anchorage of column reinforcement in drilled shaft footings (Phase II)	281
Figure 8.19 Proposed available lengths for anchorage of drilled shaft and column reinforcement in drilled shaft footings (Phase III)	282
Figure 8.20 Distribution of ultimate capacity ratios for the evaluation database	284
Figure 8.21 Geometry of the drilled shaft footing for the design example (Williams et al., 2012).....	290
Figure 8.22 Factored load: Load Case I.....	291
Figure 8.23 Factored load: Load Case II	292
Figure 8.24 Factored load: Load Case III	292
Figure 8.25 Factored load: Load Case IV	293
Figure 8.26 Factored load: Load Case V	294
Figure 8.27 Stress distribution over the column section: Load Case I	295

Figure 8.28 Applied loading and reaction forces: Load Case I	296
Figure 8.29 3D Strut-and-tie model in plan view: Load Case I.....	297
Figure 8.30 3D Strut-and-tie model in axonometric view: Load Case I.....	298
Figure 8.31 Resolving the force at Nodes A through D (CCC node)	300
Figure 8.32 Details of 3D nodal geometry at Nodes A through D	300
Figure 8.33 Determination of the confinement modification factor, m , for Nodes A through D	301
Figure 8.34 Details of 3D nodal geometry at Nodes E through H.....	303
Figure 8.35 Determination of the confinement modification factor, m , for Nodes E through H.....	304
Figure 8.36 Critical sections for the development of ties: Load Case I.....	306
Figure 8.37 Stress distribution over the column section: Load Case II.....	308
Figure 8.38 Applied loading and reaction forces: Load Case II.....	309
Figure 8.39 3D STM – plan view: Load Case II.....	310
Figure 8.40 3D Strut-and-tie model: Load Case II	310
Figure 8.41 Resolving the force at Nodes A and D (CCC node).....	312
Figure 8.42 Details of 3D nodal geometry at Nodes A and D	313
Figure 8.43 Resolving the force at Nodes B and C (CCC node)	314
Figure 8.44 Details of 3D nodal geometry at Nodes B and C	315
Figure 8.45 Details of 3D nodal geometry at Nodes E and H	317
Figure 8.46 Details of 3D nodal geometry at Nodes F and G.....	318
Figure 8.47 Critical sections for the development of ties: Load Case II	320
Figure 8.48 Stress distribution over the column section: Load Case III.....	322
Figure 8.49 Applied loading and reaction forces: Load Case III.....	323
Figure 8.50 3D STM – plan view: Load Case III	324
Figure 8.51 3D Strut-and-tie model: Load Case III.....	324
Figure 8.52 Resolving the force at Nodes A and D (CCC node).....	326
Figure 8.53 Details of 3D nodal geometry at Nodes A and D.....	327
Figure 8.54 Determination of the confinement modification factor, m , for Nodes A and D	328
Figure 8.55 Details of 3D nodal geometry at Nodes E and H	330
Figure 8.56 Details of 3D nodal geometry at Nodes F and G.....	331
Figure 8.57 Critical sections for the development of ties: Load Case III	333

Figure 8.58 Critical section for the development of column ties.....	335
Figure 8.59 Stress distribution over the column section: Load Case IV	336
Figure 8.60 Applied loading and reaction forces: Load Case IV	337
Figure 8.61 3D STM – plan view: Load Case IV	338
Figure 8.62 3D Strut-and-tie model: Load Case IV.....	338
Figure 8.63 Resolving the force at Nodes A and D (CCC node).....	342
Figure 8.64 Details of 3D nodal geometry at Nodes A and D.....	342
Figure 8.65 Determination of the confinement modification factor, m, for Nodes A and D.....	343
Figure 8.66 Details of 3D nodal geometry at Nodes E and H	345
Figure 8.67 Critical sections for the development of ties: Load Case IV.....	347
Figure 8.68 Critical section for the development of column ties and drilled shaft ties.....	348
Figure 8.69 Stress distribution over the column section: Load Case V.....	350
Figure 8.70 Positions of the subdivided loads in the equivalent force system: Load Case V.....	351
Figure 8.71 Applied loading and reaction forces: Load Case V.....	352
Figure 8.72 Strut-and-tie model – plan view: Load Case V	353
Figure 8.73 3D strut-and-tie model: Load Case V.....	353
Figure 8.74 Resolving the force at Node A (CCC node).....	355
Figure 8.75 Details of 3D nodal geometry at Node A	356
Figure 8.76 Details of 3D nodal geometry at Node E.....	358
Figure 8.77 Critical sections for the development of ties: Load Case V	361
Figure 8.78 Reinforcement details for anchorage of vertical ties.....	362
Figure 8.79 Reinforcement details for ties: elevation view	363
Figure 8.80 Reinforcement details for shrinkage and temperature reinforcement: elevation view	363
Figure 8.81 Reinforcement details for bottom mat reinforcement: plan view	364
Figure 8.82 Reinforcement details for top mat reinforcement: plan view	365
Figure D.1 Drawing of I-1: Phase I	400
Figure D.2 Drawing of I-2: Phase I	401
Figure D.3 Drawing of I-3: Phase I	402

Figure D.4 Drawing of I-4: Phase I	403
Figure D.5 Drawing of II-5: Phase I.....	404
Figure D.6 Drawing of II-6: Phase I.....	405
Figure D.7 Drawing of II-7: Phase I.....	406
Figure D.8 Drawing of III-8: Phase I.....	407
Figure D.9 Drawing of III-9: Phase I.....	408
Figure D.10 Drawing of IV-10: Phase I.....	409
Figure D.11 Drawing of IV-11: Phase I.....	410
Figure D.12 Drawing of V-12: Phase I.....	411
Figure D.13 Drawing of V-13: Phase I.....	412
Figure D.14 Drawing of VI-ST (bottom mat & side face reinforcement): Phase II.....	413
Figure D.15 Drawing of VI-ST (top mat & column reinforcement): Phase II	414
Figure D.16 Drawing of VI-HD (bottom mat & side face reinforcement): Phase II.....	415
Figure D.17 Drawing of VI-HD (top mat & column reinforcement): Phase II	416
Figure D.18 Drawing of VI-HKO (bottom mat & side face reinforcement): Phase II.....	417
Figure D.19 Drawing of VI-HKO (top mat & column reinforcement): Phase II.....	418
Figure D.20 Drawing of VI-HKI (bottom mat & side face reinforcement): Phase II.....	419
Figure D.21 Drawing of VI-HKI (top mat & column reinforcement): Phase II.....	420
Figure D.22 Drawing of VII-TD (bottom mat & side face reinforcement): Phase III.....	421
Figure D.23 Drawing of VII-TD (top mat & anti-burst & drilled shaft reinforcement): Phase III.....	422
Figure D.24 Drawing of VII-TK (bottom mat & side face reinforcement): Phase III.....	423
Figure D.25 Drawing of VII-TK (top mat & anti-burst & drilled shaft reinforcement): Phase III.....	424
Figure F.1 Plot of the applied load versus the measured deflection: I-1	427
Figure F.2 Stress distribution in main reinforcements at ultimate load: I-1	427

Figure F.3 Post-failure crack map: I-1	428
Figure F.4 Plot of the applied load versus the measured deflection: I-2	429
Figure F.5 Stress distribution in main reinforcements at ultimate load: I-2	429
Figure F.6 Post-failure crack map: I-2	430
Figure F.7 Plot of the applied load versus the measured deflection: I-3	431
Figure F.8 Stress distribution in main reinforcements at ultimate load: I-3	431
Figure F.9 Post-failure crack map: I-3	432
Figure F.10 Plot of the applied load versus the measured deflection: I-4	433
Figure F.11 Stress distribution in main reinforcements at ultimate load: I-4	433
Figure F.12 Post-failure crack map: I-4	434
Figure F.13 Plot of the applied load versus the measured deflection: II-5	435
Figure F.14 Stress distribution in main reinforcements at ultimate load: II-5	435
Figure F.15 Post-failure crack map: II-5	436
Figure F.16 Plot of the applied load versus the measured deflection: II-6	437
Figure F.17 Stress distribution in main reinforcements at ultimate load: II-6	437
Figure F.18 Post-failure crack map: II-6	438
Figure F.19 Plot of the applied load versus the measured deflection: II-7	439
Figure F.20 Stress distribution in main reinforcements at ultimate load: II-7	439
Figure F.21 Post-failure crack map: II-7	440
Figure F.22 Plot of the applied load versus the measured deflection: III-8	441
Figure F.23 Stress distribution in main reinforcements at ultimate load: III-8	441
Figure F.24 Post-failure crack map: III-8	442
Figure F.25 Plot of the applied load versus the measured deflection: III-9	443
Figure F.26 Stress distribution in main reinforcements at ultimate load: III-9	443
Figure F.27 Post-failure crack map: III-9	444
Figure F.28 Plot of the applied load versus the measured deflection: IV-10	445
Figure F.29 Stress distribution in main reinforcements at ultimate load: IV-10	445
Figure F.30 Post-failure crack map: IV-10	446

Figure F.31 Plot of the applied load versus the measured deflection: IV-11	447
Figure F.32 Stress distribution in main reinforcements at ultimate load: IV-11	447
Figure F.33 Post-failure crack map: IV-11	448
Figure F.34 Plot of the applied load versus the measured deflection: V-12.....	449
Figure F.35 Stress distribution in main reinforcements at ultimate load: V- 12.....	449
Figure F.36 Post-failure crack map: V-12	450
Figure F.37 Plot of the applied load versus the measured deflection: V-13.....	451
Figure F.38 Stress distribution in main reinforcements at ultimate load: V- 13.....	451
Figure F.39 Post-failure crack map: V-13	452
Figure G.1 Dimension of a drilled shaft footing for 3D STM calculation	453
Figure I.1 Position and reaction for the equivalent force system	464
Figure I.2 Geometric details of the equivalent force system	465
Figure I.3 3D strut-and-tie model based on the coordinates of nodes A and C	466

List of Terms

COV	coefficient of variation
ERSG	electrical resistance strain gauge
FE	finite element
FEA	finite element analysis
MCFT	modified compression field theory
PC	prestressed concrete
RC	reinforced concrete
STM	strut-and-tie method
2D	two-dimensional
3D	three-dimensional

Chapter 1. Introduction

1.1. Background

Provisions for the design implementation of the strut-and-tie method (STM) were introduced within the AASHTO LRFD Bridge Design Specifications (AASHTO LRFD) in 1994. Strut-and-tie modeling was intended to provide more realistic strength and detailing requirements for deep structural members subjected to nonlinear distributions of strain (also known as D-regions). Drilled shaft footings can be generally classified as D-regions and accordingly the use of STM is recommended for their design. Footings sitting on four (or more) drilled shafts will present three-dimensional (3D) behavior. However, current STM provisions were formulated based on research on deep structural members presenting a planar two-dimensional (2D) response, and there are no experimentally verified design guidelines for designing with the 3D STM. The lack of specific guidance results in a variation of the geometric proportions and reinforcement details used in drilled shaft footings in the field. Even though the limitations and shortcomings of legacy design methods (sectional models for flexure, one- and two-way shear) in the application of drilled shaft footing design are acknowledged, designers are reluctant to incorporate STM-based methods into the routine design of drilled shaft footings due to its 3D structure. Furthermore, detailing of the reinforcement exacerbated their concern. Figure 1.1 presents the reinforcement detail of the footing designed based on AASHTO LRFD STM provisions. Here, 180-degree hooks were utilized for terminating nearly all of the reinforcement to compensate for assumptions made during design. This approach resulted in an extremely congested reinforcement cage that was undoubtedly difficult and expensive to fabricate.



Figure 1.1 Congested reinforcement cage (footing construction at US-281 and Loop 1604 interchange)

TxDOT Project 0-5253, *Strength and Serviceability Design of Reinforced Concrete Deep Beams*, resulted in significant improvements to the application of STM to the design of planar (i.e., 2D) concrete structures. The results of TxDOT Project 0-5253, completed at The University of Texas at Austin (UT Austin), were adopted into ASHTO LRFD (2016 Interim). Furthermore, TxDOT Project 5-5253-01, *Strut-and-Tie Model Design Examples for Bridges*, also conducted by UT Austin, provided a design example of a drilled shaft footing based on the outcomes of TxDOT Project 0-5253 but with no experimental verification. Therefore, experimental research needs have been identified regarding the application of 3D strut-and-tie models to design drilled shaft footings, and the research presented in this report was designed to meet those needs.

1.2. Project Objective and Scope

The primary objective of this research is to refine the 2D STM provisions of TxDOT Project 0-5253 and establish 3D STM guidelines for drilled shaft footings. The refinement will reduce the ambiguity associated with the application of strut-and-tie modeling to drilled shaft footings. A comprehensive research program was conducted in this study, including large-scale experiments and numerical analyses of drilled shaft footings. The data and insights gathered during the project were used to establish 3D STM guidelines for drilled shaft footings. Using the newly-proposed guidelines, a design example was developed using the same drilled shaft footing as in TxDOT Project 5-5253-01. The guidelines were also used to draft a set of recommended revisions to the most recent edition of AASHTO LRFD (2020).

1.3. Organization

This research project was organized in a series of tasks including bibliographical, experimental, and analytical work. Each chapter of this report presents the results and main findings obtained from each of these tasks. Chapter 2 presents the main findings of a literature review on international provisions on 2D STM and previous research on the behavior of drilled shaft footings. In Chapter 3, drawings of the drilled shaft footings designed and constructed by TxDOT in Texas are reviewed to determine design parameters of the experimental program of this research. Chapter 4 through Chapter 6 describes and discuss the main findings of the experimental program. The experimental program comprises large-scale structural testing of drilled shaft footings subjected to various loading conditions; therefore, the program was subdivided into three phases corresponding to different loading scenarios. Each testing phase is presented in a different chapter. The first loading condition is uniaxial compression (Chapter 4), which results in uniform compression in the drilled shafts. The second loading condition is a combination of uniaxial compression and moderate uniaxial bending (Chapter 5). The moderate bending moment induces tension at one face of the column and non-uniform compression in the drilled shafts. The last loading condition is a combination of uniaxial compression and severe uniaxial bending (Chapter 6). The severe bending moment results in tension not only at one face of the column, but also at two of the four drilled shafts. In Chapter 7, results obtained from numerical parametric studies performed with additional design parameters that could not be covered in the experimental program are presented and discussed to supplement the test data. Based on the results and insights obtained from the previous chapters, Chapter 8 provides new 3D STM guidelines for design and detailing of drilled shaft footings, along with design examples. Lastly, Chapter 9 summarizes the main findings and conclusions of this research.

Chapter 2. Literature Review

2.1. Overview

In this chapter, precedent research relevant to drilled shaft footings, and the strut-and-tie modeling, and pertinent specifications and design guides are identified and summarized. Additionally, based on this literature review, the research team has compiled an experimental database of previous tests on drilled shaft footings. The findings from this literature review proved valuable to both the experimental (Chapter 4 through Chapter 6) and analytical (Chapter 7) programs.

This chapter is organized as follows. The first section examines current STM provisions, both domestic and international. The following sections will summarize key academic research investigating drilled shaft footings through design examples applying existing STM provisions to footing design, experimental testing, and proposed strut-and-tie models for different loading scenarios. After that, a section for finite element analysis (FEA) research to investigate nonlinear behavior and propose innovative strut-and-tie models of the footings will be followed. Finally, a summary of conclusions from this literature review will be presented.

2.2. Current STM Specifications

Although modern specifications addressing strut-and-tie modeling, which have largely been formulated based on research of 2D deep beams, are also conservative for 3D structures like drilled shaft footings, updating and adapting their stress limits for 3D structures could mitigate some over-conservatism. Some previous research suggested innovative strut-and-tie models for the footings by assuming specific nodal geometries, and they adopted stress limits from existing STM specifications to check stresses (Klein, 2002; Mitchell et al., 2004; Araújo, 2016; Mathern et al., 2017). Thus, it is important to review the current STM specifications.

The specifications considered include ACI 318-19 (2019), AASHTO LRFD Bridge Design Specifications (2020) (AASHTO LRFD (2020)), Canadian Highway Bridge Design Code (CSA A23.3-14) (2014), Eurocode 2 (2004), and fib Model Code 2010 (2013). The specified strengths of nodes, specified strengths for struts, and appropriate crack control reinforcement of each specification are outlined in Table 2.1, Table 2.3, and Table 2.5, respectively. Table 2.2, Table 2.4, and Table 2.6 give the definitions of the variables for each of the specifications.

Table 2.1 Nodal strength comparison for each specification

Specification		CCC	CCT	CTT
ACI 318-19		$0.85(1.00)\beta_c f'_c = 0.85\beta_c f'_c$ [§23.9.2]	$0.85(0.80)\beta_c f'_c = 0.68\beta_c f'_c$ [§23.9.2]	$0.85(0.60)\beta_c f'_c = 0.51\beta_c f'_c$ [§23.9.2]
		$\beta_c = \sqrt{A_2/A_1} \leq 2.0$ (Node includes a bearing surface) $\beta_c = 1.0$ (Other cases) [§23.4.3(b)] Increased stress is permitted if confining reinforcement is provided within the nodal zone and its effect is documented by tests and analyses [§23.9.3]		
AASHTO LRFD (2020)	Bearing Face	$0.85mf'_c$ [§5.8.2.5.3]	$0.70mf'_c$ [§5.8.2.5.3]	$\left(0.85 - \frac{f'_c}{20\text{ksi}}\right)mf'_c$ $0.45 \leq 0.85 - \frac{f'_c}{20\text{ksi}} \leq 0.65$ [§5.8.2.5.3]
	Back Face			
	Strut-Node Interface	$\left(0.85 - \frac{f'_c}{20\text{ksi}}\right)mf'_c$ $0.45 \leq 0.85 - \frac{f'_c}{20\text{ksi}} \leq 0.65$ [§5.8.2.5.3]	$\left(0.85 - \frac{f'_c}{20\text{ksi}}\right)mf'_c$ $0.45 \leq 0.85 - \frac{f'_c}{20\text{ksi}} \leq 0.65$ [§5.8.2.5.3]	

Table 2.1 (cont'd) Nodal strength comparison for each specification

Specification		CCC	CCT	CTT
	w/o crack control reinforcement		$0.45mf'_c$ [§5.8.2.5.3]	
			$m = \sqrt{A_2/A_1} \leq 2.0$ [§5.8.2.5.3]	
CSA A23.3-14		$0.85mf'_c$ [§11.4.4.1]	$0.75mf'_c$ [§11.4.4.1]	$0.65mf'_c$ [§11.4.4.1]
			$m = \sqrt{A_2/A_1} \leq 2.0$ [§10.8.1]	
Eurocode 2		$(1.00) \left(1 - \frac{f_{ck}}{250 \text{ MPa}}\right) f_{cd}$ If all three directions of the struts and the distribution of load is known, $f_{ck,c} \leq (3.00) \left(1 - \frac{f_{ck}}{250 \text{ MPa}}\right) f_{ck}$ [§6.5.4 and 3.1.9]	$(0.85) \left(1 - \frac{f_{ck}}{250 \text{ MPa}}\right) f_{cd}$ [§6.5.4]	$(0.75) \left(1 - \frac{f_{ck}}{250 \text{ MPa}}\right) f_{cd}$ [§6.5.4]
		The design compressive stress values can be increased up to 10% when:		

Table 2.1 (cont'd) Nodal strength comparison for each specification

Specification	CCC	CCT	CTT
	<ul style="list-style-type: none"> - triaxial compression is assured, - all angles between struts and ties are $\geq 55^\circ$, - the stresses applied at supports or at point loads are uniform, and the node is confined by stirrups, 	<ul style="list-style-type: none"> - the reinforcement is arranged in multiple layers, - the node is reliably confined by means of bearing arrangement or friction. 	[§6.5.4]
fib Model Code 2010	$\eta_{fc} = \left(\frac{30\text{MPa}}{f_{ck}} \right)^{\frac{1}{3}} \leq 1.00$ Under significant biaxial compression; $1.1\eta_{fc}f_{cd}$ Under triaxial compression; $\sqrt{A_{c1}/A_{c0}}f_{cd} \leq 3.0f_{cd}$ [§7.3.6.4 and 7.2.3.1.7]	$\eta_{fc} = \left(\frac{30\text{MPa}}{f_{ck}} \right)^{\frac{1}{3}} \leq 1.00$ [§7.3.6.4]	$\eta_{fc} = \left(\frac{30\text{MPa}}{f_{ck}} \right)^{\frac{1}{3}} \leq 1.00$ [§7.3.6.4]

Table 2.2 Variables referenced in Table 2.1

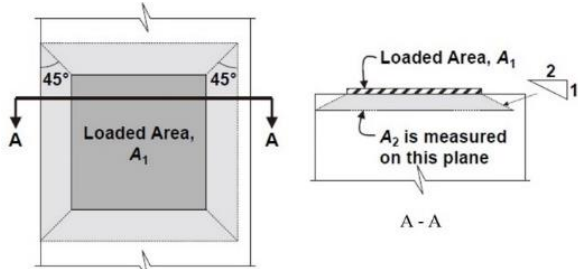
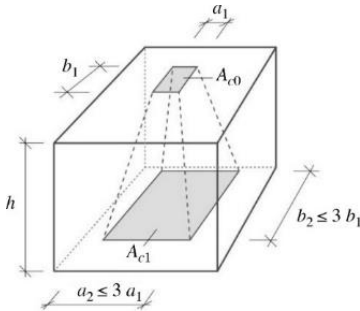
Specification	Description	
<p>ACI 318-19</p>	<p>A_1 : loaded area [in.²] A_2 : notional area for determination of β_c factor [in.²] f'_c : concrete compressive strength [ksi] β_c : confinement factor</p>	 <p style="text-align: center;">*Determination of A_2</p>
<p>AASHTO LRFD (2020)</p>	<p>A_1 : loaded area [in.²] A_2 : notional area for determination of m factor [in.²] f'_c : concrete compressive strength [ksi] m : confinement factor</p>	
<p>CSA A23.3-14</p>	<p>A_1 : loaded area [mm²] A_2 : notional area for determination of m factor [mm²] f'_c : concrete compressive strength [MPa] m : confinement factor</p>	
<p>Eurocode 2</p>	<p>f_{ck} : concrete compressive strength [MPa] $f_{ck,c}$: confined concrete compressive strength [MPa]</p> $f_{ck,c} = f_{ck}(1.000 + 5.0\sigma_2/f_{ck}) \quad \text{for } \sigma_2 \leq 0.05f_{ck}$ $f_{ck,c} = f_{ck}(1.125 + 2.5\sigma_2/f_{ck}) \quad \text{for } \sigma_2 > 0.05f_{ck}$ <p>σ_2 : effective lateral compressive stress due to confinement ($=\sigma_3$) [MPa]</p>	
<p>fib Model Code 2010</p>	<p>A_{c0} : loaded area [mm²] A_{c1} : maximum design distribution area with a similar shape to A_{c0} [mm²] f_{ck} : characteristic concrete compressive strength [MPa] η_{fc} : factor considering the effect of more brittle failure behavior of concrete of strengths greater than 30 MPa</p>	 <p style="text-align: center;">*Determination of A_{c1}</p>

Table 2.3 Strut strength comparison for each specification

Specification	Description	
ACI 318-19	For boundary struts,	$0.85(1.00)\beta_c f'_c = 0.85\beta_c f'_c$
	For interior struts 1. with satisfying minimum crack control reinforcement ratio 2. formed in sections of large dimensions enough to preclude diagonal tension failure 3. formed in beam-column joints	$0.85(0.75)\beta_c f'_c = 0.64\beta_c f'_c$
	Struts in tension members,	$0.85(0.40)\beta_c f'_c = 0.34\beta_c f'_c$
	For interior struts without crack control reinforcement but laterally restrained (drilled shaft footings)	
	All other cases,	
	[§23.4.3]	
AASHTO LRFD (2020)	N/A	
CSA A23.3-14	$\frac{1}{0.8 + 170\varepsilon_1} f'_c \leq 0.85f'_c$ $\varepsilon_1 = \varepsilon_s + (\varepsilon_s + 0.002) \cot^2 \theta_s$ <p>if the specified yield strength of the reinforcing steel < 400 MPa: $\frac{1}{1.14 + 0.68 \cot^2 \theta_s} f'_c \leq 0.85f'_c$</p> [§11.4.2.3]	
Eurocode 2	For concrete struts in a region with transverse compressive stress or no transverse stress,	f_{ck}
	For concrete struts in cracked compression zones,	$(0.60) \left(1 - \frac{f_{ck}}{250 \text{ MPa}}\right) f_{ck}$
	[§7.3.3]	

Table 2.3 (cont'd) Strut strength comparison for each specification

Specification	Description	
fib Model Code 2010	For undisturbed uniaxial compression states and for regions with transverse compression;	$1.0\eta_{fc}f_{ck}$
	For struts with cracks parallel to the direction of compression and tension reinforcement perpendicular to this;	$0.75\eta_{fc}f_{ck}$
	For struts with reinforcement running obliquely (with angles smaller than 65°) to the direction of compression;	$0.55\eta_{fc}f_{ck}$
	$\eta_{fc} = \left(\frac{30\text{MPa}}{f_{ck}}\right)^{\frac{1}{3}} \leq 1.00$	
	[§7.3.6.2]	

Table 2.4 Variables referenced in Table 2.3

Specification	Description
ACI 318-19	f'_c : concrete compressive strength [ksi] β_c : confinement factor
CSA A23.3-14	f'_c : concrete compressive strength [MPa] ε_s : tensile strain in the tie inclined at θ_s to the strut [mm/mm] θ_s : smallest angle between the strut and the adjoining ties [DEG.]
Eurocode 2	f_{ck} : characteristic concrete compressive strength [MPa]
fib Model Code 2010	f_{ck} : characteristic concrete compressive strength [MPa] η_{fc} : factor considering the effect of more brittle failure behavior of concrete of strengths greater than 30 MPa

Table 2.5 Crack control reinforcement comparison for each specification

Specification	Description
ACI 318-19	<p>Minimum distributed reinforcement ratio in each direction (orthogonal grid): 0.0025 in each direction</p> <p>Minimum distributed reinforcement ratio in one direction crossing strut at angle α_i: $0.0025/\sin^2 \alpha_i$ [§23.5.1]</p> <p>The ratio of deformed shrinkage and temperature reinforcement are to gross concrete area shall be greater than or equal to 0.0018 [§24.4.3.2]</p>
AASHTO LRFD (2020)	$\frac{A_v}{b_w s_l} \geq 0.003 \quad \& \quad \frac{A_h}{b_w s_v} \geq 0.003$ <p>Crack control reinforcement shall be distributed evenly near the side faces of the strut in each direction (longitudinal & vertical direction) [§5.8.2.6]</p> <p>Reinforcement for shrinkage and temperature stresses shall be provided near surfaces of concrete, and its ratio shall be at least 0.0018 (when $f_y=60$ ksi). This amount of reinforcement should be distributed uniformly around the perimeter of the component. [§5.10.6]</p>
CSA A23.3-14	<p>The ratio of crack control reinforcement area to gross concrete area shall not be less than 0.002 in each direction (longitudinal & vertical direction) The spacing of this reinforcement shall not exceed 300mm. [§11.4.5]</p> <p>For reinforced members with an overall depth exceeding 750mm, longitudinal skin reinforcement shall be uniformly distributed along the exposed side faces of the member. The total area of such reinforcement shall be $\rho_{sk} A_{cs}$. $\rho_{sk} = 0.008$ (interior exposure) $\rho_{sk} = 0.010$ (exterior exposure) [§10.6.2]</p>
Eurocode 2	<p>No guidance within the STM section</p> <p>Minimum reinforcement guidance for crack control in the deep elements (web depth ≥ 800mm) is given. $A_{s,min} = k_c k_{ct,eff} \frac{A_{ct}}{\sigma_s}$</p> <p>The crack control reinforcement should be provided with additional skin reinforcement, but its direction is not given. [§7.3.2]</p>

Table 2.5 (cont'd) Crack control reinforcement comparison for each specification

Specification	Description
fib Model Code 2010	<p>No guidance within the STM section</p> <p>Minimum reinforcement guidance for crack control in the fiber reinforced deep elements (web depth $\geq 800\text{mm}$) under bending is given. (Has a similar form to that of Eurocode 2 and CEP-FIP Model Code 1990)</p> $A_{s,min} = k_c k (f_{ctm} - f_{Ftsm}) \frac{A_{ct}}{\sigma_s}$ <p>[§7.7.4.3]</p>

Table 2.6 Variables referenced in Table 2.5

Specification	Description
ACI 318-19	α_i : angle between the i -th reinforcement and the axis of the strut [DEG.]
AASHTO LRFD (2020)	A_l : total area of longitudinal crack control reinforcement within spacing s_h [in. ²] A_v : total area of vertical crack control reinforcement within spacing s_v [in. ²] b_s : width of member's web [in.] f_y : specified yield strength of crack control reinforcing bars [ksi] s_l : spacing of longitudinal crack control reinforcement [in.] s_v : spacing of vertical crack control reinforcement [in.]
CSA A23.3-14	A_{cs} : sum of the area of concrete in strips [mm ²] ρ_{sk} : skin reinforcement ratio
Eurocode 2	$A_{s,min}$: minimum area of reinforcing steel within tensile zone [mm ²] A_{ct} : area of concrete within tensile zone [mm ²] $f_{ct,eff}$: effective tensile strength of concrete when first cracking occurs [MPa] k : coefficient which takes account of member depth Eurocode : ($k = 0.65$ when a member depth ≥ 800 mm / $k = 0.50$ when a member depth ≥ 1000 mm) k_c : coefficient which takes account of scheme of tensile stress distribution (For pure tension, $k_c = 1.0$) σ_s : maximum reinforcement stress after cracking (assumed to be specified yield strength in general) [MPa]
fib Model Code 2010	$A_{s,min}$: minimum area of reinforcing steel within tensile zone [mm ²] A_{ct} : area of concrete within tensile zone [mm ²] f_{ctm} : average tensile strength of concrete when first cracking occurs [MPa] f_{Ftsm} : average residual strength of fiber reinforced concrete [MPa] (assumed to be 0 in reinforced concrete) k : coefficient which takes account of member depth ($k = 0.65$ when a member depth ≥ 800 mm) k_c : coefficient which takes account of stress distribution in the cross-section just before cracking and the change of the inner lever arm (For rectangular cross-sections, $k_c = 1.0$) σ_s : maximum reinforcement stress after cracking (assumed to be specified yield strength in general) [MPa]

2.2.1. Nodal Strength Comparison

Each of the considered specifications dictate nodal strengths as the product of concrete strength and an efficiency factor. The efficiency factor differs based on the type of node in question, and there are three types of nodes: CCC (nodes bounded by compression struts only), CCT (nodes anchoring one tension tie), and CTT (nodes anchoring two or more tension ties in multiple directions). Essentially, the efficiency factor decreases as the number of ties anchored to the node increases.

In lieu of actually checking strut capacities, AASHTO LRFD (2020) performs stress checks on each face of the node. Additionally, AASHTO LRFD (2020) is the only specification that downgrades nodal strength when adequate crack control reinforcement is not provided. Instead, the other specifications downgrade strut strengths. The brittle behavior of high strength concrete is considered in the efficiency factors of all specifications except ACI 318-19 (2019). In AASHTO LRFD (2020) and CSA A23.3-14 (2014), this reduction in strength is factored into CCC and CCT bearing and back face strengths.

All specifications permit a strength increase for nodes with triaxial confinement due to surrounding concrete through an additional coefficient that increases nodal strengths. Eurocode 2 (2004) and the fib Model Code 2010 (2013) permit a triaxial confinement increase at CCC nodes only; however, ACI 318-19 (2019), AASHTO LRFD (2020), and CSA A23.3-14 (2014) permit the coefficients in all types of nodes. Eurocode 2 (2004) permits strength increases of 10% for all types of nodes if a node satisfies one of the specified conditions shown in Table 2.1.

2.2.2. Strut Strength Comparison

Except for AASHTO LRFD (2020), all specifications provide the strength of struts in addition to the nodal strengths. Only CSA A23.3-14 specifies the strut efficiency factor as a direct function of the magnitude and direction of tensile strains within the strut. The other specifications' strut efficiency factors vary depending on strut location (boundary or interior), the type and strength of concrete, whether the concrete is in a cracked or uncracked region, and whether or not adequate crack control reinforcement is provided. ACI 318-19 (2019) recognizes that interior struts of drilled shaft footing are laterally restrained by surrounding concrete. However, ACI 318-19 (2019) specifies that the strut efficiency factor for designing a drilled shaft footing shall be conservatively the minimum value ($\beta_s = 0.40$) since the crack control reinforcement requirements are difficult to be applied to the interior struts of drilled shaft footings.

2.2.3. Crack Control Reinforcement Comparison

ACI 318-19 (2019), AASHTO LRFD (2020), and CSA A23.3-14 (2014) all specify a minimum crack control reinforcement ratio for 2D strut-and-tie design, and these amounts are based on strut widths and should cross the strut axis for preventing premature splitting failure of the strut. In drilled shaft footings, it is difficult to estimate the required amount of crack control reinforcement due to indefinite strut widths in their strut-and-tie models. Furthermore, distributing crack control reinforcement around the strut axis of a 3D strut-and-tie model is also impractical.

No required distributed reinforcement for laterally restrained struts of ACI 318-19 (2019) reflects this point of view. This specification implies that the concrete surrounding struts of drilled shaft footing is equivalent to the specified minimum crack control reinforcement; however, providing adequate crack control reinforcement is still significant for STM due to serviceability.

2.3. Previous Research Review

This report reviewed previous research on drilled shaft footings under different loading conditions. For the simple loading condition results in uniform compression in drilled shafts, previous researchers investigated the behavior of drilled shaft footings by various research approaches: conducting structural testing and proposing design examples or innovative strut-and-tie modeling methods. The research team compiled an experimental database of previous tests on drilled shaft footing, and the database is provided in Appendix B. However, limited research could be conducted for the complex loading conditions inducing tension in column reinforcement or shaft reinforcement since no experimental research was planned for those loading conditions due to their complexity. The following sections organize the previous research based on the research approaches of respective loading condition.

Additionally, ample research on drilled shaft footings using FEA has been conducted in recent years, primarily making use of specialized nonlinear techniques. Some research has developed drilled shaft footing finite element models chiefly to observe nonlinear behavior; however, most took advantage of FEA specifically to obtain optimized strut-and-tie models or to propose innovative strut-and-tie methodologies. Therefore, FEA-related previous research is summarized separately from the following sections of the loading conditions.

2.3.1. Previous Research on Uniform Compressions in Drilled Shafts

2.3.1.1. Design Examples

Klein (2002)

The American Concrete Institute's Special Publication ACI SP-208 provides several design examples for the use of strut-and-tie models in accordance with ACI 318-02 (2002). In ACI SP-208, Klein (2002) provided examples for a drilled shaft footing supported by five drilled shafts under simple loading conditions.

Klein (2002) provided two examples for the use of strut-and-tie models in the design of the footing. One of them is a compression-only case. Since one of five drilled shafts is positioned on the axis of the column, the developed strut-and-tie model is the same as that of a drilled shaft footing supported by four drilled shafts, except for one vertical strut extending directly from the column to the center drilled shaft. This example defined nodal geometries of both top and bottom nodes on the basis of a required diagonal strut area computed from the strut force divided by a strut efficiency factor. The calculated strut was assumed to have a rectangular shape, and the geometries of both top and bottom nodes were obtained from the same strut area (Figure 2.1).

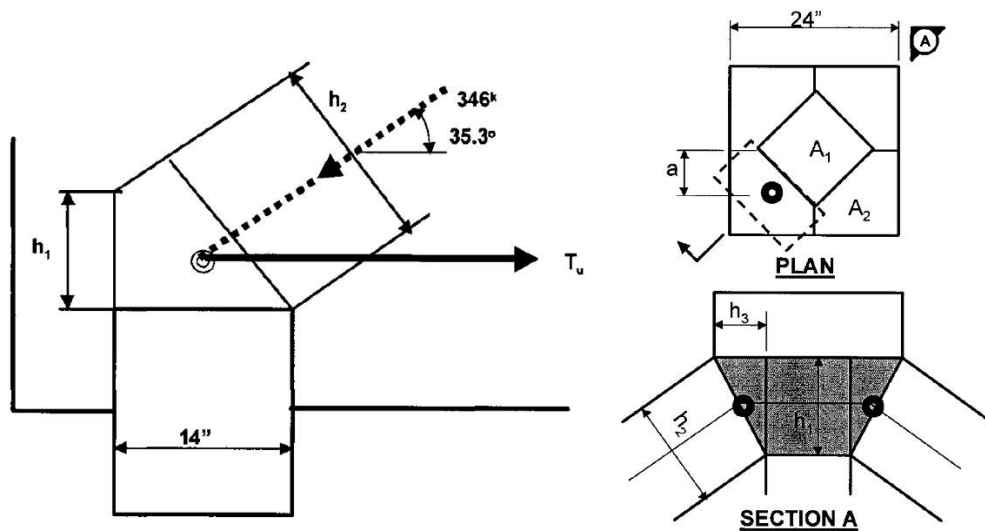


Figure 2.1 Assumed geometries of bottom node (left) and top node (right) (Klein, 2002)

Mitchell, Collins, Bhide, and Rabbat (2004)

Mitchell et al.(2004) developed a strut-and-tie model for drilled shaft footings subjected to axial compression only and provided a design procedure based on AASHTO LRFD Bridge Design Specifications (2004) (AASHTO LRFD (2004)). The developed model has top nodes that are assumed to be 2 in. below the top surface of the footing; these allow for the dimensions of the struts beneath the column. The strength of the bottom nodal zone was checked on the basis of AASHTO LRFD (2004). They approximately defined a 3D bottom nodal geometry (Figure 2.2), which also facilitated the definition of strut geometry and a check on strut strength. The anchorage length of bottom tie reinforcement was considered, as was proportioning the crack control reinforcement; however, it was provided only along the bottom surface of the footing.

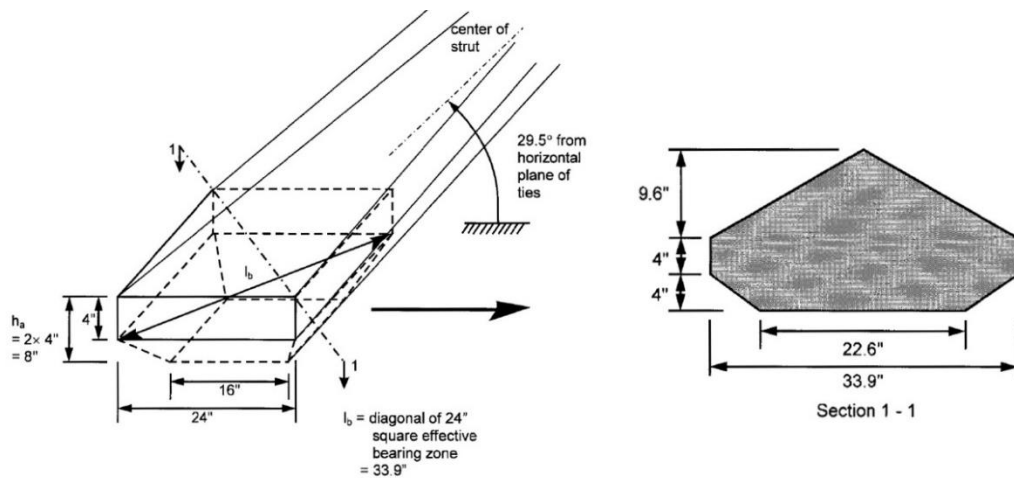


Figure 2.2 Assumed 3D nodal geometry (Mitchell et al., 2004)

2.3.1.2. Experimental Research

Blevot and Frémy (1967)

This work represents the first known experimental testing of drilled shaft footings supported by three or four drilled shafts found in the literature. Over a period of six years, Blevot and Frémy (1967) tested in direct compression 59 drilled shaft footings that had four drilled shafts, 45 drilled shaft footings that had three drilled shafts, and 12 drilled shaft footings that had two drilled shafts, nearly all of them at reduced scale. To give a sense for specimen size, the typical reduced-scale dimensions of the drilled shaft footing with four drilled shafts were approximately 24-in. x 24-in. x 12-in. A typical tested specimen is shown in Figure 2.3. Note that all their footings had tapered top surfaces.

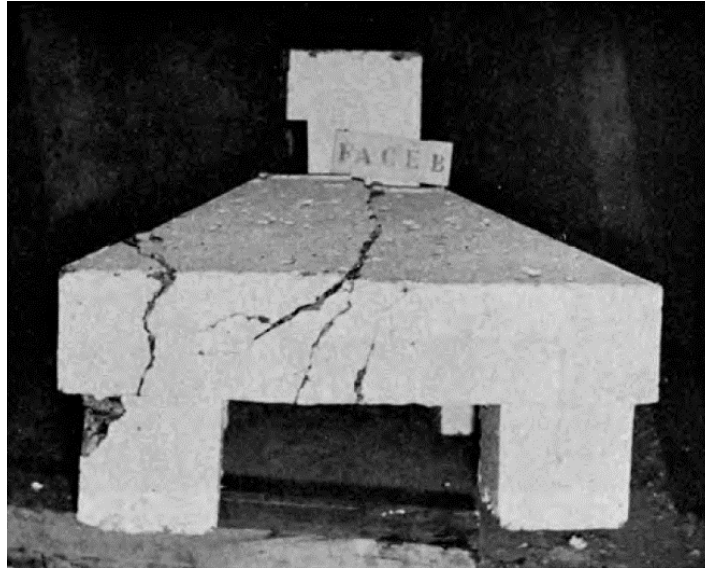


Figure 2.3 Typical specimen (Blevot and Frémy, 1967)

In their investigation of varying reinforcement layouts, Blevot and Frémy (1967) found that, for drilled shaft footings with four drilled shafts, banding the reinforcement above drilled shaft center-lines, as would be suggested by a truss model, resulted in approximately 20% greater strength than the same quantity of reinforcement spread out in a grid. For drilled shaft footings with three drilled shafts, this increase was 50%. However, they also observed that banded-only specimens exhibited wide cracking even before service loads were reached, and thus recommended a combination of banded reinforcement for strength and light grid reinforcement for crack control.

In general, Blevot and Frémy (1967) observed that the interpretation of drilled shaft footing test results is difficult due to the complicated nature of their punching failures. Unlike beams, where shear and bending behaviors can be distinctly separated, drilled shaft footings showed an interrelationship between these two phenomena: an increase in longitudinal reinforcement produced a significant increase in punching capacity. This relationship has also been well documented in the literature on the study of deep beams.

Clarke (1973)

Clarke (1973) tested 15 half-scale drilled shaft footings in direct compression with the experimental variables of footing length, drilled shaft spacing, reinforcement arrangement, and reinforcement anchorage. The typical footing shape was square with approximate dimensions of 37-in. x 37-in. x 18-in.

The tested reinforcement layouts were grid, bunched square, and bunched diagonal, the latter two concentrating reinforcement over the drilled shafts in keeping with

truss model assumptions. Like Blevot and Frémy (1967), Clarke (1973) found that banding the steel reinforcement over the drilled shafts in a square resulted in an approximate strength increase of 14% over the same quantity of reinforcement arranged in a grid. Unlike Blevot and Frémy (1967), however, Clarke (1973) did not observe a strength increase for diagonal banding.

The study observed that all 15 footings failed in shear, with failure modes taking one of two forms. The specimens tended to fail via either a beam-type shear mode or a punching-type mode (Figure 2.4). The punching mode generally revealed triangular-shaped cracking on the footing sides and pushed a conical-shaped plug out the bottom of the footing.

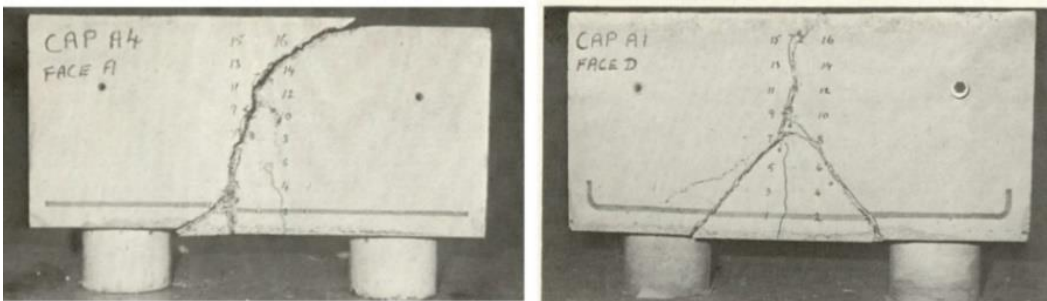


Figure 2.4 Beam-type shear failure (left) and punching shear failure (right) (Clarke, 1973)

Additionally, the study investigated four different anchorage details in his footing specimens (Figure 2.5). “Nil” represents a simple straight bar, “nominal” is a standard 90-deg bend, “full” is a 90-deg bend plus 10-in straight segment, and “full-plus-bob” adds another 90-deg bend to the end of a “full” detail.

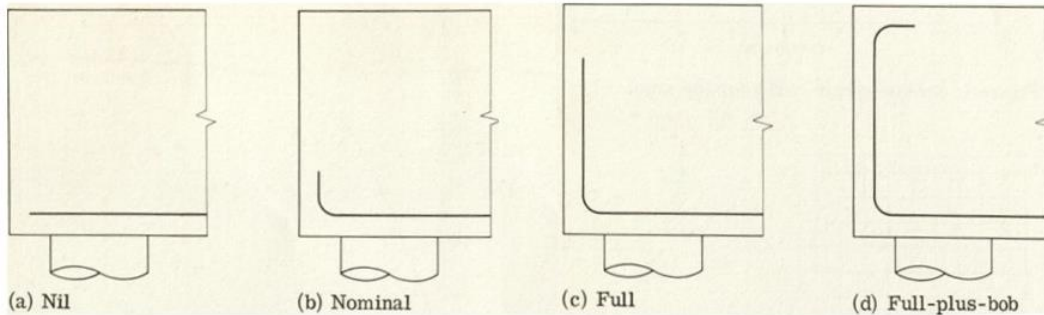


Figure 2.5 Anchorage details (Clarke, 1973)

Clarke (1973) found that the strength increase associated with replacing a “nil” with a “nominal” anchorage was minimal, only about 5%. However, the increase (compared to “nil”) associated with a “full” or “full-plus-bob” detail was more significant, approximately 30%. He suggested that this increase was due to the taller bent-up extensions acting as shear reinforcement.

Sabnis and Gogate (1984)

Sabnis and Gogate (1984) tested nine 1/5-scale drilled shaft footings in direct compression to verify a deep slab punching strength expression they had suggested previously (Gogate and Sabnis, 1980). Their specimens were very small, only 13-in. square by 6-in. deep, and reinforced with wire mesh.

In their 1980 paper, they noted the growth of research into one-way deep beam shear strength and consistent findings revealing that deep beams exhibited higher shear stresses at failure than typical shallow beams. They acknowledged that the ACI code at the time (ACI 318-77, 1977) did not specifically address thick two-way slabs, but it followed that the punching strength of these slabs should similarly be greater than that of thin two-way slabs.

In that first paper, they then suggested a punching strength expression for the design of thick footings based on the similarity between a failed footing's punching cone and the double cones formed when a typical compression cylinder fails. Their expression was very similar to the one recommended by the CRSI Handbook (CRSI, 2008), which bases punching strength on a loaded footing's two-way shear span to depth ratio (w/d) and varies shear capacity from $4\sqrt{f_c'}$ to $32\sqrt{f_c'}$ for w/d ratios ranging from 0.5 to 0. Theirs differed by proposing an upper limit of $24\sqrt{f_c'}$ rather than $32\sqrt{f_c'}$.

Their tested specimens, whose only experimental variable was reinforcement ratio, all failed in punching-type modes, consistent with their assumption. They compared their experimental failure loads to calculated capacities based on CRSI, a truss analogy, and their own expression, and found average experimental-to-theoretical load ratios of 1.35 for CRSI, 1.45 for a truss analogy, and 1.45 for their own expression. The truss analogy ratios had the widest range, varying from 0.80 to 2.04. They observed no significant dependence of punching strength on reinforcement ratio.

Adebar, Kuchma, and Collins (1990)

Adebar et al. (1990) tested six drilled shaft footings at the University of Toronto in what appears to be the first full-scale drilled shaft footing testing found in the literature. Most of their specimens were diamond-shaped and had four drilled shafts, although one was rectangular and had six drilled shafts. Their primary objective was testing the validity of how drilled shaft footings were handled by current ACI provisions of the day (ACI 318-83, 1983), which treated them as footings and required conventional two-way sectional design. They also sought to compare the ACI provisions to those of the Canadian concrete code (CAN3 A23.3-M84), which required the STM. Typical specimen dimensions were approximately

8-ft long x 6-ft wide x 2-ft deep, and details of their six specimens are shown in Figure 2.6.

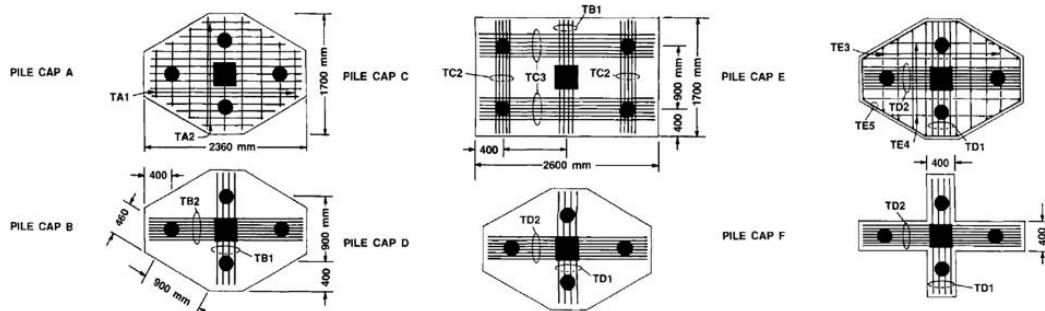


Figure 2.6 Test specimens (Adebar et al., 1990)

In comparing their specimens A and B, each was designed for a column load of 450 kips, specimen A by the ACI provisions, and specimen B by the STM. The ACI code predicted specimen A would fail by flexure at a load of 481 kips, but it instead failed via two-way punching at 401 kips, 83% of its predicted strength. Specimen B, which was predicted under STM to fail via tie yielding at a column load of 450 kips, failed at a greater load, 493 kips, and the failure mode was a combination of yielding of the short tie and punching shear.

In another interesting comparison, their specimens D and F were identical in all respects, except that, as Figure 2.6 indicates, specimen F was cast in a cruciform shape, without the same corner zones of concrete as specimen D. The ACI provisions predicted that, given its larger plan area, the shear strength of specimen D should be about 60% greater than that of specimen F. The STM, however, predicted roughly comparable strengths as the two caps were reinforced identically. Specimen D failed at 735 kips and specimen F failed at 681 kips, a difference of only 7%.

Through strain gauging of one of their specimens, Adebar et al. (1990) further confirmed the validity of the STM. Five surface-mounted gauges measured horizontal strains through the depth of specimen A, and the strains were highly nonlinear during all stages of testing. This is problematic for a sectional approach as a linear distribution of horizontal strains is a foundational assumption in this method. Additionally, by applying multiple steel-mounted strain gauges along the length of reinforcement in specimen A, these researchers found that the tie force was roughly constant along the specimen's length, falling by only 25% at the ends. This again confirms the validity of a truss model assumption.

Adebar et al. (1990) concluded that, due to its improper treatment of various parameters like amount and distribution of longitudinal reinforcement, and overemphasis of the parameter effective depth, the ACI code "fails to capture the

trend of the experimental results.” They went on to state that “strut-and-tie truss models more accurately represent the behavior of drilled shaft footings” (Figure 2.7). Note that the Canadian code, which uses STM, both follows the experimental trend and also is reliably conservative.

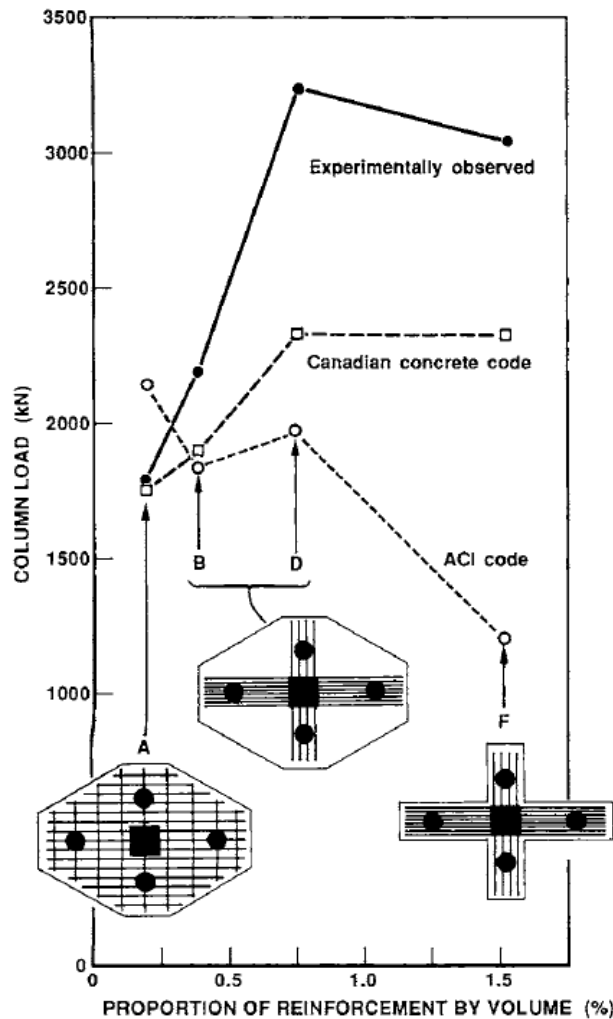


Figure 2.7 Comparison of experimental strengths and code predictions (Adebar et al., 1990)

Suzuki, Otsuki, and Tsubata (1998)

Suzuki et al. (1998) tested 28 drilled shaft footings in direct compression, varying reinforcement layouts, edge distances, and cap depths. Similar to researchers before them, they focused on only two types of reinforcement layouts: a uniformly distributed grid and square banded. Typical specimen sizes were roughly 35-in. x 35-in. x 10-in., and they tested matched pairs of specimens.

Consistent with other studies, they found that the square banded layout was stronger than the distributed grid layout for a given volume of reinforcement, with ultimate

strengths reaching approximately 10 to 15% higher. However, this effect was only visible in their deeper specimens (10-in. and 12-in.). Their thinnest specimens (8-in.) showed less than a 5% increase in strength, suggesting at this end of the spectrum a replacing of truss behavior with slab behavior.

In their other major variable in this study, Suzuki et al. (1998) considered edge distances (defined as the shortest distance from the edge of the footing to the center of drilled shaft) of $0.7d$, $1.0d$, $1.3d$, and $1.7d$, where “ d ” is drilled shaft diameter. As would be expected, they found that increasing the edge distance also increased ultimate strength, though they did observe a point of diminishing returns: there was no significant strength increase in expanding the edge distance from $1.3d$ to $1.7d$. As a result, they recommended edge distances in the practice of $1.5d$.

Miguel-Tortola, Pallarés, and Miguel (2018)

Miguel-Tortola et al. (2018) tested nine drilled shaft footings supported by three drilled shafts, with variations in shear span-depth ratio (v/d) and reinforcement layout. As international specifications (EHE-08; Spain, BS5400-4:1990; United Kingdom, and NBR 6118:2014; Brazil) recommended for designing drilled shaft footings, they designed footing specimens with different reinforcement layouts by adding horizontal and vertical secondary reinforcement into footing specimens with the banded layout of the main reinforcement, which has been widely demonstrated to be the most efficient way to design the footings (Figure 2.8). Three different span-depth ratios (1.68, 1.12, and 0.84) were employed for their specimens.

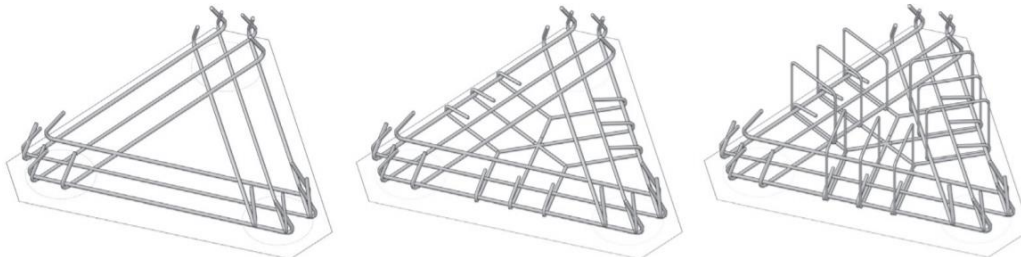


Figure 2.8 Three different reinforcement layouts adopted for test specimens (Miguel-Tortola et al., 2018)

The test results revealed that the ultimate load of the footings increases with a lower shear span-depth ratio. Furthermore, the added horizontal and vertical secondary reinforcement contributed to enhance peak loads (29% for $v/d = 1.68$, 8% for $v/d = 1.12$, and 14% for $v/d = 0.84$). Since the same depth specimens yielded at a similar load, the horizontal and vertical secondary reinforcement enabled stress redistribution to reach higher failure loads than without the secondary reinforcement. In the perspective of serviceability, the addition of horizontal secondary reinforcement also reduced the crack widths.

2.3.1.3. Proposed Strut-and-Tie Methodologies

Siao (1993)

Siao (1993) proposed an analytical method for estimating the shear capacity of drilled shaft footings failing by diagonal splitting. The diagonal compression struts of drilled shaft footings were replaced by a 3D strut-and-tie prism, as was suggested by Adebar et al. (1990), to estimate the shear capacity of the caps.

The study defined geometries of the 3D diagonal strut-and-tie prism. The compression struts act along a perimeter formed by forces radiating out from the sides of the column at an inclination of 2:1. Based on these defined geometries, this study suggested a simplified equation for the shear capacity of the footing, which was assumed to fail due to overstress of its concrete ties, on the basis of the equilibrium condition between the concrete struts and the concrete ties.

Adebar and Zhou (1996)

Adebar and Zhou (1996) proposed a simple strut-and-tie model for the design of drilled shaft footings, basing their assumptions on experimental research examining the bearing strength of unreinforced concrete cylinders.

The dependence of an STM's strength on bearing capacities had previously been well established. According to Schlaich et al. (1987), a proposed strut-and-tie model is considered safe if the maximum bearing stress in all nodal zones is below a predetermined allowable limit. Through extensive compression testing of over 60 concrete cylinders of varying heights, diameters, and volumes of confinement, Adebar and Zhou (1993) had previously developed equations that successfully predict the maximum bearing stress to cause transverse splitting of an isolated strut, and these expressions formed the basis of their proposed strut-and-tie methodology. This splitting strength was found to depend chiefly on the amount of confinement as well as a strut's cross-sectional aspect ratio.

Using a database of previous experimental testing conducted by other researchers, they went on to confirm that their proposed strut-and-tie methodology could conservatively predict capacities of footings better than the contemporary traditional methods (ACI 318-83, 1983; CRSI Handbook, 1992), which both showed up to 30% unconservatism.

Souza, Kuchma, Park, and Bittencourt (2007)

This study proposed an adaptable strut-and-tie model for designing drilled shaft footings supporting square or rectangular columns subjected to axial compression and mild biaxial moment, that is, not enough to produce tension in the column. The

axial compression and biaxial moment on the column are replaced with a single compressive axial load acting at an eccentricity, and the strut-and-tie model is developed based on the eccentric loading point and the centers of drilled shafts. In order to avoid a shear failure, this method limits the highest compressive stress acting at the corner of the column to the uniaxial compressive strength of the concrete.

Since there was no experimental test data on the performance of this type of drilled shaft footings, nonlinear FEA was applied to make predictions on the behavior of these footings. Drilled shaft footings subjected to the same loading conditions and different heights were designed on the basis of the proposed method and were analyzed through the validated nonlinear FEA. The results showed that the predicted capacities are greater than those calculated from the proposed model.

Park, Kuchma, and Souza (2008)

To evaluate the strength of struts in reinforced concrete drilled shaft footings, Park et al. (2008) proposed a strut-and-tie approach that considers strain compatibility and uses nonlinear constitutive laws for cracked reinforced concrete. Based on nodal geometries, this method computes the effective areas of a diagonal strut at the top and bottom nodes, a horizontal strut, and a concrete tie. The capacity of the model is then determined through an iterative process, incrementally increasing load until it can no longer be resisted by the assumed strut.

Interestingly, this proposed strut-and-tie model does not consider the bearing failure of a nodal zone. Further, the assumed location of the top node considered in the calculation of the effective depth of a diagonal concrete strut is incompatible with that used in determining the depth of a horizontal strut. The neutral axis depth of a singly reinforced section in an elastic state was used for the former, while a quarter of the height of the footing was used for the latter. The effective depth of a horizontal strut is based on the suggestion of Paulay and Priestley (1992) for the depth of the flexural compression zone of an elastic column.

Souza, Kuchma, Park, and Bittencourt (2009)

This work also proposed an analytical strut-and-tie model for drilled shaft footings with rectangular columns subjected to axial load only. In this methodology, the authors simplified their previous strut-and-tie approach (Souza et al., 2007) by removing the possibility of moment and requiring axial load only. In addition to this simplification, the model made use of a suggestion proposed by Siao (1993) to consider splitting of compressive struts based on the tensile strength of concrete given by CEB-FIP Model Code 1990 (1990).

Based on this proposed model, Souza et al. formulized cracking, first yielding, flexural failure, and splitting failure capacities of a footing. To evaluate test specimens containing a grid pattern of reinforcement with the proposed model, an equation for footing capacity was also suggested that predicts reinforcement yielding. To calibrate the model, the proposed formulas for cracking, first yielding, and flexural capacity were applied to an extensive experimental database consisting of 129 specimens collected from previous research (Blevot and Frémy, 1967; Clarke, 1973; Suzuki et al., 1998; Suzuki and Otsuki, 2002).

Guo (2015)

This paper presented a generalized method of spatial strut-and-tie modeling to evaluate punching shear resistance of drilled shaft footings with uniform grid reinforcement. Guo (2015) pointed out that the punching failure of a drilled shaft footing occurs due to either a strut failure or yielding of the tension tie. Strut failure is defined as a failure mechanism beginning with splitting at the middle of the strut and ending in shear-compression failure at the two ends of the strut. The yield failure of a tension tie, on the other hand, results from insufficient tension tie reinforcement but can also be accompanied by strut failure. For an area of a tension tie, Guo (2015) assumes an effective quantity of grid reinforcement based on a width equal to twice the drilled shaft diameter.

This study also evaluated strut bearing capacity, which is based on a strut area equal to 0.6 times the cross-sectional area of the drilled shaft and the average of the strengths at the two ends of the strut. The average strength was calculated using a least-squares method and was assumed to depend on two basic factors: concrete strength and punching span-to-depth ratio. A nonlinear parametric study was also conducted, producing over 100 parametric models that varied these two factors.

Araújo (2016)

This study suggested a strut-and-tie model for the design of drilled shaft footings by adopting an iterative algorithm to determine the depth of the top nodal zone so as to not to cause crushing of the struts. In the proposed model, trapezoidal-shaped struts transfer the applied load from the base of the column to the top of the footing, converging at a horizontal plane situated a small distance from the top of the footing.

According to the study, the region within the footing immediately below the column base can be seen as a virtual extension of the column. In this region, the column effectively has an enlarged base, and the crushing of the compressed concrete can be checked as such. This virtual depth of “column embedment” is determined from

the iterative algorithm based on equilibrium and the uniaxial compressive strength of concrete. Tension failure by yielding of the tie reinforcement is also considered.

The model of Araújo (2016) considers the favorable effect of triaxial confinement provided by the large concrete cover in the region of the column base. This effect is also considered at the bottom node checks by using an enlarged section measured at the axis of the tension tie. The strut stress is then computed from this enlarged section at the bottom node, using guidance from the CEP-FIP Model Code 1990 (1990) for the stress check.

Mathern, Chantelot, Svahn, Kettil, Rempling, and Engström (2017)

Mathern et al. (2017) proposed an enhanced strut-and-tie model for drilled shaft footings, which is based on consistent geometries of 3D nodal zones and struts and also integrates a strength criterion for confined bottle-shaped struts. The horizontal and vertical dimensions for the parallelepiped-shaped nodal zones under the column are calculated through iteration in order to maximize capacity. Based on the resulting 3D nodal geometries, the hexagonal cross-sectional area of the inclined struts is computed both at the nodal zones both under the column and above the drilled shafts.

The maximum allowable bearing stresses are calculated according to provisions from Eurocode 2 (2004) for triaxially compressed nodes. This study considered the inclined struts as bottle-shaped and incorporated confinement effects provided by large volumes of inactive concrete surrounding the struts. The strength of the inclined struts is then determined based on the formulation of Adebar and Zhou (1993) for the maximum bearing stress of unreinforced compressive struts confined by plain concrete and subjected to a perpendicular tension field. The maximum capacity is lastly obtained by increasing incrementally the column load, considering all possible combinations of dimensions for the nodal zones under the column until no models satisfy all the aforementioned criteria.

Table 2.7 summarizes the previously proposed methodologies; Table 2.8 defines the variables referenced in Table 2.7.

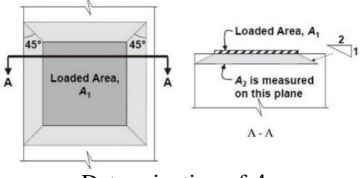
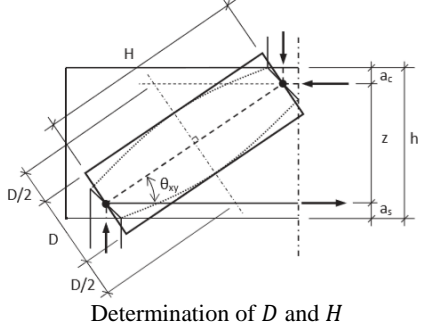
Table 2.7 Summary of previously proposed methodologies

Author	Proposed STM	Properties		Note
Siao (1993)		Equilibrium	O	<ul style="list-style-type: none"> Only splitting failure is considered in shear failure of drilled shaft footings <p>Allowable stress limits Tensile strength of concrete $f_t = 6.96\sqrt{f'_c}$ [psi]</p>
		Compatibility	X	
		Constitutive Relationship	X	
		Triaxial Confinement	X	
		Iterative Procedure	X	
		Top node Location	Column Face	
Abedar and Zhou (1996)		Equilibrium	O	<ul style="list-style-type: none"> Only the maximum bearing stress in all nodal zones is considered <p>Allowable stress limits $f_b \leq 0.6f'_c + \alpha\beta 72\sqrt{f'_c}$ [psi]</p> $\alpha = \frac{1}{3}(\sqrt{A_2/A_1} - 1) \leq 1.0$ $\beta = \frac{1}{3}(h_s/b_s - 1) \leq 1.0$
		Compatibility	X	
		Constitutive Relationship	X	
		Triaxial Confinement	O	
		Iterative Procedure	X	
		Top node Location	Column Face	
Souza et al. (2007)		Equilibrium	O	<ul style="list-style-type: none"> Generic loading condition (Axial load + Biaxial bending) is considered Bearing stress check is conducted at corners of a column <p>Allowable stress limits $\sigma_{max} \leq \lambda f_c$</p> <p>$\lambda = 1.0$ is suggested (Adebar et al., 1990)</p>
		Compatibility	X	
		Constitutive Relationship	X	
		Triaxial Confinement	X	
		Iterative Procedure	X	
		Top node Location	Column Face	
		○ Top node	●●●●● Strut	
		— Stress check locations where can cause shear failure	— Tie	

Table 2.7 (cont'd) Summary of previously proposed methodologies

Author	Proposed STM	Properties		Note
Araújo (2016)		Equilibrium	O	<ul style="list-style-type: none"> • Top nodal location $0.50x$ is determined through iteration • Triaxial confinement effect is considered by amplified nodal geometries <p>Allowable stress limits CCC : Eurocode 2(2004) CTT : CEB-FIP Model Code 1990 (1990)</p>
		Compatibility	X	
		Constitutive Relationship	X	
		Triaxial Confinement	O	
		Iterative Procedure	O	
		Top node Location	$0.50x$ from top	
Mathern et al. (2017)		Equilibrium	O	<ul style="list-style-type: none"> • Top nodal dimensions (w_c and a_c) are determined through iteration • Three-dimensional nodal geometries are considered <p>Allowable stress limits - Bearing & Back Faces Eurocode 2 (2004) - Struts $\sigma_{R,max}$ *Adebar and Zhou (1993)</p>
		Compatibility	X	
		Constitutive Relationship	X	
		Triaxial Confinement	O	
		Iterative Procedure	O	
		Top node Location	a_c from top	
		○ Top node	●●●● Strut	
		— Stress check locations where can cause shear failure	— Tie	

Table 2.8 Variables referenced in Table 2.7

Author	Description
Siao (1993)	f'_c : concrete compressive strength [psi] f_t : concrete tensile strength [psi]
Abedar and Zhou (1996)	A_1 : area of the bearing device [in ²] A_2 : notional area for determination of confinement factor [in ²] b_s : width of the compression strut f_b : maximum bearing stresses in nodal zones of footings [psi] f'_c : concrete compressive strength [psi] h_s : height of the compression strut <div style="text-align: right;">  <p style="text-align: center;">Determination of A_2</p> </div>
Souza et al. (2007)	f_c : concrete compressive strength [MPa] σ_{max} : maximum stress acting in corners of the column [MPa]
Souza et al. (2009)	f_c : concrete compressive strength [MPa] f_t : concrete tensile strength [MPa]
Mathern et al. (2017)	<p>*Strength criterion for cracked inclined struts (Adebar and Zhou (1993))</p> $\sigma_{R,max} = 0.6f_c(1 + 2\alpha\beta)$ <p style="text-align: center;">for $f_c \leq 34.5$ MPa</p> $\sigma_{R,max} = 0.6f_c \left(1 + \alpha\beta \frac{10}{\sqrt{f_c}} \right)$ <p style="text-align: center;">for $f_c > 34.5$ MPa</p> $\alpha = \frac{1}{3} \left(\frac{D}{d_{mean}} - 1 \right) \leq 1.0$ $\beta = \frac{1}{3} \left(\frac{H}{d_{mean}} - 1 \right) \leq 1.0$ $d_{mean} = \sqrt{\frac{2(A_{col} + A_{pile})}{\pi}}$ $D = \frac{z}{2 \cos \theta_{xy}}$ <div style="text-align: right;">  <p style="text-align: center;">Determination of D and H</p> </div> <p> A_{col} : hexagonal area of the inclined strut at nodal zone of the column [mm²] A_{pile} : hexagonal area of the inclined strut at nodal zone of the drilled shafts [mm²] D : assumed cylinder diameter [mm] H : length of the inclined strut [mm] d_{min} : assumed bearing diameter [mm] f_c : concrete compressive strength [MPa] $\sigma_{R,max}$: maximum allowable bearing stress [MPa] </p>

2.3.2. Previous Research on Non-uniform compression in Drilled Shafts

2.3.2.1. Design Examples

Klein (2002)

In addition to the first example of a drilled shaft footing subjected to compression-only, a drilled shaft footing of the second example was subjected to eccentric compression inducing tension in one side of the column and non-uniform compression in drilled shafts. The developed strut-and-tie model, which is identical to the assumed model of the current project, showed that dowel bars from the column should be anchored properly to the bottom of the footing. Therefore, a reinforcement detail of the longitudinal column reinforcement extending beyond the main reinforcement on the bottom was proposed (Figure 2.9). However, there was no suggestion regarding a critical section for the column reinforcement anchorage. In addition, Klein (2002) performed nodal strength checks in accordance with ACI 318-02 (2002) at the top node only by assuming square struts.

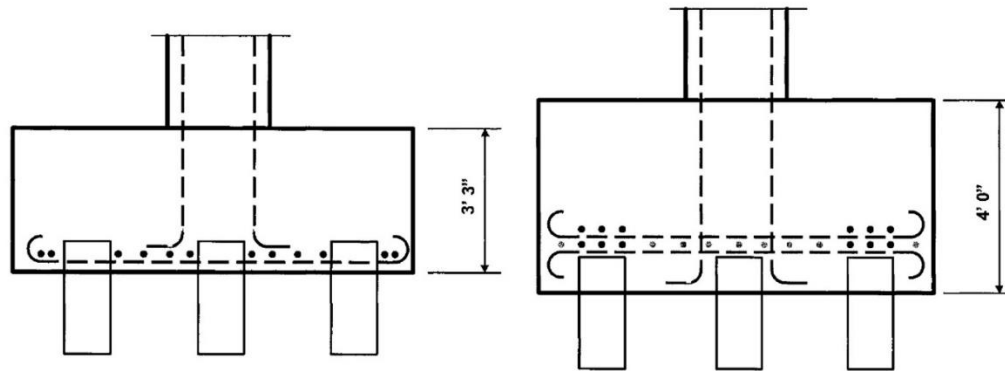


Figure 2.9 Drilled shaft footing designed by sectional design method (left) and STM (right) (Klein, 2002)

Williams, Deschenes, and Bayrak (2012)

Williams et al. (2012) authored a series of design examples on the basis of recommendations made by TxDOT Project 0-5253 (Birrcher et al., 2009), which have recently been incorporated into AASHTO LRFD (2016). They provided two design examples of drilled shaft footings subjected to a combination of axial force and moment. The first example represents a case with both significant axial load and moment results in tension in one side of the column and non-uniform compression in drilled shafts.

In the strut-and-tie model, the location of the top node was assumed at a depth of 0.1 times the total height of the footing, and locations of compressive forces applied on the column were determined based on the linear stress diagram. The stress diagram satisfied the equivalent force system, and the line of action for both forces coincided with the centroid of the compressive portion of the stress diagram. Further, based on the same logic of Widiyanto and Bayrak (2011), Williams et al. (2012) forewent determination of the complex 3D nodal geometries, instead favoring a simple bearing stress limit at the column and supports. For added conservatism in these checks, the triaxial confinement factor was neglected.

One complexity observed in the model was how to connect vertical ties from the column to the footing. The footing's nodes were considered as "smeared" (similar to a band of stirrups in a deep beam), so the point of connection was difficult to assess. Therefore, 90-degree hooks were specified in this design by considering TxDOT's long-term successful practice of using hooks to anchor column bars within deep footings (Figure 2.10). Additionally, crack control reinforcement was assumed to be necessary not only on the bottom face, but also on the footing side faces.

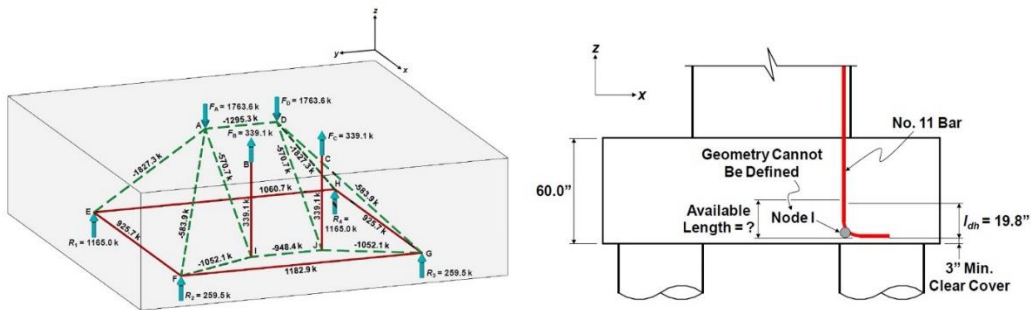


Figure 2.10 Strut-and-tie model resulting in tension at column section (left) and suggested anchorage detail of column reinforcement (right) (Williams et al., 2012)

2.3.3. Previous Research on Compression and Tension in Drilled Shafts

2.3.3.1. Design Examples

Widiyanto and Bayrak (2011)

Similar to ACI SP-208, ACI SP-273 provides several design examples for the use of strut-and-tie models in accordance with ACI 318-08 (2008). Among the examples, Widiyanto and Bayrak (2011) provided an example for the use of a strut-and-tie model in a drilled shaft footing subjected to a load combination that results tension in two of four drilled shafts. Based on the developed strut-and-tie model,

which assumes that top nodes are located at a distance from the footing's top surface equal to 0.1 times depth of the footing, the locations of compressive forces were determined based on the locations of anchor bolts in the column, as shown in Figure 2.11. This model is similar to the model corresponding to the most complex load combination of the current project.

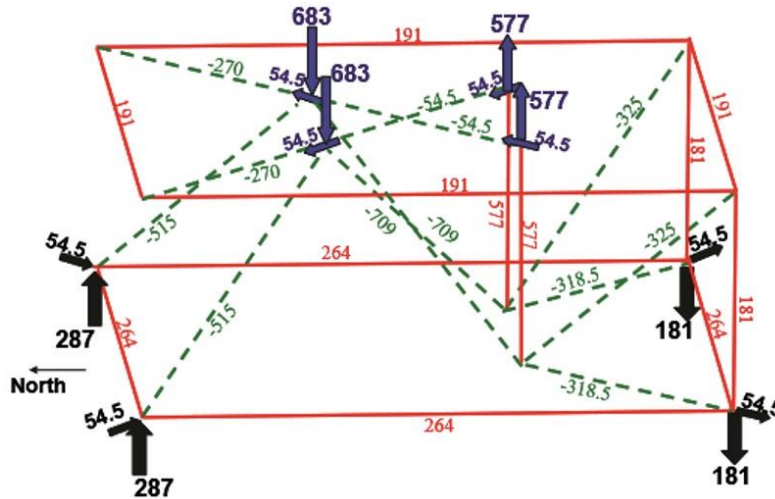


Figure 2.11 Strut-and-tie model resulting tension at drilled shafts (Widianto and Bayrak, 2011)

Typical design procedures using strut-and-tie models conduct stress checks at nodal zones and struts based on the nodal geometries; however, this example assumed that the strength of nodal zones was sufficient by simply limiting the bearing stress on the drilled shafts and columns without defining 3D nodal geometries. This reasoning was based on the fact that concrete inside 3D structures is significantly more confined than concrete inside 2D structures.

Since the nominal compressive strengths provided by ACI 318 were intended for 2D structures, using the same nominal strength may be too conservative for the well-confined concrete in a drilled shaft footing. Therefore, this example justified neglecting the determination of an exact shape of a nodal zone. The anchorage length of horizontal tie reinforcement was assumed to be measured from the interior face of the drilled shafts, and vertical tie reinforcements were assumed to be fully developed through the use of circular headed bars due to limited space beyond nodes (Figure 2.12).

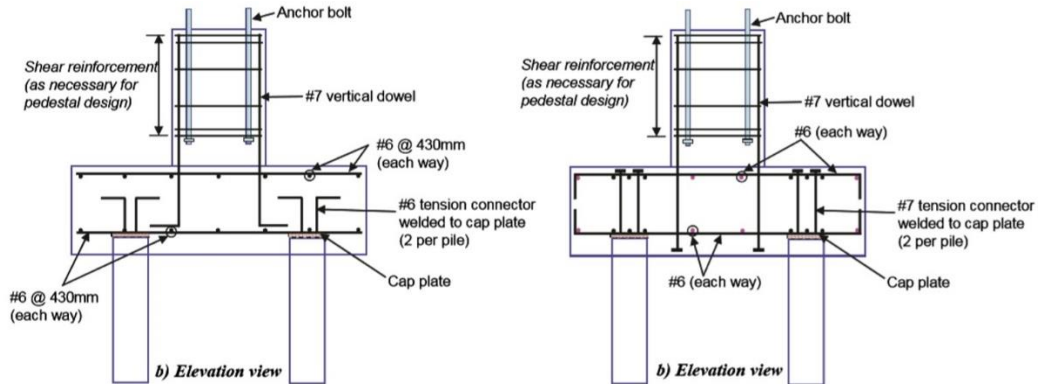


Figure 2.12 Reinforcement details based on sectional design method (left) and STM (right) (Widiyanto and Bayrak, 2011)

Williams, Deschenes, and Bayrak (2012)

Williams et al. (2012) also provided a drilled shaft footing design example of the results for tension and compression in drilled shafts. All the assumptions used for determining location of the top node and performing nodal strength checks of this model are the same as described in the former loading case (Section 2.3.2.1).

Similarly, the footing's nodes connected with vertical ties from two drilled shafts were considered as smeared; therefore, 180-degree hooks were used for drilled shaft reinforcement considering the success of past TxDOT designs as shown in Figure 2.13.

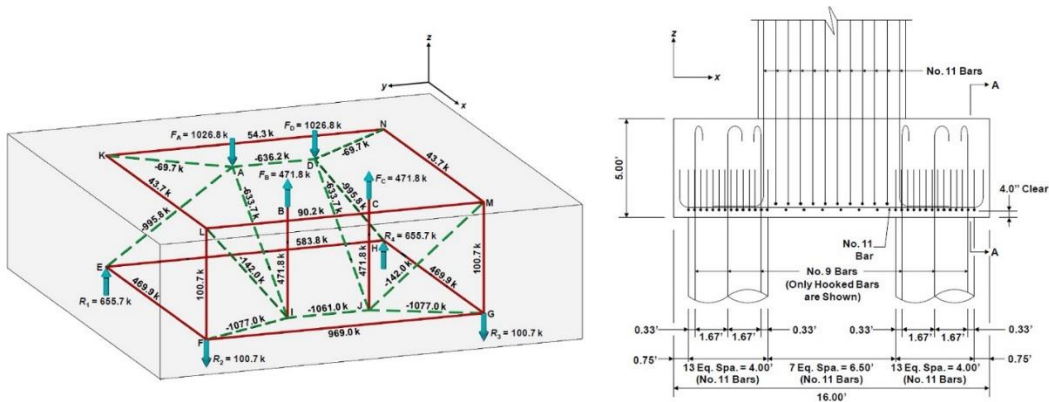


Figure 2.13 Strut-and-tie model (left) and suggested anchorage detail of drilled shaft reinforcement (right) (Williams et al., 2012)

2.3.4. Previous Research on Finite Element Analysis of Drilled Shaft Footings

2.3.4.1. Nonlinear Behavior of Drilled Shaft Footings

Sam and Iyer (1995)

Using both numerical FEA and experimentation, this research evaluated three drilled shaft footings having consistent geometry and reinforcement ratios, but with three different reinforcement layouts. The layouts were a grid distribution, bunched reinforcement over the drilled shafts in a square shape, and bunched reinforcement over the drilled shafts diagonally. The finite element models were developed using eight-noded isoparametric solid elements with incompatible modes and two-noded truss elements (Figure 2.14) and were analyzed considering various nonlinear effects: multiaxial compressive behavior of concrete, cracking of concrete, yielding of reinforcement, etc.

Regardless of the reinforcement layout, beam action was observed to dominate at low load levels, while the footing resisted load by strut action at higher load levels. Failure was caused by punching of column or drilled shafts. Both numerical and experimental results showed that the footing with a grid distribution of reinforcement resisted the highest load.

Sam and Iyer (1995) noted that this finding conflicted with the results obtained by earlier researchers (Blevot and Frémy, 1967; Clarke, 1973), but concluded their results were valid because the load carrying capacity of a drilled shaft footing is dependent on a variety of factors, including spacing of drilled shafts, footing depth, reinforcement ratio, etc.

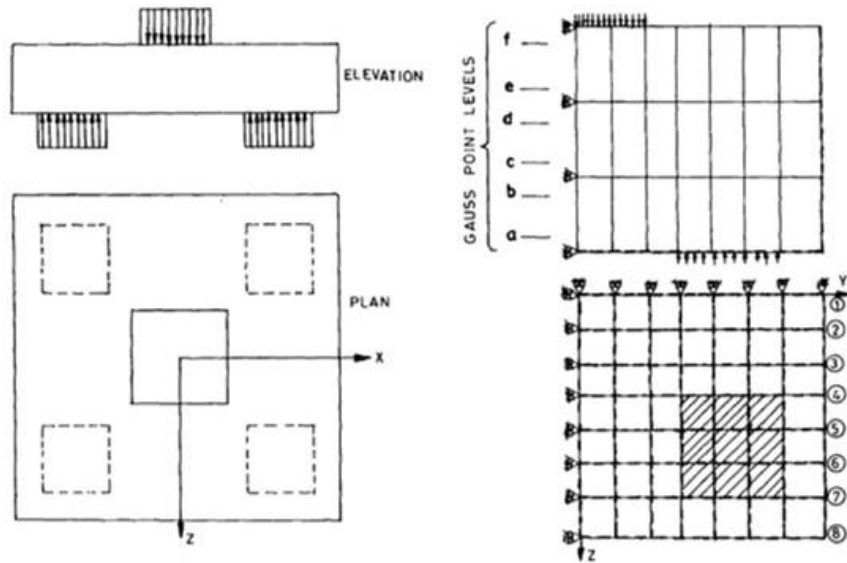


Figure 2.14 Finite element mesh for one-quarter of drilled shaft footing with slab-type reinforcement layout (Sam and Iyer, 1995)

2.3.4.2. Proposed Innovative STM

Leu, Huang, Chen, and Liao (2006)

Leu et al. (2006) suggested a refined evolutionary structural optimization (RESO) method, which uses linear elastic analysis to develop 3D strut-and-tie models for reinforced concrete structures.

The RESO method starts from a design domain informed by a finite element model with given loading and support conditions, and then an optimized topology structure can be obtained by gradually removing ineffective elements, as shown in Figure 2.15. The ineffective elements are determined from the strain energy density of each element and removed when their strain energy densities fall below a threshold relative to the average strain energy density of the structure.

By gradually removing ineffective materials, the most effective structure having a more efficient load-carrying mechanism can be obtained. In addition, this study adopted the four-parameter strength criterion of Ottosen (1977) to evaluate compressive strength for struts and nodal zones and confirmed that the criterion with the optimized topology structure agrees well with experimental results.

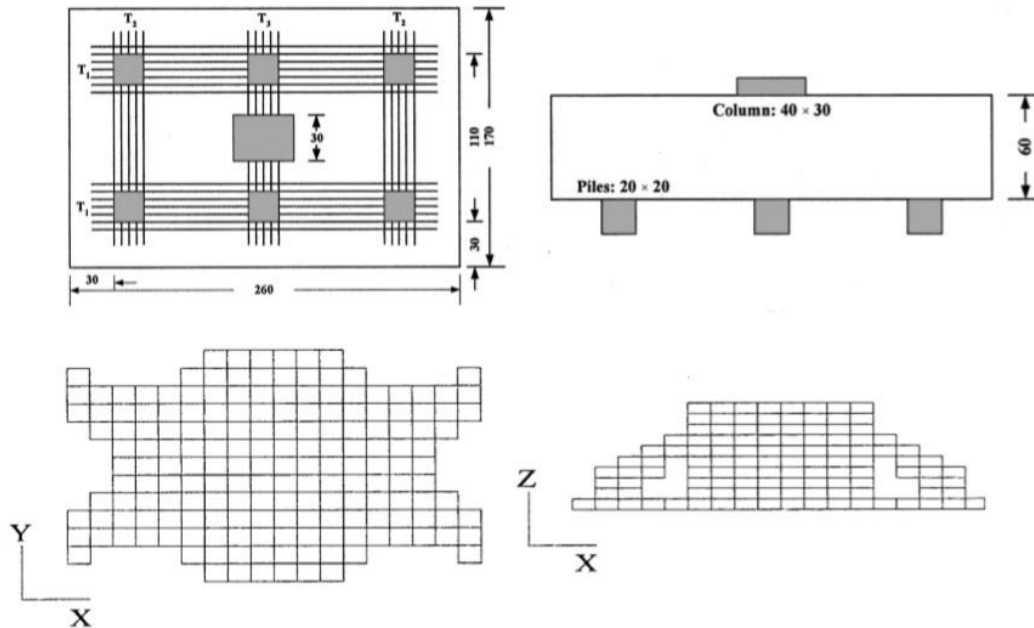


Figure 2.15 Drilled shaft footing design example (top) and topology from RESO (bottom) (Leu et al., 2006)

Yun, Kim, and Ramirez (2018)

Yun et al. (2018) proposed a 3D grid strut-and-tie model by considering all available load paths from each node to adjacent nodes within a grid element. The use of grid elements allows for complicated load-transfer mechanisms within a 3D structure (Figure 2.16).

For elements located near the longitudinal axis of a concrete strut, principal stresses and directions are limited based on the five-parameter failure model of Willam and Warnke (1975). The effective strength of the concrete strut is determined by averaging the effective strengths of the elements acting normal to the longitudinal axis of the concrete strut. The strength is also modified by multiplying a coefficient that considers the effect of concrete compressive strength. The same approach is applied to finite elements that comprise the end points of a concrete strut and helps determine the effective strength of a nodal zone.

This study found that the effective strength of a 3D nodal zone is generally greater than that of a 2D nodal zone. This study also establishes a 3D statically indeterminate strut-and-tie model for drilled shaft footings including diagonal concrete ties

The detailed 3D nodal and strut geometries are defined by comparing the required areas to the maximum areas of struts and nodal zones. The required area of a strut is obtained by dividing the cross-sectional force by its effective strength, and the

required area of a nodal zone is obtained by dividing the cross-sectional forces of the struts and ties framing into it by its effective strength. The maximum areas of each are then defined by the maximum areas that struts and ties can occupy without overlaps in grid elements. If the required area of a component exceeds the maximum area available, the component is considered to have failed.

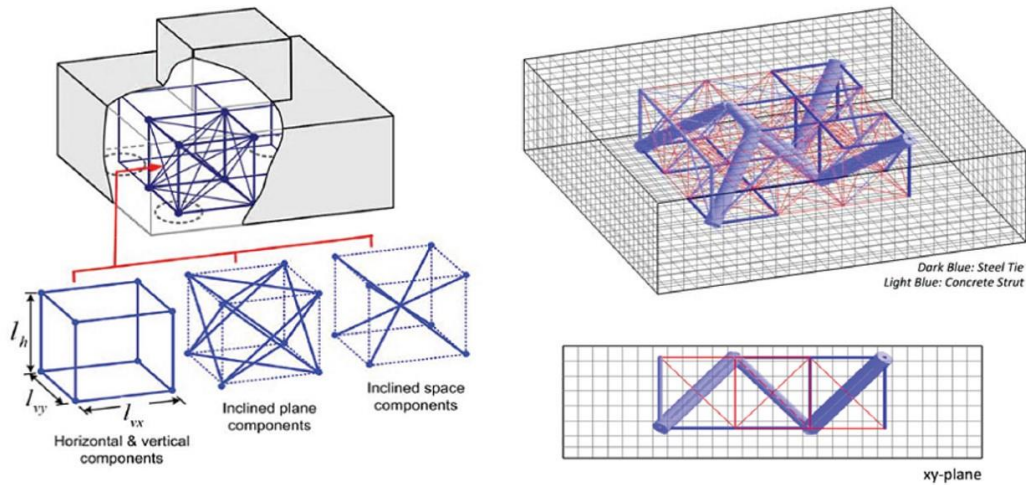


Figure 2.16 Basic grid element (left) and dimensioned shape of 3D grid strut-and-tie model for drilled shaft footing example of ACI SP-273 (right) (Yun et al., 2018)

2.4. Summary and Discussion

This chapter reviewed a broad range of research relevant to drilled shaft footings, focusing on specifications, experimental research, proposed strut-and-tie methodologies, and numerical research using FEA. Through this comprehensive review, the following conclusions can be drawn.

- A notable consensus among the various experimental researchers is that truss-based approaches like the STM are far more appropriate for the design of deep drilled shaft footings than conventional sectional approaches, which, depending on the specification, can alternately be highly over-conservative or unconservative.
- Several studies have shown that banding of reinforcement over drilled shafts consistently yielded drilled shaft footing ultimate strengths 10 to 20% higher than the same volume of reinforcement spread into a uniform grid.
- Although many STM-based design methodologies have been proposed by various researchers, the assumed top node location in each is not often based on real stress distributions, but rather on simple assumptions. Since the location of this node directly affects the forces carried by struts and ties, the

positioning of the top nodes in 3D strut-and-tie models relative to the actual stress distribution is important and requires further study.

- On the basis of the predominant shear-type failure mode observed in experimental testing, proposed strut-and-tie methodologies suggest various ways of preventing splitting failure. The criteria used to determine the appropriate stress limits can be classified into three broad categories and these vary in degrees of conservatism. The first, which is the most conservative, is a maximum bearing stress criterion. Its simplicity is rooted in the fact that it does not require defining complex nodal geometries, but it also does not incorporate the beneficial effects of triaxial confinement. The second common criterion is rooted in using concrete's tensile capacity as a predictor of splitting. The third and most complex criterion is based on limiting bearing stresses after splitting cracks occur. This approach is complicated in that it requires the full definition of complex 3D nodal geometries, but it also permits the inclusion of triaxial confinement effects.
- In general, the various proposed strut-and-tie methodologies with well-defined 3D nodal geometries tend to check nodal strengths against specifications that have been based on 2D research. However, FEA conducted by previous researchers has confirmed that the effective strength of a 3D nodal zone is generally greater than that of a 2D nodal zone.

While the literature provided several excellent STM-based design examples of drilled shaft footings with moment, which required vertical ties, there has been no in-depth research focusing on these ties' anchorage. Since they are "connected" to smeared nodes, and only limited space is available beyond these nodes, it is difficult to assess the required development lengths for these vertical ties. Some research conservatively suggested the use of headed bars or hooked bars, but this has not been confirmed experimentally. Thus, additional research strictly focusing on this anchorage detail is warranted.

Chapter 3. Design Parameter Review

3.1. Overview

The research team at The University of Texas at Austin, with support from the TxDOT project team, established a plan database of representative TxDOT bridge projects with drilled shaft footings that have been designed by TxDOT and their consultants. The database was reviewed to establish meaningful bounds for the variation of key footing parameters, including both geometric proportions and reinforcement details, which will help to inform the forthcoming experimental and analytical programs. This chapter will begin with a presentation of general information from the collected plans, including project location and year. This will be followed by a detailed investigation of each relevant design parameter, which have been broadly categorized as either geometric properties or reinforcement details. The parameters are outlined as follows:

- | | |
|----------------------------------|---------------------------|
| 1. Geometric Properties: | 2. Reinforcement Details: |
| • Span-to-Depth Ratio | • Bottom Reinforcement |
| • Footing Dimensions | • Top Reinforcement |
| • Column Dimensions | • Side Face Reinforcement |
| • Drilled Shaft Diameter | • Column Reinforcement |
| • Footing-to-Shaft Edge Distance | • Shaft Reinforcement |

3.2. TxDOT Drilled Shaft Footing Database

To develop the database, 35 different footing design cases were collected from 16 representative TxDOT projects. All the footings have four drilled shafts, one single column, and symmetric configurations. The locations of the collected footings are well distributed within Texas, coming from Austin, Bryan, Dallas, Fort Worth, Houston, San Antonio, Lubbock, and Waco, as shown in Figure 3.1. Their year of construction varies from 1999 to 2014, and their yearly distribution is shown in Figure 3.2. San Antonio has the largest number of collected footing plans (12 footing plans), and these also were among the oldest, with dates ranging from 1999 to 2002. The year 2010 had the most constructed footings among the studied projects (10 footing plans).

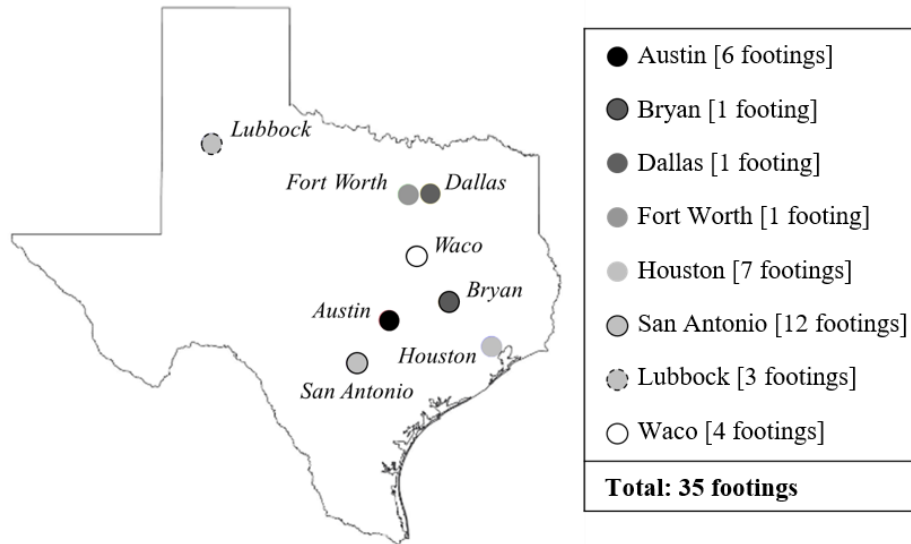


Figure 3.1 Footing locations

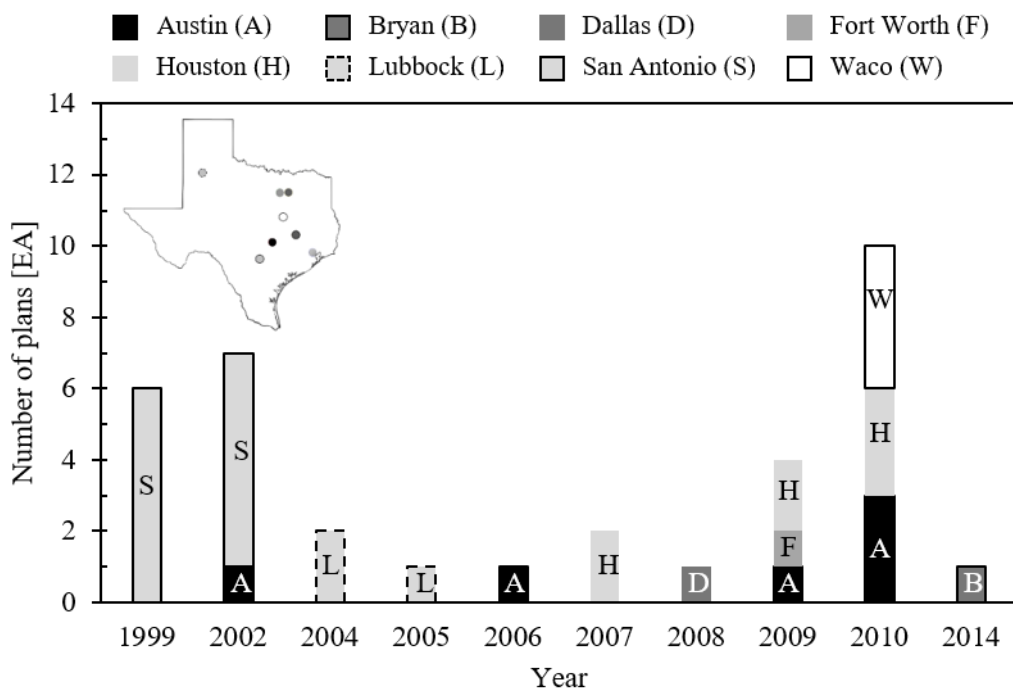


Figure 3.2 Yearly distribution of selected footing plans

Although the footing plans are not uniformly distributed over the relevant time period and geographically around the state, the parameter studies are nevertheless important and offer meaningful insights that were useful in the analytical and experimental programs of this research project. The detail of each footing plan was summarized in Appendix C.

3.3. Geometric Parameters

The geometric properties from the collected footing plans were classified with each parameter of the database and will be reviewed in the following sections.

3.3.1. Span-to-depth Ratio

Figure 3.3 shows the distribution of span-to-depth ratios of the collected footing plans by location. The ratio is expressed as z/d , in which z is the horizontal shear span measured from center of column to center of shaft, and d is the vertical distance from compression (top) face of the footing to the centroid of tensile reinforcement. Considering all the footings in the database, the minimum z/d ratio is 1.30 and the overall average is 1.86.

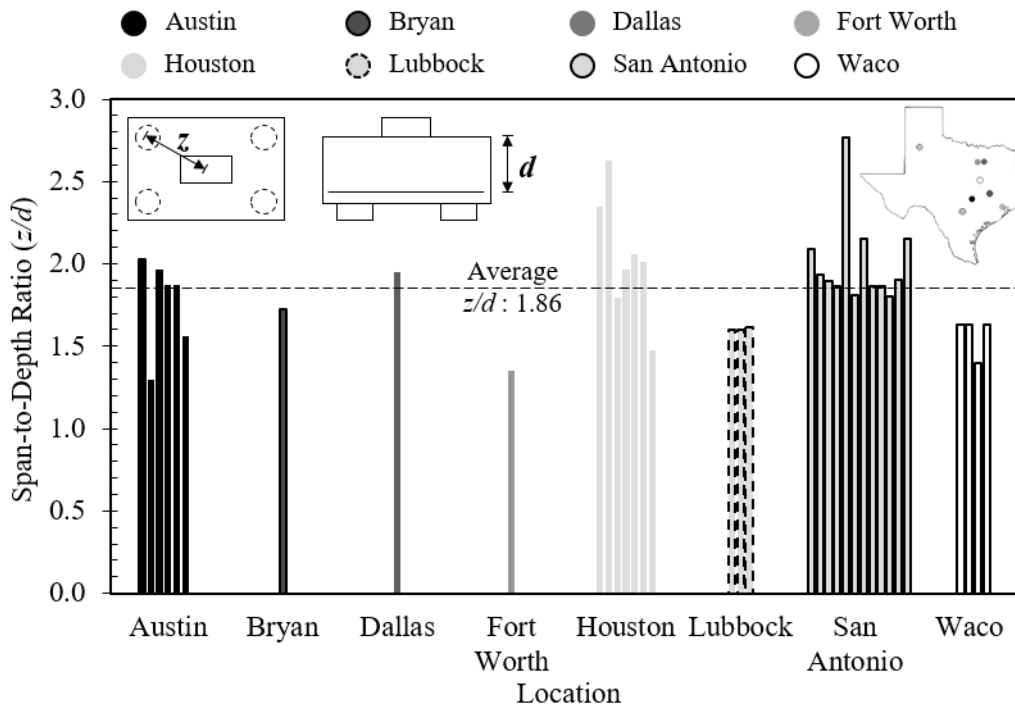


Figure 3.3 Span-to-depth ratio distribution of collected footing plans

3.3.2. Footing Dimension

Distributions of footing side lengths and footing depths of each database footing are displayed in a combined bar chart shown in Figure 3.4. Since a majority of the footings (31 out of 35 total) are square-shaped, the remaining rectangular footings were assumed to have an equivalent square length based on plan area. Among the rectangular shaped footings, the aspect ratios between lengths and widths ranged from 1.10 to 1.22. The smallest and the largest equivalent lengths of the collected footing plans are 132 in. and 294 in.; however, most of the equivalent lengths of

footings are close to the average of 219 in. The smallest and the largest footing depths are 48 in. and 84 in., respectively. The footing depth distribution also concentrated around the average of 60 in. The ratio with respect to the equivalent length was 0.28 on average and ranged from 0.20 to 0.39.

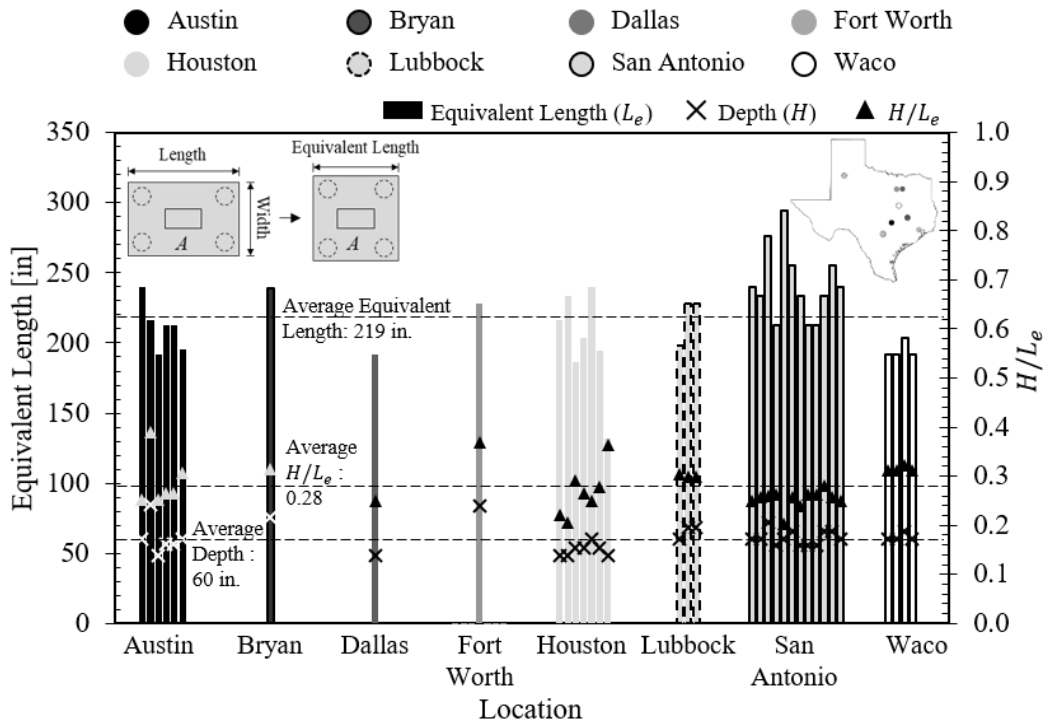


Figure 3.4 Footing dimensions of collected footing plans

3.3.3. Column Dimension

The depths and widths of column cross sections are displayed in a combined bar chart shown in Figure 3.5. Only 21 cases were considered due to insufficient information for 14 of the plans. All columns were rectangular-shaped except one case in Houston. It should be noted that the equivalent square geometry was considered for the circular column section. The shape of the column section was rectangular in all cases except for one instance of a circular column section. The average, minimum, and maximum aspect ratios of column dimensions were 1.78, 1.56, and 2.25 when the case of the circular column section was excluded. The average column length and width were 107 in. and 61 in., respectively. In addition, the ratios of column area to footing plan area were calculated to determine whether there was any meaningful relationship. The results show that the area ratios tend to vary with respect to the change of column dimensions since the collected footing dimensions were relatively constant compared to those of the columns. The average ratio was observed to be 13%.

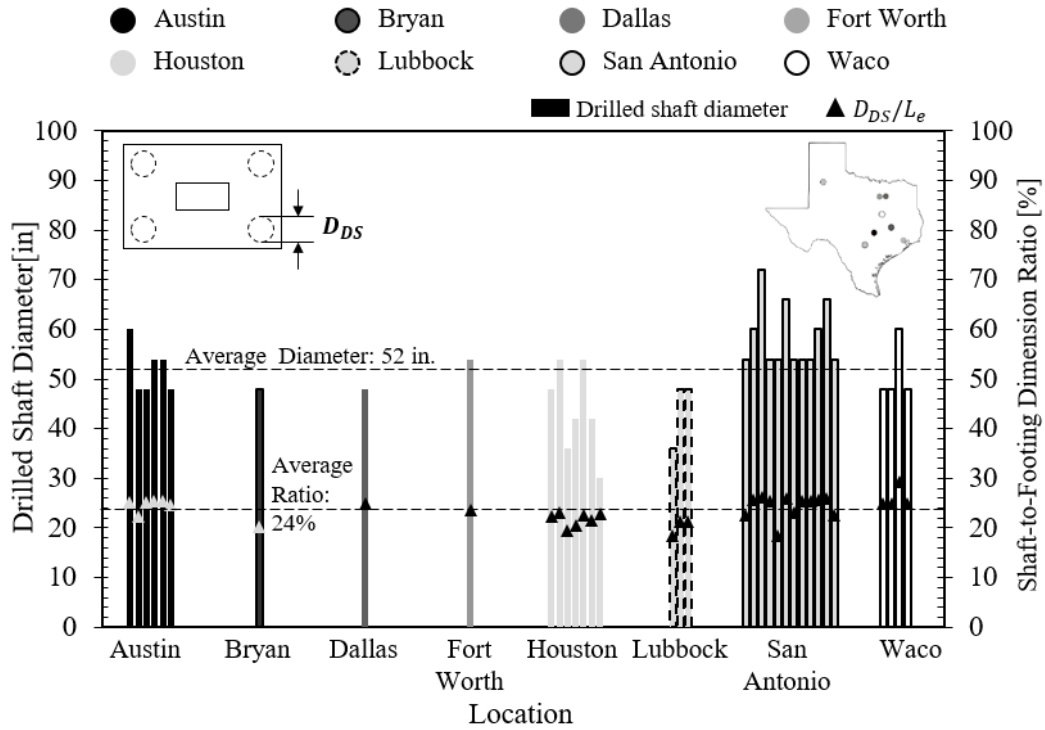


Figure 3.6 Drilled shaft diameters of collected footing plans

3.3.5. Footing-to-shaft Edge Distance

According to AASHTO LRFD (2020) (Article 10.7.1.2), the distance from the side of any pile to the nearest edge of footing, which this report terms the “footing-to-shaft edge distance,” shall not be less than 9 in. for driven piles only, not for drilled shafts. Figure 3.7 provides the footing-to-shaft edge distances of the collected footing plans.

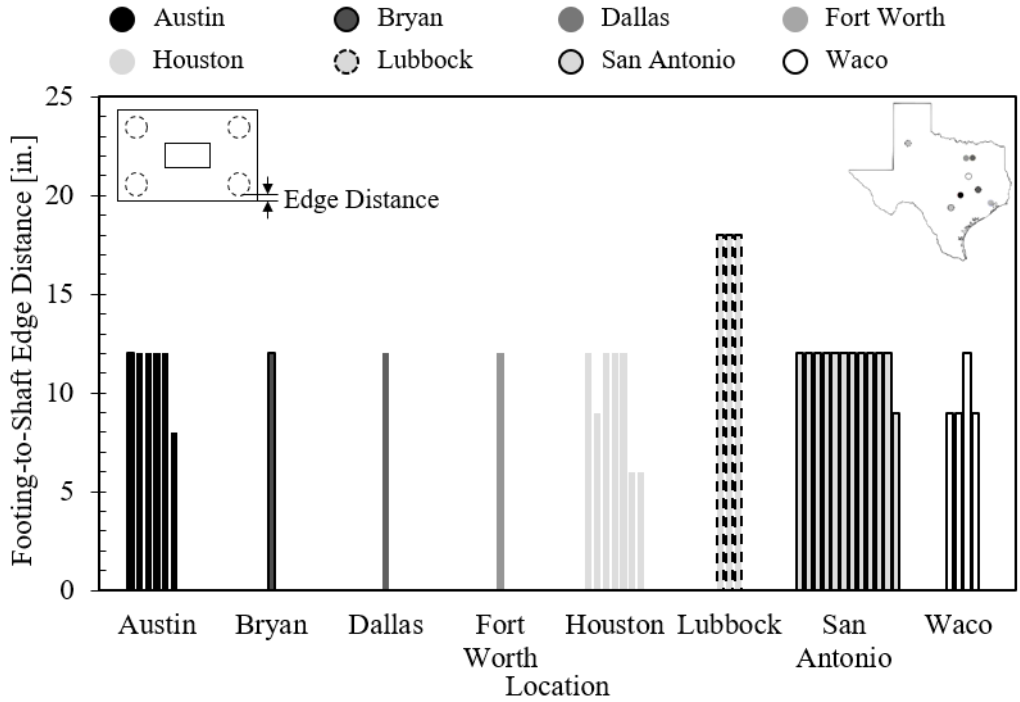


Figure 3.7 Footing-to-shaft edge distances of collected footing plans

3.4. Reinforcing Details

The reinforcement details from the collected footing plans were classified based on reinforcement location: bottom reinforcement, top reinforcement, face reinforcement, and dowel bars from columns and drilled shafts. Quantity, distribution, and anchorage type of each reinforcement location are described in the following sections.

3.4.1. Bottom Mat Reinforcement

3.4.1.1. Quantity

The overall quantity of bottom reinforcement in each footing was examined in terms of average reinforcement ratio ($\rho_{tb, Avg.}$) of a footing, regardless of configuration types, as shown in Figure 3.8. The configuration types of the bottom reinforcement will be discussed later. The range of the collected bottom reinforcement ratios is 0.21% to 0.60%, with an average ratio of 0.37%. Relatively low ratios of bottom reinforcement were mainly observed in the San Antonio projects, which, as mentioned previously, represent the oldest footings in the database.

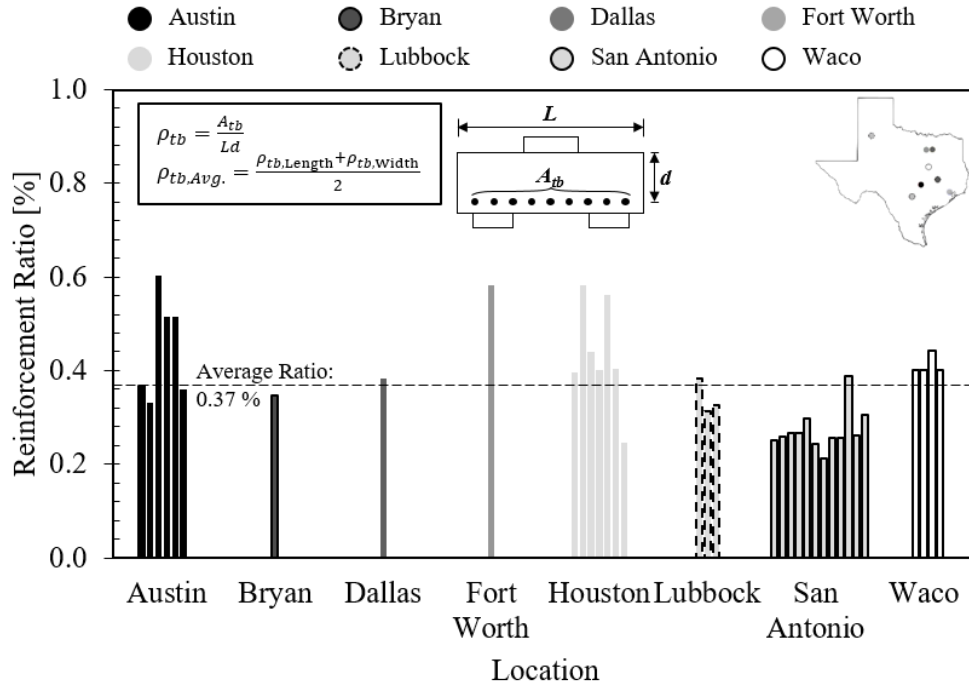


Figure 3.8 Average bottom mat reinforcement ratios of collected footing plans

The trend can also be examined through a combined chart putting reinforcement ratio data organized by year onto the chart of yearly distribution of the collected footing plans (Figure 3.2), as shown in Figure 3.9. Although the span-to-depth ratios of the footings located in San Antonio are relatively high compared to those of other locations (Figure 3.3), they contain the lowest levels of bottom reinforcement ratio. Since all of them were constructed 16 to 18 years ago (in 1999 and 2002), it is possible that the footings were designed on the basis of traditional beam theory, not the strut-and-tie model method. The relationship between bottom reinforcement ratios and span-to-depth ratios was also examined, and Figure 3.10 shows the relationship between the two parameters. It is difficult to observe any significant dependence between them when all the footings are plotted. However, a positive relationship can be observed between these two parameters within 22 footing plans, which exclude footing plans constructed in 1999 and 2002 and those in Fort Worth.

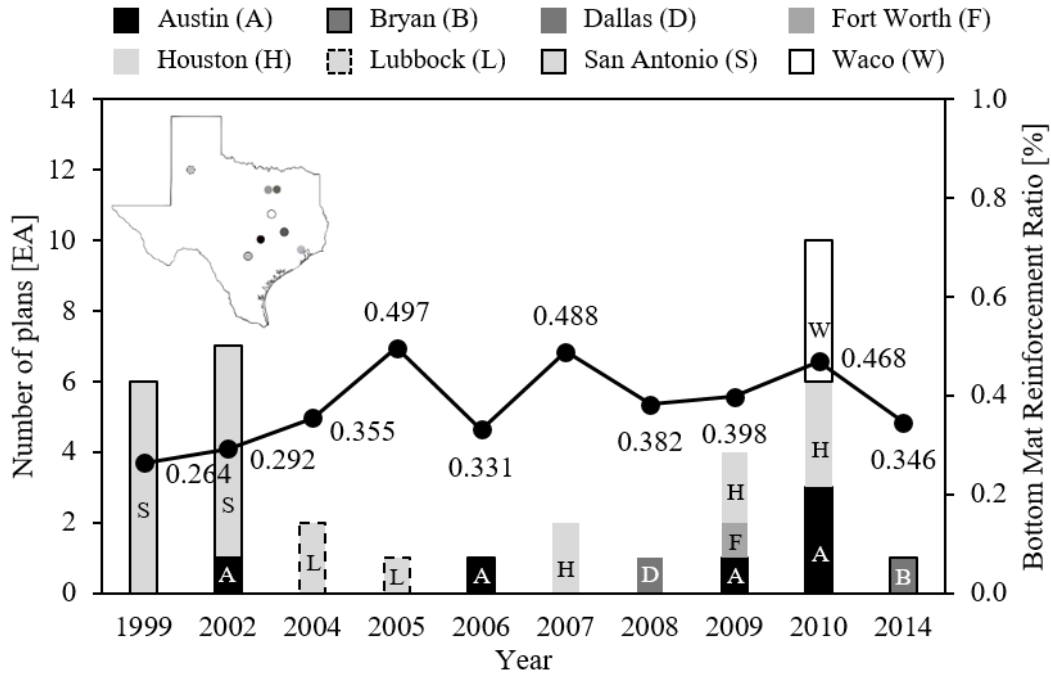


Figure 3.9 Average bottom mat reinforcement ratio by year

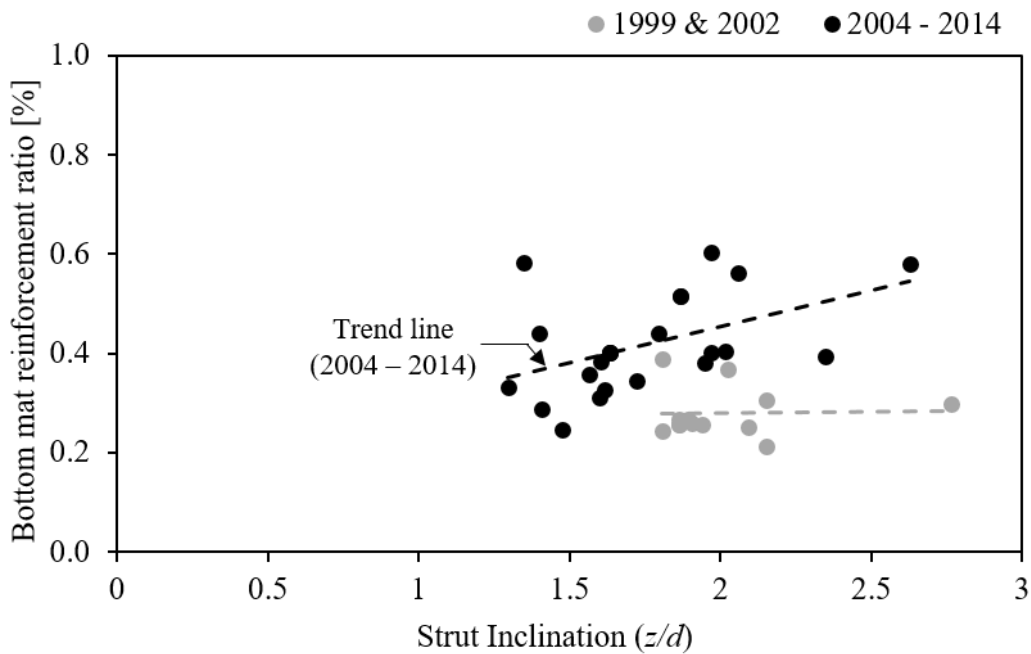


Figure 3.10 Relationship between strut inclination and bottom mat reinforcement ratio

3.4.1.2. Reinforcement Configuration

Two different types of bottom reinforcement configuration are used for drilled shaft footings in practice. One is a uniformly distributed bottom mat reinforcement (grid),

and the other concentrates the bottom mat reinforcement over the drilled shafts (banding). Among banded configurations, nominal distributed reinforcement between bands is still typically provided due to shrinkage and temperature requirements. The types of configurations used in the collected footing plans, and the numbers of each type, are shown in Figure 3.11.

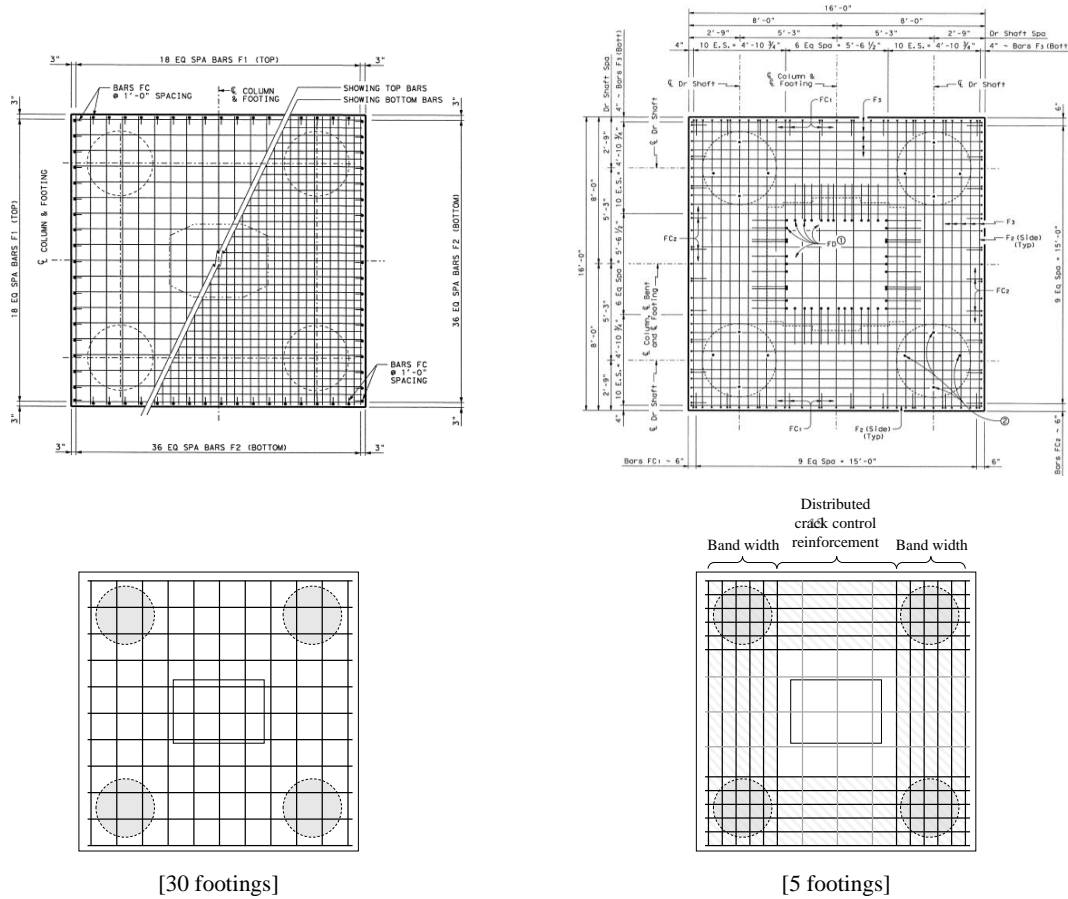


Figure 3.11 Grid configuration (left) and banding configuration (right) used in drilled shaft footings

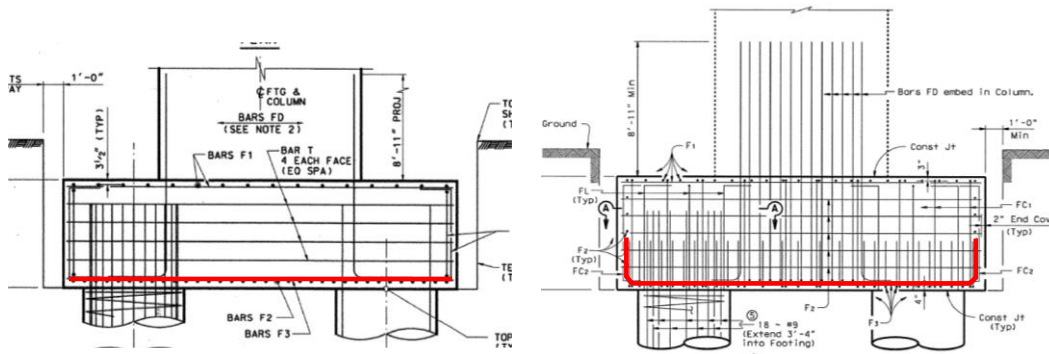
Additional details of the footings containing the banded configuration are tabulated in Table 3.1. The overall reinforcement ratio was calculated with the total amount of bottom reinforcement. The banding and distributed ratios were computed from the amounts of bottom reinforcement placed within a banding width (L_b) and placed between the banding widths, respectively. A banding width is defined as the region where primary bottom mat reinforcement (not reinforcement to control cracks for shrinkage and temperature effect) was placed. In order to observe how much bottom reinforcement is concentrated within the banding zones, a concentration ratio is also defined as the ratio of the amount of banded reinforcement to overall reinforcement in one direction. The result shows that approximately 84% of total reinforcement is concentrated within the banding widths on average.

Table 3.1 Details of banding configuration in TxDOT drilled shaft footing database

City	Year	Overall Ratio $^* \rho_t$ [%]	Banded Ratio $^{**} \rho_b$ [%]	Distributed Ratio $^{***} \rho_d$ [%]	Equivalent Length L_e [in.]	Shaft Diameter D_{DS} [in.]	Band Width L_b [in.]	Concentration Ratio $(2\rho_b L_b / \rho_t L_e)$
Bryan	2014	0.346	0.611	0.089	239	48	59	0.87
Waco	2010	0.307	0.535	0.192	192	48	58.75	0.81
Waco	2010	0.307	0.535	0.192	192	48	58.75	0.81
Waco	2010	0.442	0.553	0.140	204	60	74.5	0.91
Waco	2010	0.307	0.535	0.192	192	48	58.75	0.81
							Average	0.84

3.4.1.3. Anchorage

Most footing plans (31 footing plans) used straight bars for anchorage of bottom reinforcement, whereas others (4 footing plans) used hooked bars. The typical footing plans of these two types of anchorage are shown in Figure 3.12.



Using straight bars for anchorage
[31 footings]

Using hooked bars for anchorage
[4 footings]

Figure 3.12 Anchorage using straight bars (left) and using hooked bars (right)

3.4.2. Top Mat Reinforcement

The overall quantity of top reinforcement for each footing plan was also examined in terms of the average reinforcement ratio ($\rho_{tt,Avg.}$), as shown in Figure 3.13. The range of the collected top reinforcement ratios is 0.05% to 0.31%, having an average ratio of 0.16%. Compared to the bottom reinforcement ratios, the collected footings used only modest amounts of top reinforcement. All the footing plans used the grid reinforcement layout for top reinforcement. Straight bars were employed for anchorage of the top reinforcement in all cases.

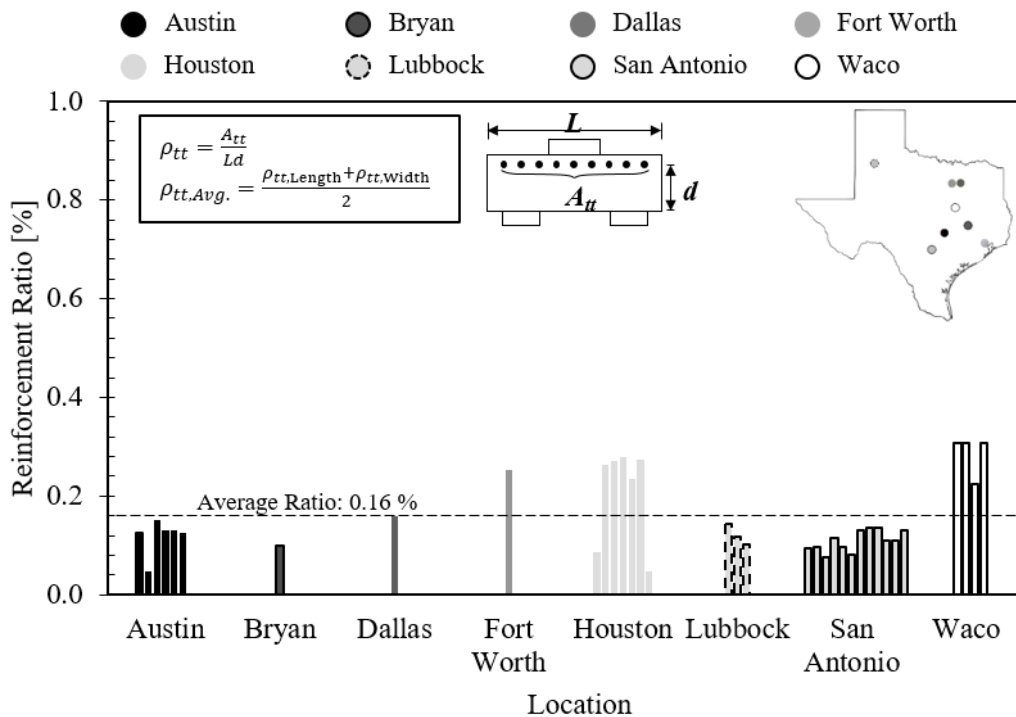


Figure 3.13 Average top mat reinforcement ratios of collected footing plans

3.4.3. Side Face Reinforcement

AASHTO LRFD (2020) (Article 5.10.6), for shrinkage and temperature reinforcement, establishes the following requirement (provided as Eq. (3.1)) for the area of face reinforcement per foot, on each face and in each direction of a reinforced concrete member.

$$A_s/s \geq \frac{1.30A_g}{(Perimeter)f_y} \quad \text{Eq. (3.1)}$$

where:

A_s/s = the area of face reinforcement per foot [in.²/ft]

A_g = the concrete gross area of the section [in.²]

$Perimeter$ = the perimeter of a section where the uniformly distributed face reinforcement is to be provided in a direction perpendicular to the section [in.]

f_y = the yield strength of the face reinforcement [ksi]

By rearranging terms in Eq. (3.1), changing the units of A_s/s to [in.²/in.] and considering $f_y = 60$ ksi, Eq. (3.2) is obtained.

$$\frac{A_s/s(Perimeter)}{A_g} \geq 0.0018 \quad \text{Eq. (3.2)}$$

Hence, the requirement in Eq. (3.2) is comparable to providing an equivalent uniformly distributed reinforcement around the perimeter of the section of at least 0.0018 A_g or 0.18% of the overall section) when $f_y = 60$ ksi. Based on this, the following face reinforcement ratio Eq. (3.3)) is proposed to compare the amount of face reinforcement provided to each footing with the required equivalent 0.18% ratio.

$$\rho_{t \text{ or } l} = \frac{A_{s,t \text{ or } s,l} Perimeter f_y}{s_{s,t \text{ or } s,l} A_g 60} \quad \text{Eq. (3.3)}$$

where:

$\rho_{t \text{ or } l}$ = a ratio of the provided face reinforcement in longitudinal or transverse directions

$A_{s,t \text{ or } s,l}$ = a nominal area of the provided face reinforcement in longitudinal or transverse directions [in.²]

$s_{s,t \text{ or } s,l}$ = spacing of reinforcement in longitudinal or transverse directions [in.]

3.4.3.1. Longitudinal Side Face Reinforcement

The quantity of longitudinal (horizontal) side face reinforcement in each footing is examined in terms of an average reinforcement ratio using Figure 3.14. The range of the collected longitudinal face reinforcement ratios is 0.08% to 0.43%, with an average ratio of 0.25% as shown in Figure 3.14. Longitudinal side face reinforcement was provided for the majority of footing plans (30 out of 35 total), although not provided for five footing plans in Houston. In all, 22 footing plans (63% of the total footing plans and 73% of footing plans having side face reinforcement) contain a longitudinal face reinforcement ratio greater than 0.18%, which is the requirement for shrinkage and temperature reinforcement of AASHTO LRFD (2020).

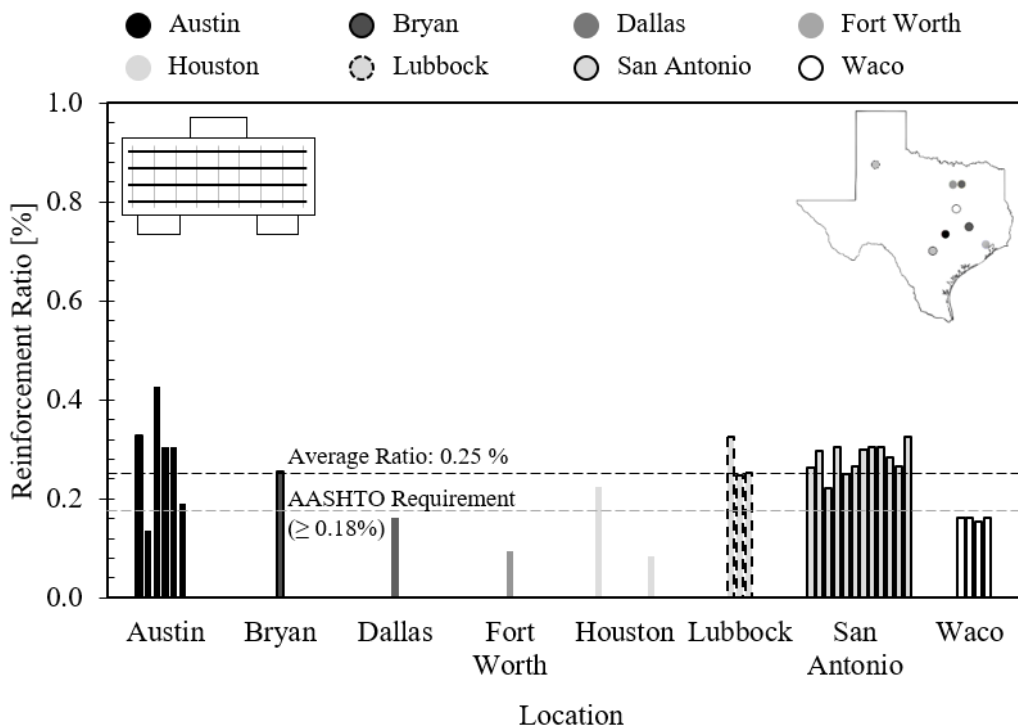


Figure 3.14 Average longitudinal side face reinforcement ratios of collected footing plans

3.4.3.2. Transverse Side Face Reinforcement

The quantity of transverse (vertical) side face reinforcement for each footing plan was also examined in terms of average reinforcement ratio using Figure 3.15. It should be noted that the Fort Worth footing plan was excluded due to the insufficient and ambiguous information regarding transverse side face reinforcement. The collected footing in Fort Worth used hooked bars for the bottom reinforcement, and both ends of the hooked legs reach the top reinforcement. Considering this type of reinforcement as transverse face reinforcement is debatable because the upper ends of the hooked bottom reinforcement are not fully

configurations of dowel bars connecting columns to footings are common among the database plans. The most prevalent detail is hooked dowel bars sitting directly above the bottom reinforcement, which is the case in all plans except for those of Fort Worth. In the case of Fort Worth, these dowels are anchored below the bottom reinforcement.

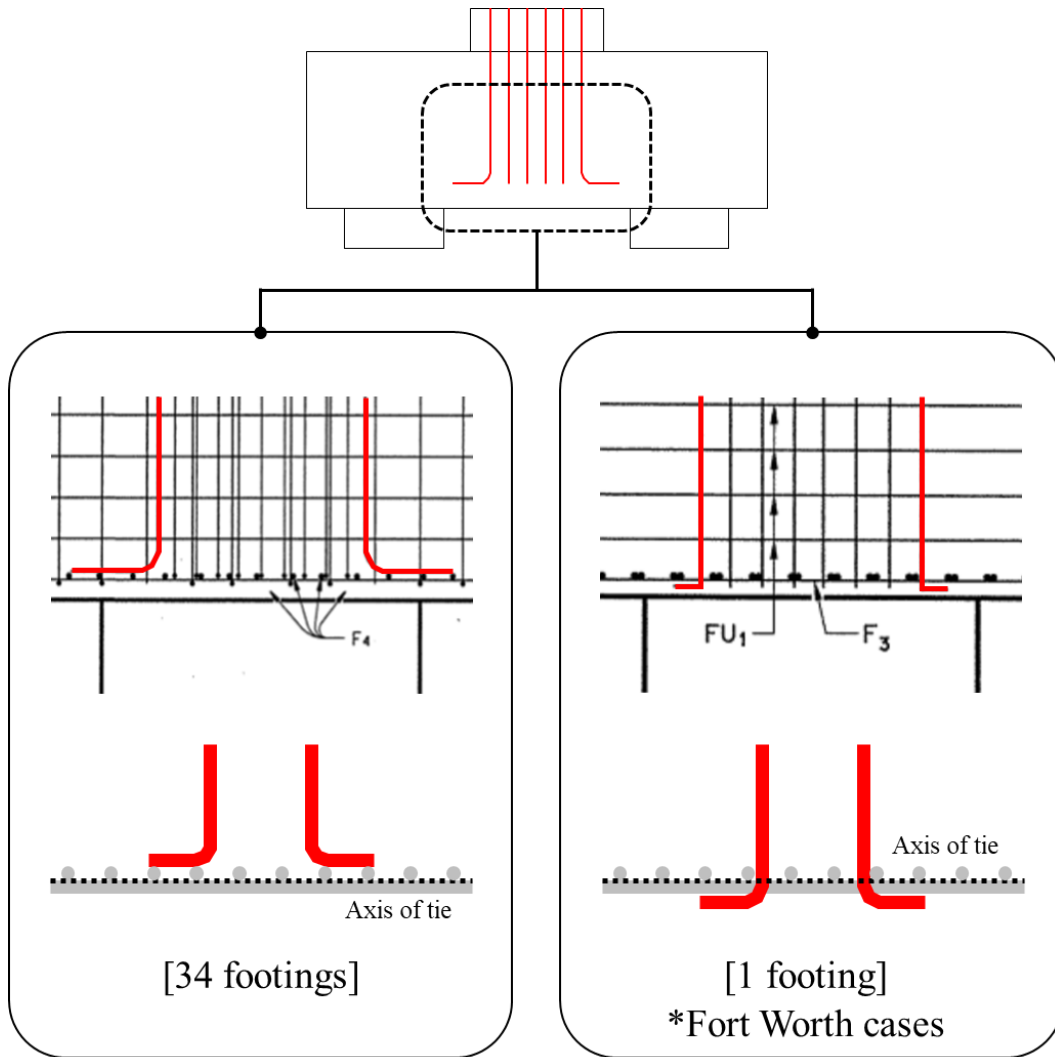


Figure 3.17 Two types of dowel bars coming from columns in the TxDOT Drilled shaft footing database

3.4.5. Shaft Reinforcement

In contrast to the column dowels, the shaft dowels did not always extend to the top reinforcement of footings. Since three of the footing plans did not contain detailed information on drilled shafts, 32 footing plans were reviewed in this section. Straight bars for shaft reinforcement were employed for all 32 cases. The provided lengths of the dowel bar extending into the footings were reviewed relative to a provision pertaining to tension development length for straight bars in AASHTO

LRFD (2020) (Article 5.10.8.2), which was adapted from ACI 318-14 (2014). The required development length, $l_{d,req}$ [in.] should satisfy the following requirement. This length can be also modified by multiplying several factors in accordance with AASHTO LRFD (2020) (Article 5.10.8.2.1a), provided here as Eq. (3.4). Generally, the minimum of reinforcement confinement factor (λ_{rc}) of 0.4 was applied for all cases since the center-to-center spacing and the distance from bars to the nearest concrete surface were much larger with respect to the diameter of shaft reinforcement. Other factors were not applicable to database or assumed conservatively.

$$l_{d,req} = 2.4d_{b,shaft} \frac{f_{y,shaft}}{\sqrt{f'_c}} \times \left(\frac{\lambda_{rl} \times \lambda_{cf} \times \lambda_{rc} \times \lambda_{er}}{\lambda} \right) \quad \text{Eq. (3.4)}$$

where:

- $d_{b,shaft}$ = the nominal diameter of a shaft dowel bar [in.²]
- f'_c = specified compressive strength of concrete at 28 days [ksi]
- $f_{y,shaft}$ = yield strength of shaft reinforcement (No. 11 bar and smaller and less than 100 ksi) [ksi]
- λ_{rl} = reinforcement location factor
- λ_{cf} = coating factor
- λ_{rc} = reinforcement confinement factor ($0.4 \leq \lambda_{rc} \leq 1.0$)
- λ_{er} = excess reinforcement factor
- λ = concrete density modification factor

The required development length is compared to the provided length of dowel bars, $l_{d,prov}$, specified in each drawing as shown in Figure 3.18. It can be confirmed that most of the collected footing plans (30 of 32 footing plans) satisfy the requirement. Furthermore, Figure 3.19 depicts that some footing plans (four footing plans constructed in Waco) provided short spliced hooked bars that effectively extended shaft reinforcing to the top of the footing and decreased the development length by the hooked end, but they do not extend beyond the top reinforcement and do not connect at all to the shaft reinforcement.

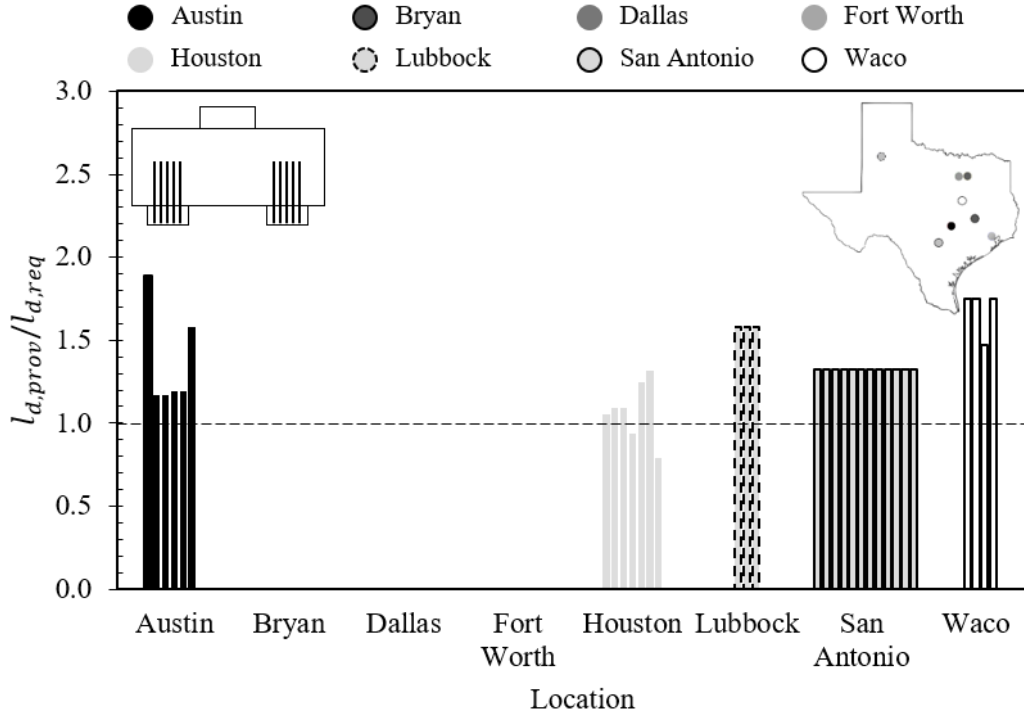


Figure 3.18 Ratio of provided to required lengths of dowel bars coming from shafts

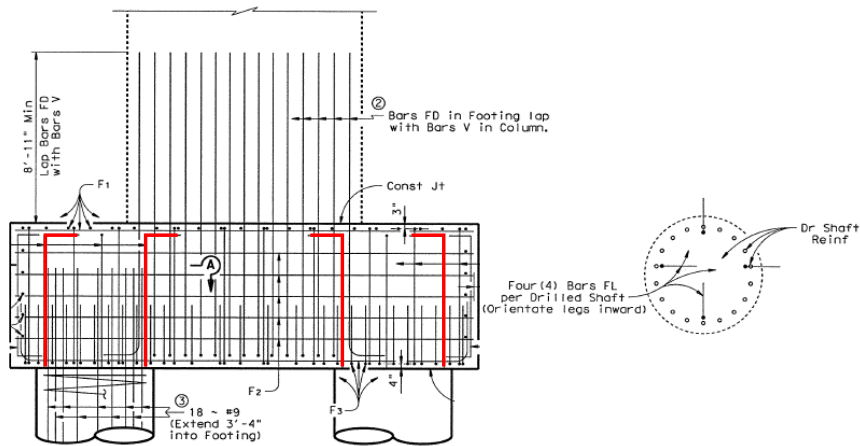


Figure 3.19 Details of hooked dowel bars spliced to dowel bars coming from shafts

3.5. Summary and Discussion

This chapter presented the findings from the review of the TxDOT bridge plan database constructed for this project. Table 3.2 summarizes geometric properties and Table 3.3 summarizes reinforcement details.

Table 3.2 Summary of TxDOT plan database (Geometry)

Properties		Min.	Average	Max.
Span-to-Depth Ratio (z/d)		1.30	1.86	2.77
Footing Dimensions	Equivalent Length (L_e)	132 in.	221 in.	294 in.
	Depth (H)	48 in.	60 in.	84 in.
	H/L_e	0.20	0.28	0.39
Column Dimensions	Aspect Ratio	1.56*	1.74	2.25
	Column-to-Footing Area Ratio	7 %	13 %	23 %
Drilled Shaft Dimensions	Diameter (D_{DS})	30 in.	52 in.	72 in.
	D_{DS}/L_e	0.18	0.24	0.29

* Footing plan with a circular shaped column was excluded

Table 3.3 Summary of TxDOT plan database (Reinforcement)

Properties		Min. Ratio	Average Ratio	Max. Ratio
Bottom Mat Reinforcement		0.21 %	0.37 %	0.60 %
Top Mat Reinforcement		0.05 %	0.16 %	0.31 %
Side Face Reinforcement	Longitudinal	0.08 %	0.25 %	0.43 %
	Transverse	0.04 %	0.11 %	0.23 %

- Most of the footings (31 out of 35 total) are square-shaped, and all columns are rectangular-shaped; the average aspect ratio is 1.86.
- A minor positive relationship between bottom reinforcement ratios and span-to-depth ratios was observed in footings constructed in the period from 2004 to 2014.
- The banding configuration was used for bottom reinforcement of several footings (5 out of 35 total), concentrating an average of 80% total reinforcement within band widths.

- The hooked anchorage of the bottom reinforcement was used only in some footings (4 out of 35 total), and all top reinforcement used straight bars for its anchorage.
- With the exception of 13 cases, all footing plans contain a longitudinal face reinforcement ratio greater than 0.18%, which is the requirement for shrinkage and temperature reinforcement of AASHTO LRFD (2020).
- In contrast, most of the footings have a much smaller amount of transverse face reinforcement than that of longitudinal face reinforcement.
- All dowel bars coming from columns are placed on bottom mat reinforcement except in one footing plan constructed in Fort Worth, in which the dowel bars extend below the bottom reinforcement.
- With the exception of two footing plans, all dowel bars coming from shafts satisfy the tension development length assuming their full yield strength specified in AASHTO LRFD (2020).
- Some footing plans (four cases constructed in Waco) used hooked bars, which are spliced to straight dowel bars coming from shafts, to reach top reinforcement and decrease the development length.

Chapter 4. Experimental Program – Phase I: Uniform Compression in Drilled Shafts

4.1. Overview

A comprehensive experimental program comprising a series of large-scale drilled shaft footing specimens subjected to uniform compression loading—Phase I testing—was planned and conducted as part of the research project. The objectives of this experimental program were to understand the structural behavior of a large-scale footing with uniform compression in drilled shafts and to investigate the effects of various design parameters on the structural response. The analysis of test results was used to validate the numerical models of Chapter 7 and to inform the new design recommendations of Chapter 8. The test program is subdivided into five series of tests to elucidate the strength and serviceability effects of the following variables: bottom mat reinforcement details (Series I), strut inclination (Series II), shaft diameter (Series III), face reinforcement (Series IV), and footing depth (Series V). In this chapter, Section 4.2 describes the design variables and the details of design and testing setup for the large-scale footing specimens. Section 4.3 presents and discusses the results of the structural tests conducted on the footing specimens.

4.2. Experimental Program

4.2.1. Test Variables

Phase I testing program was designed to examine different design parameters that are expected to affect the structural performance of a drilled shaft footing; these parameters may also influence the definition of the 3D strut-and-tie model representing the internal flow of forces. Figure 4.1 illustrates the typical 3D strut-and-tie model of a drilled shaft footing subjected to uniform compression loading. It is assumed that the loading from column can be divided equally into four quadrants and applied at the center of each quadrant. The bottom nodes can be developed at the center of drilled shafts at the elevation of the centroid of bottom mat reinforcement. Ties connect between bottom nodes and struts develop between top and bottom nodes. The detailed strut-and-tie model and calculations will be described in Section 4.4.

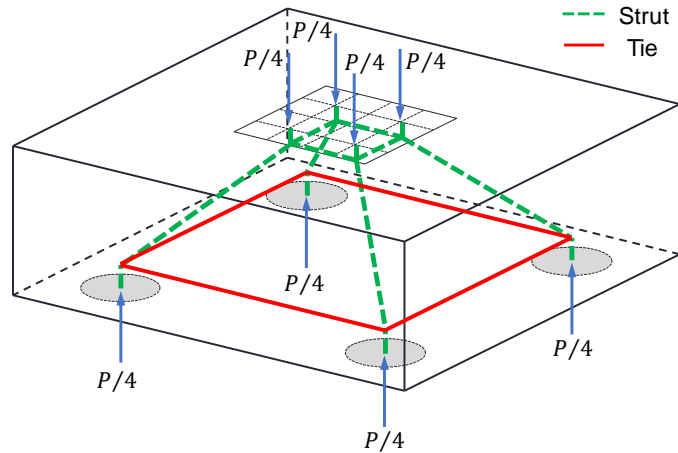


Figure 4.1 Generalized 3D strut-and-tie model for drilled shaft footings subjected to compression loading

Table 4.1 summarizes the matrix of test parameters. The geometry and test variables were comprehensively investigated and selected, as reported in Chapter 2 and Chapter 3. Test variables were independent for each series. It should be noted that bottom mat reinforcement details of specimens from 5 through 13 in Table 4.1 were determined by the conclusion of Series I testing as explained in Section 4.3.2. Test No. 7 is the baseline model to compare the results with different specimens except Series I. The research significance and objectives of the selected design parameters is described below.

Table 4.1 Test matrix of Phase I testing

Series	Test No.	Length x Width $L_1 \times L_2$ [in.]	Bottom mat of reinforcement		Strut inclination z/d [in.]	Shaft diameter D_{DS} [in.]	Side face reinf. ratio ρ_{face} [%]	Footing depth H [in.]	
			Layout	Anchorage					
I	1	96 x 96	Grid	Straight	1.70	16	0.30 [‡]	32	
	2 ^{**}	96 x 96	Grid	90-degree Hooked					
	3	96 x 96	Banded	Straight					
	4	96 x 96	Banded	90-degree Hooked					
II	5	96 x 72	Grid	90-degree Hooked	1.10	16	0.30 [‡]	40	
	6	96 x 96			1.35				
	7 [*]	96 x 132			1.70				
III	8	96 x 132			1.70	12	16	0.30 [‡]	40
	7 [*]	96 x 132				16			
	9	96 x 132				20			
IV	10	96 x 132			1.70	16	0.00	40	
	11	96 x 132					0.18 [†]		
	7 [*]	96 x 132					0.30 [‡]		
V	12 ^{**}	96 x 96			1.70	16	0.30 [‡]	32	
	7 [*]	96 x 132						40	
	13	96 x 164						48	

* Test No. 7 provides data for Series II through V

** Test No. 2 and Test No.12 have different amount of bottom mat reinforcement

† Shrinkage and temperature reinforcement per AASHTO LRFD (2020) Article 5.10.6

‡ Crack control reinforcement for deep planar members per AASHTO LRFD (2020) Article 5.8.2.6

4.2.1.1. Series I: Bottom Mat Reinforcement Details

Series I investigated the effects of bottom mat reinforcement configuration (grid vs. banded) and the anchorage type (straight vs. 90-degree hooked) on the structural performance of a footing specimen. A grid layout is defined as the uniform distribution of reinforcement over the entire cross section. In a banded layout, the reinforcing bars are located in the bandwidth such that the spreading area is extended by 45 degrees from the edge of the drilled shaft, according to TxDOT Bridge Design Guide (2020) as illustrated in Figure 4.2. According to the literature review in Chapter 2, banding of the bottom mat reinforcement within the bandwidth of a footing generates high structural efficiency compared to evenly distributed bottom mat reinforcement over the cross section. However, the design parameter review in Chapter 3 reported that banded layout was not preferable in current design

practice for two reasons. First, the use of banding results in a net increase of bottom mat reinforcement by adding secondary reinforcing bars to satisfy crack control reinforcement requirements. Moreover, the protruding drilled shaft reinforcement can congest the region near the shafts when the banding of bottom mat reinforcement is adopted. In addition to the bar layout, anchorage of the bottom mat reinforcement is also critical to ensure full-yield strength of reinforcement. Nevertheless, it is uncertain how to measure the provided development length of bottom mat reinforcement above shafts due to the complicated 3D nodal geometry in this region. Therefore, four different combinations of the bottom mat configurations were tested to identify the reinforcement layout and anchorage details that provide the most rational design based on structural performance (strength and serviceability) and constructability. The selection of the bottom mat configuration based on the analysis of test results in Series I was applied to the rest of the test series.

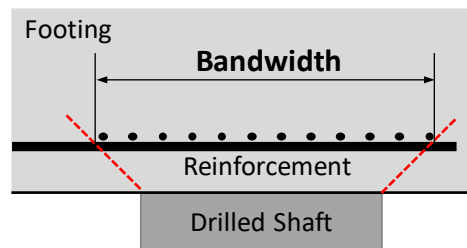


Figure 4.2 Definition of the bandwidth

4.2.1.2. Series II: Strut Inclination

The failure mechanism of a 2D deep structural member such as a deep beam is greatly influenced by the ratio of the shear span (a) to the effective member depth (d). At relatively small shear spans ($a/d < 1.2$), the failure is generally controlled by splitting the direct strut between the load and support. However, it gradually shows a transition to a diagonal tension mode, which is characteristic of sectional shear models as the shear span increases ($a/d > 2.0$). Similarly, the strut inclination of a drilled shaft footing, defined as the ratio of the column-to-shaft centerline distance (z) to the effective depth (d) in Figure 4.2, was selected as a test parameter to investigate its effect on the failure mechanism of a drilled shaft footing representing 3D deep structural members.

4.2.1.3. Series III: Shaft Diameter

Variation of the shaft diameter within a footing affects the bearing area of the node above drilled shafts and edge distance, which is defined as the shortest distance between the center of the shaft and the edge of the footing by Suzuki et al. (2008). As described earlier, the bearing area primarily contributes to the nodal strength of

a drilled shaft footing. Furthermore, the edge distance represents the amount of concrete surrounding the bottom node of the 3D STM developed in a drilled shaft footing as illustrated in Figure 4.1, and it directly relates to the triaxial confinement effect provided by the surrounding concrete. In general, the nodes in 3D STM are much more confined by the surrounding concrete than those in 2D STM, while current design examples (Williams et al., 2012) did not consider the confinement effect to add conservatism. Therefore, the relationship between bearing area and ultimate capacities of drilled shaft footings and the nodal efficiency due to the triaxial confinement effect were examined in the test results obtained from this test series.

4.2.1.4. Series IV: Side Face Reinforcement

According to Article 5.8.2.6 of AASHTO LRFD (2020), footing members do not need to satisfy the requirement of crack control reinforcement ratio (0.3% for each axis) that current 2D STM provisions specify to ensure a minimum ductility for redistribution of internal stresses in the region of struts. The 2D STM limits the nodal efficiency factors if a minimum amount of crack control reinforcement is not provided in accordance with both ACI 318-19 (2019) and AASHTO LRFD (2020) provisions. However, it is ambiguous whether side face reinforcement, which contributes to control cracks by temperature and shrinkage in the serviceability condition, plays a similar role in drilled shaft footings since face reinforcement is not located in the same plane as the 3D inclined struts contained within the footing. This is the reason why the minimum nodal efficiency factor defined in the Article 13.4.6.4 of ACI 318-19 (2019) is used for the 3D STMs of drilled shaft footings conservatively. However, the use of this efficiency factor has not been substantiated by any tests or analyses, although most of design examples presented in Chapter 3 had side face reinforcement. Therefore, testing the specimens with varying face reinforcement is beneficial to examine the effect of side face reinforcement on the strength and the serviceability of footing as well as to determine a minimum amount of face reinforcement required for the drilled shaft footings designed with 3D STM. Three variables of side face reinforcement ratio were selected for the objective. No side face reinforcement is representative of previous test specimens. The ratios required are 0.18% and 0.30%, to control cracks for the serviceability by temperature and shrinkage effect and to provide a minimal ductility by redistributing internal stresses in accordance with Article 5.10.6 and 5.8.2.6 in AASHTO LRFD (2020), respectively.

4.2.1.5. Series V: Footing Depth

Some legacy sectional methods would consider that the shear strength of the footing is proportional to the depth of the footing. However, a size effect (i.e., reduction of

ultimate shear stress with increasing effective depth) should be considered in design of large-scale structural members such as drilled shaft footings. The specimens designed in Series V will be tested to characterize this size effect.

4.2.2. Specimen Design

4.2.2.1. Footings Specimen

As shown in Table 4.1, details of a total of 13 footing test specimens were designed for Phase I testing. The geometry of each specimen was determined in accordance with the selected test parameters as shown in Figure 4.3 and summarized in Table 4.2. Detail drawings of the dimension for each specimen are provided in Appendix D. Each test specimen consisted of a deep footing section and a 4-in.-tall intersecting column section that was laterally encased with steel plates to prevent premature column failures, and four circular support plates were used to simulate drilled shafts.

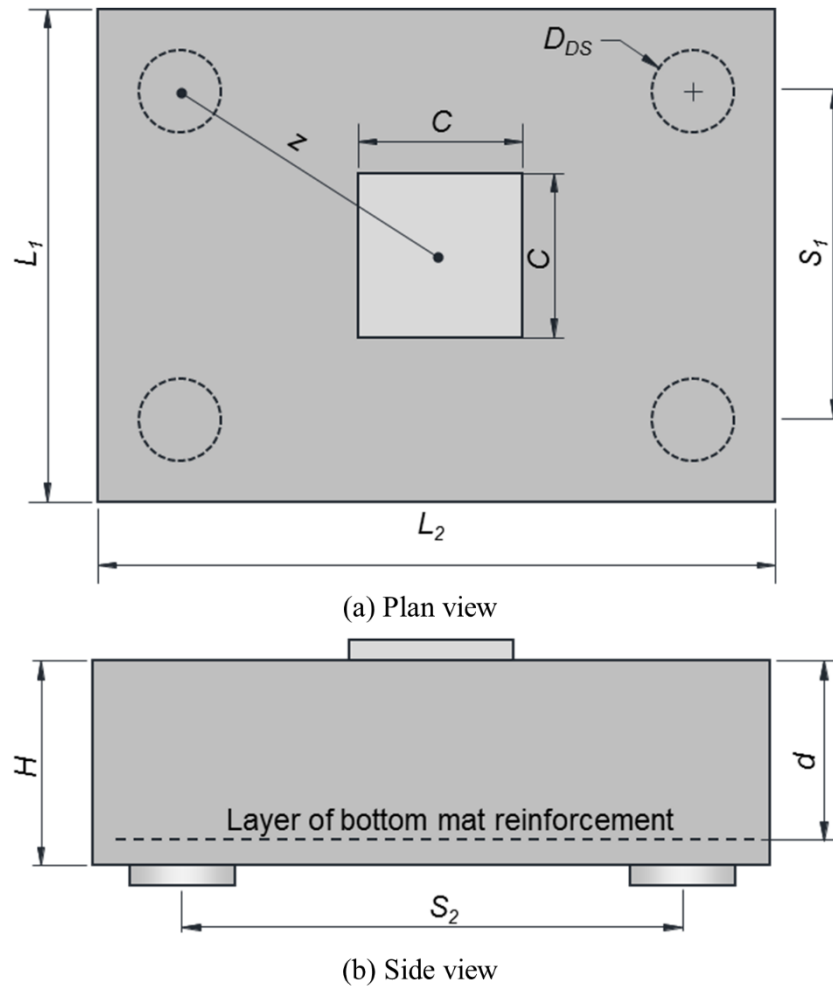


Figure 4.3 Geometry of a footing specimen

Table 4.2 Summary of dimensions of specimens

Series	Test No.	Specimen ID	L_1 [in.]	L_2 [in.]	H [in.]	S_1 [in.]	S_2 [in.]	D_{DS} [in.]	z [in.]	C [in.]
I	1	I-1	96	96	32	65.00	65.00	16	45.96	32
	2	I-2								
	3	I-3								
	4	I-4								
II	5	II-5	96	72	40	65.10	41.10	16	38.49	32
	6	II-6	96	96		66.75	66.75		47.20	
	7	II-7	96	132		64.00	100.25		59.47	
III	8	III-8	96	132	40	64.00	100.25	12	59.47	32
	7	II-7						16		
	9	III-9						20		
IV	10	IV-10	96	132	40	64.00	100.25	16	59.47	32
	11	IV-11								
	7	II-7								
V	12	V-12	96	96	32	65.00	65.00	16	45.96	32
	7	II-7	96	132	40	64.00	100.25		59.47	
	13	V-13	96	164	48	64.00	132.00		73.35	

4.2.2.2. Reinforcement Details

The reinforcement details of all specimens are summarized in Table 4.3. As discussed earlier, the bottom mat reinforcement configuration was selected for Series II through V based on the results of Series I testing as discussed in Section 4.3.2. In Series I testing, the combination of two layouts (grid vs. banded) and the anchorage type (straight vs. 90-degree hooked) was employed in order to investigate the effect of bottom mat reinforcing details, as shown in Figure 4.4. It should be noted that one bundle was placed outside of the bandwidth in I-3 and I-4 due to the limitations of clear spacing and the narrow bandwidth of scaled specimens. As a result of Series I testing, hooked bars were distributed evenly (grid layout) over the cross section for the bottom mat in all specimens of Series II through V.

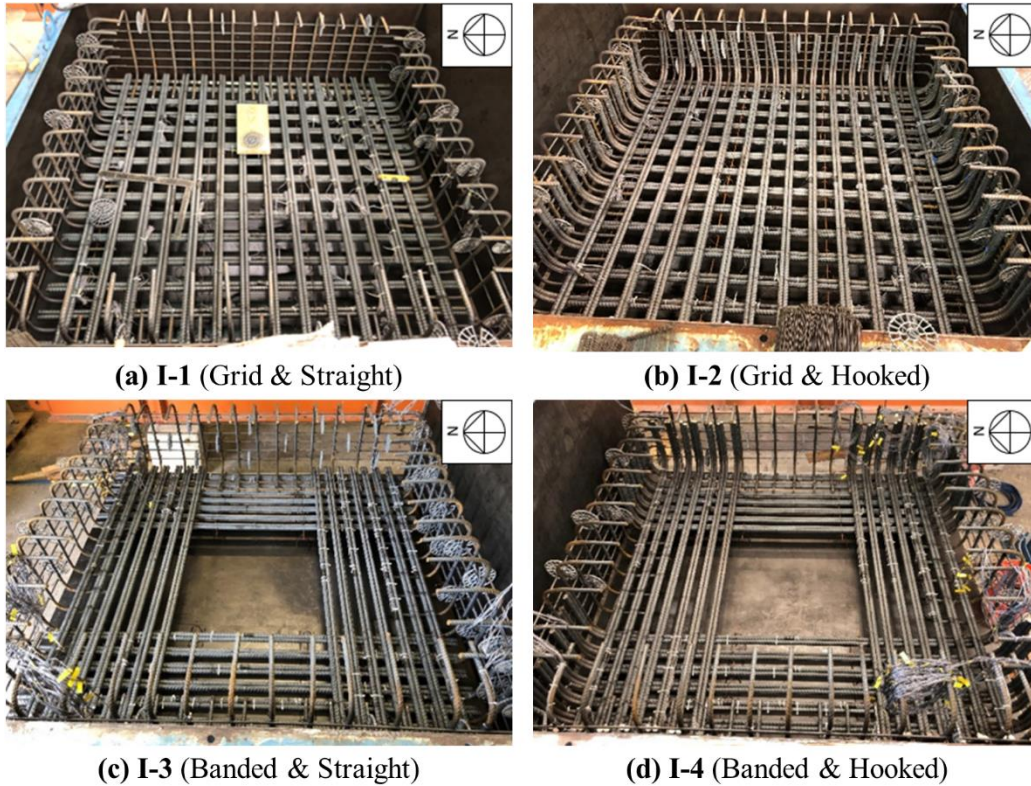


Figure 4.4 Bottom mat reinforcement configuration and anchorage of specimens in Series I

The amount of the reinforcement was determined on the basis of a series of finite element analyses so that failures of specimens would be induced by shear-critical failure mechanisms, which are related to nodal capacity in terms of STM. Investigating nodal region failure, not tie-yielding, in the footing specimens is critical to evaluate suitable strut and nodal strengths for the purposes of 3D STM refinement. Consequently, 0.85% and at least 0.96% of the reinforcement ratio were provided to the specimens in Series I and Series II through V, respectively. According to AASHTO LRFD (2020), at least 0.30% of side face reinforcement on each surface and along each axis was provided in all specimens except Series IV. Specimens of Series IV testing, which examined the influence of side face reinforcement ratio, contained different amounts of the side face reinforcement as a test parameter. Figure 4.5 depicts the typical reinforcement details.

Table 4.3 Summary of details of reinforcement

Specimen ID	Bottom mat reinforcement						Side Face Reinforcement		
	Layout	Anchorage	<i>d</i> [in.]	<i>L</i> ₁ (WE) - Direction	<i>L</i> ₂ (NS)- Direction	Avg. Ratio	Longitudinal	Transverse	Avg. Ratio
I-1	Grid	Straight	27.0	14-2x#8 at 6.00 in.	14-2x#8 at 6.00 in.	0.85%	#3 at 3.00 in.	#6 at 6.00 in	0.31%
I-2	Grid	Hooked	27.0	14-2x#8 at 6.00 in.	14-2x#8 at 6.00 in.	0.85%	#3 at 3.00 in.	#6 at 6.00 in	0.31%
I-3	Banded	Straight	27.0	7-2x#8 at 3.75 in. in the bandwidth	7-2x#8 at 3.75 in. in the bandwidth	0.85%	#3 at 3.00 in.	#6 at 6.00 in	0.31%
I-4	Banded	Straight	27.0	7-2x#8 at 3.75 in. in the bandwidth	7-2x#8 at 3.75 in. in the bandwidth	0.85%	#3 at 3.00 in.	#6 at 6.00 in	0.31%
II-5	Grid	Hooked	34.9	12-2x#9 at 5.00 in.	16-2x#9 at 5.00 in.	0.96%	#5 at 6.00 in.	#5 at 5.00 in.	0.34%
II-6	Grid	Hooked	34.9	16-2x#9 at 5.00 in.	16-2x#9 at 5.00 in.	0.96%	#5 at 6.00 in.	#6 at 5.00 in.	0.38%
II-7	Grid	Hooked	34.9	22-2x#9 at 5.25 in.	16-2x#9 at 5.00 in.	0.96%	#5 at 6.00 in.	#6 at 5.25 in. #6 at 5.00 in.	0.33%
III-8	Grid	Hooked	34.9	22-2x#9 at 5.25 in.	16-2x#9 at 5.00 in.	0.96%	#5 at 6.00 in.	#6 at 5.25 in. #6 at 5.00 in.	0.33%
III-9	Grid	Hooked	34.9	22-2x#9 at 5.25 in.	16-2x#9 at 5.00 in.	0.96%	#5 at 6.00 in.	#6 at 5.25 in. #6 at 5.00 in.	0.33%
IV-10	Grid	Hooked	34.9	22-2x#9 at 5.25 in.	16-2x#9 at 5.00 in.	0.96%	N/A	N/A	0.00%
IV-11	Grid	Hooked	34.9	22-2x#9 at 5.25 in.	16-2x#9 at 5.00 in.	0.96%	#4 at 6.00 in.	#5 at 5.25 in. #5 at 5.00 in.	0.22%
V-12	Grid	Hooked	27.0	16-2x#8 at 5.25 in.	16-2x#8 at 5.25 in.	0.98%	#5 at 8.00-in.	#6 at 5.25-in.	0.34%
V-13	Grid	Hooked	42.7	27-2x#10 at 5.50 in.	16-2x#10 at 5.00 in.	0.98%	#5 at 5.50 in.	#7 at 5.50 in. #7 at 5.00 in.	0.35%

Note: A-B#C at D (A: number of bars or bundles, B: if bundled, 2x, C: bar size, D: spacing)

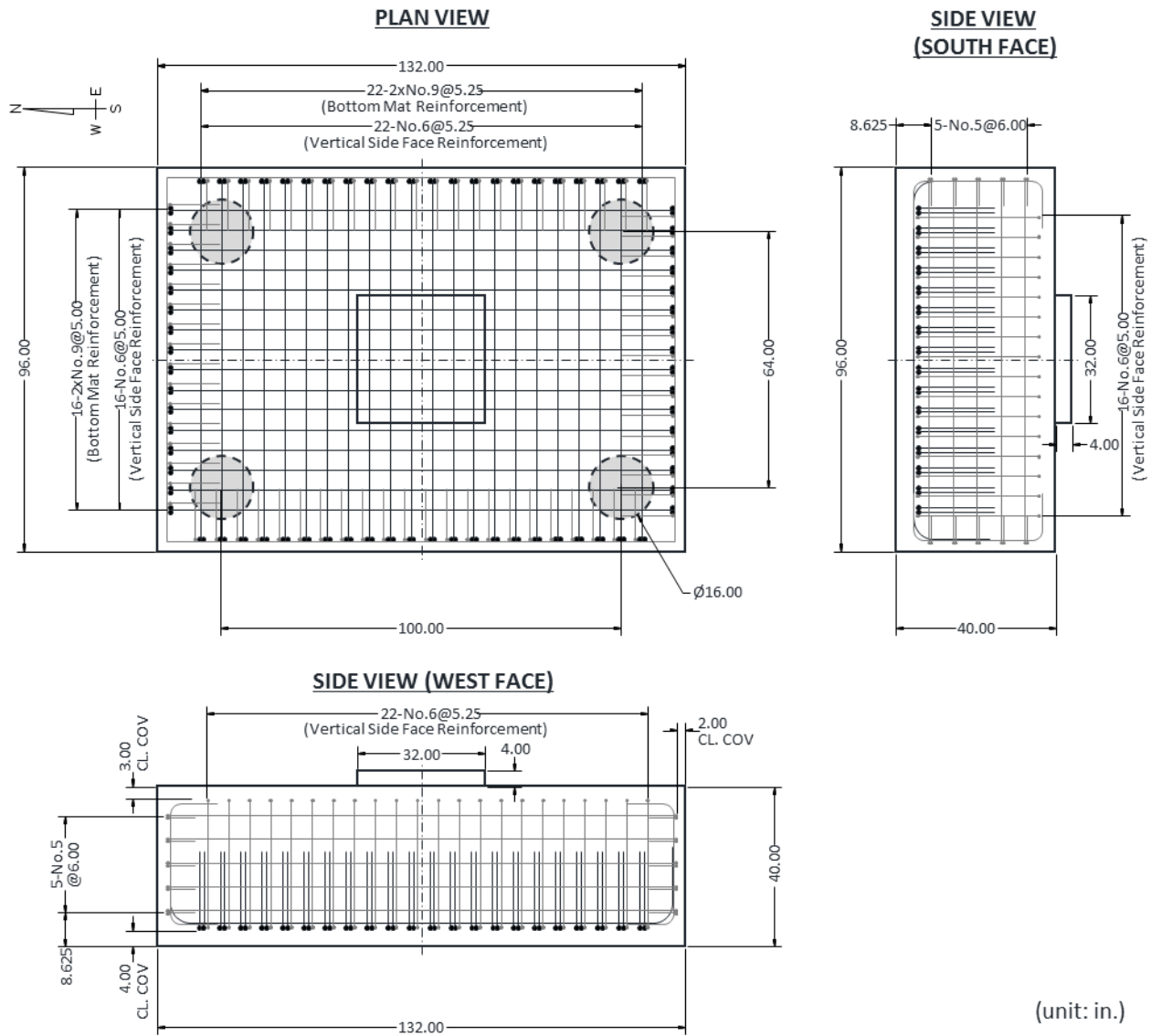


Figure 4.5 Drawings of reinforcing details (II-7)

4.2.2.3. Summary and Comparison with Previous Studies

Previous research studies have also conducted experimental programs on drilled shaft footings considering similar test parameters. However, the scale of the specimens was significantly smaller than actual footings constructed in bridge projects. Since the drilled shaft footings are deep elements governed by shear, the size effect should be considered. Therefore, the research team has designed specimens that are significantly larger than those considered in previous studies. In addition, size effect has been included as one test parameter (Series V) to observe its impact on the strength of a footing. The largest specimen designed in Phase I testing (V-13) is approximately half scale of the representative footings identified from TxDOT projects in Chapter 3 and considerably larger than previously tested specimens, as shown in Figure 4.6.

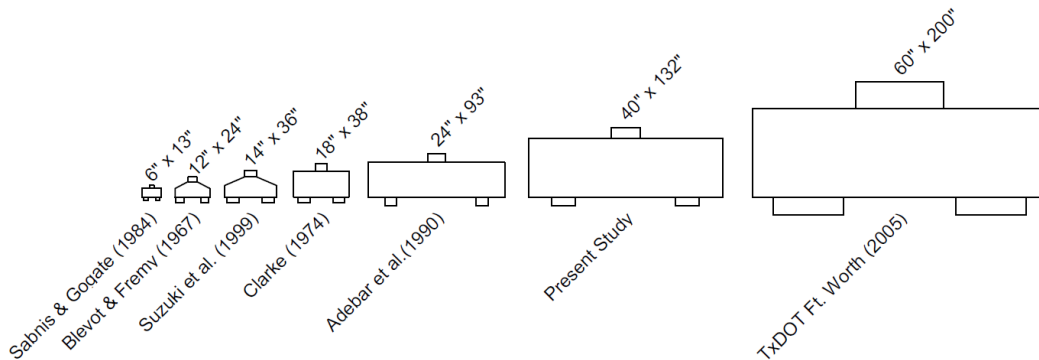


Figure 4.6 Historical scaled testing of footings relative to actual TxDOT example

Moreover, earlier researchers specifically focused on parameters affecting the ultimate strength of a footing. A parameter that can affect serviceability is side face reinforcement (Series IV), which has not been previously investigated. The face reinforcement on the side faces could allow redistribution of the internal stress in a footing even though it is not placed on the same axis of the strut forming inside the footing. Therefore, providing an appropriate amount of side face reinforcement may affect both serviceability and strength. The test results obtained from Series IV and analyses will be utilized to achieve a better understanding of this effect.

4.2.3. Materials

4.2.3.1. Concrete

- Mixture Design

The design concrete strength was taken to be 3.6 ksi, in accordance with what has commonly been used in practice, as summarized in Chapter 3. The two mixture designs that were provided by the concrete supplier for the casting of the specimens

in Phase I testing are summarized in Table 4.4. The difference between two design mixtures was the quantity of Class F fly ash, which affects long-term concrete compressive strength. Using a smaller quantity of fly ash helped prevent excessive increase in concrete strength over the long-term age.

Table 4.4 Concrete mixture design

Mixture design (Code)		A (S3135314)	B (S3130310)
Specimens		I-1, I-2, I-3, I-4, II-7	II-5, II-6, III-8, III-9, IV-10, IV-11, V-12, V-13
Mixture components	Type I/II cement [lb/yd ³]	352	338
	Class F fly ash [lb/yd ³]	118	112
	Fine aggregate [lb/yd ³]	1461	1479
	Coarse aggregate [lb/yd ³]	1915	1915
	Water [lb/yd ³]	250	250
	Water reducer [oz/cwt CM]	3.00 ~ 10.00	4.0
	High-range water reducer, [oz/cwt CM]	2.00 ~ 12.00	5.5
	Water-cementitious ratio	0.53	0.56
Maximum aggregate size [in.]		1.0	
Specified slump [in.]		7.0 ± 2.0	

- Material Tests

Mechanical properties of each material were examined through a planned series of material tests and utilized in the analysis of structural test results to obtain actual strength-based insights. Several types of concrete material test specimens, as shown in Figure 4.7, were prepared for the purpose of evaluating mechanical properties. Cylinders were stored fully submerged in a water tank (wet condition) in accordance with ASTM C31.



Figure 4.7 Concrete cylinders (left) and dog-bone direct tension specimens (right)

Relevant mechanical properties of the concrete were evaluated, including 28-day compressive strength, compressive strength at test day (i.e., test day of the parent footing specimen), and the modulus of elasticity (MOE) at test day. Figure 4.8 shows each material test. Results obtained from the concrete compressive strength testing and the MOE testing are summarized in Table 4.5. The capacity of diagonal struts forming in the footing specimens is governed by the tensile strength of concrete. In an effort to obtain tensile strength of concrete, direct tensile strength and split tensile strength were measured for all concrete cast on footing specimens. To measure the direct tensile strength, dog-bone shaped concrete specimens were fabricated and cured in the water until test day, as was done for cylinder specimens. After the evaluation of Series I test results, it was decided not to measure the direct tensile strength, and the split tensile strength was performed only for the remaining test series. Splitting tensile strength test was performed in accordance with ASTM C496. Split tensile strength testing, which is known as indirect tensile strength, is widely used in construction practice due to the simplicity of the test procedure and reliability of test results.

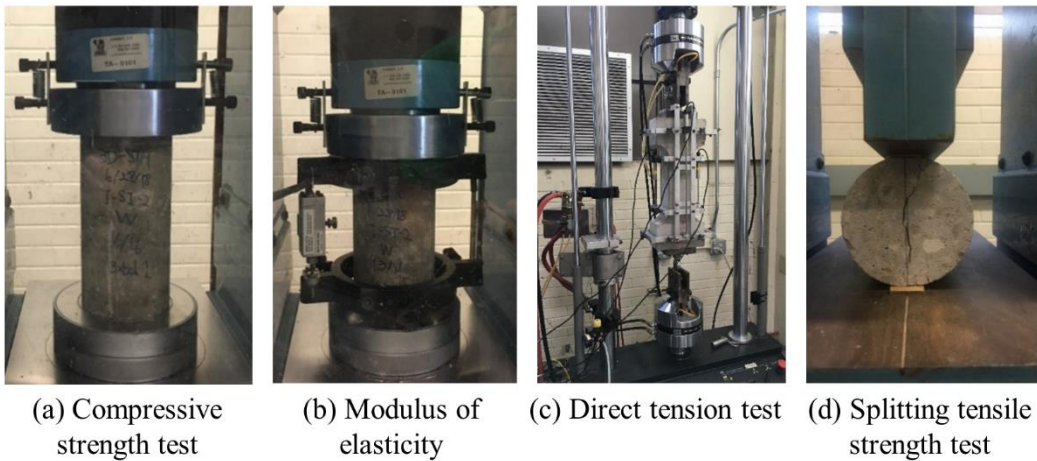


Figure 4.8 Concrete cylinder tests

- Test Results

Concrete material test results are summarized in Table 4.5.

Table 4.5 Measured Strengths of Cylinders

Specimen ID / Batch No.		Casting Date	28-days	Test Day			
			Compressive Strength (f'_c) [ksi]	Test Date	Compressive Strength (f'_c) [ksi]	Modulus of Elasticity (E_c) [ksi]	Tensile Test (f'_t) [ksi]
I-1	2	06/28/18	4.24	08/31/18	5.07	6,725	0.46 ¹⁾
I-2	1		4.36	09/17/18	5.22	6,753	0.53 ¹⁾
I-3	2	07/31/18	4.56	10/03/18	5.09	5,948	0.56 ¹⁾
I-4	1		4.45	10/12/18	5.06	5,835	0.53 ¹⁾
II-5	1	10/18/19	3.62	11/06/19	3.24	6,485	0.29
II-6	2		4.62	11/15/19	4.62	-*	0.38
II-7	1	04/17/19	5.39	07/12/19	6.74	6,556	0.67
	2		3.39		4.99	6,461	0.43
III-8	1	07/16/19	5.06	08/13/19	5.06	6,363	0.46
	2		4.25		4.25	6,645	0.35
III-9	2		4.25	08/06/19	3.29	6,645 ²⁾	0.35
	3		4.29		4.13	6,738	0.36
IV-10	1	06/7/19	4.17 ²⁾	07/3//19	4.81	5,224	0.45
	2		3.96 ²⁾		4.51	5,171	0.36
IV-11	2		3.96 ²⁾	07/22/19	4.33	5,724	0.48
	3		4.57 ²⁾		4.97	6,156	0.49
V-12	1	08/6/19	3.52	08/27/19	3.50	5,995	0.31
V-13	1	08/16/19	3.85	09/11/19	4.05	-*	0.33
	2		3.78		4.18	6,757	0.36

1) Result from direct tension test

2) Test was carried out 7 days after test due to the malfunction of test machine

3) Test was carried out 31 days after casting due to the malfunction of test machine

* Incomplete test data

4.2.3.2. Reinforcing Bars

Three reinforcement samples were tested for each reinforcing bar size and series used in the construction of the footing specimens, in accordance with ASTM A370. A summary of the average test results obtained for bottom mat reinforcements by series are provided in Table 4.6. Appendix E contains the detail test results for each specimen and Figure 4.9 depicts the test setup.

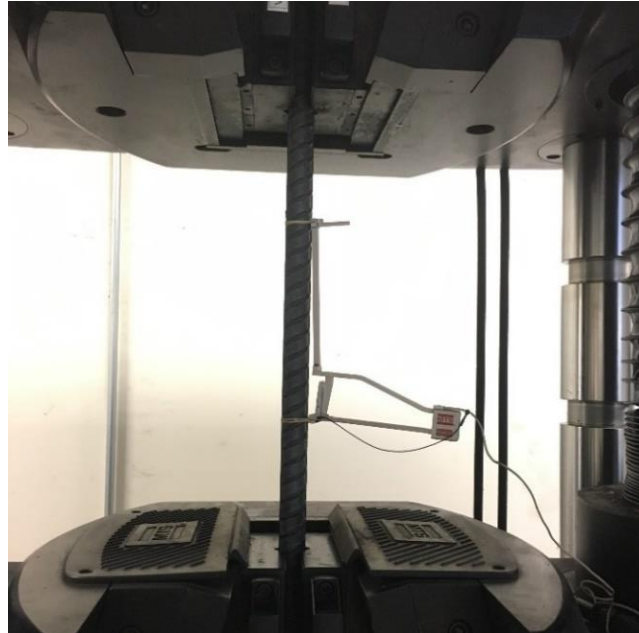


Figure 4.9 Reinforcement sample test

Table 4.6 Mechanical properties of bottom mat reinforcement

Specimen ID	Bar Size	Yield Strength (f_y) [ksi]	Tensile Strength (f_u) [ksi]
I-1	#8	71.9	106.4
I-2, I-3, & I-4	#8	64.1	107.6
II-5, II-6	#9	63.5	106.6
II-7	#9	62.8	105.8
III-8 & III-9	#9	67.5	108.2
IV-10 & IV-11	#9	78.3	113.2
V-12	#8	67.0	109.5
V-13	#10	68.2	103.7

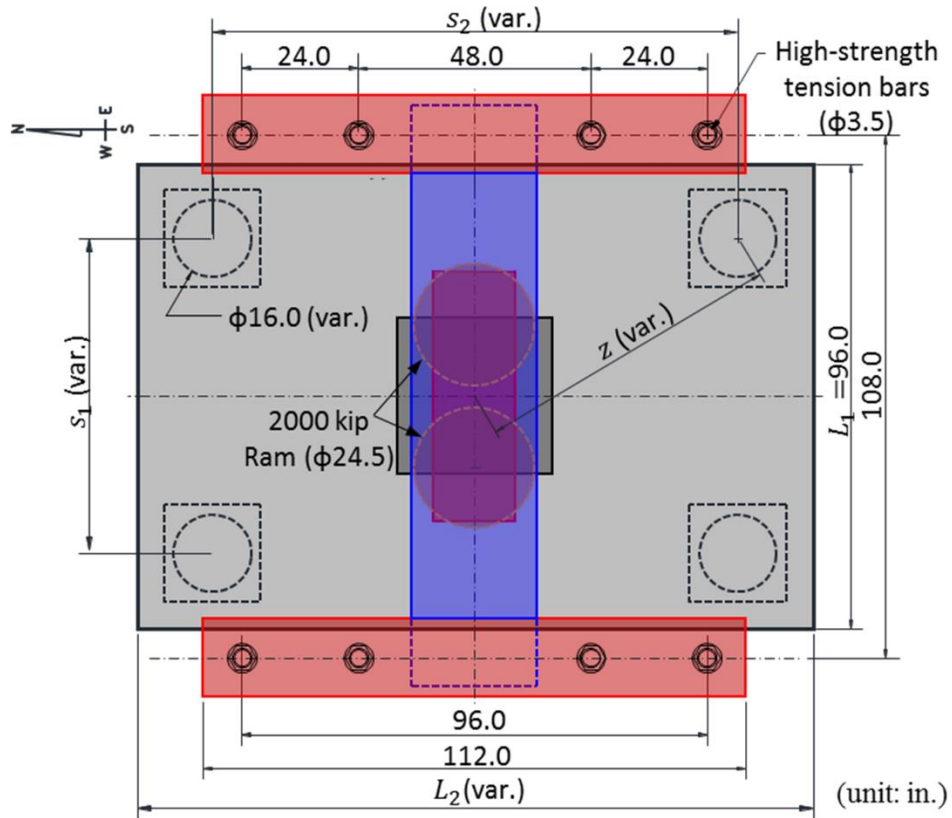
4.2.4. Testing Setup

4.2.4.1. Layout and Configuration

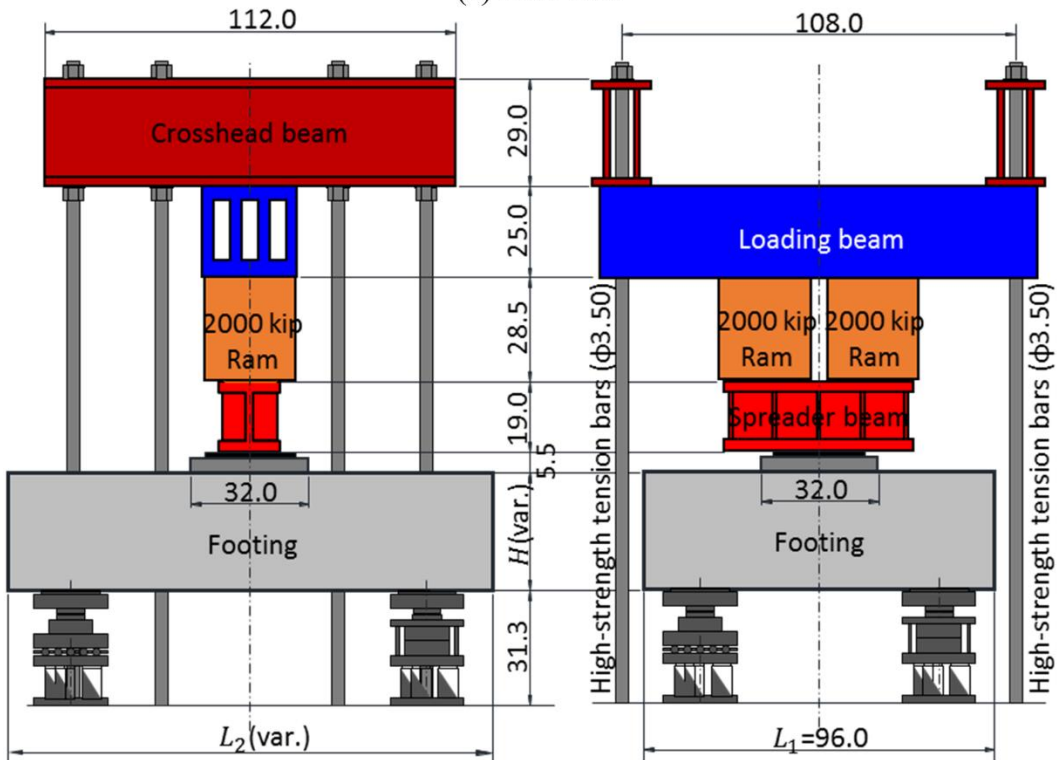
All specimens comprising Phase I were tested under uniform compressive loading only conditions, as shown in Figure 4.10. Figure 4.11 depicts the typical test setup configuration. The specimens were subjected to concentrated loads that were applied using two 2,000-kip capacity hydraulic rams that loaded the center-points of the specimens. The load was applied to the test specimens through a steel spreader beam and the rams reacted against a steel frame attached to the strong floor. In Figure 4.11, the distance between the center of the specimen and the centroids of the four supports is variable as it depends on the strut inclination and the dimension of the specimens. The test setup for II-7 through V-11 has the same configuration due to their identical dimensions.



Figure 4.10 Structural test setup



(a) Plan view



(b) Side view (East/West)

(c) Front view (North/South)

Figure 4.11 General test configuration for Phase I testing

4.2.4.2. Support Fixtures

Figure 4.12 shows the layout and restraint conditions provided by test supports. The support design and configuration were determined to avoid lateral and rotational restraint effects caused by the supports. The specimens were supported on circular steel plates representing the drilled shaft footings. The steel plates were 16 in. in diameter, except for two specimens in Series III testing, which were used to study the effects of the shaft diameter. III-8 and III-9 had 12 in. and 20 in. diameter steel discs, respectively.

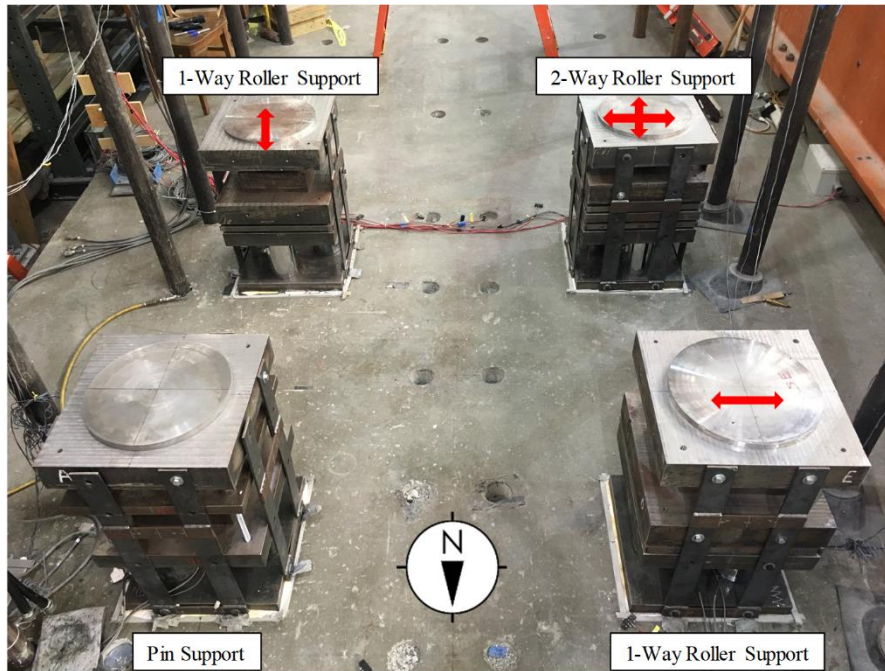
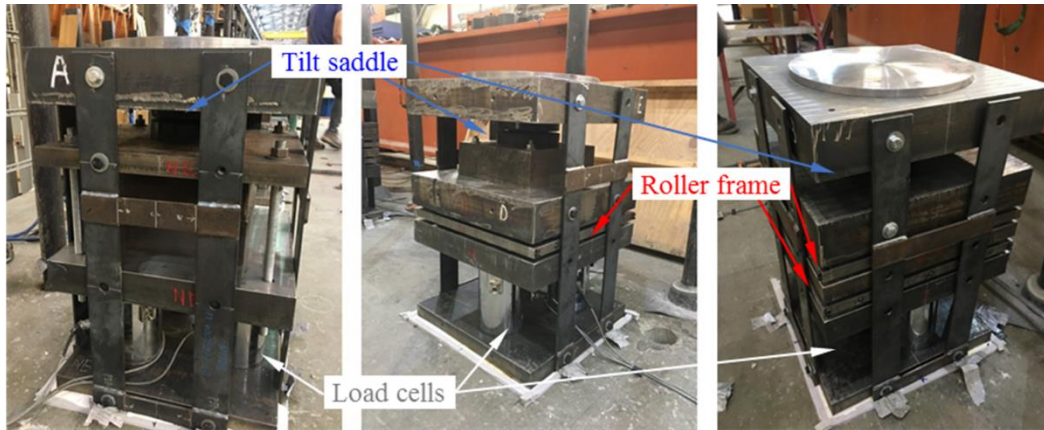


Figure 4.12 Layout of supports

The four bearing plates were designed to be supported by a pinned support fixture at one corner, two one-way roller support fixtures at the corners adjacent to the pin support, and a two-way roller support fixture at the corner opposite to the pinned support. Tilt-saddles were placed below the upper plates of each support fixture, as shown in Figure 4.13, which allowed the specimen to rotate at the support. Figure 4.14 shows the roller frames, which consist of five 2-in. diameter rollers that permitted the supports to translate freely. Three 500-kip capacity load cells were provided at the base of each support as a means of measuring the applied loading during structural testing, as well as the weights of the specimen, the loading frame, and the spreader beam.

All support fixtures were carefully designed to ensure proper functionality under the large-magnitude reactions that were anticipated to be developed. Furthermore, support fixtures were also fabricated precisely by milling and machining to ensure

that different support assemblies provided at each corner of the footing specimens maintained nominally identical support stack heights, permitting idealized boundary conditions.



(a) Pin support

(b) One-way roller support

(c) Two-way roller support

Figure 4.13 Support fixtures



(a) During fabrication

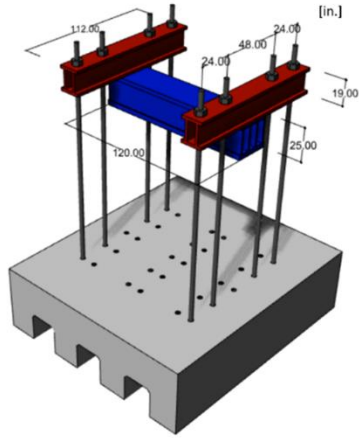


(b) After assembly

Figure 4.14 Roller frame

4.2.4.3. Loading Frame and Spreader Beam

Load was applied to the footing specimens using two 2,000-kip capacity hydraulic rams that were uniformly pressurized by means of one pneumatically controlled hydraulic pump. Figure 4.15 illustrates how the hydraulic rams reacted against a stiff loading frame that was connected to a reinforced concrete strong floor by way of eight high-strength steel rods. Loading frames with 29 in. height and 19 in. height were used for specimens with 32 in. depth and those deeper than 40 in., respectively. Figure 4.16 shows the spreader beam located below the hydraulic ram as a means of transferring the applied load from the rams to the footing specimen.

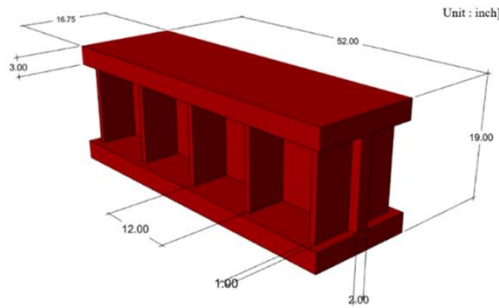


(a) Schematic drawing with dimension



(b) Loading frame during Installation

Figure 4.15 Loading frame



(a) Dimension



(b) Spreader beam after setup

Figure 4.16 Spreader beam

4.2.5. Fabrication of Specimens

- General Specimens

A summary of the overall test specimen fabrication procedures (applied to all specimens except for the largest, V-13) is depicted in Figure 4.17. Firstly, planned strain gauges were attached to reinforcement, and reinforcing cages were assembled in accordance with designed reinforcing details. After side forms had been installed and adjusted with top and bottom ties for desired dimensions, concrete casting was scheduled. The concrete casting was processed in two steps: casting the footing section first, and the 4-in.-high column section subsequently. Several key steps of the procedure are summarized in the following paragraphs.

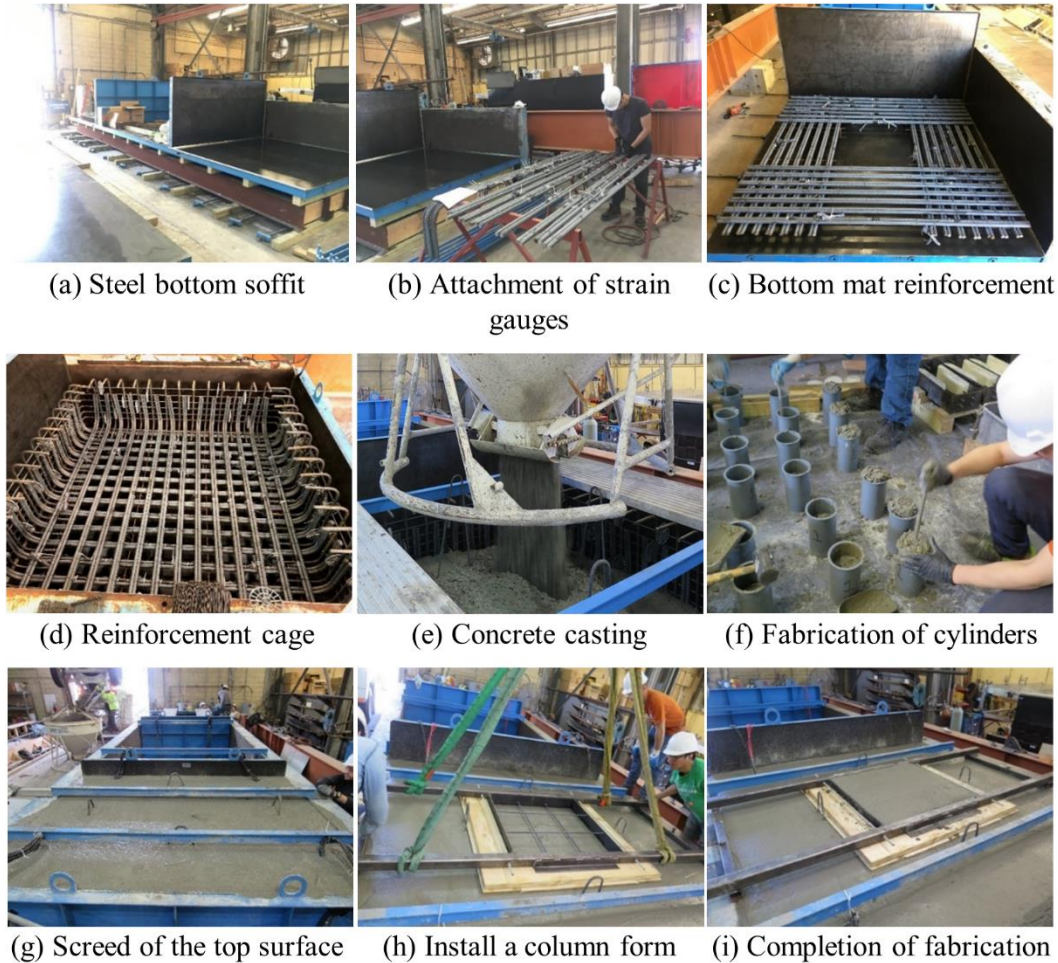


Figure 4.17 Procedure of specimen fabrication

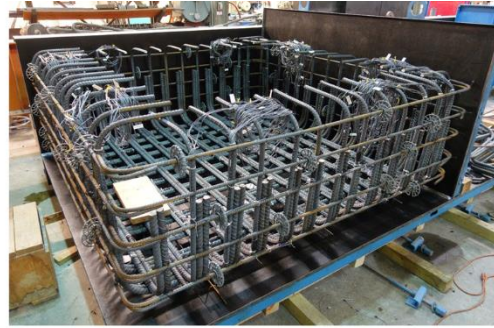
Before placing the bottom mat reinforcement, electrical resistance strain gauges (ERSGs) were attached at different locations on selected bars to measure strains during testing. The desired installation locations on the reinforcing bars were ground to ensure a flat surface. After installation, the ERSGs were painted with waterproof material and epoxy for protection from damage caused by physical impact, according to a lab procedure and the manufacturer’s guidelines. Bar stresses were estimated from the strain measurements and the tensile test results of reinforcing bars.

The lower layer of bottom mat reinforcement (provided in the north-south direction) was first placed to maintain the minimum vertical clear spacing requirement. Next, the upper layer of bottom mat reinforcement (provided in the east-west direction) was placed directly above the bottom layer and secured in place with the desired layout, using steel tie wire. Transverse side face reinforcement was placed after the bottom mat had been secured and, finally, the longitudinal side face reinforcement was placed last and tied to the outside surface of the transverse side

face reinforcing bars. Plastic spacers were anchored to the longitudinal side face bars to ensure satisfactory clear spacing was maintained between the rebar cage and the side forms. Figure 4.18 presents the completed reinforcing bar cages for the typical footing test specimens.



(a) I-2



(b) II-6

Figure 4.18 Typical rebar cage of Phase I testing

The steel formwork used to facilitate the concrete casting process is shown in Figure 4.19-(a). The modular forms were configured to accommodate three types of plan dimensions (72 in., 96 in., and 132 in. by 96 in.) at three heights (32 in., 40 in., and 48 in.) To cast the intersecting column stub, column formwork, which also served as column stub confining reinforcement, was designed as shown in Figure 4.19-(b).



(a) Bottom soffit and side forms



(b) Column form

Figure 4.19 Assembled formwork prior to concrete placement

The steel formwork permitted two footing test specimens to be cast simultaneously. Thus, the footing test specimens were cast two at a time; however, it should be noted that each footing test specimen, and its associated material test specimens, were cast using a single batch of concrete that was delivered via one ready-mix truck. Column stubs of the first four specimens were cast using the same concrete as in the footing specimens, and at the same time of concrete placement. The high-strength grouting mortar was cast a couple of days after the footing casting, instead

of at the same time as the concrete, to ensure high quality of construction and strength.

- The Largest Specimen (V-13)

The fabrication and handling of V-13, the largest in the series, required a unique approach due to its unprecedented size and weight. The special fabrication process is summarized below. The largest specimen weighed approximately 67 kips, which exceeds the rated lifting capacity of the overhead crane; therefore, the specimen was fabricated adjacent to the testing area and moved via skates attached beneath a traveler frame to the testing area, as shown in Figure 4.20. To accommodate the move, a custom-made bottom soffit formwork was fabricated in three parts—two bottom soffits on the side and one traveler frame at the center, as illustrated in Figure 4.21. The two side soffits were dismantled after casting and the center traveler frame carried the specimen over the support fixtures. Four skates under the center traveler were able to move V-13 by remarkably little force relative to the weight of the specimen. The center of the specimen was re-positioned by a crane or rams so that the specimen was positioned correctly relative to the skate rail and the center of supports for the safety and quality control of the loading test, respectively. The process is depicted graphically in Figure 4.22. The reinforcement cage was fabricated at the fabrication area where the research team had previously fabricated other specimens. Figure 4.23 shows that the cage was installed on the bottom soffit formwork of V-13 using the overhead crane. Significantly careful design and fabrication of the center traveler, as well as travel protocol, allowed V-13 to move without any critical concern about or damage to the specimen or the laboratory facilities, as shown in Figure 4.24 and Figure 4.25.

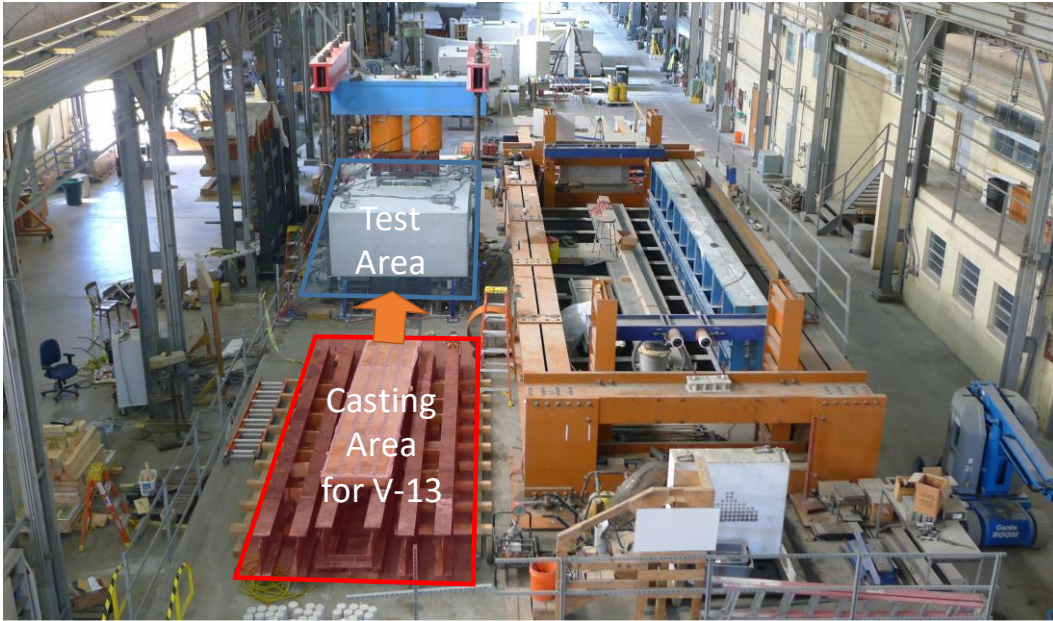


Figure 4.20 Aerial view of casting and testing area on the elevated slab at FSEL

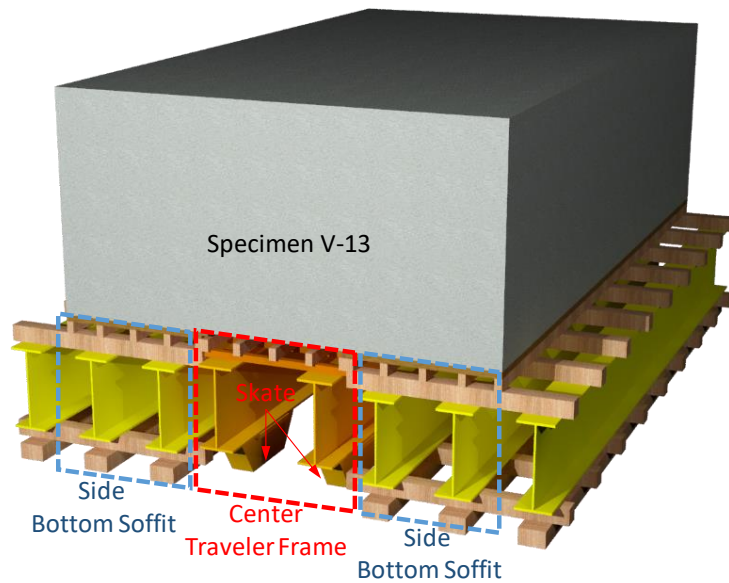


Figure 4.21 The section of the bottom soffit formwork for V-13

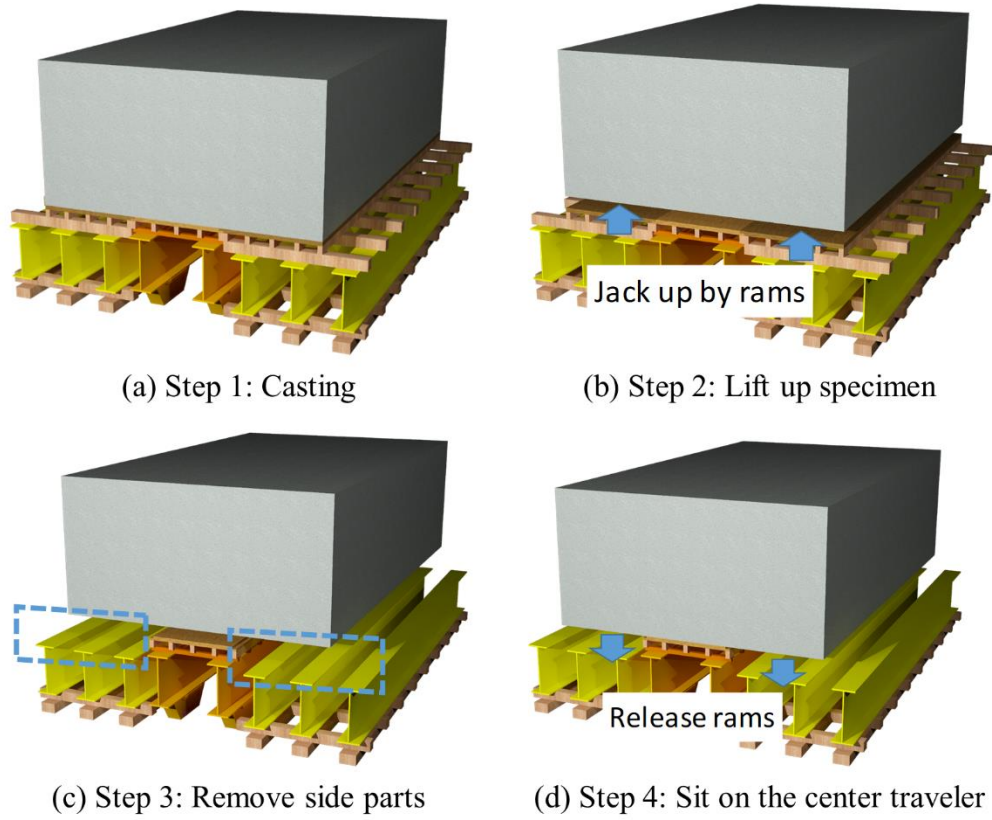


Figure 4.22 The process of removing the bottom soffit for V-13

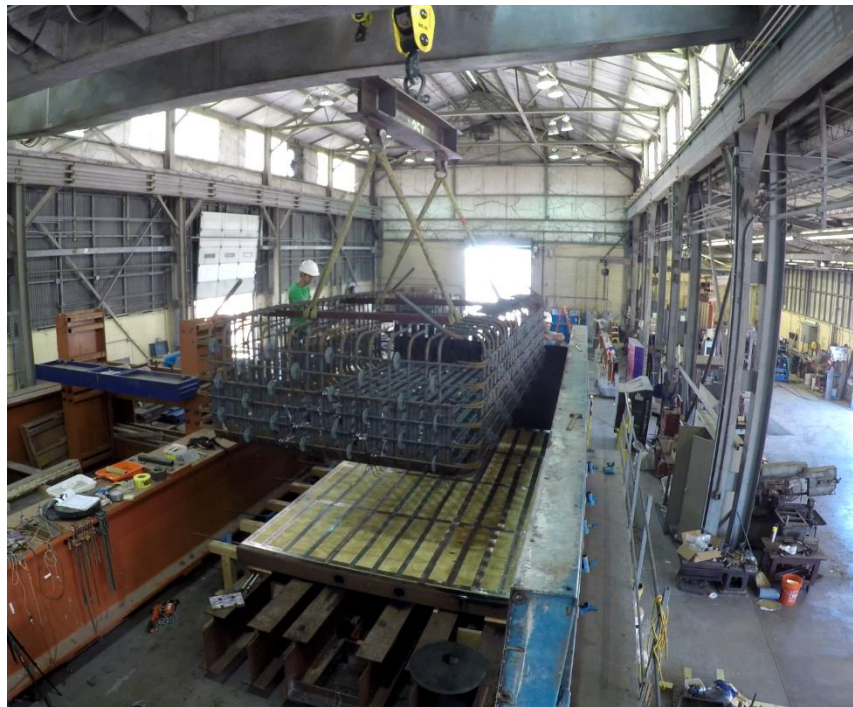


Figure 4.23 Moving reinforcement cage of V-13



Figure 4.24 Travelling of V-13 to test area



Figure 4.25 V-13 after setting up the loading test

4.2.6. Instrumentation

The test specimens were extensively instrumented to monitor reactions, displacements, and strain development over the course of testing. Figure 4.26 illustrates the instrumentation map of the typical specimen (II-7). Appendix D contains instrumentation maps for each specimen.

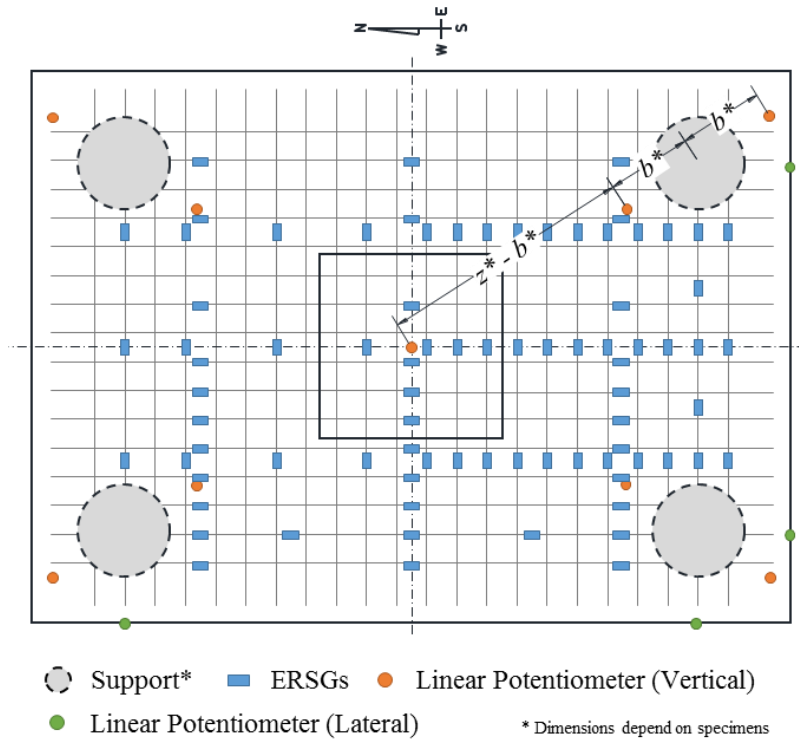


Figure 4.26 Instrumentation map of II-7

- Strain Measurements: Reinforcing bars

Stress development in the reinforcing bars will be estimated by means of measured ERSG measurements obtained from gauges installed during specimen fabrication (refer to Section 4.2.4). ERSGs were attached on selected bottom mat and side face reinforcement locations where large values of strains were expected—for example, the vicinity of drilled shafts and the mid-span of side faces. Figure 4.27 shows the attached ERSG.

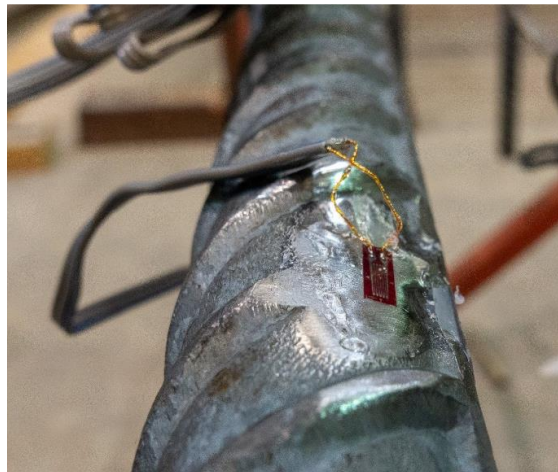


Figure 4.27 ERSG attached on reinforcement to measure strains

- Load and Displacement Measurements

The load for each test was measured using a total of twelve 500-kip capacity load cells (refer to Figure 4.28) that were placed beneath the support fixtures. These load cells monitored the self-weight and the loading frame weight during the initial placement of the specimens and the test frame components, and also the applied loading during structural testing. Figure 4.29 shows that linear potentiometers were placed on the bottom surface of the footings, below the loading point and near the four supports, to measure the vertical displacements at the loading point and at the location of supports, respectively. In addition, linear potentiometers were provided on the side surfaces of the specimen to monitor lateral displacement.



Figure 4.28 Load cells in the support fixtures

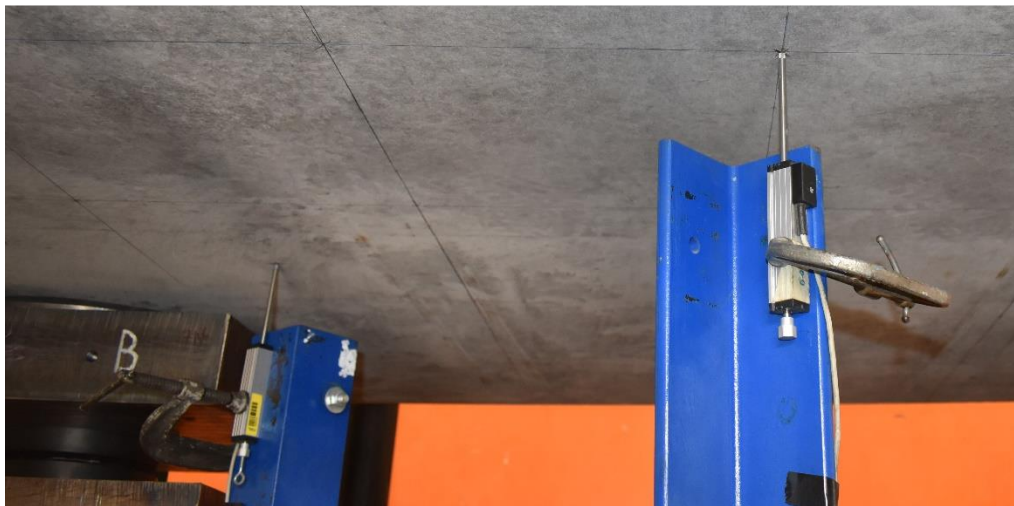
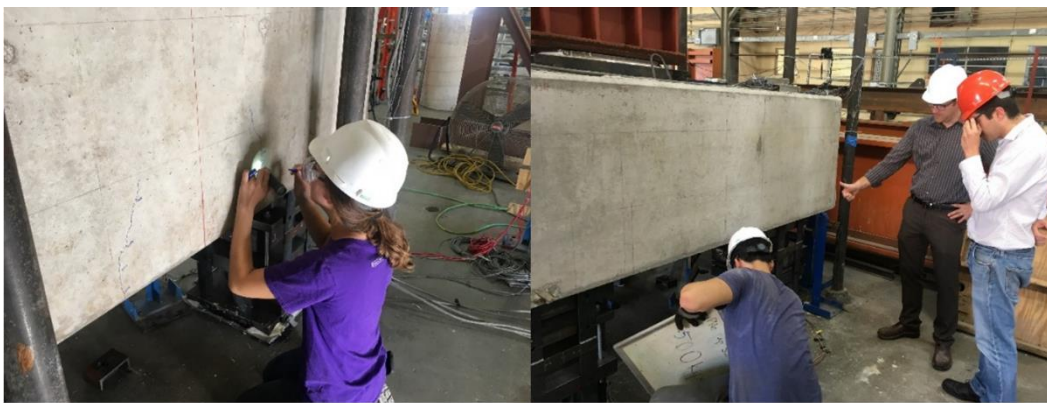


Figure 4.29 Linear potentiometers to measure displacements on the bottom surface

4.2.7. Test Procedure

Loading was applied using a series of predefined stages, each corresponding to an increase in the load level that is smaller than one-tenth of the nominal capacity estimates obtained from preliminary nonlinear finite element analyses (FEA). As a result, typical load increments of 100 kips were employed. A monotonically increasing and quasi-static loading was applied at each loading stage. Upon reaching each of the predefined load levels, the condition of the specimens was visually inspected and documented via crack mapping and digital photographs as shown in Figure 4.30. The performance of all digital instrumentation and monitoring equipment was verified during test. The specimen was subsequently subjected to a higher level of load until footing failure occurred.



(a) Visual check on side surfaces

(b) Optical check by high-resolution camera (GoPro) on bottom surface

Figure 4.30 Crack mapping at predefined loading stages

4.3. Experimental Results and Discussion

4.3.1. Summary of Experimental Results

In this section, observations and measurements from the specimens during and after tests are presented and discussed in depth from a variety of viewpoints: visual observations, load-deflection behavior, and strain distribution in bottom mat reinforcement at ultimate state to investigate the effect of each test variable on the structural performance of drilled shaft footings. Comparison and discussion of results for each series are provided in the following sub-sections; detailed data for all specimens are provided in Appendix F. The following paragraphs explain how the research team interpreted the results from each perspective. The notations used in this section are listed as follows:

$f'_{c,test}$ =	Average compressive strength of concrete for each batch at the time of testing measured in accordance with ASTM C39 [ksi]
f_{yb} =	Yield strength of bottom mat reinforcement measured in accordance with ASTM A370 [ksi]
z =	Shear span, distance from the centroid of the footing to the center of the shafts [in.]
d =	Effective depth, distance from top surface to centroid of bottom mat reinforcement [in.]
z/d =	Strut inclination, the slope of shear span with respect to effective depth
ρ_{face} =	Average side face reinforcement ratio [%]
P =	Total applied load [kip]
$P_{cr,v}$ =	Load at cracking on the side face by visual inspection [kip]
P_y =	Load at the first yielding of bottom mat reinforcement [kip]
P_u =	Ultimate load of the test specimen [kip]
P_N =	Normalized applied of the test specimen ($= \frac{P}{f'_c A_{col}}$)
P_{N-u} =	Normalized ultimate load of the test specimen ($= \frac{P_u}{f'_c A_{col}}$)
A_{col} =	Column stub cross-section area [in. ²]
Δ_m =	Measured deflection under the center of loading area [in.]
Δ =	Deflection under the center of loading area compensating the deflection of the support ($= \Delta_m - \Delta_{supp}$) [in.]
Δ_N =	Normalized deflection under the center of loading area ($= \frac{\Delta}{z}$)
Δ_{N-max} =	Normalized deflection under the center of loading area (point) at the ultimate strength ($= \frac{\Delta_{max}}{z}$)
Δ_{max} =	Deflection under the center of loading area compensating the deflection of the supports at ultimate strength [in.]
Δ_{supp} =	Average deflection at the center of four support plates [in.]

To begin with, visual observation involves the evaluation of a cracking pattern, failure mechanism, and post-failure conditions, as well as comparison between specimens in each series. Cracking propagation during the testing and at the post-failure conditions provided the serviceability of the specimen, stress distribution, and redistribution of internal stress after cracks developed. The brittle failures of specimens were expected since specimens were designed to control a nodal capacity that is relevant to shear-induced failure, rather than tie yielding. The research team interpreted the major failure mechanism from inspection of post-failure conditions as well as the load-deflection behavior data.

Furthermore, load-deflection responses were used to evaluate ultimate strength, stiffness, and ductility of each specimen. The load data included only total applied load, not self-weight of footing. Total applied load was the summation of the measurement from load cells underneath four supports. As described in the previous section, the displacement measured at the center of footing, which is identical to the centroid of loading area and two locations near four drilled shafts to measure the deformation of supports. The load and displacement data needed to be normalized due to different concrete strengths on test day and footing sizes. For normalizing, the load was divided by the concrete strengths since those strengths affected the ultimate capacities of the footing specimen. In addition, the load had to be divided by the area of the column, which corresponds to the same area in all specimens, in order to remove the engineering unit. The normalized deflection was calculated by subtracting the support deflections from measured deflection at the center of the footing and dividing by the span of the footing, the distance between the center of the footing to the center of supports as illustrated in Figure 4.31. Therefore, a normalized load-carrying capacity provides a level basis of comparison for specimens at different concrete strengths and footing sizes. The strength data of all specimens are summarized in Table 4.7.

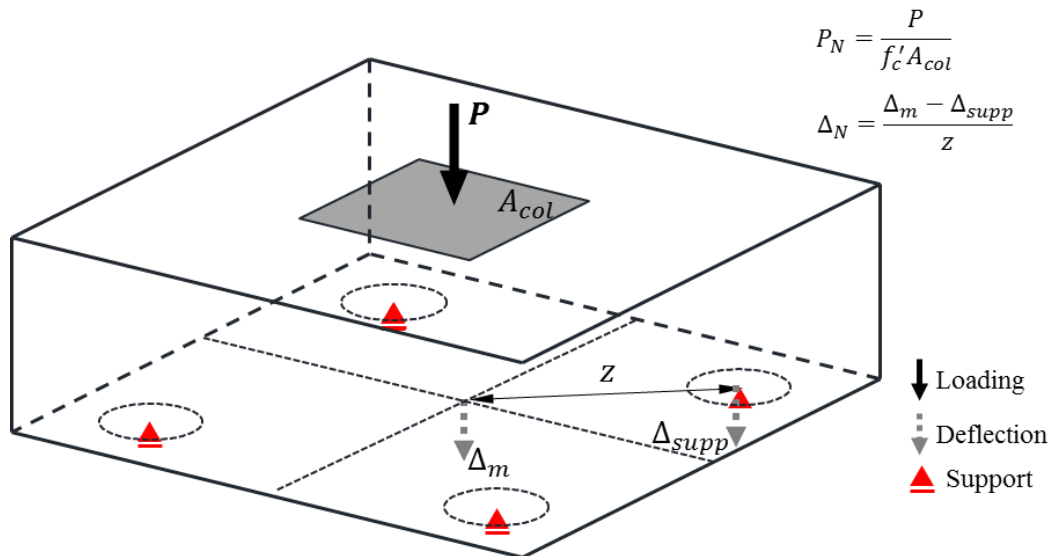


Figure 4.31 Dimension used for normalization of load and deflection

Moreover, strains in bottom mat reinforcement were monitored from ERSGs attached to the bottom mat reinforcing bars. The ratios of measured strain to yield strain were plotted by circle markers whose areas and colors indicate the ratio. Monitoring strain by increase of the total applied load resulted in data on when reinforcing bars yielded, how strain distributed at varying stages of the loading condition (for example, the ultimate state), and where ties developed effectively.

Lastly, serviceability and constructability were investigated for Series I testing only so that key findings from the discussion of Series I could inform the details of bottom mat reinforcement selected for the rest of the specimens. The crack pattern and crack widths on the bottom surface were examined by optical measurement, in lieu of crack gauges, due to the safety issue of working below specimens under heavy loading.

Table 4.7 Summary of experimental results

Series	Specimen ID	Footing Dimension ($L_1 \times L_2$) [in.]	Material properties				Bottom mat reinforcement details		Test variables				Test Results		
			$f'_{c,test}$ [ksi]	f_{yb} [ksi]	f_{yl} [ksi]	f_{yt} [ksi]	Layout	Anchorage	z/d	D_{DS} [in.]	ρ_{face} [%]	H [in.]	P_u [kip]	P_{N-u}	Δ_{N-max}
I	I-1	96 × 96	5.07	71.9	66.9	68.8	Grid	Straight	1.70	16	0.30	32	2,107	0.41	5.60
	I-2	96 × 96	5.22	64.1	66.9	68.8	Grid	Hooked	1.70	16	0.30	32	2,775	0.52	4.92
	I-3	96 × 96	5.09	64.1	82.2	60.8	Banded	Straight	1.70	16	0.30	32	2,703	0.52	4.36
	I-4	96 × 96	5.06	64.1	82.2	60.8	Banded	Hooked	1.70	16	0.30	32	2,884	0.56	4.84
II	II-5	96 × 72	3.24	63.5	61.8	63.0	Grid	Hooked	1.10	16	0.30	40	3,273	0.99	3.00
	II-6	96 × 96	4.62	63.5	61.8	63.0	Grid	Hooked	1.35	16	0.30	40	3,648	0.77	3.34
	II-7*	96 × 132	5.86	62.8	63.6	62.2	Grid	Hooked	1.70	16	0.30	40	3,387	0.56	6.00
III	III-8	96 × 132	4.66	67.5	61.8	62.6	Grid	Hooked	1.70	12	0.30	40	2,886	0.60	4.46
	III-9	96 × 132	3.71	67.5	61.8	62.6	Grid	Hooked	1.70	20	0.30	40	2,902	0.76	5.06
IV	IV-10	96 × 132	4.66	78.3	N/A	N/A	Grid	Hooked	1.70	16	0.00	40	2,523	0.53	4.18
	IV-11	96 × 132	4.65	78.3	65.6	63.6	Grid	Hooked	1.70	16	0.18	40	2,990	0.63	4.88
V	V-12	96 × 96	3.52	67.0	62.4	64.5	Grid	Hooked	1.70	16	0.30	32	2,239	0.62	3.58
	V-13	96 × 164	3.82	68.2	62.4	65.0	Grid	Hooked	1.70	16	0.30	48	3,354	0.86	4.88

* Baseline model: Results are compared in Series II through V

4.3.2. Series I: Bottom Mat Reinforcement Details

The test results of Series I are summarized for comparison in Table 4.8.

Table 4.8 Test results: Series I

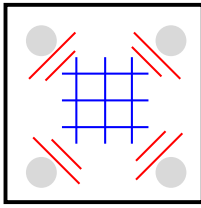
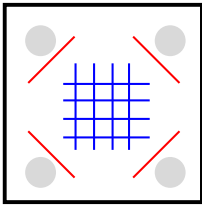
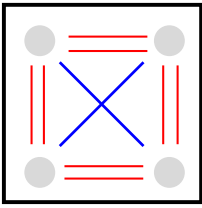
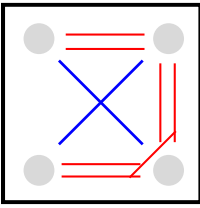
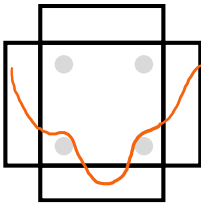
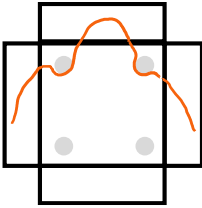
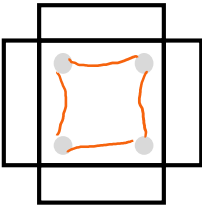
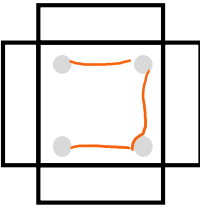
Specimen ID	I-1 (Grid & Straight)	I-2 (Grid & Hooked)	I-3 (Banded & Straight)	I-4 (Banded & Hooked)
$f'_{c,test}$ [ksi]	5.07	5.22	5.09	5.06
$P_{cr,v}$ [kip]	600	700	600	600
P_y [kip]	1,897	2,072	2,465	2,380
P_u [kip]	2,107	2,775	2,703	2,884
P_{N-u}	0.41	0.52	0.52	0.56

4.3.2.1. Strength Results

- Visual Observation

The observed visual conditions of each specimen are summarized in Table 4.9. In the lower level of the applied load (0~1,600 kips), specimens with grid layout (I-1 and I-2) had cross-patterned cracks on the bottom surface. In contrast, cracks extended from the center of the specimen to the center of the supports (X-shaped) in specimens with banded layout (I-3 and I-4). Crack maps of each series are included in Appendix F. Crack widths on the bottom face in I-3 and I-4 were generally larger than the cross-shaped cracks in I-1 and I-2 from the comparison of visual inspection and photos taken by a high-resolution camera (GoPro). Severe damage in the vicinity of supports on the bottom face, as shown in Figure 4.32-(a), and large multiple arch-shaped cracks on side surfaces, in Figure 4.32-(b), contributed to the failures of the specimens employing the grid reinforcement layout. I-3 and I-4 experienced only minor failure near supports; however, significant cracks propagated along the centerline of the banded area, as shown in Figure 4.32-(c). It should be noted that bond-related damage on the south face of I-1, which appears in Figure 4.32-(d), adversely affected the ultimate capacity, as explained in the following section.

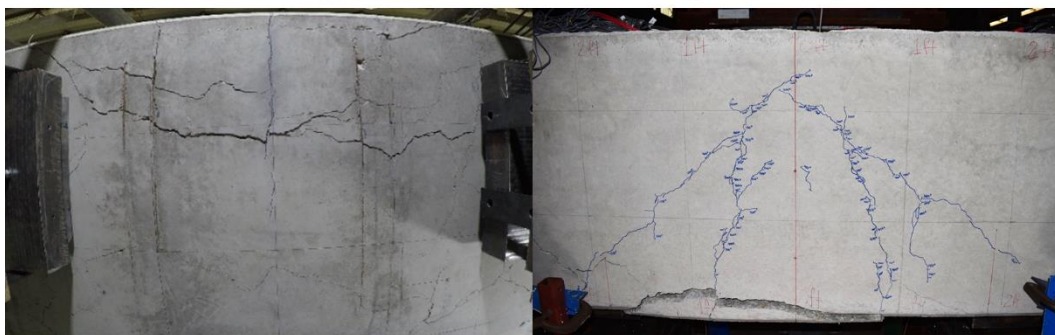
Table 4.9 Summary of visual observations in Series I testing

Specimen ID	I-1 (Grid & Straight)	I-2 (Grid & Hooked)	I-3 (Banded & Straight)	I-4 (Banded & Hooked)
Cracks on bottom surface				
Failure surface				
Major cracks in the banded area	Near Edge	Near Edge	Centerline	Centerline
Punching shear near supports	Severe	Severe	Minor	Minor



(a) Damage near supports: I-2

(b) Multiple arch-shaped cracks: I-2



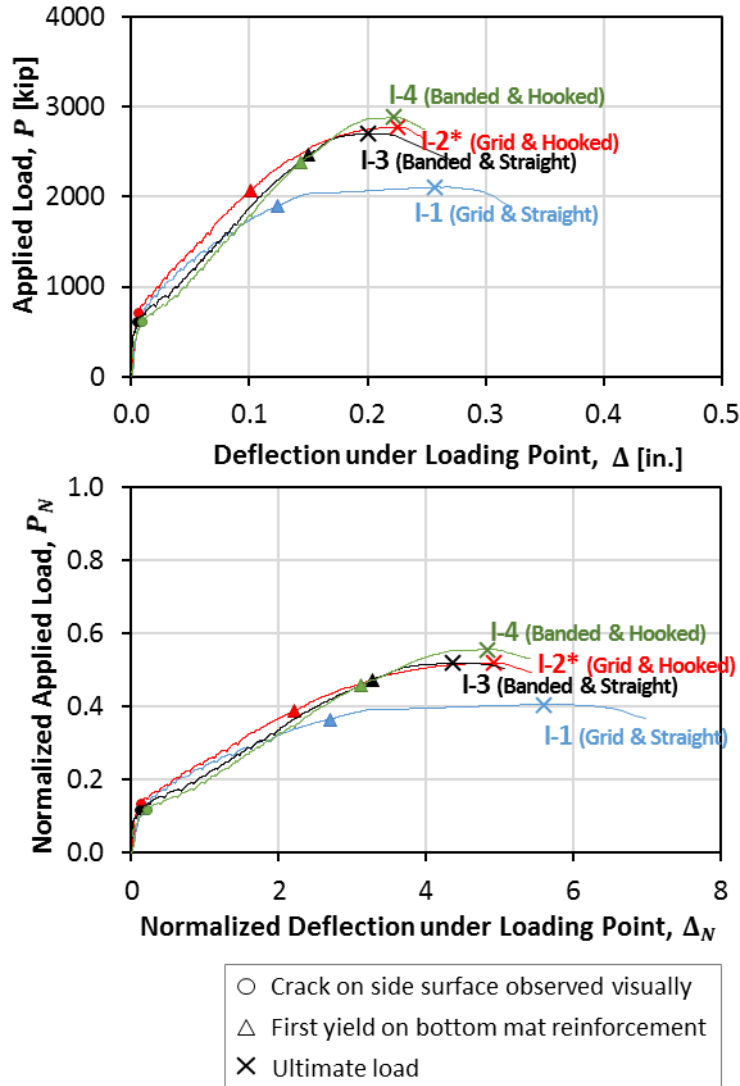
(c) Large cracks in the direction parallel to the centerline of the bandwidth: I-3

(d) Bond related crack on South face: I-1

Figure 4.32 Details of the damage observed in Specimen I-1 after failure

- Load-deflection Response

The normalized load-normalized deflection responses of specimens I-1 through I-4 are compared in Figure 4.33. It should be noted that the normalized deflection of I-2 was incomplete due to the malfunction of instrumentation near supports. Consequently, the normalized load of I-2 is compared with that of other specimens. Based on both measured and normalized data, I-2, I-3, and I-4 indicated comparable load resistances while I-1 failed at the significantly lower applied load. This lower failure load-carrying capacity was caused by the loss of bond in the bottom mat reinforcement of the first specimen, due to the insufficient development length provided by the straight anchorage. Moreover, the specimens constructed with the banded layout of hooked bars (I-4) provided a 4% and 7% greater ultimate capacity based on measured and normalized data, respectively, than those with the grid layout and the same anchorage (I-3). Note that this increase of the ultimate capacities can be achieved only if the full development length is provided. The conclusion that the banded specimen provided 4% greater failure load is consistent with findings obtained from previous studies that found capacity increases of 6% (Clarke, 1973) and 8% (Suzuki et al., 1998).



* The deflection of I-2 is incomplete due to the misreading of the deflection near supports
 Figure 4.33 Load-deflection responses of specimens: Series I

- Strains in Bottom Mat Reinforcement

The strains in the bottom mat reinforcing bars were estimated on the basis of the ERSGs' measurements. The strains developed in the bottom mat reinforcement at ultimate state are presented in Figure 4.34. Most reinforcing bars in the banded area, as indicated by the yellow, in all specimens yielded or converged to yielding condition at failure. In specimens with hooked bars (I-2 and I-4), the reinforcing bars outside the bandwidth reached yield condition practically. It should be noted that greater than 90% of yielding strain can be regarded as the yielding since it is greatly possible that reinforcement near the location where ERSGs were attached was yielded. ERSGs have a limitation that the measurements indicate local strain, not average strain. Further, despite the insufficient development lengths provided

for the bottom mat reinforcing bars in specimens having straight bars (I-1 and I-3), the reinforcement above the supports had achieved full yield.

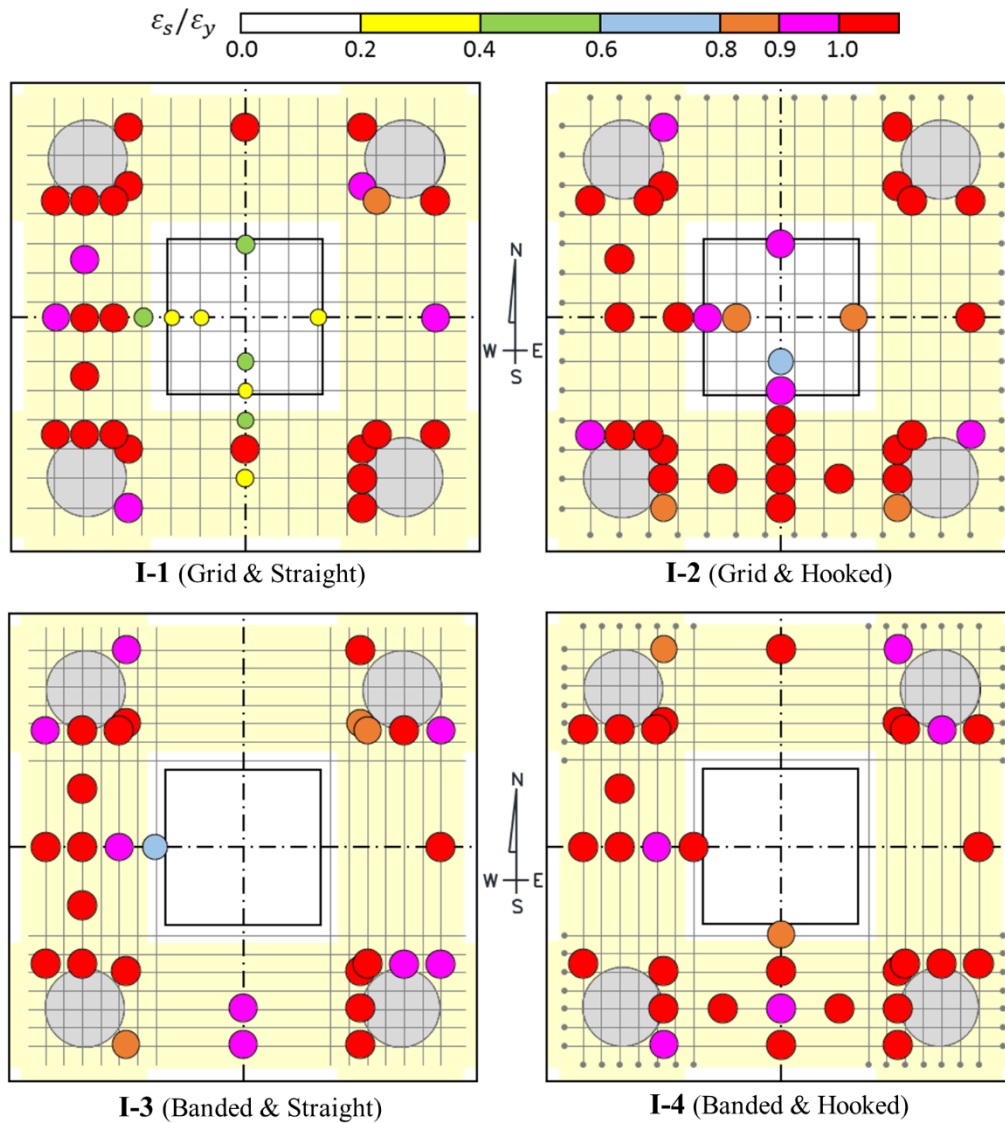


Figure 4.34 Strain distribution in bottom mat reinforcement at the ultimate load: Series I

4.3.2.2. Serviceability and Constructability Results

- Serviceability

To evaluate the serviceability of each bottom mat reinforcement detail, the crack patterns of the bottom surface of each specimen at the service load level was reviewed. Table 4.10 and Figure 4.35 show the simplified bottom surface crack patterns of each specimen under the service load level, 1,600 kips as defined earlier, were examined to evaluate the serviceability of each bottom reinforcement detail. By comparing the crack patterns with respect to the reinforcement layout, it can be

seen that specimens with the grid layout showed grid-shaped crack patterns under service load levels; however, those with the banded layout showed radial crack patterns. While the radial cracks could be observed by the naked eye, the grid cracks could not, due to their small crack widths. It was obvious that the cracks with large width developed at the center of the banded layout specimens since no reinforcement was placed at the region. The reinforcement placed at the center of the grid layout specimens made the grid layout have higher serviceability than the banded layout by controlling crack widths at the service load level. The effect of providing fully developed hooked bars to the bottom mat reinforcement could be evaluated by comparing crack patterns of the specimens having the grid layout. Smaller width and a greater number/density of cracks developed at the center of the bottom surface in the specimen with the hooked bars than in the specimen with straight bars under the same service load as shown in Figure 4.35. Therefore, specimens constructed with fully developed hooked bars better controlled the crack widths than did the specimens constructed using straight bars without full development length. However, this effect was not notably observed in the banded layout specimens since there was no reinforcement controlling cracks at the center.

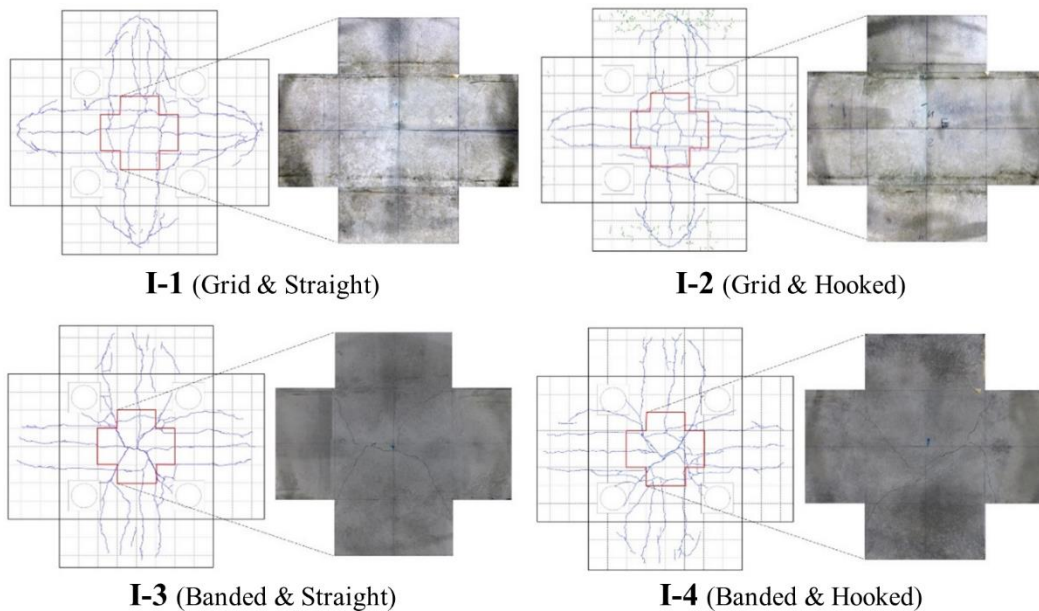
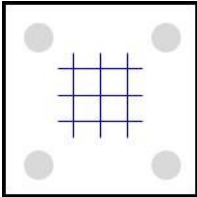
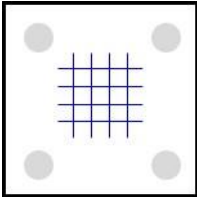
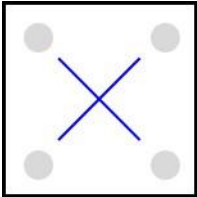
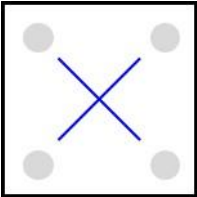


Figure 4.35 Crack patterns on the bottom face under serviceability load

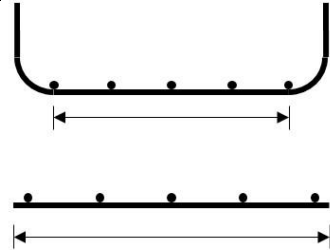


Table 4.10 Summary of the serviceability condition: Series I

Specimen ID	I-1 (Grid & Straight)	I-2 (Grid & Hooked)	I-3 (Banded & Straight)	I-4 (Banded & Hooked)
Crack Pattern				
Crack Width Control	Good	Very Good	Poor	Poor

- Constructability

Consideration of the constructability of each bottom mat reinforcement detail provides another insight for determining an appropriate bottom reinforcement detail for drilled shaft footings. Through a multifaceted consideration, some drawbacks in using the banded layout or hooked bars could be confirmed from the perspective of constructability, as shown in Table 4.11. Several factors associated with the banded layout could negatively affect constructability. The vertical reinforcement coming from the drilled shaft is also likely to interfere with the bottom mat reinforcement.

Table 4.11 Summary of constructability issues: Series I

Hooked Reinforcement	Hooked Reinforcement	Banded Layout
		
reinforcement cannot be placed within bend radius	may affect vertical crack control reinforcement spacing	insufficient space for dowel bars come from drilled shafts
Constructability ↓	Constructability ↓	Constructability ↓

4.3.2.3. Discussion and Conclusion

Significant discrepancy of crack patterns between grid and banded layout was observed in both the serviceability and the ultimate condition. The specimens with the grid layout showed grid-shaped crack patterns under service load levels; however, those with the banded layout showed radial crack patterns with large widths. In post-failure conditions, wide cracks developed at the center of the banded layout specimens since no reinforcement was placed in this region whereas severe

damage in the vicinity of supports and diagonal cracks were major contribution to failure of specimens having grid layout.

Series I testing confirmed that all of the bottom mat reinforcement combinations had comparable load-carrying efficiency, except for the grid layout with straight bars (I-1). I-1 failed under far lower load than the others due to the premature failure caused by reinforcement slip. Results from strain distribution found that most bottom mat reinforcement yielded in the bandwidth as well as outside of the bandwidth if reinforcing bars were sufficiently anchored. It can be concluded that the ultimate capacity is not significantly affected by the configuration of bottom mat reinforcement, either grid or banded layout, if sufficient development length was provided.

Several factors associated with the banded layout could negatively affect constructability. The vertical reinforcement from the drilled shaft is likely to interfere with the bottom mat of reinforcement. In the event that there is no interference between the vertical and horizontal reinforcement located at the shafts, this layout could result in an extremely congested reinforcement cage, which is likely to complicate construction.

The bottom mat reinforcement details used in the rest of Phase I specimens were determined based on multifaceted considerations. Table 4.12 summarizes the evaluation of each specimen from the observations and discussions. In conclusion, the specimen that employed the grid layout and hooked anchors had the best performance from a variety of perspectives.

Table 4.12 Comparison table for determining bottom mat reinforcing detail

Specimen ID	I-1 (Grid & Straight)	I-2 (Grid & Hooked)	I-3 (Banded & Straight)	I-4 (Banded & Hooked)
Configuration	Grid layout	Grid layout	Banded layout	Banded layout
Anchorage	Straight	90-degree hooked	Straight	90-degree hooked
Details of Post-Failure Conditions	Cracks near supports Loss of bond	Cracks near supports	Cracks in the banded area	Cracks in the banded area
Strength	Poor	Very good	Very good	Very good
Serviceability	Good	Very good	Poor*	Poor*
Constructability	Very good	Good	Poor	Very poor

* If sufficient crack control reinforcement was provided, the specimen would have less cracking, but the additional reinforcement would be necessary, which means not economical design

4.3.3. Series II: Strut Inclination

The test results of Series II are summarized for comparison in Table 4.13.

Table 4.13 Test results: Series II

Specimen ID	II-5 ($z/d=1.10$)	II-6 ($z/d=1.35$)	II-7 ($z/d=1.70$)
$f'_{c,test}$ [ksi]	3.24	4.62	5.86
$P_{cr,v}$ [kip]	600	700	400
P_y [kip]	1,293	1,683	2,459
P_u [kip]	3,273	3,648	3,387
P_{N-u}	0.99	0.77	0.56

4.3.3.1. Strength Results

- Visual Observation

All specimens of Series II failed in a brittle manner and, as shown in Figure 4.36, exhibited the similar cross-shaped cracking pattern on the bottom face to that found in the I-1 with a grid layout and hooked bars for the bottom mat reinforcement. Typical cracking and damage patterns of specimens with a grid layout and hooked bars are described in Figure 4.37.

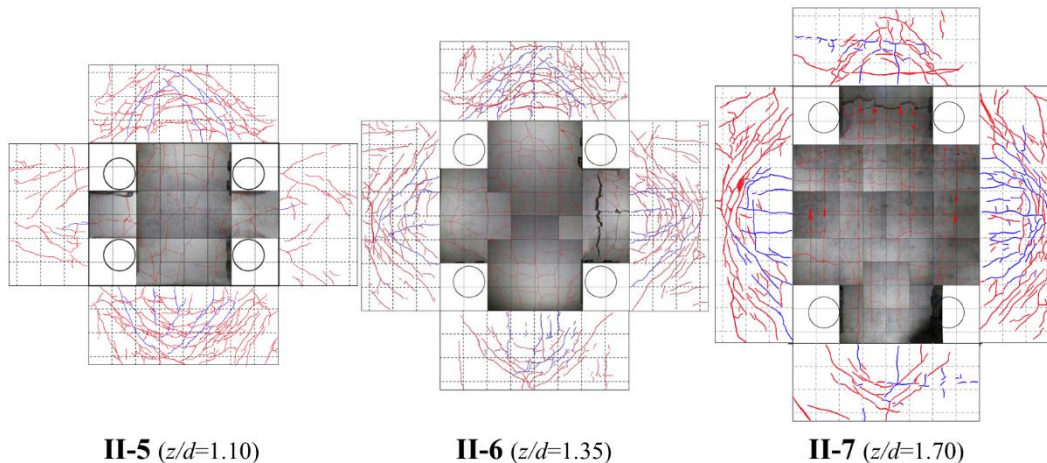
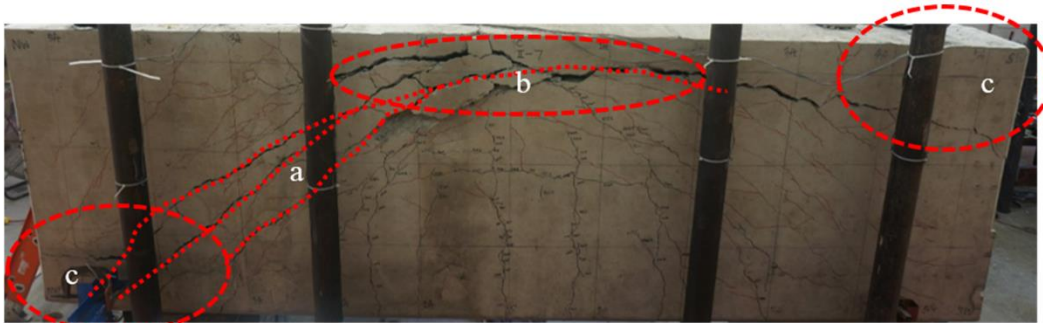
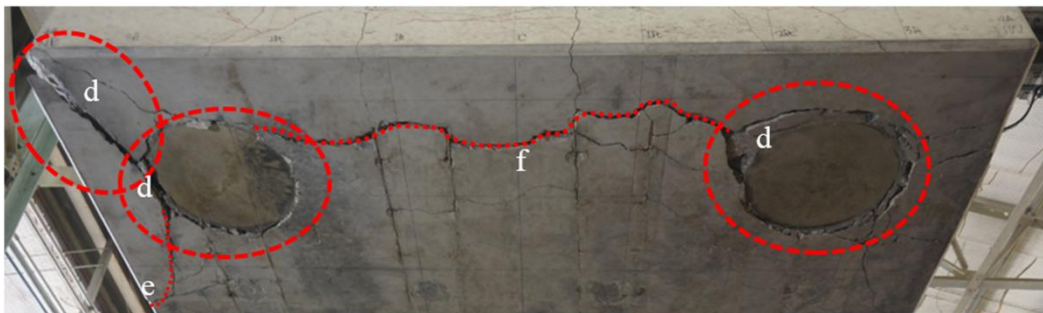


Figure 4.36 Crack maps: Series II



- a) Multiple arch-shaped diagonal cracks from the bottom to the top
- b) Damage on the top
- c) Damage at the top corner or the bottom corner near drilled shafts

(a) Side face



- d) Severe damage in the vicinity of drilled shafts (supports)
- e) Cracks that developed near drilled shafts connected with diagonal cracks on side surfaces
- f) Cracks in the direction parallel to the line between centers of drilled shafts

(b) bottom face

Figure 4.37 Typical cracking and damage pattern

- Load-deflection Response

Figure 4.38 presents a comparison of the load-deflection response among the three specimens of Series II testing. The load-deflection plots were used to compare the strength, stiffness, and ductility of each specimen.

The primary test results and findings are as follows:

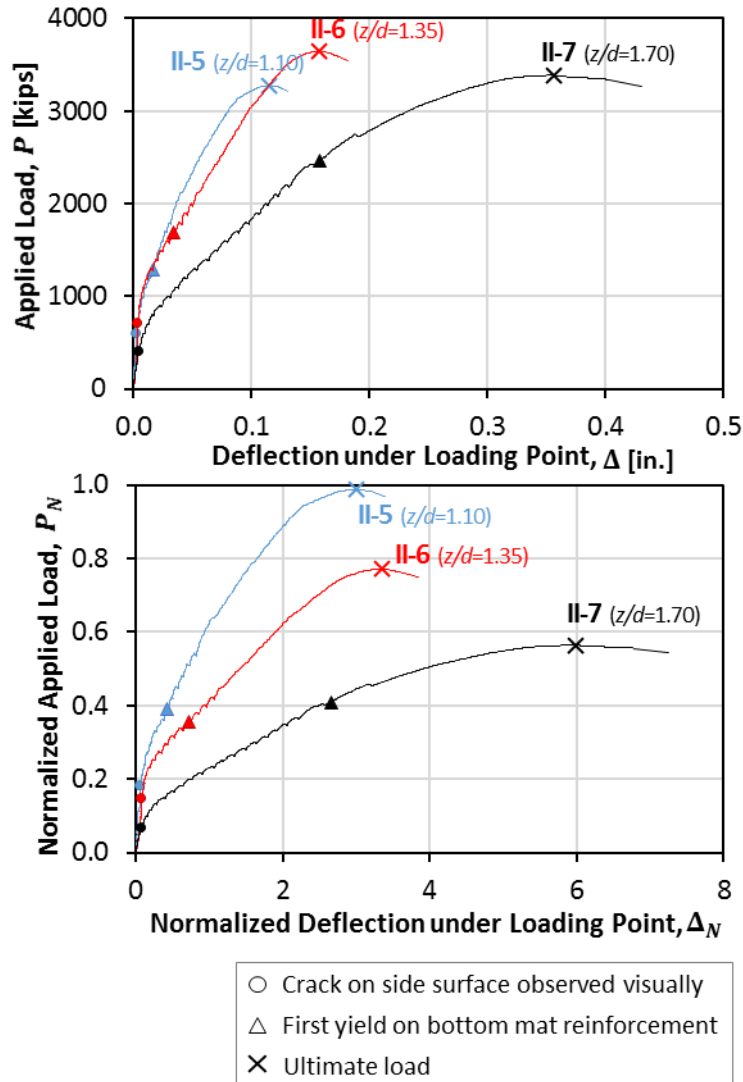


Figure 4.38 Load-deflection responses of specimens: Series II

- Stiffness at the pre- and post-cracking states has the tendency to increase with smaller (steeper) strut inclination.
- Steeper strut inclination resulted in the smaller load at the first yielding in spite of similar yielding strength and ratio of bottom mat reinforcement.
- The load from the first yielding point (triangle marker) to the failure (X-shaped marker) tends to increase when strut inclination decreases.
- The normalized ultimate strengths increased when strut inclination reduced. The normalized ultimate strength of II-5 was substantially larger (0.99) even though both the ultimate load and the concrete strength were the smallest among specimens in Series II.

- e. The normalized deflection of II-7 at the ultimate load was notably the largest among specimens.
 - f. Deflection of II-7 increased greater from the peak to the total failure than other specimens. Ductile behavior in II-5 and II-6 was barely observed.
- Strains in Bottom Mat Reinforcement

Figure 4.39 shows the strain development in bottom mat reinforcement of specimens at ultimate load. II-6 experienced more widespread bar yielding at failure compared to the other two specimens due to the square-shaped footing. II-5 and II-7 had 7 out of 9 bars and all bars, where strain gauges were installed, along the long span, respectively, yielded or were close to yielding both inside and outside the bandwidth, while strains along the other directions were lower than 40% of the yield strain in most of the measured locations outside of the bandwidth. This result supports the finding from Series I testing that most reinforcing bars both inside and outside of the bandwidth yielded or were close to yielding.

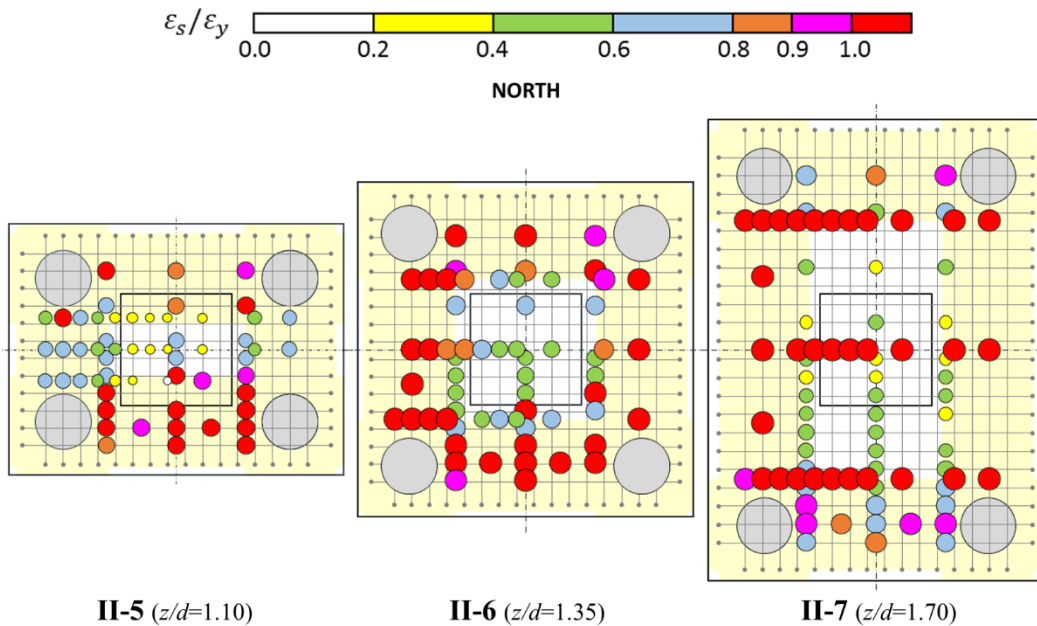


Figure 4.39 Strain distribution in bottom mat reinforcement at the ultimate load: Series II

4.3.3.2. Discussion

The results obtained from the visual observations, load-deflection responses, and strain distribution was evaluated. The structural behavior clearly differed between specimens in terms of the load-deflection response in Series II. Steeper strut inclination resulted in greater stiffness and ultimate load. The plot in Figure 4.40 indicates that the inverse correlation between strut inclination and ultimate loads is

significant. The ultimate loads increase proportionally to the decrease of strut inclination (steeper inclination). Specimens with steeper strut inclination failed in a more brittle manner with a small increase of deflection in the post-peak state. Strain distribution of bottom mat reinforcement could support the statement since specimens with steeper strut inclination failed at greater loads in spite of having fewer locations where bottom mat reinforcement along the longer axis yielded. The reinforcement in the longer direction experienced higher level of stress than the reinforcement in the shorter direction when the longer dimension increased.

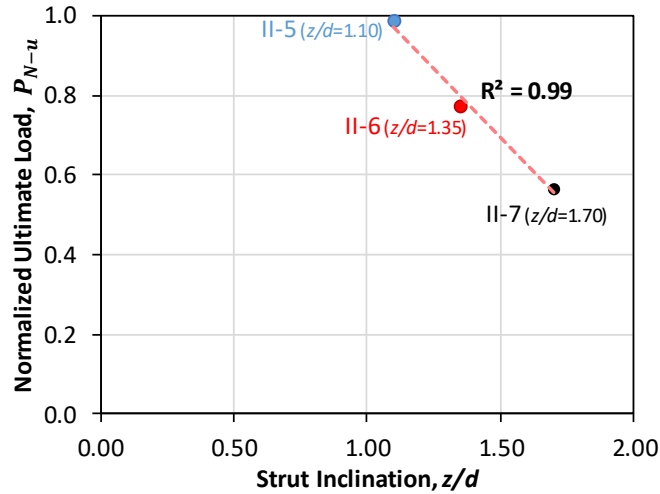


Figure 4.40 Relationship between normalized ultimate loads and strut inclinations

4.3.4. Series III: Shaft Diameter

The test results of Series III are summarized for comparison in Table 4.14.

Table 4.14 Test results: Series III

Specimen ID	III-8 ($D_{DS} = 12$ in.)	II-7 ($D_{DS} = 16$ in.)	III-9 ($D_{DS} = 20$ in.)
$f'_{c,test}$ [ksi]	4.66	5.86	3.71
$P_{cr,v}$ [kip]	600	400	500
P_y [kip]	2,558	2,459	2,728
P_u [kip]	2,886	3,387	2,902
P_{N-u}	0.60	0.56	0.76

4.3.4.1. Strength Results

- Visual observation

Entire crack patterns of specimens are similar to the typical pattern described in Section 4.3.3.1. As shown in Figure 4.41, it was observed that concrete at the bottom corner near the drilled shaft spalled severely in III-8 compared to other specimens. Otherwise, cracks at the bottom corner were found in II-7 and III-9 in lieu of concrete spalling damage. The most considerable cracks connected from the edge of drilled shaft to the corner of the loading plate, as found in the diagonal cutting sections after failure of Figure 4.42.

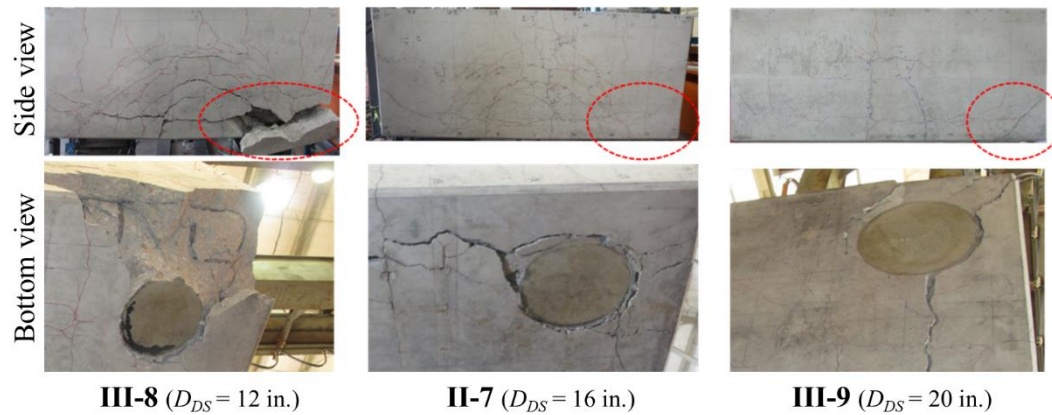


Figure 4.41 Post-failure conditions near the failed drilled shaft



Figure 4.42 Post-failure conditions on top surface of III-9

- Load-Deflection Response
 - a. The primary test results and findings from load-deflection response as plotted in Figure 4.43 are as follows:
 - b. All specimens presented comparable stiffness in pre- and post-cracking state from measured load-deflection response.
 - c. The loads at the first yielding of bottom mat reinforcement were comparable.
 - d. The response of III-9 reached a greater normalized capacity as compared to III-8 and II-7, which have similar normalized ultimate loads.

- e. Increment of deflection beyond the peak to the failure was the smallest in III-9.

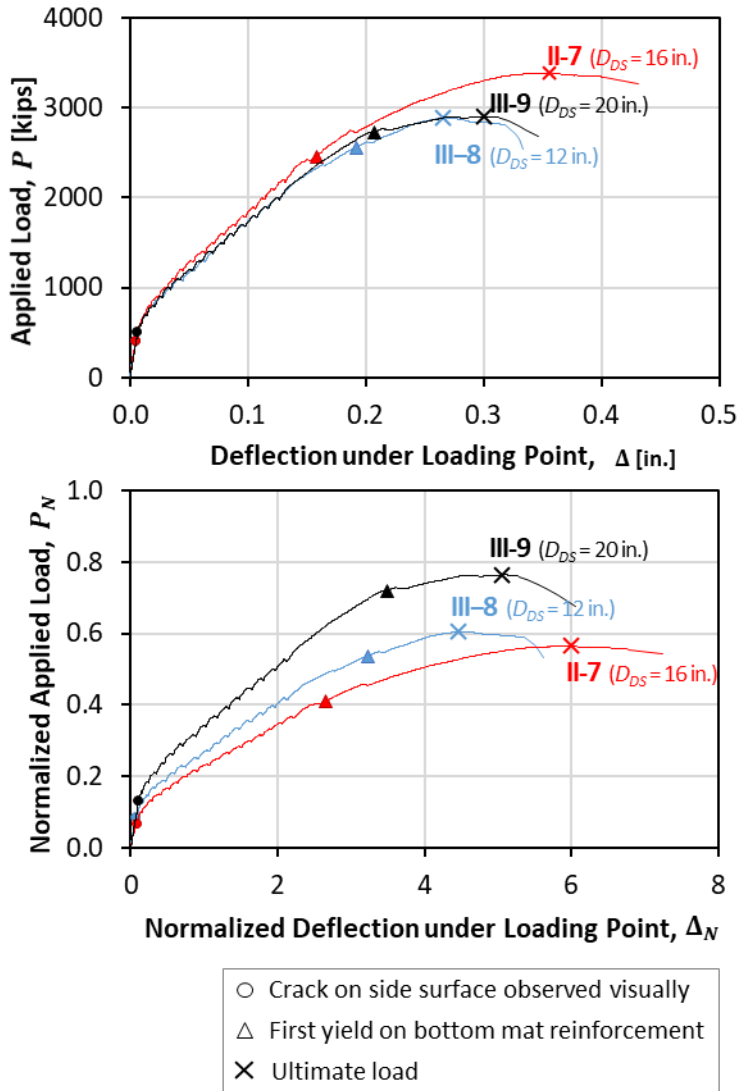


Figure 4.43 Load-deflection responses of specimens: Series III

- Strains in Bottom Mat Reinforcement

Figure 4.44 shows the strains in the bottom mat reinforcement of III-8, II-7, and III-9 at the ultimate capacity. II-7 ($D_{ds} = 16$ in.), which provided the greatest ultimate load, also experienced the greatest number of yielding locations at failure compared to the other two specimens. Bottom mat reinforcement of III-8 ($D_{ds} = 12$ in.) yielded at the fewest measurement locations.

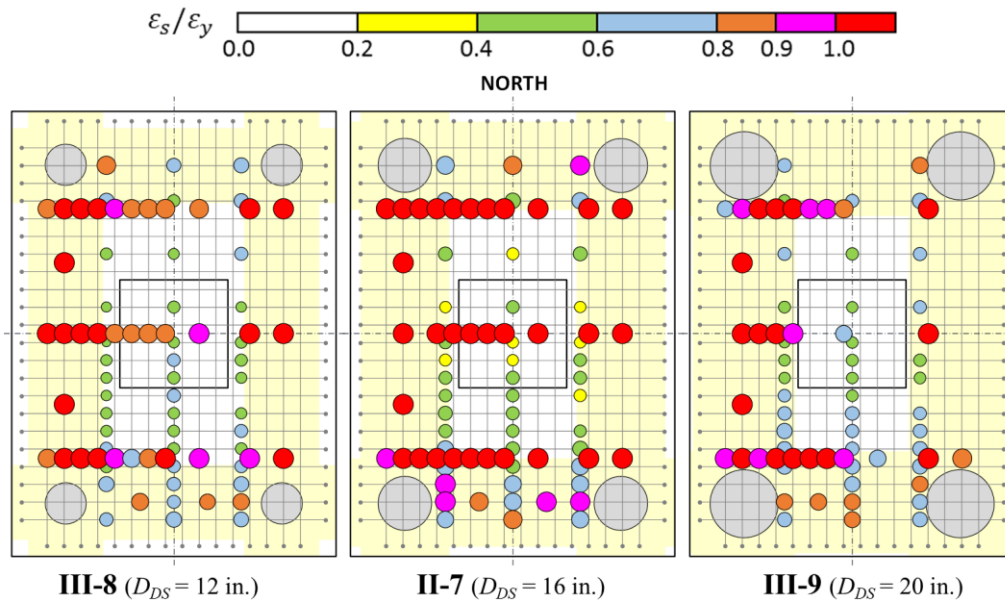


Figure 4.44 Strain distribution in bottom mat reinforcement at ultimate load: Series III

4.3.4.2. Discussion

Noticeable damage at the corner in the vicinity of the failed drilled shaft was found in the specimen with the smallest shafts (III-8). This damage may stem from greater stress concentration near the drilled shaft when the shaft diameter decreases. On the other hand, severe concrete spalling near the edge between the side and top surface was observed in III-9, which had the largest shafts, since the stress of the node below the column was greater than that of the node above the drilled shafts, whose area was greater than the area of a quadrant of the column. Load-carrying capacity did not show any strong relationship, with both shaft diameter and shaft area as plotted in Figure 4.45. Shaft area seemingly had a stronger correlation with normalized ultimate loads than shaft diameter; however, the r-square of 0.64 value was not sufficient to verify the trend. Theoretically, the ultimate capacities are proportionally related to the shaft area if the failure mechanisms were the same. This discrepancy between the test results and the theory will be discussed in the following section in-depth. The result of strain distribution diagrams in Figure 4.44 indicates that smaller bearing area (shaft diameter) could slightly hinder the stress spread further, which negatively affects the ultimate load and ductility. In spite of the negative effect of smaller shaft diameter, it was reported again that most reinforcing bars with proper anchorage (90-degree hook) along the longer axis yielded, which is similar to the findings of Series I and II. It can be concluded that the shaft diameter had no effect on the overall pattern of the strain distribution that experienced the same as all three specimens.

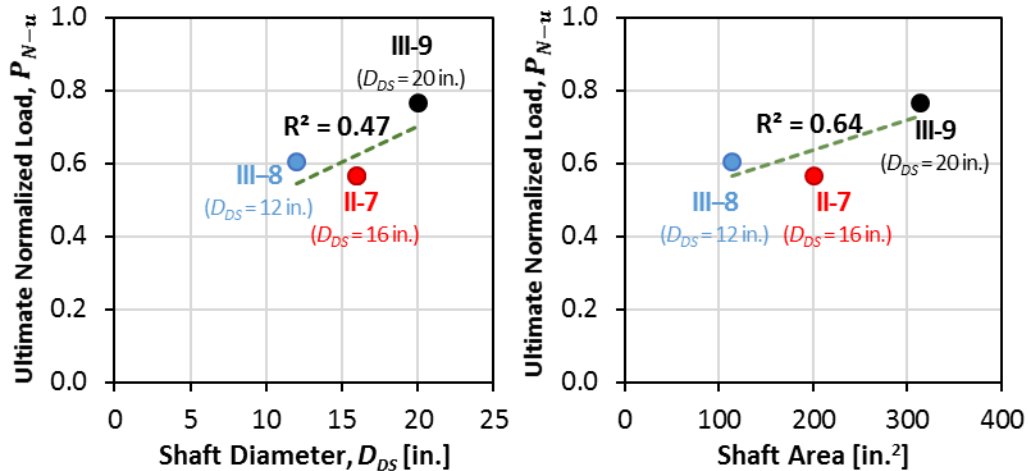


Figure 4.45 Relationship between normalized ultimate loads and shaft diameters and shaft area

4.3.5. Series IV: Side Face Reinforcement Ratio

The test results of Series IV are summarized for comparison in Table 4.15.

Table 4.15 Test results: Series IV

Specimen ID	IV-10 ($\rho_{face} = 0.00\%$)	IV-11 ($\rho_{face} = 0.18\%$)	II-7 ($\rho_{face} = 0.30\%$)
$f'_{c,test}$ [ksi]	4.66	4.65	5.86
$P_{cr,v}$ [kip]	400	500	400
P_y [kip]	2,375	2,644	2,459
P_u [kip]	2,523	2,990	3,387
P_{N-u}	0.53	0.63	0.56

4.3.5.1. Strength Results

- Visual observation

The specimen without side face reinforcement (IV-10) experienced the most brittle and catastrophic failure among all of specimens in Phase I testing. An obviously different crack pattern and post-failure conditions compared to specimens having side face reinforcement (IV-11 and II-7) were observed. Figure 4.46 shows that single large diagonal crack on side surfaces led to the brittle failure and spalling concrete cover that was notable in IV-10, while multiple diagonal cracks in IV-11 and II-7 were observed. Moreover, spalling of the concrete cover on the side surface of the short span and distinguishable horizontal cracks at the elevation of the end

of hooks on the side surfaces were found to be dissimilar to other specimens, as depicted in Figure 4.47. Another important observation from crack maps on the bottom faces in Figure 4.48 was the presence of relatively fewer cracks with larger spacing on the bottom face; this means that crack width was greater when the side face reinforcement ratio decreased, even though there was no face reinforcement on bottom faces in all cases.



Figure 4.46 Comparison of post-failure conditions on the side faces between specimens: Series IV

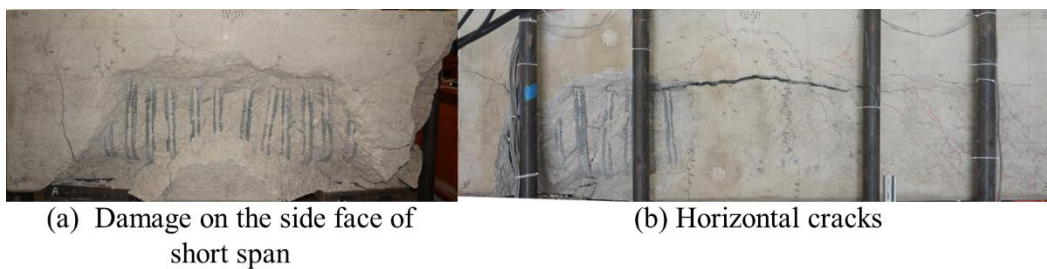


Figure 4.47 Post-failure conditions: IV-10

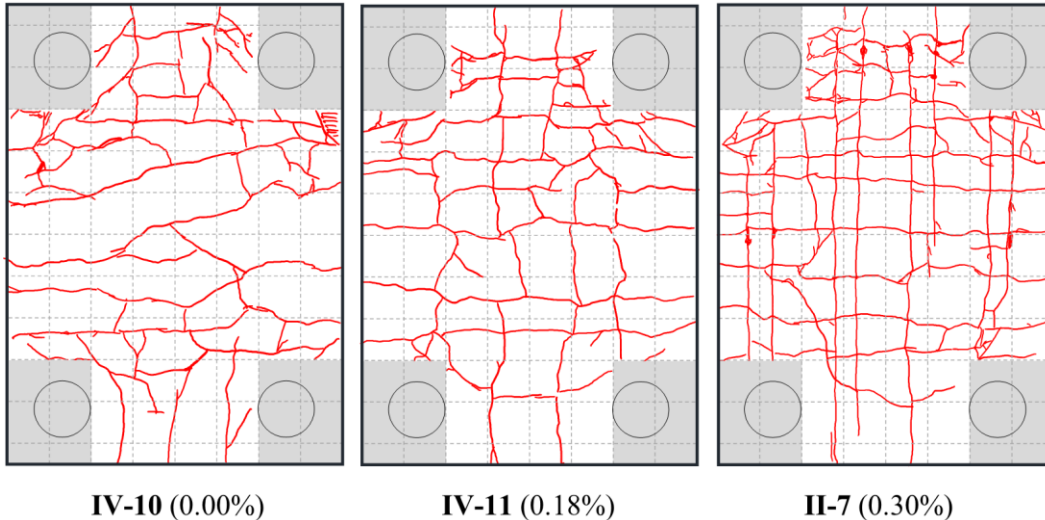


Figure 4.48 Comparison of post-failure conditions on the bottom face between specimens: Series IV

- Load-Deflection Response

Figure 4.49 presents both measured and normalized load-deflection response of specimens in Series IV. The primary test results and findings from the plots are as follows:

- a. Stiffness of the specimen without side face reinforcement (IV-10) was smaller from around 2,000 kips, where diagonal cracks on side surfaces might develop compared to other specimens
- b. IV-10 exhibited the lowest ultimate load and lowest load at the first yielding of bottom mat reinforcement.
- c. The deflection of specimens at the first yield of bottom mat reinforcement (triangle marker) and ultimate load (X-shaped marker) increased with increasing face reinforcement ratio.
- d. IV-10 had the lowest ultimate load, followed by IV-11 with 0.18% of side face reinforcement, and finally II-7 with 0.3% of side face reinforcement.
- e. The ultimate normalized load of IV-11 was the greatest, followed by II-7.
- f. The increment of deflection from the ultimate load (X-shaped marker) to total failure (the end of line) was greater with increasing face reinforcement ratio.

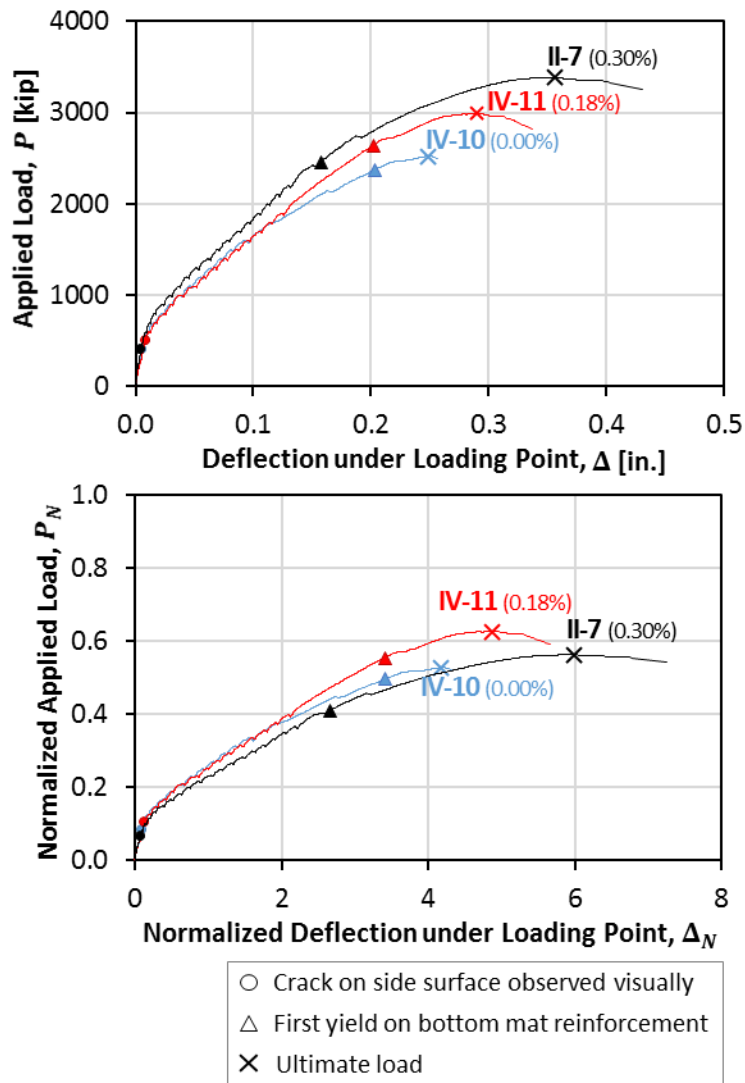


Figure 4.49 Load-deflection responses of specimens: Series IV

- Strains in Bottom Mat Reinforcement

As shown in Figure 4.50, IV-10 (no side face reinforcement) experienced lower strains on the bottom reinforcement than IV-11 (half side face reinforcement) and II-7 (full side face reinforcement). Because the face reinforcement aids in preventing cracks from opening on the side faces, more face reinforcement allowed for a more ductile response in which more bars yielded at failure.

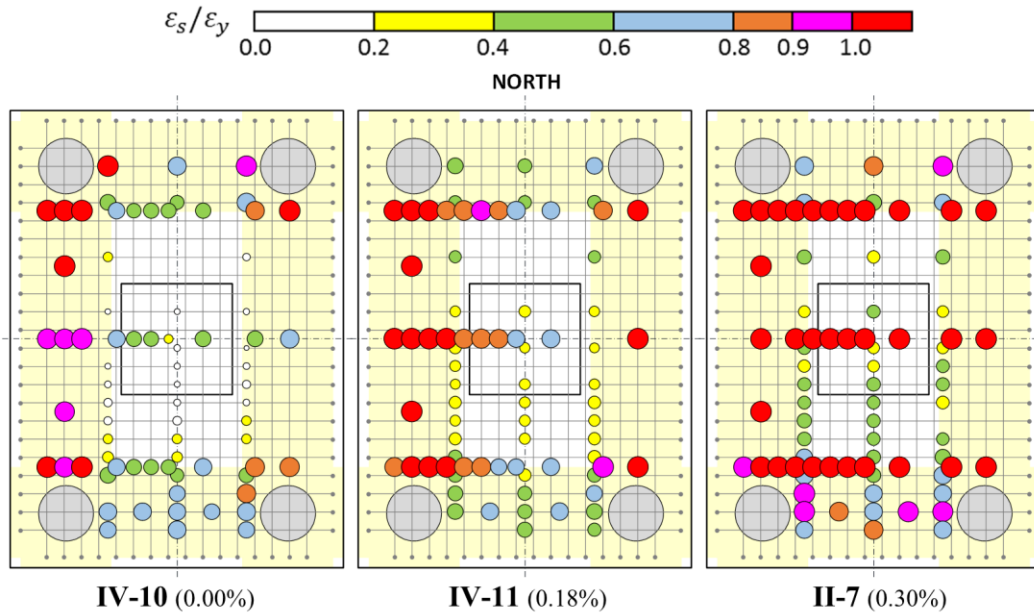


Figure 4.50 Strain distribution in bottom mat reinforcement at ultimate load: Series IV

4.3.5.2. Discussion

The Series IV results show that side face reinforcement enhanced the structural performance at the ultimate failure as well as in the service condition. The load-carrying capacities of specimens with side face reinforcement, regardless of the amount, were notably greater than those without side face reinforcement. The structural behaviors—such as load-deflection responses in the post-peak state, the spacing and number of cracks on the bottom faces, and strain distribution in bottom mat reinforcement—improved when side face reinforcement ratio increased. These phenomena can be caused by the enhanced redistribution of internal stresses redistribution in the post-cracking state. The confining effect by side face reinforcement can be an evidence of more yielding of bottom mat reinforcement. As a result, the research team can suggest that side face reinforcement shall be provided to avoid not only lower quality in the service condition, as shown in Figure 4.48, but also the significantly lower ultimate capacity that resulted, as demonstrated in Figure 4.49. Further studies that investigate the reasonable amount of side face reinforcement numerically—for example, greater than 0.18% or 0.30%—will support the findings from Series IV.

4.3.6. Series V: Footing Size

The test results of Series V are summarized for comparison in Table 4.16.

Table 4.16 Test results: Series V

Specimen ID	V-12 (H = 32 in.)	II-7 (H = 40 in.)	V-13 (H = 48 in.)
$f'_{c,test}$ [ksi]	3.52	5.86	3.82
$P_{cr,v}$ [kip]	500	400	600
P_y [kip]	2,122	2,459	2,990
P_u [kip]	2,239	3,387	3,354
P_{N-u}	0.62	0.56	0.86

4.3.6.1. Strength Results

- Visual observation

The research team found distinct differences in the failure between V-12 and other specimens. Unlike other specimens, V-12 failed without any brittle actions, accompanied by slow dropping of the applied load in the post-peak state. In addition, the large opening diagonal cracks and the typical crack pattern of footings employing grid and hooked layout as described in Section 4.3.3.1, were not found in V-12, as Figure 4.51 attests. Otherwise, Figure 4.52-(a) shows that failure of V-13 occurred with huge spalling and breaking of concrete on the side face near the top surface, which was similar to III-9. Furthermore, the most damage was found among all specimens of Series V, as shown in Figure 4.52-(b).

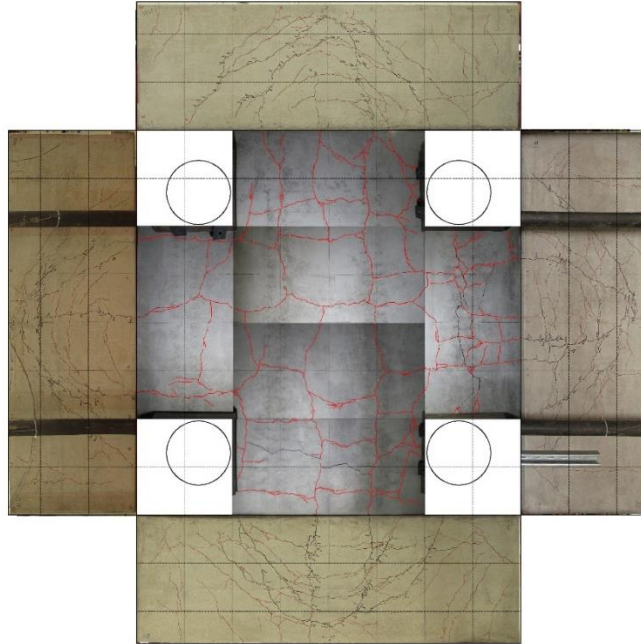


Figure 4.51 Crack map of V-12



(a) Damage on the top of side face of V-13

(b) Southeast support

Figure 4.52 Post-failure conditions: V-13

- Load-Deflection Response

Figure 4.53 presents the load-deflection response obtained from measurements and normalized values of specimens in Series V. The primary test results and findings from the plots are as follows:

- The ultimate capacity of V-12 ($H = 32$ in.) was roughly 66% lower than both those of II-7 ($H = 40$ in.) and V-13 ($H = 48$ in.).
- The ultimate loads of II-7 and V-13 were comparable, whereas the normalized capacity of V-13 was considerably greater than that of II-7.
- The deflection of V-12 in the post-yielding and post-peak states increased considerably more as compared with other two specimens

- d. Measured deflection of V-13 at the ultimate load was comparable with that of II-7, which was the largest of the specimens in Phase I testing.

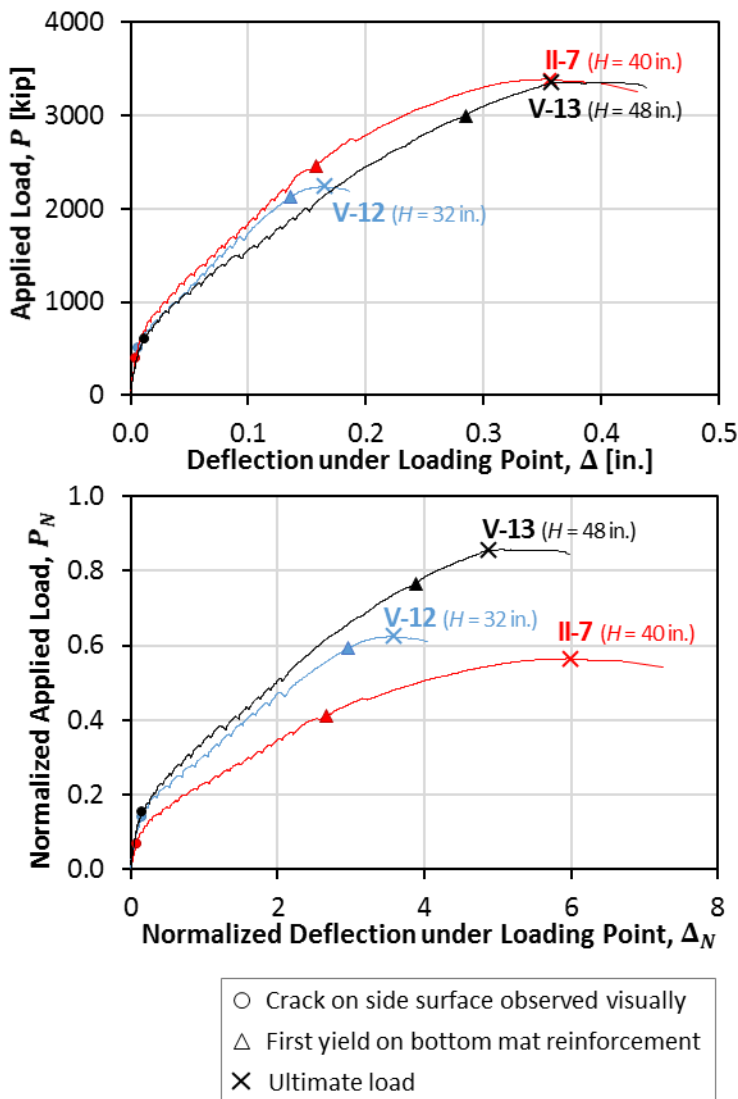


Figure 4.53 Load-deflection response of specimens: Series V

- Strains in Bottom Mat Reinforcement

Figure 4.54 shows the strains in the bottom mat reinforcement of V-12 ($H = 32$ in.), II-7 ($H = 40$ in.), and V-13 ($H = 48$ in.) at ultimate load. More widespread bar yielding at failure was found in II-7, which had the highest failure load. Specimen V-12 experienced yielding at fewer locations even in the bandwidth than II-7. Specimen V-13 had many bars in the east-west direction (short span) with strains lower than 40% of yield strain. In conclusion, the reinforcement along the longer direction experienced higher strain demands than the reinforcement in parallel to the axis of shorter length when the longer dimension was increased.

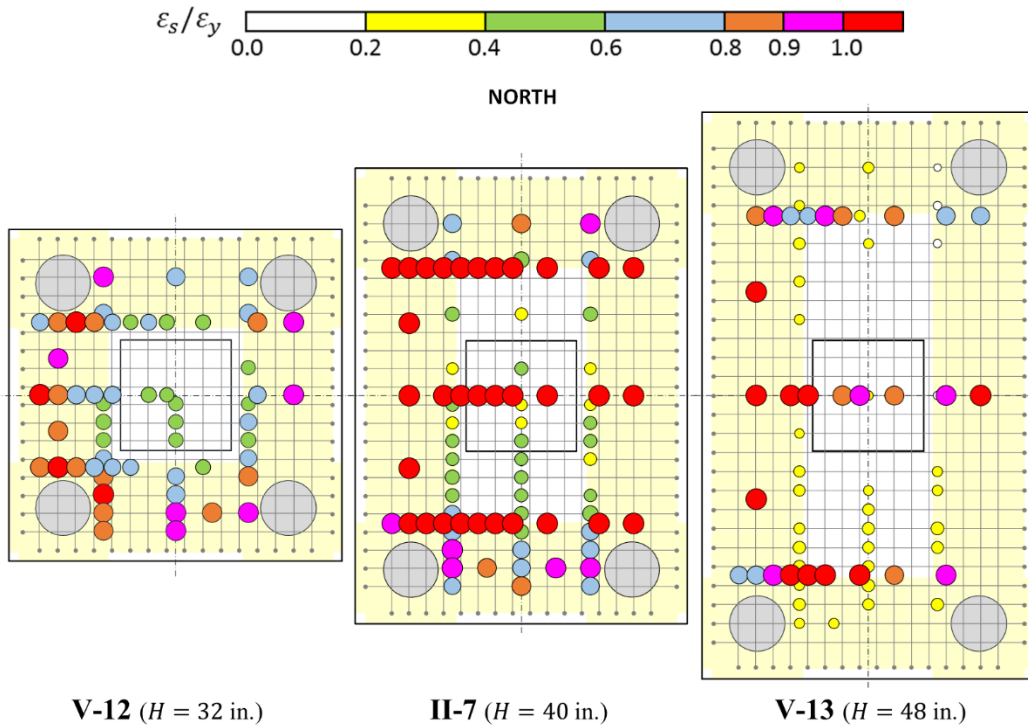


Figure 4.54 Strain distribution in bottom mat reinforcement at ultimate load: Series V

4.3.6.2. Discussion

The results of the correlational analysis between both ultimate loads and normalized ultimate loads and footing heights are presented in Figure 4.55. Neither plot reveals a clear trend of increasing by footing height. The trend line seems linear; however, the R-square value did not guarantee a strong proportional increase of the footing height. In any case, Phase V results seem to indicate that size effect had no relevance on the capacity of the footings.

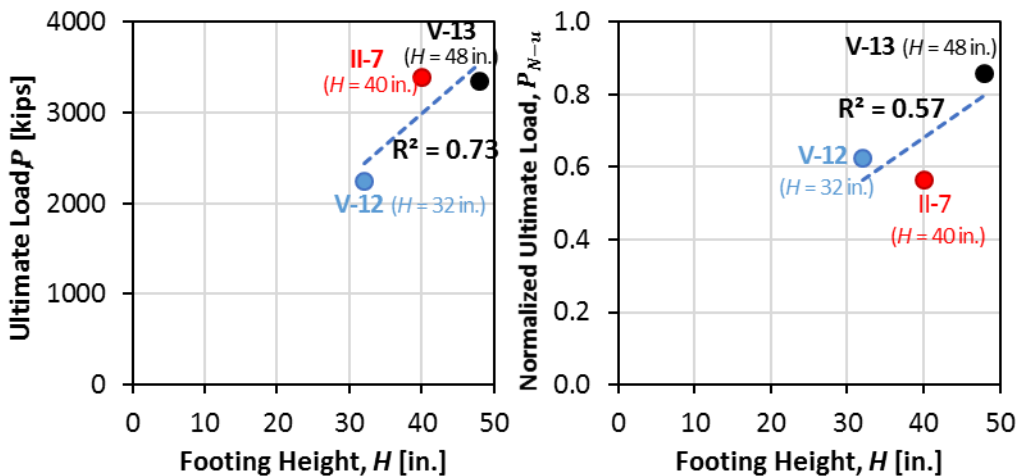


Figure 4.55 Relationship between normalized ultimate loads and footing height

4.4. Summary and Discussion

The Phase I testing program was designed to evaluate a variety of parameters affecting the structural performance and the analysis using 3D STM of a drilled shaft footing. The design parameters are reinforcement layout and anchorage types (Series I), strut inclination (Series II), shaft diameter (Series III), face reinforcement ratio (Series IV), and size effect (Series V). The following findings and suggestions from both experimental and analytic results were used to develop the refined 3D STM recommendations in Chapter 8.

Series I testing included four specimens with two different reinforcement layouts (grid vs. banded) and anchorage details (straight vs. 90-degree hook). All specimens in Series I, with the exception of Specimen I-1 (grid layout and straight anchorage), had reasonably comparable strength. It can be concluded that if reinforcing bars developed properly with any anchorage details, the structural behaviors of drill-shaft footings would be similar. In conclusion, the research team decided to employ a grid layout and 90-degree hooked bars for the design of all other specimens in the test series based on the results of Series I testing.

Series II specimens were designed with varying strut inclinations (z/d): 1.10, 1.35, and 1.70 for II-5, II-6, and II-7, respectively. A comparison of the behavior of Series II specimens shows greater stiffness for the steeper strut inclination, in pre- and post-cracking states. It can be concluded that ultimate strengths increased proportionally when strut inclination decreased.

The principal experimental parameter of Series III is the shaft diameter, which was selected to be 12 in., 16 in., and 20 in. for specimens III-8, II-7, and III-9, respectively. The specimen with the smallest shaft size exhibited the most brittle behavior at failure among Series III. The concrete near one of the supports spalled severely, and researchers could see conical cracks inside of the concrete. It was observed that smaller diameter adversely affected strain development outside of the bandwidth.

Series IV testing considered varying side face reinforcement ratio. IV-10 and IV-11 contained side face reinforcement ratios of 0.00% and 0.18%, respectively. These were compared to II-7, which had 0.30% of side face reinforcement. The specimen with zero face reinforcement (IV-10) failed most severely among Phase I specimens. Post-failure conditions of IV-10 were clearly different from other specimens. Slightly improved deformation capacity of II-7 (0.3%) in post-peak state from test results. Side face reinforcements provided similar ultimate capacities, regardless of side face reinforcement ratios (if present).

Series V specimens were designed with the same strut inclination of 1.7 and various heights of specimen (H): 32, 40, and 48 in. for V-12, II-7, and V-13, respectively. Specialized fabrication and installation methods were applied for V-13, which was the largest specimen in the history of research on footing tests under axial loading condition. The structural performance of V-13 showed the greatest normalized ultimate capacity and slightly improved deformation capacity in the post-peak state. The relevance of size effect is not supported by the current findings.

Chapter 5. Experimental Program – Phase II: Non-uniform Compression in Drilled Shafts

5.1. Overview

This chapter covers the Phase II experimental program of large-scale drilled shaft footings subjected to a load combination of uniaxial compression and moderate bending moment that results in non-uniform compression in drilled shafts. The primary objective was to investigate the behavior of the longitudinal column reinforcement that extends into the footing and establish the minimum anchorage requirements for it. In order to accomplish the objective, four tests were conducted using different anchorage details: straight, headed, and two hooked reinforcing bars with different hook orientations. The test results were used for planning an additional parametric study in Chapter 7 and the basis of design recommendations related to minimum anchorage of the column reinforcement, a component of Chapter 8 as well.

In this chapter, Section 5.2 provides the basic information about the planned experimental program, including the design variables, details of design, and testing setup for the large-scale footing specimens. Section 5.3 presents the testing results on the basis of the measured data during the tests and proposes the critical section of the column reinforcement for the anchorage requirement.

5.2. Experimental Program

5.2.1. Test Variable

As shown in Figure 5.1, the 3D strut-and-tie model of drilled shaft footings subjected to uniaxial compression and moderate bending moment results in tension at one face of the column, and the vertical ties are provided to resist it. In order to ensure yielding of the tie element, anchorage requirements for its end node inside of the footing need to be defined. Therefore, Phase II specimens have been designed to explore the behavior of the longitudinal column reinforcement embedded in drilled shaft footings with the chief purpose of establishing the performance of different anchorage details for the reinforcement.

A total of four test specimens having different anchorage type of the longitudinal column reinforcement was planned for Phase II testing to investigate its effect on the behavior of the footing of which the ultimate state is governed by yielding of the column reinforcement. Figure 5.2 illustrates general geometry of test specimens, and the test matrix for Phase II testing is given in Table 5.1.

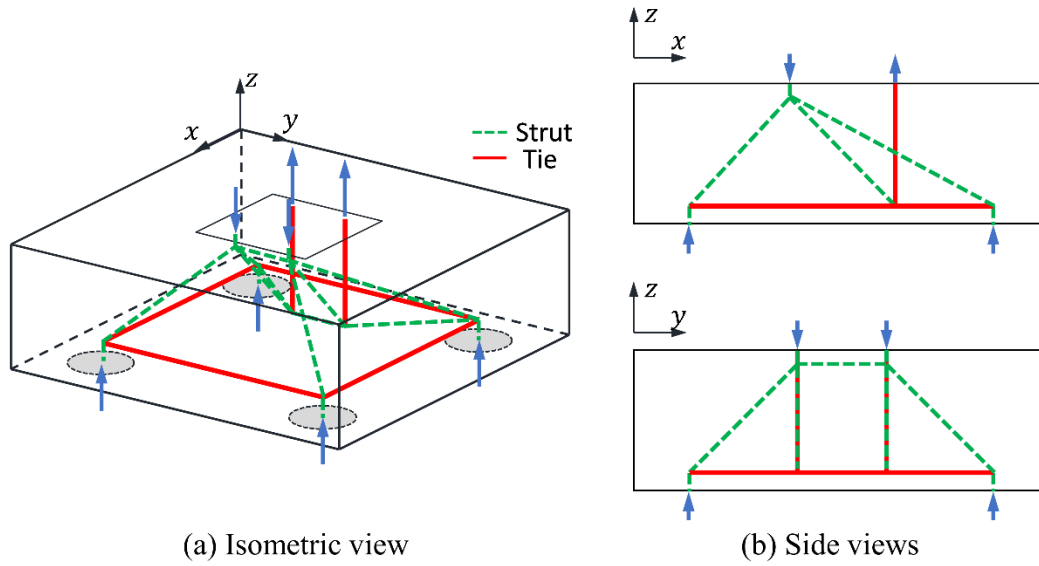


Figure 5.1 3D strut-and-tie model for drilled shaft footing where shafts are in non-uniform compression (isometric view: left / side views: right)

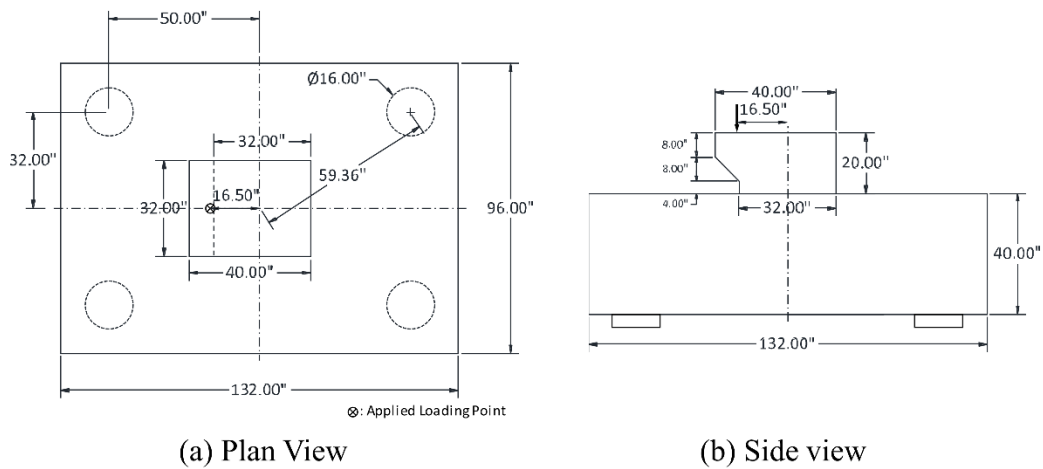


Figure 5.2 Dimension of specimen: Phase II

Table 5.1 Test matrix: Phase II

Series	Specimen No.	Specimen ID	Top/Bottom mat of reinforcement		Shaft Diameter z/d [in.]	Load eccentricity e [in.]	Column Reinforcement Anchorage
			Layout	Anchorage			
VI	1	VI-ST	Grid	Straight (Top Mat) & Hooked (Bottom Mat)	1.70	16.5"	Straight
	2	VI-HD					Headed
	3	VI-HKO					Hooked (Orientation: Outward)
	4	VI-HKI					Hooked (Orientation: Inward)

The tail end of the hook embedded in the footing is typically oriented in the direction away from the column for constructability. However, the hook anchorage resists the tensile force by bond stresses on bar surface and bearing on concrete inside the hook. In order to activate the bearing action inside the hook properly, the hook orientation needs to be determined based on internal force flow near the anchorage, similar to the orientation of hook in a beam-column joint.

Similarly, the compressive struts applied near the end of the column reinforcement may also affect force transfer mechanism of the column reinforcement depending on the orientation of hook, and it needs to be investigated through structural tests. Therefore, two hooked anchorage specimens with different hook orientations (VI-HKO and VI-HKI) were planned, in addition to the specimens with straight and headed anchorages, as shown in Figure 5.3.

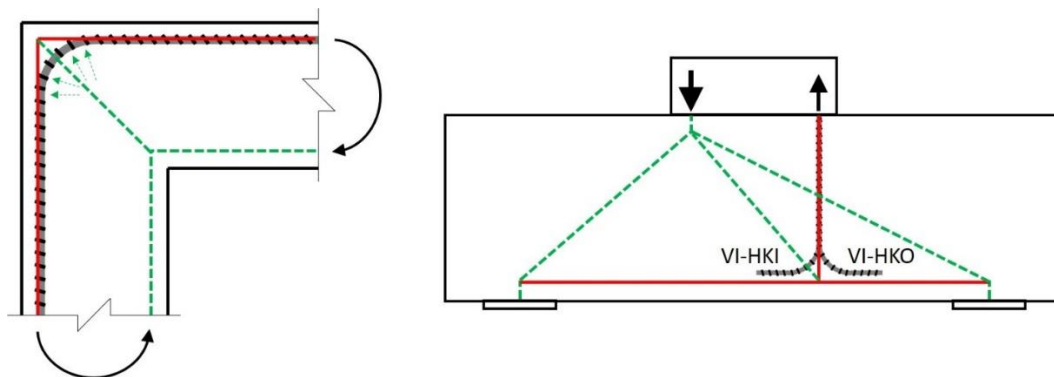


Figure 5.3 Typical hook orientation in a beam-column joint (left) and hook orientations planned for Phase II testing (right)

5.2.2. Specimen Design

5.2.2.1. Drilled Shaft Footing

Details of the specimen design were selected to augment the general specimen geometry and construction details of Phase I and were largely based on II-7 which represented the most common specimen in the experimental program. In addition, Phase II specimens included an integral corbel for applying an eccentric load in order to produce non-uniform compression at the supports. Other general details of the shaft-supported footing design are as follows:

Most details of geometry—length, width, height, drilled shaft diameter, drilled shaft pitch, and the column size at the interface—are identical to II-7. Reinforcement detailing is also identical to that of II-7 except for the column reinforcement and top mat reinforcement. Those details are regarded as a conservative design with sufficient structural capacity sufficient to investigate the post-yielding behavior of the column reinforcement without failure of the footing based on the test result of II-7. The provided top reinforcement ratio (0.20%) satisfied the minimum reinforcement requirement ratio specified in AASHTO LRFD (2020) ($> 0.18\%$), and it can also prevent premature conical cracks, which can affect bond behavior of the column reinforcement. Detail drawings of Phase II specimens are provided in Appendix D.

5.2.2.2. Column Corbel

Phase II tests utilized an eccentric externally applied load to the column corbel to simulate combined axial force and uniaxial bending moment imposed by a column. The eccentricity of the load was carefully determined since a large eccentricity can result in large reactions at two of four supports, and it may cause failure at the support region in the footing. Furthermore, the eccentricity should be enough to induce tensile yielding in the longitudinal column reinforcement prior to exceeding the strength of the footing. To that end, an eccentricity of 16.5-in. was selected, and the longitudinal column reinforcement and integral corbel were designed accordingly.

The 20-in. tall column corbel was sized to provide sufficient area to apply the eccentric load and was over-designed to preclude premature failure in the corbel. The amount of the crack control reinforcement more than 0.30% (0.48%) was provided in both longitudinal and transverse directions to satisfy the crack control reinforcement requirement of the current 2D strut-and-tie provision specified in AASHTO LRFD (2020) and to confine the concrete. A relatively high tie force is applied to the top horizontal ties developed in the STM of the corbel; therefore,

reinforcement was added and anchored with welding at both ends. Additionally, the corbel was laterally encased with 9/16-in. thick steel plates to preclude any undesired anchorage splitting failure or concrete crushing failure and eliminate the possibility of a premature failure in the corbel.

5.2.2.3. Column Reinforcement

To determine the column reinforcement size to be used in the tests, a parameter study was conducted using the TxDOT drilled shaft footing database described in Chapter 3. By filtering the footing plans with missing information for the study, a total of 24 drilled shaft footing plans were reviewed from the TxDOT drilled shaft footing database. The embedment lengths of the column reinforcement into the drilled shaft footing ($l_{b,c}$) were determined from the drawings, and divided by the diameter of the column reinforcing bars ($d_{b,c}$). The average $l_{b,c} / d_{b,c}$ ratio was 39.4. The $l_{b,c} / d_{b,c}$ coefficients for each drilled shaft footing plan are summarized in Figure 5.4. To have a similar l_b / d_b ratio in the test specimens, #7 reinforcement was selected given the available embedment length as tabulated in Table 5.2.

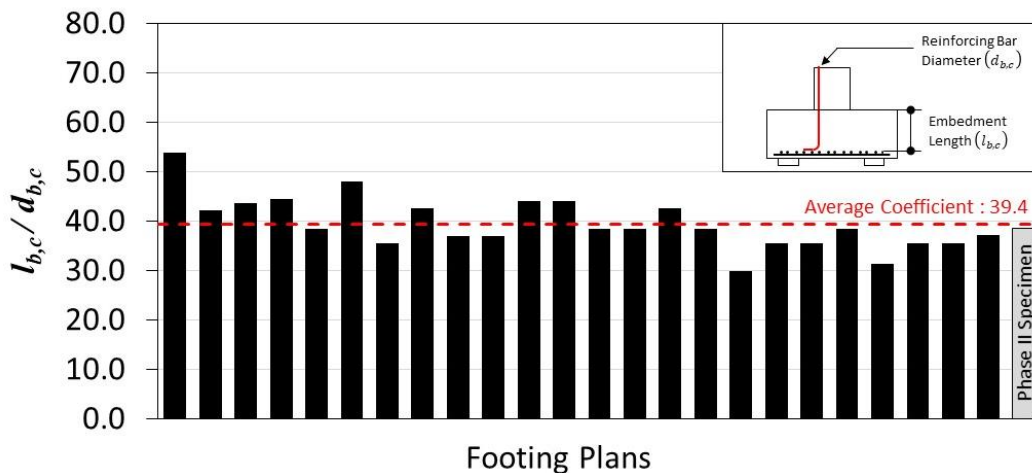


Figure 5.4 Embedment lengths of TxDOT drilled shaft footing database and Phase II specimens

Table 5.2 Comparison between column reinforcement embedment lengths of TxDOT drilled shaft footing database and Phase II specimens

TxDOT Drilled Shaft Footing Database		
Column Reinforcement Embedment Length ($l_{b,c}$) [in.]	Reinforcement Diameter ($d_{b,c}$) [in.]	$l_{b,c}/d_{b,c}$
Maximum	76.0	53.9
Minimum	42.0	29.8
Average	54.9	39.4
Phase II Specimens		
Column Reinforcement Embedment Length ($l_{b,c}$) [in.]	Reinforcement Diameter ($d_{b,c}$) [in.]	$l_{b,c}/d_{b,c}$
33.7	0.875	38.6

5.2.3. Materials

5.2.3.1. Concrete

- Mixture Design

As in Phase I testing, the design concrete strength of the footings was taken to be 3.6 ksi. Additionally, high-strength concrete with a design concrete strength of 10.0 ksi was used for the column corbel. The concrete design mix for the normal-strength concrete is the same as one used for Phase I testing (Design code: S3130310). The two mixture designs are summarized in Table 5.3.

Table 5.3 Concrete mix design for Phase II specimens

Mixture design (Code)		S3130310	293830-DLS
Component of Specimen		Footing	Column Corbel
Mixture components	Type I/II cement, [lb/yd ³]	338	665
	Class F fly ash, [lb/yd ³]	112	285
	Fine aggregate, [lb/yd ³]	1479	1087
	Coarse aggregate, [lb/yd ³]	1915	1760
	Water, [lb/yd ³]	250	276
	Water reducer, [oz/cwt CM]	4.0	-
	High-range water reducer, [oz/cwt CM]	5.5	-
	Water-cementitious ratio	0.56	0.29
Maximum aggregate size, [in.]		1.0	3/8
Specified slump, [in.]		7.0 ± 2.0	9.0 ± 1.5

- Material Tests

Since bond-slip behavior of reinforcement is governed by the concrete strength, only compressive strength of both footing and column corbel were examined by testing concrete cylinders. The details of the conducted compression test for the cylinders are presented in Section 4.2.3.

- Test Results

Concrete material test results are summarized in Table 5.4.

Table 5.4 Measured strengths of cylinders: Phase II

Specimen ID	Structure Type	Batch No.	Casting Date	28-days	Test Day	
				Compressive Strength (f'_c) [ksi]	Test Date (Age) [days]	Compressive Strength (f'_t) [ksi]
VI-ST	Footing	1	12/05/19	3.77	01/29/20 (55)	4.57
		2		4.05		4.68
	Column Corbel	1	12/20/19	11.14*		11.97
VI-HD	Footing	2	12/05/19	4.05	02/07/20 (64)	5.24
		3		3.82		4.78
	Column Corbel	1	12/20/19	11.14*		11.79
VI-HKO	Footing	1	02/05/20	4.69	03/19/20 (42)	5.30
		2		4.27		4.70
	Column Corbel	1	02/19/20	10.18*		10.36
VI-HKI	Footing	1	12/18/20	4.01	04/19/20 (122)	5.30
		2		4.10		5.20
	Column Corbel	1	03/16/21	10.02		10.02

5.2.3.2. Reinforcing Bars

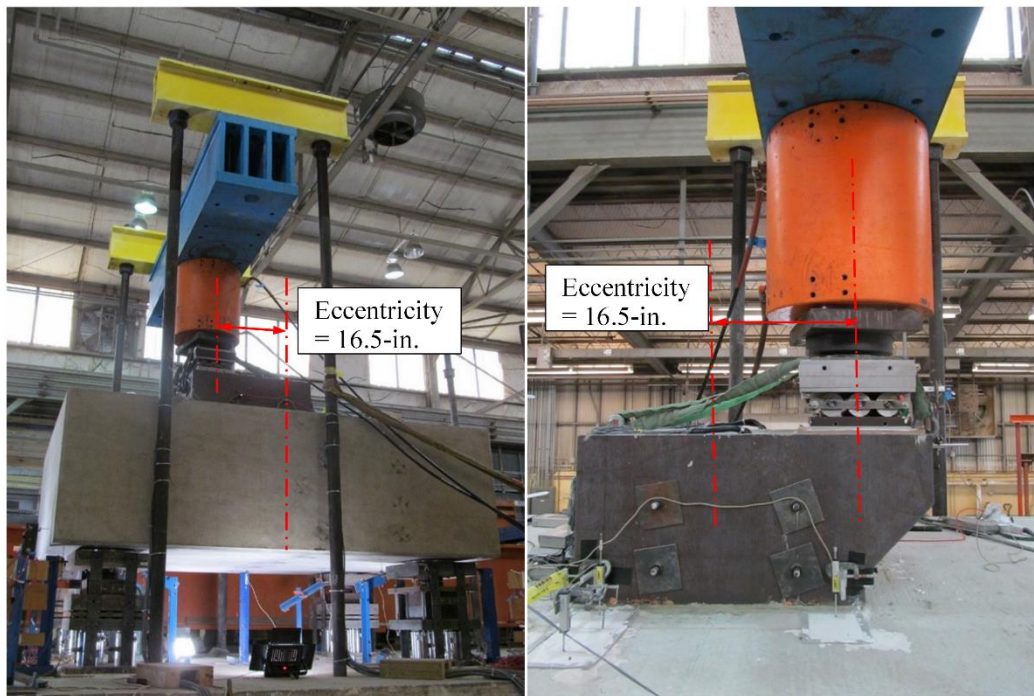
ASTM A706 Grade 60 reinforcing bars were used for the vertical column reinforcement such that the column reinforcement embedded in the corbel could be sufficiently anchored through welding. ASTM A615 Grade 60 reinforcing bars were used for all the other reinforcing bars. The average test results for each reinforcing bar size and set are summarized in Table 5.5.

Table 5.5 Mechanical properties of reinforcement: Phase II

Specimen ID	Bar Size	Location	Yield Strength (f_y) [ksi]	Tensile Strength (f_u) [ksi]
VI-ST	#7	Column	70.3	101.3
	#9	Bottom Mat	67.0	109.5
	#6	Top Mat	64.1	104.5
	#5	Face (Footing)	63.5	104.8
	#5	Face (Column)	68.2	103.7
VI-HD	#7	Column	72.1	101.3
	#9	Bottom Mat	67.0	109.5
	#6	Top Mat	64.1	104.5
	#5	Face (Footing)	63.5	104.8
	#5	Face (Column)	68.2	103.7
VI-HKO	#7	Column	70.3	101.3
	#9	Bottom Mat	67.0	109.5
	#6	Top Mat	63.6	104.4
	#5	Face (Footing)	63.5	104.8
	#5	Face (Column)	68.2	103.7
VI-HKI	#7	Column	76.8	105.0
	#9	Bottom Mat	69.9	109.6
	#6	Top Mat	63.5	104.1
	#5	Face (Footing)	70.5	105.7
	#5	Face (Column)	66.5	106.8

5.2.4. Testing Setup

All specimens comprising the Phase II experimental program were tested under an eccentric loading condition to generate non-uniform compression in the supports. Figure 5.5-(a) shows the test setup configuration. Each specimen was subjected to an eccentric load (16.5-in. eccentricity with respect to the centroid of pile cap) that was applied using one 2,000-kip capacity hydraulic ram and reaction frame bolted to the elevated strong floor. A custom-designed and machined loading fixture composed of a spherical saddle and a series of rollers was placed between the column corbel and the loading ram, as shown in Figure 5.5-(b), so that the column corbel was allowed to both rotate and translate. The supports of the specimen were identical to those utilized in Phase I testing as described in Section 4.2.4. Detailed drawings of the test configuration are provided in Figure 5.6.



(a) Test setup

(b) Loading part on the column corbel

Figure 5.5 Eccentric loading test setup for Phase II testing

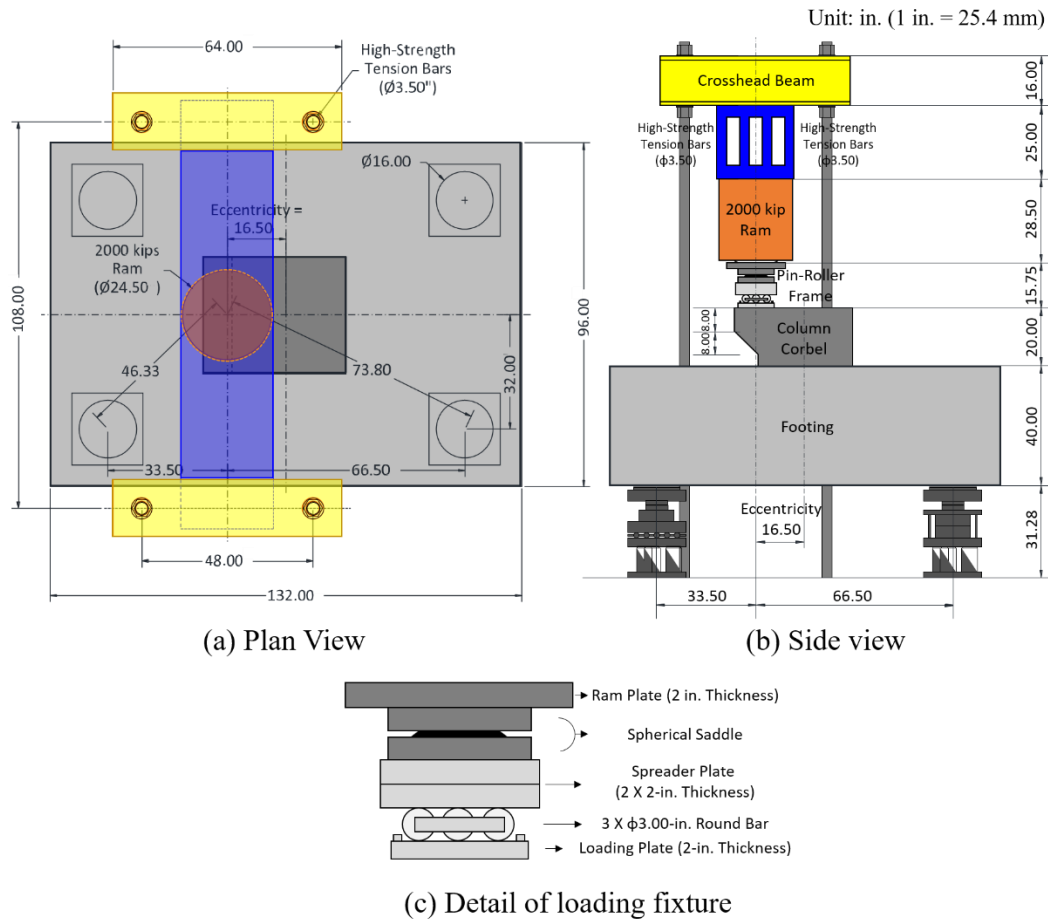


Figure 5.6 General test configuration for Phase II testing

5.2.5. Fabrication of Specimens

5.2.5.1. Drilled Shaft Footing

Drilled shaft footings were fabricated following the same methods used with Phase I testing specimens except for the column and top mat reinforcement. Figure 5.7 shows a specimen during fabrication after the installation of the top mat reinforcement and the longitudinal column reinforcement. Column reinforcement will be explained in the following section. More details about other identical fabrication procedures for footings are presented in Section 4.2.5.

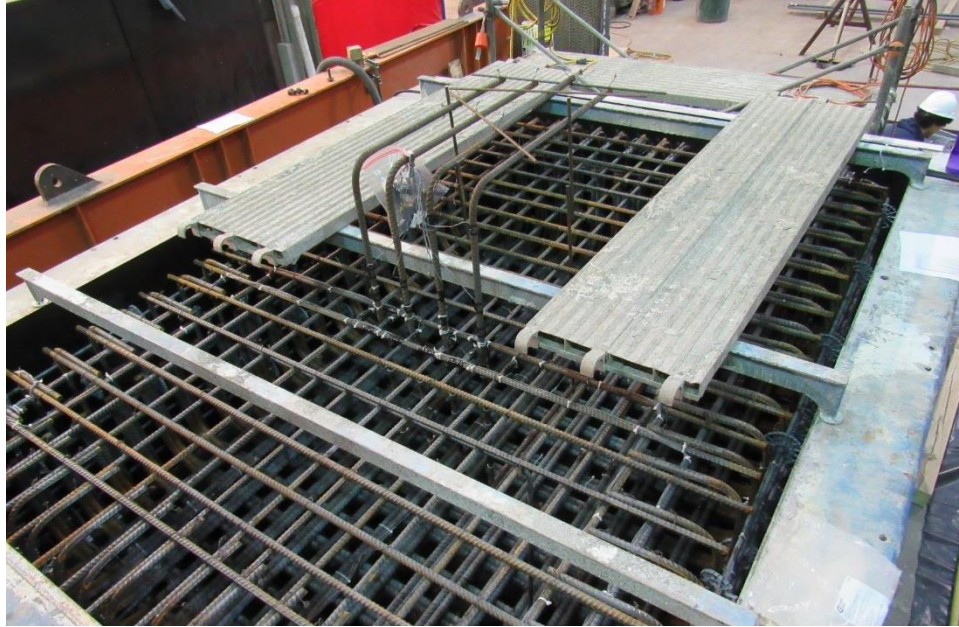


Figure 5.7 Top mat reinforcement and column reinforcement

5.2.5.2. Column Corbel

A summary of the column corbel fabrication procedure is depicted in Figure 5.8. The following outlines the sequence for fabricating the column corbels:

- (a) Chip the interface between drilled shaft footing and the column corbel
- (b) Assemble rebar cage
- (c) Attach strain gauges on top ties and crack control reinforcement
- (d) Install the steel jacket/permanent formwork. A 0.5-in. gap was provided between the steel jacket and the footing to prevent contact between the steel jacket and the top of the footing during testing.
- (e) Install threaded rods in the steel jacket.
- (f) Place concrete.



(a) Chipping the interface



(b) Completed rebar cage



(c) Strain gauges on reinforcement



(d) Install the steel jacket with the 0.5-in. gap (plywood)



(e) Install threaded rods



(f) Concrete placement

Figure 5.8 Procedure of column corbel fabrication

- Column Reinforcement

There are several types of head connections—friction welded, forged, and tapered thread. This project used Lenton Terminators produced by nVent LENTON, as shown in Figure 5.9, for headed anchorage detail. Lenton Terminators were carefully installed by applying the required torque. The net bearing area of the provided head was equal to four times the cross-section area of the reinforcing bar. Four longitudinal column reinforcing bars were installed at the tension side of the corbel. The amount of the column reinforcement was determined to induce reinforcement yielding prior to the failure of the footing and provide the reinforcement ratio close to the minimum reinforcement ratio for a column as

specified in AASHTO LRFD (2020) (1.00%) when the same amount of the reinforcement is provided at four sides of the column (0.93%).

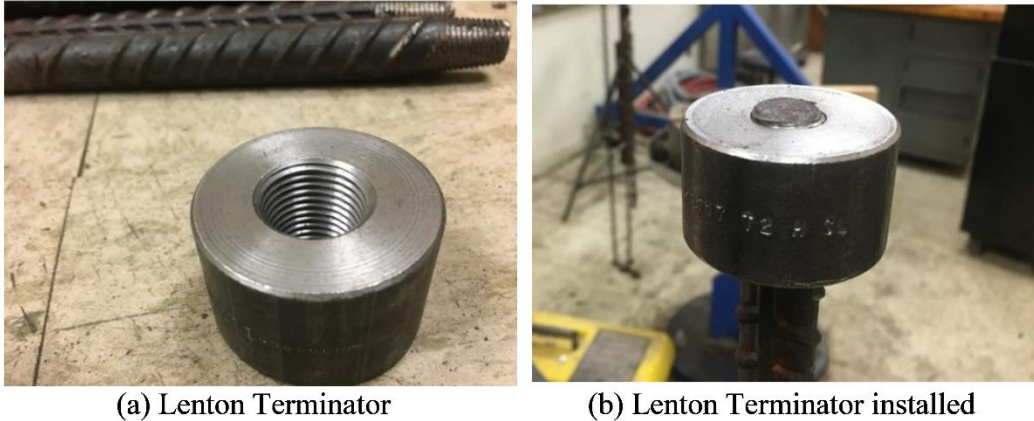


Figure 5.9 Lenton Terminators for headed bars

5.2.6. Instrumentation

In order to monitor loads, reactions, displacements, and strain development during testing, Phase II test specimens were also extensively instrumented, similar to Phase I test specimens.

In addition to the linear potentiometers placed beneath and sides of the footing to measure the deflection of the footing during the tests, linear potentiometers were installed at both sides of the column corbel to measure relative deformation of the column corbel at the interface, as shown in Figure 5.10. The tension-side displacement was measured at the location of column reinforcement on the top of drilled shaft footing, which indicates the relative uplift of the column corbel at its tension face with respect to the drilled shaft footing. Similarly, the compression-side displacement was measured at the symmetric position of the column reinforcement.

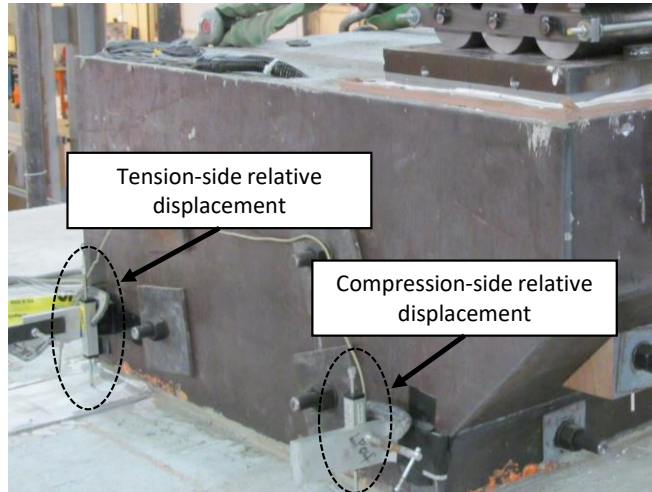


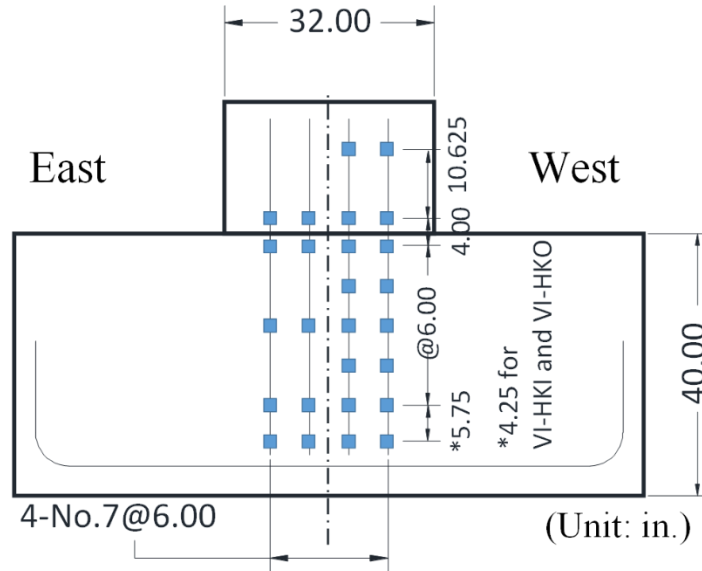
Figure 5.10 Linear potentiometers to measure relative displacement of column corbel

Furthermore, each longitudinal column reinforcement was instrumented with a series of ERSG measurements along its length so that the measured data can develop a stress profile of the reinforcement. The obtained stress profiles represent the behavior of the column reinforcement; therefore, they can be utilized for defining a critical section for anchorage requirements of the column reinforcement. The gauges were attached on longitudinal ribs of the column reinforcement, as shown in Figure 5.11, to minimize grinding of reinforcement and waterproof protection area, which might adversely affect the bond.

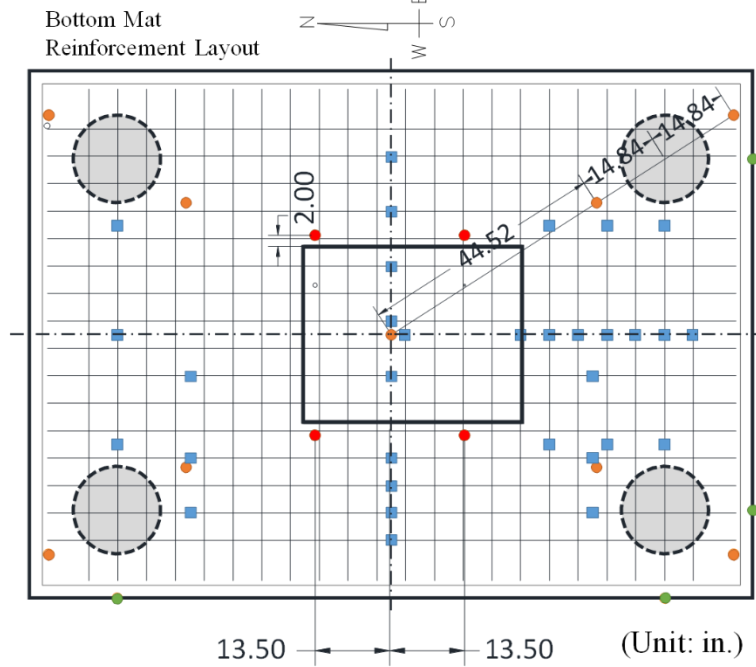


Figure 5.11 Polished longitudinal rib (left) and minimized protection area (right)

Instrumentation maps for VI-ST, VI-HD, and VI-HKO are provided in Figure 5.12. Since VI-HKI was tested later than the others, the specimen was instrumented with more ERSGs. Appendix D contains instrumentation maps for each specimen. Detailed descriptions of the other instrumentation are the same as those of Phase I testing and presented in Section 4.2.6.



(a) Instrumentation map of longitudinal column reinforcement



- Linear Potentiometer (Vertical – installed underneath footing)
- Linear Potentiometer (Vertical – installed on footing)
- Linear Potentiometer (Lateral)
- Support
- ERSGs

(b) Instrumentation map of footing

Figure 5.12 Instrumentation map of Phase II specimens (VI-ST, VI-HD, VI-HKO)

5.2.7. Test Procedure

Test specimens were loaded in 100-kip increments up to the load when the maximum column reinforcement reaches 75% of yield strain. Between load increments, the condition of the specimens was visually inspected and documented, and the performance of instrumentation and monitoring equipment was checked. After reaching 75% of yield strain of the column reinforcement, the specimen was continuously loaded until any signs of failure observed while simultaneously recording instrumentation and video data.

However, the second test specimen (VI-HD) failed by fracture of the column reinforcement, and it led to a catastrophic failure of the specimen. Therefore, the research team decided to apply the loading up to 2,000 kips only from the third specimen even though the specimen did not fail for safety reasons.

5.3. Experimental Results and Discussion

5.3.1. Overview

In this section, observations and data obtained from test specimens during and after tests will be provided and discussed based on visual observation, load-deflection behavior, stress distribution in bottom mat reinforcement, and stress profiles of the column reinforcement to examine the column reinforcement with various anchorage types. The notations used in this chapter are listed as follows:

$f'_{c,f}$	Average compressive strength of concrete for each batch comprising the footing at the time of testing measured in accordance with ASTM C39 [ksi]
$f'_{c,c}$	Average compressive strength of concrete comprising the column corbel at the time of testing measured in accordance with ASTM C39 [ksi]
$f_{y,b}$	Yield strength of bottom mat reinforcement measured in accordance with ASTM A370 [ksi]
$f_{y,c}$	Yield strength of column reinforcement measured in accordance with ASTM A370 [ksi]
P	Total applied load [kip]
$P_{fy,b}$	Load at the first yielding of bottom mat reinforcement [kip]
$P_{fy,c}$	Load at the first yielding of column reinforcement [kip]
$P_{y,c}$	Load at yielding of all column reinforcement [kip]
P_u	Ultimate load of the test specimen [kip]
Δ	Deflection under the center of loading area compensating the deflection of the support ($= \Delta_m - \Delta_{supp}$) [in.]

$\Delta_c =$	Measured compression-side relative displacement of column corbel [in.]
$\Delta_m =$	Measured deflection under the center of loading area [in.]
$\Delta_{supp} =$	Average deflection at the center of four support plates [in.]
$\Delta_t =$	Measured tension-side relative displacement of column corbel [in.]

Firstly, visual observations of test specimens are discussed based on post-failure conditions of test specimens loaded up to failure since some Phase II specimens were not loaded up to failure due to the safety issue. Instead, all Phase II specimens were dissected orthogonally after testing at the west-end column reinforcement position to compare interior crack patterns between the specimens. By comparing the internal crack patterns, the behavior of the tested various anchorage types could be evaluated visually.

To investigate load-deflection response of the test specimens, the normalized deflection of the footing and the relative displacement of the column corbel were exploited. The displacement measured at the center of the footing and that measured vicinity of the support were used to normalize deflection of the footing as described in Section 4.3. The relative tension and compression-side displacements of the column corbel measured at both sides were also compared between test specimens to represent the relative deformation at the interface. The applied load corresponding to the deflection data was obtained by the summation of the measurement from load cells underneath supports.

Furthermore, the monitored strains in bottom mat reinforcement from the ERSGs attached on the reinforcing bars were plotted by circle markers similar to Phase I test specimens. The strains are expressed in the ratios of the measured strain to yield strain. The plot could provide strain distribution of the bottom mat reinforcement at varying load levels.

Lastly, strains of the primary column reinforcement embedded in the footing were monitored through a series of ERSGs during each test. The stress-strain relationships obtained from tension tests on the column reinforcing bars were employed to convert strains to stresses. The stresses measured at a column reinforcing bar were plotted at their respective elevation to develop a stress profile of the column reinforcement. The stress discrepancy between two measuring locations was resisted by the bond stress acting on the surficial area of reinforcement. Therefore, a bond stress profile of the column reinforcement could also be developed based on the stress profile, as illustrated in Figure 5.13.

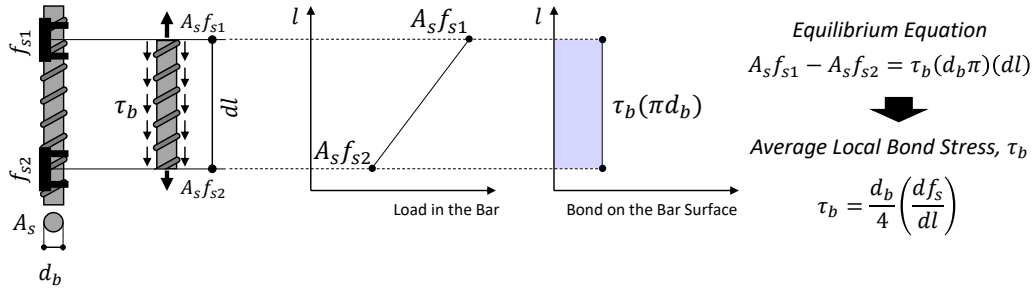


Figure 5.13 Average bond stress acting between two adjacent strain measurement locations

The computed bond stresses at varying load stages were also developed to examine the column reinforcement with various anchorage types. Additionally, the research team compared the computed bond stresses to the local splitting bond strength, $\tau_{bu,split}$ specified in fib Model Code 2010 (2013) as follows in Eq. (5.1):

$$\tau_{bu,split} = \eta_2 6.5 \left(\frac{f_{cm}}{25} \right)^{0.25} \left(\frac{25}{\phi} \right)^{0.2} \left[\left(\frac{c_{min}}{\phi} \right)^{0.33} \left(\frac{c_{max}}{c_{min}} \right)^{0.1} + k_m K_{Tr} \right] \quad \text{Eq. (5.1)}$$

where:

$\tau_{bu,split}$ = local splitting bond strength [MPa]

η = 1.0 (good bond condition: 90-degree to the horizontal during concreting)

f_{cm} = mean cylinder concrete compressive strength [MPa]

ϕ = diameter of the anchored bar considered [mm]

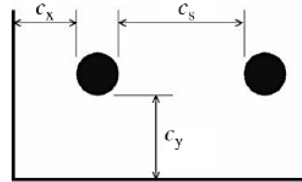
c_{min} = $\min\{c_s/2, c_x, c_y\}$ [mm]

$$\left(0.5 \leq \left(\frac{c_{min}}{\phi} \right) \leq 3.5 \right)$$

c_{max} = $\max\{c_s/2, c_x\}$ [mm]

$$\left(1.0 \leq \left(\frac{c_{max}}{c_{min}} \right) \leq 5.0 \right)$$

$k_m K_{Tr}$ = passive confinement factor from transverse reinforcement
 (=0; not considered in this section since no transverse reinforcement was provided to the column reinforcement)



5.3.2. Series VI: Anchorage Type of Column Reinforcement

5.3.2.1. Strength Results

The test results of Series VI are summarized for comparison in Table 5.6. After testing the specimen failed by rupture of the column reinforcement (VI-HD), the research team stopped loading the remainder Phase II specimens (VI-HKO and VI-HKI) at 2,000 kips. All column reinforcing bars of the test specimens yielded in the middle of testing, whereas the bottom mat reinforcement of the teste specimens did

not experience yielding until 2,000 kips loading. Therefore, the column reinforcement embedded in the specimens was considered to experience post-yielding behavior sufficient to evaluate anchorage types, even though they were not able to reach their ultimate state until 2,000 kips loading.

Table 5.6 Summary of experimental results: Phase II

Specimen ID	VI-ST	VI-HD	VI-HKO	VI-HKI
Anchorage detail of column reinforcement	Straight	Headed	Hooked (Outward to column)	Hooked (Inward to column)
$f'_{c,f}$ [ksi]	4.62	5.01	5.00	5.25
$f'_{c,c}$ [ksi]	11.97	11.79	10.36	10.02
$f_{y,b}$ [ksi]	67.0	67.0	67.0	69.9
$P_{fy,b}$ [kip]	2,025	2,080	N/A*	N/A*
$f_{y,c}$ [ksi]	70.3	72.1	70.3	76.8
$P_{fy,c}$ [kip]	1,189	1,146	1,195	1,241
$P_{y,c}$ [kip]	1,564	1,540	1,416	1,422
P_u [kip]	2,079	2,154	2,000*	2,000*
Failure mode	Failure in footing	Fracture of column reinforcement	N/A*	N/A*

* Testing stopped prior to failure (at 2,000 kips)

5.3.2.2. Visual Observation

As described in the previous section, different failure modes were observed in VI-ST and VI-HD (specimens of straight and headed column reinforcement). Overall failure patterns observed in those two specimens are provided in Figure 5.14.



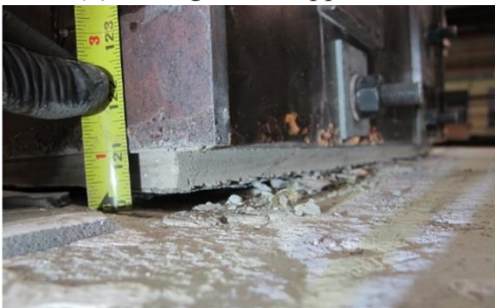
(a) Damage on side surface of footing (west)



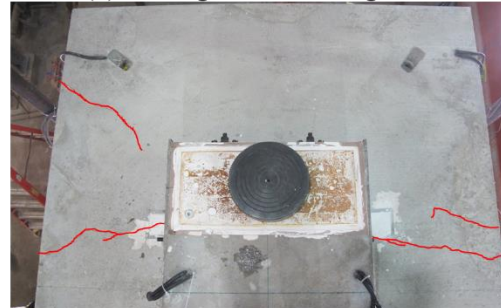
(b) Damage near support side



(c) Damage near loading side



(d) Deformation on tension side



(e) Damage on top surface of footing

Figure 5.14 Post-failure conditions of VI-ST

The failure of VI-ST occurred from the footing. The crack pattern of the footing after testing was similar to that observed in Phase I footings. However, most of the damage was concentrated near the half span of the footing on the side of supports

subjected to a high reaction. On the other hand, no damage was detected visually on the column corbel confined by steel plates. Instead, concrete crushing and crack opening (3/8-in. width) could be identified easily via visual inspection at the compression side and tension side of the 0.5-in. gap between the steel jacket and the footing, respectively. The concrete crushing at the compression side made the steel jacket contact directly with the footing. As a result, several cracks propagated from the compression side of the column corbel on the top surface of the footing.

Figure 5.15 shows the post-failure conditions of VI-HD. Since the concrete strength of the footing component of VI-HD is approximately 10% higher than that of VI-ST, VI-HD was failed by rupture of the column reinforcement. The small amount of the longitudinal column reinforcement (two No. 3) embedded in the footing on the compression side of the column corbel could not resist the sudden overturning force at the rupture of the tensile column reinforcement. Therefore, the column corbel fell off the specimen at the failure. This failure mode was so catastrophic that some elements of the test setup were damaged; therefore, the research stopped testing at 2,000 kips loading of the remaining Phase II specimens for safety. The 2,000-kip load limit was determined to evaluate the post-yielding behavior of the column reinforcement with various anchorage types since yielding of the column reinforcement embedded in both specimens occurred around 1,550 kips.

Even though the failure of VI-HD was not governed by the footing, the crack pattern of the footing after the test was almost identical to that observed in VI-ST. This indicates that the footing component of VI-HD was also close to the ultimate state at the failure. Furthermore, the interface between the column corbel and the footing could be investigated. A small concrete cone was formed surrounding the column reinforcement, and apparent splitting cracks between the column reinforcement could be found at the tension-side of the interface. Crushed concrete debris originated from the 0.5-in. gap was found on the compression side of the interface, but the footing part seemed undamaged.



(a) Damage on side surface of footing (west)



(a) Cracks on top surface



(b) Crushing of column corbel on loading side



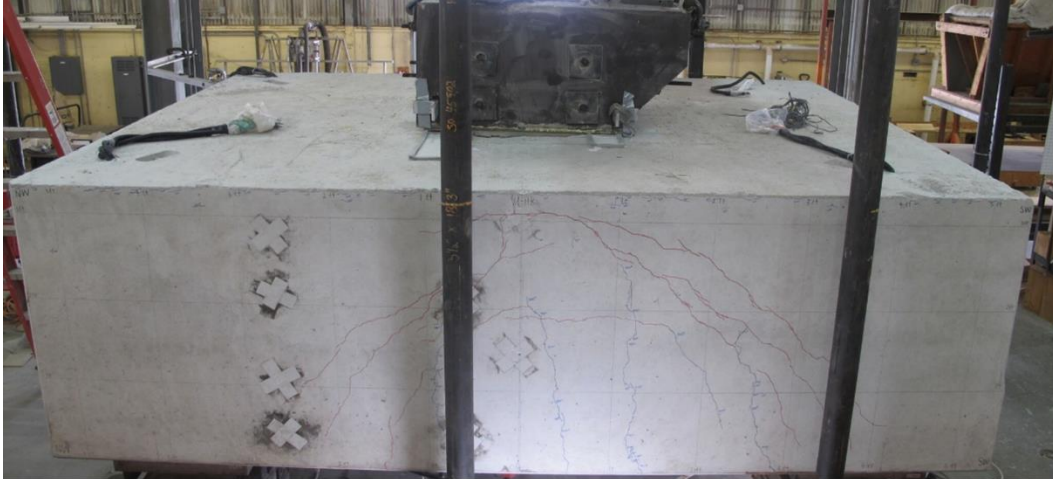
(c) Split cracks near column reinforcement



(d) Fracture of column reinforcement

Figure 5.15 Post-failure condition of VI-HD

The other Phase II specimens (VI-HKO and VI-HKI) were able to be loaded to the test limit; 2,000 kips, without failure, and their crack patterns were inspected after unloading. The crack patterns were comparable to the aforementioned specimens, as shown in Figure 5.16.



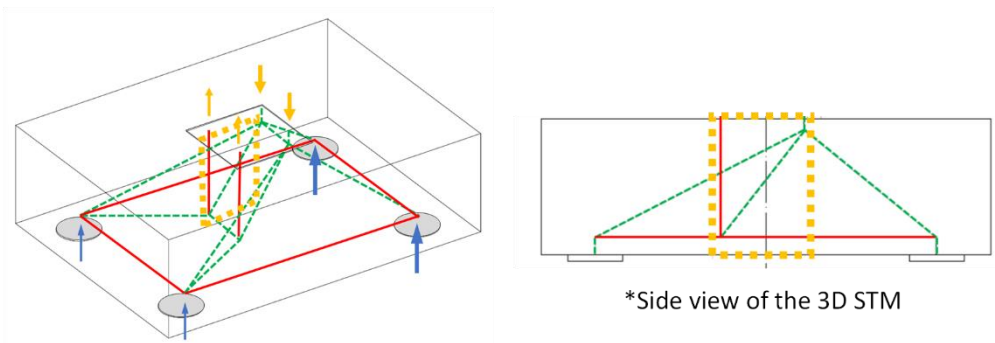
(a) Side surface (west) of VI-HKO after testing



(a) Side surface (west) of VI-HKI after testing

Figure 5.16 Post-failure condition of VI-HKO and VI-HKI

Additionally, the research team dissected all Phase II specimens orthogonally after testing at the column reinforcement position to compare interior crack patterns, as shown in Figure 5.17.

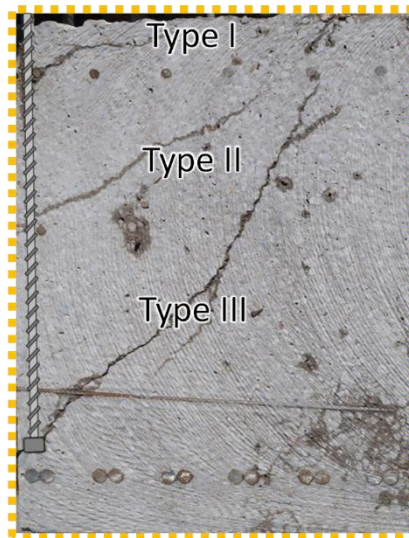


*Side view of the 3D STM

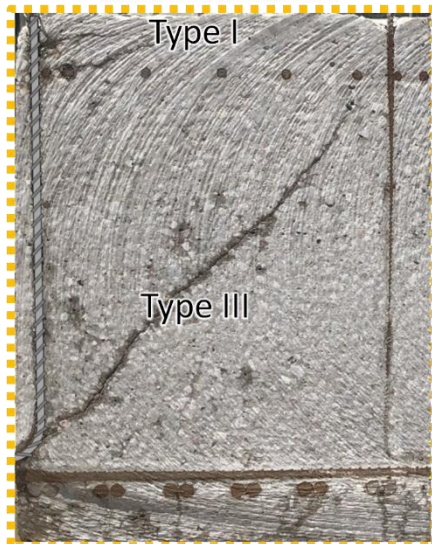
(a) Position of cut section in the 3D strut-and-tie model



(b) VI-ST



(c) VI-HD



(d) VI-HKO



(e) VI-HKI

Figure 5.17 Cut sections of Phase II specimens

Three cracking types were identified in the cut sections. The first type (Type I) is a conical crack formed near the top surface of the footing starting from the level of the top mat reinforcement induced by highly-concentrated tensile strain near the interface. The second and third cracking types are splitting cracks formed at the middle (Type II) and bottom tip of the column reinforcement (Type III) induced by the diagonal struts flowing down to the drilled shaft and bottom end of the column tie element, respectively. The crack induced by the diagonal strut flowing down to the drilled shaft does not intersect with the vertical tie element. Still, the crack was formed over the entire width of the footing, as shown in Figure 5.18. All those types of cracking were notably formed at the section of VI-ST and VI-HD. However, the first and second type cracking was not formed at the section of VI-HKI and VI-HKO, respectively. Furthermore, the third type of cracking formed in VI-HKO did not cross the column reinforcement but passed underneath the bend radius of its hook. In contrast, the crack passed through the bend radius and the tail of the hook in the specimen of the opposite hook orientation (VI-HKI).



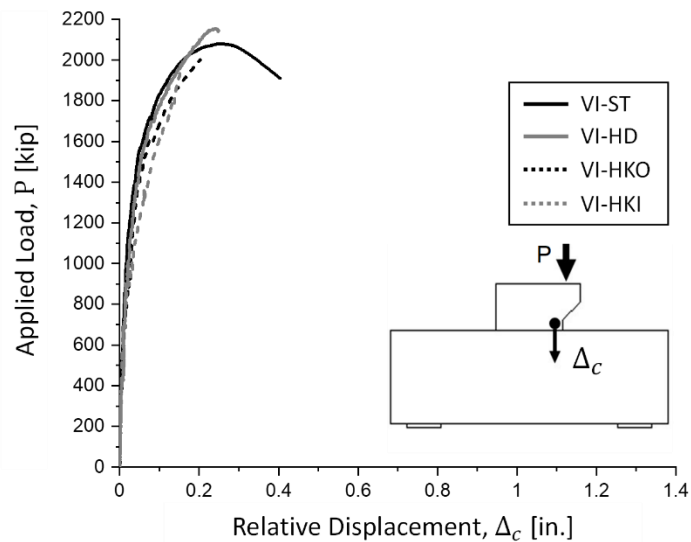
Figure 5.18 Internal cracks formed entire with of specimen (VI-ST)

5.3.2.3. Load-deflection response

To compare load-deflection responses between test specimens designed with various anchorage types, the research team compared the normalized deflection of the footing, compression-side, and tension-side relative displacements of the column corbel measured during the tests. Each displacement measured for all Phase II specimens was compared to all the others, as shown in Figure 5.19. The primary test results and findings from the load-deflection response are as follows:

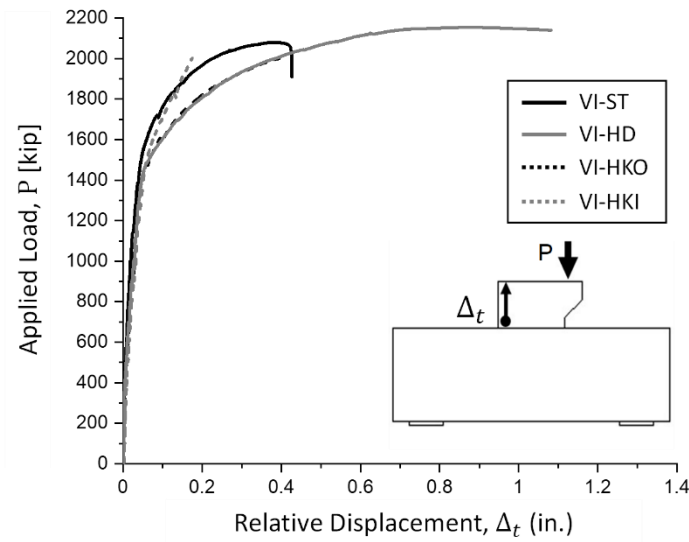
- The load-normalized deflection responses of the footing measured at all Phase II specimens are comparable to each other until 2,000 kips loading.
- The tension-side relative displacement of VI-HKI did not increase significantly compared to that of the compression-side even beyond the yielding load of all column reinforcing bars.

The tension-side relative displacement of the other Phase II specimens increased rapidly after exceeding the yielding load of all column reinforcing bars.

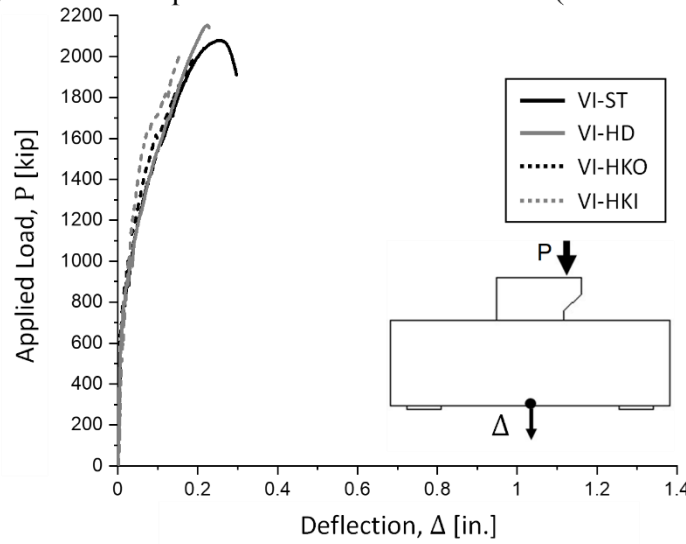


(a) Relative displacement of column corbel (compression-side)

Figure 5.19 Load-deflection responses of specimens: Phase II



(b) Relative displacement of column corbel (tension-side)



(c) Deflection of footing

Figure 5.19 (cont'd) Load-deflection responses of specimens: Phase II

5.3.2.4. Strain distribution in bottom mat reinforcement

Figure 5.20 shows the strain development in bottom mat reinforcement of Phase II specimens at ultimate load. Regardless of the anchorage types, the bottom mat reinforcement did not yield until 2,000 kips loading. The reinforcing bars along the long span experienced higher strain than those in the short span. Overall, the bottom mat reinforcement of all Phase II specimens behaved similarly regardless of the anchorage type on the basis of the strain distribution.

NORTH

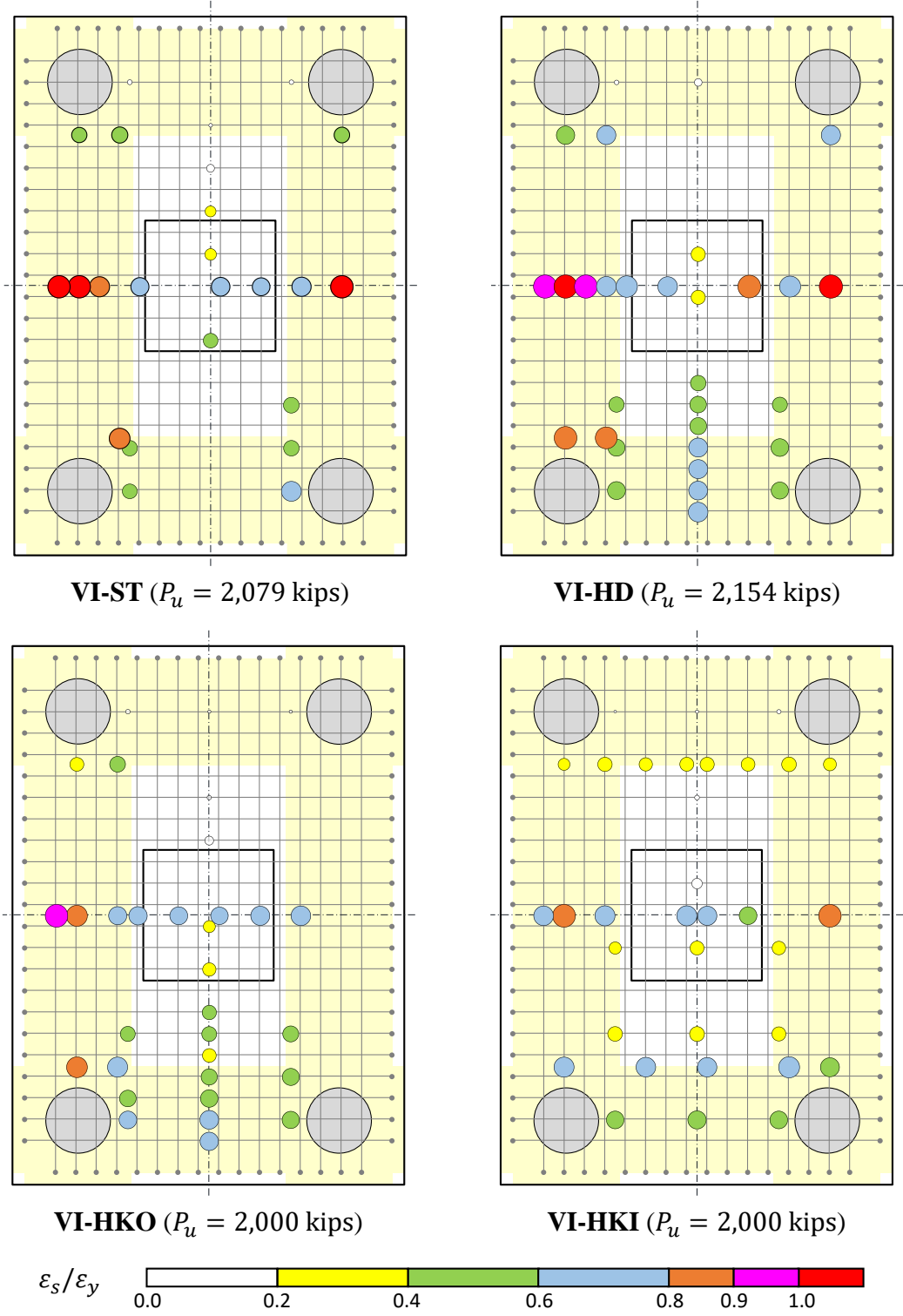
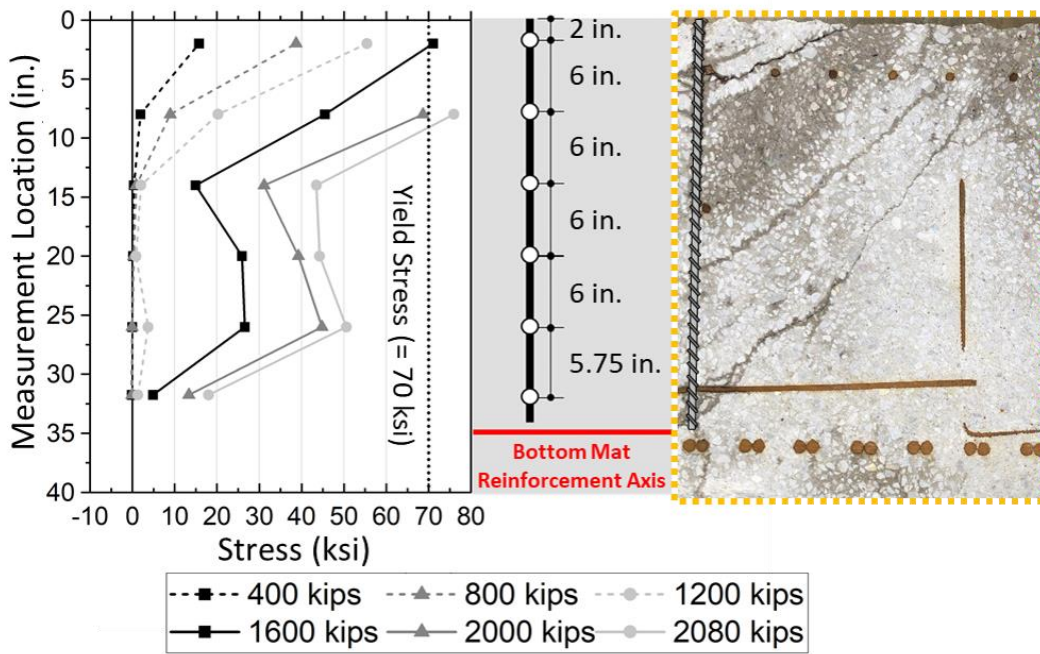


Figure 5.20 Strain distribution in bottom mat reinforcement at ultimate load: Phase II

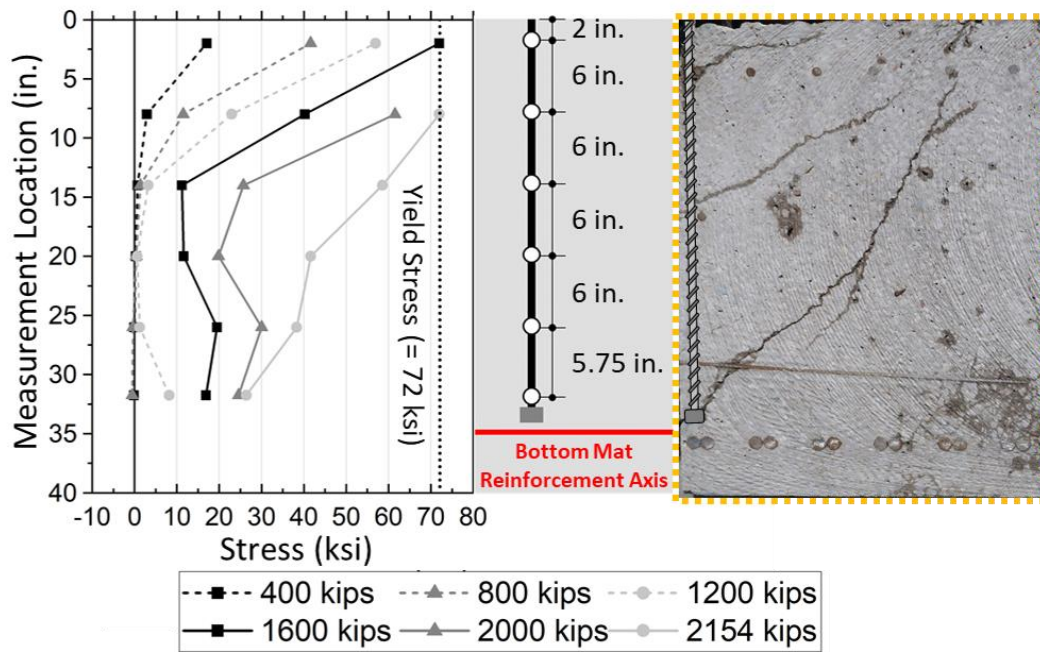
5.3.2.5. Stress Profiles and Bond Stress Profiles of Column Reinforcement

The stress profiles of the column reinforcement were developed based on the measured strains through the ERSGs attached to the column reinforcement and the stress-strain relationship obtained from the material tests. Since the position of the column reinforcement in the test specimen did not influence the overall shape of the stress profile significantly, the stress profile of the column reinforcement positioned at the west-end was selected for comparing the profiles between Phase II specimens. The profiles are presented with the cut section, as shown in Figure 5.21. Following are the primary test results and findings obtained from the stress profiles:

- Column reinforcement was able to develop most of its yield strength (85%) within the upper 16 in. of their embedment length inside the footing. In the case of VI-HKO, the yield strength was fully developed within 20 in. from the top.
- The embedment lengths provided to all three specimens were sufficient to develop the full yield strength of the bars.
- Stresses near the bottom tip of reinforcement increased in all specimens except VI-HKO. Instead, the column reinforcement of VI-HKO experienced a relatively higher stress level near the interface with the column than that of the other specimens.
- For VI-ST, the non-uniform stress distribution near the bottom of the straight bars can be explained by activation of bond stresses due to bar slip.
- For VI-HD and VI-HKI, stresses near the bottom tip of the column reinforcement show a rather uniform distribution. This indicates that small bond stresses were activated in this region.
- When the column reinforcement yielding was identified from the attached gauge near the column interface, the tensile stresses developed right above the inner-oriented hook (VI-HKI) and the head (VI-HD) at the bottom of the bar were 17 ksi (24% of the yield strength) and 41 ksi (53% of the yield strength), respectively.

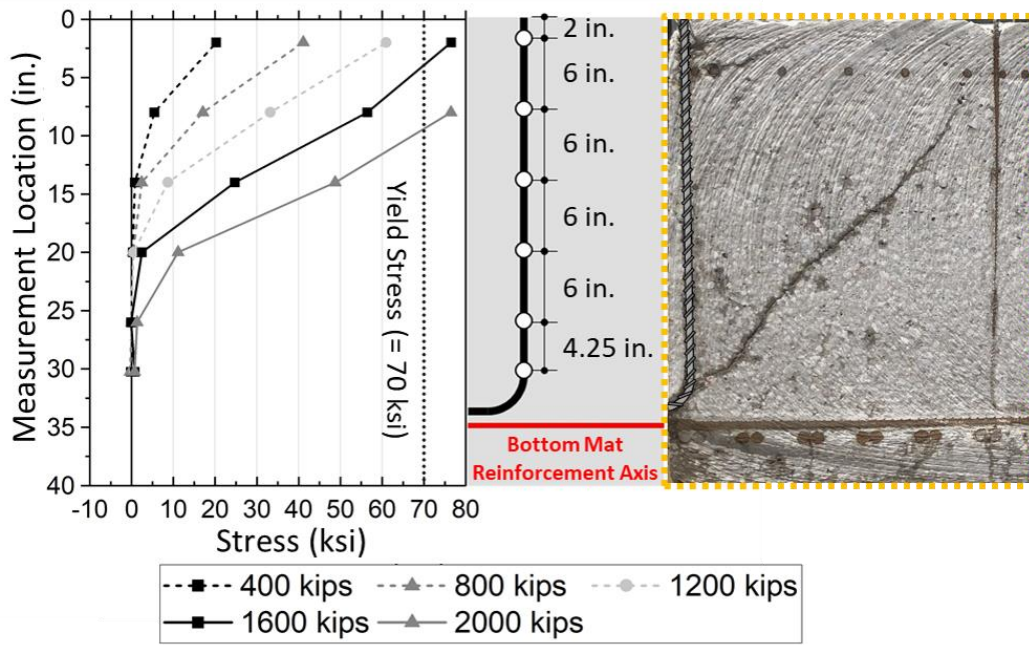


(a) VI-ST

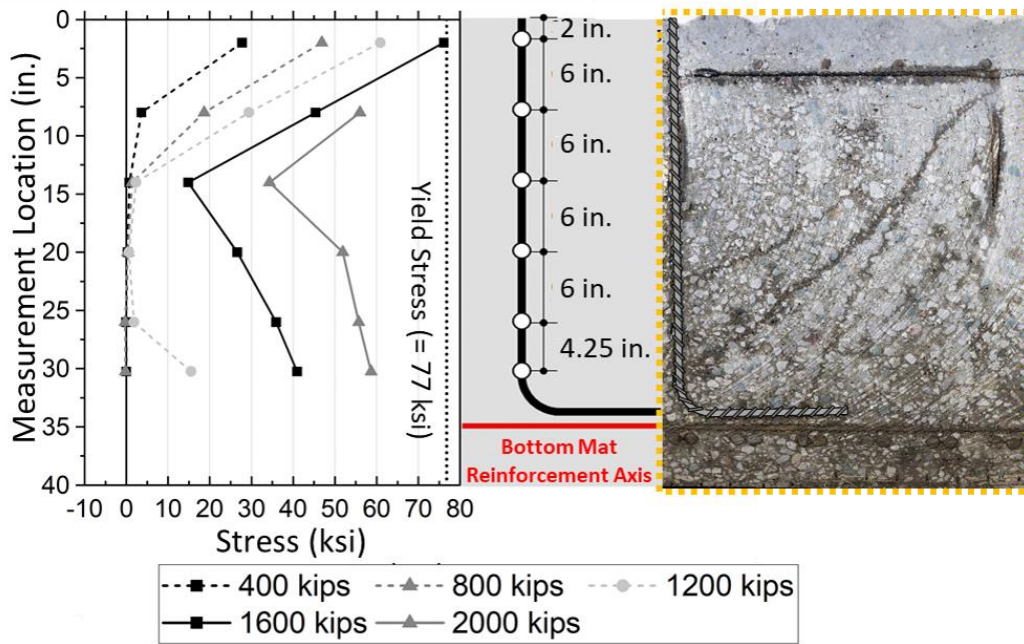


(b) VI-HD

Figure 5.21 Stress profiles of column reinforcement



(c) VI-HKO

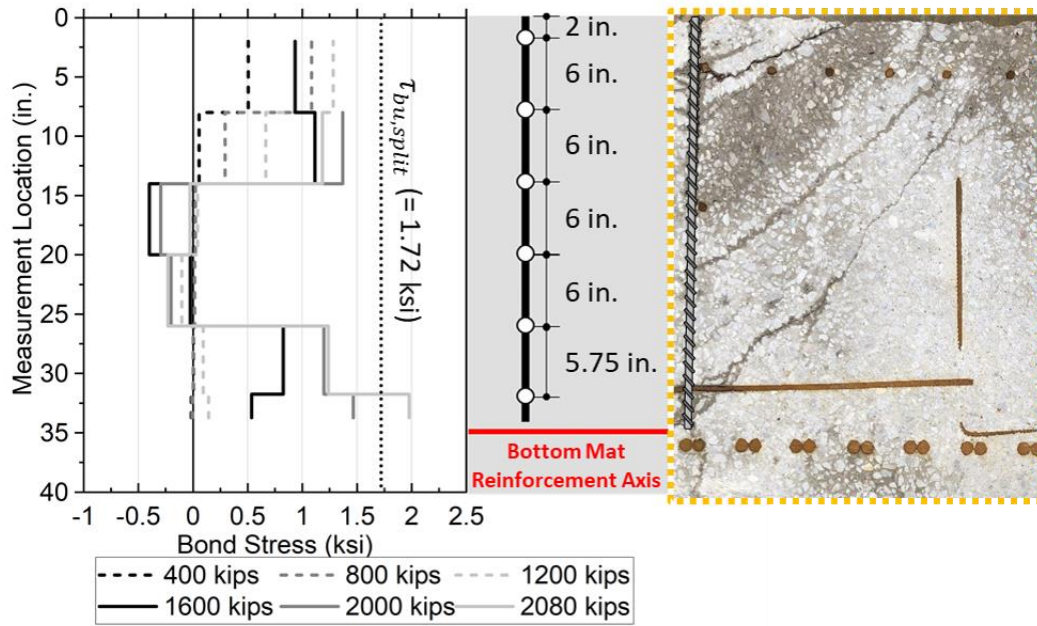


(d) VI-HKI

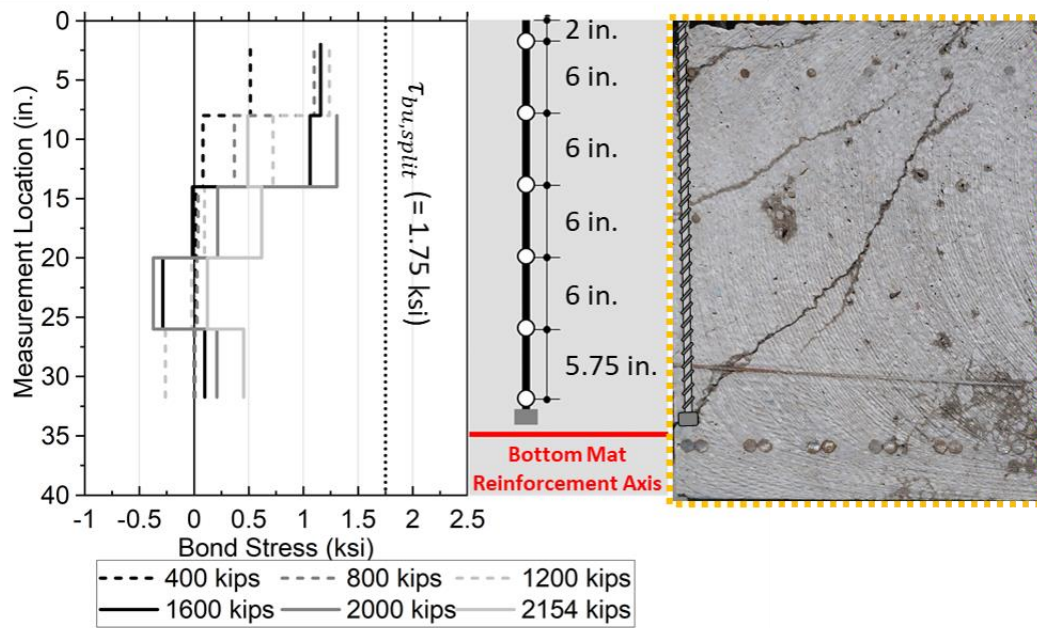
Figure 5.21 (cont'd) Stress profiles of column reinforcement

Based on the developed stress profiles, bond stress profiles were developed, as shown in Figure 5.22. A uniform bond stress distribution was assumed between two adjacent gauges, and the profiles are presented with the cut section as well. Following are the primary test results and findings obtained from the bond stress profiles:

- The peak bond stresses computed near the interface during Phase II tests were comparable to each other. However, they are smaller than the local bond resistance, $\tau_{bu.split}$ specified in fib Model Code 2010 (2013) since the computed bond stresses were not able to catch the local bond stress but were averaged between two measurement locations.
- The bond stress near the bottom tip of the straight column reinforcement was significantly higher than the other types of anchorages.
- Almost no bond stresses developed near the bottom end of the headed and inner-oriented hooked column reinforcement at the load when the gauge near the interface exceeds the yield strain (1,600 kips). A slight increase of bond stresses was identified at the loading beyond 1,600 kips for both anchorage types.
- Since small tensile stresses developed near the bottom end of the outer-oriented hooked column reinforcement, the bond stress near the bottom end of the outer-oriented hook was negligible.

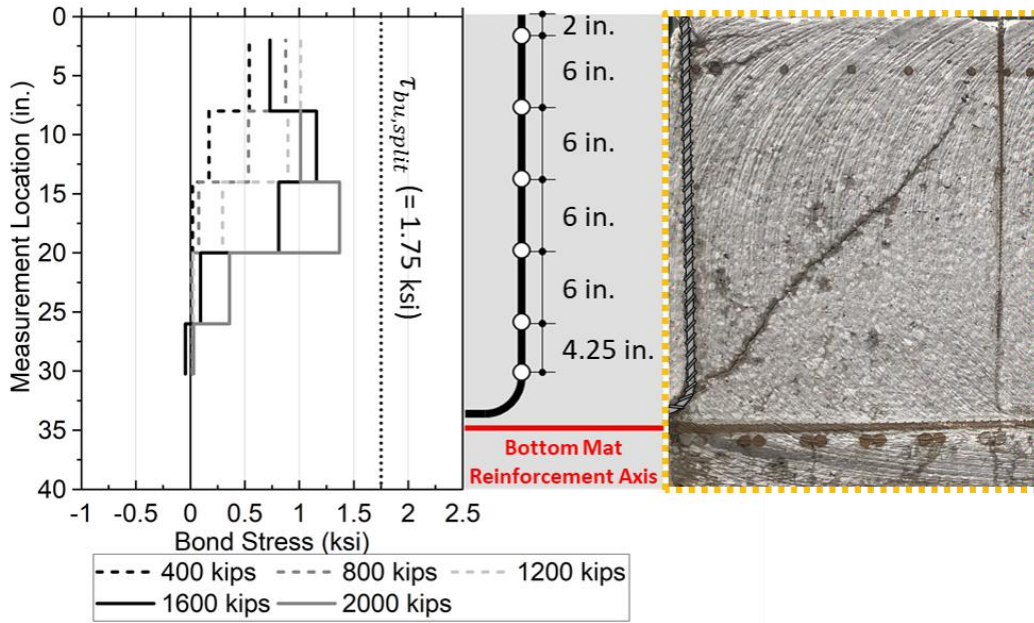


(a) VI-ST

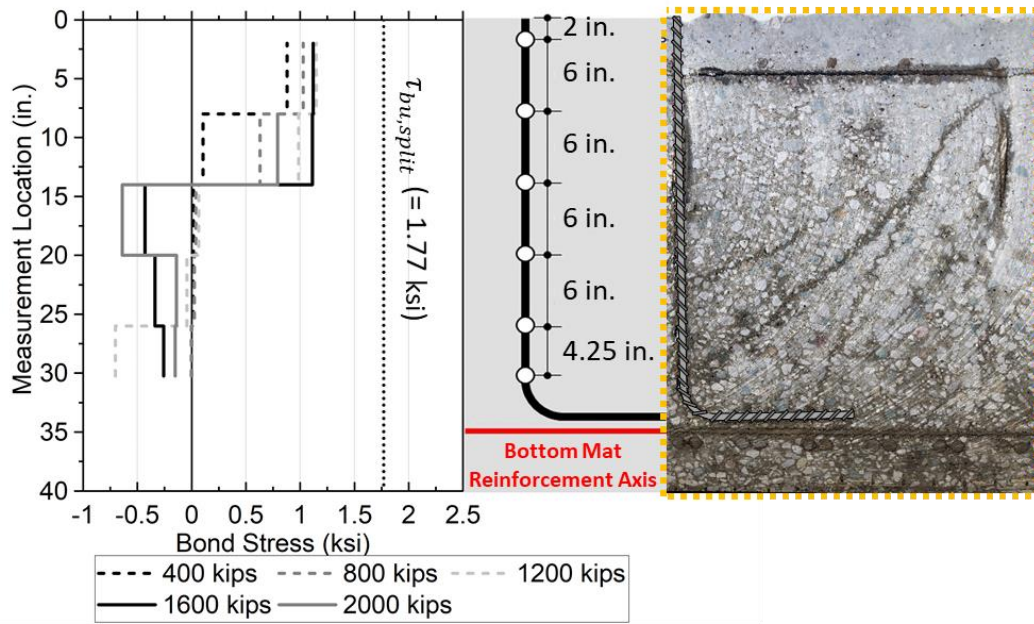


(b) VI-HD

Figure 5.22 Bond stress profiles of column reinforcement



(c) VI-HKO



(d) VI-HKI

Figure 5.22 (cont'd) Bond stress profiles of column reinforcement

5.3.3. Critical Section of Column Reinforcement

The research team identified the stress increment at the middle of the column reinforcement in all properly anchored column reinforcement of Phase II specimens (i.e., all Phase II specimens except for VI-HKO). The stress increment was caused by the diagonal crack formed at the middle of the column reinforcement, and the cut sections showed that the crack was induced by the diagonal strut flowing down to the drilled shaft of the opposite loading side. Further, the column reinforcement experienced another diagonal cracking induced by the diagonal strut flowing down to the bottom end of the column reinforcement.

Therefore, the vicinity of the bottom end of the column reinforcement is influenced by a large compression field bounded by two diagonal struts flowing down to the drilled shaft and the bottom end of the column reinforcement, respectively. The large compression field performs the same role as an extended nodal zone, despite the fact that the diagonal strut flowing down to the drilled shaft does not intersect the column tie element. Based on the defined compression field, the critical section of the column reinforcement can be defined in a simple way as the intersection of the diagonal struts and the column ties in the 3D STM viewed from its side view, as illustrated in Figure 5.23.

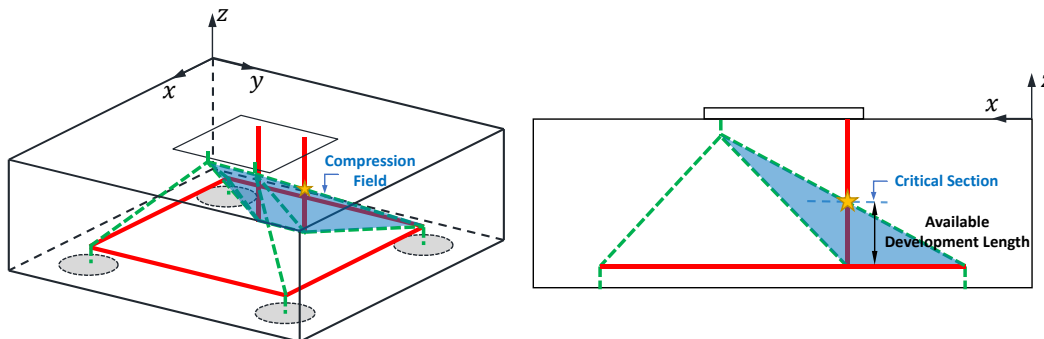


Figure 5.23 Compression field formed by diagonal struts and proposed critical section of column reinforcement

5.3.4. Summary and Discussion

The Phase II testing program was designed to evaluate various anchorage types of column reinforcement. Four footing specimens with different types of anchorage for the column reinforcement were planned and loaded sufficient to evaluate post-yielding behavior of the column reinforcement. The experimental results were used to propose the critical section of the column reinforcement for the anchorage requirement of the refined 3D STM recommendations in Chapter 8.

Different behaviors of the column reinforcement depending on the anchorage types can be identified, although all anchorage types were able to develop the full yield

strength during the tests. The diagonal struts flowing down to the drilled shaft and the bottom end of the column reinforcement induce the stress increment in the vicinity of the bottom end of the column reinforcement at all anchorage types except for the outer-oriented hooked, which is the practically employed anchorage detail for drilled shaft footings. The inner-oriented hooked bar and headed bar primarily resist the stress increment with bearing action of the anchorage, whereas the straight bar solely resists it with bond stress. However, the outer-oriented hooked bar cannot activate its bearing action, and the stress is not developed near the anchorage. It results in a relatively high-stress level developing near the interface of VI-HKO.

Based on this fact, the research team was able to conclude that hook orientation significantly affects the behavior of the column reinforcement. Although the outer-oriented hooked bar could develop its yield strength, the negligible stress development near its bottom end indicates inefficient structural performance of the anchorage detail. In order to ensure proper behavior of the hooked column reinforcement, the hook orientation needs to be placed towards the diagonal strut to include the vertical force component, and this conclusion is in line with the research conducted by Nilsson and Losberg (1976), who investigated the effect of hook orientation on the behavior of a beam-column joint against seismic loading.

On the basis of the test results, the critical section of the column reinforcement for the anchorage requirement was proposed. The large compression field formed by diagonal struts near the bottom end of the column reinforcement was considered for the critical section. The validity of the proposed critical section will be supplemented with a parametric study planned in Chapter 7.

Chapter 6. Experimental Program – Phase III: Compression and Tension in Drilled Shafts

6.1. Overview

This chapter covers the Phase III experimental program of large-scale drilled shaft footings subjected to a load combination of uniaxial compression and severe bending moment that results in tension and compression in drilled shafts. The primary objective of Phase III testing was to investigate behavior of the drilled shaft reinforcement that extends into the footing and establish the minimum anchorage requirements for it. The loading condition was idealized for the large-scale structural tests to accomplish the objective. Three different anchorage details of the drilled shaft reinforcement—straight, headed, and hooked reinforcing bars—were evaluated. The test results were used for planning an additional parametric study in Chapter 7 and the basis of design recommendations related to minimum anchorage of the drilled shaft reinforcement, a component of Chapter 8.

In this chapter, Section 6.2 describes the planned equivalent loading condition for large-scale structural tests of Phase III testing, and provides details of the design variables, design and fabrication of test specimens, and test setup for the loading condition. Test results are presented and discussed from various points of view based on measured data, and the critical section of the drilled shaft reinforcement for the anchorage requirement is proposed in Section 6.3.

6.2. Experimental Program

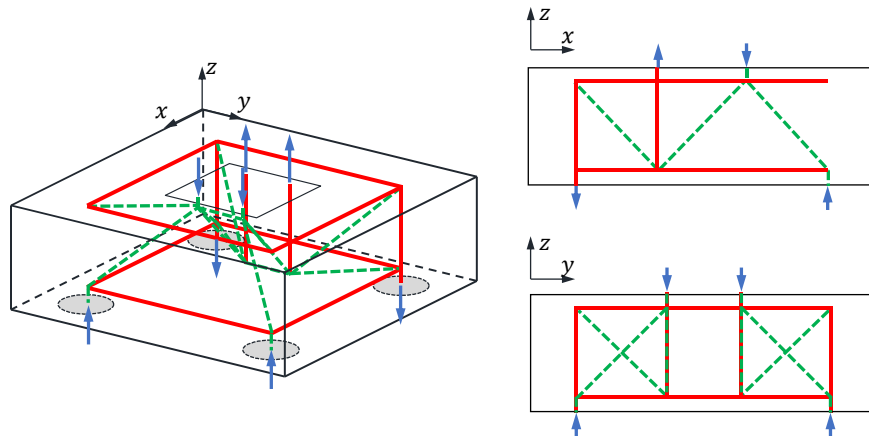
6.2.1. Equivalent Loading Condition

The high bending moment applied at the interface results in tensile reactions at two of four drilled shafts. To achieve that amount of moment by applying the load to a column similar to the Phase II testing, a large load eccentricity or lateral load needs to be applied to the column. However, imposing this boundary condition is too complicated to be obtained in large-scale structural testing. Furthermore, yielding of the column element needs to be prevented before drilled shaft reinforcement yielding for the purpose of testing despite a large amount of force applied to the column tie elements. Therefore, the research team planned an equivalent loading condition for the experimental program by applying tensile load at two drilled shafts where tensile reactions are generated. Moreover, the column tie elements in the model were substituted by post-tensioning forces applied on the top surface of

the footing to prevent the failure induced by the column tie elements, as illustrated in Figure 6.1.

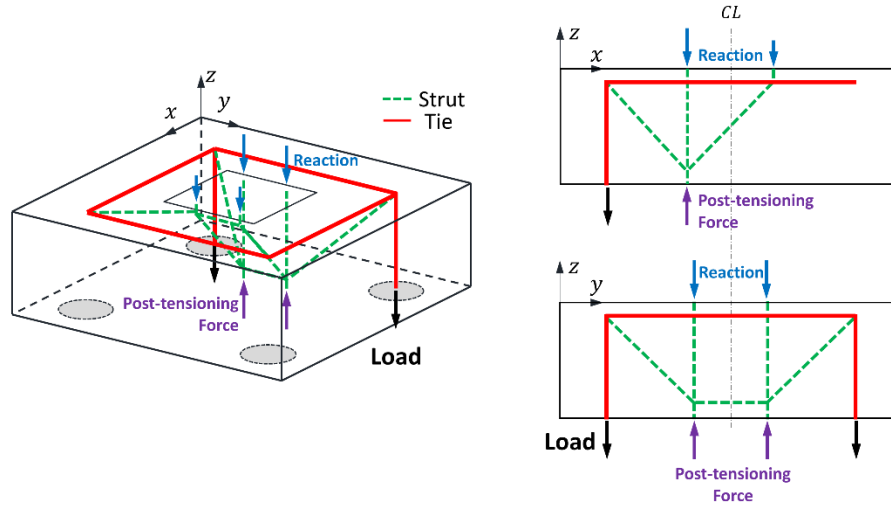
The strut-and-tie model obtained from the equivalent loading is simpler than that of the Phase III loading. However, the configuration of the models near the tip of vertical tie elements for drilled shaft reinforcement, which represent the force transfer mechanism of the force in the vertical drilled shaft tie element, are identical to each other. Although the horizontal strut placed on the plane of the bottom mat reinforcement ring does not exist in the equivalent model, it will not affect anchorage behavior at the top smeared node of the vertical tie element for drilled shaft reinforcement. The depth of the strut shall depend on the concrete cover of the bottom mat reinforcement since the axis of the strut is parallel to the plane of the bottom surface of the footing. Therefore, the influence of the strut on the anchorage region of the drilled shaft reinforcement can be negligible due to the depth of the footing.

The discrepancies between the models are caused by the existence of compressive reaction at the other two drilled shafts of the footing subjected to the Phase III loading, and the discrepancies are not considered to affect the behavior of drilled shaft reinforcement subjected to the tensile reaction.



(a) 3D strut-and-tie model for drilled shaft footing where shafts are in tension-compression (isometric view: left / side views: right)

Figure 6.1 Comparison of 3D strut-and-tie models under original and equivalent loading scenario of Phase III testing



(b) 3D strut-and-tie model for drilled shaft footing under equivalent loading scenario (isometric view: left / side views: right)

Figure 6.1 (cont'd) Comparison of 3D strut-and-tie models under original and equivalent loading scenario of Phase III testing

6.2.2. Test Variable

As shown in Figure 6.1, the 3D strut-and-tie model of drilled shaft footings subjected to uniaxial compression and severe bending moment results in tension at both one face of the column and two of four drilled shafts, and the vertical ties are provided to resist it. The drilled shaft tie elements are stretched up to the top tie ring representing the top mat reinforcement of the footing. Therefore, the drilled shaft ties need to be properly anchored to ensure yielding of the drilled shaft reinforcement. Phase III specimens have been designed to investigate the performance of different anchorage details for the reinforcement embedded in drilled shaft footings.

Since the drilled shaft reinforcement behavior in two drilled shafts can be investigated per test without influencing the opposite-side drilled shafts, the research team planned two sets of tests for each footing test specimen through the equivalent loading scenario. Therefore, two footing specimens were fabricated, and each specimen contained two different anchorage types of drilled shaft reinforcement for testing twice a single specimen. To compare the behavior of drilled shaft reinforcement depending on the anchorage type, one specimen had drilled shaft reinforcement with straight and headed anchorages, and another one had reinforcement with straight and hooked anchorages. Figure 6.2 illustrates general geometry of test specimens, and the Phase III test matrix is shown in Table 6.1.

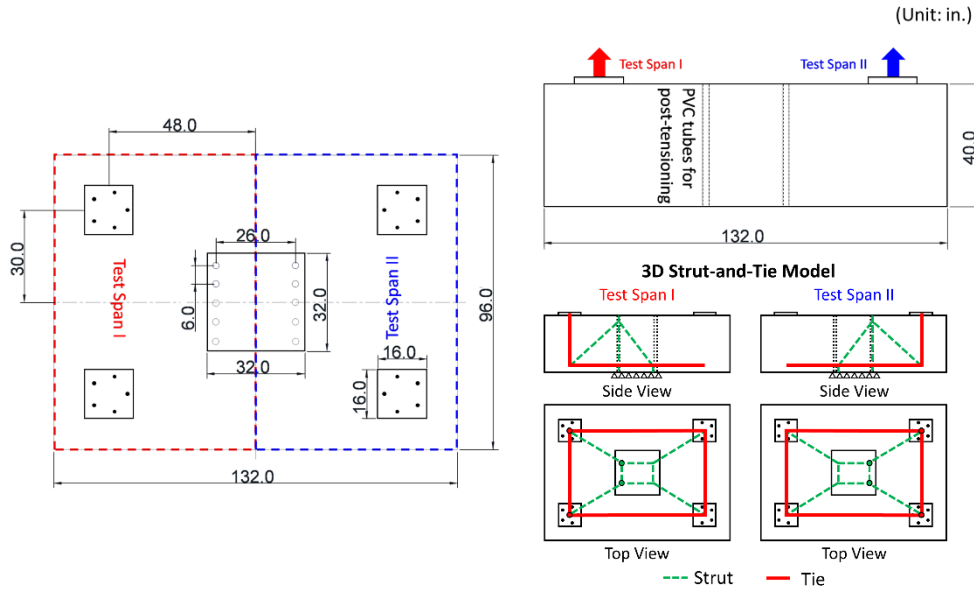


Figure 6.2 Dimension of specimen: Phase III

Table 6.1 Test matrix: Phase III

Series	Specimen ID	Test No.	Test ID	Drilled Shaft Reinforcement			
				Amount	Anchorage Detail		
					Straight	Headed	Hooked
VII	VII-TD	1	VII-TD-ST	5 - #6 (*Ratio: 1.09%)			
		2	VII-TD-HD				
	VII-TK	3	VII-TK-ST				
		4	VII-TK-HK				

*for 16-in. diameter drilled shaft

6.2.3. Specimen Design

6.2.3.1. Drilled Shaft Footing

The amount of the bottom mat reinforcement and the column reinforcement within the footing specimens was determined based on the tie forces of the strut-and-tie model at the ultimate state of the drilled shaft reinforcement. The minimum amount of reinforcement ratio for shrinkage and temperature reinforcement ($> 0.18\%$) was provided at the top of the footing in accordance with AASHTO LRFD (2020). In the context of the strut-and-tie design, transverse and longitudinal crack control reinforcement ($> 0.30\%$ in both directions) was provided at the side surfaces of the footing, just as in Phase I and Phase II specimens.

In order to preclude any premature failures in the footing, a conservative amount of the bottom mat reinforcement was provided to the specimen, and large-diameter

prestressed threaded rods (1.625-in. diameter) were inserted through PVC pipes embedded in the footing to resist high tensile force in the tie elements of the column. Those rods were post-tensioned and bolted to a supporting frame to prevent a slack between the specimen and the frame during the testing. The post-tensioning force can cause transverse tension, bursting force at the mid-height of the footing, and local damage at the bearing faces; therefore, transverse reinforcement and spiral reinforcement were provided at the mid-height of the footing and bearing faces near the PVC pipes. The bursting force was calculated based on AASHTO LRFD (2020).

Also, the specimens were turned upside down to allow direct application of an upward force to the drilled shaft reinforcement for the equivalent loading scenario, as shown in Figure 6.3. Most of the geometric properties—length, width, height, drilled shaft diameter, and the column size at the interface—are identical to those of II-7. Detail drawings of Phase III specimens are provided in Appendix D. The design concrete strength was taken to be 3.6 ksi, in accordance with what has commonly been used in practice, as summarized in Chapter 3.

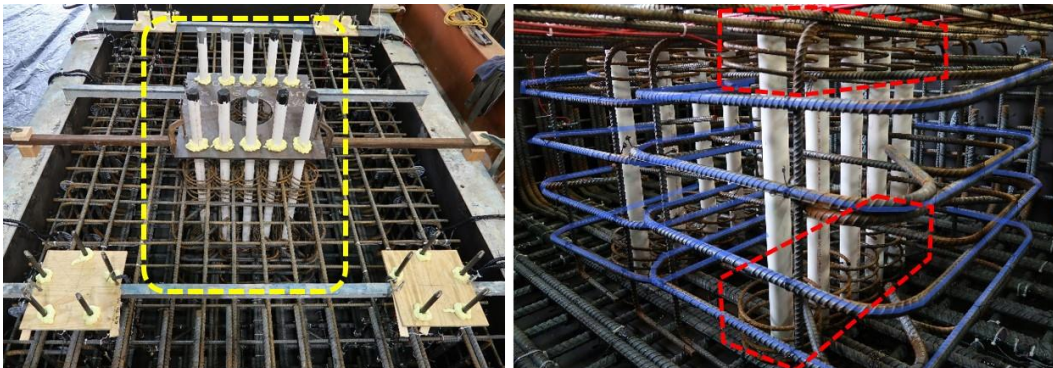


Figure 6.3 Reinforcing bar cage before cast concrete (left) and reinforcement detail to resist post-tensioning force (right)

6.2.3.2. Drilled Shaft Reinforcement

Similar to the procedure employed to determine the column reinforcement size in Phase II testing (Section 5.2.2.3), the research team decided the size and amount of the drilled shaft reinforcement for Phase III testing based on a design parameter study using the footing database established in Chapter 3. All column reinforcement in the database extended down to the bottom mat reinforcement regardless of the footing depth. On the other hand, the drilled shaft reinforcement in the database usually did not extend to the top mat reinforcement, as shown in Figure 6.4. Instead, it extended into the footing just enough to develop its yield strength at the interface between the footing and the drilled shaft, since the collected footings might not be designed for the complex loading similar to the Phase III loading scenario.

Therefore, the research team defined an assumed embedment length—a pseudo-embedment length—to determine an adequate size for the drilled shaft reinforcement. The pseudo-embedment length is an extended embedment length of drilled shaft reinforcement that extends up to the elevation of the top mat reinforcement for the vertical tie element for the drilled shaft reinforcement.

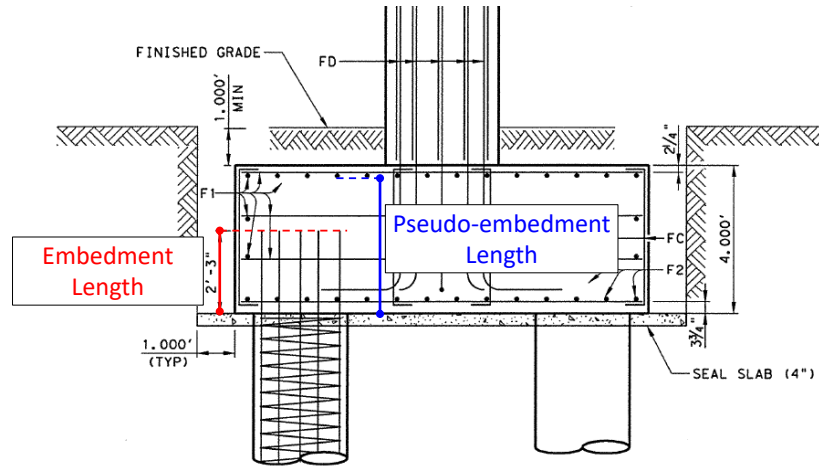


Figure 6.4 Definition of pseudo-embedment length of drilled shaft reinforcement in a TxDOT footing plan

A total of 31 of drilled shaft footing plans were reviewed. The set of 31 was selected by filtering out the footing plans in the TxDOT drilled shaft footing database lacking information on the drilled shaft reinforcement used. The pseudo-embedment lengths ($l_{p,e}$) of the drilled shaft reinforcement into the footings and the drilled shaft reinforcement ratios (ρ_{shaft}) were determined and divided by the diameters ($d_{b,s}$) of the reinforcing bars. The average $l_{p,e} / d_{b,s}$ ratio was 43.1, and the average drilled shaft reinforcement was 1.05%, respectively. The collected $l_{p,e} / d_{b,s}$ coefficients and reinforcement ratios are summarized, with drilled shaft reinforcement ratios provided for each footing plan, in Figure 6.5. To reproduce the same $l_{p,e} / d_{b,s}$ ratio and drilled shaft reinforcement ratio typically employed in practice, five No. 6 reinforcement bars were provided and extended up to the top mat reinforcement at each drilled shaft of the specimens, as tabulated in Table 6.2.

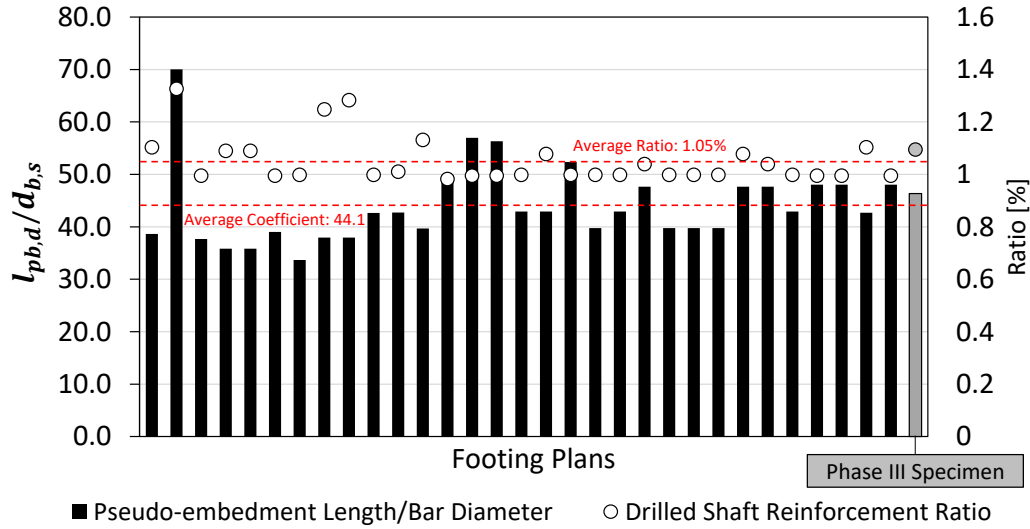


Figure 6.5 Pseudo-embedment lengths and drilled shaft reinforcement amount of TxDOT drilled shaft footing database

Table 6.2 Comparison between drilled shaft reinforcement embedment lengths of TxDOT drilled shaft footing database and Phase III specimens

TxDOT Drilled Shaft Footing Database (31 of 41 plans)		
Maximum l_b/d_b	Minimum l_b/d_b	Average
70.0	33.7	44.1
Maximum ρ_{shaft}	Minimum ρ_{shaft}	Average
1.32 %	0.98 %	1.05 %
Phase III Specimen		
Drilled Shaft Reinforcement Embedment Length (l_b) [in.]	Reinforcement Diameter (d_b) [in.]	l_b/d_b
34.7	0.75	46.3
Amount of Reinforcement	Drilled Shaft Diameter [in.]	ρ_{shaft}
5 – No. 6 (2.20 in ²)	16.0	1.09 %

6.2.4. Materials

6.2.4.1. Concrete

- Mixture Design

As in Phase I and Phase II testing, the design concrete strength of the footings was taken to be 3.6 ksi. Therefore, the concrete design mix for the normal-strength concrete for the footing is the same as the one used for Phase I and Phase II testing (Design code: S3130310); the mixture design is provided in Section 4.2.3.

- Material Tests

Since the bond-slip behavior of reinforcement is governed by the concrete strength, only compressive strength was examined by testing concrete cylinders. The details of the conducted compression test for the cylinders are presented in Section 4.2.3.

During the specimen casting process, bleeding in concrete was confirmed in a batch, as shown in Figure 6.6. The bleeding can adversely affect the compressive strength of the concrete; therefore, four cylinders were cored from the specimen in which the bleeding had occurred and tested to evaluate the real concrete strength of the batch, as shown in Figure 6.7.



Figure 6.6 Bleeding occurred in batch #3 (left) and surface of the specimen after curing (right)



Figure 6.7 Coring work (left) and position of coring on the north face of the specimen (right)

- Test Results

Concrete material test results are summarized in Table 6.3.

Table 6.3 Measured strengths of cylinders: Phase III

Test ID	Batch No.	Casting Date	28-days	Test Day	
			Compressive Strength (f'_c) [ksi]	Test Date (Age) [days]	Compressive Strength (f'_t) [ksi]
VII-TK-ST	1	09/24/20	4.01	01/15/21 (113)	4.87
	2		4.50		5.49
VII-TK-HK	1		4.01	01/29/21 (127)	5.11
	2		4.50		5.76
VII-TD-ST	2		4.50	03/04/21 (160)	5.44
	3		3.11		4.07
					*03/10/21 (166)
VII-TD-HD	2		4,50	02/11/21 (139)	5.68
	3		3.11		4.24
					*03/10/21 (166)

* Tested from the cored cylinders

6.2.4.2. Reinforcing Bars

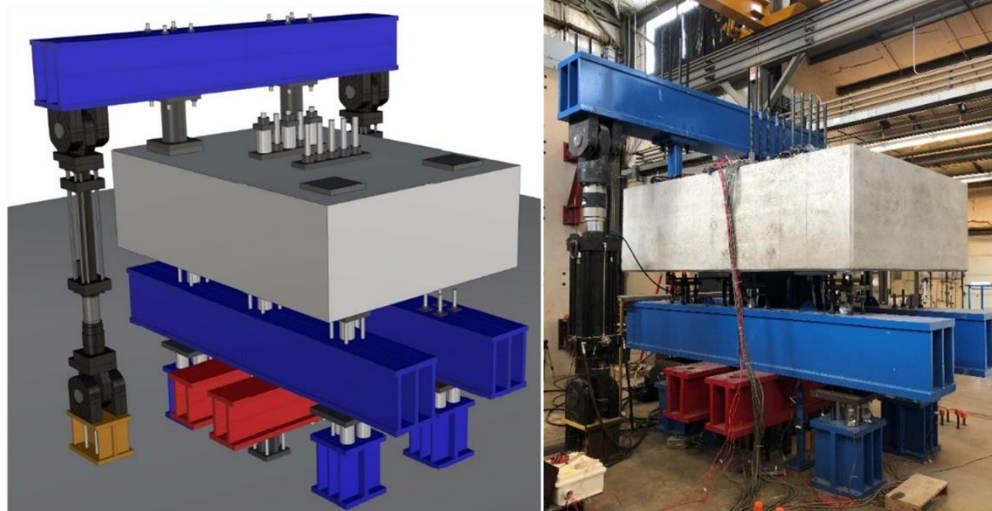
ASTM A706 bars were chosen to be able to weld them to a steel plate needed to apply the tensile load, as it will be discussed later. The rest of the reinforcement in the test specimens were ASTM A615 Grade 60 reinforcing bars. The average test results for each reinforcing bar size and set are summarized in Table 6.4.

Table 6.4 Mechanical properties of reinforcing bars: Phase III

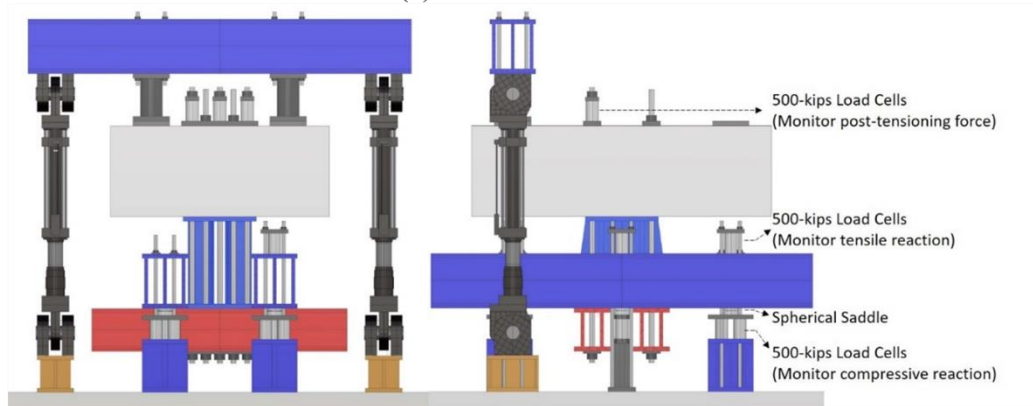
Specimen ID	Bar Size	Location	Yield Strength (f_y) [ksi]	Tensile Strength (f_u) [ksi]
All Phase III Specimens	#6	Drilled Shaft	68.2	102.8
	#9	Bottom Mat	62.9	107.9
	#8	Transverse Face	74.2	112.3
	#7	Top Mat	64.1	104.4
	#6	Transverse Face	66.0	103.9
	#5	Top Mat & Longitudinal Face	63.9	103.4

6.2.5. Testing Setup

The equivalent loading scenario was planned to investigate the anchorage behavior of drilled shaft reinforcement, and a test setup was deliberately designed to apply the load properly and transfer it to the strong floor. The test setup configuration is illustrated in Figure 6.8.



(a) Isometric view



(b) Front view

(c) Side view

Figure 6.8 Test setup for planned equivalent loading of Phase III testing

The eccentrically applied upward force (48-in. eccentricity with respect to the centroid of the specimen) results in a large overturning moment at the center region on the bottom surface of the footing, which simulates the interface between the column and the footing. Therefore, a support frame was designed to redistribute the moment to the strong floor with tensile and compressive reactions. The supporting frame consists of a big pedestal supporting the specimen, and staggered box beams are placed under it to transfer the moment to six support pedestals on the strong floor.

Each support pedestal was connected to the box beam with four grade B7 rods, and the rods were post-tensioned with 50 kip respectively to compensate for tensile reactions caused by the overturning moment. The test specimen was anchored to the support frame with two rows of five large-diameter post-tensioning threaded rods through the embedded PVC pipes. For each test, the rods in a row located at the axis of the vertical tie elements on the column side were post-tensioned with

150 kips per rod to prevent a slack between the specimen and the supporting frame before yielding the drilled shaft reinforcement.

Figure 6.9 illustrates the detail of the connection between the drilled shaft reinforcement extended out from the footing and an adapter plate. The drilled shaft reinforcement was welded to the adapter plate inside a 0.75-in.-deep and 2.5-in.-diameter pocket to apply the load to the bars directly. The connection should not fail until the ultimate state of the drilled shaft reinforcement for the purpose of the testing; therefore, the research team conducted a mock-up test to verify the detail and confirmed its validity, as shown in Figure 6.10. The connection detail was verified to be safe for the tests since no damage was found at the connection until the reinforcement was fractured in tension. The adapter plate was connected to a crosshead box beam through a squat steel pedestal. Two 330-kip capacity MTS actuators were placed at both sides of the specimen under the crosshead box beam to apply a tensile force to the drilled shaft reinforcement. The MTS actuator has a swivel head at both ends, permitting some amount of rotation and translation of the specimen.

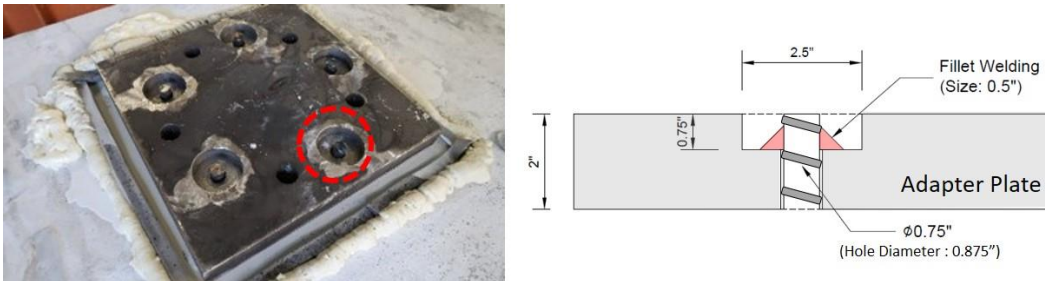


Figure 6.9 Detail of connection between drilled shaft reinforcement and adapter plate



Figure 6.10 Mock-up test plan (left) and fracture of reinforcement after mock-up test (right)

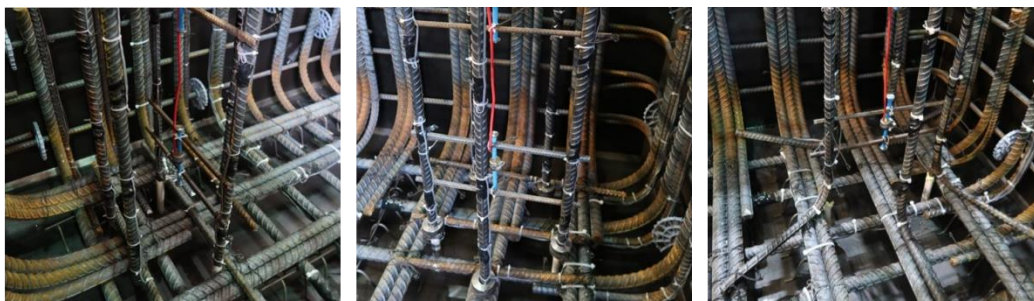
6.2.6. Fabrication of Specimens

6.2.6.1. Drilled Shaft Footing

Fabrication of the footing part of the specimens was almost identical to that of Phase I and Phase II specimens. In addition to the side, top mat, and bottom mat reinforcement, additional reinforcement such as anti-burst reinforcement and spiral reinforcement was provided at the center of the footing to preclude any damages due to the post-tensioning, as mentioned in the previous section. PVC pipes were also embedded in the footing to install the specimen to the supporting frame through high-strength threaded rods. More details about other identical fabrication procedures for footings are reported in Section 4.2.5.

6.2.6.2. Drilled Shaft Reinforcement

The drilled shaft reinforcing bars were carefully installed to the reinforcing cages since they also had the purpose of a connection to the loading frame. Figure 6.11 illustrates three different anchorage types—straight, hooked, and headed—of drilled shaft reinforcement installed to the footing cages. Hook orientations of the hooked drilled shaft reinforcement were radially placed as shown in Figure 6.11-(c) to examine the effect of the hook orientation on the drilled shaft reinforcement behavior. The same as the headed anchorage specimen in Phase II testing, Lenton Terminators produced by nVent LENTON, were employed for the headed anchorage detail in Phase III testing. Lenton Terminators were also carefully installed by applying the requirement of torque, as described in Section 5.2.5.2.



(a) Straight anchorage

(b) Headed anchorage

(c) Hooked anchorage

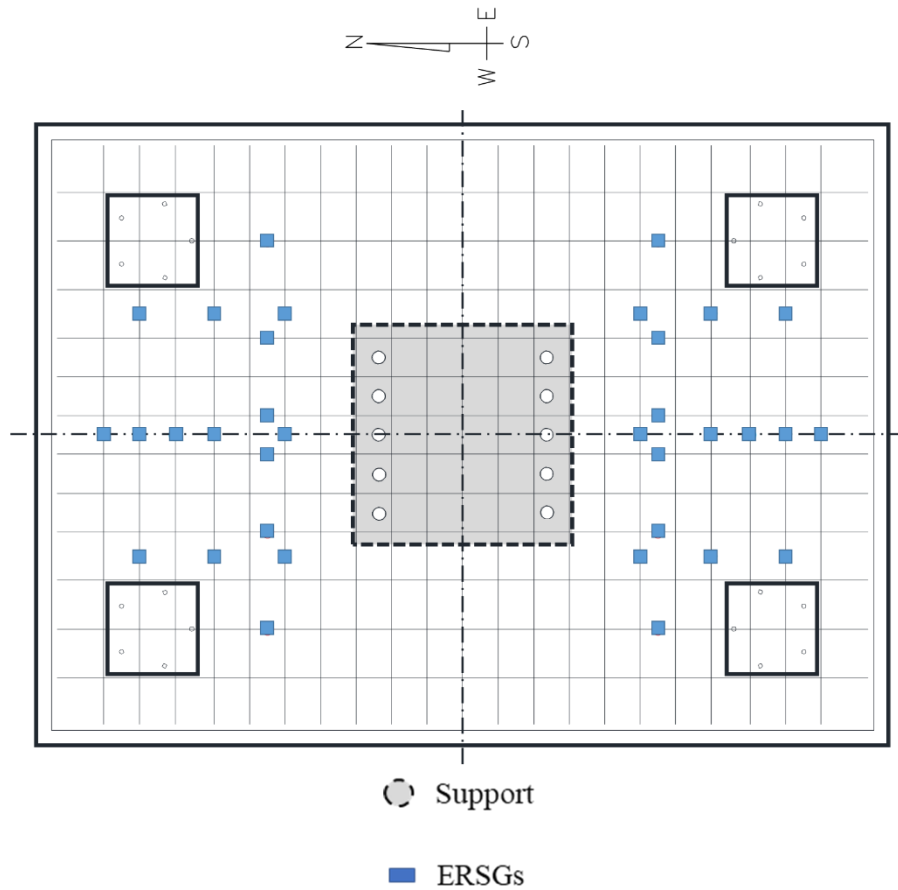
Figure 6.11 Type of anchorage detail for drilled shaft reinforcement

6.2.7. Instrumentation

6.2.7.1. Strain Measurements: Reinforcing Bars

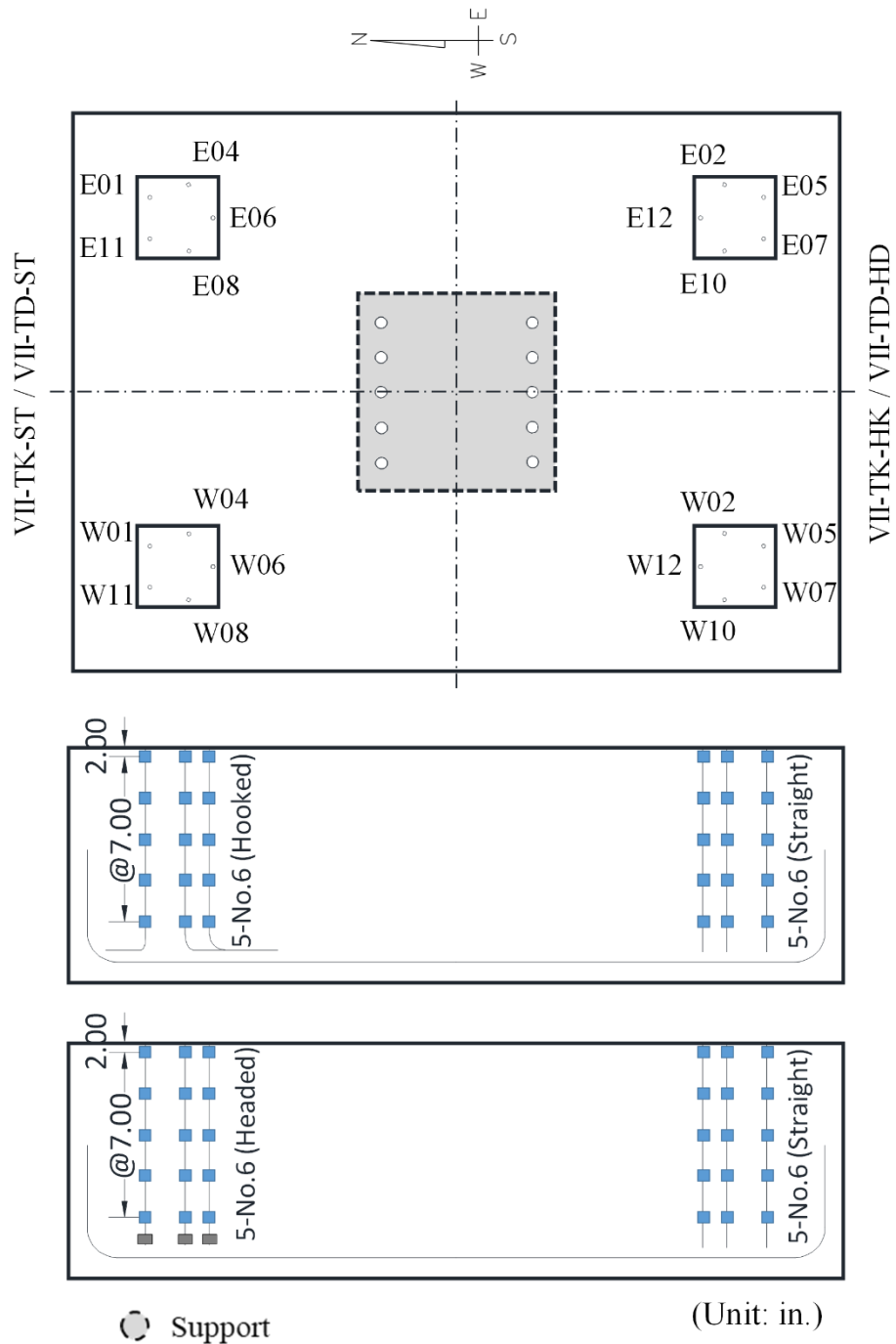
To investigate the strain development along the length of the drilled shaft reinforcement, the drilled shaft reinforcement was instrumented with ERSGs. Similar to the instrumentation plan employed in Phase II tests for monitoring the

column reinforcement strain development, a series of gauges were also installed on longitudinal ribs of drilled shaft reinforcement as illustrated in Figure 5.11 to minimize the adverse effect on the bond. In addition, bottom mat reinforcement was also instrumented with strain gauges to monitor its strain development during the tests. Instrumentation maps for Phase III specimens are provided in Figure 6.12 as an example, and Appendix D contains detailed instrumentation maps for each specimen.



(a) Instrumentation map of bottom mat reinforcement

Figure 6.12 Instrumentation map of Phase III specimens



(b) Instrumentation map of drilled shaft reinforcement
 Figure 6.12 (cont'd) Instrumentation map of Phase III specimens

6.2.7.2. Load and Displacement Measurements

The applied loading was monitored in two ways; load cells embedded in the MTS actuators and load cells in the support pedestals. The support frame is supported by

four corner support pedestals and two center-located pedestals, as described in Section 6.2.5. A total of three 500-kip capacity load cells were provided at the base of each corner support pedestal, and one 500-kip capacity load cell was provided at the base of each center-located pedestal. In general, load cells were instrumented for monitoring applied compressive forces; however, the designed supports can also monitor tensile forces since each support pedestal is subjected to 200-kips compression due to the post-tensioning grade B7 rods. Therefore, the load cell reading decreases when a tensile reaction is applied to the support. The post-tensioning forces applied to anchor the test specimen to the support frame were also monitored through 500-kip capacity load cells. Three of five large-diameter post-tensioning threaded rods were monitored during the testing. The installed 500-kip load cell locations in the test setup are shown in Figure 6.8.

To examine the anchorage behavior of the drilled shaft reinforcement, reinforcement slips at both ends of the drilled shaft reinforcement were measured. On the top surface of the footing, linear potentiometers were installed near two corners of the adopter plates. In addition, deep but small voids were provided right under the tip of two of five drilled shaft reinforcing bars per each drilled shaft, and linear potentiometers were installed through the holes to measure the slip. While the straight and the headed anchorages have a flat surface at the bottom tip, the hooked anchorage does not due to its bend radius. Therefore, a small steel rod was welded at the bend radius of the hooked anchorage to make a flat surface at its tip, as shown in Figure 6.13.

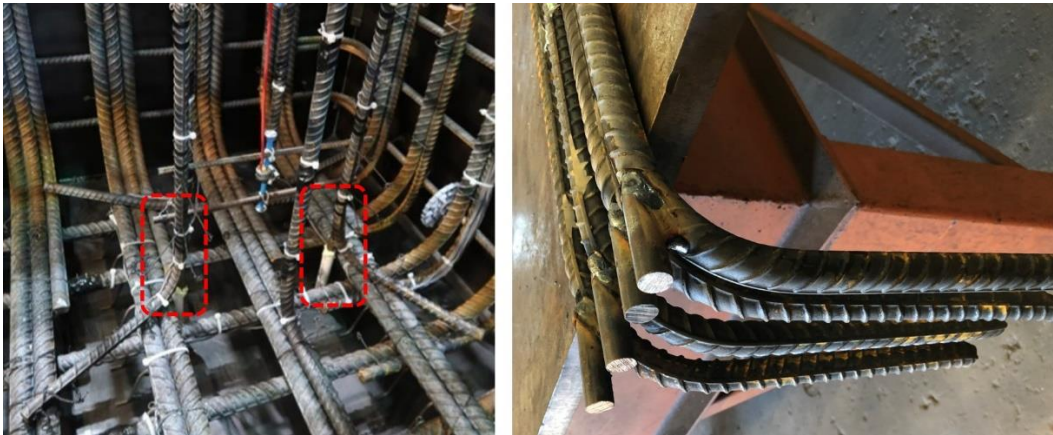


Figure 6.13 Welded hooked reinforcement to measure drilled shaft reinforcement slip

Displacement the footing during each test were monitored from linear potentiometers placed near the pedestal supporting the specimen. As an example, the locations of installed linear potentiometers for VII-TD-HD test are illustrated in Figure 6.14.

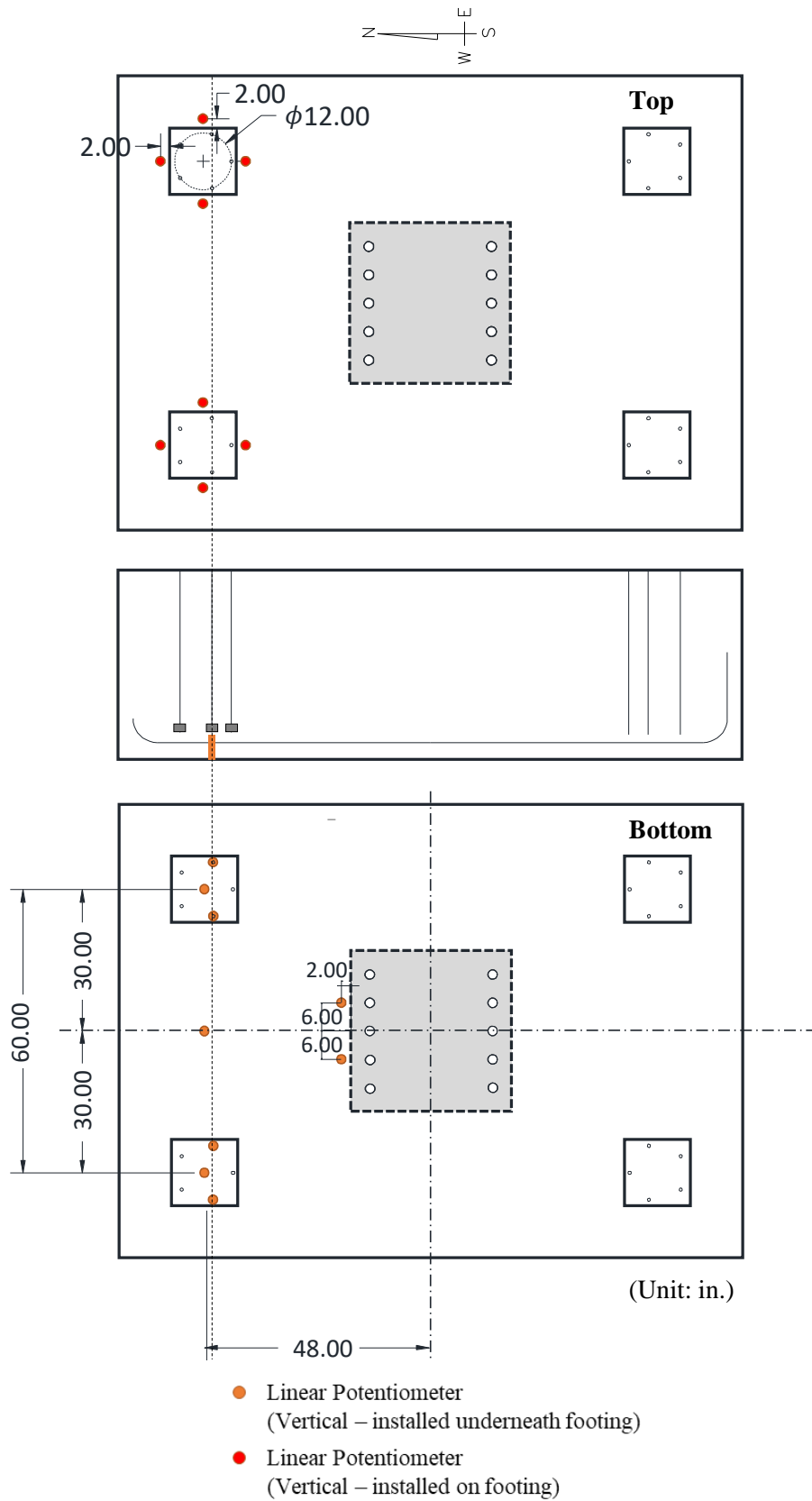


Figure 6.14 Instrumentation map of linear potentiometers for VII-TD-HD

6.2.8. Test Procedure

Test specimens were loaded with displacement-controlled load from the MTS actuators with 0.025-in. per a minute loading rate. During the displacement steps, the testing was stopped in 50-kip increments manually up to the load when at least one drilled shaft reinforcement yields to inspect and document the condition of the specimens. After all drilled shaft reinforcement exceeds yield stress, the specimens were continuously loaded with displacement-controlled until about 90% of the expected ultimate load (400 kips) was attained. The testing stopped at 400 kips loading to prevent impact damage caused by the fracture of the drilled shaft reinforcement.

6.3. Experimental Results and Discussion

6.3.1. Overview

In this section, observations and data obtained from test specimens during and after tests will be provided and discussed based on visual observation, load-deflection behavior, stress distribution in bottom mat reinforcement, and stress profiles of the drilled reinforcement to examine the drilled shaft reinforcement with various anchorage types. The notations used in this chapter are listed as follows:

A_s	Total amount of drilled shaft reinforcement [in. ²]
f'_c	Average compressive strength of concrete for each batch comprising the footing at the time of testing measured in accordance with ASTM C39 [ksi]
$f_{s,a}$	Average drilled shaft reinforcement stress ($= P/A_s$) [ksi]
$f_{t,s}$	Tensile strength of drilled shaft reinforcement measured in accordance with ASTM A370 [ksi]
$f_{y,s}$	Yield strength of drilled shaft reinforcement measured in accordance with ASTM A370 [ksi]
P	Total applied load [kip]
$P_{fy,s}$	Load at the first yielding of drilled shaft reinforcement [kip]
$P_{y,c}$	Load at yielding of all drilled shaft reinforcement [kip]
Δ_a	Average relative displacements measured at four sides of adopter plate, [in.]
Δ_s	Measured slips at the anchorage of drilled shaft reinforcement [in.]

Visual observations of test specimens are discussed based on the visual inspection conducted after each test since Phase III test specimens were not loaded up to failure. The inspection was mainly focused on the side surfaces of the specimen and the vicinity of the adopter plates on the loading side.

To investigate the load-deflection response of the test specimens and compare the responses between the specimens, the linear potentiometers placed next to four faces of the drilled shaft plates for measuring the relative displacement of the adopter plate against the footing were exploited. The averaged displacement represents the average elongation of the drilled shaft reinforcement above the top surface of the footing. Additionally, the linear potentiometers placed at the tip of the drilled shaft reinforcement measured the slip at the anchorage of the drilled shaft reinforcement. The measured slips were compared between the anchorage types to examine the anchorage behavior of the drilled shaft reinforcement embedded in the footing.

Similar to Phase II testing, strains of the drilled shaft reinforcement embedded in the footing were monitored through a series of ERSGs during each test. The measured strains were converted to stresses based on the stress-strain relationships obtained from the material tests conducted for the drilled shaft reinforcing bars. Based on the converted stresses, the stress profiles of the drilled shaft reinforcement were developed. Additionally, the bond stress profiles of the drilled shaft reinforcement were also developed based on the stress profiles following the same scheme specified in Section 5.3.1. The bond stress profiles were compared with the code-specified (fib Model Code 2010, 2013) local peak bond resistance governed by splitting, $\tau_{bu,split}$ in the same plot, and the equation for it is provided in the previous chapter: Section 5.3.1.

6.3.2. Series VII: Anchorage Type of Drilled Shaft Reinforcement

6.3.2.1. Strength Results

The test results of Series VII are summarized for comparison in Table 6.5. Since the applied load cannot be evenly distributed to all drilled shaft reinforcement, there was a difference between the specimens at the first yielding load. However, when comparing the loads when all the reinforcing bars yielded in each of the four tests, there was no significant difference, and the error range was within 10% compared to the average value of 347 kips of the four tests. Furthermore, the research team compared the maximum stresses of the drilled shaft reinforcement between the tests at the maximum applied load of 400 kips. Regardless of the anchorage types, the maximum stresses were developed at the measurement location closest to the top surface of the footing (2 in. below the top surface), and they exceeded 90% of the tensile strength of the drilled shaft reinforcement.

Table 6.5 Summary of experimental results: Phase III

Test ID	VII-TK-ST	VII-TK-HK	VII-TD-HD	VII-TD-ST
Anchorage detail of drilled shaft reinforcement	Straight	Hooked	Headed	Straight
f'_c [ksi]	5.18	5.43	**4.44	**4.56
$f_{y,s}$ [ksi]	68.2			
$f_{t,s}$ [ksi]	102.8			
$P_{fy,s}$ [kip] (*Reinforcing bar position)	209 (E04)	249 (W10)	290 (E02)	277 (E06)
$P_{y,s}$ [kip]	344	329	374	342
$f_{s,max}$ [ksi] (*Reinforcing bar position)	94.8 (E04)	90.5 (W07)	92.4 (W10)	90.3 (E06)

*Refer to Figure 6.12

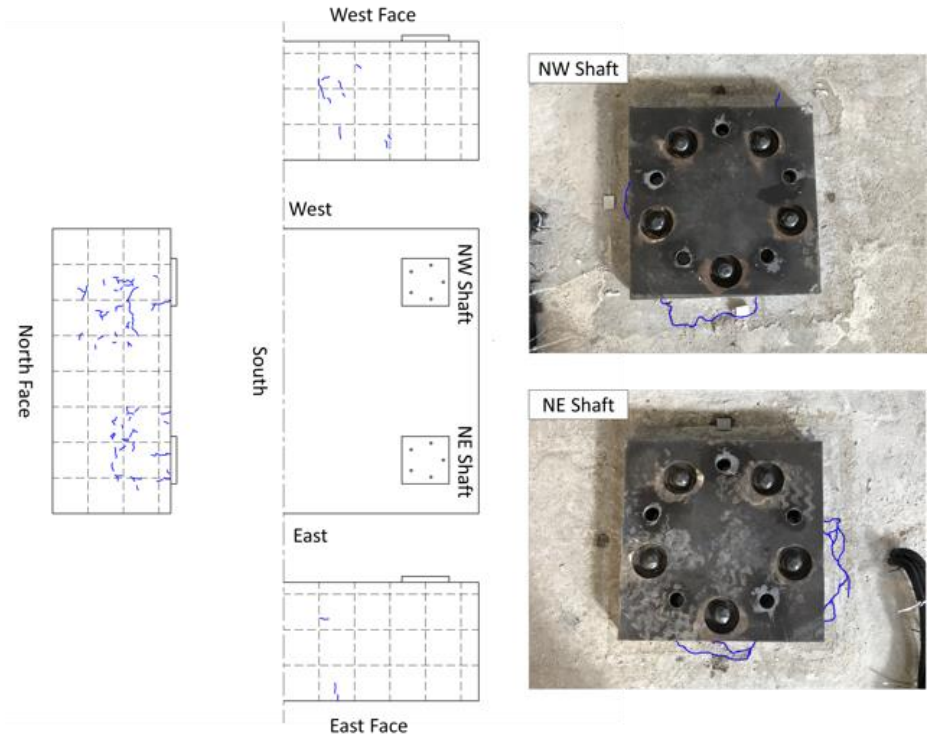
**Additional concrete cylinders were cored from the specimen to estimate the strength as described in Section 6.2.4.1.

6.3.2.2. Visual Observation

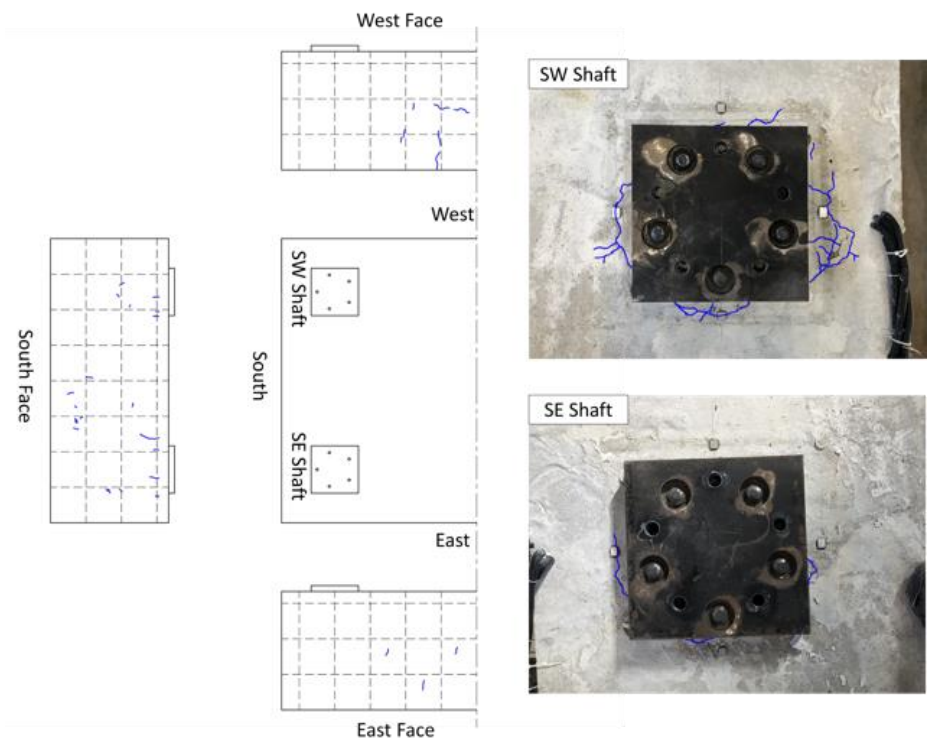
During each test, all faces of the tested span of the footing were inspected. During testing of VII-TK-ST, a series of horizontal cracks occurred on the middle of the north face of the specimen as the load increased. Those cracks are presumed to be micro-cracks that already existed before the test because of the cold joint at the boundary of two concrete batches. Most of the cracks were formed at the loading steps of 100 kips and 150 kips, and no additional cracks were propagated from the already existing ones. Furthermore, those cracks were not observed in the other tests.

Otherwise, all specimens showed a similar crack pattern. Only a few hairline cracks occurred on the side surfaces of the footing in all specimens during the tests though a bottom tie ring exists in the 3D STM under the equivalent loading condition. The post-tensioning forces applied for anchoring the test specimen to the support frame increased during the testing as load increases. It indicates that the post-tensioning rods were elongated during the testing; therefore, the desired fixed support condition could not be provided to the test specimen. Because of the boundary

condition, the test specimens showed a rocking behavior during the testing, which hindered flexural cracks on the footing component of the specimens. In spite of the rocking behavior, all tested drilled shaft reinforcement could be loaded up to close to the ultimate state by showing the maximum stress of over 90% of the tensile strength. Therefore, concrete spalling around the drilled shaft plates was observed after the tests due to the tensile behavior of the drilled shaft reinforcement. Figure 6.15 presents the inspected crack maps after testing the span of each drilled shaft reinforcement anchorage type.

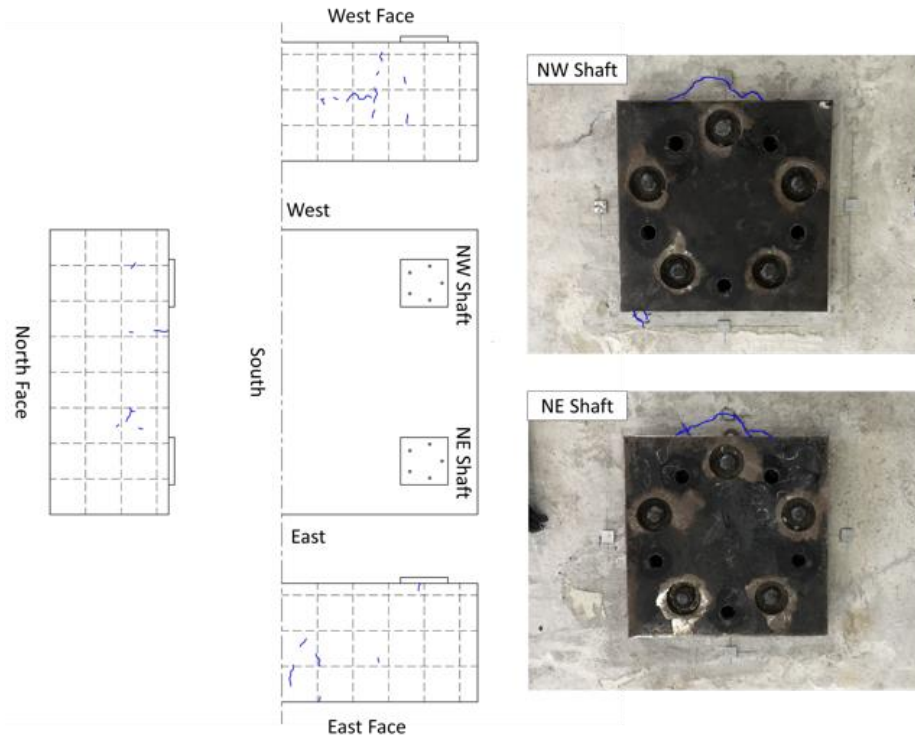


(a) VII-TK-ST

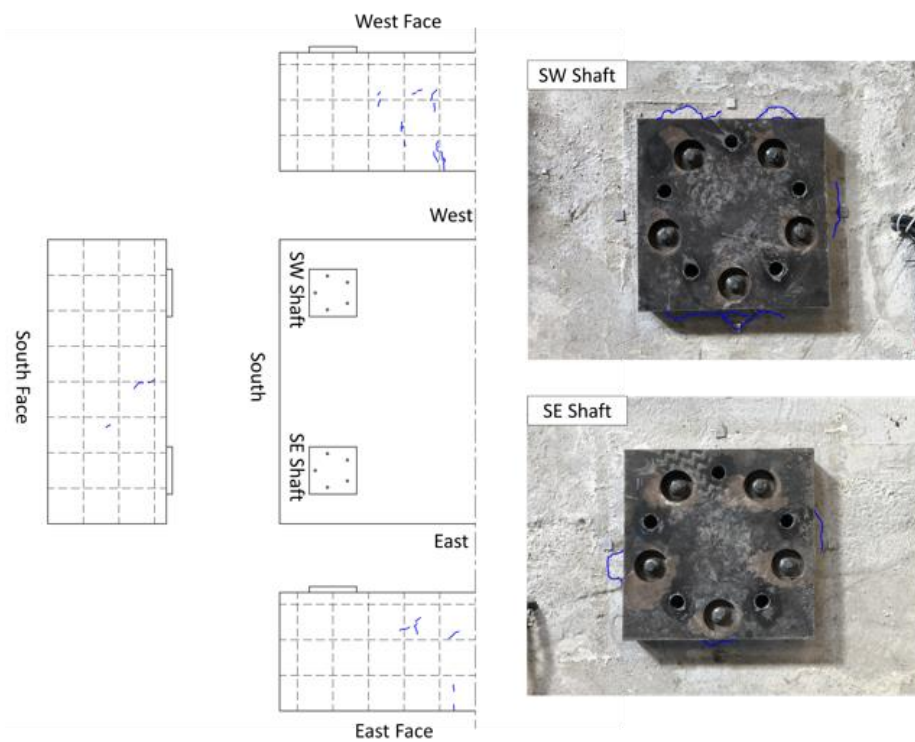


(b) VII-TK-HK

Figure 6.15 Crack map of Phase III specimens after testing



(c) VII-TD-ST



(d) VII-TD-HD

Figure 6.15 (cont'd) Crack map of Phase III specimens after testing

6.3.2.3. Load-deflection Response

The linear potentiometers, which were placed next to four faces of the drilled shaft plates to measure the relative displacement of the shaft plate against the footing, were exploited to compare behaviors between the specimens. They were averaged to calculate the average relative displacement of the shaft plate, which also represents the average elongation of the shaft reinforcement above the top surface of the footing. Some linear potentiometers installed at one shaft plate on the specimen measured unstable data after drilled shaft reinforcement yielding due to the conical cracks formed around the shaft plate. Therefore, the west-side plate was selected for VII-TK-ST (straight drilled shaft reinforcement), and the east-side plate was selected for the other specimens to represent the behavior of the drilled shaft reinforcement embedded in the footing.

A graph with the average relative displacement of one shaft plate as the x-axis and the applied load through the same side's MTS actuator as the y-axis was developed for each specimen and compared. Furthermore, the average stress level of the drilled shaft reinforcement, dividing the applied load by a total amount of drilled shaft reinforcement in a shaft plate, could be confirmed in the same curve by the secondary axis, as shown in Figure 6.16.

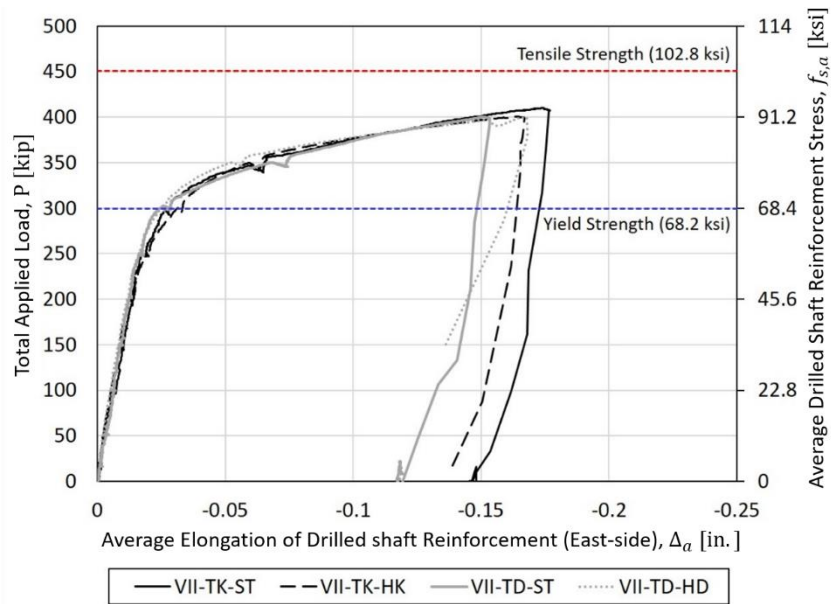


Figure 6.16 Overall behavior of Phase III tests

The primary test results and findings from load-deflection response are as follows:

- The average drilled shaft reinforcement stress exceeded the yield stress at around 300 kips loading and reached about 90 ksi stress level at 400 kips loading.
- The overall responses of the tests are comparable to each other regardless of the anchorage types.

The slips measured at the bottom tip of the drilled shaft reinforcement showed a trend as load increases; however, the values were negligible regardless of the anchorage types, as shown in Figure 6.17.

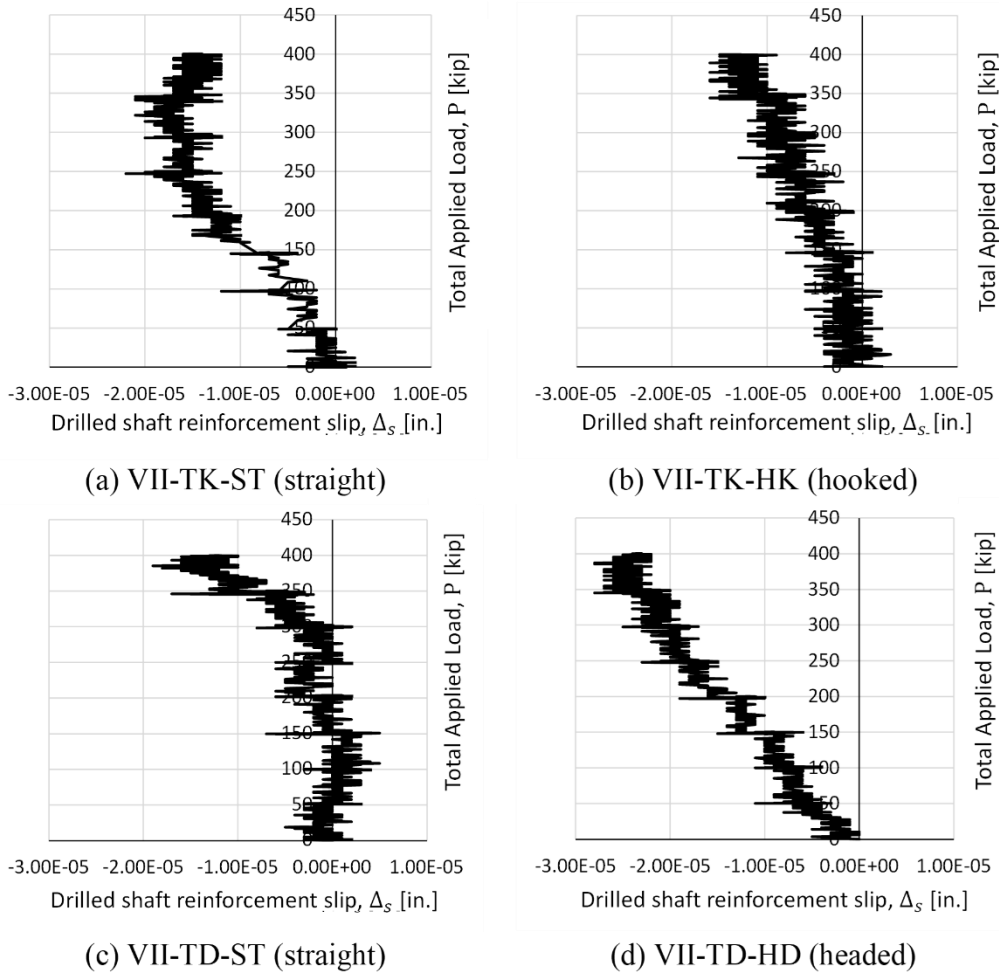


Figure 6.17 Measured slips at anchorage ends of drilled shaft reinforcement

6.3.2.4. Strain Distribution in Bottom Mat Reinforcement

The bottom mat reinforcement experienced a low-strain level (less than equivalent to the stress of 1.50 ksi) until the end of the test due to the aforementioned boundary condition in all Phase III specimens. This result is in line with the few hairline cracks formed on the specimens.

6.3.2.5. Stress Profiles and Bond Stress Profiles of Drilled Shaft Reinforcement

The drilled shaft reinforcement behavior during the testing was investigated through the ERSGs installed at 7-in. spacing, and the stress-strain relationships obtained from tension tests on reinforcing bars were used to convert measured strains to stresses.

The drilled shaft reinforcing bars in a shaft plate were subjected to different loads because of the deformation of the specimen and the horizontality of the shaft plate. However, the stress profiles of all drilled shaft reinforcing bars showed a similar tendency regardless of their position and anchorage type. To compare the behavior between different anchorage types of the drilled shaft reinforcement, the reinforcing bar in the east-side drilled shaft reinforcement group positioned closest to the central axis of the footing was selected to investigate the behavior of the drilled shaft reinforcement and compare between the specimens. Figure 6.18 presents a comparison of the stress profiles at the loading from 50 kips to 400 kips.

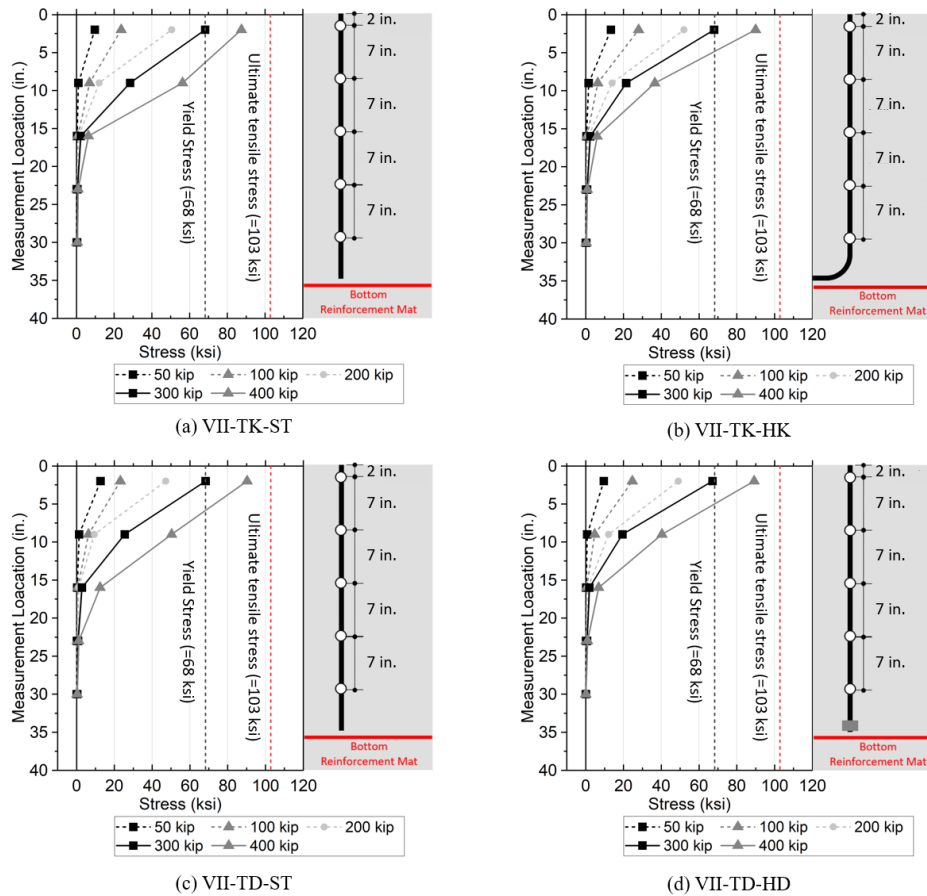


Figure 6.18 Stress profiles of drilled shaft reinforcement

The main outcomes of the results obtained from the stress profiles are as follows:

- Drilled shaft reinforcement was able to develop yield strength within 15.5 inches of its embedment length measured from the topmost strain gauge, installed at 2 inches below the top surface of the footing regardless of their anchorage types. This indicates that the headed and hooked drilled shaft reinforcement did not activate the bearing action of the head and the hook to resist the tensile force in the reinforcing bar, and bond stress on the surface of the reinforcing bar solely resisted the tension applied to the bar. This fact can be confirmed again with the bond stress profiles, which will be covered in the next section.
- The bottom portion of the bars did not experience a strain increase, regardless of the anchorage. Stresses near the bottom tip of drilled shaft reinforcement did not increase significantly.
- Even after yielding of the stresses at 2 in. below the top surface of the footing, the stress level monitored near the interface with the shaft increased consistently close to about 90 ksi, or 90% of the tensile strength (99 ksi) of the reinforcement.
- The radially placed hook orientations did not affect the behavior of hooked drilled shaft reinforcing bars since the bearing action of the hook was not activated during the tests.

To examine bond behavior of the drilled shaft reinforcement, the bond stresses were calculated based on the stress profiles, as described in the chapter on Phase II testing (Section 5.3.1). Figure 6.19 presents the average bond stress profiles of the drilled shaft reinforcement. The profiles are presented with the local splitting bond strength proposed in fib Model Code 2010 (2013), which considers several aspects of the bond.

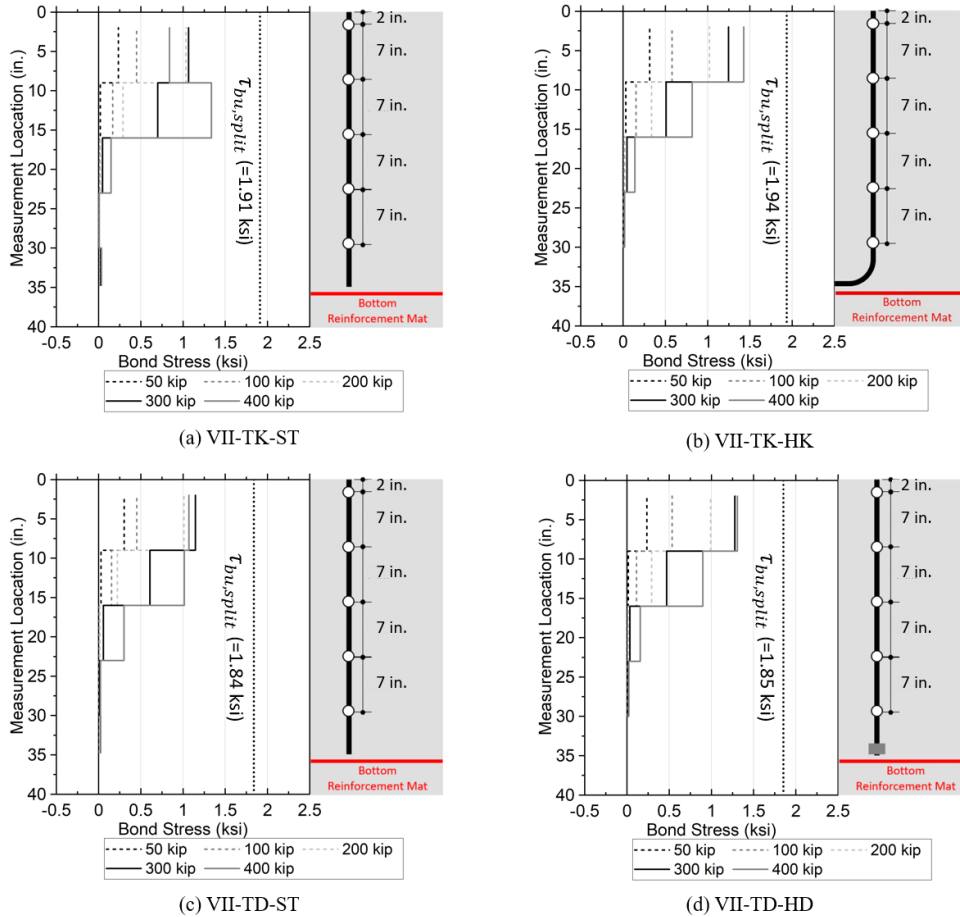


Figure 6.19 Bond stress profiles of drilled shaft reinforcement

The main outcomes of the results obtained from the bond stress profiles are as follows:

- The average bond stress increased from the top surface of the footing as the load increased and reached its maximum, which is comparable to the code-specified strength; $\tau_{bu,split}$. However, the bond stress could not exceed $\tau_{bu,split}$ since the computed average bond stress for 7-in. strain measurement locations could not catch the local maximum bond stress within that range.
- The bond stress was activated on the reinforcing bar surface only near the top surface of the footing to resist the tensile force applied in the reinforcing bar during the testing, and almost no bond stress distribution was confirmed near the end of drilled shaft reinforcement regardless of its anchorage type.
- The radially placed hook orientations did not affect the behavior of hooked drilled shaft reinforcing bars since the bearing action of the hook was not activated during the tests.

6.3.3. Critical Section of Drilled Shaft Reinforcement

The drilled shaft reinforcement of the test specimens under the equivalent loading condition of Phase III testing experienced high-stress level near the interface regardless of the anchorage types. In order to propose the critical section of the drilled shaft reinforcement conservatively, the internal force flow of Phase III specimens was reviewed.

The diagonal strut acting at the end of the drilled shaft reinforcement embedded is classified as a fan-shaped strut since this end corresponds to a smeared node, as shown in Figure 6.20. Therefore, the strut boundary spreads out from the edge of the bearing pad placed on the test specimen for applying the post-tensioning force. The minimum strut angle specified in AASHTO LRFD (2020), 25 degrees, is employed for defining the upper boundary of the fan-shaped strut. The resulting compression field, shaded in blue in Figure 6.20, is assumed to perform the same role as an extended nodal zone for the purpose of developing tensile forces of the tie. The point at which the drilled shaft reinforcing bar intersects the boundary of the fan-shaped strut would correspond to the critical section at which the bar starts to be developed, between 12.1 in. and 17.2 in. from the top surface depending on the bar. Figure 6.20 also indicates the section at which the yield strength of the bar was actually developed at the end of the test, which lies somewhere between 9 in. and 16 in. from the top surface. This indicates that the critical section of the drilled shaft reinforcement defined from the assumed boundary of the fan-shaped strut is conservative enough to ensure yielding of the drilled shaft reinforcement. Therefore, the critical section of a group of drilled shaft reinforcing bars in a drilled shaft can be safely assumed to be at the point where the theoretical compression field meets the vertical tie of the drilled shaft regardless of the bar position in the drilled shaft.

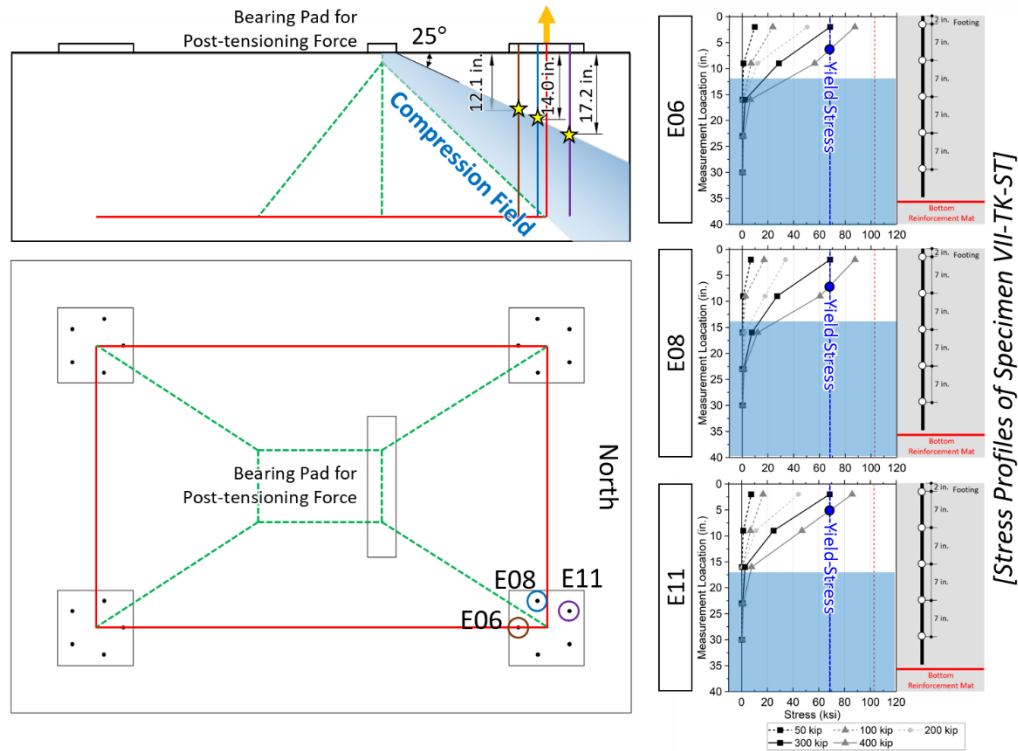


Figure 6.20 Assumed compression field and proposed critical section of drilled shaft reinforcement (equivalent Phase III loading condition)

It should be noted that the equivalent loading condition substitutes the column reinforcement to the post-tensioning forces; therefore, the research team assumed a compression field formed between the drilled shaft reinforcement and the column reinforcement in drilled shaft footings subjected to the original Phase III loading condition, as shown in Figure 6.21. The assumed compression field represents a non-contact lap splice behavior between the column and drilled shaft reinforcement. The minimum strut angle of 25 degrees is also employed to define the compression field. Therefore, the critical section of the drilled shaft reinforcement can be defined at the position where the drilled shaft tie element intersects with the boundary of the assumed compression field. The same concept can be applied to the column reinforcement in determining its critical section under the original Phase III loading condition, as illustrated in Figure 6.21.

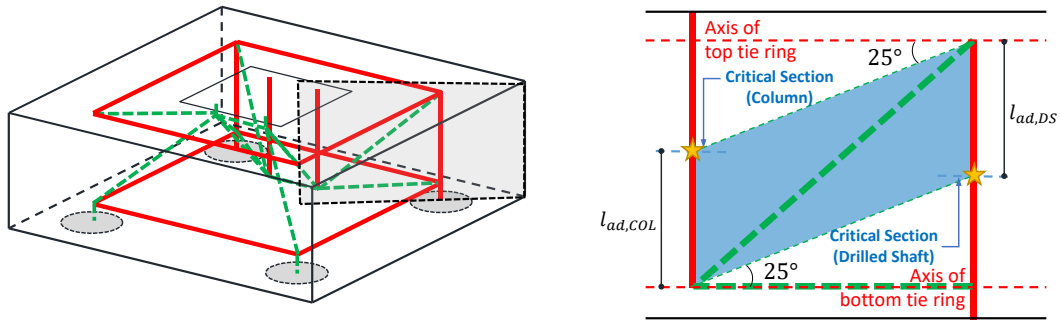


Figure 6.21 Assumed compression field and proposed critical sections of column and drilled shaft reinforcement (original Phase III loading condition)

6.3.4. Summary and Discussion

The purpose of the Phase III testing program was to establish the minimum anchorage requirements for the drilled shaft reinforcement in footings containing two of four drilled shafts in tension and the others in compression. The force condition in the drilled shafts can be achieved by a large amount of uniaxial bending moment in addition to the uniaxial compression load applied to the column. In order to investigate the anchorage behavior of the drilled shaft reinforcement, the ultimate state of the test specimens should be governed by drilled shaft reinforcement, and failure of the other structural components in the footing needs to be prevented. However, imposing the loading condition is restrictive in large-scale structural testing. Therefore, an equivalent loading condition appropriate for the testing was planned based on the strut-and-tie model near the end of the drilled shaft reinforcement to be the same as that under the original loading condition.

Test specimens containing various types of drilled shaft anchorages—straight, hooked, and headed—were designed and fabricated for the test program. Similar to Phase II testing, the drilled shaft reinforcement in the test specimens was detailed on the basis of the typical embedment length-to-bar diameter ratios used in drilled shaft footing projects in the state of Texas. The test specimens were subjected to displacement-controlled loading; loading was stopped before the failure of specimens to prevent damages to the test setup, which was deliberately designed for the equivalent loading condition.

All anchorage types of drilled shaft reinforcement were able to develop the full yield strength during the tests, and the behavior of the drilled shaft reinforcement was investigated through a series of strain gauges installed on the longitudinal rib of the bars. The strain data collected from the gauges were used to develop stress profiles and bond stress profiles of the drilled shaft reinforcement based on the strain-stress relationship obtained from tension tests of the reinforcing bars.

The overall behavior of the drilled shaft reinforcement observed in Phase III testing was comparable among the various iterations regardless of the anchorage type. The reinforcement stress increment was observed near the top surface of the footing, whereas almost no stress was developed near the end of drilled shaft reinforcement. The maximum stresses within the drilled shaft reinforcement length during the tests were measured at the strain gauges installed closest to the interface between the shaft plate and the footing, and they reached about 90% of the tensile strength of the drilled shaft reinforcement at 400 kips loading. Similarly, the bond stress was activated near the top surface of the footing; however, almost zero bond stress was computed near the end of the drilled shaft reinforcement during the tests.

The test results indicated that the drilled shaft reinforcement stress increases from the interface between footing and shaft, and consistently increases even after yielding up to its fracture. The tensile force applied to the drilled shaft reinforcement is resisted solely by bond along the top and central portion of the embedment lengths. Therefore, the bearing action of the head or hook anchorage near the drilled shaft end was excluded for the tensile force resisting mechanism.

The research team also proposed an assumed compression field defined by the boundary of the fan-shaped strut. The critical section of the drilled shaft reinforcement defined by the assumed compression field was conservative enough to ensure yielding of the drilled shaft reinforcement when the critical section is displayed on the developed stress profiles from the tests. Following the same scheme, a compression field representing the non-contact lap splice behavior between the column and drilled shaft tie elements was assumed. The conservativeness of the assumed compression field will be verified in Chapter 7.

Chapter 7. Finite Element Modeling

7.1. Introduction

The objectives of this chapter were to develop finite element (FE) models, calibrate and validate the FE results using experimental results, and carry out a parametric study. In the study, the software modified version of VecTor4 in which Goh and Hrynyk (2018) implemented solid continuum elements was used to develop and analyze FE models. VecTor4 was originally dedicated to nonlinear FEA for 3D plate or shell type elements. The FE model was then validated under loading conditions based on Phase I through Phase III of the experimental program. An equivalent FE model identical to the model used for testing experimental footing specimens and a full FE model were developed and compared for the loading condition of Phase III testing—large uniaxial eccentric loading. Numerical parametric analyses were performed using the validated FE model to investigate the effect of design parameters and provide supplement data for the experimental program. That is, the research team expanded both the parameters that were not investigated and the parameters that were included in the experimental program.

This chapter is organized as follows: Section 7.2 briefly introduces the results of the model verification procedure through comparison with previous test results. The FE results for Phase I, II, and III testing are presented in Section 7.3, 7.4, and 7.5, respectively. Each of these three subsections presents and discusses the development of the FE model, the investigation of FE results through comparison with test results of this project, and the numerical parametric study for each loading condition.

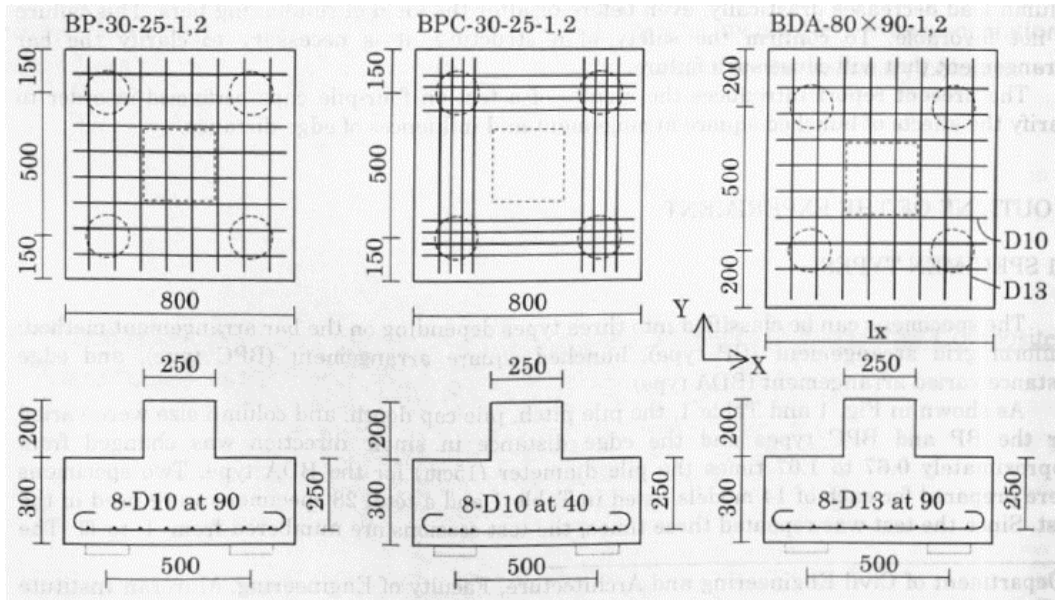
7.2. Preliminary FE Model Assessment

FE modeling and analysis in this research project was conducted using VecTor4, a nonlinear FE analysis program developed by the Vector Analysis Group at the University of Toronto. VecTor4 is designed to analyze 3D reinforced concrete continuum structures. A cracked reinforced concrete material modeling scheme in accordance with the equations of the disturbed stress field model and modified compression field theory was employed. VecTor4 can provide displacement at each node, crack information such as crack width and angle in each concrete element, and stress/strain information in any elements. As a result, the research team can predict the structural response, crack pattern, and stress distribution from FE analysis.

The validation process of FE modeling assumptions and methodologies was performed in two stages. In a preliminary assessment stage, experimental data from previous experimental programs in the literature was utilized to develop FE models and initially validate modeling assumptions for simulating the behavior of drilled shaft footings subjected to axial compressive force under quasi-static loading conditions. In a second stage, the FE models were validated with results from the specimens tested in the experimental programs of the current project, by comparing the experimental and computational results presented in Sections 7.3 through 7.5.

7.2.1. Footing Research Database for the FE Validation

For preliminary FE model assessment, 17 of specimens from two experimental studies, as summarized in Table 7.1, were collected from the footing research database introduced in Chapter 2. Collected database for FE validation was established by filtering out those footing specimens not supported by four drilled shafts or tested with different boundary conditions to that of the experimental program of this study. Figure 7.1 and Figure 7.2 provide the dimensions and details of test specimens.



(Unit: mm)

Figure 7.1 Dimension and details of test specimens (Suzuki et al. 1998)

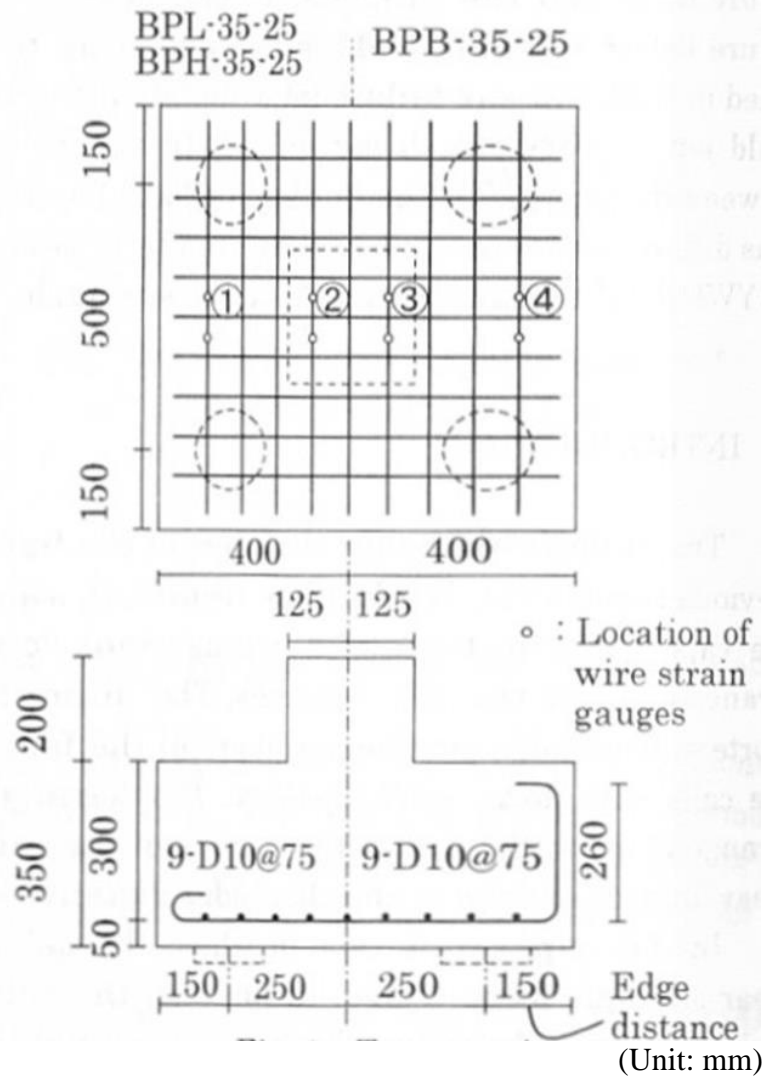


Figure 7.2 Dimension and details of test specimens (Suzuki and Otsuki, 2002)

Table 7.1 Summary of FE Validation Database

Researchers (Years)	Specimen ID	Footing Size [in.]			Bottom Mat Reinforcement Layout	Concrete Strength [ksi]	Ultimate Capacity [kip]
		Length	Width	Height			
Suzuki et al. (1998)	BP-20-2	35.4	35.4	7.9	Grid	2.96	107.9
	BPC-20-2	35.4	35.4	7.9	Banded	2.89	118.9
	BP-25-2	35.4	35.4	9.8	Grid	3.12	169.7
	BPC-25-2	35.4	35.4	9.8	Banded	3.19	182.8
	BP-20-30-2	31.5	31.5	7.9	Grid	4.32	107.9
	BPC-20-30-2	31.5	31.5	7.9	Banded	4.32	111.3
	BP-30-30-2	31.5	31.5	11.8	Grid	4.13	203.9
	BPC-30-30-2	31.5	31.5	11.8	Banded	4.48	231.3
	BP-30-25-2	31.5	31.5	11.8	Grid	3.81	163.0
	BPC-30-25-2	31.5	31.5	11.8	Banded	4.23	196.0
	BDA-70x90-2	27.6	35.4	11.8	Grid	4.38	169.7
	BDA-80x90-2	31.5	35.4	11.8	Grid	4.25	191.8
	BDA-90x90-2	35.4	35.4	11.8	Grid	4.57	207.1
	BDA-100x90-2	39.4	35.4	11.8	Grid	4.54	209.3
Suzuki and Otsuki (2002)	BPL-35-30-1	31.5	31.5	13.8	Grid	3.49	215.8
	BPL-35-25-1	31.5	31.5	13.8	Grid	3.93	202.8
	BPL-35-20-1	31.5	31.5	13.8	Grid	3.26	169.7

7.2.2. Finite Element Model

The FE models for the specimens contained in the FE Validation Database modeled with a quarter of test specimens taking advantage of symmetry conditions as shown in Figure 7.3. Figure 7.4 illustrates two types of FE models which were modeled with two different sizes of mesh (2 in. and 1 in).

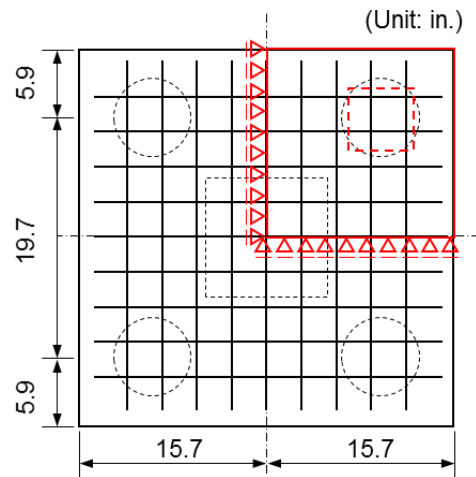


Figure 7.3 Sample FE model of FE Validation Database (Suzuki and Otsuki, 2002)

First-order (eight-noded) hexahedral solid concrete elements were used for the concrete elements. Two types of concrete elements were designated. One is the footing concrete element with the measured compressive strength of concrete for test specimens, while the other concrete element was assigned a much higher compressive strength and modulus of elasticity to simulate loading and supporting parts so that they remain elastic. Only the compressive strength of concrete was specified by users and the other parameters were automatically calculated from the input of concrete compressive strength by the program. For simplicity, a square bearing plate with the same area as the circular drilled shaft was used instead of a circular shape.

Reinforcing bars were modeled using 3D truss elements with two nodes. The yield strength and tensile strength of the steel were determined based on the material properties reported in the experimental studies. The elastic-plastic model with linear hardening was implemented. A perfect bond was assumed between concrete and reinforcement.

Loading was applied as prescribed displacements onto all nodes of the loading plate with increments of 0.004 in. until the convergence error occurred due to failure or the designated number of loading steps (100 steps) was reached. Long term deformation effects of concrete such as creep and shrinkage were not considered.

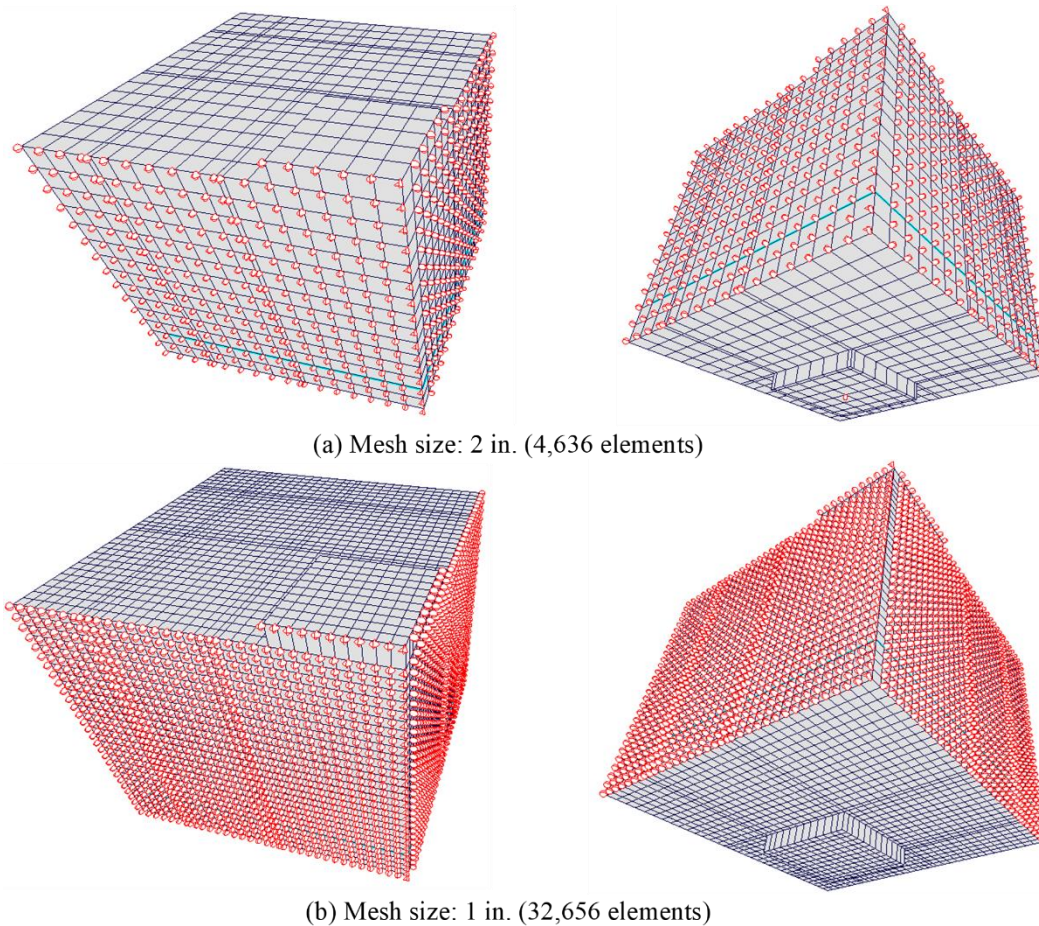


Figure 7.4 Two types of mesh size for mesh sensitivity analysis (BPB-35-25)

7.2.3. Results and Discussion

7.2.3.1. Mesh Sensitivity Analysis

Mesh density for the FE models presenting stress concentration is a critical factor to determine the accuracy of results, the convergence rate, and the efficiency of running time (CPU time). Less stress was predicted for coarse FE mesh as compared to finer FE mesh. The finer model can predict more accurate results, but is computationally expensive in terms of resources such as memory and CPU. As high magnitude of force was applied on the loading plate, stress concentration was expected near the edge and tip of shaft and loading plates in the FE models provided in this chapter. Therefore, mesh sensitivity analysis can provide the most efficient mesh size for optimizing the accuracy and running resources. As shown in Figure 7.4, two types of mesh sizes —1 in. and 2 in.—for a total of four test specimens (BPC-20-2, BPC-25-2, BPL-35-25-1, and BPL-35-30-1) were employed for the mesh sensitivity analysis.

Table 7.2 summarizes the measured and the computed ultimate capacities for two types of FE models. The ratios of measured to computed ultimate capacities for four FE models were comparable. It can be seen from Figure 7.5 and Figure 7.6 indicate that load-deflection responses from both FE mesh sizes were similar as well. The levels of accuracy were sufficient. The findings reveal that 2 in. mesh size could optimize the accuracy of numerical results and the computational efficiency.

Table 7.2 Summary of sensitivity analysis

Specimen ID	Mesh size	Ultimate capacity [kN]		$\frac{P_u}{P_{FEA}}$
		Computed (P_{FEA})	Measured (P_u)	
BPC-20-2	1 in.	487	529	1.03
	2 in.	512		1.09
BPC-25-2	1 in.	810	813	1.00
	2 in.	767		1.06
BPL-35-25-1	1 in.	920	902	0.98
	2 in.	917		0.98
BPL-35-30-1	1 in.	999	960	0.96
	2 in.	1,003		0.96

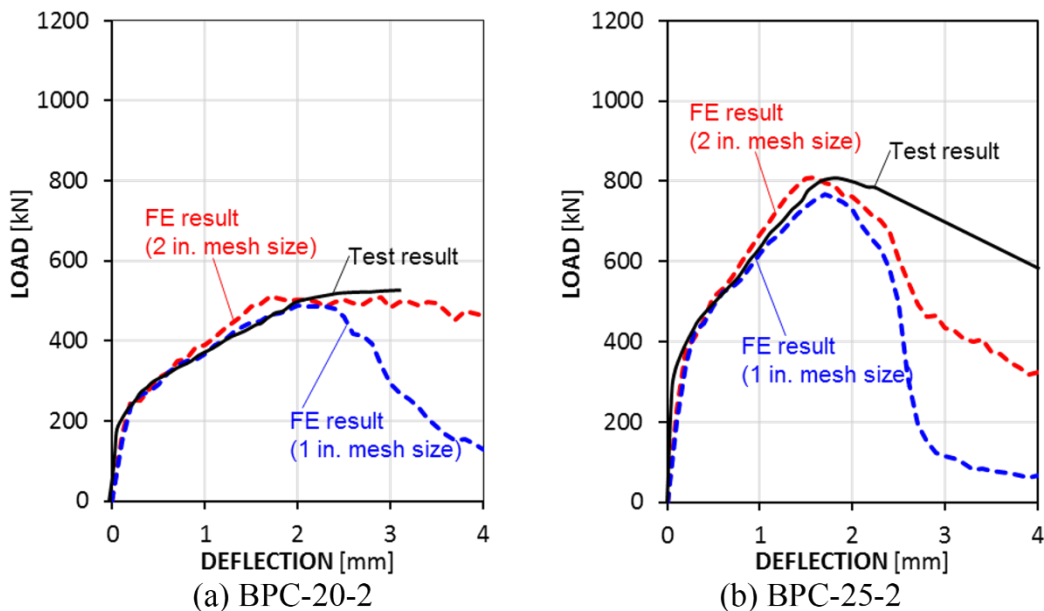


Figure 7.5 Load-deflection responses of test specimens and FE models with 1 in. and 2 in. mesh size: Banded layout

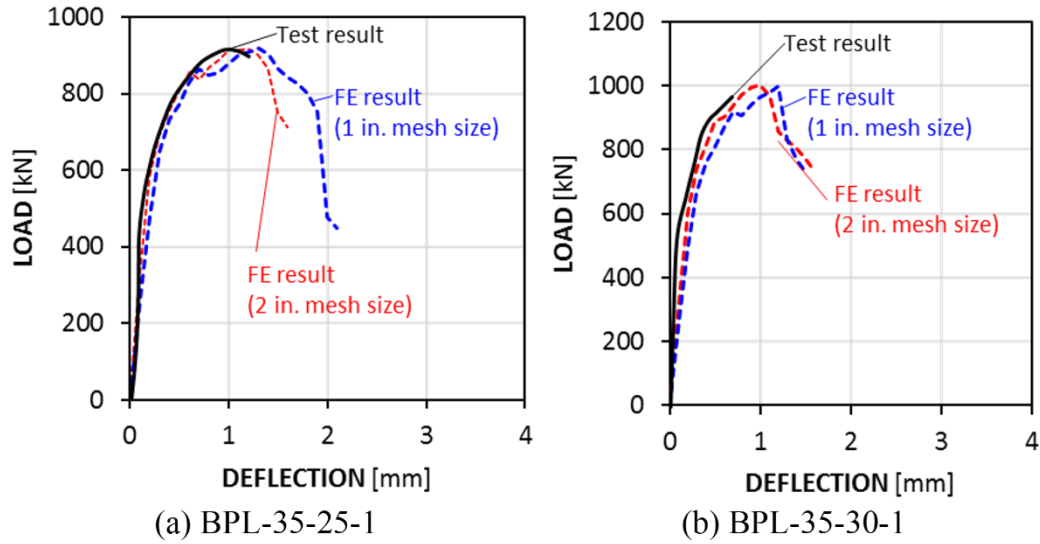


Figure 7.6 Load-deflection responses of test specimens and FE models with 1 in. and 2 in. mesh size: Grid layout

7.2.3.2. Ultimate Capacities

Ultimate capacity is the primary factor used to validate the FE model compared to test specimens. As tabulated in Table 7.3, the FE models in the FE Validation Database predicted ultimate capacities accurately since the ultimate capacity ratio (P_u/P_{FEA}) is 1.01 on average and ranged from 0.94 to 1.11%. The coefficient of variation (COV) was 0.05. In conclusion, the FE model methodology for footing structures can be accepted and can be applied to the FE models in the following sections.

Table 7.3 Summary of measured and computed ultimate capacities of FE Validation Database

Researchers (Years)	Specimen ID	Bottom Mat Reinforcement Layout	Ultimate Capacity [kip]		$\frac{P_u}{P_{FEA}}$
			Computed (P_{FEA})	Measured (P_u)	
Suzuki et al. (1998)	BP-20-2	Grid	102.4	107.9	1.05
	BPC-20-2	Banded	115.0	118.9	1.03
	BP-25-2	Grid	153.6	169.7	1.11
	BPC-25-2	Banded	182.0	182.8	1.00
	BP-20-30-2	Grid	98.5	107.9	1.10
	BPC-20-30-2	Banded	118.1	111.3	0.94
	BP-30-30-2	Grid	192.9	203.9	1.06
	BPC-30-30-2	Banded	225.8	231.3	1.02
	BP-30-25-2	Grid	163.2	163.0	1.00
	BPC-30-25-2	Banded	189.8	196.0	1.03
	BDA-70x90-2	Grid	180.2	169.7	0.94
	BDA-80x90-2	Grid	193.8	191.8	0.99
	BDA-90x90-2	Grid	210.4	207.1	0.98
	BDA-100x90-2	Grid	200.3	209.3	1.04
Suzuki and Otsuki (2002)	BPL-35-30-1	Grid	225.4	215.8	0.96
	BPL-35-25-1	Grid	206.2	202.8	0.98
	BPL-35-20-1	Grid	175.2	169.7	0.97
Average P_u/P_{FEA}					1.01
Coefficient of Variation (COV=standard deviation / mean)					0.05

7.3. Phase I Testing: Uniform Compression in Shafts

The research team developed FE models of the test specimens of Phase I testing to further investigate the response of footings under uniform compression conditions and to further validate the FE modeling approach.

7.3.1. Finite Element Model

Figure 7.7 illustrates a sample of 3D FE mesh used for test specimen, II-7, that was the baseline model of which results were compared with other specimens and had

the most common dimension among specimens of Phase I testing. The same modeling approach as described in Section 7.2 was used: the concrete was modeled using first-order (eight-noded) hexahedral (brick) solid concrete elements; 3D truss elements with two nodes were used to model the reinforcement. To reduce the degree of freedom, only one-quarter of the symmetrical footing specimen was modeled which conserved computational resources. Based on the results of mesh sensitivity analysis conducted in the FE model assessment of Section 7.2, an element size of 2.0 in. was applied to all specimens.

The research team defined two concrete types when modeling the footing and the auxiliary part—the column (loading part) and the drilled shaft (support part). The compressive strength of concrete measured in the experimental program was used to define the footing concrete material. On the other hand, the auxiliary part, where the significant stress concentration developed, was simulated as a concrete model with extremely high strength and so that the part would remain in elastic during analysis and the failure at the auxiliary part was prevented, which is caused by the non-existence of a linear elastic model. This FE model had a square bearing plate whose area was identical to the circle drilled shaft. Both the tensile and compressive stress-strain relationships of concrete such as tension stiffening, tension softening, and concrete softening were automatically determined based on the measured concrete compressive strength for each specimen in Phase I testing.

Reinforcing bars were modeled by truss element with measured mechanical properties (yield strength and ultimate strength) through the test protocol complying with ASTM A370. Trilinear stress-strain relationship was defined for the reinforcing bars with these values and default setting of VecTor4. As shown in Figure 7.8, both hooked and straight bars for bottom mat reinforcement were implemented depending on the bottom mat reinforcement layout of each specimen. Straight bars were used for vertical (transverse) side face reinforcement. Perfect bond was assumed between concrete and reinforcement. Figure 7.9 shows the boundary and loading conditions for the test specimens. Symmetry was considered in the two internal faces of the quarter-footing model. A vertical restraint was applied at the center of the bearing plate to represent the support in the experimental program. Prescribed displacement as shown in Figure 7.9 was applied onto all nodes of the loading plate with increments of 0.008 in. (0.2 mm) until the FE model did not converge after peak or designated number of loading steps was reached. The self-weight was neglected since the measured applied load during test was a primary comparison parameter. In addition, long-term effects such as creep or shrinkage was not applied due to the lack of accurate measured test data.

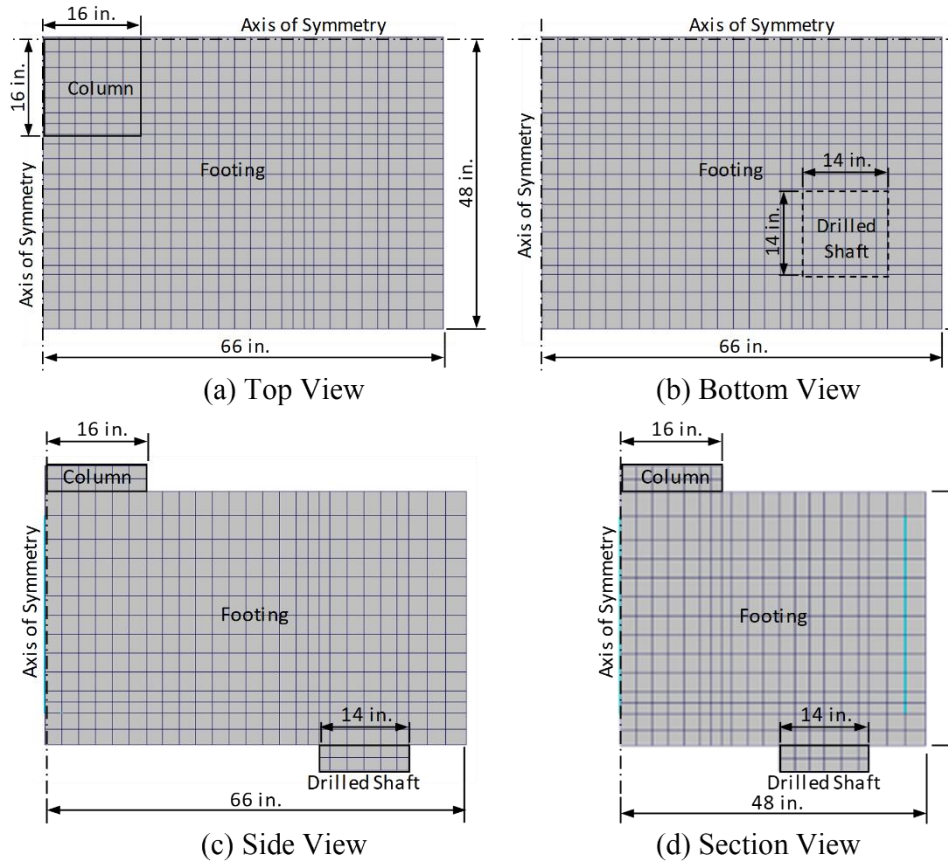


Figure 7.7 FE mesh example for Phase I testing (II-7)

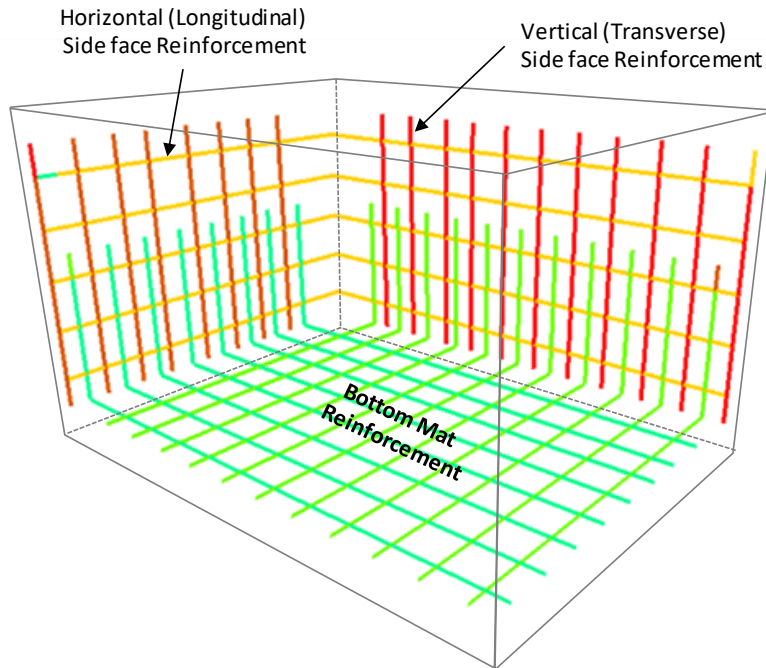


Figure 7.8 Example of truss elements for reinforcement in FE models for Phase I testing

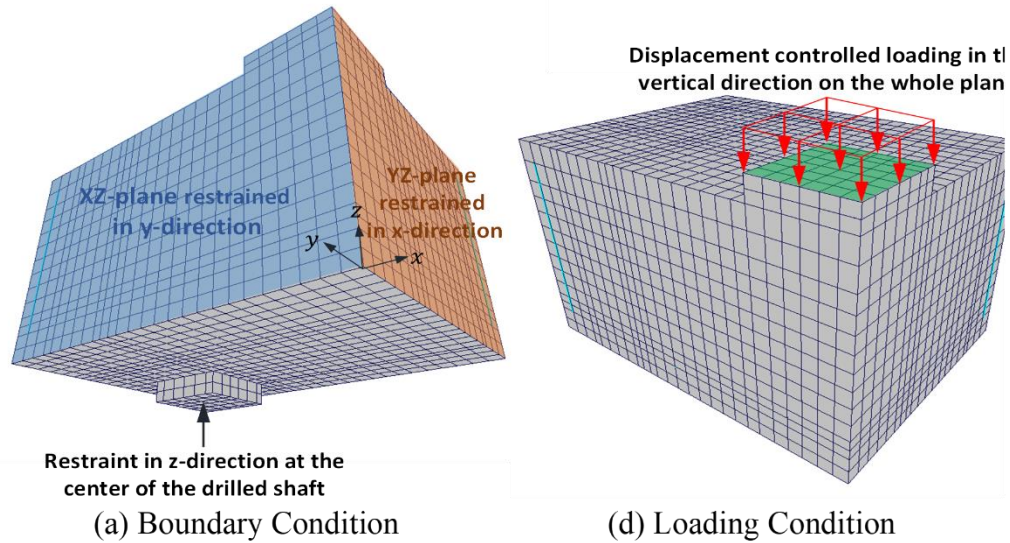


Figure 7.9 Example of boundary and loading conditions in FE models for Phase I testing

7.3.2. Results and Validation with Experimental Data

The ultimate capacity, load-deflection response, and cracking pattern on the external face or internal section of the footing were used to validate the FE models by comparing model outputs with experimental results.

7.3.2.1. Ultimate Capacity

Table 7.4 summarizes the measured and computed ultimate capacities for each test series. The average ratio of experimental to numerical ultimate capacities was 1.12. The difference ranged from 0.2% to 33% and the COV was 0.08. The numerical results of specimens with straight bars (I-1 and I-3) as well as those with smaller side face reinforcement (IV-10 and IV-11) differed slightly (less than 10%) from the experimental results. Numerical tests on the specimens with hooked bars and side face reinforcement provided more conservative analytical predictions in terms of the ultimate capacity. Based on the average and dispersion of the strength ratios, it can be concluded that the computed ultimate capacities by FEA provided reasonably accurate predictions within an acceptable tolerance.

Table 7.4 Summary of measured and computed ultimate capacities

Series	Specimen ID	Test variables					Ultimate Capacities [kip]			
		Bottom Mat Details [†]	z/d	D_{DS} [in]	ρ_{face} [%]	H [in]	Measured (P_u)	Computed (P_{FEA})	$\frac{P_u}{P_{FEA}}$	Average $\frac{P_u}{P_{FEA}}$
I	I-1	GS	1.70	16	0.30	32	2,107	1,977	1.07	1.15
	I-2	GH	1.70	16	0.30	32	2,775	2,089	1.33	
	I-3	BS	1.70	16	0.30	32	2,703	2,485	1.09	
	I-4	BH	1.70	16	0.30	32	2,884	2,568	1.12	
II	II-5	GH	1.10	16	0.30	40	3,273	2,655	1.23	1.19
	II-6	GH	1.35	16	0.30	40	3,648	3,224	1.13	
	II-7 *	GH	1.70	16	0.30	40	3,387	2,843	1.19	
III	III-8	GH	1.70	12	0.30	40	2,886	2,714	1.06	1.13
	II-7 *	GH	1.70	16	0.30	40	3,387	2,843	1.19	
	III-9	GH	1.70	20	0.30	40	2,902	2,583	1.12	
IV	IV-10	GH	1.70	16	0.00	40	2,523	2,528	1.00	1.08
	IV-11	GH	1.70	16	0.18	40	2,990	2,869	1.04	
	II-7 *	GH	1.70	16	0.30	40	3,387	2,843	1.19	
V	V-12	GH	1.70	16	0.30	32	2,239	2,152	1.04	1.15
	II-7 *	GH	1.70	16	0.30	40	3,387	2,843	1.19	
	V-13	GH	1.70	16	0.30	48	3,354	2,890	1.23	
Average P_u/P_{FEA}									1.13	
Coefficient of Variation (COV)									0.08	

* Baseline model: Results are compared in Series II through V

† GS: Grid layout and straight anchorage, GH: Grid layout and 90-degree hooked anchorage, BS: Banded layout and straight anchorage, BH: Banded layout and 90-degree hooked anchorage

7.3.2.2. Load-Deflection Response

Figure 7.10 shows the comparison of experimental and numerical load-deflection responses of specimens that provided the most accurate computed prediction (IV-10), the least accurate computed prediction (II-5), the best fit of load-deflection response (III-8), and the baseline specimen (II-7). It should be noted that I-2 was excluded from this comparison because the measured deflection was incomplete. As shown in these plots, the FE models successfully captured the ultimate capacities and the load-deflection responses, except for the FE model of II-5 shown in Figure 7.10-(b). Generally, the numerical ultimate capacities and the load-deflection response were comparable with the experimental results in all cases except for II-5 and II-6, which had smaller strut inclinations. The initial stiffnesses obtained from experimental and computational results were almost identical. Post-cracking stiffness up to the first loading drop obtained from FEA results (around 2,000 kips in most cases) were slightly larger than for experimental results. After the first load dropped initially, the FE models presented a higher residual load as compared to experimental results. The numerical peak loads in 12 out of 13 specimens are less than experimental ultimate capacities as summarized in Table 7.4. The numerical behaviors of II-5 and II-6 provided smaller stiffness than measured behavior.

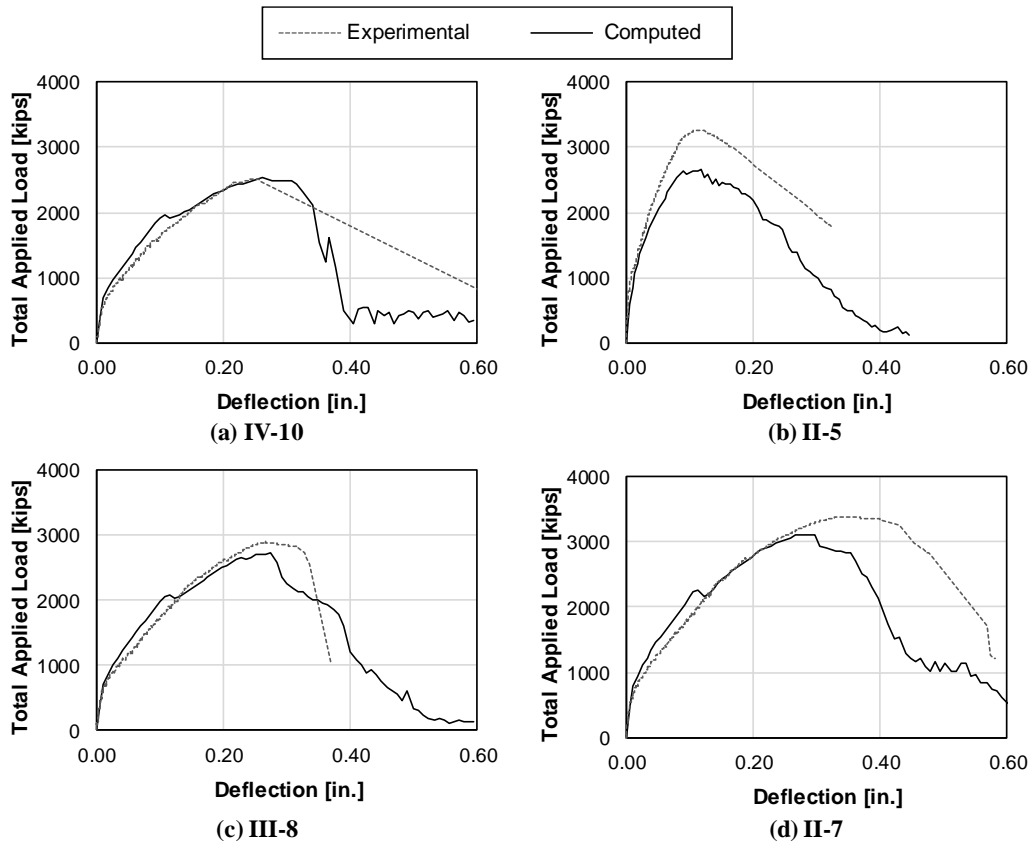
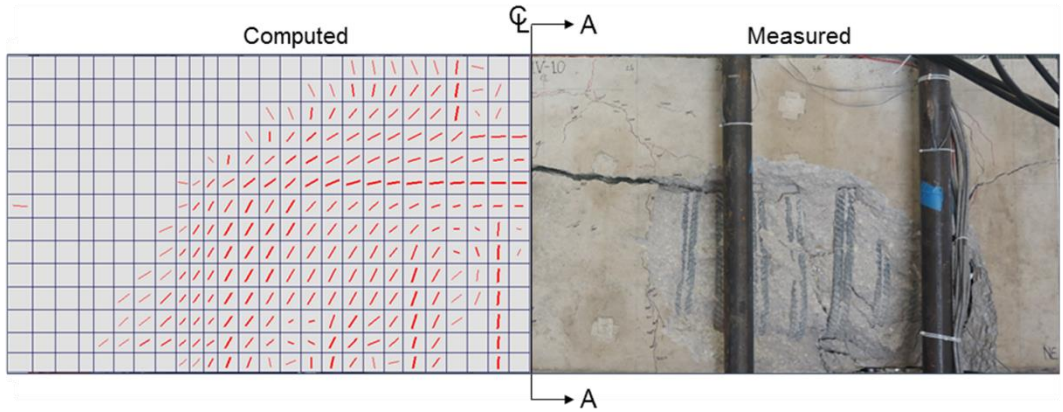


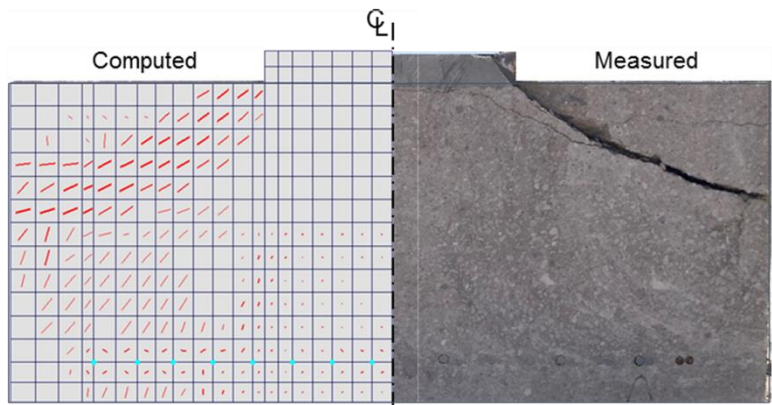
Figure 7.10 Comparison of measured and computed load-deflection plots

7.3.2.3. Crack Patterns

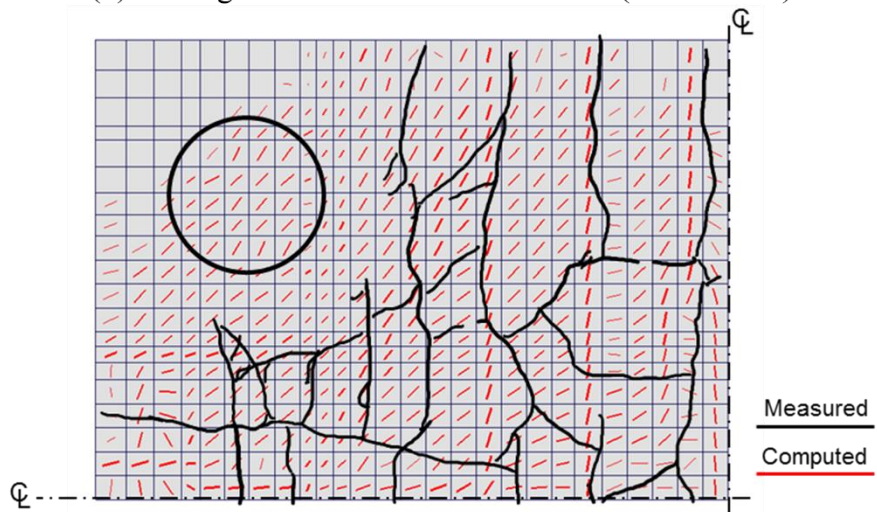
As shown in Figure 7.11 through Figure 7.14, crack patterns on a side face or bottom face of the footings are compared between experimental and numerical results. The numerical and experimental results were reported at the ultimate load and after total failure, respectively. Note that crack widths were not included in the comparison since crack widths were not measured during testing. Figure 7.11 shows the experimentally mapped and computed post-failure conditions in IV-10, for which the most accurate numerical load-deflection response was obtained. As shown in the figure, both the major damage and the crack patterns generated from the numerical tests were successfully captured. A large horizontal crack at mid-height in Figure 7.11-(a) and crack developed from the edge of column to the mid-height of the side face in Figure 7.11-(b) were comparable between mapped and computed results. Figure 7.11-(c) depicts the quadrant of the bottom face with experimental and FEA results overlapping. It should be noted that damage in the region near drilled shafts was not reported. The locations of cracks in the orthogonal direction were accurately captured by FEA. The FE model of II-5 also successfully predicted the crack pattern as shown in Figure 7.12, although the computed load-deflection response was the least accurate. The pattern and angle of the arch-shaped cracks on the north side face and orthogonal cracks at the bottom face in the FE model of II-5 were reasonably comparable. As illustrated in Figure 7.13 and Figure 7.14, the computed results of III-8 and II-7 provided similar post-failure conditions as well. The FE models of both specimens successfully predicted the severe damage near the top edge of the side face observed in both III-8 and II-7. It can be concluded that predictions of overall crack patterns in FE models provided satisfactory performance when compared to the experimental results.



(a) Side face (East)

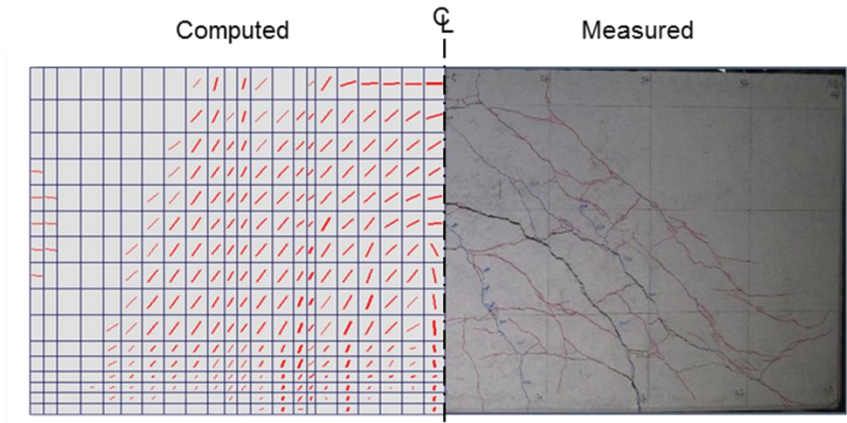


(b) Cutting section in the short direction (Section AA)

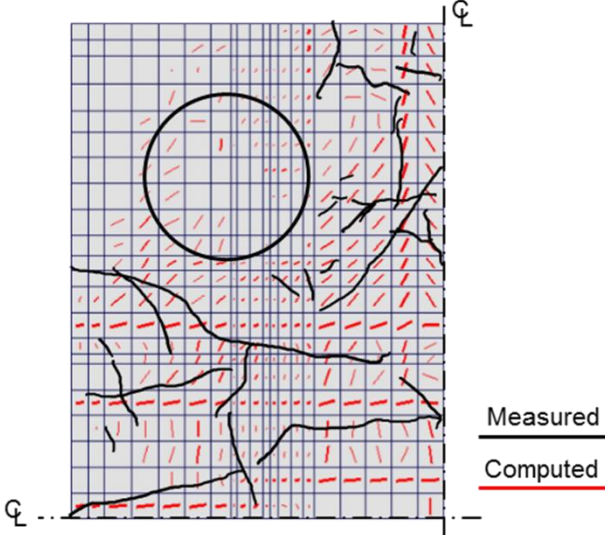


(c) Quadrant of the bottom face

Figure 7.11 Experimentally measured versus computed post-failure crack patterns in IV-10

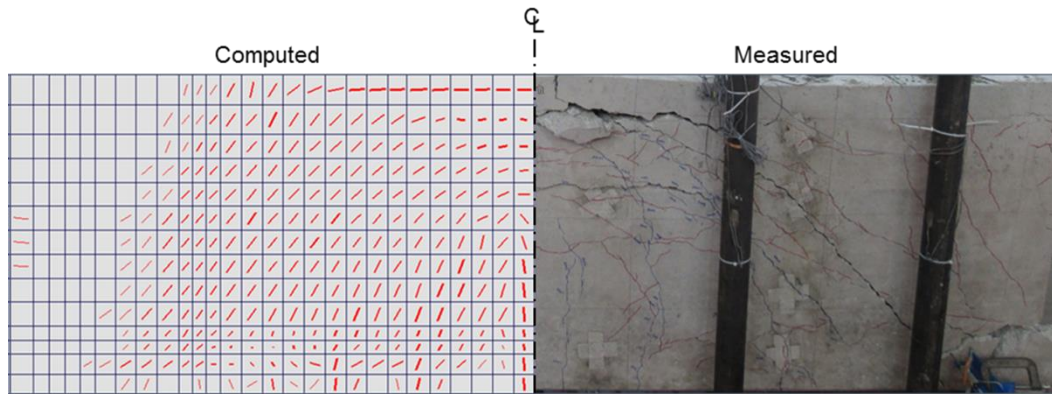


(a) Side face (North)

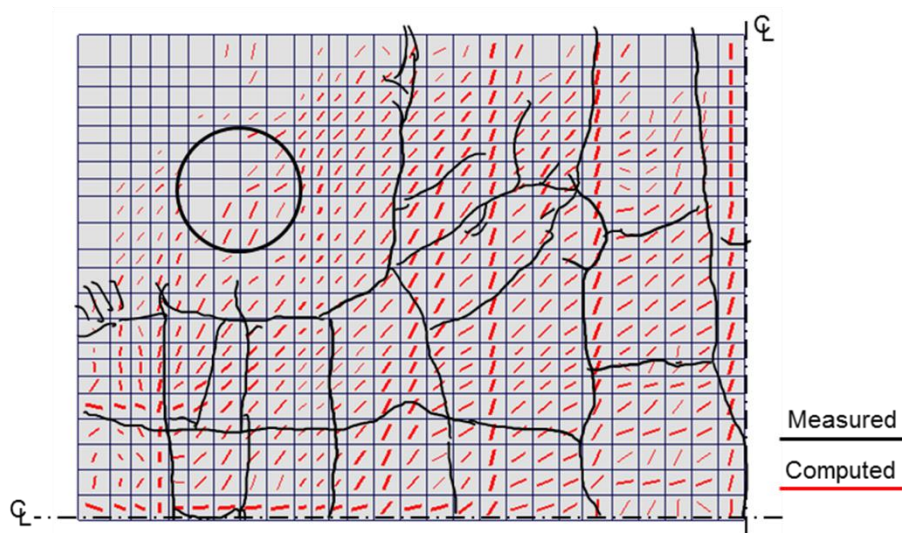


(b) Quadrant of bottom face

Figure 7.12 Experimentally measured versus computed post-failure crack patterns in II-5

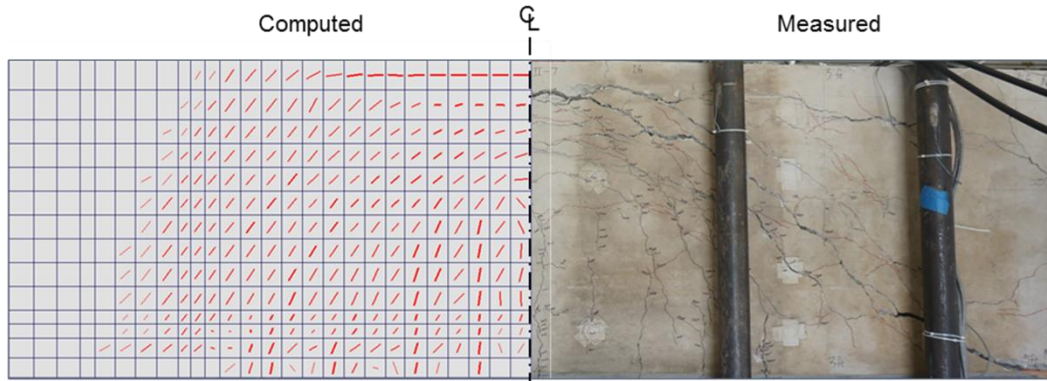


(a) Side face (East)

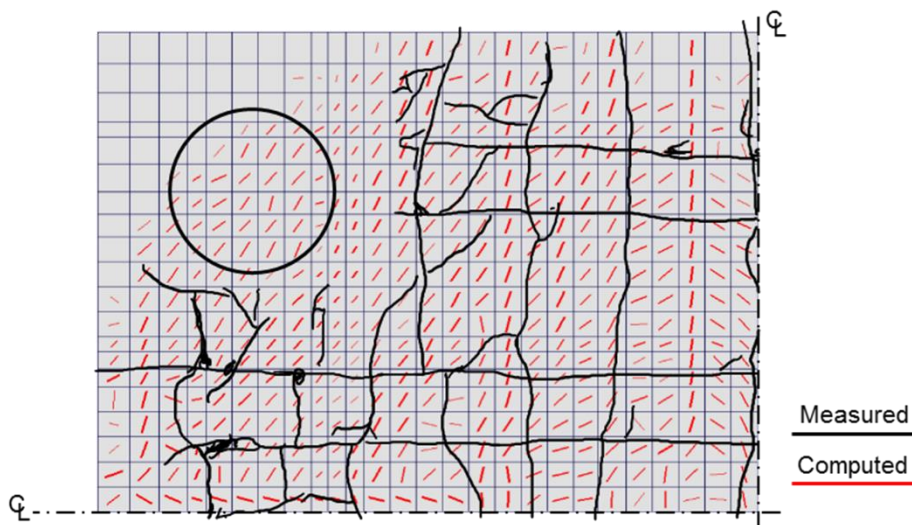


(b) Quadrant of bottom face

Figure 7.13 Experimentally measured versus computed post-failure crack patterns in III-8



(a) Side face (East)



(b) Quadrant of bottom face

Figure 7.14 Experimentally measured versus computed post-failure crack patterns in II-7

7.3.3. Numerical Parametric Study

7.3.3.1. Overview

The research team has identified and experimentally investigated key factors that affect the design and the ultimate capacity of drilled shaft footings throughout the current research project. Although all the test specimens were developed to best represent existing drill shaft footings, the extent of studied parameters in the experimental program was constrained due to time management, economy, and capacity of the test setup. To expand the study domain, validated FE models introduced in the previous section were employed to conduct a numerical parametric analysis as a replacement of additional large-scale structural tests. In addition, the numerical parametric analysis could allow more extensive investigation than the experiments by controlling input parameters to any values,

and reducing the time and effort required for testing. In this section, the numerical parametric studies provide the supplementary assessment of various design parameters that were not covered by the experimental results. In addition, the research team expanded the range of design parameters already included in the testing program.

7.3.3.2. Modeling

The baseline model of drilled shaft footing as shown in Figure 7.15 was designed to be as representative as possible of existing footings in Texas bridges based on the design parameter investigation in Chapter 3. This baseline model provided a basis for comparison with all other numerical results. The footing is square, and the size is a half-scale of the average footing size. The dimensions of the column and footing were determined by the average ratio with respect to footing size. The material properties—compressive strength of concrete (3.6 ksi) and yield strength of steel (60 ksi) were representative of the design material properties typically used in current practice in Texas. A ratio of bottom mat reinforcement (0.9%) and side face reinforcement (0.3%) similar to that used for Phase I test specimens was provided, but the top mat reinforcement was excluded in the baseline model. The area and diameter of reinforcement was calculated from the exact reinforcement area defined as the product of multiplying the reinforcement ratio by the gross sectional area in lieu of the dimensioning based on common reinforcing bar sizes.

The same FE modeling methodology as introduced in Section 7.3.1 was used. As illustrated in Figure 7.16, a doubly symmetric FE model was used and the dimensions of both loading and supporting plate were greater than those in the experimental program. The mesh size ranged from 1.25 to 2.25 in. and was 1.7 in. in average. The center on the bottom face of drilled shaft footing was restrained in the axis of gravity and allowed to translate in other orthogonal directions. A displacement-controlled loading applied in all nodes on the top surface of the loading plate with increments of 0.005 in.

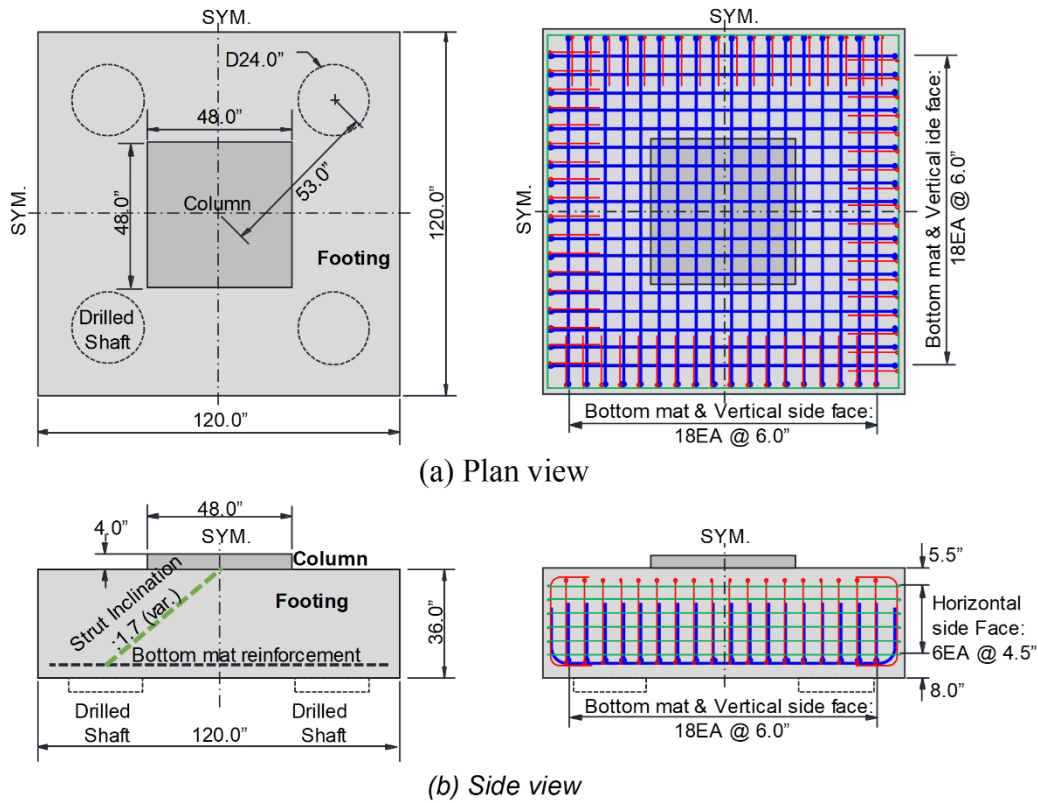


Figure 7.15 Dimension (left) and reinforcing details (right) of the baseline model for numerical parametric study

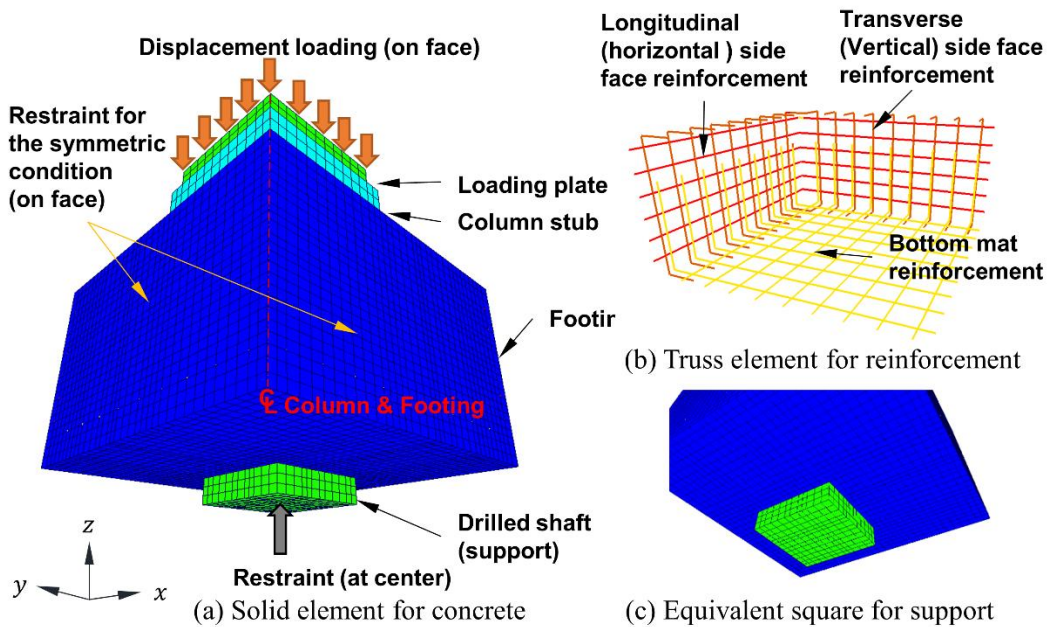


Figure 7.16 Details of the FE model for numerical parametric study

7.3.3.3. Studied Parameters

Ten design parameters and 29 cases were examined in this numerical parametric analysis, as summarized in Table 7.5. The parameters were categorized into four groups—Geometry, Material Properties, Reinforcing Details and Expansive Experimental Variables. The range of each analysis variable was selected from the statistical values such as the minimum, the maximum, or the mean from the footing research database in Chapter 2; the investigation of design parameter reviewed in Chapter 3; and experimental footing specimens in Chapter 4.

The impact of the aspect ratios of a footing and a column on the ultimate capacity was assessed in the category Geometry due to the discrepancy of aspect ratios observed between testing specimens and existing footings in current practice as identified in Chapter 3. The most common shape of the existing footings in the plan view identified in Chapter 3 was square. A rectangular column with an aspect ratio of two was the most commonly used. On the other hand, the shape of testing specimens was square or rectangular and the cross section of all column stubs in the testing specimen was square. The research team studied various aspect ratios in the series focused on the aspect ratios of footing (Series ARF); the series investigating the aspect ratio of column (Series ARC) evaluated the effect of the aspect ratios. The findings of the aspect ratio investigation would affect the design of the baseline model.

The compressive strength of concrete in common practice is usually greater than 3.6 ksi which is design concrete strength. In the series focused on concrete strength (Series CS), the research team examined the effect of higher concrete compressive strength on the ultimate capacity.

Various design parameters are related to reinforcing details. This numerical study investigated varying reinforcement ratios of bottom mat, top mat, and side face reinforcement. The bottom mat reinforcement ratio (Series BM) in the experimental program (Chapter 4) was greater than that in common practice Top mat reinforcement (Series TM) was not provided in the experimental program, but existing footings have top mat reinforcement to resist a flexural loading from other loading cases or controlling shrinkage and temperature cracks. The effect of the side face reinforcement ratio (Series SF) was investigated to validate whether the experimental finding was consistent or not with a computed result. Moreover, Figure 7.17 shows that two types of side face reinforcement (Series SFT) employed in existing footings from the investigation of the design parameter review (Chapter 3). In one type, separate side face reinforcement was placed beside bottom mat reinforcement (Series SFT-SF) as illustrated in Figure 7.17-(a). The other type,

shown in Figure 7.17-(b), is side face reinforcement as an extension of the bottom mat reinforcement (Series SFT-EB) from either straight or hook anchorage.

The last category was intended to expand test variables of Phase I testing (Chapter 4). In specific, the effects of strut inclination (Series SI), shaft diameter (Series SD), and footing height (Series FH) on the structural behavior of a drilled shaft footing were investigated with both experimental tests and numerical parametric studies. As introduced earlier, the parametric analysis results were compared with the experimental results to validate consistency between experiment and numerical analysis.

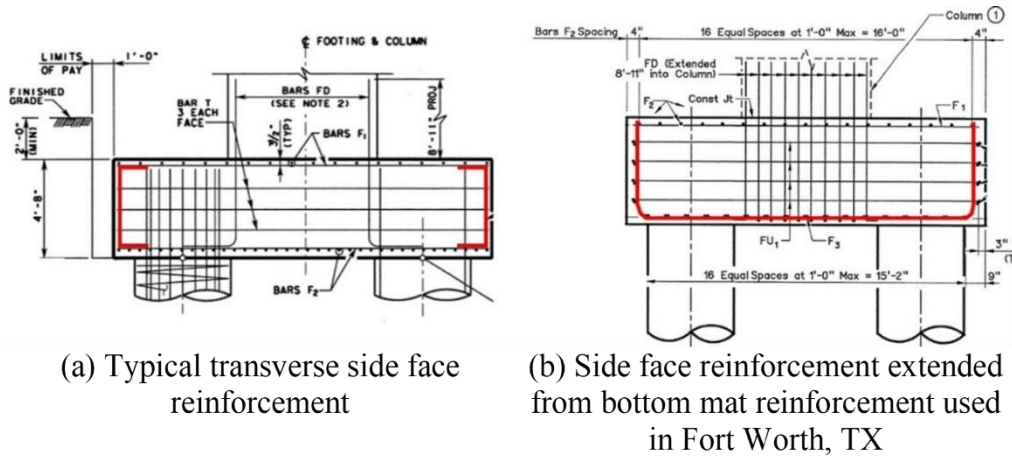


Figure 7.17 Types of traverse side face reinforcement

Table 7.5 Analysis matrix of the numerical parametric study (Phase I)

Category	Series	Model ID	Geometry							Material Properties	Reinforcing Details			
			Footing	Column	Footing Height (H) [in.]	Shaft Diameter (D _{DS}) [in.]	Strut Inclination (z/d)	Aspect Ratio		Concrete compressive strength (f' _c) [ksi]	Ratio [%]			Side face type
			L ₁ x L ₂ [in.]	L _{c,1} x L _{c,2} [in.]				Footing	Column		Bottom Mat	Top Mat	Side Face	
Geometry	Aspect Ratio of Footing (ARF)	<u>ARF-1.000</u>	120 x 120	48 x 48	36	24	1.7	1.00	1.000	3.6	0.9	0.0	0.3	SF
		ARF-1.125	126 x 114						1.125					
		ARF-1.250	135 x 107						1.250					
		ARF-1.375	140 x 103						1.375					
	Aspect ratio of Column (ARC)	<u>ARC-1.00</u>	120 x 120	48 x 48	36	24	1.7	1.000	1.00	3.6	0.9	0.0	0.3	SF
		ARC-1.25		54 x 42					1.25					
		ARC-1.50		60 x 39					1.50					
		ARC-1.75		63 x 36					1.75					
		ARC-2.00		68 x 34					2.00					
	Material Properties	Concrete Strength (CS)	CS-2.4	120 x 120	48 x 48	36	24	1.7	1.000	1.00	2.4	0.9	0.0	0.3
<u>CS-3.6</u>			3.6											
CS-4.8			4.8											
CS-6.0			6.0											
Reinforcing Details	Bottom Mat Ratio (BM)	BM-0.3	120 x 120	48 x 48	36	24	1.7	1.000	1.00	3.6	0.3	0.0	0.3	SF
		BM-0.5									0.5			
		BM-0.7									0.7			
		BM-0.9									0.9			
	Top Mat Ratio (TM)	TM-0.00	120 x 120	48 x 48	36	24	1.7	1.000	1.00	3.6	0.9	0.00	0.3	SF
		TM-0.10										0.10		
		<u>TM-0.18</u>										0.18		
		TM-0.30										0.30		

Note: Underline (Baseline model), SF (Separate face reinforcement), EB (extension of bottom mat reinforcement)

Table 7.5 (cont'd) Analysis matrix of the numerical parametric study (Phase I)

Category	Series	Model ID	Geometry							Material Properties	Reinforcing Details			
			Footing	Column	Footing Height (H) [in.]	Shaft Diameter (D _{DS}) [in.]	Strut Inclination (z/d)	Aspect Ratio		Concrete compressive strength (f' _c) [ksi]	Ratio [%]			Side face type
			L ₁ x L ₂ [in.]	L _{c,1} x L _{c,2} [in.]				Footing	Column		Bottom Mat	Top Mat	Side Face	
Reinforcing Details	Side Face Ratio (SF)	SF-0.00	120 x 120	48 x 48	36	24	1.7	1.000	1.00	3.6	0.9	0.0	0.00	SF
		SF-0.10											0.10	
		SF-0.18											0.18	
		SF-0.30											0.30	
	Side Face Type (SFT)	SFT-SF	120 x 120	48 x 48	36	24	1.7	1.000	1.00	3.6	0.9	0.0	0.71*	SF
		SFT-EB											0.71*	EB
Test Variables	Strut Inclination (SI)	SI-1.2	96 x 96	48 x 48	36	24	1.2	1.000	1.00	3.6	0.9	0.0	0.3	SF
		SI-1.7	120 x 120				1.7							
		SI-2.2	138 x 138				2.2							
	Shaft Diameter (SD)	SD-18	120 x 120	48 x 48	36	18	1.7	1.000	1.00	3.6	0.9	0.0	0.3	SF
		SD-24				24								
		SD-30				30								
		SD-36				36								
	Footing Height (FH)	FH-30	105 x 105	48 x 48	30	24	1.7	1.000	1.00	3.6	0.9	0.0	0.3	SF
		FH-36	120 x 120		36									
		FH-42	132 x 132		42									

Note: Underline (Baseline model), SF (Separate face reinforcement), EB (extension of bottom mat reinforcement)

* Total volume of side face reinforcement divided by total volume of footing

7.3.3.4. Results

Load-deflection responses are compared for each series and the relationship between ultimate load and variables are investigated in this section. A black solid line and a marker in the following plots indicated the result of the baseline model.

Series Aspect Ratio of Footing (Series ARF)

As shown in Figure 7.18, it was found that, at initial degrading of stiffness, the cracking load and post-cracking stiffness decreased when the aspect ratio of footing increased. However, the ultimate loads were comparable. Hence, the analytical results indicate that the aspect ratio of footing is insensitive on ultimate load. As a result, the structural behavior of rectangular footing test specimens in Phase I testing (Chapter 4) can represent the behavior of square footings, which are more common in current practice.

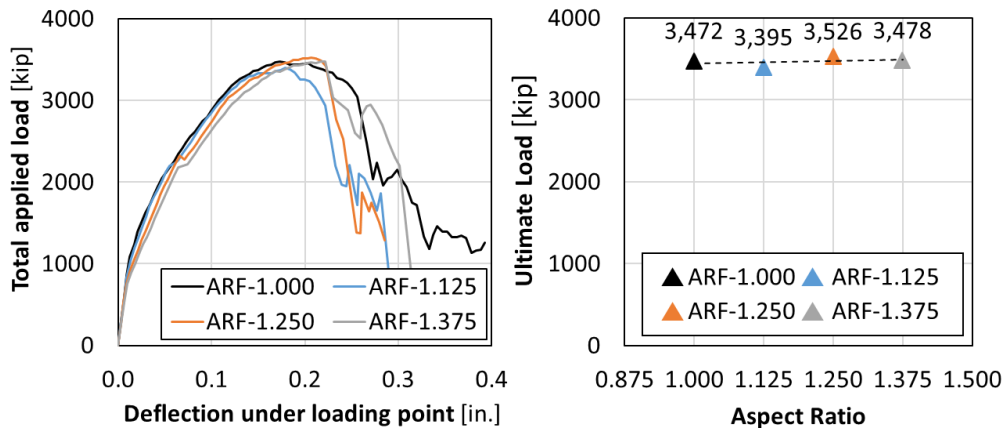


Figure 7.18 Load-deflection plot (left) and plot of ultimate load versus aspect ratio of footing (right): Series ARF

Aspect Ratio of Column (Series ARC)

Figure 7.19 shows little differences in in the pre-peak state and ultimate loads (differences were 3% or smaller) among specimens with different column geometry. Hence, the aspect ratio of the column did not affect the ultimate load and the structural response. Consequently, a square column section that used in the experimental program (Chapter 4) can provide the comparable behavior of a rectangular column section, which are more common in current practice.

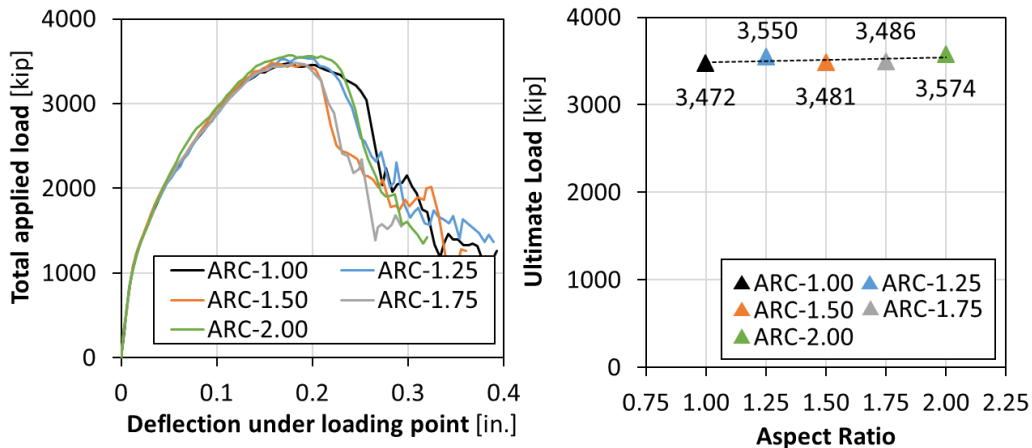


Figure 7.19 Load-deflection plot (left) and plot of ultimate load versus aspect ratio of column (right): Series ARC

Compressive Strength of Concrete (Series CS)

It was observed that greater compressive strength of concrete resulted in greater stiffness and ultimate load, as shown in Figure 7.20. The ultimate load increased proportionally to the square root of compressive concrete strength. This would indicate that the failure was caused by the splitting of the diagonal concrete strut, which depends on the tensile strength of concrete.

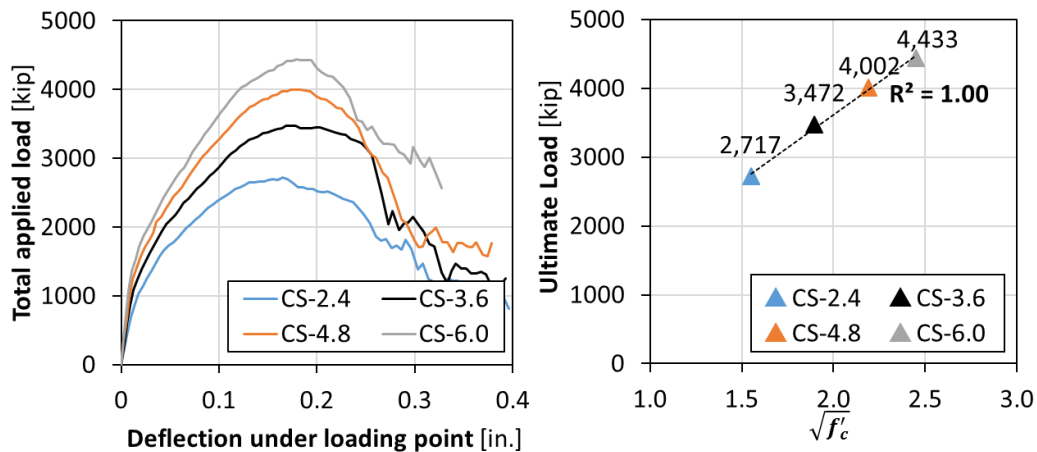


Figure 7.20 Load-deflection plot (left) and plot of ultimate load versus concrete compressive strength (right): Series CS

Bottom Mat Reinforcement Ratio (Series BM)

The initial stiffness is identical regardless of the bottom mat reinforcement ratio. However, post-cracking stiffness, deflection at peak point, and ultimate load increased when the reinforcement ratio increased. As shown in Figure 7.21, the

increase of ultimate load was not linear with the increase of the reinforcement ratio. Rather, the increase rate declined as the ratio increased. Further investigation is necessary to find a relationship between bottom mat reinforcement ratio and ultimate load.

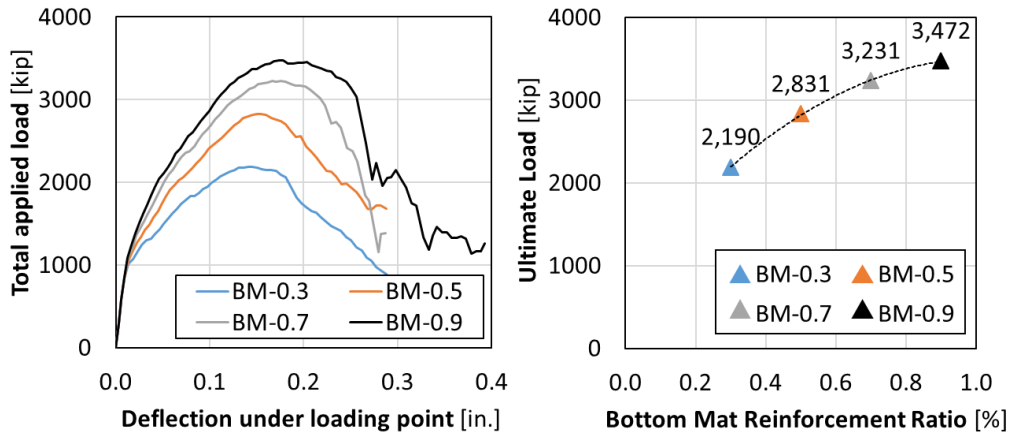


Figure 7.21 Load-deflection plot (left) and plot of ultimate load versus bottom mat reinforcement ratio (right): Series BM

Top Mat Reinforcement Ratio (Series TM)

As shown in Figure 7.22, the load-deflection responses of all cases were comparable up to around 3,200 kips (88% of average numerical ultimate capacity). When top mat reinforcement was not provided (TM-0.00, black solid line in Figure 7.22), the ultimate load was around 7% (230 kips) lower than the average of the other cases (3,706 kips). In contrast, load-deflection responses and ultimate loads of FE models with top mat reinforcement, regardless of the specific reinforcement ratio, were comparable within a 2% difference.

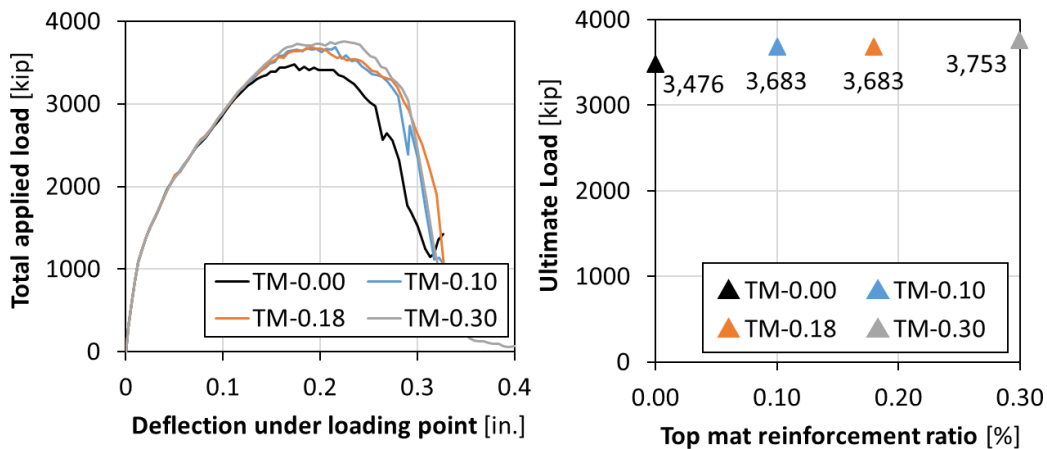


Figure 7.22 Load-deflection plot (left) and plot of ultimate load versus top mat reinforcement ratio (right): Series TM

Side Face Reinforcement Ratio (Series SF)

Figure 7.23 shows the computed results of FE models in Series SF. Regardless of the existence of side face reinforcement, similar load-deflection responses were observed under the lower-level loading stage (less than 2,000 kips). The FE model without side face reinforcement (SF-0.00) exhibited lower stiffness after 2,000 kips, when diagonal cracks developed on the side surfaces, than did other FE models, as well as an ultimate load that was 8% lower. If side face reinforcement was provided, the ratio increase resulted in slightly greater stiffness after 2,000 kips. The ultimate loads of FE models with side face reinforcement, regardless the reinforcement ratio, were comparable. This trend is similar to the experimental result of Series IV in Phase I testing (Chapter 4).

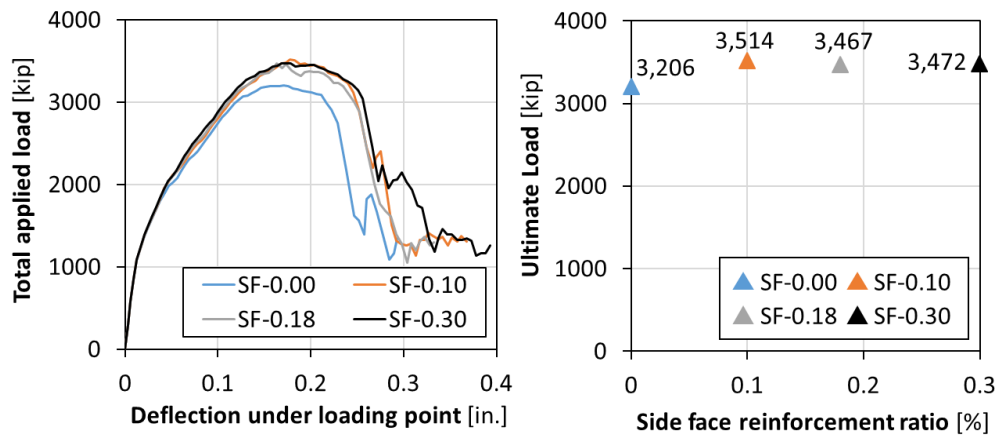


Figure 7.23 Load-deflection plot (left) and plot of peak load versus side face reinforcement ratio (right): Series SF

Side Face Reinforcement Type (Series SFT)

Figure 7.24 indicates that there are no differences in the load-deflection response and ultimate load between side face reinforcement types. Because the side face reinforcement ratio in SFT-EB could not be defined, the total volume of side reinforcement and the extension of bottom mat reinforcement on the side face was considered as the factor of analysis. The total volume of reinforcement on the side face for both types is close (925 in^3 for SFT-EB and 919 in^3 for SFT-SF). Thus, no significant difference of structural behavior was found. It can be concluded that for the same level of side reinforcement volume, using separate side face reinforcement (SFT-SF) does not provide any advantage.

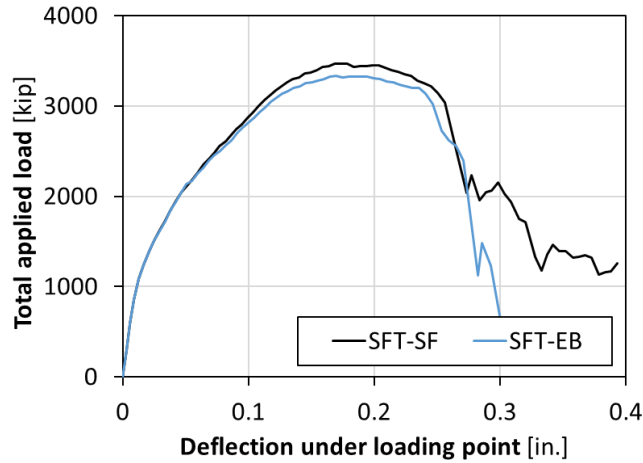


Figure 7.24 Load-deflection plot: Series SFT

Strut Inclination (Series SI)

Figure 7.25 compares the structural behavior and ultimate load obtained for footing with different strut inclination. As provided in the figure and the experimental result of Series II in Phase I testing (Chapter 4), the strut inclination significantly affected the stiffness, ultimate load, and deflection at ultimate load. Stiffness and ultimate load increased when strut inclination decreased. The plot of ultimate load versus strut inclination revealed the linearly decreasing trend of ultimate load when strut inclination increases. This finding supports the conclusion of Series II in Phase I testing (Chapter 4), where steeper strut inclinations resulted in greater stiffness and normalized ultimate load.

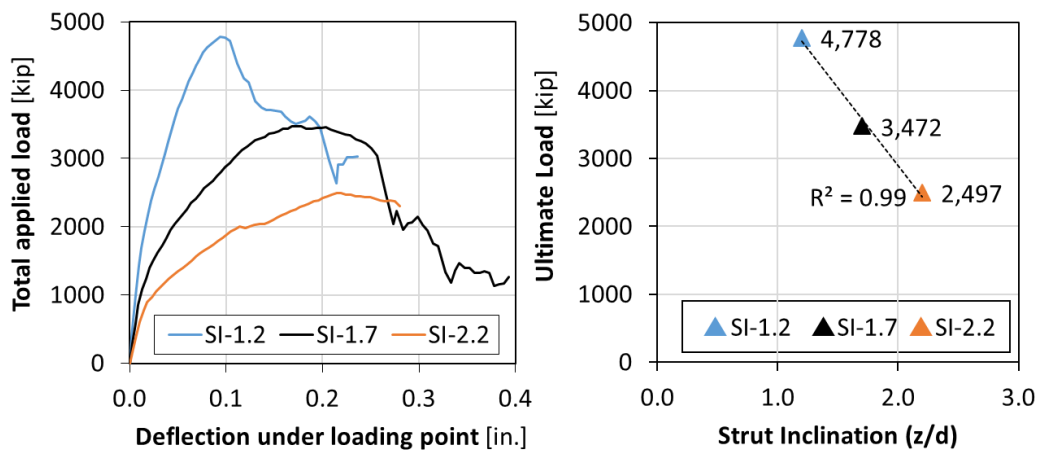


Figure 7.25 Load-deflection plot (left) and plot of ultimate load versus strut inclination (right): Series SI

Shaft Diameter (Series SD)

It can be observed from Figure 7.26 that greater shaft diameter resulted in greater ultimate load; however, no sign of linear relationship with either shaft diameter or shaft area was found.

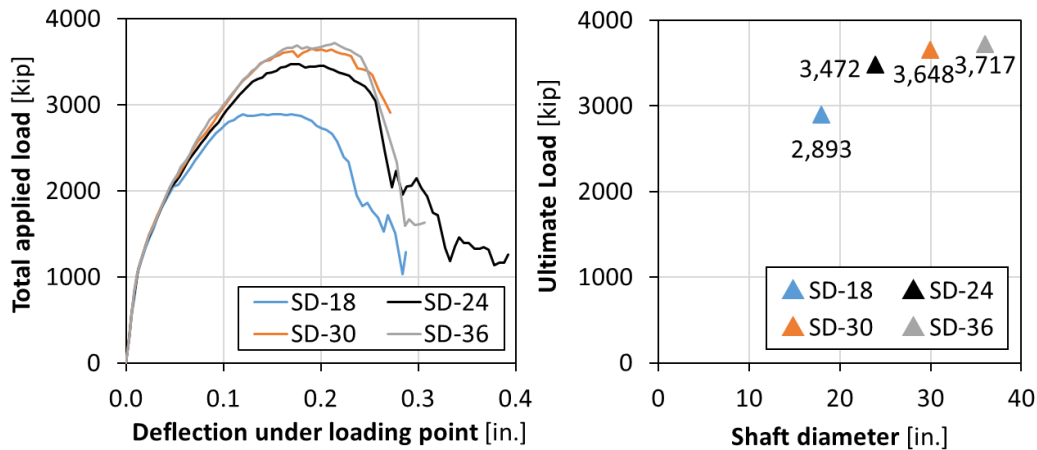


Figure 7.26 Load-deflection plot (left) and plot of ultimate load versus shaft diameter (right): Series SD

Footing Height (Series FH)

There was no clear sign of the impact of footing height (size) since the structural behavior and the ultimate load did not show a trend with footing height, as shown in Figure 7.27.

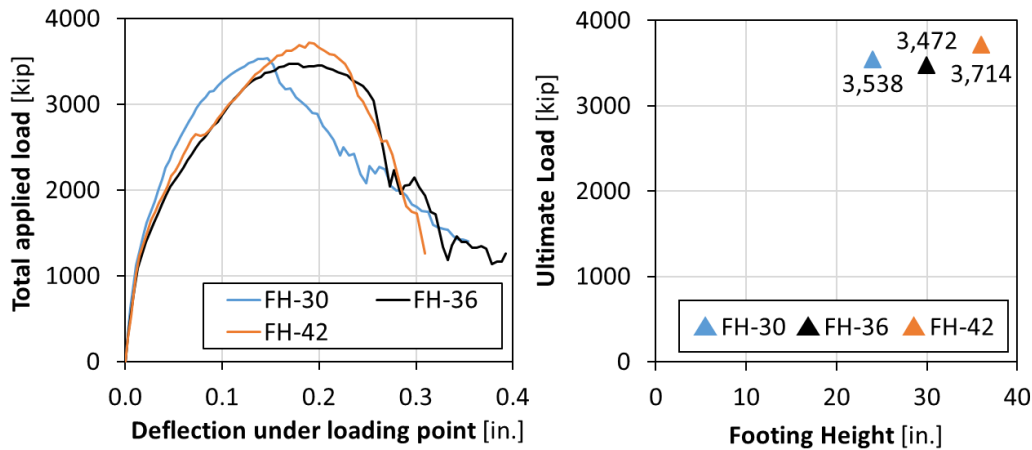


Figure 7.27 Load-deflection plot (left) and plot of ultimate load versus footing height (right): Series FH

7.3.4. Summary and Discussion

The research team developed the FE models of Phase I based on the validated FE model strategy as introduced in Section 7.2. These validated FE models of Phase I successfully predicted the ultimate loads and crack patterns. Computed load-deflection responses under low- and high-levels of loading conditions (less than 1,000 kips and greater than 2,000 kips) were estimated accurately, but the estimates were slightly less accurate for mid-level loading states (between 1,000 and 2,000 kips). FE models of II-5 and II-6 with steeper strut inclination provided less successful load-deflection responses.

Numerical parametric analysis was performed to examine different design characteristics that the experimental program could not cover and as a supplement to the experimental result. The FE model for the numerical parametric study was designed to represent the existing footing of TxDOT as determined in TM3. The observations and findings for each series are summarized as follows:

- Aspect ratios of footing and column did not affect the ultimate loads. Therefore, it is concluded that the experimental specimen can represent the structural behavior of existing footings in Texas even though the aspect ratios of the test specimens had a little discrepancy with actual practice.
- The parametric analysis of the compressive strength of concrete led to the fact that splitting of the strut was a major controlling failure mechanism.
- The ultimate loads, the load-deflection responses, and the trend of the ultimate load depending on strut inclination were consistent with the conclusion of the experimental results.
- It was observed that the existence of top mat and side face reinforcement resulted in greater ultimate load; however, the specific amounts of top and side face reinforcement did not affect the computed ultimate capacity. If the top mat and side face reinforcement was not provided, the numerical ultimate capacity was significantly lower.
- The shaft diameter and footing height did not practically affect the predicted ultimate load.

7.4. Phase II Testing: Non-uniform Compression in Shafts

7.4.1. Finite Element Model

Figure 7.28 presents the 3D FE mesh for the Phase II test specimens. Similar to the experimental program of Phase II, the FE model consisted of a footing component and a column corbel component and applied the uniaxial bending moment at the column-footing interface with eccentric loading. As in the Phase I FE models, eight-noded hexahedral solid concrete elements and truss elements with two nodes for reinforcement were employed to model both Phase II specimens and footing specimens for the numerical parametric study. To accurately model the different types of anchorages tested in Phase II, the region surrounding the column truss elements was modeled with fine meshes. Still, a typical element size of 2.0 in. was also applied in all the other regions of the specimens based on the FE model assessment of Section 7.2.

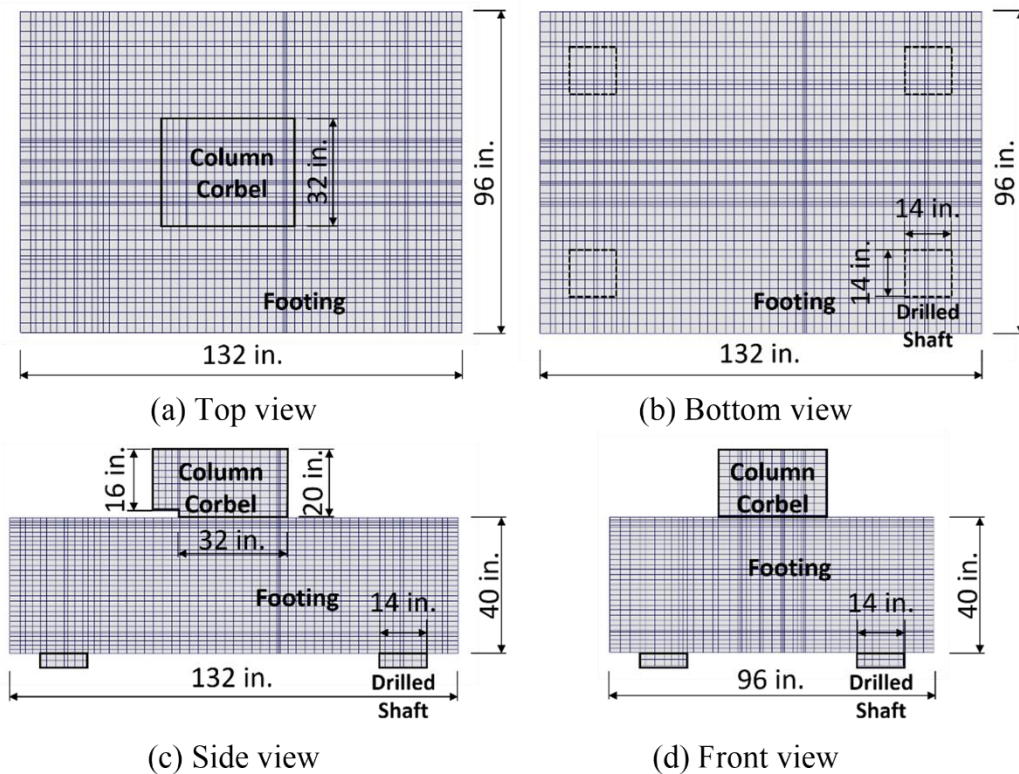


Figure 7.28 FE mesh for Phase II testing

The research team defined three concrete types for modeling the footing, the column corbel, and the auxiliary components — supports representing the drilled shaft. The measured compressive strength of concrete was used to define the concrete model for validating the FE model of each test specimen. Since the column corbel of the experimental program was confined with 0.5-in. thickness steel plates,

the column corbel of the FE model used high-strength concrete (120 ksi) in both compression and tension with the modulus of elasticity of the concrete (5,700 ksi) computed from the concrete strength of the column corbel (10 ksi) to simulate the highly-confined column corbel of the test specimen and preclude any premature failures at the column corbel. Both longitudinal and transverse side reinforcement confining the column corbel was modeled as smeared reinforcement (0.30% in both directions), employing the same concrete type used for modeling the column corbel. The concrete for the auxiliary component was assumed to be extremely high strength concrete on the basis of the same methodology as Phase I FE models, as introduced in Section 7.3.1.

All reinforcing bars of the footing and horizontal reinforcing bars placed at the top of the column corbel were modeled with truss elements connected by nodes that are also connected to adjacent concrete elements, as shown in Figure 7.29. Link elements were employed to simulate the bond-slip behavior of the vertical column reinforcing bars embedded into the footing to examine the anchorage behavior with the FE models.

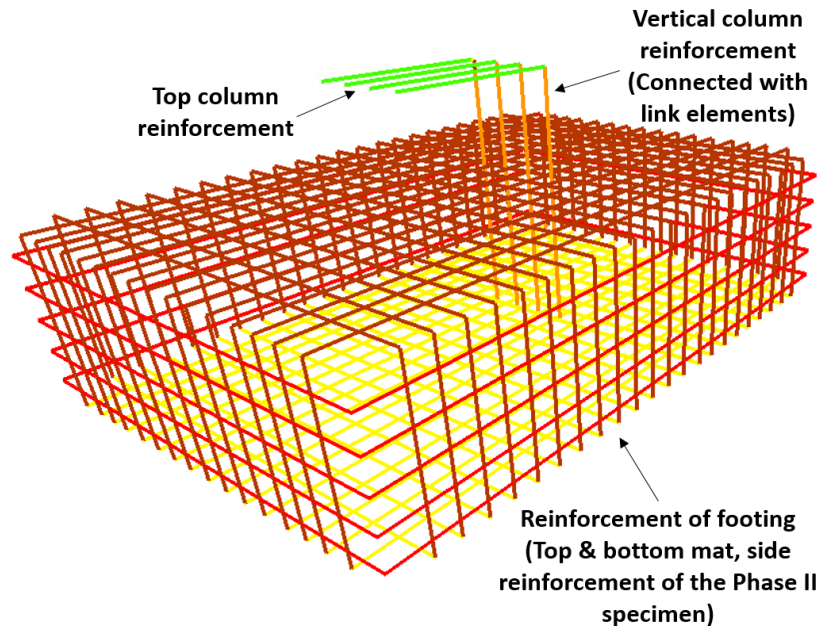


Figure 7.29 Truss elements for reinforcement in FE models for Phase II testing

The link element is a non-dimensional element consisting of two nodes sharing the same coordinate (Ngo and Scordelis, 1967). One node (node i in Figure 7.30) must be linked to a concrete element, and the other node (node j in Figure 7.30) must be linked to a truss element. As shown in Figure 7.30, the link element can be visualized with two orthogonal springs linking those two nodes (node i and j in Figure 7.30). One spring deforms tangentially to the truss element, representing the bond-slip behavior of the reinforcement. The other spring deforms radially to the

truss element, representing the radial displacements and stresses. The bond-slip model of Eligehausen et al. (1983) was implemented on the link elements to permit the bond-slip behavior of the column reinforcement.

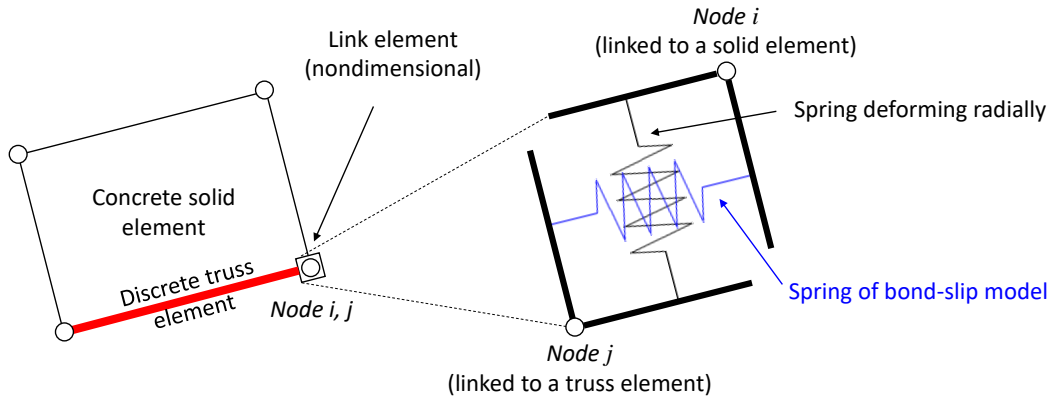


Figure 7.30 Link element

The column reinforcement of the FE models for Phase II test specimens was modeled using link elements. Each anchorage type was modeled differently according to the corresponding detailing and force-resisting mechanism, as illustrated in Figure 7.31. The straight bar anchorage was solely modeled with the discrete truss elements with link elements since the stress of a straight bar is developed through surficial bond stress only. However, the headed bar and hooked bar are developed with both bond stresses and the bearing action stemming from the head and the hook. Therefore, the truss elements were locally modeled at the head and hook regions without link elements to exclude the slip and the anchorage devices were modeled separately.

To model the head, the material properties of the steel used for modeling the column corbel were applied to the solid elements surrounding the truss elements. The size of the head was determined to be equivalent to the dimension of the nVent LENTON Terminator used in the experimental program. The bend radius and the tail of the hook were modeled with truss elements linked with general nodes. Since VecTor4 does not allow modeling curved truss elements, the bend radius was subdivided into two straight truss elements.

Figure 7.32 shows the boundary condition of the developed FE model for Phase II specimens. Using the same boundary condition planned for the experimental program, four modeled bearing parts were supported by a pinned support at the center of one corner bearing pad, two one-way pin-roller supports at the center of the bearing pads adjacent to that of the pinned support, and a two-way pin-roller support at the center of the bearing pad opposite to that of the pinned support.

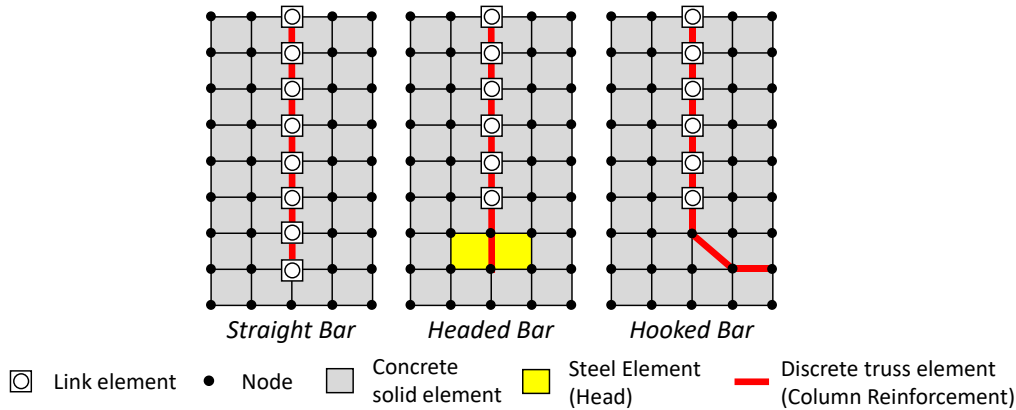


Figure 7.31 Modeling strategy for anchorage types tested in Phase II

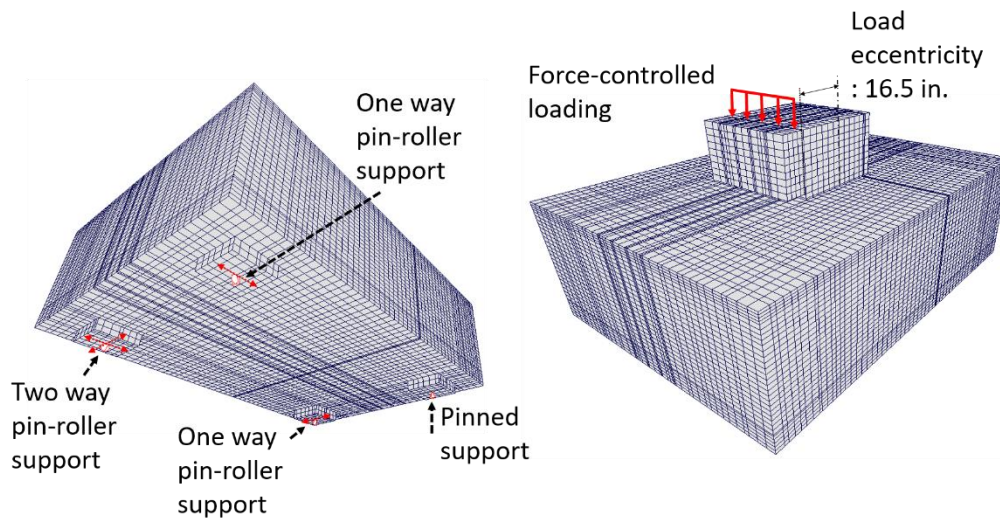


Figure 7.32 Boundary and loading conditions in FE models for Phase II testing

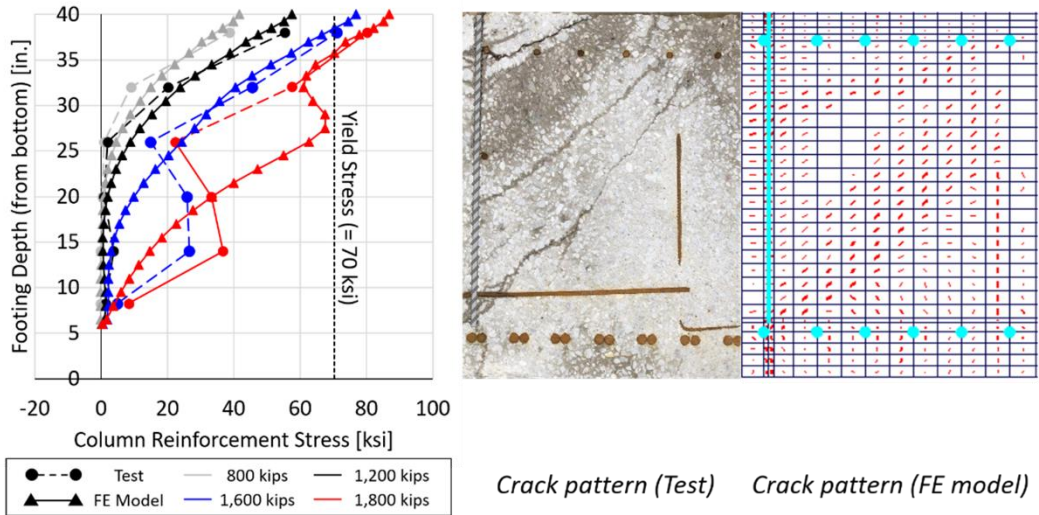
The loads were applied to the top of the column corbel at the nodes positioned on the axis of the same load eccentricity (16.5 in.) used in the experimental program. The self-weight of a footing specimen and long-term effects such as creep or shrinkage were not considered in the analyses due to the limit of accurate measuring reference.

7.4.2. Results and Validation with Experimental Data

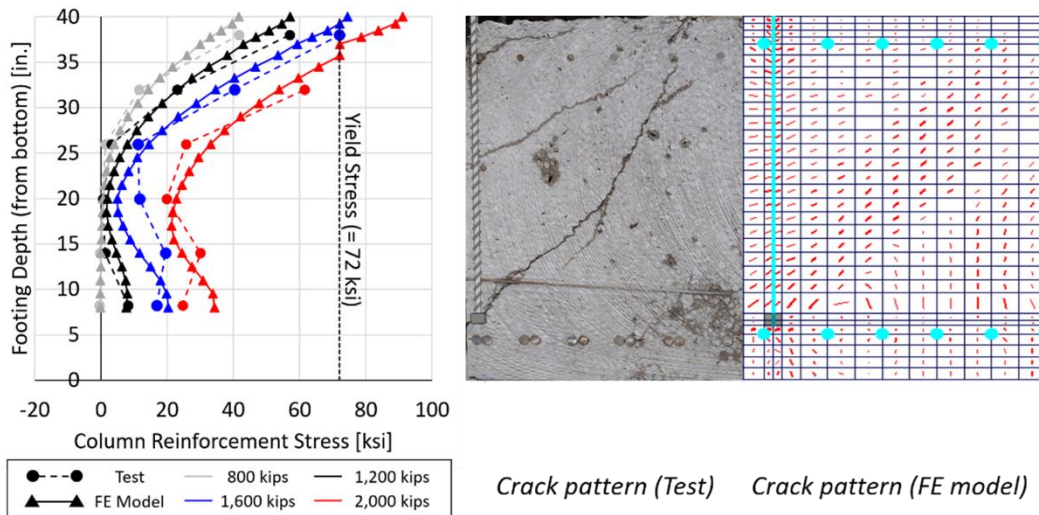
7.4.2.1. Column Reinforcement Stress Profile and Crack Patterns

To study the response of the anchorages, the stress profiles of the column bars along their anchorage were examined. The stress profiles of the column reinforcement obtained from each Phase II test specimen were compared with those obtained from the respective FE model. In addition, the crack patterns obtained at a vertical section near the anchorage were compared. The stress profile of each test specimen and

corresponding FE model was compared to each other at load steps from 800 kips to 2,000 kips with 200-kip intervals depending on the anchorage types as shown in Figure 7.33. All developed FE models were able to be converged until 2,000 kips loading, except for that of the straight column reinforcement, which ultimately converged at 1,800 kips loading.

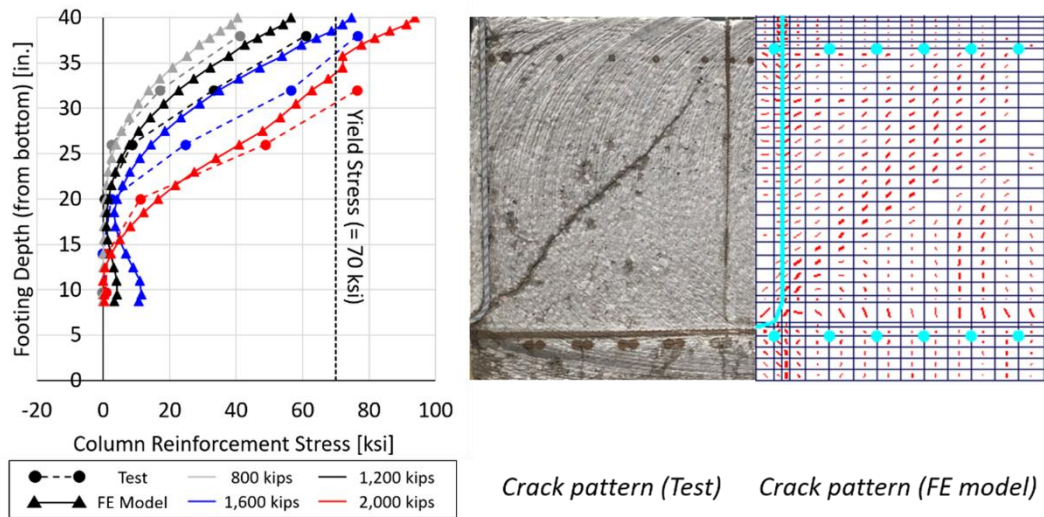


(a) FE model validation (Specimen VI-ST)

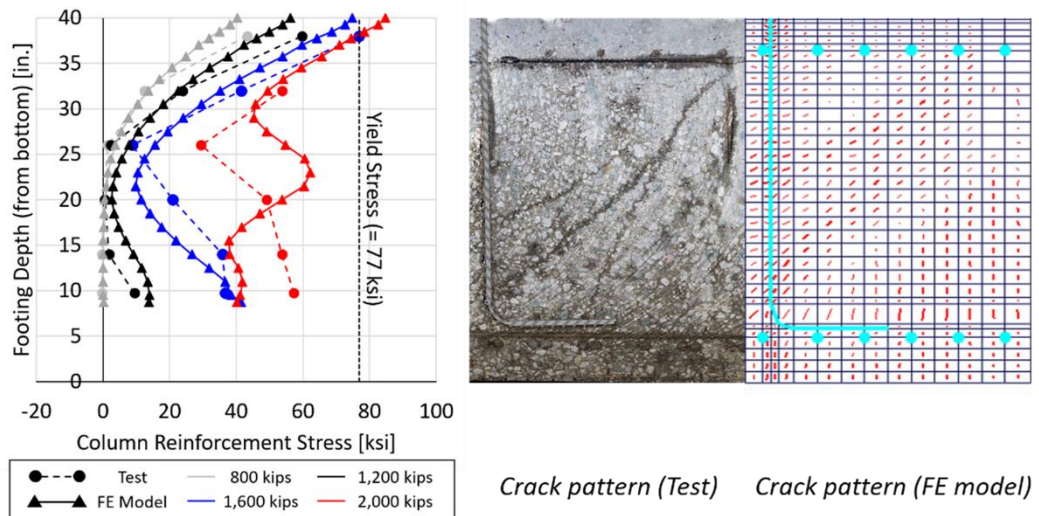


(b) FE model validation (Specimen VI-HD)

Figure 7.33 FE model validation with stress profiles (Phase II)



(c) FE model validation (Specimen VI-HKO)



(d) FE model validation (Specimen VI-HKI)

Figure 7.33 (cont'd) FE model validation with stress profiles (Phase II)

Since the column reinforcement of all Phase II test specimens yielded at around 1,400 kips loading, the selected set of load steps is appropriate for validating both pre-yielding and post-yielding behavior of the FE models having different column reinforcement anchorages.

The experimental and numerical stress distributions are in general consistent, which indicates that the development of the bars by bond is well captured by the model. However, the stress variations at the mid-height of the straight column reinforcement cannot be predicted accurately by the FE model since the stress increment is caused by the internal crack due to the diagonal strut, the location of which is not well captured by the model. Furthermore, the stresses developed right

above the inner-oriented hook and the head at the load level when the column reinforcement of the FE models experienced yielding (1,600 kips) were 41 ksi (53% of the yield stress) and 20 ksi (28% of the yield stress) in the tests, respectively. Alike, the stresses predicted in the FE models were 37 ksi (48% of the yield stress) and 17 ksi (24% of the yield stress), respectively. In conclusion, the anchorage response of all three types of anchorages is predicted with reasonable accuracy.

7.4.3. Numerical Parametric Study

7.4.3.1. Overview

The research team tested large-scale drilled shaft footings with different column anchorages and examined the behavior of the column reinforcement in Phase II testing (Chapter 5) to propose the critical section of the column reinforcement for establishing the anchorage requirements of the 3D strut-and-tie modeling guidelines. However, the experimental program was planned with a single test parameter; the anchorage type of the column reinforcement; therefore, additional design parameters that can affect the critical section of the column reinforcement were investigated for the numerical parametric study in this section. After that, a series of FE models were developed based on the modeling strategy validated in the previous section. The numerical parametric study conducted with the additional design parameters can solidify the validity of the proposed critical section.

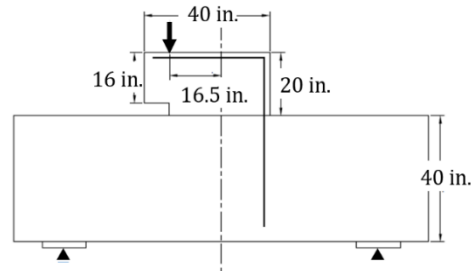
7.4.3.2. Modeling

The proposed critical section of the column reinforcement is defined at the intersecting point of the diagonal strut and the vertical tie on the side view. The validated FE model of the straight column reinforcement (i.e., modeled for VI-ST) was determined as a control model for the numerical study, and the FE models for the numerical parametric study were modeled with the same material properties as those used for developing the control FE model to investigate the effect of design parameters on the anchorage response. The same modeling strategy described in Section 7.4.1 was employed to develop the FE models of the numerical parametric study.

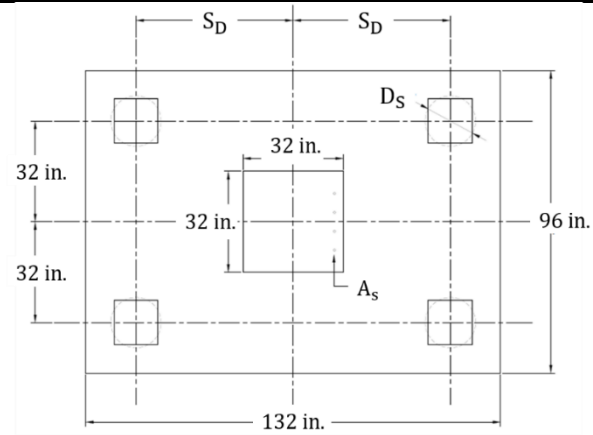
7.4.3.3. Studied Parameters

Three design parameters were selected, and three models per each design parameter were planned for the numerical parametric study, as tabulated in Table 7.6. The design parameters were assumed as factors that can influence the behavior of the column reinforcement or cracking position due to the diagonal strut as follows.

Table 7.6 Analysis matrix of the numerical parametric study (Phase II)



*Column reinforcement was modeled with straight anchorage



Category	Model ID	# of column reinforcement (Total area: 2.40 in. ²)			Drilled Shaft Pitch (S_D) [in.]			Drilled Shaft Diameter (D_S) [in.]		
		9 Bars (ϕ 0.583 in.)	4 Bars (#7) (ϕ 0.875 in.)	2 Bars (ϕ 1.236 in.)	36	42	50	16	20	24
Column Reinforcement Size	<u>COL-9R</u>									
	<u>COL-4R</u>									
	<u>COL-2R</u>									
Drilled Shaft Pitch	<u>DSP-36</u>									
	<u>DSP-42</u>									
	<u>DSP-50</u>									
Drilled Shaft Diameter	<u>DSD-16</u>									
	<u>DSD-20</u>									
	<u>DSD-24</u>									

Note: Underline (Control model)

The size of the column reinforcing bars used in the experimental program was No. 7 selected based on the dimension of the footings identified from the TxDOT drilled shaft footing database in Chapter 3. Maintaining the total area of the column reinforcement (four – No.7; \emptyset 0.875 in. @6 in.; 2.40 in.²) of the control FE model, two FE models were additionally planned by increasing (nine bars - \emptyset 0.583 in. @3 in.) or decreasing (two bars - \emptyset 1.236 in. @18 in.) the column reinforcement. The diameter of the reinforcement was computed to be the equivalent reinforcement area based on the number of bars. The models were compared to each other and to the control model to investigate the effect of reinforcing bar size on the behavior of the column reinforcement.

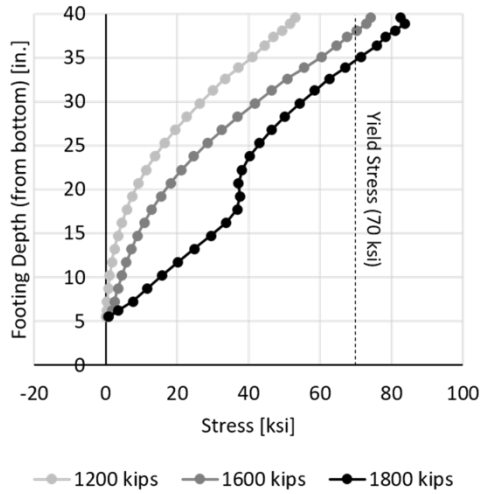
The drilled shaft pitch is directly related to the configuration of the strut-and-tie model; it also affects the cracking position due to the diagonal strut. This fact was proved experimentally from Series II specimens in Phase I testing (Chapter 4). Therefore, the research team analyzed two FE models developed with shorter drilled shaft pitches and investigated the results to elucidate the effect of the drilled shaft pitch on the proposed critical section of the column reinforcement. Furthermore, the reinforcement positioned near the centerline of the column could less be influenced by the assumed large compression field used for defining the critical section than the reinforcement positioned at corners of the column. This assumption could be verified by comparing the column reinforcement stress profiles placed at the same position between the FE models having different drilled shaft pitches.

Lastly, the research team studied the effect of the drilled shaft diameter on the behavior of the column reinforcement. The stress intensity of the assumed compression field decreases as the drilled shaft diameter increases. Therefore, two FE models with larger drilled shaft diameters than the control model were planned to investigate their effect on the stress profile of the column reinforcement.

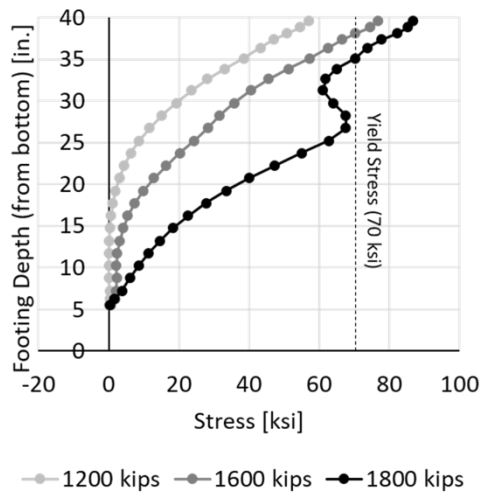
7.4.3.4. Results

- Column Reinforcement Size (Series COL)

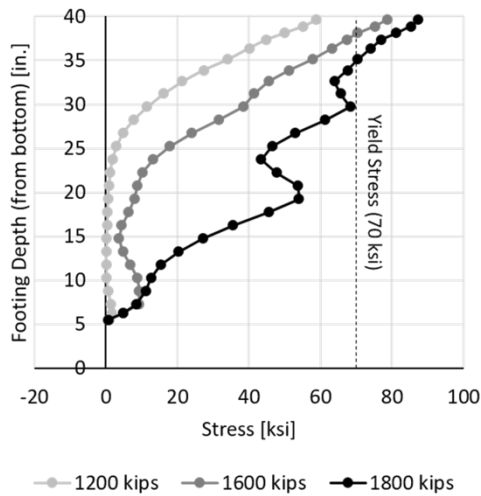
The stress profiles of each FE model at 1,200 kips, 1,600 kips, and 1,800 kips are presented in Figure 7.34.



(a) COL-2R



(b) COL-4R



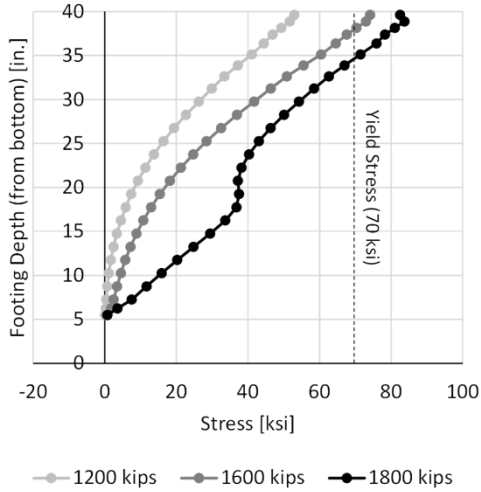
(c) COL-9R

Figure 7.34 Stress profiles of FE models (COL Series – Phase II)

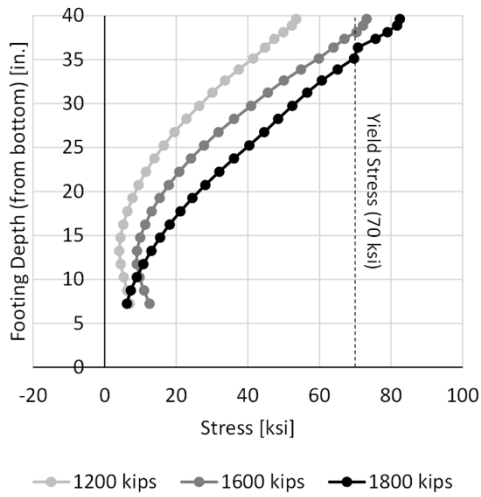
The stress profiles of the FE model developed with nine reinforcing bars (\emptyset 0.583 in.) were most influenced by the diagonal cracks among the FE models in the same series. The behavior is induced by a wider tensile stress field formed by widespread column reinforcement than that of the other FE models. In contrast, the stress increment due to the diagonal crack was delayed in the FE model developed with only two reinforcing bars (\emptyset 1.236 in.) at the column corners.

As the column reinforcement size increased, the bond stress level near the anchorage also increased. Furthermore, the use of large-diameter column reinforcement resulted in a large and almost uniform bond stress near the anchorage indicating the reinforcement is close to the onset of significant slip along the entire anchorage, which would eventually lead to a bar pullout. Therefore, the research team modified the FE model of the large diameter straight column reinforcement (COL-2R) to hooked anchorage (COL-2R(HK)). The tail of the hook is oriented inward to the column to activate the bearing action of the hook. As shown in Figure 7.35, the truss element right above the hook developed 13 ksi (19% of the yield stress) at the analysis step when the stress of the column reinforcement first exceeded the yield stress. Furthermore, the bond stress near the bottom tip of the large diameter column reinforcement decreased by modifying the anchorage from straight to hooked.

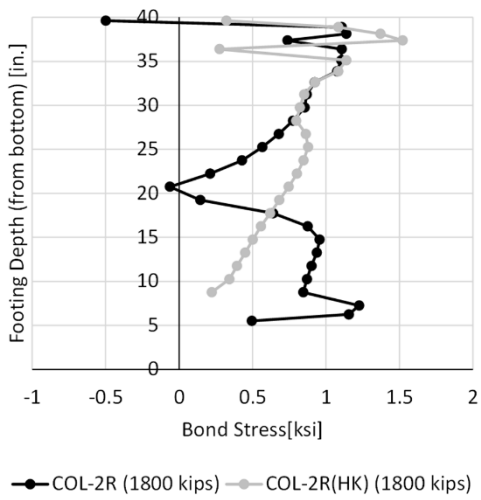
The available development length determined based on the proposed critical section is displayed on the stress profiles with the required minimum development length for each size of the reinforcement modeled computed based on AASHTO LRFD (2020), as shown in Figure 7.36. The conservativeness of the proposed critical section can be confirmed from the plots.



(a) COL-2R

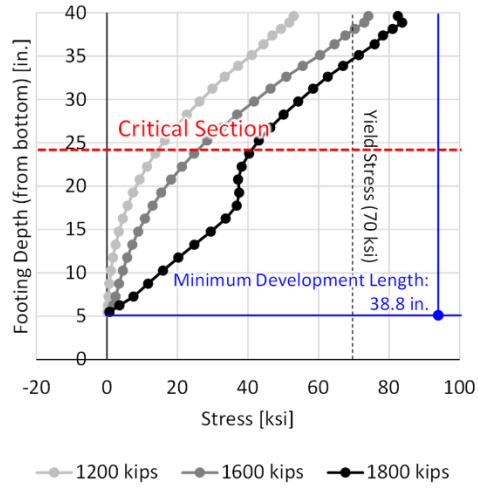


(b) COL-2R(HK)

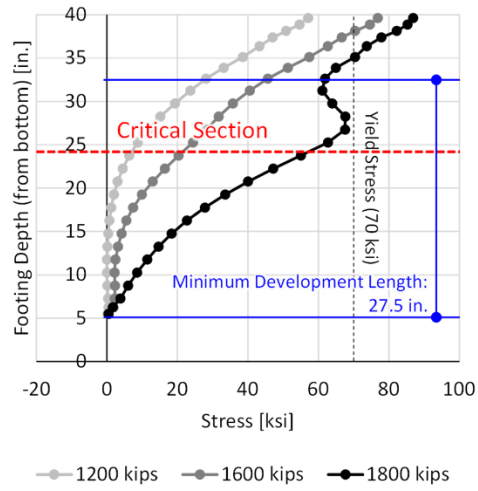


(c) COL-2R vs. COL-2R(HK)

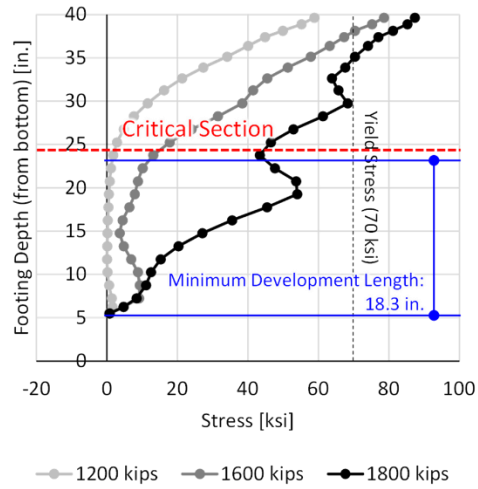
Figure 7.35 Behavior of COL-2R modeled with hooked anchorage (COL-2R(HK))



(a) COL-2R



(b) COL-4R



(c) COL-9R

Figure 7.36 Assumed critical section compared with required development lengths (COL Series – Phase II)

- Drilled Shaft Pitch (Series DSP)

Since the drilled shaft pitch is directly related to the capacity of the footing, the FE models developed with shorter drilled shaft pitches (DSP-42 and DSP-36) than the control model (DSP-50) were able to converge at higher loads than 1,800 kips. The analyses of DSP-42 and DSP-36 could converge until 2,000 kips loading and 2,200 kips loading, respectively. Therefore, the research team compared the stress profiles of the FE models in this series at the same load of 1,800 kips. Additionally, the stress profiles of the FE models at the load level of the last analysis step of each model were compared to investigate the effect of the drilled shaft pitch on the stress profile, as shown in Figure 7.37.

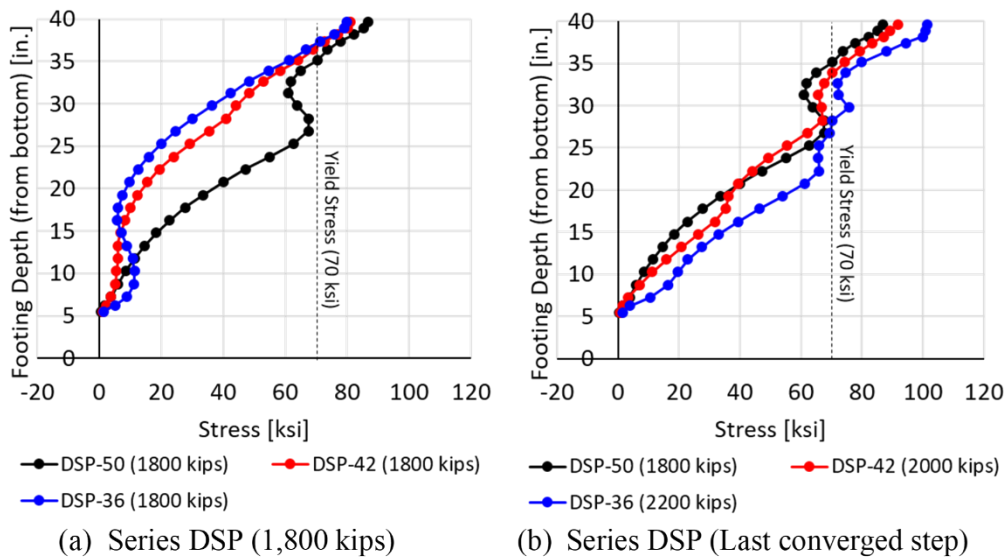


Figure 7.37 Stress profiles of FE models (Series DSP – Phase II)

As the drilled shaft pitch decreased, the bottom tip of the column reinforcement was influenced more by the diagonal strut flowing down to the drilled shaft; therefore, the bottom end of the column reinforcement experienced a relatively high-stress level in the FE model of the shortest drilled shaft pitch (DSP-36) than the other FE models. By comparing the stress profiles of DSP-42 and DSP-36 at 1,800 kips to those at respective maximum load, the research team was able to identify that the stress profile near the bottom end of the column reinforcement developed almost tangentially to the stress increase at the bottom end. As a result, the shorter drilled shaft made the column reinforcement stress profile shift downward; therefore, the available development length decreased when a footing is designed with a shorter drilled shaft pitch. The trend can be easily recognized when the proposed critical section for each FE model is displayed on the same plot, as shown in Figure 7.38.

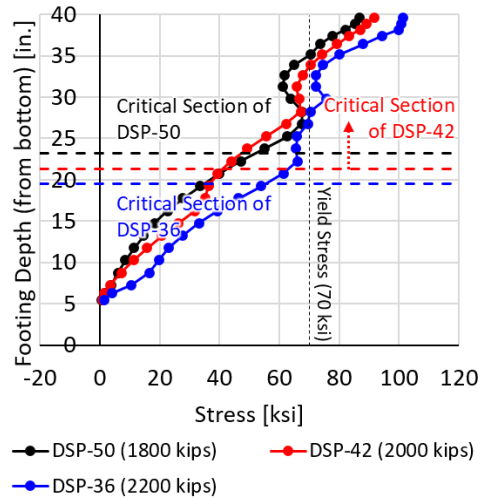


Figure 7.38 Stress profiles of FE models with critical sections (Series DSP – Phase II)

- Drilled Shaft Diameter (Series DSD)

The drilled shaft diameter affects the strut width of the diagonal strut that influences the drilled shaft profile. As shown in Figure 7.39, the stress profiles of the FE models at the same load level of 1,800 kips were compared to verify the effect of this parameter on the stress profile of the column reinforcement.

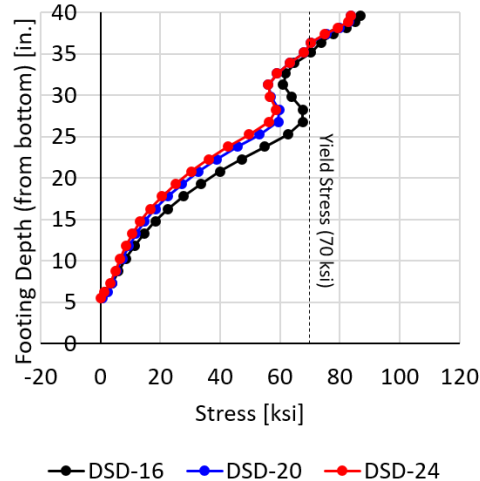


Figure 7.39 Stress profiles of FE models (DSD Series – Phase II)

The overall shapes of the stress profiles were comparable regardless of the drilled shaft diameter; however, a little difference in the stress increment induced by the diagonal crack was able to be confirmed. Since the strut force passing through wider strut width results in smaller tensile stress acting perpendicular to the axis of the strut, the large drilled shaft diameter made the stress increment induced by the diagonal crack decrease.

7.4.4. Summary and Discussion

The research team developed the FE models of Phase II test specimens with various anchorage types. Different modeling strategies were employed to develop each type of anchorage depending on the behavior of the anchorages observed in the experimental program. The validation of the FE models was verified through both stress profiles and bond stress profiles obtained from the tests.

Based on the validated FE model of the straight column reinforcement, the numerical parametric analysis was conducted to supplement the assumption of the critical section proposed for the anchorage requirement of the column reinforcement by analyzing FE models designed with several design parameters. The observations and findings made for each series are summarized as follows:

- The large diameter column reinforcement resulted in high and almost uniform bond stress distribution near the anchorage region. The bond stress level could be decreased by employing the inner-oriented hooked reinforcement.
- The widespread of column reinforcement formed a wider tensile stress field within the footing vicinity of the column reinforcement, and the column reinforcement was more likely to be influenced by the diagonal cracks than the use of fewer column reinforcing bars placed farther apart.
- The decreased drilled shaft pitch increased the stress increment level near the bottom end of the column reinforcement. The stress profile of the lower part of the column reinforcement was developed tangentially to the stress profile of the bottom end; therefore, the shorter drilled shaft pitch made the column reinforcement stress profile shift downward.
- The overall shape of the stress profile was not affected by the drilled shaft diameter. Instead, the stress increment level induced by the crack of the diagonal strut was influenced by the drilled shaft diameter since the larger drilled shaft diameter results in the smaller tensile stress acting perpendicular to the axis of the diagonal strut.
- The proposed critical section for the anchorage requirement of the column reinforcement is conservative for all FE models in this study.

7.5. Phase III Testing: Tension-Compression in Shafts

7.5.1. Finite Element Model

The footing loading conditions inducing tension in two of four drilled shafts are generated from a significant uniaxial bending moment with axial compression at the interface. However, the exact loading and boundary conditions are challenging to recreate in large-scale structural testing due to the capacity of the test setup and safety. Therefore, the research team planned and conducted the simplified experimental program in Chapter 6 by idealizing the loading condition for the strut-and-tie model to keep the same configuration vicinity of the end of the drilled shaft tie element as that of the original loading condition. Given the nature of the force flow in the equivalent strut-and-tie model, no experimental data could be collected about the effect of the compressive reactions applied at the other two drilled shafts. Alternatively, the data could be obtained by FE models of full footing specimens that have drilled shafts subjected to the original boundary condition. Furthermore, a numerical parametric study using the models could provide additional insight into the anchorage behavior of the drilled shaft reinforcement comprising the footing.

The FE model validation was performed in two steps. First, an FE model for the Phase III test specimen with straight drilled shaft reinforcement designed for the equivalent loading (equivalent FE model) was developed, and the result obtained from the FE model was compared with the test data. The FE models of headed and hooked drilled shaft reinforcement were not developed in this case since the anchorages were not found to play a role in the experimental program. After that, the analysis result of the validated model was compared with that of an FE model of a footing modeled with four drilled shafts subjected to the original boundary condition (original FE model). The details of each model validated are described as follows.

7.5.1.1. FE Model of Equivalent Loading Condition

Figure 7.40 presents the 3D FE mesh for Phase III test specimens. The FE model consisted of a footing component and four drilled shafts. The concrete elements and the reinforcement were modeled with eight-noded hexahedral solid elements and truss elements connected with two nodes, respectively. Although the large-diameter post-tensioning bars penetrated the test specimen through PVC pipes, they were also considered as truss elements embedded in the footing for the FE model.

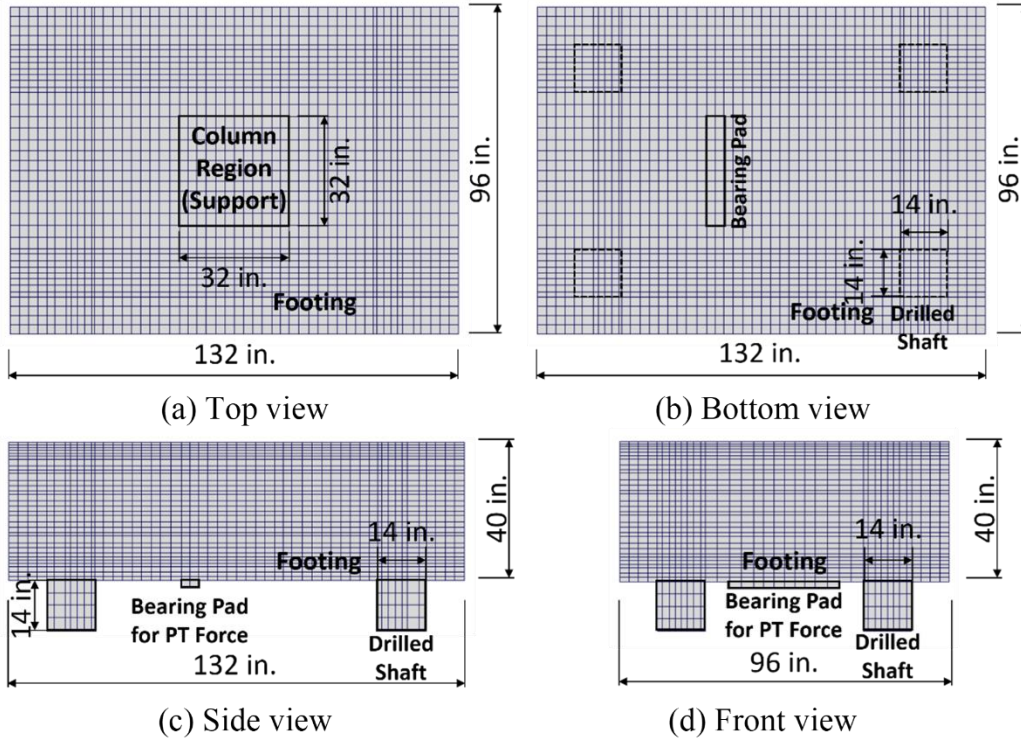


Figure 7.40 FE mesh for Phase III testing (Equivalent loading condition)

Different concrete types were assigned to the footing and the drilled shaft. To validate the model, the measured properties of the materials comprising VII-TK-ST were assigned to the concrete element and truss elements. The drilled shaft was considered as an auxiliary component following the same as Phase I FE modeling methodology, as introduced in Section 7.3.1, in order to remain in elastic and preclude any premature failure at the drilled shaft. The height of the drilled shaft was determined based on the elevation of the MTS actuator measured from the top surface of the footing in the test setup of the experimental program.

Similar to the truss elements for the column in Phase II FE models, the drilled shaft reinforcement of the equivalent FE model was modeled as truss elements connected with link elements to consider the bond-slip behavior of the drilled shaft reinforcement. The same modeling strategy as that established for modeling the straight column reinforcement in Section 7.4.1 was also employed to model the drilled shaft reinforcement. The developed truss elements are shown in Figure 7.41.

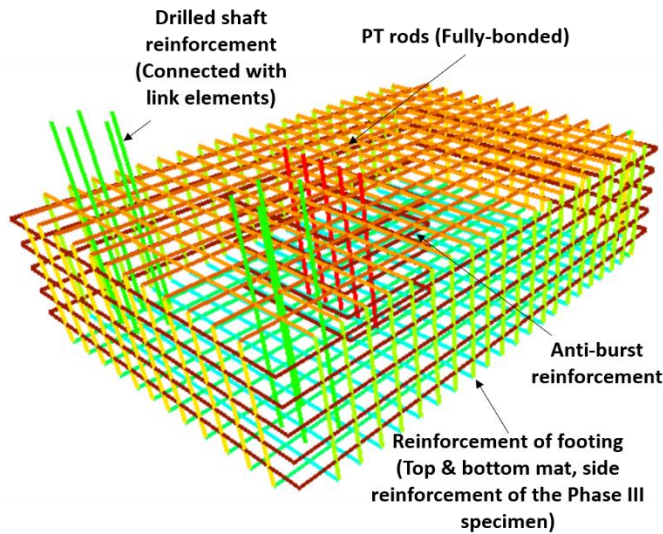


Figure 7.41 Truss elements for reinforcement in FE models for Phase III testing (Equivalent loading condition)

Figure 7.42 illustrates the boundary condition of the equivalent FE model. Vertical and lateral restraints were assigned to all nodes positioned at the region corresponding to the interface in the equivalent FE model. The equivalent FE model was subjected to the external loads at two of four drilled shafts to induce tension in drilled shafts. The load applied at each drilled shaft was controlled to increase by 25 kips per analysis step, with the intent to compare the drilled shaft reinforcement profiles from the analysis with those from the test at the same load level. In addition, the equivalent FE model was subjected to a constant load of 750 kips in compression to simulate the post-tensioning force applied to the test specimen to prevent a slack forming during the testing. The self-weight of a footing specimen and long-term effects such as creep or shrinkage were not considered in the analysis.

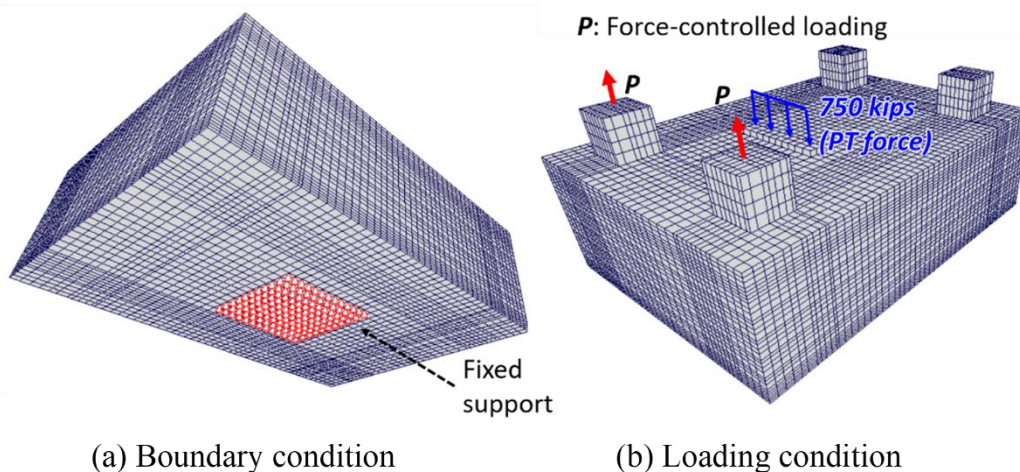


Figure 7.42 Boundary and loading conditions in FE models for Phase III testing (Equivalent loading condition)

7.5.1.2. FE Model of Actual Loading Condition

The FE model subjected to the actual loading conditions was modeled with the same modeling strategy used for the equivalent FE model. Since the reinforcement of the footing for the Phase III specimens was designed based on the equivalent loading, some adjustments were applied for the original FE model. Figure 7.43 presents the 3D mesh for the original FE model.

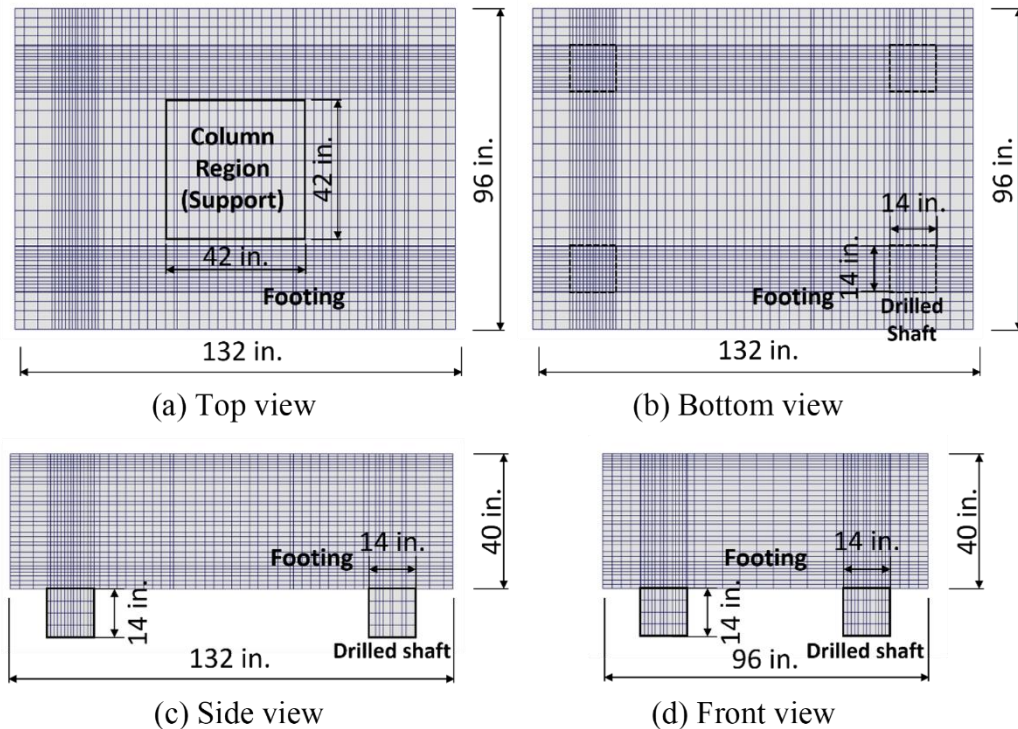


Figure 7.43 FE mesh for Phase III testing (Original loading condition)

First, the area of the column region where the boundary condition was assigned became enlarged to resist a large uniaxial moment. To be specific, the dimension of the interface adjusted from 32 in. square-shaped to 42 in. square-shaped. Furthermore, the post-tensioning load was removed and replaced with a large amount of column reinforcement in the form of straight anchorage (eight bars at 5 in. each [total area: 40in.^2]). The column reinforcement was provided on the tension side of the column with truss elements connected by two link elements sufficient to resist the tension induced by the moment.

Second, the reinforcement details of the footing (bottom mat, top mat, and side reinforcement) were substituted with those of the Phase II footing specimen due to the modified force flow in the footing as compared to the equivalent loading condition for the large-scale testing. The same material properties were assigned to the concrete solid elements and truss elements of the drilled shaft reinforcement as those employed in the equivalent FE model. The design yield strength (60 ksi) was

assigned to the truss elements of the modified reinforcing bars in the footing. The reinforcement cage represented with truss elements is shown in Figure 7.44.

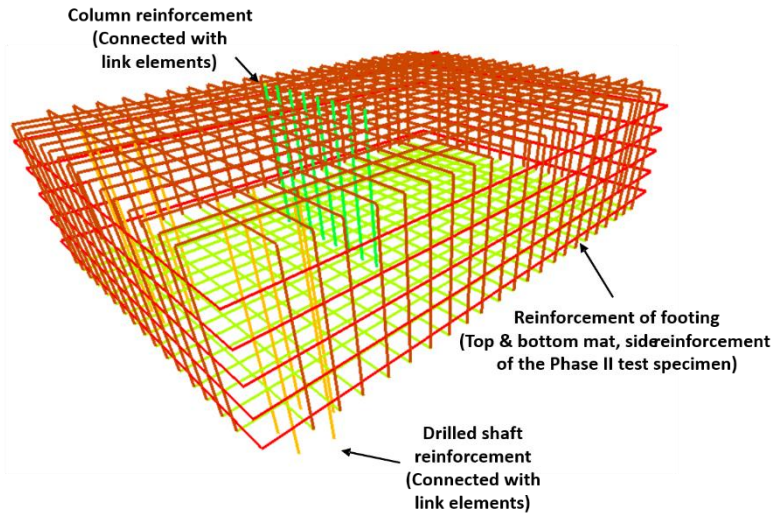


Figure 7.44 Truss elements for reinforcement in the typical footing specimen (Original loading condition)

Lastly, the original loading condition was imposed by applying tension at two drilled shafts and the same load in compression at the other drilled shafts, as shown in Figure 7.45. This loading condition was equivalent to the drilled shaft supported footing subjected to uniaxial bending moment without axial compression at the interface; however, the configuration of the developed strut-and-tie model was not affected by this modification. As with the equivalent FE model, the load applied at each drilled shaft was controlled to increase by 25 kips per each analysis step. The results are presented in terms of the stress profile along the anchorage of the drilled shaft reinforcement and are compared to the results obtained using the equivalent FE model.

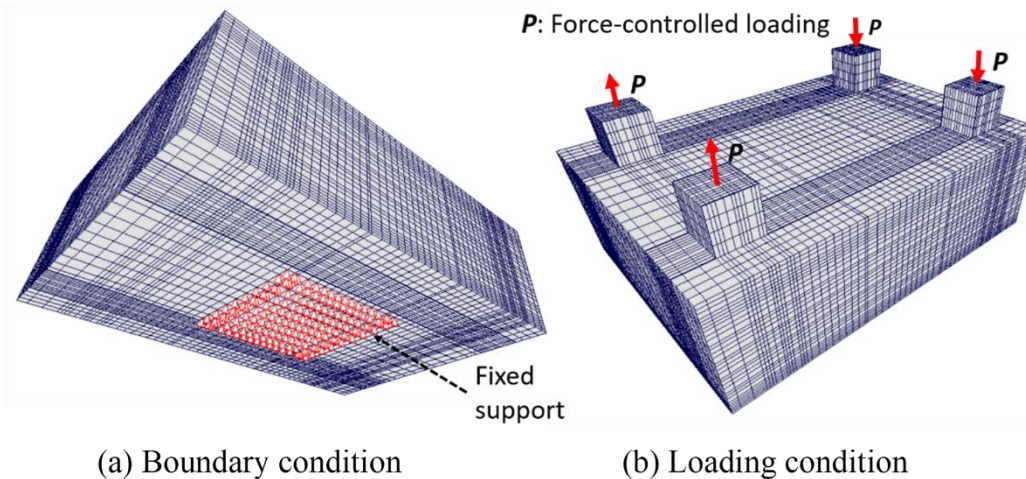


Figure 7.45 Boundary and loading conditions in FE models for Phase III testing (Original loading condition)

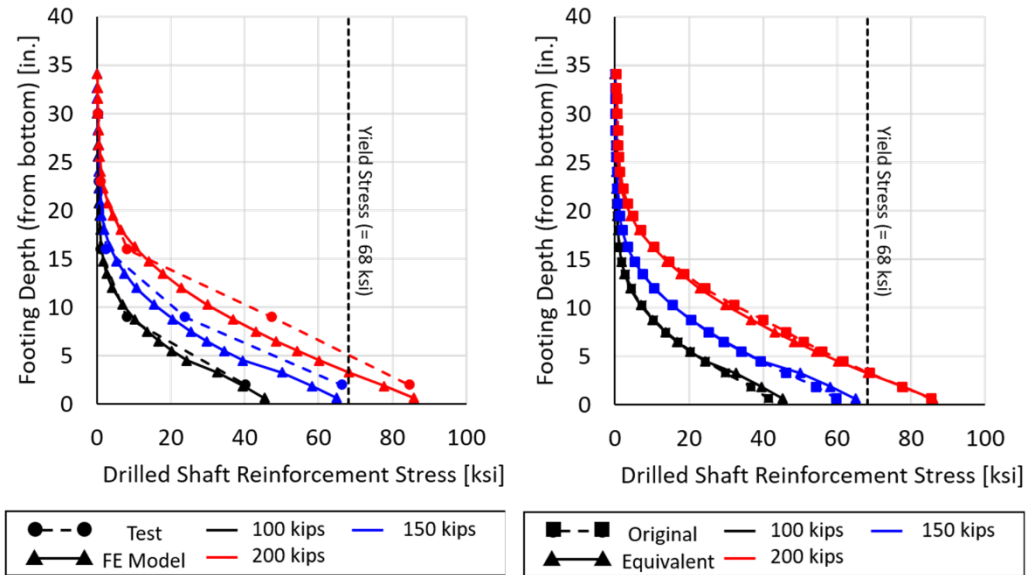
7.5.2. Results and Validation with Experimental Data

7.5.2.1. Drilled Shaft Reinforcement Stress Profile

The stress profiles obtained from the straight drilled shaft reinforcing bars embedded in the Phase III test specimen (Specimen VII-TK-ST) were compared to those analyzed from the equivalent FE model for the first step of the validation. The drilled shaft reinforcing bars could not be subjected to a perfectly uniform load in both the experimental program and the FE model due to the deformation of the footing even though the loading is applied at the center of the drilled shaft. Therefore, the stress profiles of five drilled shaft reinforcing bars—constituting one drilled shaft—were averaged for comparison under the same load level for comparison purposes.

As shown in Figure 7.46-(a), the stress profiles of the test specimen and those of the equivalent FE model were compared at several load steps applied at a single drilled shaft from 100 kips loading to 200 kips loading with 50-kip intervals. All drilled shaft reinforcing bars yielded at around 170 kips loading in testing; therefore, the selected set of load steps is appropriate for validating both pre-yielding and post-yielding behavior of the equivalent FE model. The stress profiles at the same load level are comparable to each other enough to verify the validity of the equivalent FE model.

Similarly, the stress profiles of the original FE model were compared with those of the equivalent FE model already validated, as shown in Figure 7.46-(b). Based on the result, the equivalent loading condition provided similar stress profiles and anchorage responses as the actual loading conditions being studied.



(a) Validation (Test vs. Equivalent FE model) (b) Validation (Equivalent vs. Original FE model)

Figure 7.46 FE model validation with stress profiles (Phase III – Equivalent & Original)

7.5.3. Numerical Parametric Study

7.5.3.1. Overview

The research team examined the behavior of the footing with drilled shaft reinforcement under tension, according to the experimental program planned for the equivalent loading condition. However, the testing was conducted for a single test parameter—anchorage types of the drilled shaft reinforcement—and all drilled shaft reinforcing bars behaved similarly regardless of the anchorage type. The research team proposed the critical section for the drilled shaft reinforcement conservatively based on the stress field defined by the non-contact lap splice behavior between the column and the drilled shaft tie elements. Therefore, some additional design parameters need to be studied through the numerical parametric study to verify the model’s validity.

7.5.3.2. Modeling

The validated original FE model was selected as a control model for the numerical parametric study, and the model was modified for each design parameter. Therefore, the modeling strategy specified in Section 7.5.1.2 was also employed to develop the models for the numerical parametric study.

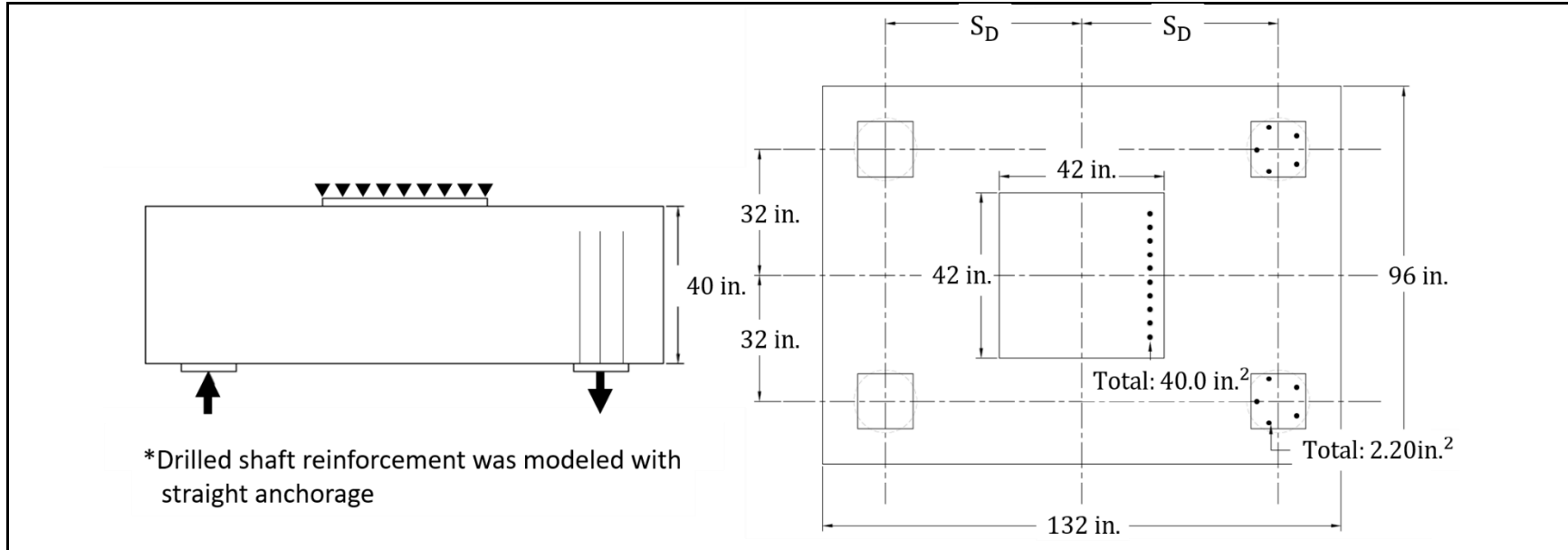
7.5.3.3. Studied Parameters

Two design parameters were selected and two models were developed per design parameter for the numerical parametric study, as tabulated in Table 7.7. The design parameters were assumed as factors that can influence the assumed stress field forming between the column and the drilled shaft tie elements on the basis of the non-contact lap splice behavior.

Similar to the column reinforcement size in Phase II testing, the No. 6 drilled shaft reinforcing bars used in the experimental program were used, selected based on the dimensions of the footings identified in TxDOT drilled shaft footing database in Chapter 3. To verify the conservatism of the proposed critical section of the drilled shaft reinforcement for the anchorage requirement, the total area of the drilled shaft reinforcement of the original FE model was maintained (five No. 6; 2.20 in.² per each drilled shaft), and two FE models were developed by changing the size and number of drilled shaft reinforcement bars constituting each drilled shaft. The FE models were modeled with 3 bars (\varnothing 0.966 in.) and 10 bars (\varnothing 0.529 in.) per drilled shaft, respectively. The diameter of the reinforcement was computed to be the equivalent reinforcement area based on the number of bars. The FE models developed with this design parameter were compared to the control model to investigate the effect of reinforcing bar size on the behavior of the drilled shaft reinforcement.

The assumed critical section is significantly influenced by the drilled shaft pitch since the position of the critical section is determined by the assumed stress field proportional to the drilled shaft pitch. Therefore, the research team planned two FE models developed with shorter drilled shaft pitches. The planned drilled shaft pitches are the same as those employed for the numerical parametric study for Phase II testing. The analysis results were also utilized to examine the conservatism of the suggested critical section of the drilled shaft reinforcement for the anchorage requirement.

Table 7.7 Analysis matrix of the numerical parametric study (Phase III)



Category	Model ID	# of drilled shaft reinforcement per each shaft (Total area: 2.20 in. ²)			Drilled Shaft Pitch (S_D) [in.]		
		3 Bars (Ø 0.966 in.)	5 Bars (#6) (Ø 0.750 in.)	10 Bars (Ø 0.529 in.)	36	42	50
Drilled Shaft Reinforcement Size	<u>DSR-3R</u>						
	<u>DSR-5R</u>						
	<u>DSR-10R</u>						
Drilled Shaft Pitch	<u>DSP-36</u>						
	<u>DSP-42</u>						
	<u>DSP-50</u>						

Note: Underline (Control model)

7.5.3.4. Results

The first conclusion from the analyses is that all drilled shaft reinforcing bars in the different models were able to yield in tension. Further, the stress profiles at several load steps before and after yielding were compared. To eliminate confusion caused by the concentration of stress on one specific bar of the drilled shaft reinforcement group, the stress profiles of the bars corresponding to the same drilled shaft were averaged, allowing investigation of the effect of each design parameter on the drilled shaft reinforcement behavior.

- Drilled Shaft Reinforcement Size (Series DSR)

The averaged stress profiles of the FE models in this series at the same load level before yielding (150 kips applied at each drilled shaft) and after yielding (200 kips applied at each drilled shaft) were compared, as shown in Figure 7.47. When a larger bar size was used, the penetration of tensile stresses into the anchorage region increased. This is consistent with the need for longer development lengths for larger bars. However, the size and number of drilled shaft reinforcement bars did not significantly affect the overall anchorage capacity since the provided anchorage length was sufficient to develop the full capacity of the bars.

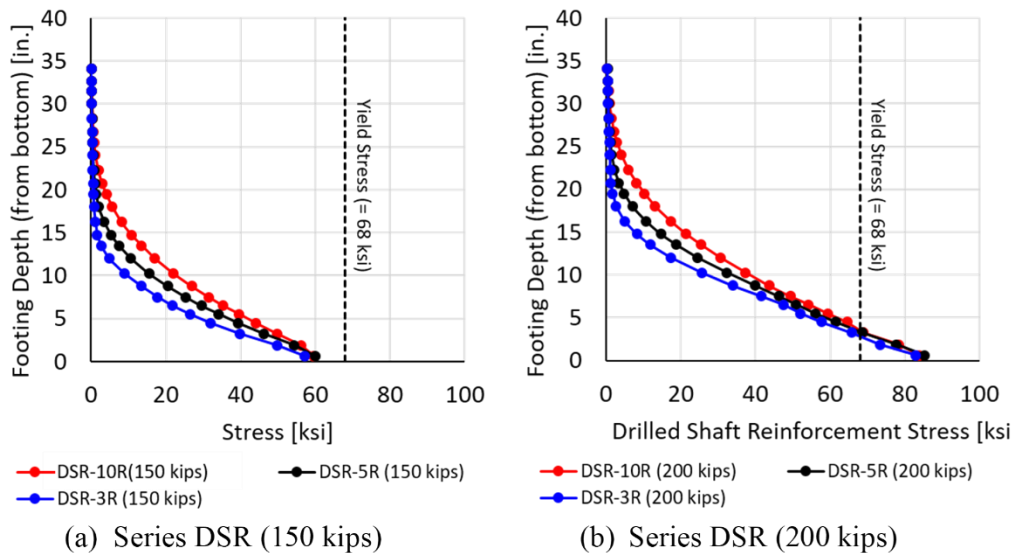


Figure 7.47 Stress profiles of FE models (Series DSR – Phase III)

The available development length determined based on the proposed critical section is displayed on the stress profiles with the required minimum development length for each size of the reinforcement modeled computed based on AASHTO LRFD (2020), as shown in Figure 7.48. The conservativeness of the proposed critical section can be confirmed from the plots.

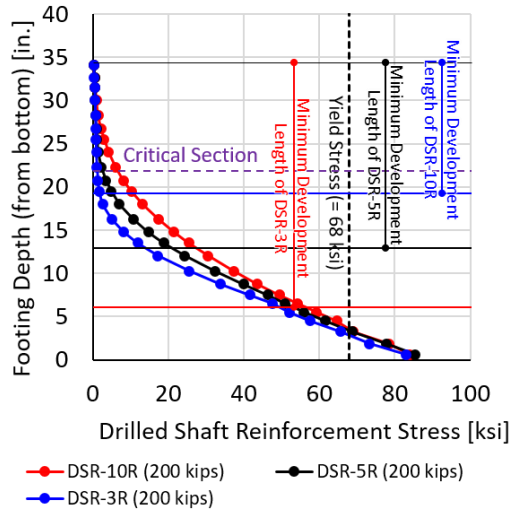


Figure 7.48 Assumed critical section compared with required development lengths (Series DSR – Phase III)

- Drilled Shaft Pitch (Series DSP)

Similarly, the average stress profiles of the FE models in this series were compared at the same load levels of 150 kips and 200 kips. The stress profiles were almost identical to each other regardless of the drilled shaft pitch, as shown in Figure 7.49.

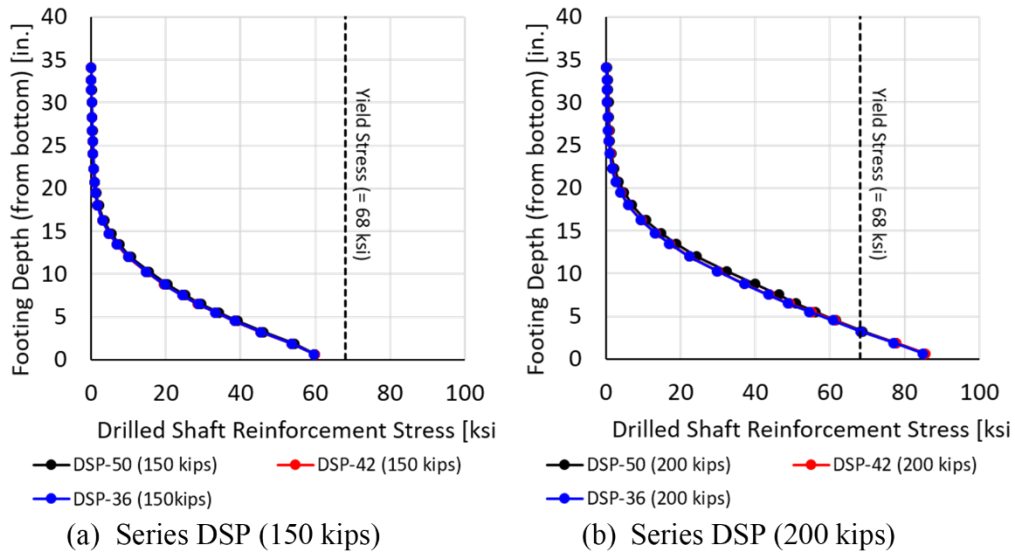


Figure 7.49 Stress profiles of FE models (Series DSP – Phase III)

Figure 7.50 displays the assumed critical sections of the FE models planned in both DSR and DSP series together with the average stress profile of the original FE model at 200 kips loading, which is the load inducing almost 85% of the tensile strength. The yield penetration in the depth of the footing measured from the bottom of the footing is much shallower than the assumed critical sections. It indicates the

conservatism of the proposed critical section of the drilled shaft reinforcement for the anchorage requirement.

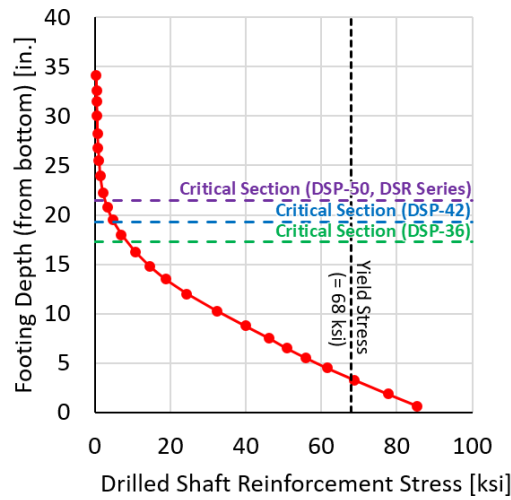


Figure 7.50 Conservativeness of the proposed critical section of the drilled shaft reinforcement

7.5.3.5. Summary and Discussion

The research team developed the FE models of the Phase III test specimen of the straight drilled shaft reinforcement designed for the equivalent loading condition. To validate the model, the drilled shaft reinforcement stress profiles obtained from the testing and the FE model were compared at several load levels. The validated FE model was designed for the equivalent loading condition; the equivalent FE model was taken as the replacement of FE model of the same dimensional footing designed for the original loading condition, which was complicated to recreate in large-scale structural testing. Similarly, the stress profiles of reinforcing bars in a drilled shaft obtained from the FE model were designed for the original loading; the original FE model results were compared to those of the equivalent FE model, which was already validated with the test results.

A numerical parametric study was conducted using the validated FE models to provide supplement data not available through the experimental program. The investigated parameters included the size of drilled shaft reinforcement and drilled shaft pitch. The analytical result reveals that both parameters had little effect on the stress profile in the reinforcing bars in the drilled shaft. Nevertheless, the depth of yield penetration indicated that the proposed critical section in the current study is conservative.

Chapter 8. Development of Strut-and-Tie Modeling Guidelines

8.1. Overview

Design guidelines for drilled shaft footings based on 3D STM are proposed and a design example for a drilled shaft footing are presented using the proposed 3D STM in this chapter. The analysis of experimental results obtained from a series of large-scale footing specimens (Chapter 4 through Chapter 6 of the project) and from experimentally validated finite element models (Chapter 7) elucidated the behavior of drilled shaft footings subjected to three types of uniaxial load combinations. Based on these efforts, the guidelines for using 3D STM in drilled shaft footings were refined, resulting in a more accurate prediction of the ultimate capacity and a consistent level of safety. Using the proposed guidelines, the research team also provides the design example of a drilled shaft footing subjected to a variety of loading conditions.

This chapter is organized as follows: Section 8.2 briefly re-states the current STM provisions and the recommendation for design of drilled shaft footings. The predictions are evaluated with a filtered footing research database. The refined 3D STM guidelines for drilled shaft footings are proposed and examined through comparison with a filtered footing test database in Section 8.3. Section 8.4 presents the design example of a drilled shaft footing subjected to five loading conditions—pure axial compression (load condition studied experimentally in Chapter 4), axial compression with mild uniaxial moment (not studied experimentally), axial compression with moderate uniaxial moment (studied experimentally in Chapter 5), axial compression in combination with severe uniaxial moment (studied experimentally in Chapter 6), and axial compression in combination with mild biaxial moments (not studied experimentally). Finally, the proposed guidelines and their application to the design example are summarized in Section 8.5.

8.2. Current STM Provision for Drilled Shaft Footings

The literature provides several design examples of drilled shaft footings, as described in Chapter 2. The American Concrete Institute's Special Publication, ACI SP-208 (2002), provided several design examples of drilled shaft footings under uniform compression loading for the use of 3D STM in accordance with ACI 318-02 (2002). The STM provision has changed little since first introduced. In ACI SP-208 (2002), Klein (2002) provided examples for a five-pile cap under compressive loading alone—the identical loading condition investigated in Phase I testing (Chapter 4)—and flexure loading, as well as compressive loading over the cross

section of the column, to determine the depth of the column and the amount of the reinforcement. Mitchell et al. (2004) provided a pile cap design example illustrating the use of STM in accordance with past AASHTO LRFD Bridge Design Specifications (AASHTO LRFD) (2004). They defined a 3D bottom nodal geometry that also facilitated the definition of strut geometry and a check on strut strength. Williams et al. (2012) reported two calculation examples of a drilled shaft footing subjected to a combination of axial and flexure loading as part of a comprehensive investigation of STM. To check nodal capacities, a simple bearing stress limit was favored without triaxial confinement effect to add conservatism.

Several assumptions about the strength calculations were identical among the three aforementioned design examples. The first assumption was that only the bottom mat reinforcement in the bandwidth (not all reinforcing bars) contributed to the tie force. When considering the different shapes of drilled shafts, the critical section for anchorage ties was the interior edge of a shaft for a square shaft or the equivalent square area for a circular type. In addition to tie forces, nodal capacities were checked in accordance with the provisions of either ACI or AASHTO LRFD provisions. None of the examples incorporated triaxial confinement effects contrary to 2D structures. With respect to 3D strut-and-tie model for the drilled shaft footing, the loading over the column section was equally divided into four loadings, applied at the center of each quadrant of the column section in all cases. Working with these common assumptions, the studies suggested different approaches to determining the top nodal elevation. In Klein (2002), top nodal elevation was dependent on the strut force and nodal geometries near the top node. Mitchell et al. (2004) employed a distance of 2 in. below the interface. Williams et al. (2012) adopted 0.1 times the height of the footing, which was close to the level of the top mat reinforcement.

In this study, the measured ultimate loads are compared with those predicted from 3D STM equations based on the recommendation by Williams et al. (2012) because it is the most consistent approach with the current STM provision in AASHTO LRFD (2020).

8.2.1. AASHTO LRFD (2020) and Williams et al. (2012)

The 3D STM procedure recommended by Williams et al. (2012) is briefly summarized below and detailed in the following subsections:

- 1) Developing 3D strut-and-tie model
- 2) Proportioning ties
- 3) Performing nodal strength checks
- 4) Proportioning shrinkage and temperature reinforcement
- 5) Providing necessary anchorage for ties

8.2.1.1. 3D Strut-and-Tie Model

To develop 3D strut-and-tie models for several loading cases (as shown in Figure 8.1), the first step is to calculate loads from the column and drilled shaft reactions. Williams et al. (2012) provided 3D strut-and-tie models for the loading cases of axial compression in combination with mild and severe uniaxial moments, which are identical to the loading conditions used in Phase II (Chapter 5) and Phase III (Chapter 6) testing of this research project. The strut-and-tie model for footings subjected to pure axial compression over the column, which correspond to the loading case of Phase I (Chapter 4) testing of the current study, can be straightforwardly developed and confirmed by other studies (Klein, 2002; Mitchel et al., 2004). For the case of pure compression loading only, the load from the column can be divided into four quadrants and assumed to be applied at the center of each quadrant. Four drilled shafts provide equal reactions. If a bending moment is applied in the column and it induces tension at one face of the column, the equivalent force system needs to be developed from the applied axial force and moment under the assumption of an elastic linear stress distribution over the column section. The compressive force is subdivided into two forces, and the forces act at the centroid of the compressive portion of the stress diagram. The positions of tensile resultant forces are determined based on the position of the longitudinal column reinforcement. As a result, the magnitude of the member forces can be determined by equilibrium. The reaction of each drilled shaft is computed by equilibrium as well.

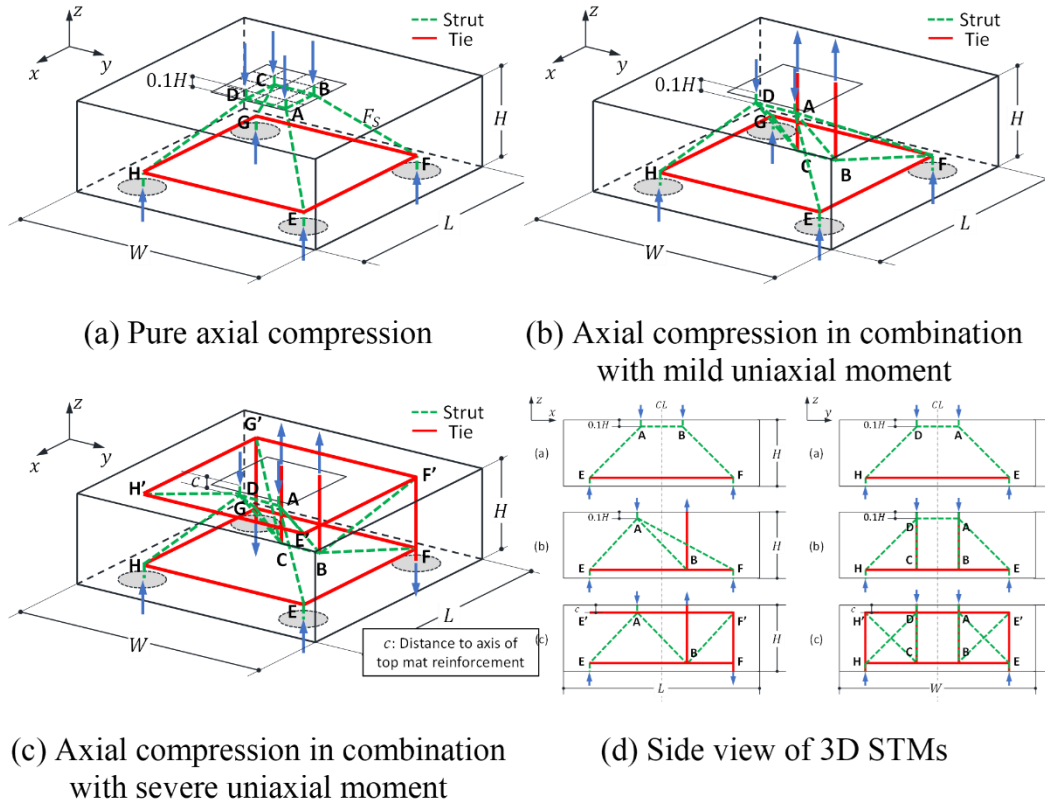


Figure 8.1 Typical 3D strut-and-tie models for loading cases

The basic concepts used to develop STMs for drilled shaft footings are as follows:

- The nodes beneath the column are located 0.1 times the height in z -axis if there is no top tie ring in the 3D STM (Figure 8.1-(a), (b)).
- The position of the four nodes for the top tie ring (Figure 8.1-(c)) is the projection of the center of the drilled shafts at the elevation of top mat reinforcement, and the nodes beneath the column are positioned on the same horizontal plane of the tip tie ring.
- The position of the four nodes above the drilled shafts is the projection of the center of the drilled shafts at the elevation of bottom mat reinforcement.
- Ties on the plane of bottom/top tie ring are placed along the axis of bottom/top mat reinforcement.
- Column ties stretched down to the plane of the bottom tie ring are positioned at the axis of the tensile column reinforcement array.
- A compressive strut is placed to meet the equilibrium condition with applied forces and reaction forces in each axis at each node. The angle of a diagonal

strut with the plane of bottom mat reinforcement and that between a strut and a tie on the same plane shall be between 25 and 65 degrees.

- Tie and strut forces can be computed using statics (method of joints or method of sections).

- *Phase I: Uniform Compression in Shafts*

Figure 8.1 illustrates the 3D strut-and-tie model used for each case considered in this study. The case of uniform compression loading only presents the simplest strut-and-tie model, as shown in Figure 8.1-(a). The nodes beneath the column (Nodes A through D) are located 0.1 times the footing height below the center of each quadrant. The position of the four nodes above the drilled shafts (Nodes E through H) is the center of the drilled shafts at the elevation of tension reinforcement. Bottom horizontal ties that represent the bottom mat reinforcement (Ties EF, FG, GH, and HE) are connected at these four nodes. Diagonal struts (Struts AE, BF, CG, and DH) are developed between nodes below the column and above drilled shafts for each quadrant. A strut ring is needed beneath the column (Struts AB, BC, CD, and DA) to satisfy the requirement of the equilibrium.

- *Phase II: Non-uniform Compression in Shafts*

The STM subjected to the load combination of the axial compression and moderate uniaxial moment is shown in Figure 8.1-(b). As a tensile resultant force is formed on the column section due to bending, vertical tie elements are developed and extend to the plane of the bottom mat reinforcement. Therefore, an additional set of diagonal struts (Struts AB and CD) are formed from the compression side of the column to the end of vertical column ties for equilibrating the tension. Similar to the case of uniform compression loading, a bottom tie ring (Ties EF, FG, GH, and HE) is formed at the axis of the bottom mat reinforcement, and diagonal struts (Struts AE, AF, DH, and DG) are developed between the nodes beneath the column and those at the corners of the bottom tie ring. Additionally, horizontal struts (Struts AD, BC, BF, and CG) are placed on the x-y plane to balance the lateral forces in the STM.

- *Phase III: Compression and Tension in Shafts*

The severe uniaxial moment causing tensile reaction at two of four drilled shafts results in a STM with a complicated configuration, as shown in Figure 8.1-(c). Two vertical tie elements, passing through the center of each drilled shaft, are required at the two drilled shafts exhibiting tensile reaction forces. Diagonal struts (Struts BF' and CG') are formed between the vertical tie elements of the column

reinforcement and the drilled shaft reinforcement to transfer the tension between the two tie elements. This force transfer is equivalent to that of a non-contact lap splice. In addition to the bottom tie ties above the drilled shafts (Ties EF, FG, GH, and HE), a set of top ties (Ties E’F’, F’G’, G’H’, and H’E’) is also needed near the top surface of the footing to carry hoop tensile forces generated by the non-contact lap splice. The compressive resultant forces on the column section flow to the nearest drilled shafts through diagonal struts (Struts AE and DH). Finally, horizontal struts (Struts AD, BC, BF, CG, AE’, and DH’) are developed on the x-y plane to satisfy equilibrium for lateral forces of the STM.

8.2.1.2. Proportioning Ties

As noted in Chapter 3, two types of reinforcement configurations for top and bottom mats are used in current practice. One is a grid layout in which reinforcing bars are distributed uniformly; the other is a banded layout in which bars are concentrated within a bandwidth (Figure 4.2) such that the spreading area is extended by 45 degrees from the edge of the drilled shaft, in accordance with the TxDOT Bridge Design Guide (2020). While banding of reinforcement can meet the concept of STM, a grid layout can result from the conventional sectional design. The survey of constructed footings in Chapter 3 reported that a majority of the footing designs examined on Texas bridges (36 out of 41 total) had a grid layout for the bottom mat. Williams et al. (2012) and other previous researchers suggested a banded layout for their drilled shaft footing design examples. Reinforcing bars in the bandwidth are considered to contribute to tie forces when predicting the ultimate capacity of the tie forces to be consistent with previous design examples. In such a case, the equation of 5.8.2.4.1-1 in AASHTO LRFD (2020) can be updated, as shown in Eq. (8.1):

$$P_{n,tie} = f_y A_{st} \quad \text{Eq. (8.1)}$$

where:

$P_{n,tie}$ = nominal resistance of a tie [kip]

f_y = yield strength of nonprestressed longitudinal reinforcement in the bandwidth [ksi]

A_{st} = total area of nonprestressed longitudinal reinforcement in the bandwidth [in.²]

8.2.1.3. Nodal Strength Checks

The strengths of three node faces—bearing face, back face, and strut-to-node interface—need to be checked with Eq. (8.2) in accordance with AASHTO LRFD (2020).

$$P_{n,n} = f_{cu}A_{cn} \quad \text{Eq. (8.2)}$$

where:

$P_{n,n}$ = nominal resistance of a node face [kip]

f_{cu} = limiting compressive stress at the node face, taken as mvf'_c [ksi]

where:

m = confinement modification factor, taken as $\sqrt{A_2/A_1} \leq 2.0$ as defined in Article 5.6.5

v = concrete efficient factor as shown in Table 5.8.2.5.3a-1

f'_c = compressive strength of concrete for use in design [ksi]

A_{cn} = effective cross-sectional area of the node face as specified in Article 5.8.2.5.2 [in.²]

The equation for checking the nodal strength as provided in Eq. (8.2) is based on 2D structural members, such as deep beams. However, different assumptions and modifications should be applied when evaluating the nodal strength developed in drilled shaft footings, as reported in Chapter 2. First, nodal strength checks are performed at bearing faces only, since it is difficult to define the full 3D geometry of the node due to its complexity. Previous methodologies suggest several criteria to failure. The most conservative criterion among them is a maximum bearing stress limit. While this criterion does not incorporate the beneficial effects of triaxial confinement, it also does not necessitate defining the complex nodal geometries required to check the nodal strength at the strut-to-node interface. As a result, using the nodal strength in drilled shaft footings led to significantly simpler calculations. Moreover, the researchers who reported design examples of drilled shaft footings as mentioned in the previous section proposed that the triaxial confinement effect is neglected ($m = 1.0$) for additional conservatism. Last, applying crack control reinforcement near struts to redistribute internal stresses is not required for footing structures according to AASHTO LRFD (2020). Therefore, the concrete efficiency factor is not affected by the lack of crack control reinforcement, compared to that of 2D structures.

8.2.1.4. Proportioning Shrinkage and Temperature Reinforcement

As described in the previous subsection, the crack control requirement for STMs in accordance with Article 5.8.2.6 of AASHTO LRFD (2020) does not apply to footings. Rather, footings require face or skin reinforcement to control cracks for shrinkage and temperature effect on any faces. Article 5.10.6 of AASHTO LRFD (2020), as shown in Eq. (8.3), stipulates that more than 0.18% of face reinforcement should be provided for each face and direction. According to the review of design parameters (Chapter 3), most footings do not satisfy this requirement on all side

faces. Bottom and top faces generally contain more than the required amount due to primary longitudinal reinforcement. Crack control reinforcement on the bottom face is located outside of the bandwidth for footings with a banded layout. However, the lack of sufficient side face reinforcement does not influence predictions of the ultimate capacity, because this requirement is intended to enhance the serviceability, not the strength.

$$A_s \geq \frac{1.30bh}{2(b+h)f_y} \quad \text{Eq. (8.3)}$$

except that

$$0.11 \leq A_s \leq 0.60$$

where:

A_s = area of reinforcement in each direction and each face [in.²/ft]

b = least width of component section [in.]

h = least thickness of component section [in.]

f_y = specified minimum yield strength of reinforcement ≤ 75.0 ksi [ksi]

8.2.1.5. Anchorage for Ties

- *Minimum Development Length*

Article 5.10.8.2.1 of AASHTO LRFD (2020) provides the minimum tension development length of straight bars according to Eq. (8.4).

$$l_d = 2.4d_b \frac{f_y}{\sqrt{f'_c}} \times \left(\frac{\lambda_{rl}\lambda_{cf}\lambda_{rc}\lambda_{er}}{\lambda} \right) \quad \text{Eq. (8.4)}$$

where:

d_b = nominal diameter of reinforcing bars [in.]

f_y = specified minimum yield strength of reinforcement [ksi]

f'_c = compressive strength of concrete for use in design [ksi]

λ_{rl} = reinforcement location factor

λ_{cf} = coating factor

λ_{rc} = reinforcement confinement factor, taken as $d_b/(c_b + k_{tr})$, $0.4 \leq \lambda_{rc} \leq 1.0$

c_b = the smaller of distance from center of bar or wire being developed to the nearest concrete surface and one-half the center-to-center spacing of bars or wires being developed [in.]

k_{tr} = transverse reinforce index, taken as $40A_{tr}/(sn)$

A_{tr} = total cross-sectional area of all transverse reinforcement which is within the spacing s and which crosses the potential plane of splitting through the reinforcement being developed [in.²]

- s = maximum center-to-center spacing of transverse reinforcement within l_d [in.]
- n = number of bars or wires developed along plane of splitting
- λ_{er} = excess reinforcement factor, taken as $A_{s,req'd}/A_{s,provided} \leq 1.0$
- λ = concrete density modification factor

The equation to calculate the required development length for a hooked bar in accordance with Article 5.10.8.2.4 of AASHTO LRFD (2020) is provided in Eq. (8.5):

$$l_{dh} = \frac{38.0d_b}{60.0} \frac{f_y}{\sqrt{f'_c}} \times \left(\frac{\lambda_{rc}\lambda_{cw}\lambda_{er}}{\lambda} \right) \quad \text{Eq. (8.5)}$$

where:

- d_b = nominal diameter of reinforcing bars [in.]
- f_y = specified minimum yield strength of reinforcement [ksi]
- f'_c = compressive strength of concrete for use in design [ksi]
- λ_{rc} = reinforcement confinement factor
- λ_{cw} = coating factor
- λ_{er} = excess reinforcement factor, taken as $A_{s,req'd}/A_{s,provided} \leq 1.0$
- λ = concrete density modification factor

- **Bottom/Top Mat Reinforcement**

Sufficient length behind the critical section is required so that the tie reinforcement can be fully developed. If the required development length is not satisfied, the tie force should be reduced proportionally to the ratio of the available development length to the required length. If a nodal region can be defined, the tie reinforcement should be developed at the intersection between the centroid of the reinforcement and an extended nodal zone, in accordance with AASHTO LRFD (2020), as shown in Figure 8.2-(a). However, the extended nodal zone in drilled shaft footings is difficult to define in three dimensions since multiple ties and struts are connected and they are not contained in the same plane. Therefore, the assumption of the available development length (l_{ad})—conservatively defined as the length measured from the interior edge of the equivalent square shaft, as depicted in Figure 8.2-(b)—is adopted as suggested by previous researchers, including Williams et al. (2012).

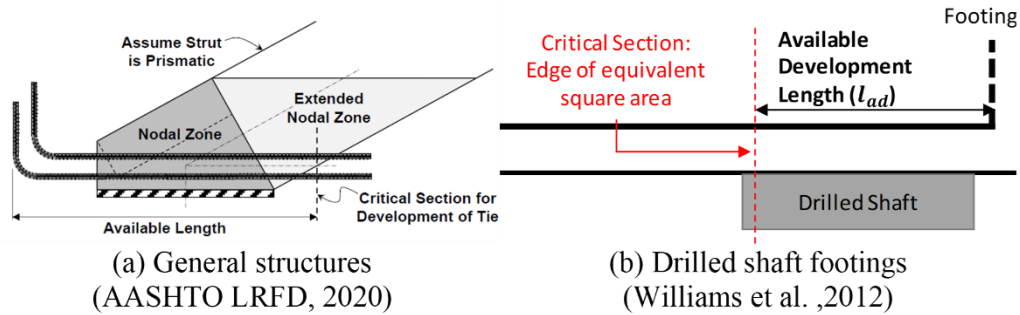


Figure 8.2 Available development length of tie reinforcement

- **Column/Drilled Shaft Reinforcement**

To ensure full yield strength of the tie elements of the column reinforcement and drilled shaft reinforcement employed for the STMs subjected to uniaxial moment, the available development lengths at the end nodes of the tie elements need to be specified. However, the nodes are classified as smeared nodes since they are positioned at a bearing face. Therefore, the available lengths cannot be determined from the extended nodal concept based on the defined nodal geometry. There is no specified method to define the available length for the anchorage requirement of the smeared node in current STM provisions, including AASHTO LRFD (2020). Williams et al. (2012) suggested using the conventional anchorage types adopted in past TxDOT designs, such as hooked anchorage for the column and drilled shaft reinforcement, conservatively. Still, the anchorage detail was not verified experimentally prior to the current project.

8.2.1.6. Outline of Predictions Based on 3D STM

The procedure used to generate the 3D STM predictions for drilled shaft footings subjected to pure axial loading (Phase I test loading condition) is summarized below:

- 1) Calculation of equivalent loads from the column and drilled shaft reactions
 - o Resultant loads from the column can be divided into four quadrants and assumed to be applied at the center of each quadrant.
 - o The four drilled shafts react to the loads equally.
- 2) Development of a 3D strut-and-tie model as illustrated in Figure 8.1-(a)
 - o The nodes beneath the column are located 0.1 times the effective depth below the center of each quadrant.

- o The position of the four nodes above the drilled shafts is the center of the drilled shafts at the elevation of tension reinforcement.
 - o The bottom horizontal ties that represent the bottom mat reinforcement are connected between each node above the drilled shafts.
 - o Diagonal struts are developed between nodes below the column and above the drilled shafts for each quadrant.
 - o Strut rings at the vertical position of the nodes beneath the column can be determined to satisfy the requirement of the equilibrium.
 - o Tie and strut forces (T_x , T_y , and F_s) can be computed by the equilibrium of each axis at each node and the geometric properties.
- 3) Material properties
- o The actual concrete strength ($f'_{c,test}$) on test date and yield strength of bottom mat reinforcement (f_{yb}) were used in the strength calculations. In the case of the specimens cast with concrete from two different ready-mix trucks, the average strength obtained from these two concrete batches was used for $f'_{c,test}$.
- 4) Proportion of ties
- o Steel in the bandwidth—defined as the width within 45-degree distribution angle from the edge of drilled shafts, as shown in Figure 4.2—is considered to contribute to tie forces.
 - o $T_x = \frac{P/4}{\sin \theta} \cos \theta \cos \alpha = A_{st,x} f_{yb,x} \rightarrow P_{tie,x} = 4A_{st,x} f_{yb,x} \frac{\tan \theta}{\cos \alpha}$
 - o $T_y = \frac{P/4}{\sin \theta} \cos \theta \sin \alpha = A_{st,y} f_{yb,y} \rightarrow P_{tie,y} = 4A_{st,y} f_{yb,y} \frac{\tan \theta}{\sin \alpha}$
- 5) Nodal strength checks
- o Nodal strength checks are performed at bearing faces only since it is difficult to define the full 3D geometry of the nodes due to its complexity.
 - o The maximum bearing stress on a bearing face, f_{cu} is limited to mvf'_c , where m is the triaxial confinement factor and v is the concrete efficiency factor in accordance with Article 5.8.2.3 in AASHTO LRFD (2020). The triaxial confinement effect is neglected ($m = 1.0$) for added conservatism.

- o $F_{DS,b} = \frac{P/4}{\sin \theta} = A_{DS} m v f'_{c,test} \rightarrow P_{DS,b} = 4 A_{DS} m v f'_{c,test} \sin \theta$ (CTT)
- o $F_{COL,b} = \frac{P/4}{\sin \theta} = \frac{A_{COL}}{4} m v f'_{c,test} \rightarrow P_{COL,b} = A_{COL} m v f'_{c,test} \sin \theta$ (CCC)

6) Proportion of shrinkage and temperature reinforcement

- o The requirement of crack control for STM calculation in accordance with Article 5.8.2.6 of AASHTO LRFD (2020) is not applied to footings.
- o Face reinforcement (crack control reinforcement used to control the shrinkage and temperature effect on footing faces) can be installed along each axis on each face in accordance with Article 5.10.6 of AASHTO LRFD (2020).
- o This requirement is for the purpose of design regarding the serviceability; therefore, it does not influence the prediction of the ultimate capacity.

7) Anchorage check for ties

- o Figure 8.2-(b) depicts the available development length (l_{ad}), conservatively defined as the length from the interior edge of the equivalent square shaft to the section of the end of the bottom mat reinforcement due to undefined extended nodal zone above drilled shaft.
- o If the required development length is not satisfied, the tie force should reduce proportional to the ratio of the available development length to the requirement ($l_{ad}/l_{d,req'd}$).

8) Prediction of the ultimate capacity

- o The minimum value of $P_{tie,x}$, $P_{tie,y}$, $P_{DS,b}$ and $P_{COL,b}$ would be P_{STM} .

8.2.2. Evaluation of Current STM Provision

This section compares experimental ultimate strengths and predicted ultimate capacities achieved by the current STM provision. A footing research database was created and Phase I testing results evaluated. It should be noted that the analytical predictions were done using the average measured compressive strength of concrete cylinders at the time of testing, and that the resistance factor was not considered.

8.2.2.1. Footing Research Database

Building on the Chapter 2 findings, the research team compiled a database of drilled shaft footing tests conducted in previous research projects. The database is intended to provide an alternative method of evaluating the current provision.

Using the database, the research team identified footing specimens that had four shafts and were subjected to axial compression only over the column section. As summarized in Table 8.1, 160 footing tests, including 13 tests carried out in Phase I (Chapter 4) of the current project, were collected. This database is referred to as the *collection database*. Only Phase I testing was incorporated into the database because those specimens were tested in a loading condition similar to the other collected studies in the database. Further, the database contained no record of footings tested with uniaxial eccentric loads. Therefore, Phase II and III testing results were not used to evaluate predictions of ultimate capacities by the current STM provision.

Table 8.1 Number of tests from previous research and this study

Researchers (Years)	No. of tests	Researchers (Years)	No. of tests
Blevot and Frémy (1967)	27	Clarke (1973)	13
Sabnis and Gogate (1984)	8	Adebar et al. (1990)	5
Suzuki et al. (1998)	28	Suzuki et al. (1999)	19
Suzuki et al. (2000)	30	Suzuki and Otsuki (2002)	18
Present Study (2021)	13	Total	160

The collection database was filtered in two stages, as summarized in Table 8.2. The first stage began with the elimination of any test results involving impractical material properties and out-of-scope tests. Tests that employed specimens with less than 2.4 ksi of compressive concrete strength were excluded, since AASHTO LRFD (2020) specifies that the minimum concrete strength for structural purposes is 2.4 ksi. Two specimens from Blevot and Frémy (1967) were filtered out in this stage. In addition, cases whose specimens' reinforcing bars had a yielding strength of less than 50 ksi were eliminated as well. Even though the yield strength of reinforcement is required to be 60 ksi in accordance with both AASHTO LRFD (2020) and ACI 318-19 (2019), the yield strength criterion was set at 50 ksi because some specimens were fabricated more than 50 years ago. Seven cases from Blevot and Frémy (1967) were filtered out due to low yield strength. Furthermore, 31 cases were removed for meeting the criterion that any failure of a footing specimen stemmed only from tie yielding or flexure, as determined by the sectional analysis

(since a footing generally fails due to the interrelationship between flexure and shear, not flexure only, according to previous researchers). Another five cases were excluded because the governing failure mode was unspecified. After this first filtering stage, 115 tests remained; this set was referred to as the *filtered database*.

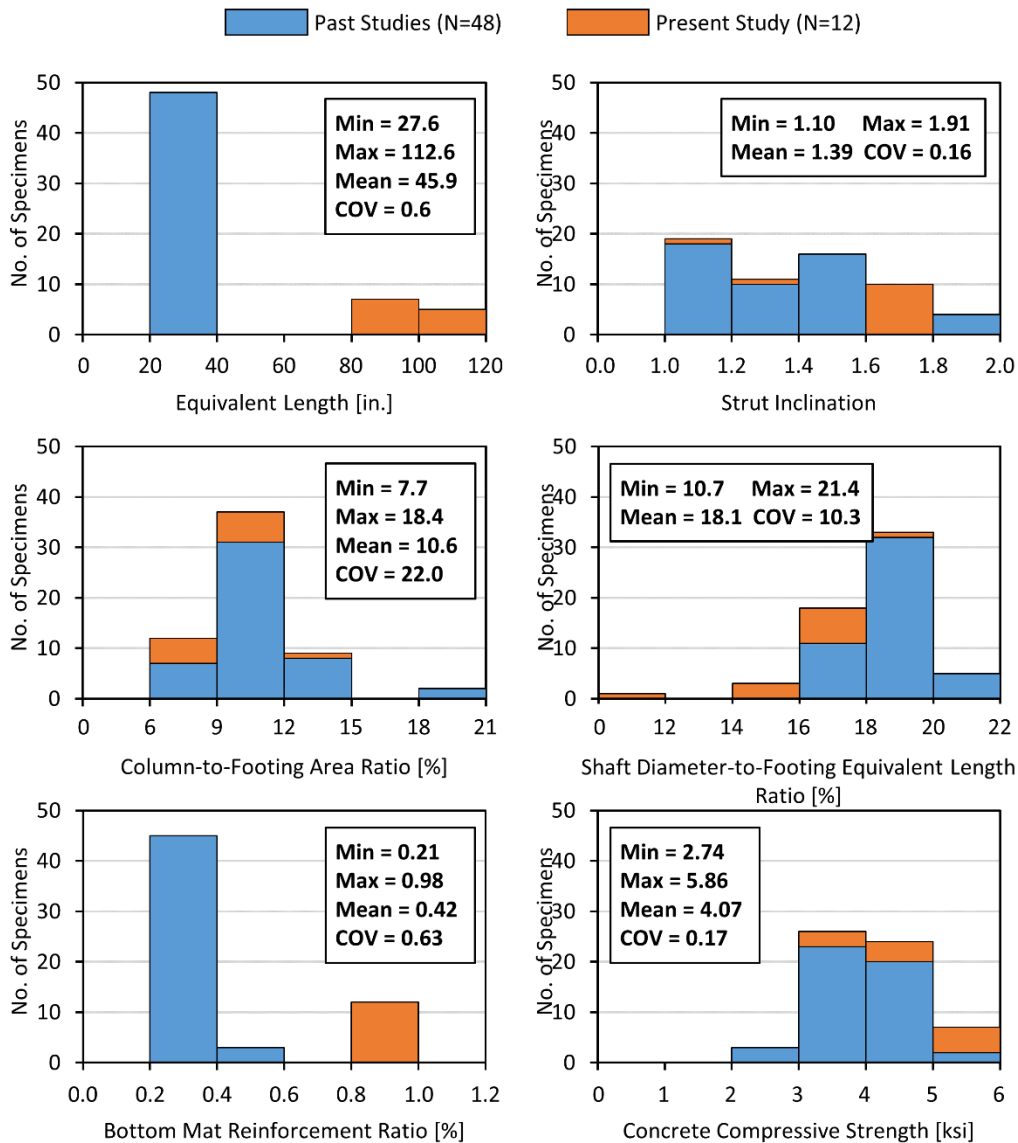
In the second stage, specimens that were representative of current practice and could be classified as D-regions, as defined in Chapter 3, were selected from the *filtered database*. In selecting these cases, three criteria were used for additional filtering: strut inclination, column-to-footing ratio, and bottom mat reinforcement ratio. The criteria range was set as the minimum and maximum value of each attribute established in the TxDOT drilled shaft footing database in Chapter 3. First, 31 tests were eliminated because strut inclinations were not between 1:1.1 and 1:2.3, which can be defined as the D-region. Removed next were 15 tests that met the filtering range of bottom mat reinforcement ratio, from 0.20 and 0.98%. Lastly, 9 tests whose specimens had excessively large or small column size with respect to footing size, using minimum and maximum area ratios of column to footing of 7% and 21% were excluded. Ultimately, 60 tests were found to satisfy all three Stage II filtering criteria simultaneously; this final filtered database is referred to as the *evaluation database*.

Table 8.2 Filtering criteria used for the footing research database

<i>Collection Database</i>		160 tests
Stage I filtering	$f'_c < 2.4$ ksi	-2 tests
	$f_y < 50$ ksi	-7 tests
	Failed by tie yielding only or no specified failure mode	-36 tests
<i>Filtered Database</i>		115 tests
Stage II filtering	Strut inclination (z/d): ≤ 1.1 or ≥ 2.3	-31 tests
	Bottom mat reinforcement ratio: ≤ 0.20 or $\geq 0.98\%$	-9 tests
	$A_{col}/A_{footing} : \leq 7\%$ or $\geq 21\%$	-15 tests
<i>Evaluation Database</i>		60 tests

Figure 8.3 shows the distribution of primary attributes in the evaluation database and Appendix B contains details about the records in the *evaluation database*. The blue and orange bars in Figure 8.3 indicate past studies and the present study, respectively. The statistical values are presented in each plot. The equivalent length, which can represent the footing size, is defined as the side length of a square that has the same area as the footing plan. The footing size used in the present study is significantly larger than those of past studies. Strut inclination ranges from 1.0 to

2.0 and is relatively uniformly distributed. The average of column-to-footing area ratio is 10.6% and most cases fall between 9% and 12%. The ratio of shaft area to footing area is mainly distributed on both sides of 18%, considerably close to the average of 18.1%. Previous footing specimens had less bottom mat reinforcement than the present study. As a result, previous researchers usually observed incidents of failure induced by both flexure and shear. This study used a high bottom mat reinforcement ratio to ensure that the nodal capacity would be eventually exceeded in the tests, as described in Chapter 4. Concrete compressive strengths of both past studies and the present study are mainly distributed between 3.0 to 5.0 ksi.



Note: COV = Coefficient of Variation = Standard Deviation / Mean

Figure 8.3 Histograms of attributes of the footing specimens in the evaluation database (N=60)

The distribution of ultimate capacity ratios of footing test specimens in the evaluation database is presented in Figure 8.4. It should be noted that the resistance factor is not included in this calculation. The ultimate capacity ratio is defined as the ratio of experimental ultimate load to the predicted capacity based on 3D STM recommended by Williams et al. (2012). The predictions of the ultimate capacities of all footing specimens in the evaluation database are conservative. The average of these ratios is 1.97 and 82% of the cases are distributed between 1.5 and 2.5. The calculated ultimate capacities in the majority of cases (45%) are excessively conservative, with ultimate capacity ratios greater than two. Appendix G contains the 3D STM calculation of *evaluation database*.

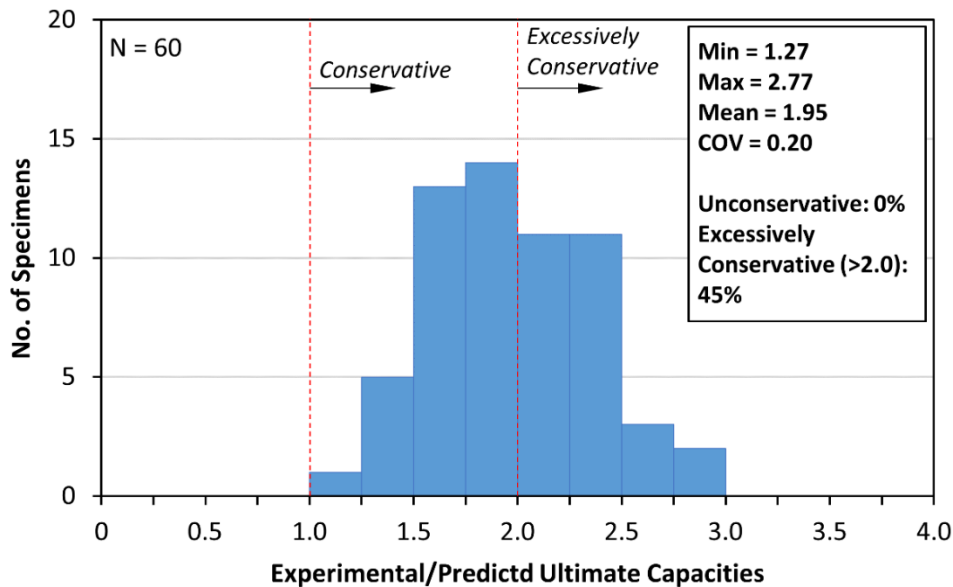


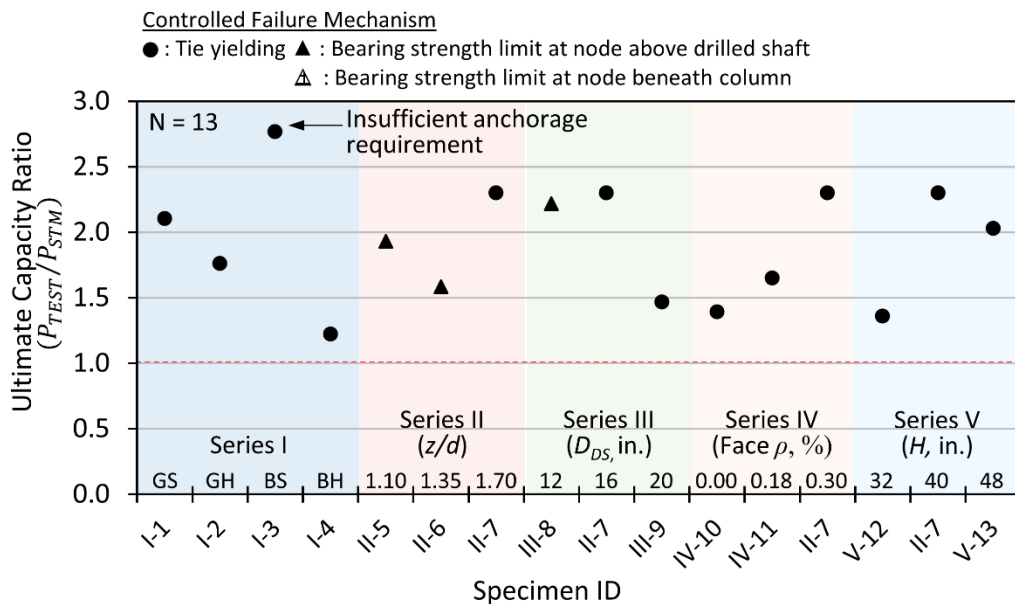
Figure 8.4 Distribution of ultimate capacity ratios for the evaluation database

8.2.2.2. Phase I Testing Results

A more detailed interpretation of the experimental and predicted test results for Phase I testing of this study is presented in this section, examining the effect of each design parameter. Table 8.3 summarizes the experimental and calculated results. Using the design recommendations by Williams et al. (2012), the actual ultimate loads are on average 83% lower than calculated ultimate capacities, which means that 3D STM estimation provides conservative results. Tie yielding is the controlling failure mechanism used in 3D STMs for most cases since it is assumed that only the reinforcing bars in the bandwidth contribute to tie force. Failure to consider the steel located outside of the bandwidth as a component of the ties leads to excessively conservative results and a discrepancy between failure mechanisms observed and test results. Tie yielding or near-yielding was observed in all specimens; however, the failures resulted from the interrelationship between tie yielding and nodal stress limit, not from tie yielding alone, as the investigation of

post-failure conditions and load-deflection responses revealed. The discrepancy pertaining to the controlling failure mechanism needs to be resolved. The controlling failure mechanism of specimens with steeper strut inclinations (II-5 and II-6) were well-predicted. The ultimate capacity ratios (P_u/P_{STM}) ranged from 1.22 to 2.76. For specimens with straight bars for bottom mat steel arranged in a banded layout (I-3), the overly conservative ultimate capacity predictions resulted from the consideration of insufficient development length. The research team did not observe any signs of local or global failure due to tie yielding in I-3. Consequently, the ultimate capacity ratio of I-3, 2.77, which is related to anchorage ties, resulted in the most conservative ultimate capacity prediction among all cases. If sufficient anchorage of I-3 were assumed according to the experimental result, the prediction would be 2,361 kips, roughly 13% less than the measured ultimate capacity, resulting in an ultimate capacity ratio of 1.14.

The effects of test variables corresponding to different series in the ultimate capacity ratio are illustrated in Figure 8.5. The marker shapes used in the figure indicate the controlling failure mechanisms. The average ultimate capacity ratio is 1.83; 5 out of 13 specimens were over an ultimate capacity ratio of 2.0, which means the predictions are excessively conservative. The predicted ultimate capacity of I-4, which has a banded layout, was the most accurate. The plotted data show that the controlling failure mechanism was tie yielding in the majority of specimens. However, the experimental result indicated that specimens could provide more load-carrying capacity after yielding.



Note) z : Shear span, d : effective depth, D_{DS} : Shaft Diameter, ρ_{face} : Side face reinforcement ratio, H : footing height, G (Grid layout), B (Banded layout), S (Straight anchorage), H (Hooked anchorage)

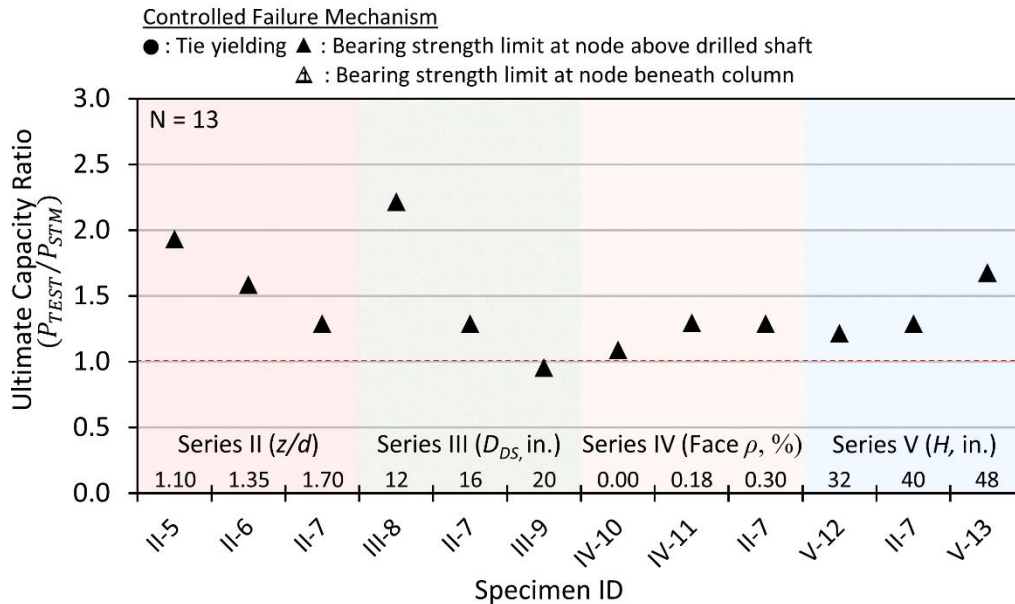
Figure 8.5 Comparison of experimental and predicted ultimate capacities

Table 8.3 Summary of predicted ultimate capacities based on current 3D STM provision

Series	Specimen ID	Material Properties		Geometric properties			STM prediction by Controlled Failure mechanism				Ultimate load (P_u) [kip]	Predicted ultimate capacity (P_{STM}) [kip]	$\frac{P_u}{P_{STM}}$
		$f'_{c,test}$ [ksi]	f_{yb} [ksi]	θ [deg.]	α [deg.]	$\frac{l_{ad}}{l_{d,req'd}}$	Tie length-dir. [kip]	Tie width-dir. [kip]	CCC bearing [kip]	CTT bearing [kip]			
I	I-1	5.07	71.9	34.5	45.0	0.57	<u>1,002</u>	<u>1,002</u>	2,432	4,413	2,107	1,002	2.10
	I-2	5.22	64.1	34.5	45.0	1.35	<u>1,574</u>	<u>1,574</u>	2,473	4,543	2,775	1,574	1.76
	I-3	5.09	64.1	34.5	45.0	0.41	<u>978</u>	<u>978</u>	2,438	4,430	2,703	978	2.76
	I-4	5.06	64.1	34.5	45.0	1.33	<u>2,361</u>	<u>2,361</u>	2,429	4,404	2,884	2,361	1.22
II	II-5	3.24	63.5	48.2	27.1	0.99	4,999	2,555	<u>1,694</u>	2,820	3,273	1,694	1.93
	II-6	4.62	63.5	40.7	45.0	1.13	2,472	2,472	<u>2,300</u>	4,021	3,648	2,300	1.59
	II-7*	5.86	62.8	32.5	29.7	1.37	2,585	<u>1,473</u>	2,625	5,101	3,387	1,473	2.30
III	III-8	4.66	67.5	32.5	29.7	1.04	2,778	1,583	<u>1,301</u>	4,056	2,886	1,301	2.22
	III-9	3.71	67.4	32.5	29.7	1.11	3,468	<u>1,976</u>	3,030	3,229	2,902	1,976	1.47
IV	IV-10	4.66	78.3	32.5	29.7	0.98	3,180	<u>1,812</u>	2,312	4,056	2,523	1,802	1.39
	IV-11	4.65	78.3	32.5	29.7	0.98	3,178	<u>1,811</u>	2,309	4,047	2,990	1,800	1.65
V	V-12	3.52	67.0	34.5	45.0	1.10	<u>1,645</u>	<u>1,645</u>	1,840	3,064	2,239	1,645	1.36
	V-13	3.82	68.2	31.1	22.5	0.91	3,993	<u>1,652</u>	1,997	3,325	3,354	1,652	2.03

Note: *(baseline model), underline (controlled failure mechanism)

To explore the discrepancy between the STM estimation and the experimental finding as regards the failure mechanism, Figure 8.6 plots the ultimate capacity ratio from Series II to Series V by focusing on the bearing stress limit at the node above the drilled shaft. The bearing capacity values were used to investigate the discrepancy for two reasons. First, the bearing capacity was generally critical if the underestimated tie forces were neglected. This underestimation arose because a small portion of the bottom mat reinforcing bars in specimens with grid layouts (Series II through V) was located in the bandwidth region. In addition, tie yielding forces that are strongly affected the yield strength of steel governed the ultimate capacities in most cases. As a result, investigating the effect of concrete on the ultimate capacity is limited. It should be noted that specimens in Series I are excluded from Figure 8.6. Calculations for specimens with the banded layout (I-3 and I-4) did not underestimate tie forces; an insufficient anchorage length was predicted in I-1 with straight bars.



Note) z: Shear span, d: effective depth, D_{DS}: Shaft Diameter, ρ_{face}: Side face reinforcement ratio, H: footing height

Figure 8.6 Comparison of experimental and predicted ultimate capacities controlled by bearing strength at node above drilled shafts

The findings and discussions for each series are as follows:

- Series I: Bottom mat reinforcing details
 - o Calculations for specimens with straight bars (I-1 and I-3) yielded more conservative predictions than for specimens with hooked bars, because the development length requirement was not satisfied for straight bars, as previously discussed.

- o For reinforcement arrangements with proper anchorage conditions (I-2 and I-4), the presence of a banded layout (I-4) resulted in an ultimate prediction that was 50% greater than that of a grid layout (I-2) because more reinforcing bars were contained in the bandwidth (in accordance with the 3D STM design). However, the measured ultimate loads in the testing program were 4% different between both specimens.
- o The experimental results of Series I indicated that reinforcing bars—even those outside of the bandwidth—can contribute tie forces if properly anchored.
- o Strength predictions were more accurate for those specimens with a banded layout and full anchorage (I-4).
- Series II: Strut inclination
 - o The predicted failure mechanisms for specimens with steeper strut inclination (II-5 and II-6) were controlled by the bearing stress limit at the node above drilled shafts while II-7 was controlled by tie yielding.
 - o If comparing the bearing strengths at the node above the drilled shafts of all specimens in Series II, as shown in Figure 8.6, the ultimate capacity ratios decreased when the strut inclination decreased proportionally.
 - o Therefore, nodal strength at the strut-to-node interface, which strongly depends on strut inclination, needs to be considered rather than the nodal capacity limit at the bearing face.
- Series III: Shaft diameter
 - o The smallest shaft diameter (III-8) resulted in the lowest predicted ultimate capacity among specimens in Series III since shaft size directly affected the nodal strength, which resulted in the most conservative prediction and a different controlling failure mechanism: the bearing strength at the node above the drilled shafts. For other specimens, tie yielding was the controlling mechanism.
 - o The presence of more reinforcing bars in the bandwidth, enabled by the larger shaft diameter (III-9), resulted in more accurate prediction.
 - o The confinement factor affected by the edge distance needs to be considered in the 3D STM prediction scheme since greater edge distance, created by a smaller shaft diameter, can induce a greater confinement effect due to the greater mass of the surrounding concrete.

- Series IV: Side face reinforcement ratio
 - The ultimate capacities depend on the yield strength of bottom mat reinforcement, as shown in Table 8.3.
 - Specimens without side face reinforcement (IV-10) provided the least conservative predictions, as shown in both Figure 8.5 and Figure 8.6. However, IV-10 has to be the most conservative due to the most brittle failure and the lowest level of stress redistribution predicted.
 - The ultimate capacity ratios in Figure 8.6 were slightly less widespread compared to other series.
 - The side face reinforcement ratio did not affect any calculation, although the experimental results found that no side face reinforcement exhibited significantly lower strength. It can be recommended that a penalty should be enforced on calculating the ultimate strength when no side face reinforcement is used in STM. This is similar to the requirement of crack control reinforcement.
- Series V: Footing height
 - Estimated ultimate capacities were not affected by footing height (size).
 - The ultimate capacity ratio of V-13 in Figure 8.6 was the greatest, although two other specimens experienced a similar level of conservativeness.
 - Shaft diameter and edge distance with respect to footing size were smaller in the largest specimen, V-13, whose ultimate strength ratio was greater than 2. As a result, examining the confinement effect in 3D STM would be recommended.

8.3. Proposal of 3D STM Guidelines for Drilled Shaft Footings

8.3.1. Proposal of 3D STM

The proposed guidelines employ the same general 3D STM procedure for drilled shaft footings as described in Section 8.2.1, but with key modifications that are detailed in the following subsections.

- 1) Develop 3D strut-and-tie model
- 2) Proportion ties
- 3) Perform nodal strength checks
- 4) Proportion shrinkage and temperature reinforcement
- 5) Provide necessary anchorage for ties

8.3.1.1. 3D Strut-and-Tie Model

The basic concepts used to develop 3D STMs of drilled shaft footings under various loading combinations are adopted from Williams et al. (2012), as detailed in Section 8.2.1.1. However, the research team proposes an adjustment in determining the position of resultant forces on the column section when a large amount of uniaxial moment is applied to induce tension on one face of the column. In specific, the compression resultant is determined based on the actual loading-based stress distribution of the reinforced concrete column section as explained next.

The column section is assumed to remain plane during loading, so a linear strain distribution characterized by the extreme compressive fiber strain (ϵ_{ct}) and the neutral axis depth (c) is assumed. The constitutive relationships for concrete and reinforcing steel are used to convert the strain distribution into a stress distribution. A simplified rectangular stress block is used for concrete in compression, and the equivalent stress block factors (α_1 and β_1) proposed by Collins and Mitchell (1991) can be computed from Eq. (8.6) based on ϵ_{ct} . The geometry and magnitude of the stress block is then used to determine the compressive resultant force and its position on the column section, as shown in Figure 8.7. An iterative procedure is needed to determine the values of ϵ_{ct} and c that will satisfy force and moment equilibrium, as shown in Figure 8.7.

By taking the nonlinear stress distribution with the equivalent stress block concept into the decision of the configuration of the STM, the developed STM can maintain the consistency of the force flow between a B-region and a D-region, whether the column section behaves essentially as a cracked elastic section or approaches ultimate conditions. Therefore, the member forces of the STM determined based on the nonlinear stress distribution of the column can contribute to a more realistic representation of the demands and more efficient design for this loading conditions.

$$\alpha_1 = \frac{1}{\beta_1} \left[\left(\frac{\epsilon_{ct}}{\epsilon'_c} \right) - \frac{1}{3} \left(\frac{\epsilon_{ct}}{\epsilon'_c} \right)^2 \right] \quad \text{Eq. (8.6)-(a)}$$

$$\beta_1 = \frac{4 - (\epsilon_{ct}/\epsilon'_c)}{6 - 2(\epsilon_{ct}/\epsilon'_c)} \quad \text{Eq. (8.6)-(b)}$$

where:

- α_1 = equivalent stress factor
- β_1 = equivalent stress block depth factor
- ϵ'_c = concrete strain at peak stress (= -0.002 in./in.)
- ϵ_{ct} = strain at extreme compressive fiber [in./in.]

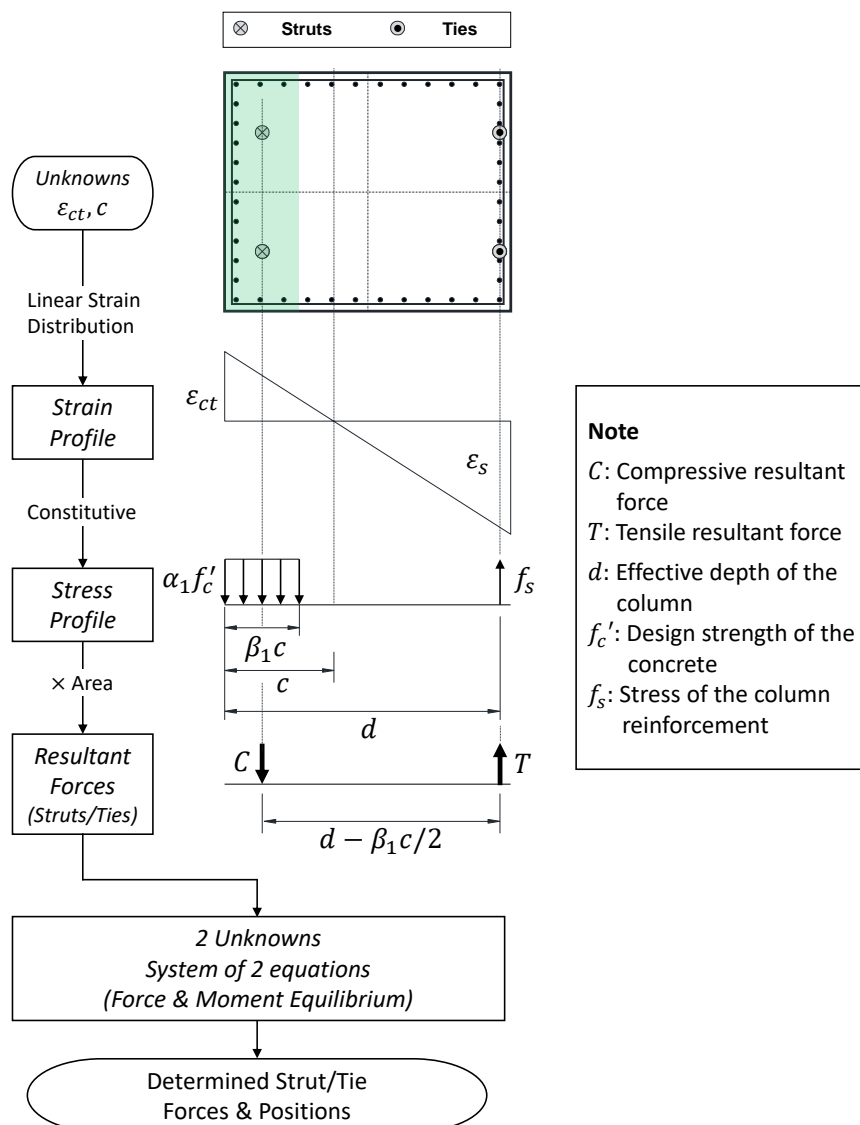


Figure 8.7 Flow chart to determine forces and position of struts and ties on the column section

8.3.1.2. Proportion Ties

Based on the findings from Phase I testing and the evaluation of the current provision, the research team concluded that reinforcing bars both outside and inside the bandwidth can be included as the total tie area. In other words, all bottom mat reinforcement, regardless of bottom mat configuration, can be engaged to take the tie forces if the reinforcement is sufficiently anchored. It was observed that the ultimate capacities of specimens with both grid and banded layouts were comparable; however, the predicted ultimate capacity of specimens with a banded layout was 50% greater, revealing that the current provision underestimated the tie force when bars were arranged uniformly. Therefore, the research team proposed to update Eq. (8.1) as shown in Eq. (8.7):

$$P_{n,tie} = f_y A_{st} \quad \text{Eq. (8.7)}$$

where:

$P_{n,tie}$ = nominal resistance of a tie [kip]

f_y = yield strength of nonprestressed longitudinal reinforcement [ksi]

A_{st} = area of nonprestressed longitudinal reinforcement engaged to take the tie force [in.²]

In a 3D strut-and-tie model of footings with four drilled shafts, two horizontal ties are placed in each direction. Therefore, A_{st} in Eq. (8.7) represents half the amount of bottom mat reinforcement in one direction when calculating the tie capacity.

8.3.1.3. Nodal Strength Checks

This section proposes the refinement of 3D nodal geometry, confinement modification factor, and concrete efficiency factor.

- *3D Nodal Geometry*

This study suggests 3D nodal geometry for drilled shaft footings subjected to various loading combinations.

- PHASE I: UNIFORM COMPRESSION IN SHAFTS

Figure 8.8 shows the 3D strut-and-tie model of a drilled shaft footing subjected to pure compression only that is the equivalent loading case of Phase I. Williams et al. (2012) proposed a simplified 3D nodal evaluation: the bearing stress limit is applied to the 3D STM for drilled shaft footing due to complex nodal geometry. It results in excessive conservatism of the design examples also provided by the same study. Instead of evaluating the bearing stress only, the research team proposes a procedure to define the nodal dimensions for each face in the following sections.

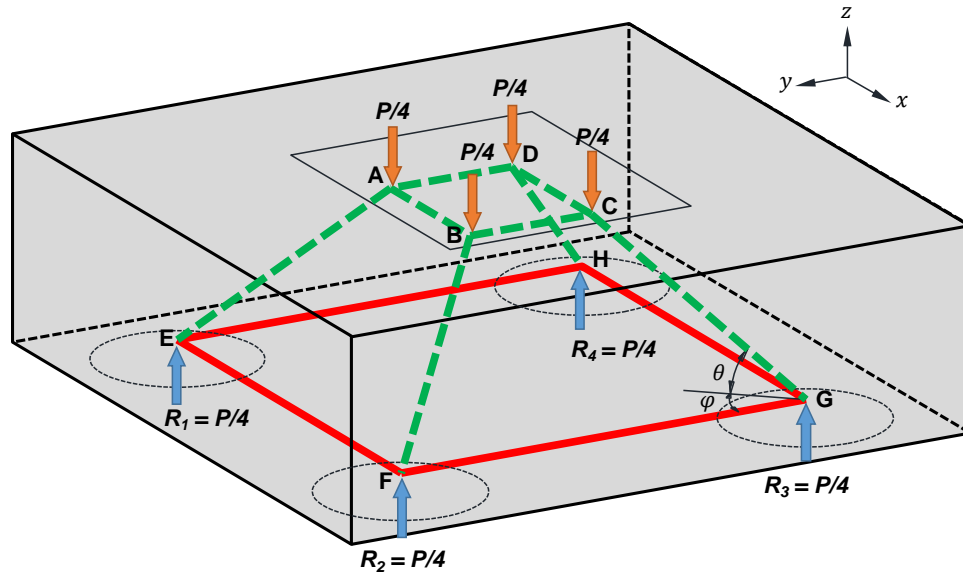
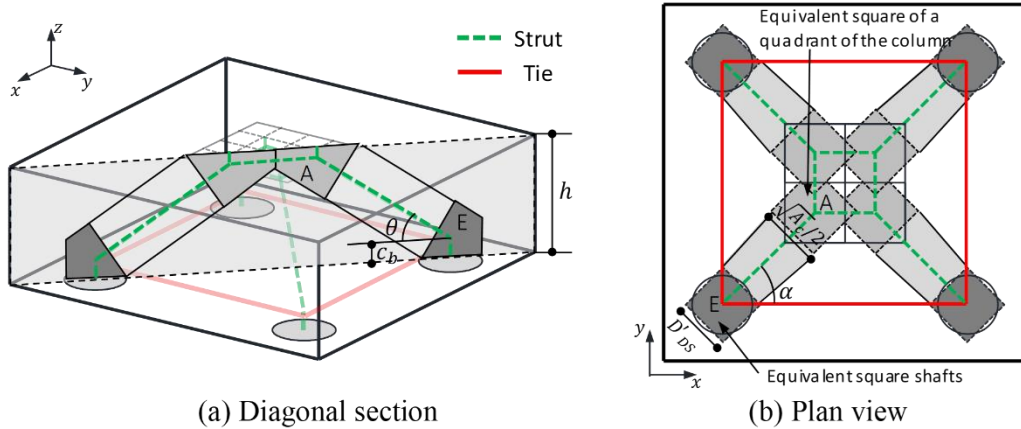


Figure 8.8 3D Strut-and-tie model of drilled shaft footings under uniform compressive loading

To define the 3D nodal geometry, the section of the diagonal struts is utilized as illustrated in Figure 8.9-(a) with assumptions described as follows: 1) non-hydrostatic nodes and prismatic struts with a rectangular cross section are used; 2) the strut width at the node is taken as the width of the equivalent square bearing face, and 3) the back face height of the CCC node is taken as twice the distance from the top surface to the CCC node (Node A in Figure 8.9 for example), or twice of $0.1h$. For CTT nodes above the drilled shafts, the height of the back face is twice the distance from the bottom surface to the centroid of the tie (c_b). If multiple struts are connected to a node forming multiple back faces as shown in Figure 8.9-(b), the strut forces are resolved into a single force applied perpendicularly to a single back face. With the specified dimensions, the length of the strut-to-node interface can be derived from the generalized 3D nodal geometry, as illustrated in Figure 8.10. For example, the bearing face of the CCC node beneath the column (Node A in Figure 8.9) can be defined as the quadrant area of the column; the bearing face of the CTT node above drilled shafts (Node E in Figure 8.9) can be taken as the area of the drilled shaft. The width of the equivalent square bearing face is the same as the width of the strut determined by aligning the horizontal equivalent square of the bearing face perpendicular to the axis of the strut in the plane view, as shown in Figure 8.9-(b). The length of the equivalent square bearing face and angle of struts are used to compute the length of strut-to-node interface using simple geometric relations.



Note α : Angle between x-axis and projected strut AB to the plane of the bottom mat reinforcement
 θ : Angle between strut AE and the plane of bottom mat reinforcement
 A_c : Area of the column
 D_{DS} : Shaft diameter
 D'_{DS} : Length of the equivalent square shaft ($= D_{DS}\sqrt{\pi/4}$)
 c_b : Distance from bottom surface to the centroid of bottom mat reinforcement
 h : Height of the footing

Figure 8.9 The sectional views to define 3D nodal geometry (Phase I)

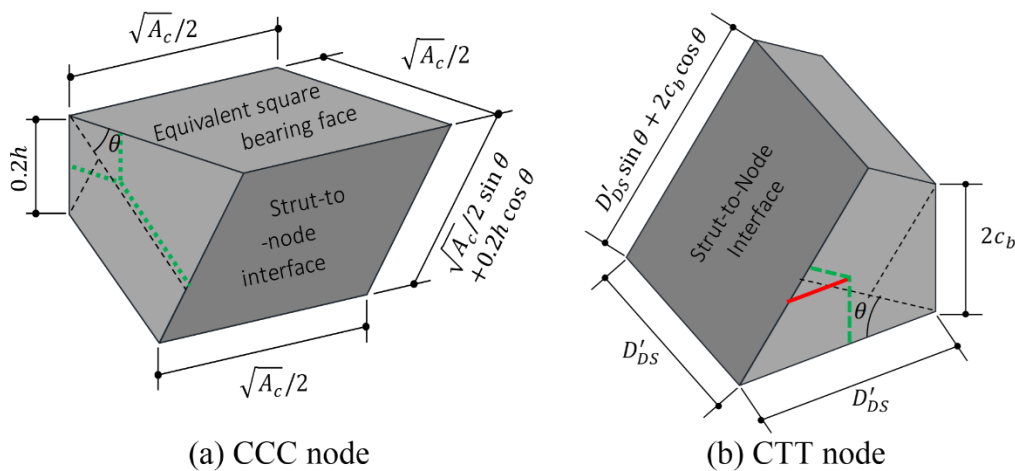
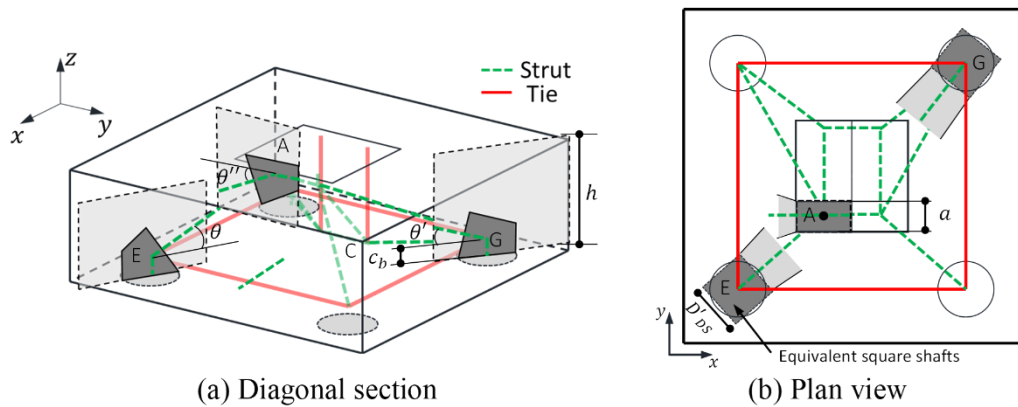


Figure 8.10 Detail of 3D nodal geometries in drilled shaft footings (Phase I)

- PHASE II: NON-UNIFORM COMPRESSION IN SHAFTS

The internal force flow of the footing becomes more complicated as the moderate uniaxial moment is applied to the column section. It results in a larger number of elements and nodes comprising the STM than the STM developed for the Phase I case, but allows for visualization of the force flow, as shown in Figure 8.11. In this case, the nodal strength check is performed at all faces of the CCC nodes beneath the column (Nodes A and D) and the CTT nodes positioned above the drilled shafts (Nodes E, F, G, and H).

As the evaluation of the CCC nodes remains the same as introduced, the 3D nodal geometry of the CTT nodes is determined on the basis of the same assumptions made for the CTT nodes in the footing under uniform compression. One additional assumption was made for this model to perform the nodal strength check at nodes subjected to more than two struts acting in different directions (Nodes A and G in Figure 8.11). When the node is subjected to more than two strut forces—having more than two strut-to-node interfaces facing different directions—it is too complicated to define the nodal geometry. Therefore, the struts are resolved to simplify the nodal strength check, and the strut-to-node interface dimension of this node should be determined based on the axis of the resolved strut, as shown in Figure 8.12.



- Note**
- θ : Angle between strut AE and the plane of bottom mat reinforcement
 - θ' , θ'' : Angle between the resolved strut and the plane of the bearing face
 - D_{DS} : Shaft diameter
 - D'_{DS} : Length of the equivalent square shaft ($= D_{DS}\sqrt{\pi/4}$)
 - a : Equivalent stress block depth
 - c_b : Distance from bottom surface to the centroid of bottom mat reinforcement
 - h : Height of the footing

Figure 8.11 The sectional views to define 3D nodal geometry (Phase II)

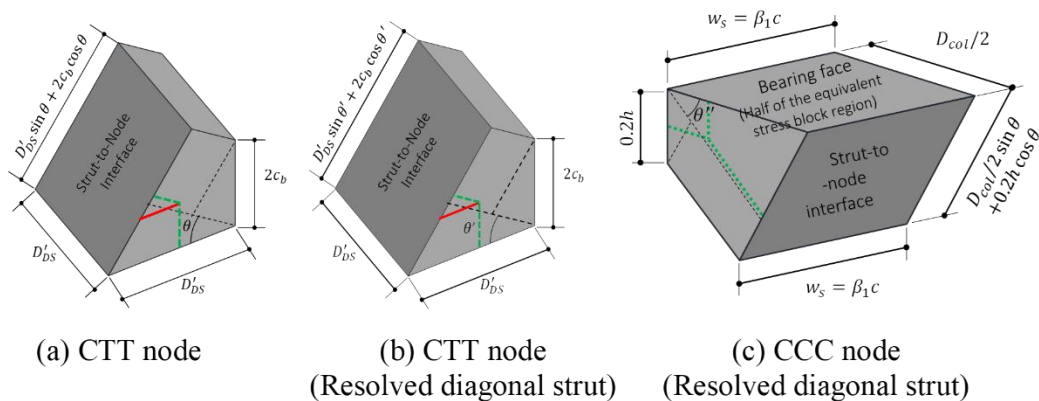
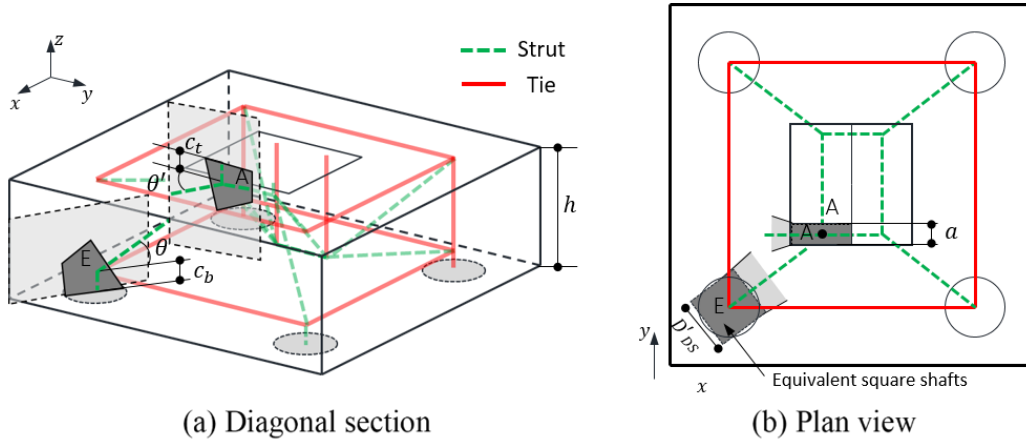


Figure 8.12 Detail of 3D nodal geometries in drilled shaft footings (Phase II)

• PHASE III: TENSION-COMPRESSION IN SHAFTS

Similarly, the evaluation of the 3D nodal geometry for Phase III loading conditions includes the CTT nodes above drilled shafts (Node E) and the CCC nodes beneath the column (Node A), as shown in Figure 8.13 and Figure 8.14.



- Note
- θ : Angle between strut AE and the plane of bottom mat reinforcement
 - θ' : Angle between the resolved strut and the plane of the bearing face
 - D_{DS} : Shaft diameter
 - D'_{DS} : Length of the equivalent square shaft ($= D_{DS}\sqrt{\pi/4}$)
 - a : Equivalent stress block depth
 - c_b : Distance from bottom surface to the centroid of bottom mat reinforcement
 - c_t : Distance from top surface to the centroid of top mat reinforcement
 - h : Height of the footing

Figure 8.13 The sectional views to define 3D nodal geometry (Phase III)

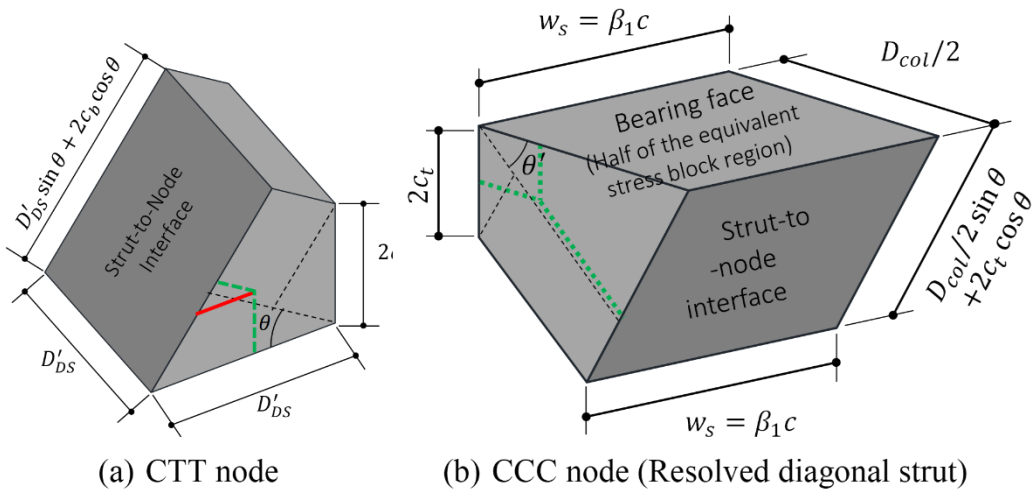


Figure 8.14 Detail of 3D nodal geometries in drilled shaft footings (Phase III)

- **Confinement Modification Factor**

According to the recommendation by Williams et al. (2012), a unit number of the confinement modification factor was employed in order to add conservatism. Article 5.6.5 of AASHTO LRFD (2020) allows the confinement modification factor to increase up to 2.0 for all node types of 2D structures, as provided in Eq. (8.8). The review of current STM specifications in the literature review (Chapter 2) reported that ACI 318-19 (2019) and CSA A23.3-14 (2014) used the same equation. However, Eurocode 2 (2004) and fib Model Code 2010 (2013) permit the maximum confinement of 3.0 for CCC nodes under triaxial compression condition, as shown in Eq. (8.9). As nodes in a drilled shaft footing are significantly confined by massive surrounding concrete for all types of nodes (CCC nodes, CCT nodes, and CTT nodes), it is recommended that up to 3.0 and 2.0 of confinement modification factors be used for CCC and other node types, respectively.

$$m = \sqrt{A_2/A_1} \leq 2.0 \quad \text{Eq. (8.8)}$$

where:

m = confinement modification factor

A_1 = area under bearing device [in.²]

A_2 = notional area defined as shown in Figure 8.15 [in.²]

$$F_{Rdu} = A_{c0}f_{cd}\sqrt{A_{c1}/A_{c0}} \leq 3.0f_{cd}A_{c0} \quad \text{Eq. (8.9)}$$

where:

F_{Rdu} = resistance force [kip]

f_{cd} = design value of f_c [ksi]

A_{c0} = loaded area (equivalent to A_1 in Figure 8.15) [in.²]

A_{c1} = maximum design distribution area with a similar shape to A_{c0} (equivalent to A_2 in Figure 8.15) [in.²]

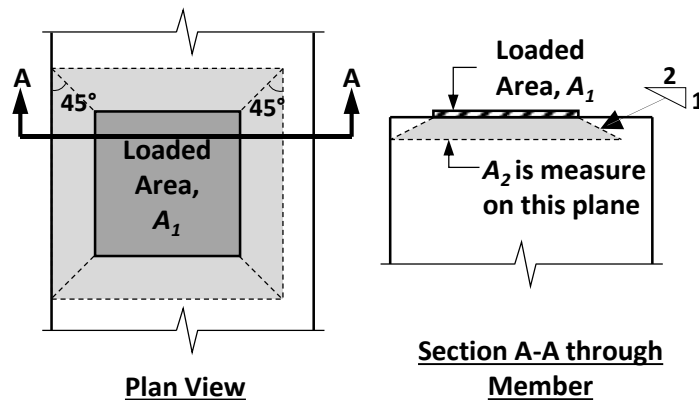


Figure 8.15 Determination of notional area (AASHTO LRFD, 2020)

- **Concrete Efficiency Factor**

The requirement of crack control reinforcement is not applied to footing structures in accordance with AASHTO LRFD (2020). Consequently, any secondary reinforcement does not affect strength calculation in the 3D STM. However, test results of Series IV in Phase I testing showed that the lack of side face reinforcement resulted in lower ultimate capacity, the most brittle failure, and different post-failure conditions as compared to other specimens with side face reinforcement. This result indicates that the side face reinforcement can contribute to redistributing internal stresses on the surface between two supported regions (drilled shafts), exemplified as the force system introduced by Clarke (1973) illustrated in Figure 8.16. In the current provision, the contribution of side face reinforcement to the ultimate capacity was underestimated. The assessment of the current 3D STM provision in Section 8.2.2.2 reported that although the predicted ultimate strength of the specimen without side face reinforcement (IV-10) was relatively accurate, the failure mode was brittle and not desired. The research team concluded that the side face reinforcement can improve the structural safety of the drilled shaft footings. If side face reinforcement is under the requirement, the footing would fail brittlely and therefore, the concrete efficiency factor should be taken as a lower value. The concept is analogous to the case for lacking crack control reinforcement. Two criteria of side face reinforcement in AASHTO LRFD (2020) were assessed in the experimental program: 0.18% to control shrinkage and temperature effect (Article 5.10.6), and 0.30% to provide a minimal ductility by redistributing internal stresses (Article 5.8.2.6). The results indicated that the specimens with both 0.18 and 0.30% of side face reinforcement provided had comparable normalized ultimate capacities. From the experimental results, II-7 (0.30%) showed a slightly improved deformation capacity in the post-peak state. However, the numerical analysis did not exhibit clear sign of this improvement. In conclusion, the research team proposes using the minimum concrete efficiency factor (0.45) if the side face reinforcement ratio is smaller than 0.18%; otherwise, the efficiency factor can remain the same as the current provision.

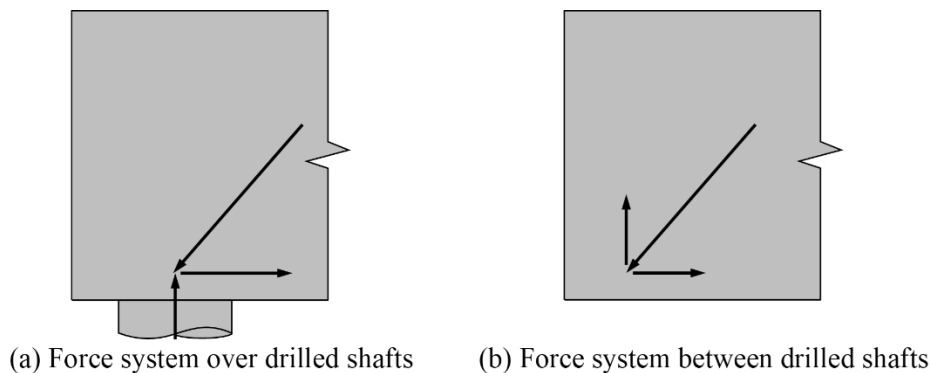


Figure 8.16 Force system in a drilled shaft footing (Clarke, 1973)

- **Summary**

This study proposes to refine the nodal strength at all faces of drilled shaft footings by 3D STM through application of Eq. (8.10):

$$P_{n,n} = f_{cu}A_{cn} \quad \text{Eq. (8.10)}$$

where:

$P_{n,n}$ = nominal resistance of a node face [kip]

f_{cu} = limiting compressive stress at the node face, taken as mvf'_c [ksi]

m = confinement modification factor, taken as $\sqrt{A_2/A_1} \leq 3.0$ and 2.0 as defined in Article 5.6.5 for CCC node and other node types (CCT and CTT), respectively

v = the minimum concrete efficient factor (0.45) if side face reinforcement requirement (0.18%) is not satisfied in accordance with Article 5.10.6
 = concrete efficiency factor as shown in Table 5.8.2.5.3a-1 if side face reinforcement requirement (0.18%) is satisfied in accordance with Article 5.10.6

Table 5.8.2.5.3a-1—Efficiency Factors for Nodes with Crack Control Reinforcement (AASHTO LRFD, 2020)

Face	Node Type		
	CCC	CCT	CTT
Bearing Face	0.85	0.70	$0.85 - \frac{f'_c}{20 \text{ ksi}}$ $0.45 \leq v \leq 0.65$
Back Face			
Strut-to-Node Interface	$0.85 - \frac{f'_c}{20 \text{ ksi}}$ $0.45 \leq v \leq 0.65$		

f'_c = compressive strength of concrete for use in design [ksi]

A_{cn} = effective cross-sectional area of the node faces as specified in Article 5.8.2.5.2; and Figure 8.10, Figure 8.12, and Figure 8.14 for strut-to-node interface [in.²]

8.3.1.4. Anchorage for Ties

- **Bottom Mat Reinforcement**

The research team suggests the available development length by using the proposed 3D nodal geometry in this section. Similar to the approach using the extended nodal zone to define the critical section based on 2D STM as depicted in Figure 8.2-(a), Figure 8.17-(b) visualizes the extended nodal zone in the 3D STM on the plane parallel to the tie, as specified in Figure 8.17-(a). The critical section on the plane of the strut can be defined as the point where the tie centroid intersects with the extended nodal zone. With the defined extended nodal zone, the available development length can be calculated using Eq. (8.11) based on geometry. The

reinforcing bars are considered sufficiently developed if available development length by Eq. (8.11) is greater than the required development length.

$$l_{ad} = c_b / \tan \theta_{s,proj} + D'_{DS}/2 + D_{DS}/2 + OH - c \quad \text{Eq. (8.11)}$$

where:

- l_{ad} = available development length [in.]
- c_b = distance from bottom surface to the centroid of bottom mat reinforcement [in.]
- $\theta_{s,proj}$ = projected strut angle on the plane parallel to ties [degrees]
- D'_{DS} = length of the equivalent square drilled shaft [in.]
- D_{DS} = diameter of the drilled shaft [in.]
- OH = edge distance (the minimum distance from the edge of drilled shaft to the closest surface) [in.]
- c = clear cover between bottom mat reinforcement and the side face [in.]

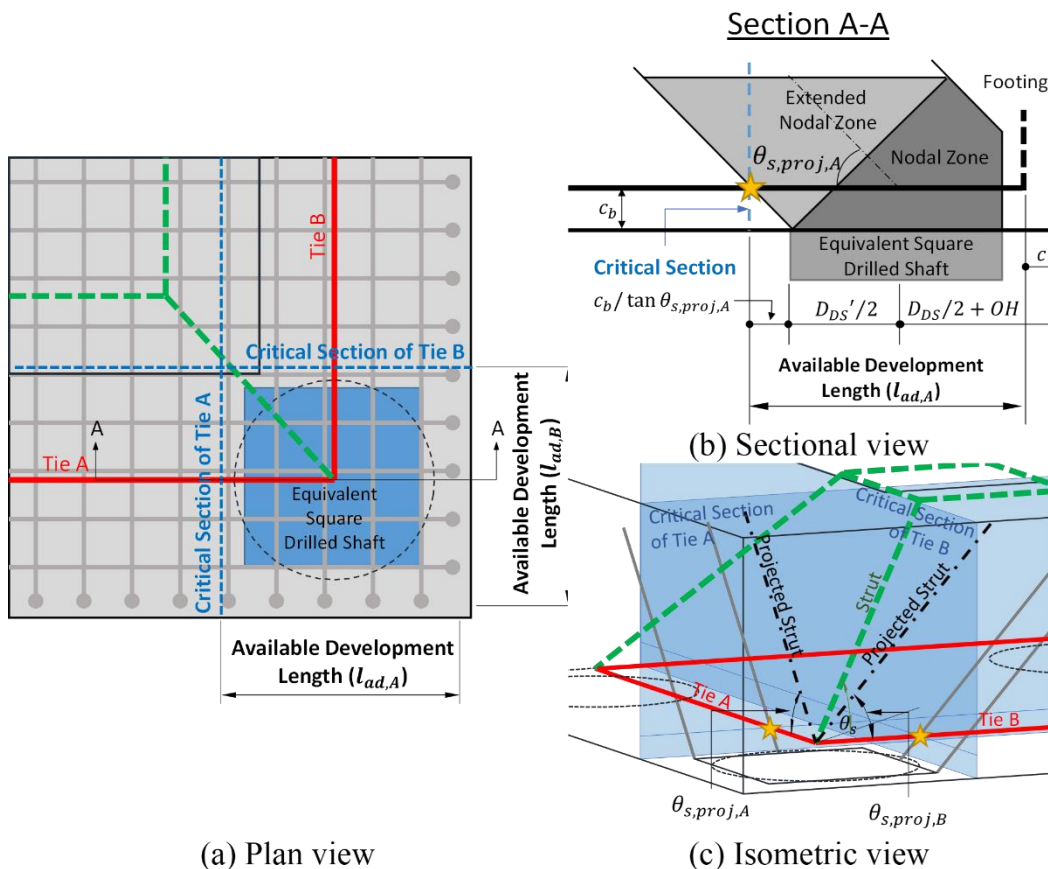


Figure 8.17 Proposed available length for anchorage of bottom mat reinforcement in drilled shaft footings

- *Column Reinforcement (Phase II: Non-uniform Compression in Shafts)*

Different from the suggestions for the horizontal ties, the available development length for the vertical column reinforcement is not determined using the corresponding nodal geometry, given the smeared nature of the bottom node of the vertical tie. Instead, the critical section for the column reinforcement can be defined from a large compression field bounded by diagonal struts flowing down to the drilled shafts. Even though the diagonal struts do not actually intersect the column tie elements, the large compression field serves the same role as the extended nodal zone.

Therefore, the critical section of the column reinforcement can be defined as the intersection of the diagonal struts and the column ties in the 3D STM viewed from its side view, as shown in Figure 8.18. Based on the critical section, the calculation for the available length of the column reinforcement is provided in Eq. (8.12). For constructability, the column reinforcement is assumed to be placed above the bottom mat reinforcement.

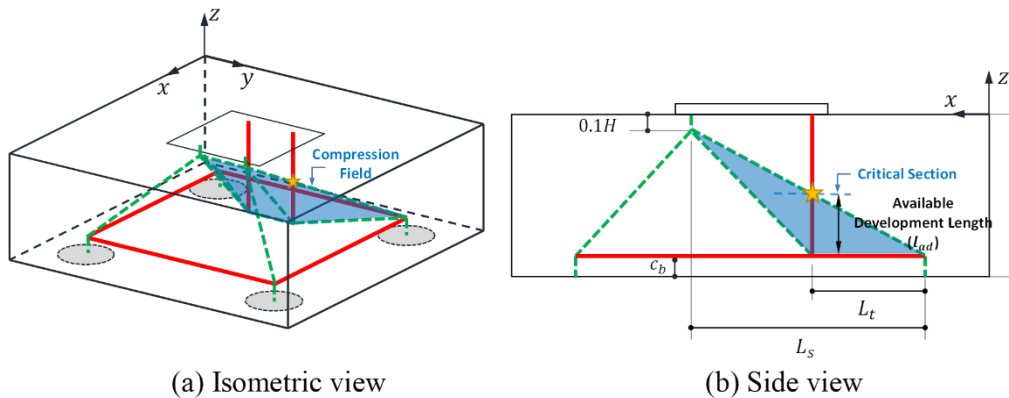


Figure 8.18 Proposed available length for anchorage of column reinforcement in drilled shaft footings (Phase II)

$$l_{ad} = \left(\frac{L_t}{L_s}\right) (0.9H - c_b) - (d_{b,bu}) \quad \text{Eq. (8.12)}$$

where:

- l_{ad} = available development length [in.]
- L_t = projected distance from the axis of the vertical strut to the axis of the center of drilled shaft [in.]
- L_s = projected distance from the axis of the vertical tie to the axis of the center of drilled shaft [in.]
- H = footing height [in.]
- c_b = distance from bottom surface to the centroid of bottom mat reinforcement [in.]
- $d_{b,bu}$ = diameter of upper layer bottom mat reinforcement [in.]

- **Drilled Shaft/Column Reinforcement (Phase III: Tension-Compression in Shafts)**

The force transfer mechanism between the tie elements of the column and drilled shaft reinforcement resembles a non-contact lap splice behavior. Therefore, the research team assumed a compression stress field developed between the tie elements of the drilled shaft and column reinforcement in the 3D STM to define the critical sections of the drilled shaft and column reinforcement, as shown in Figure 8.19. The assumed stress field is determined by an inclination of 25 degrees of the stress field, which is equivalent to the minimum strut angle specified in AASHTO LRFD (2020). The available development length for the drilled shaft and column reinforcement is defined within the compressive stress zone as shown in Figure 8.19-(b), as expressed in Eq. (8.13). The column reinforcement is assumed to be placed above the bottom mat reinforcement, and the drilled shaft reinforcement is assumed to be able to extend up to the bottom layer of the top mat reinforcement.

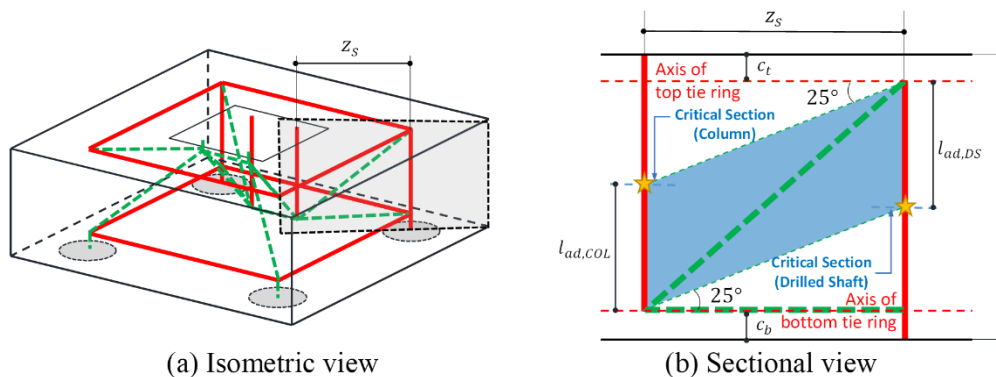


Figure 8.19 Proposed available lengths for anchorage of drilled shaft and column reinforcement in drilled shaft footings (Phase III)

$$\begin{aligned}
 l_{ad,COL} &= H - (c_b + c_t) - (d_{b,bu}) - z_s \tan 25^\circ \\
 l_{ad,DS} &= H - (c_b + c_t) - (d_{b,tl}) - z_s \tan 25^\circ
 \end{aligned}
 \tag{Eq. (8.13)}$$

where:

- $l_{ad,DS}$ = available development length of drilled shaft reinforcement [in.]
- $l_{ad,COL}$ = available development length of column reinforcement [in.]
- H = footing height [in.]
- c_b = distance from bottom surface to the centroid of bottom mat reinforcement [in.]
- c_t = distance from top surface to the centroid of top mat reinforcement [in.]
- $d_{b,bu}$ = diameter of upper layer bottom mat reinforcement [in.]
- $d_{b,tl}$ = diameter of lower layer top mat reinforcement [in.]
- z_s = aligned distance between the axis of the column and drilled shaft tie element [in.]

8.3.2. Assessment of Proposed 3D STM

8.3.2.1. 3D STM for Drilled Shaft Footings

The ultimate capacity ratios of footing test specimens in the evaluation database, based on the proposed 3D STM of this study, are plotted in the histogram shown in Figure 8.20. Detailed calculations of the evaluation database are summarized in Appendix H.

Predicted ultimate capacities of all footing specimens in the evaluation database are conservative, with the exception of two. Even though two cases were predicted unconservatively (0.92 and 0.97), the predictions of two cases had an acceptable margin of safety since the ratios of two cases were greater than the resistance factor (ϕ) for tension failure (0.9) or compression failure (0.7) in accordance with Article 5.5.4.2 of AASHTO LRFD (2020). The strength ratios range from 0.92 from 1.84 with the average being 1.45, as summarized in Table 8.4 and Figure 8.20. The average and range of ultimate capacity ratios improve significantly compared to the recommendation of Williams et al. (2012). The maximum ultimate capacity ratio improved from 2.77 for Williams et al. (2012) to 1.84 for the current guidelines, and an excessively conservative cases with an ultimate ratio greater than 2.0 were eliminated altogether. Moreover, the coefficient of variation (COV) reduced from 0.20 to 0.17, which means that data were less scattered. The most conservative prediction obtained with the new recommendations is for specimen II-3, due to the discrepancy between the experimental result and 3D STM prediction for the anchorage level of bottom ties, as described in Section 8.2.2.2. According to the experimental result described in Chapter 4, 17 out of 20 measurement locations of bottom mat reinforcing bars in the vicinity of drilled shafts reached or converged

to yielding condition (90% of the yield strain) and no signs of bond-related issues were observed, which means ties were sufficiently anchored. On the other hand, 3D STM predicted that ties in specimen II-3 were not fully developed at the critical section. Consequently, measured load-carrying capacity was much larger than the prediction based on the proposed 3D STM. If it were assumed that ties were fully developed, the ultimate capacity ratio would become 0.98.

Table 8.4 Statistical data of predicted ultimate capacities

Recommendation	Min.	Max.	Mean	COV	Unconservative Cases	Excessive Conservative Cases (>2.0)
Williams et al. (2012)	1.22	2.77	1.97	0.20	0%	45%
Present Study	0.92	1.84	1.44	0.17	3%	0%

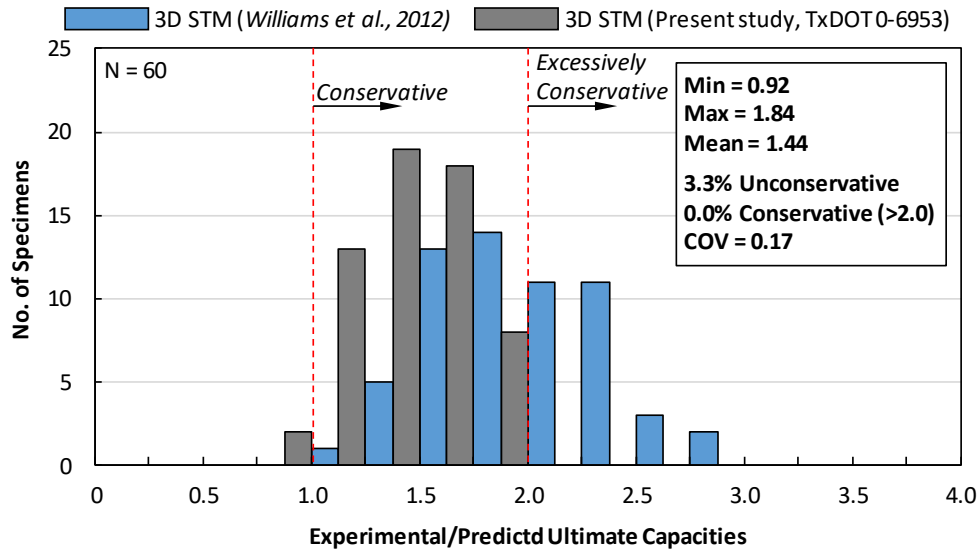


Figure 8.20 Distribution of ultimate capacity ratios for the evaluation database

Table 8.5 summarizes the controlling failure mechanisms obtained using the recommendations of Williams et al. (2012) and those obtained with the new recommendations. The predicted ultimate loads of past footing specimens with a grid layout of the bottom mat reinforcement increase due to the proposed proportion ties, such that the total amount of steel contains all bottom mat reinforcing bars. Based on the proposed 3D STM, tie yielding, regardless of grid or banded layout, is still the most common controlling failure mechanism for previous footing specimens since relatively lower bottom mat reinforcement, 0.29% on average, was provided, as shown in Figure 8.3. Note that this average ratio is significantly lower than current practices in Texas (0.49% on average) according to Chapter 3. All but three specimens are predicted to fail by tie yielding when using the

recommendation of Williams et al. (2012). Failure in these three cases is predicted to be controlled by the bearing stress limit. Those specimens had lower strut inclination (< 1.7) or the smallest shaft diameter. When using the recommendations of the present study, 10 specimens out of 60 are not predicted to fail by tie yielding. In this case, the controlling failure mechanism of the six specimens in this study that had a greater bottom mat reinforcement ratio is the nodal capacity at the strut-to-node interface at the CTT node, where the node is located above drilled shaft. The strength of the remaining four cases is predicted to be governed by the failure of the back face at the CCC node. The minimum concrete efficiency factor, 0.45, was applied since the side face reinforcement ratio was less than the requirement, 0.18%, which resulted in a lower concrete compressive stress limit and lower nodal capacity at the back face of the CCC node beneath the column. This result was observed for specimens with relatively higher reinforcement ratio than average and no satisfaction of the side reinforcement requirement.

In conclusion, the proposed 3D STM improved both accuracy and consistency of the calculation. Furthermore, controlling failure mechanisms were predicted more consistently with the experimental results.

Table 8.5 Controlling failure mechanism by 3D STM

Controlling failure mechanism		Williams et al. (2012)	Present Study
Tie yielding		57	50
CCC Node (below the column)	Bearing face	0	0
	Back face	N/A	4
	Strut-to-node interface	N/A	0
CTT Node (above the shaft)	Bearing face	3	0
	Strut-to-node interface	N/A	6

8.3.2.2. Data Analysis with Strength Models in Current AASHTO LRFD

Experimental databases comprising shear-critical loading tests for panels, reinforced concrete (RC) beams, and prestressed concrete (PC) beams have been used to assess the accuracy of the simplified modified compression field theory (MCFT) as well as that of STM for design of deep beams.

Hawkins et al. (2005) reported a simplified shear design method for RC and PC members in NCHRP Report 549. The authors selected 64 RC beams and 83 PC beams and compared the strength ratios predicted from the simplified MCFT method, which is equivalent to the method used in CSA A23.3 (2004), the current AASHTO LRFD (2020), AASHTO Standard Specifications for Highway Bridges (1996) approach, AASHTO LRFD (2004) approach. The simplified MCFT led to

a mean ratio of measured-to-predicted strength of 1.105 with a COV of 0.156 for RC beams and 1.245 with a COV of 0.134 for PC beams. When the same dataset was used to evaluate the MCFT method in accordance with the previous AASHTO LRFD (2004), which used the simple table for the parameters, the mean ratios were 1.214 and 1.227 for RC and PC members, respectively. The corresponding COVs were 0.179 for RC members and 0.145 for PC members. The researchers investigated the cases where the shear strength ratio was less than the resistance factor, ϕ , taken as 0.9 for shear strength; in other words, the cases in which the design strength was lower than the experimental strength. The simplified MCFT resulted in 11.7% and 1.9% of unconservative predicted design strength for RC and PC members, respectively. The approach, which is in accordance with AASHTO LRFD (2004), provided unconservative predictions: 7.3% for RC members and 0.9% for PC members.

Bentz et al. (2006) performed database analysis using 102 test results in pure shear or shear combined with uniaxial stress loading conditions. The authors computed the predictions for three strength models—full MCFT, simplified MCFT, and the ACI approach. The shear strength ratio, V_{test}/V_{calc} , used in the simplified MCFT was 1.11 on average and ranged from 0.86 to 1.46 with a COV of 0.23. The computed design strengths were unconservative in two cases (2%), when the strength ratio was less than 0.9 (resistance factor).

Bircher et al. (2009) investigated the ultimate strength ratios, P_{test}/P_{calc} , of deep beam test specimens using six shear design procedures by examining 179 cases. The STM that the authors proposed was adopted in the current AASHTO LRFD provision. The minimum and maximum ultimate strength ratios from the proposed STM were 0.73 and 4.14, respectively. The ultimate strength ratio was 1.54 on average and the COV of the ratio was 0.28. The STM predicted that the strength was higher than that obtained experimentally (without including the resistance factor) in only one case (0.6%).

Nakamura et al. (2013) examined the shear strength ratios, V_{test}/V_{calc} , of PC test specimens using eight different shear design procedures. The authors investigated 171 tests after filtering. The shear strength ratios from the simplified MCFT method in AASHTO LRFD (2010) ranged from 0.98 to 3.11. The average and COV of shear strength ratio were 1.43 and 0.25, respectively. The computed shear strengths for 15 cases (8.8%) were predicted unconservatively when the resistance factor was not accounted for.

Bentz and Collins (2017) compared the shear strength of shear test specimens subjected to concentrated loads with the predictions obtained with the simplified MCFT. The researchers provided statistics data for two cases: 1) members without

stirrups and 2) members with stirrups. It is noted that the statistics value was based on the bottom half of the data because the predicted strengths of several tests were excessively conservative. For members without stirrups, the average was 1.18 and COV was 0.12. The test-to-predicted ratio for members with stirrups was 1.27 on average and 0.15 for COV. No information pertaining to the percentage of an unconservative predictions was provided.

8.3.2.3. Discussion and Conclusion

The research team performed database analysis using a simple method to get a sense of the level of safety associated with the proposed 3D STM method. Table 8.6 summarizes the statistics data of the strength ratios (SR) obtained with the design methods introduced in the previous section. All design procedures except the proposed 3D STM by the current research project were employed in previous or current version of AASHTO LRFD. By comparing each statistical data type reported in Table 8.6, the following observations can be made about the improvements to the accuracy and consistency of the footing capacity predictions achieved when using the proposed 3D STM guidelines:

- The mean shear strength ratio determined using simplified MCFT ranged from 1.11 to 1.43. For RC structures, the average ratio is 1.17 from four data sets using the simplified MCFT. The STM for deep beams provided a slightly higher value (1.54) than the simplified MCFT method did.
- When considering the evaluation database compiled in the present project, The mean and COV of the strength ratio of the proposed 3D STM (1.44 and 0.17) are more consistent with simplified MCFT and STM than the values generated using the recommendations proposed in TxDOT project 5-5253 (1.97 and 0.22).
- The mean strength ratio of the proposed 3D STM is similar to one obtained in Birrcher et al. (2009). As described in Birrcher et al. (2009), : “the experimental strength was approximately 1.5 times the strength calculated using the proposed provisions, which is appropriate for the scatter in deep beam shear strength.”
- When using the statistics values from this project’s Phase I testing results (13 specimens), the mean ratio and corresponding COV (1.19 and 0.21) obtained using the proposed 3D STM, as presented in Table 8.4, are more consistent with MCFT when compared to the statistic value provided in the evaluation database (1.44 and 0.17).

- The proposed method did not predict unconservative design capacities when considering the resistance factor, while the MCFT method did generate a limited number of unconservative predictions.

In conclusion, the proposed 3D STM for drilled shaft footings improves the accuracy of the prediction to an acceptable mean strength ratio while avoiding over-conservative designs, since the mean strength ratio decreases from 1.97 (from previous 3D STM recommendations) to 1.44 and the COV (0.17) is similar to COVs from the simplified MCFT according to the current AASHTO LRFD. There are also no predictions for which $P_{test} < \phi P_{calc}$; hence, these results provide an acceptable level of safety. Finally, the new 3D STM guidelines for drilled shaft footings will impact the current method minimally.

Table 8.6 Summary of statistics of SR

Researchers	Design Method	Structural Members	No. Tests	Mean	COV	% SR < ϕ
Hawkins et al. (2005)	MCFT (AASHTO 3 rd Ed.,2004)	RC beams	64	1.21	0.18	7.3
		PC beams	83	1.23	0.14	0.9
	Simplified MCFT	RC beams	64	1.11	0.16	11.7
		PC beams	83	1.25	0.13	1.9
Bentz et al. (2006)	Simplified MCFT	RC panels	102	1.11	0.13	2.0
Bentz and Collins (2017)	Simplified MCFT	RC beams (without stirrups)	740	1.18	0.12	-
		RC beams (with stirrups)	170	1.27	0.16	-
Nakamura et al. (2013)	Simplified MCFT	PC beams	171	1.43	0.25	-
Bircher et al. (2009) TxDOT 0-5253	STM	RC deep beams	179	1.54	0.28	-
Williams et al. (2012) TxDOT 5-5253-01	3D STM	RC drilled shaft footing	60	1.97	0.22	0.0
Present Study TxDOT 0-6953	PROPOSED 3D STM	RC drilled shaft footing	60	1.44	0.17	0.0

Note: %SR< ϕ : the percentage of cases in which the strength ratio is less than the resistance factor (0.9 for shear in RC and PC members, 0.9 for tension in STM, and 0.7 for compression in STM)

8.4. Design Example

8.4.1. Overview

This chapter presents the design example of a drilled shaft footing subjected to five general loading cases in current practice according to the 3D STM proposed by this study. The design target footing is identical to the footing used in Williams et al. (2012). The footing for the design example is square-shaped and has one single rectangular column and four drilled shafts. The drilled shaft footing example is designed according to the recommendation of this study. The first loading case is pure compression that resulted in uniform compression in shafts. The second through fourth loading cases are compression with varying uniaxial flexural loading. The last loading case is compression loading with biaxial flexural loading that leads to non-uniform compression in all drilled shafts. It is noted that the second and third loading cases were structured to match the design example of Williams et al. (2012). As a result, the design product can be compared with that of Williams et al. (2012) for two loading cases.

8.4.2. Design Task

8.4.2.1. Drilled Shaft Footing Geometry

As noted, the drilled shaft footing example has the same geometry as Williams et al. (2012) to facilitate comparison. Figure 8.21 shows the plan and side views of the drilled shaft footing example. The 16-foot square drilled shaft footing is 5 feet thick. Four drilled shafts with 4 feet diameter support the footing with a span of 10.50 feet. The column is a rectangle that is 7.50 by 6.25 feet. The footing and the column are doubly symmetric with respect to x - and y -axes.

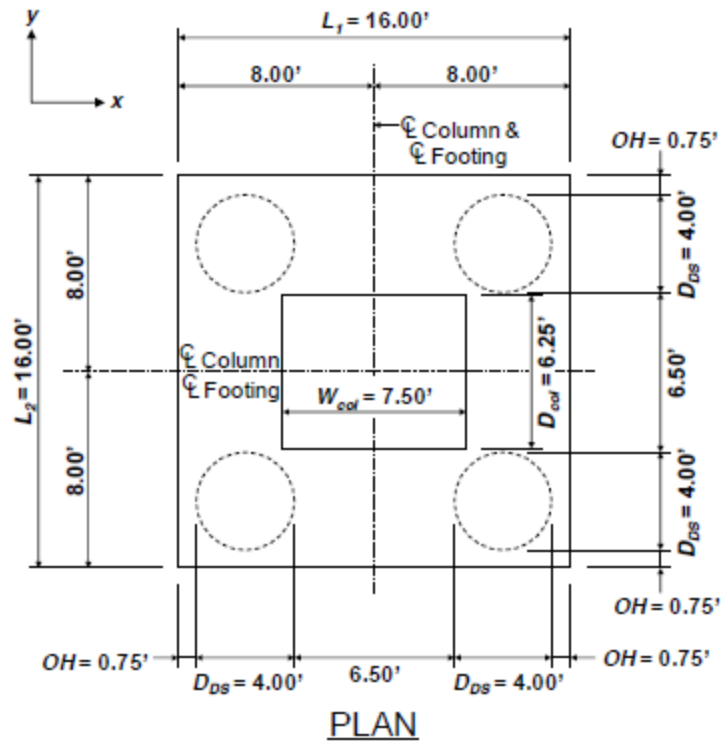
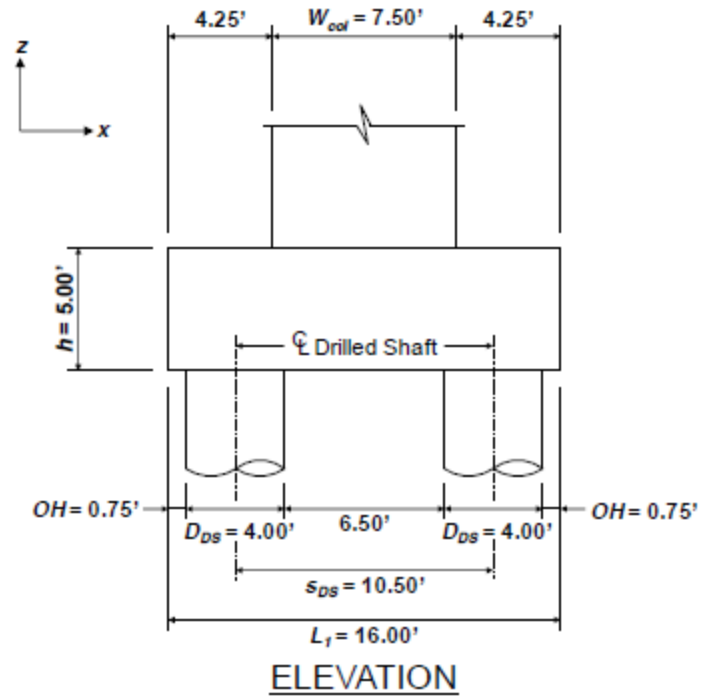


Figure 8.21 Geometry of the drilled shaft footing for the design example (Williams et al., 2012)

8.4.2.2. Load Cases

- *Load Case I: Pure axial compression*

The first loading condition is the case in which the column is subjected to axial compression only. The uniform compressive stress develops over the column section. The reactions of all drilled shafts will remain in the equal amounts of compression. Figure 8.22 shows the factored axial load for the first loading case.

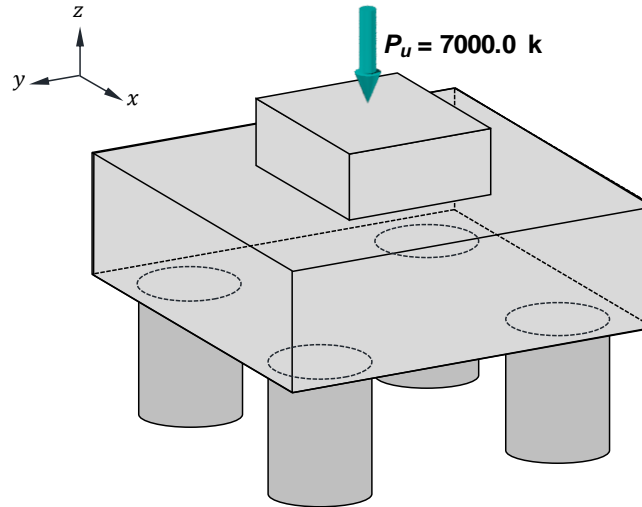


Figure 8.22 Factored load: Load Case I

- *Load Case II: Axial compression in combination with mild uniaxial flexural loading*

In Load Case II, the axial compression and mild uniaxial flexural loading about the strong axis (i.e., y-axis) applies to the column section. The factored axial and flexural loads for the second loading case are illustrated in Figure 8.23. The eccentricity of mild uniaxial flexural loading was determined so that the reaction distribution of $0.4P_u$ at one pair of shafts and $0.6P_u$ at the other pair of shafts is generated. As a result, the stress distribution of the column section will remain in compression over the entire section.

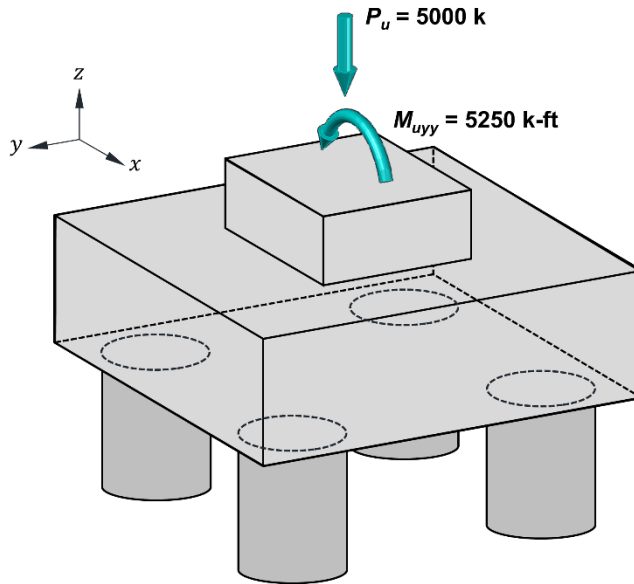


Figure 8.23 Factored load: Load Case II

- *Load Case III: Axial compression in combination with moderate uniaxial flexural loading*

Here the column is subjected to uniaxial flexural loading with greater eccentricity that generates the compression-tension linear stress distribution over the column section. This loading condition results in non-uniform compression of two groups of drilled shafts. This loading case is equivalent with the first load case of Williams et al. (2012). Figure 8.24 depicts the factored load and moment for Load Case III.

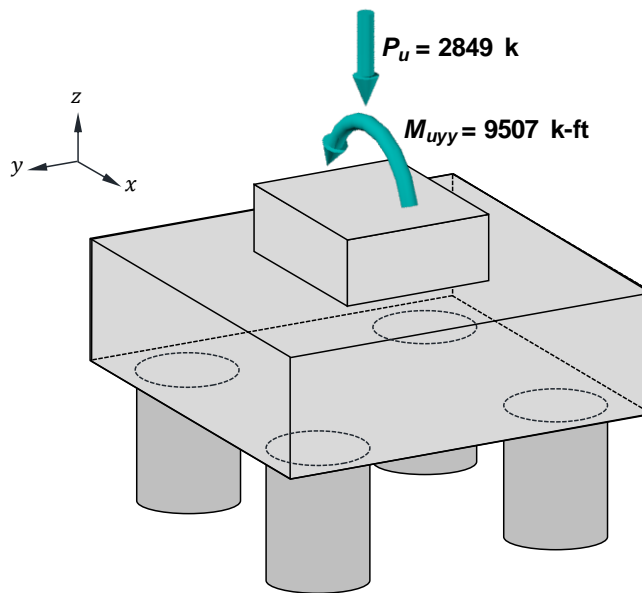


Figure 8.24 Factored load: Load Case III

- *Load Case IV: Axial compression in combination with severe uniaxial flexural loading*

Load Case IV is identical to the second loading case of Williams et al. (2012). In this loading case, the eccentric load is located outside of the column section and two of the drilled shafts react in tension. The factored load for the fourth loading case is shown in Figure 8.25.

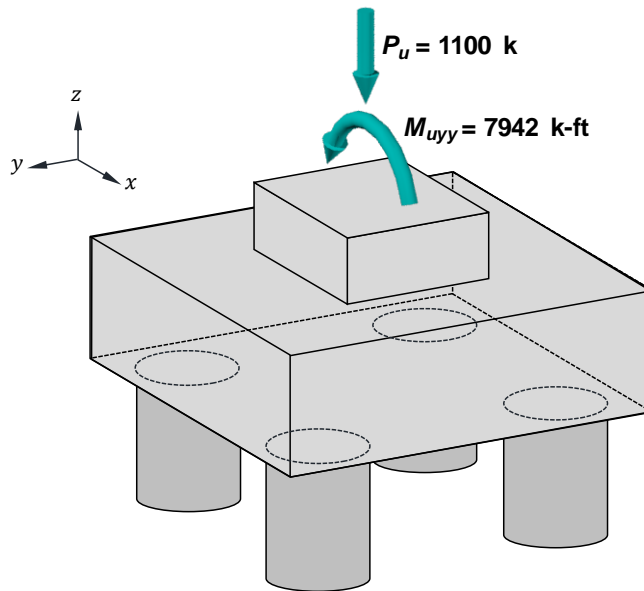


Figure 8.25 Factored load: Load Case IV

- *Load Case V: Axial compression in combination with mild biaxial flexural loading*

Mild biaxial flexural loading results in non-uniform compression in all drilled shafts. The column section will remain in compression, but the distribution will be more complicated than in the uniaxial flexural loading case. Figure 8.26 illustrates the factored axial load and flexural load on both axes for the last loading case.

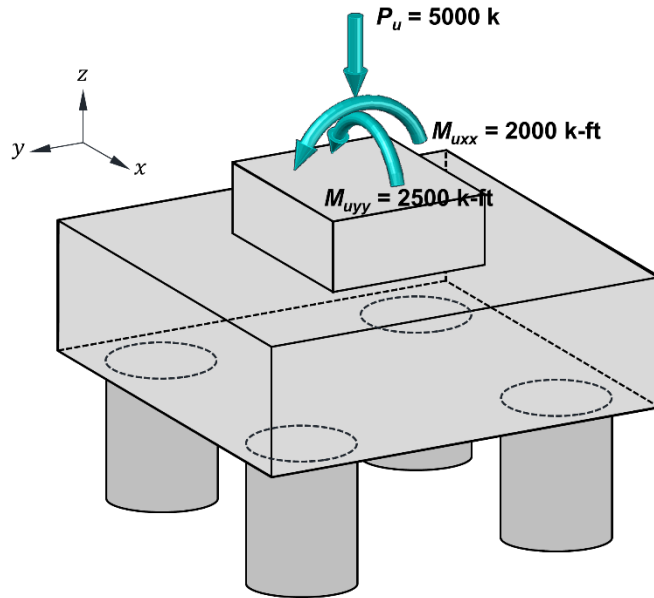


Figure 8.26 Factored load: Load Case V

8.4.2.3. Material Properties

A concrete compressive strength, f'_c , of 3.6 ksi and yield strength of reinforcement, f_y , of 60 ksi are used in the design example. These meet the minimum requirement of concrete and reinforcement for structural purposes in accordance with AASHTO LRFD (2020) and TxDOT specifications. The No. 11 bars that Williams et al. (2012) used for the design example will be used for bottom mat reinforcement to compare the final design product.

8.4.2.4. Design Procedure

The general STM design procedure introduced in Section 8.2.1, listed below, is applied to design the footing examples. The detail calculation follows the 3D STM recommendation in Section 8.3.

- Step 1: Determine loads
- Step 2: Analyze structural components
- Step 3: Develop strut-and-tie model
- Step 4: Proportion ties
- Step 5: Perform strength checks
- Step 6: Proportion the shrinkage and temperature reinforcement
- Step 7: Provide necessary anchorage for ties

8.4.3. Design Calculations: Load Case I

8.4.3.1. Step 1: Determine the Loads

The same stress level as illustrated in Figure 8.27 is distributed over the column cross section against pure compression loading. It can be assumed that the loading on the column transferred through the footing to four drilled shafts equally due to the double symmetric geometry. Therefore, the load can be divided into four identical compressive loading components (pushing downward on the footing) applied at the center of each quadrant, as shown in Figure 8.27.

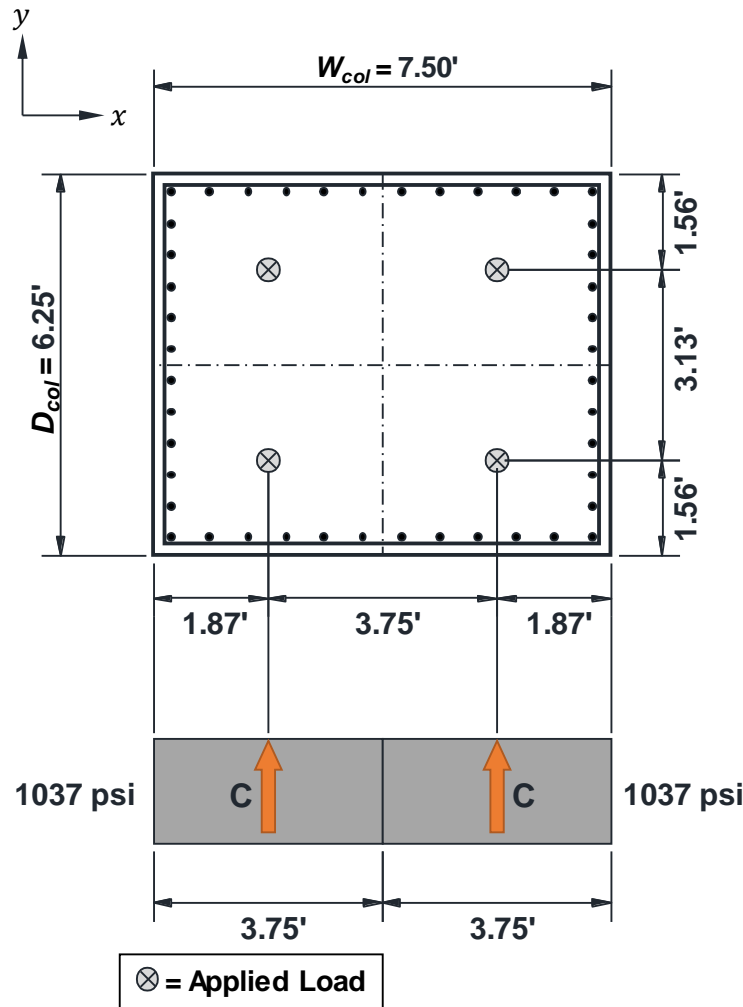


Figure 8.27 Stress distribution over the column section: Load Case I

8.4.3.2. Step 2: Analyze Structural Component

The reaction force of each drilled shaft can be easily calculated by dividing the total reaction force equally, as described in Eq. (8.14). Figure 8.28 shows the calculation result of the structural analysis.

$$R_1 = R_2 = R_3 = R_4 = \frac{P_u}{4} = \frac{7000 \text{ kip}}{4} = 1750.0 \text{ kip (Compression)} \quad \text{Eq. (8.14)}$$

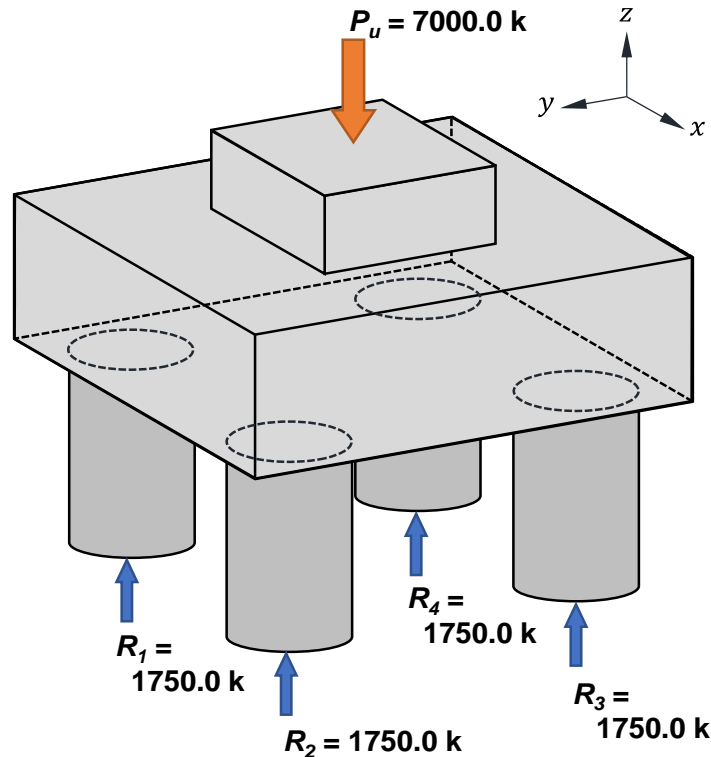


Figure 8.28 Applied loading and reaction forces: Load Case I

8.4.3.3. Step 3: Develop Strut-and-Tie Model

The procedure of the development of 3D strut-and-tie model in accordance with Section 8.3.1.1 is as follows:

- The nodes beneath the column are located 0.1 times height below the centroid of loading components as specified in Step 1 (Nodes A through D).
- The four nodes above the drilled shafts are positioned at the center of each drilled shaft at the elevation of the centroid of tension reinforcement (Nodes E through H).
- The bottom horizontal ties that represent the bottom mat reinforcement are connected between each node above the drilled shaft (Ties EF, FG, GH, and EH).
- Diagonal struts are developed between nodes below the column and above drilled shafts for each quadrant (Struts AE, BF, CG, and DH).

- Strut rings at the vertical position of the nodes beneath the column can be determined to satisfy the requirement of the equilibrium (Struts AB, BC, CD, and DA).

Tie forces and strut forces, illustrated in Figure 8.29 and Figure 8.30, can be computed by the equilibrium of each axis at each node.

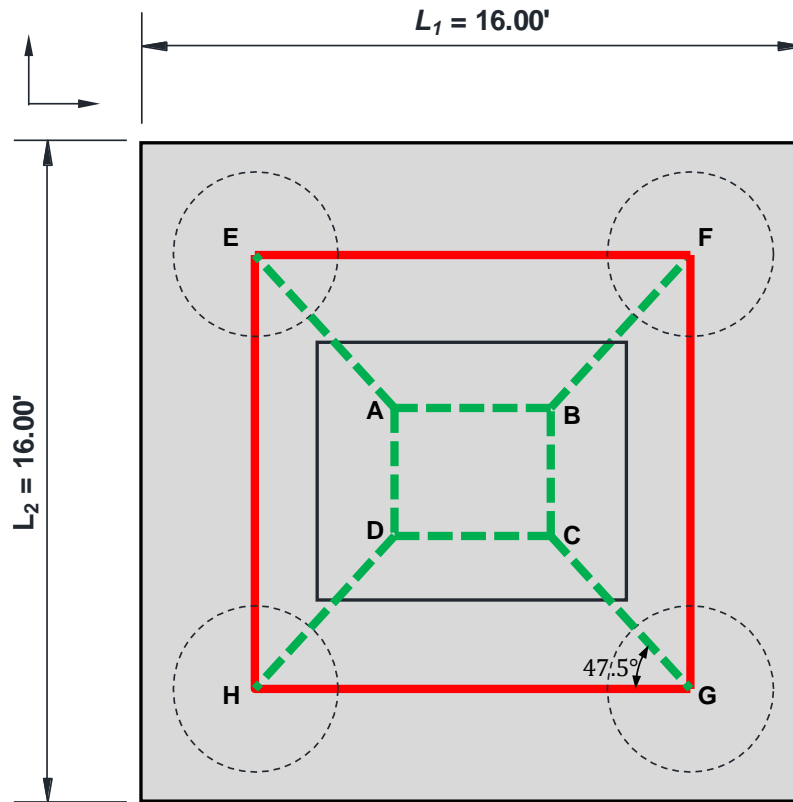


Figure 8.29 3D Strut-and-tie model in plan view: Load Case I

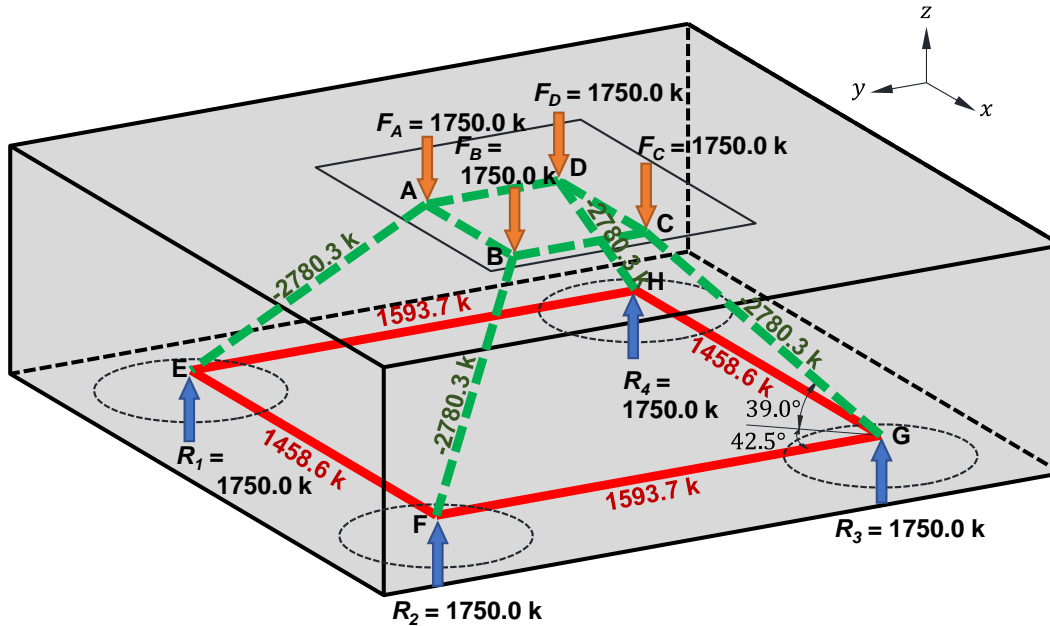


Figure 8.30 3D Strut-and-tie model in axonometric view: Load Case I

8.4.3.4. Step 4: Proportion Ties

The required total area of bottom mat horizontal reinforcement is calculated from horizontal tie forces provided in Figure 8.30. As mentioned in the above section, No. 11 bars ($A_s = 1.56 \text{ in.}^2$) are used for the bottom mat reinforcement.

- Ties EF and GH

Factored tie force:	$F_{u,tie} = 1458.6 \text{ kip}$
Tie capacity:	$\phi \cdot f_y \cdot A_{st} = F_{u,tie}$
	$(0.9)(60 \text{ ksi})A_{st} = 1458.6 \text{ kip}$
	$A_{st} = 27.01 \text{ in.}^2$
Number of No. 11 bars required:	$27.01 \text{ in.}^2 / 1.56 \text{ in.}^2 = 18 \text{ bars}$

- Ties EH and FG

Factored tie force:	$F_{u,tie} = 1593.7 \text{ kip}$
Tie capacity:	$\phi \cdot f_y \cdot A_{st} = F_{u,tie}$
	$(0.9)(60 \text{ ksi})A_{st} = 1593.7 \text{ kip}$
	$A_{st} = 29.51 \text{ in.}^2$
Number of No. 11 bars required:	$29.51 \text{ in.}^2 / 1.56 \text{ in.}^2 = 19 \text{ bars}$

The same number of bars (19 bars) is provided for each tie for practical purposes. As proposed in Section 8.3.1.2, the reinforcement will be distributed uniformly

instead of being concentrated over the drilled shaft. Therefore, 38 bars with 5-in. spacing in both orthogonal directions were used for bottom mat reinforcement.

8.4.3.5. Step 5: Perform Strength Checks

In lieu of the conservative approach to check nodal strength at bearing face in the previous recommendations (Section 8.3.1.3), this study performs the refined nodal strength checks at all faces. The recommendation of this study led to considering the triaxial confinement factor, to update the concrete efficiency factor and determine 3D nodal geometry. In accordance with Section 8.3.1.3, 3D nodal geometries of Nodes A (CCC node) and E (CTT node) are developed and nodal strengths at each face are checked below.

- Nodes A through D (CCC node)

The dimensions and forces at Nodes A through D are identical. At first, the calculation of bearing area at the nodes is necessary to define the detailed 3D nodal geometry. The bearing area of the nodes, as indicated by the shaded regions on the column section in Figure 8.27, is:

$$A_{cn,bearing} = \frac{W_{col} D_{col}}{2} = \left(\frac{7.5 \text{ ft}}{2}\right) \left(\frac{6.25 \text{ ft}}{2}\right) = 11.72 \text{ ft}^2 = 1687.5 \text{ in.}^2$$

The length of the equivalent square bearing face, $L'_{cn,b}$, is:

$$L'_{cn,b} = \sqrt{A_{cn,bearing}} = \frac{\sqrt{W_{col} D_{col}}}{2} = 41.1 \text{ in.}$$

In Load Case I, the axes of forces at two back faces are not perpendicular to the normal axis of the back face of 3D nodal geometry, as shown in Figure 8.30. Consequently, the resolving force from two forces at two orthogonal back faces is applied in the normal direction of the back face at the 3D normal geometry (Figure 8.31). Reflecting the recommendation made in Section 8.3.1.3, Figure 8.32 illustrates nodes A through D in three dimensions, including the force at each face, so that nodal capacities at each face can be checked.

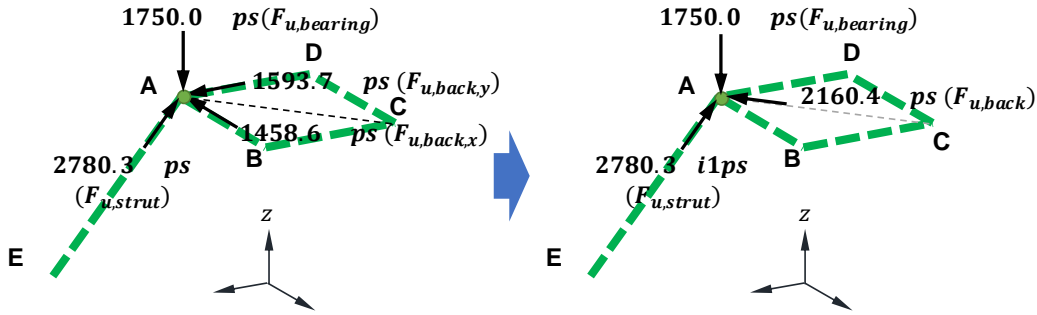
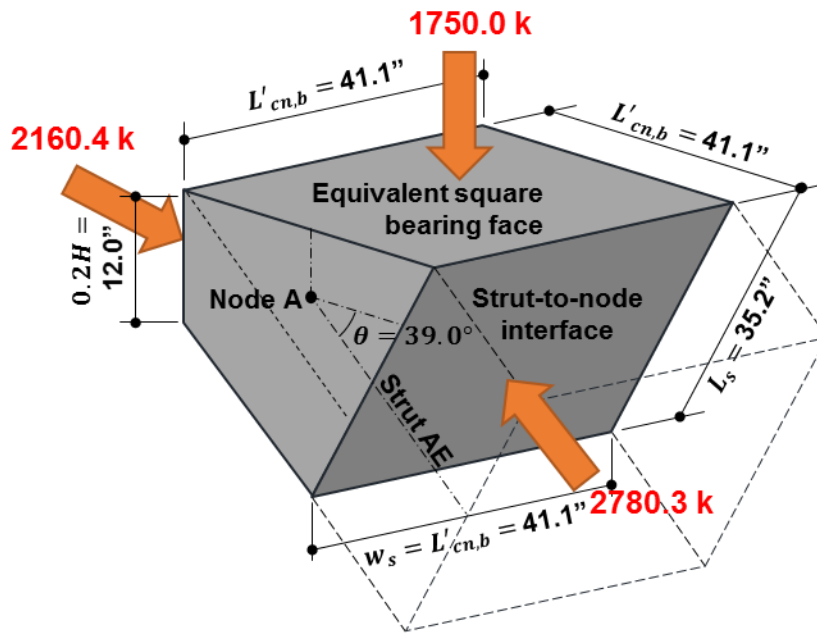


Figure 8.31 Resolving the force at Node s A through D (CCC node)



$$\begin{aligned}
 L_s &= L'_{cn,b} \sin \theta + 0.2H \cos \theta \\
 &= 41.1'' \sin 39.0^\circ + 0.2 \times 60'' \cos 39.0^\circ \\
 &= 25.86'' + 9.32'' = 35.2''
 \end{aligned}$$

Figure 8.32 Details of 3D nodal geometry at Nodes A through D

The triaxial confinement factor is calculated from the equivalent square area of entire column section as specified in Figure 8.33.

$$m = \sqrt{\frac{A_2}{A_1}} = \sqrt{\frac{16.00 \times 16.00}{6.85 \times 6.85}} = 2.34 \leq 3 \quad \therefore \text{se } m = 2.34$$

The concrete efficiency factor, ν , is determined in accordance with Table 5.8.2.5.3a-1 of AASHTO LRFD (2020). It should be noted that the concrete efficiency factor does not have to decrease to 0.45 because side face reinforcement of more than 0.18% will be provided.

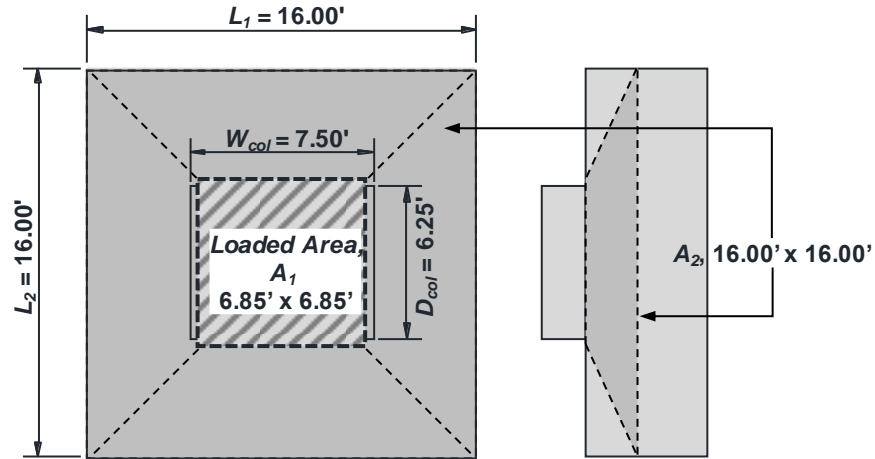


Figure 8.33 Determination of the confinement modification factor, m , for Nodes A through D

o NODAL STRENGTH AT BEARING FACE

Factored load: $F_{u,bearing} = 1750.0 \text{ kip}$

Concrete efficiency factor: $\nu = 0.85$

Concrete capacity: $f_{cu} = m \cdot \nu \cdot f'_c = (2.34)(0.85)(3.6 \text{ ksi}) = 7.16 \text{ ksi}$

Nodal capacity: $\phi F_{n,bearing} = \phi f_{cu} A_{cn,bearing} = (0.7)(7.16 \text{ ksi})(1687.5 \text{ in.}^2) = 8458.2 \text{ kip} > 1750.0 \text{ kip} \quad \mathbf{OK}$

o NODAL STRENGTH AT BACK FACE

Factored load: $F_{u,back} = \sqrt{1458.6^2 + 1593.7^2} = 2160.4 \text{ kip}$

Effective area: $A_{cn,back} = L'_{cn,b} \cdot 0.2H = 493.0 \text{ in.}^2$

Concrete efficiency factor: $\nu = 0.85$

Concrete capacity: $f_{cu} = m \cdot \nu \cdot f'_c = (2.34)(0.85)(3.6 \text{ ksi}) = 7.16 \text{ ksi}$

Nodal capacity: $\phi F_{n,back} = \phi f_{cu} A_{cn,back} = (0.7)(7.16 \text{ ksi})(493.0 \text{ in.}^2) = 2470.8 \text{ kip} > 2160.4 \text{ kip} \quad \mathbf{OK}$

o NODAL STRENGTH AT STRUT-TO-NODE INTERFACE

Factored load:	$F_{u,SNI} = 2780.3 \text{ kip}$
Effective area:	$A_{cn,SNI} = w_s \cdot L_S = (41.1 \text{ in.})(35.2 \text{ in.})$ $= 1446.7 \text{ in.}^2$
Concrete efficiency factor:	$\nu = 0.85 - \frac{f'_c}{20 \text{ ksi}} = 0.85 - \frac{3.6 \text{ ksi}}{20 \text{ ksi}}$ $= 0.67 > 0.65 \quad \therefore \text{ se } \nu = 0.65$
Concrete capacity:	$f_{cu} = m \cdot \nu \cdot f'_c = (2.34)(0.65)(3.6 \text{ ksi})$ $= 5.48 \text{ ksi}$
Nodal capacity:	$\phi F_{n,SNI} = \phi f_{cu} A_{cn,SNI}$ $= (0.7)(5.48 \text{ ksi})(1446.7 \text{ in.}^2)$ $= 5549.5 \text{ kip} > 2780.3 \text{ kip} \quad \mathbf{OK}$

- Nodes E through H (CTT node)

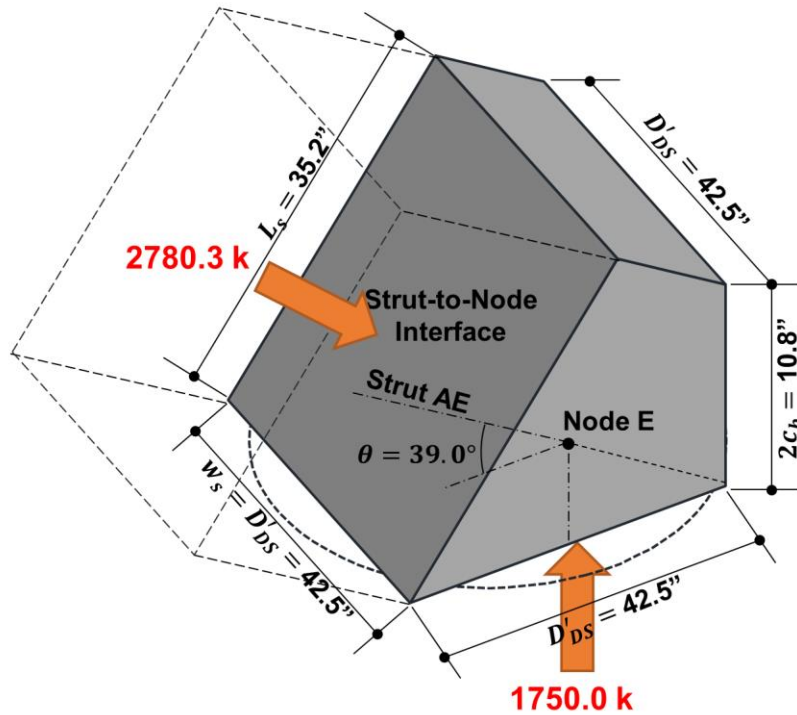
The dimensions and forces at Nodes E through H are identical. At first, the calculation of bearing area at the nodes is necessary to define the detailed 3D nodal geometry. The bearing area of the nodes is:

$$A_{cn,bearing} = \frac{\pi}{4} (D_{DS})^2 = \frac{\pi}{4} (4 \text{ ft})^2 = 12.57 \text{ ft}^2 = 1809.6 \text{ in.}^2$$

In lieu of a circular-shaped bearing face, the equivalent square-shaped bearing face is considered to define the 3D nodal geometry. The length of the equivalent square bearing face, D'_{DS} , is:

$$D'_{DS} = \sqrt{A_{cn,bearing}} = \frac{\sqrt{\pi} \cdot D_{DS}}{2} = 42.5 \text{ in.}$$

Figure 8.34 illustrates nodes E through H in three dimensions, in keeping with this study's recommendations.



$$\begin{aligned}
 L_s &= D'_{DS} \sin \theta + 2c_b \cos \theta \\
 &= 42.5'' \sin 39.0^\circ + 2 \times (4'' + 1.41'') \cos 39.0^\circ \\
 &= 26.78'' + 8.41'' = 35.2''
 \end{aligned}$$

Figure 8.34 Details of 3D nodal geometry at Nodes E through H

The triaxial confinement factor is calculated from the dimension as specified in Figure 8.35.

$$m = \sqrt{\frac{A_2}{A_1}} = \sqrt{\frac{5.50 \times 5.50}{3.54 \times 3.54}} = 1.55 \leq 2 \quad \therefore \text{se } m = 1.55$$

The concrete efficiency factor, ν , is determined in accordance with Table 5.8.2.5.3a-1 of AASHTO LRFD (2020). It should be noted that the concrete efficiency factor does not have to decrease to 0.45 because side face reinforcement of more than 0.18% will be provided. For the CTT node, the concrete efficiency factors at each face are equivalent, as in the following calculation:

$$\nu = 0.85 - f'_c / 20 \text{ ksi} = 0.85 - 3.6 \text{ ksi} / 20 \text{ ksi} = 0.67 > 0.65 \quad \therefore \text{se } \nu = 0.65$$

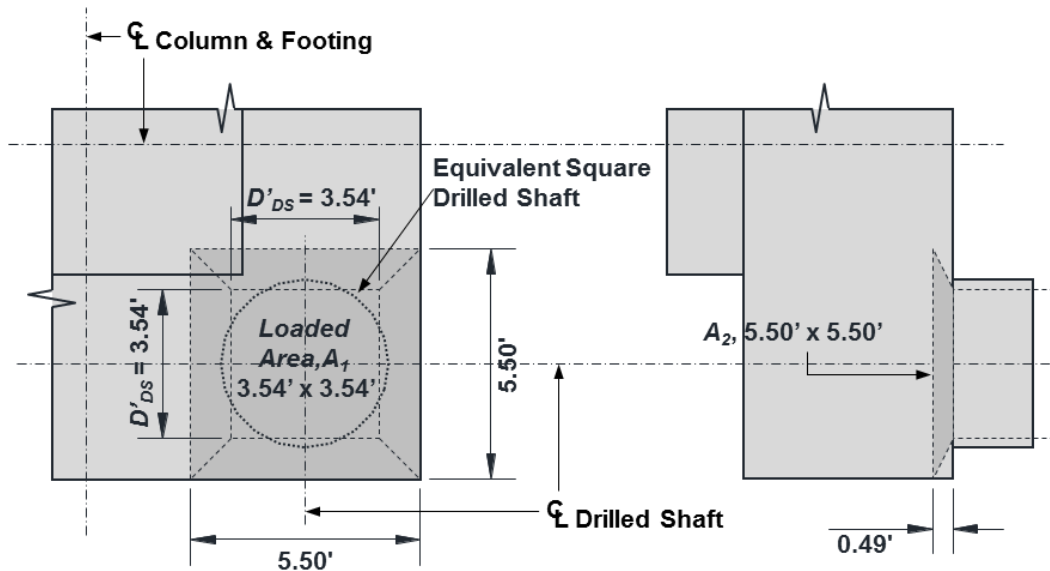


Figure 8.35 Determination of the confinement modification factor, m , for Nodes E through H

Note that the nodal strength checks at back faces are not necessary since an adequate development length that satisfies the anchorage requirement is provided in this example.

o NODAL STRENGTH AT BEARING FACE

Factored load: $F_{u,bearing} = 1750.0 \text{ kip}$

Concrete efficiency factor: $\nu = 0.65$

Concrete capacity: $f_{cu} = m \cdot \nu \cdot f'_c = (1.55)(0.65)(3.6 \text{ ksi}) = 3.63 \text{ ksi}$

Nodal capacity: $\phi F_{n,bearing} = \phi f_{cu} A_{cn,bearing} = (0.7)(3.63 \text{ ksi})(1809.6 \text{ in.}^2) = 4598.8 \text{ kip} > 1750.0 \text{ kip} \quad \mathbf{OK}$

o NODAL STRENGTH AT STRUT-TO-NODE INTERFACE

Factored load: $F_{u,SNI} = 2780.3 \text{ kip}$

Effective area: $A_{cn,SNI} = w_s \cdot L_s = (42.5 \text{ in.})(35.2 \text{ in.}) = 1496.0 \text{ in.}^2$

Concrete capacity: $f_{cu} = m \cdot \nu \cdot f'_c = (1.55)(0.65)(3.6 \text{ ksi}) = 3.63 \text{ ksi}$

Nodal capacity: $\phi F_{n,SNI} = \phi f_{cu} A_{cn,SNI} = (0.7)(3.63 \text{ ksi})(1496.0 \text{ in.}^2) = 3801.3 \text{ kip} > 2780.3 \text{ kip} \quad \mathbf{OK}$

Therefore, the nodal capacities of Nodes E through H satisfy the proposed strength check procedure.

8.4.3.6. Step 6: Proportion Shrinkage and Temperature Reinforcement

The least width in both directions is 192 inches and the least thickness is 60 in. The required amount for shrinkage and temperature reinforcement for this footing is $0.50 \text{ in.}^2/\text{ft.}$ for each face and in each direction, as the following calculation indicates.

$$A_s \geq \frac{1.30bh}{2(b+h)f_y} = \frac{1.30(192 \text{ in.})(60 \text{ in.})}{2(192 \text{ in.} + 60 \text{ in.})(60 \text{ ksi})} = 0.50 \text{ in.}^2/\text{ft.}$$

To determine the spacing of side face reinforcement, the spacing of bottom mat reinforcement (5 in.) is doubled, for practical purposes. This spacing (10 in.) satisfies the maximum requirement of spacing, which is 12 in. for components thicker than 36.0 in. On four side faces, No. 6 bars with 10 in. spacing ($A_s = 0.53 \text{ in.}^2/\text{ft.}$) will be provided in both horizontal and vertical directions. On the top face, No. 6 bars with 10 in. spacing will be provided in both orthogonal directions; however, the top mat reinforcement can be varied the requirement for the other loading cases. The shrinkage and temperature reinforcement is not necessary on the bottom face because uniformly distributed bottom mat reinforcement exists over the entire bottom face. The reinforcing details are provided in Section 8.4.8.

8.4.3.7. Step 7: Provide Necessary Anchorage for Ties

As described in Section 8.3.1.4, all ties have to be completely developed at the section where the tie centroid intersects with the extended nodal zone. For Load Case I, it is necessary to check whether the available development length for bottom mat reinforcement is greater than the minimum requirement. Figure 8.36 depicts the available length for ties in both directions. According to Eq. (8.11), the available development lengths for the bottom ties are 55.8 in. for Tie EF (GH) and 56.2 in. for Tie EH (FG), as the following calculation indicates:

$$\begin{aligned} l_{ad,EF} &= \frac{c_b}{\tan \theta_{s,proj,EF}} + D_{DS}'/2 + D_{DS}/2 + OH - c \\ &= \frac{(5.41 \text{ in.})}{\tan 50.2^\circ} + (42.5 \text{ in.})/2 + (48.0 \text{ in.})/2 + 9 \text{ in.} - 3 \text{ in.} = 55.8 \text{ in.} \end{aligned}$$

$$\begin{aligned} l_{ad,EH} &= \frac{c_b}{\tan \theta_{s,proj,EH}} + D_{DS}'/2 + D_{DS}/2 + OH - c \\ &= \frac{(5.41 \text{ in.})}{\tan 47.7^\circ} + (42.5 \text{ in.})/2 + (48.0 \text{ in.})/2 + 9 \text{ in.} - 3 \text{ in.} = 56.2 \text{ in.} \end{aligned}$$

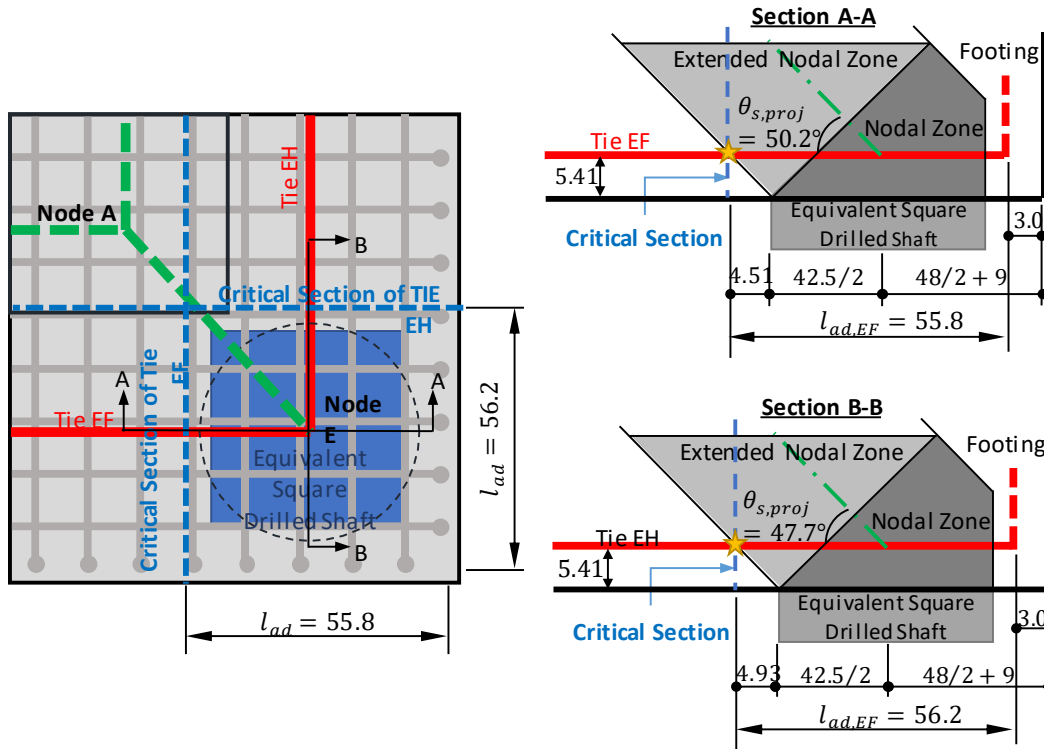


Figure 8.36 Critical sections for the development of ties: Load Case I

The minimum required development length of a straight bar is calculated in accordance with Article 5.10.8.2 of AASHTO LRFD (2020), as provided in Eq. (8.4). The reinforcement location factor, λ_{rl} , is 1.0, the reinforcement coating factor, λ_{cf} , is 1.0 for uncoated reinforcement, the reinforcement confinement factor, λ_{rc} , is 0.54 by given reinforcing details of the example, and the concrete density modification factor, λ , is 1.0 for normal weight concrete. The excess reinforcement factors, λ_{er} , for Tie EF and EH are 0.911 and 0.996, respectively. The required development length of a straight No. 11 bar is calculated as below:

$$l_{d,EF} = (2.4)(1.41 \text{ in.}) \frac{60}{\sqrt{3.6}} \left(\frac{1.0 \cdot 1.0 \cdot 0.54 \cdot 0.911}{1.0} \right) = 52.6 \text{ in.} < l_{ad,EF} (= 55.8 \text{ in.})$$

$$l_{d,EH} = (2.4)(1.41 \text{ in.}) \frac{60}{\sqrt{3.6}} \left(\frac{1.0 \cdot 1.0 \cdot 0.54 \cdot 0.996}{1.0} \right) = 57.6 \text{ in.} > l_{ad,EH} (= 56.2 \text{ in.})$$

Although straight bars for Tie EH are slightly insufficient to reach the required strength within the available length specified in the previous paragraph, 2.5% of shortness might not cause a structural issue due to conservatism in the equation.

Additionally, the research team calculated the required development length of 90-degree and 180-degree hooked bars as introduced in Eq. (8.5). The reinforcement confinement factor, λ_{rc} , is 0.8 by given reinforcing details of the example; the

coating factor, λ_{cw} , is 1.0 for uncoated reinforcement; the excess reinforcement factor, λ_{er} , is 1.0 to add conservatism; and the concrete density modification factor, λ , is 1.0 for normal weight concrete. The required development length of a hooked No. 11 bar is calculated as below:

$$l_{ah} = \frac{38.0(1.41 \text{ in.})}{60.0} \cdot \frac{60 \text{ ksi}}{\sqrt{3.6 \text{ ksi}}} \times \left(\frac{0.8 \cdot 1.0 \cdot 1.0}{1.0} \right) = 22.6 \text{ in.} < l_{ad,EF} (= 55.8 \text{ in.})$$

In conclusion, both straight and hooked No. 11 bars are adequate for the development in proposed available lengths for both ties, 55.8 in. and 56.2 in. The research team suggests straight reinforcing bars for the bottom mat, as is the most common current practice.

8.4.4. Design Calculations: Load Case II

Figure 8.23 shows the factored load case that the column is subjected to axial compressive force and mild uniaxial flexural loading. Despite the applied flexural loading, the column section remains in compression with varied stress level. Moreover, two sets of drilled shafts carry non-uniform amounts of compressive reactions, with the ratio of 1.5:1 in the second load case.

8.4.4.1. Step 1: Determine the Loads

The stress on the column section varied along the x-axis and the distribution was symmetric on the x-axis. The maximum and the minimum compressive stress are 1363 psi and 119 psi respectively with the assumption of linear stress distribution. The load can be divided into two sets of loading, with resultant components that are equivalent with the reaction forces of adjacent drilled shafts, as provided in the following step, so that the equilibrium condition at each node is satisfied. The positions of loading resultant forces are located at the centroid of stress distribution as shown in Figure 8.37.

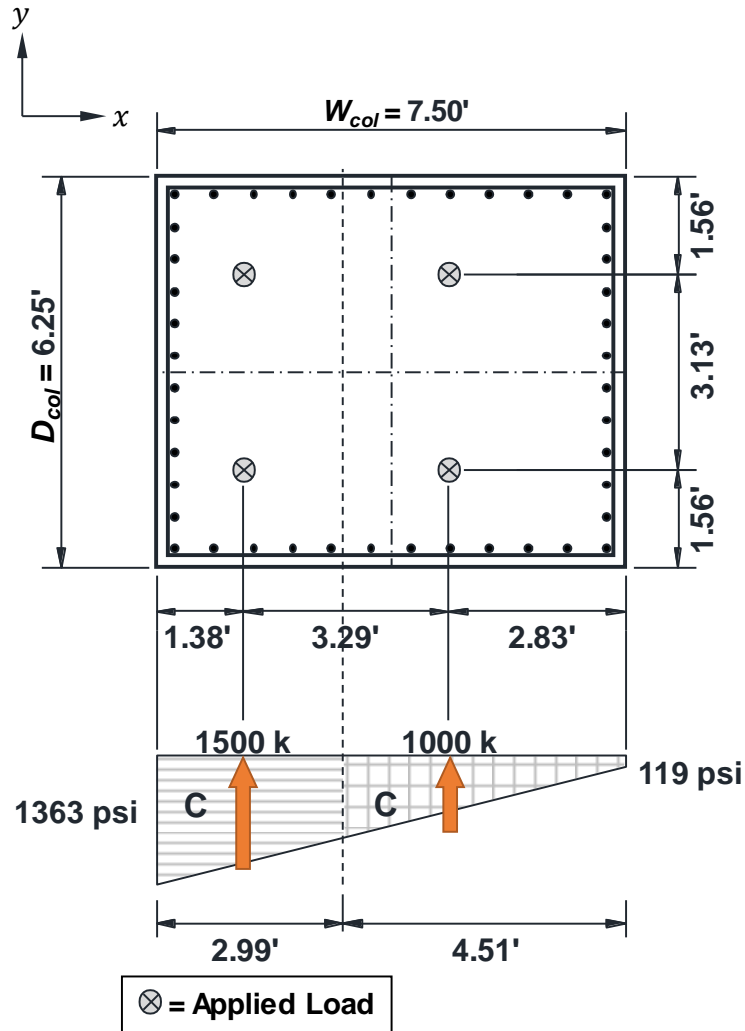


Figure 8.37 Stress distribution over the column section: Load Case II

8.4.4.2. Step 2: Analyze Structural Component

The reaction force of each drilled shaft can be calculated by the equilibrium conditions of the external loading and reactions at four shafts as described in Eq. (8.15). Figure 8.38 shows the result of the structural analysis.

$$R_1 = R_4 = \frac{P_u}{4} + \frac{1}{2} \left(\frac{M_{uyy}}{S_{DS,x}} \right) = \frac{5000 \text{ kip}}{4} + \frac{1}{2} \left(\frac{5250 \text{ k-ft}}{10.50 \text{ ft}} \right) = 1500.0 \text{ kip} \quad \text{(Compression)} \quad \text{Eq. (8.15)}$$

$$R_2 = R_3 = \frac{P_u}{4} - \frac{1}{2} \left(\frac{M_{uyy}}{S_{DS,x}} \right) = \frac{5000 \text{ kip}}{4} - \frac{1}{2} \left(\frac{5250 \text{ k-ft}}{10.50 \text{ ft}} \right) = 1000.0 \text{ kip} \quad \text{(Compression)}$$

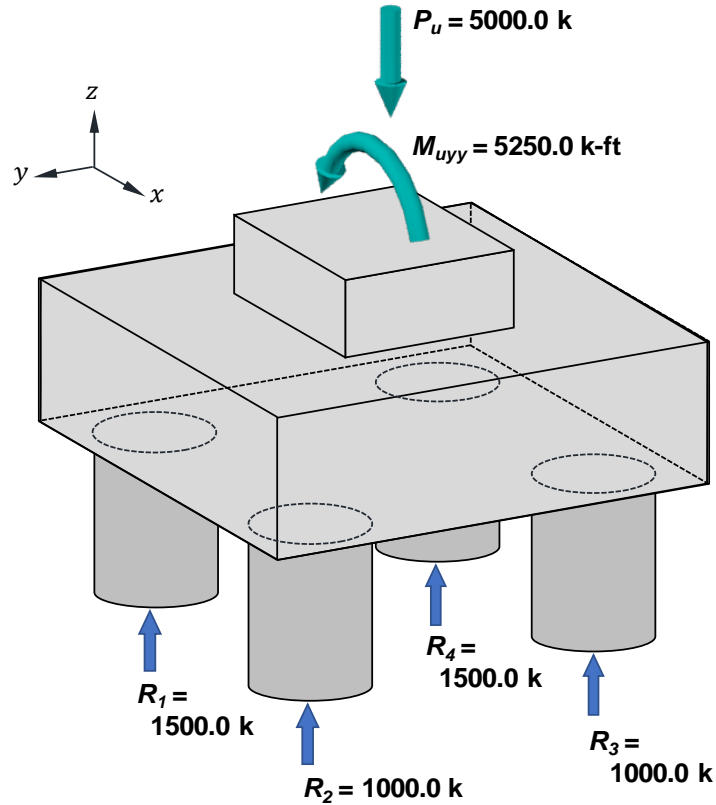


Figure 8.38 Applied loading and reaction forces: Load Case II

8.4.4.3. Step 3: Develop Strut-and-Tie Model

A 3D strut-and-tie model can be developed according to the principle of 3D STM specified in Section 8.3.1.1. The elevation (z -coordinate) of top nodes is 0.6 ft ($0.1h$) below the top surface. The x - and y -coordinates of the nodes below the column (Nodes A through D) are adopted from the centroid of subdivided four resultant forces that calculated over the column section in the previous section. The coordinates of nodes above shafts (Nodes E through H) are identical to Load Case I. Tie forces and strut forces, as illustrated in Figure 8.39 and Figure 8.40, can be computed by the equilibrium of each axis at each node and the geometric properties.

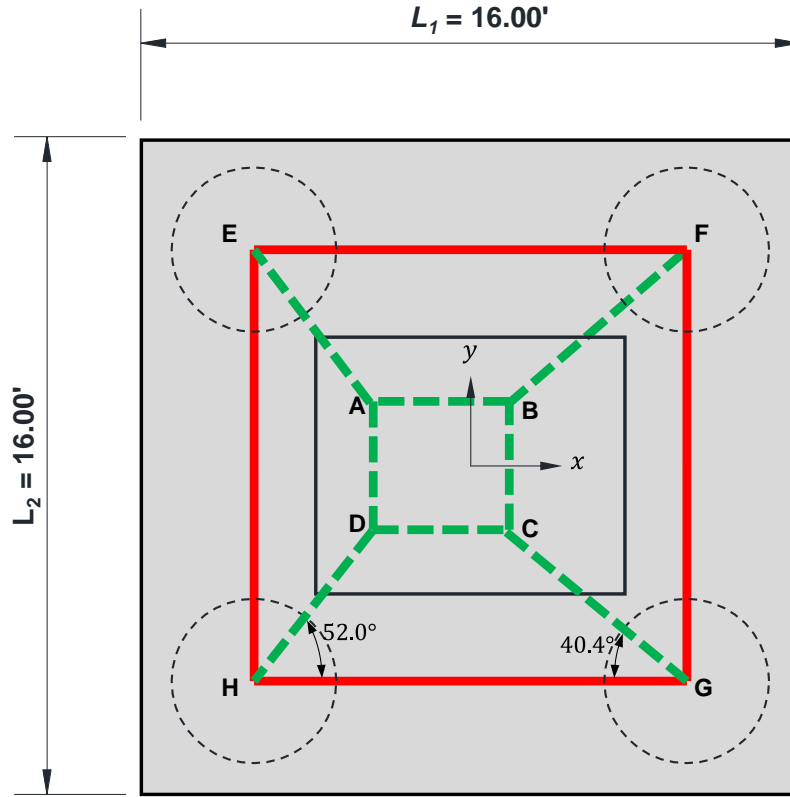


Figure 8.39 3D STM – plan view: Load Case II

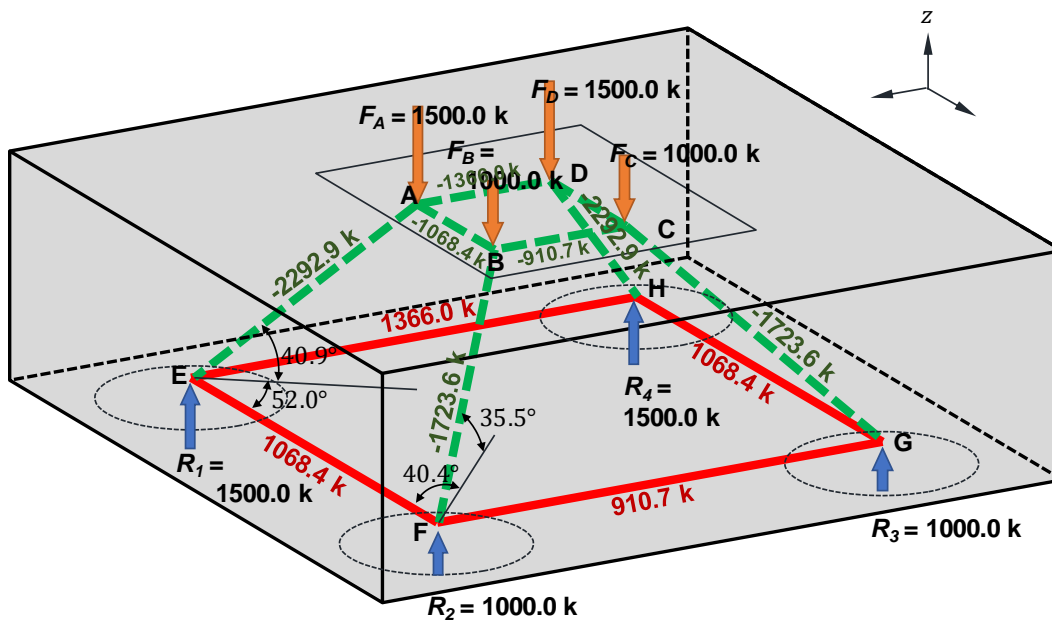


Figure 8.40 3D Strut-and-tie model: Load Case II

8.4.4.4. Step 4: Proportion Ties

As shown in Figure 8.40, tie EH is the most critical to calculate the required amount of reinforcement. Similar to Load Case I, No. 11 bars will be used for the bottom mat reinforcement.

- Ties EF and HG

$$\begin{aligned}\text{Factored tie force:} & F_{u,tie} = 1068.4 \text{ kip} \\ \text{Tie capacity:} & \phi \cdot f_y \cdot A_{st} = F_{u,tie} \\ & (0.9)(60 \text{ ksi})A_{st} = 1068.4 \text{ kip} \\ & A_{st} = 19.78 \text{ in.}^2 \\ \text{Number of No. 11 bars required:} & 19.78 \text{ in.}^2 / 1.56 \text{ in.}^2 = 13 \text{ bars}\end{aligned}$$

- Ties EH

$$\begin{aligned}\text{Factored tie force:} & F_{u,tie} = 1366.0 \text{ kip} \\ \text{Tie capacity:} & \phi \cdot f_y \cdot A_{st} = F_{u,tie} \\ & (0.9)(60 \text{ ksi})A_{st} = 1366.0 \text{ kip} \\ & A_{st} = 25.30 \text{ in.}^2 \\ \text{Number of No. 11 bars required:} & 25.30 \text{ in.}^2 / 1.56 \text{ in.}^2 = 17 \text{ bars}\end{aligned}$$

- Ties FG

$$\begin{aligned}\text{Factored tie force:} & F_{u,tie} = 910.7 \text{ kip} \\ \text{Tie capacity:} & \phi \cdot f_y \cdot A_{st} = F_{u,tie} \\ & (0.9)(60 \text{ ksi})A_{st} = 910.7 \text{ kip} \\ & A_{st} = 16.86 \text{ in.}^2 \\ \text{Number of No. 11 bars required:} & 16.86 \text{ in.}^2 / 1.56 \text{ in.}^2 = 11 \text{ bars}\end{aligned}$$

In conclusion, the same number of bars (19 bars for each tie element) as used in Load Case I is provided in both orthogonal directions since the required amount of bottom mat reinforcement for Load Case I is greater than that of Load Case II.

8.4.4.5. Step 5: Perform Strength Checks

Four nodes—Nodes A, B, E, and F—need to be checked for the nominal capacity at the bearing face, back face, and strut-to-node interface. Nodes E and H are critical locations for nodal strength checks, as the force at the bearing face and strut force are the greatest; further, the node type is CTT node, which has the smallest concrete

efficiency factor. In this example, nodal strength checks of all nodes will be performed.

- Nodes A and D (CCC node)

The dimensions and forces at Nodes A and D are identical. At first, the calculation of bearing area at the nodes is necessary to define the detailed 3D nodal geometry. The bearing area of the nodes, as indicated by the horizontal patterned region on the column section in Figure 8.37, is:

$$A_{cn,bearing} = (2.99 \text{ ft}) \left(\frac{6.25 \text{ ft}}{2} \right) = 9.34 \text{ ft}^2 = 1345.4 \text{ in.}^2$$

The length of the equivalent square bearing face, $L'_{cn,b}$, is:

$$L'_{cn,b} = \sqrt{A_{cn,bearing}} = 36.7 \text{ in.}$$

Figure 8.41 illustrates resolving the force at Nodes A and D from multiple loads at back faces. In accordance with the recommendation in Section 8.3.1.3, Figure 8.42 illustrates nodes A and D in three dimensions, including the forces at each face, so that nodal capacities at each face can be checked.

When calculating the triaxial confinement factor, this study recommends considering the entire column section since entire column section is in compression. The triaxial confinement factor is the same as used in Load Case I ($m = 2.34$). Concrete efficiency factor, ν , is determined in accordance with Table 5.8.2.5.3a-1 of AASHTO LRFD (2020). It should be noted that the concrete efficiency factor does not have to decrease to 0.45 because the side face reinforcement provided will be more than 0.18%.

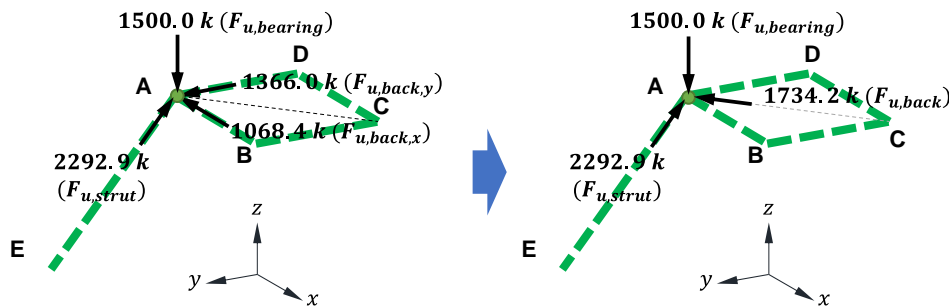


Figure 8.41 Resolving the force at Nodes A and D (CCC node)

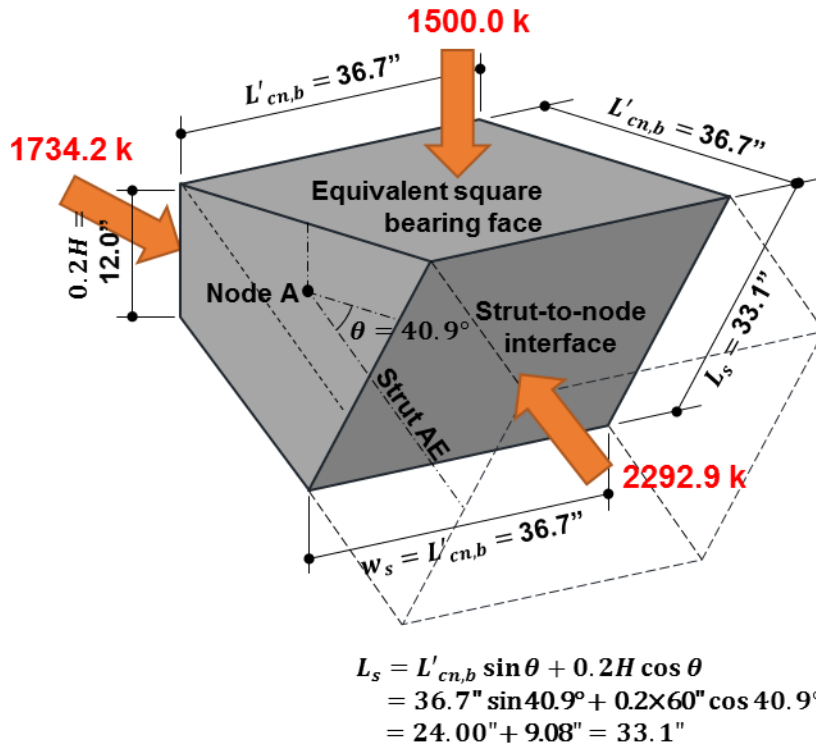


Figure 8.42 Details of 3D nodal geometry at Nodes A and D

o NODAL STRENGTH AT BEARING FACE

Factored load: $F_{u,bearing} = 1500.0 \text{ kip}$

Concrete efficiency factor: $\nu = 0.85$

Concrete capacity: $f_{cu} = m \cdot \nu \cdot f'_c = (2.34)(0.85)(3.6 \text{ ksi}) = 7.16 \text{ ksi}$

Nodal capacity: $\phi F_{n,bearing} = \phi f_{cu} A_{cn,bearing} = (0.7)(7.16 \text{ ksi})(1345.4 \text{ in.}^2) = 6743.1 \text{ kip} > 1500.0 \text{ kip} \quad \mathbf{OK}$

o NODAL STRENGTH AT BACK FACE

Factored load: $F_{u,back} = \sqrt{1068.4^2 + 1366.0^2} = 1734.2 \text{ kip}$

Effective area: $A_{cn,back} = L'_{cn,b} \cdot 0.2H = 440.2 \text{ in}^2$

Concrete efficiency factor: $\nu = 0.85$

Concrete capacity: $f_{cu} = m \cdot \nu \cdot f'_c = (2.34)(0.85)(3.6 \text{ ksi}) = 7.16 \text{ ksi}$

Nodal capacity: $\phi F_{n,back} = \phi f_{cu} A_{cn,back} = (0.7)(7.16 \text{ ksi})(440.2 \text{ in.}^2) = 2206.3 \text{ kip} > 1734.2 \text{ kip} \quad \mathbf{OK}$

o NODAL STRENGTH AT STRUT-TO-NODE INTERFACE

Factored load:	$F_{u,SNI} = 2292.9 \text{ kip}$
Effective area:	$A_{cn,SNI} = w_s \cdot L_s = (36.7 \text{ in.})(33.1 \text{ in.})$ $= 1214.8 \text{ in.}^2$
Concrete efficiency factor:	$\nu = 0.85 - f'_c / 20 \text{ ksi} = 0.85 - 3.6 \text{ ksi} / 20 \text{ ksi}$ $= 0.67 > 0.65 \quad \therefore \text{se } \nu = 0.65$
Concrete capacity:	$f_{cu} = m \cdot \nu \cdot f'_c = (2.34)(0.65)(3.6 \text{ ksi})$ $= 5.48 \text{ ksi}$
Nodal capacity:	$\phi F_{n,SNI} = \phi f_{cu} A_{cn,SNI}$ $= (0.7)(5.48 \text{ ksi})(1214.8 \text{ in.}^2)$ $= 4660.0 \text{ kip} > 2292.9 \text{ kip} \quad \text{OK}$

- Nodes B and C (CCC node)

Nodes B and C are under the same loading condition. To determine the detailed 3D nodal geometry, the bearing area of the nodes, as indicated by the grid pattern region on the column section in, is calculated thusly:

$$A_{cn,bearing} = (4.51 \text{ ft}) \left(\frac{6.25 \text{ ft}}{2} \right) = 14.09 \text{ ft}^2 = 2029.6 \text{ in.}^2$$

The length of the equivalent square bearing face, $L'_{cn,b}$, is:

$$L'_{cn,b} = \sqrt{A_{cn,bearing}} = 45.1 \text{ in.}$$

Figure 8.43 illustrates the resolved force that is applied at the back face. Reflecting the recommendation made in Section 8.3.1.3, Figure 8.44 illustrates nodes B and C in three dimensions, and the applied forces that are calculated using the same method as Load Case I to perform nodal strength checks. The same triaxial confinement factor calculated in Load Case I ($m = 2.34$) is used.

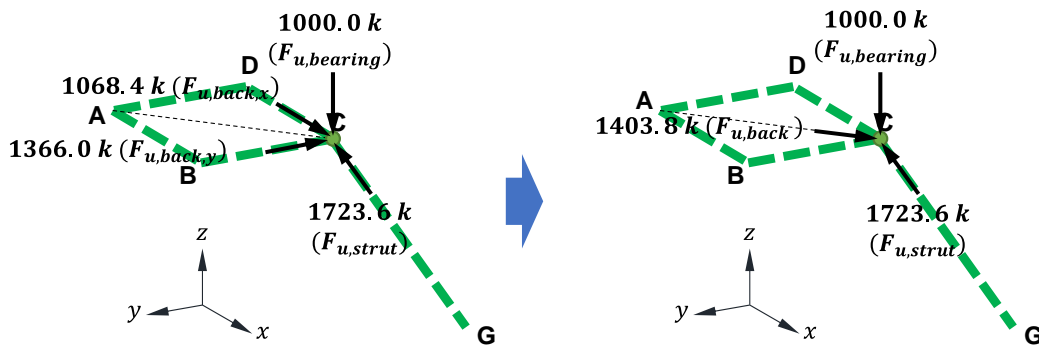
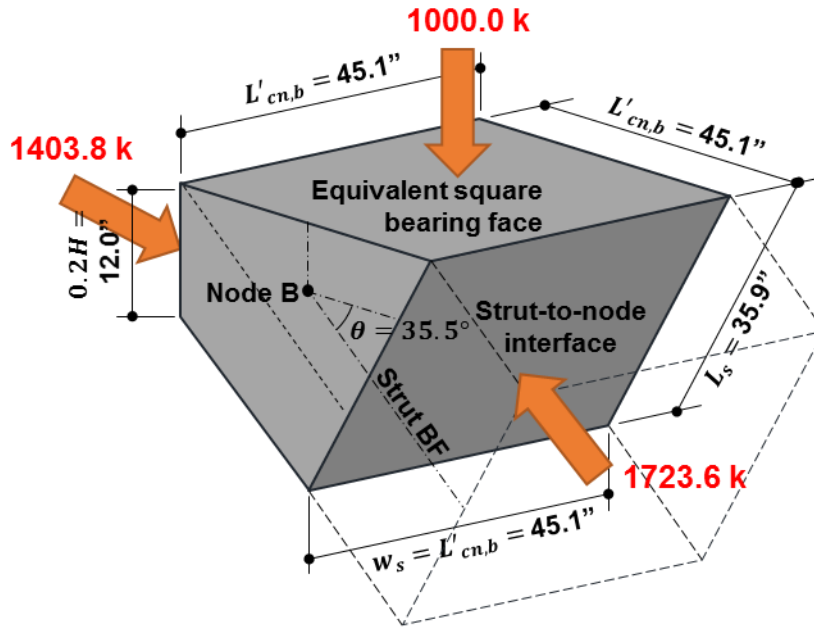


Figure 8.43 Resolving the force at Nodes B and C (CCC node)



$$\begin{aligned}
 L_s &= L'_{cn,b} \sin \theta + 0.2H \cos \theta \\
 &= 45.1'' \sin 35.5^\circ + 0.2 \times 60'' \cos 35.5^\circ \\
 &= 26.14'' + 9.77'' = 35.9''
 \end{aligned}$$

Figure 8.44 Details of 3D nodal geometry at Nodes B and C

o NODAL STRENGTH AT BEARING FACE

Factored load: $F_{u,bearing} = 1000.0 \text{ kip}$

Concrete efficiency factor: $\nu = 0.85$

Concrete capacity: $f_{cu} = m \cdot \nu \cdot f'_c = (2.34)(0.85)(3.6 \text{ ksi}) = 7.16 \text{ ksi}$

Nodal capacity: $\phi F_{n,bearing} = \phi f_{cu} A_{cn,bearing} = (0.7)(7.16 \text{ ksi})(2029.6 \text{ in.}^2) = 10172.4 \text{ kip} > 1000.0 \text{ kip} \quad \mathbf{OK}$

o NODAL STRENGTH AT BACK FACE

Factored load: $F_{u,back} = \sqrt{1068.4^2 + 910.7^2} = 1403.8 \text{ kip}$

Effective area: $A_{cn,back} = L'_{cn,b} \cdot 0.2H = 540.6 \text{ in}^2$

Concrete efficiency factor: $\nu = 0.85$

Concrete capacity: $f_{cu} = m \cdot \nu \cdot f'_c = (2.34)(0.85)(3.6 \text{ ksi}) = 7.16 \text{ ksi}$

Nodal capacity: $\phi F_{n,back} = \phi f_{cu} A_{cn,back} = (0.7)(7.16 \text{ ksi})(540.6 \text{ in.}^2) = 2709.5 \text{ kip} > 1403.8 \text{ kip} \quad \mathbf{OK}$

o NODAL STRENGTH AT STRUT-TO-NODE INTERFACE

Factored load:	$F_{u,SNI} = 1723.6 \text{ kip}$
Effective area:	$A_{cn,SNI} = w_s \cdot L_S = (45.1 \text{ in.})(35.9 \text{ in.})$ $= 1617.9 \text{ in.}^2$
Concrete efficiency factor:	$\nu = 0.85 - \frac{f'_c}{20 \text{ ksi}} = 0.85 - \frac{3.6 \text{ ksi}}{20 \text{ ksi}}$ $= 0.67 > 0.65 \quad \therefore \text{se } \nu = 0.65$
Concrete capacity:	$f_{cu} = m \cdot \nu \cdot f'_c = (2.34)(0.65)(3.6 \text{ ksi})$ $= 5.48 \text{ ksi}$
Nodal capacity:	$\phi F_{n,SNI} = \phi f_{cu} A_{cn,SNI}$ $= (0.7)(5.48 \text{ ksi})(1617.9 \text{ in.}^2)$ $= 6206.3 \text{ kip} > 1723.6 \text{ kip} \quad \mathbf{OK}$

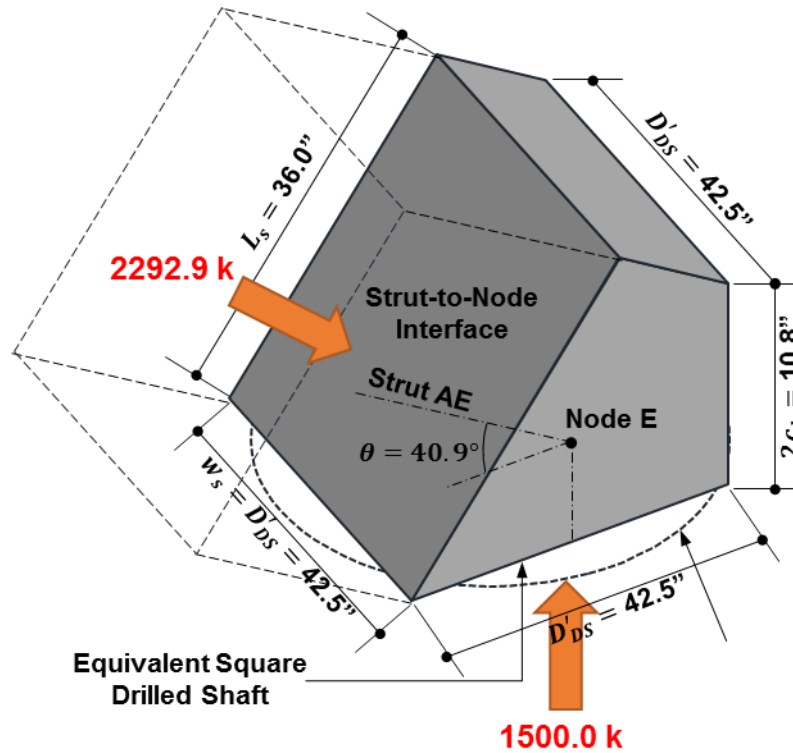
- Nodes E and H (CTT node)

Figure 8.45 illustrates the dimension and applying forces of nodes E and H in three dimensions based on this study's proposed recommendations. The confinement modification factors of Nodes E and H in Load Case II are the same as those in Load Case I ($m = 1.55$) as illustrated in Figure 8.35. In addition, the length of the equivalent square bearing face ($D'_{DS} = 42.5 \text{ in.}$) is identical as well.

For the CTT node, the concrete efficiency factors at each face are identical to the following:

$$\nu = 0.85 - \frac{f'_c}{20 \text{ ksi}} = 0.85 - \frac{3.6 \text{ ksi}}{20 \text{ ksi}} = 0.67 > 0.65 \quad \therefore \text{se } \nu = 0.65$$

Note that the nodal strength check at back faces is not necessary since an adequate development length that satisfies the anchorage requirement is provided in this example.



$$\begin{aligned}
 L_s &= D'_{DS} \sin \theta + 2c_b \cos \theta \\
 &= 42.5'' \sin 40.9^\circ + 2 \times (4'' + 1.41'') \cos 40.9^\circ \\
 &= 27.83'' + 8.18'' = 36.0''
 \end{aligned}$$

Figure 8.45 Details of 3D nodal geometry at Nodes E and H

o NODAL STRENGTH AT BEARING FACE

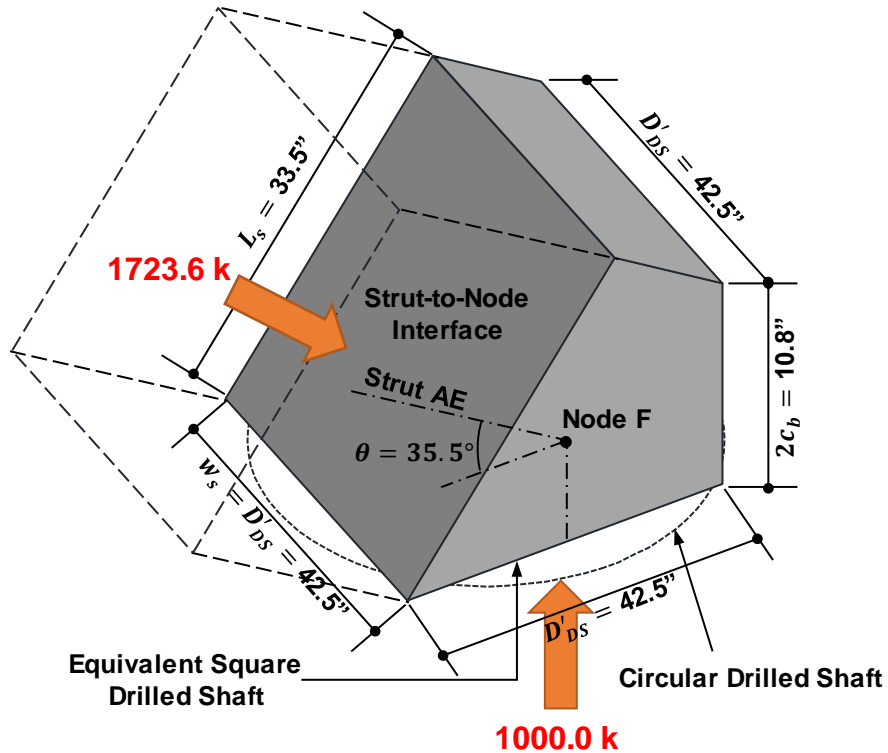
- Factored load: $F_{u,bearing} = 1500.0 \text{ kip}$
- Concrete efficiency factor: $\nu = 0.65$
- Concrete capacity: $f_{cu} = m \cdot \nu \cdot f'_c = (1.55)(0.65)(3.6 \text{ ksi}) = 3.63 \text{ ksi}$
- Nodal capacity: $\phi F_{n,bearing} = \phi f_{cu} A_{cn,bearing} = (0.7)(3.63 \text{ ksi})(1809.6 \text{ in.}^2) = 4598.2 \text{ kip} > 1500.0 \text{ kip} \quad \text{OK}$

o NODAL STRENGTH AT STRUT-TO-NODE INTERFACE

- Factored load: $F_{u,SNI} = 2292.9 \text{ kip}$
- Effective area: $A_{cn,SNI} = w_s \cdot L_s = (42.5 \text{ in.})(36.0 \text{ in.}) = 1531.0 \text{ in.}^2$
- Concrete capacity: $f_{cu} = m \cdot \nu \cdot f'_c = (1.55)(0.65)(3.6 \text{ ksi}) = 3.63 \text{ ksi}$
- Nodal capacity: $\phi F_{n,SNI} = \phi f_{cu} A_{cn,SNI} = (0.7)(3.63 \text{ ksi})(1531.0 \text{ in.}^2) = 3890.3 \text{ kip} > 2292.9 \text{ kip} \quad \text{OK}$

- Nodes F and G (CTT node)

Nodes F and G have the same 3D nodal geometry and are subjected to the identical applying forces as shown in Figure 8.46. As mentioned earlier, the confinement modification factors ($m = 1.55$) and concrete efficiency factor ($\nu = 0.65$) of Nodes F and G are the same as Nodes E and H.



$$\begin{aligned}
 L_s &= D'_{DS} \sin \theta + 2c_b \cos \theta \\
 &= 42.5'' \sin 35.5^\circ + 2 \times (4'' + 1.41'') \cos 35.5^\circ \\
 &= 24.68'' + 8.81'' = 33.5''
 \end{aligned}$$

Figure 8.46 Details of 3D nodal geometry at Nodes F and G

o NODAL STRENGTH AT BEARING FACE

Factored load:	$F_{u,bearing} = 1000.0 \text{ kip}$
Concrete efficiency factor:	$\nu = 0.65$
Concrete capacity:	$f_{cu} = m \cdot \nu \cdot f'_c = (1.55)(0.65)(3.6 \text{ ksi})$ $= 3.63 \text{ ksi}$
Nodal capacity:	$\phi F_{n,bearing} = \phi f_{cu} A_{cn,bearing}$ $= (0.7)(3.63 \text{ ksi})(1809.6 \text{ in.}^2)$ $= 4598.2 \text{ kip} > 1000.0 \text{ kip} \quad \mathbf{OK}$

o NODAL STRENGTH AT STRUT-TO-NODE INTERFACE

Factored load:	$F_{u,SNI} = 1723.6 \text{ kip}$
Concrete efficiency factor:	$\nu = 0.65$
Effective area:	$A_{cn,SNI} = w_s \cdot L_s = (42.5 \text{ in.})(33.5 \text{ in.})$ $= 1424.8 \text{ in.}^2$
Concrete capacity:	$f_{cu} = m \cdot \nu \cdot f'_c = (1.55)(0.65)(3.6 \text{ ksi})$ $= 3.63 \text{ ksi}$
Nodal capacity:	$\phi F_{n,SNI} = \phi f_{cu} A_{cn,SNI}$ $= (0.7)(3.63 \text{ ksi})(1424.8 \text{ in.}^2)$ $= 3620.4 \text{ kip} > 1723.6 \text{ kip} \quad \mathbf{OK}$

Therefore, the nodal capacities of Nodes A through H are greater than factored loads.

8.4.4.6. Step 6: Proportion Shrinkage and Temperature Reinforcement

The necessary shrinkage and temperature reinforcement for the footing was specified in Section 8.4.3. On the side faces, No. 6 bars with 10 in. spacing ($A_s = 0.53 \text{ in.}^2/\text{ft.}$) are required in both horizontal and vertical directions. On the top face, No. 6 bars with 10 in. spacing A_s ($0.53 \text{ in.}^2/\text{ft.}$) are provided; however, the top mat reinforcement can be dependent on the other loading cases.

8.4.4.7. Step 7: Provide Necessary Anchorage for Ties

Figure 8.47 shows the available development length for ties in each direction. Tie EF has different projected angles at each node. The research team suggests calculating the available development length at each node and checking the minimum length against the requirement. According to Eq. (8.11), the available development lengths for each bottom tie are 55.1 in. for Tie EF (HG) and 56.2 in. for Ties FG and EH, as determined by the following calculations:

$$l_{ad,EF,E} = \frac{c_b}{\tan \theta_{s,proj,EF,E}} + D_{DS}'/2 + D_{DS}/2 + OH - c$$

$$= \frac{(5.41 \text{ in.})}{\tan 54.5^\circ} + (42.5 \text{ in.})/2 + (48.0 \text{ in.})/2 + 9 \text{ in.} - 3 \text{ in.} = 55.1 \text{ in.}$$

$$l_{ad,EF,E} = \frac{c_b}{\tan \theta_{s,proj,EF,F}} + D_{DS}'/2 + D_{DS}/2 + OH - c$$

$$= \frac{(5.41 \text{ in.})}{\tan 43.1^\circ} + (42.5 \text{ in.})/2 + (48.0 \text{ in.})/2 + 9 \text{ in.} - 3 \text{ in.} = 57.0 \text{ in.}$$

$$l_{ad,FG} = \frac{c_b}{\tan \theta_{s,proj,FG}} + D_{DS}'/2 + D_{DS}/2 + OH - c$$

$$= \frac{(5.41 \text{ in.})}{\tan 47.7^\circ} + (42.5 \text{ in.})/2 + (48.0 \text{ in.})/2 + 9 \text{ in.} - 3 \text{ in.} = 56.2 \text{ in.}$$

$$l_{ad,EH} = \frac{c_b}{\tan \theta_{s,proj,EH}} + D_{DS}'/2 + D_{DS}/2 + OH - c$$

$$= \frac{(5.41 \text{ in.})}{\tan 47.7^\circ} + (42.5 \text{ in.})/2 + (48.0 \text{ in.})/2 + 9 \text{ in.} - 3 \text{ in.} = 56.2 \text{ in.}$$

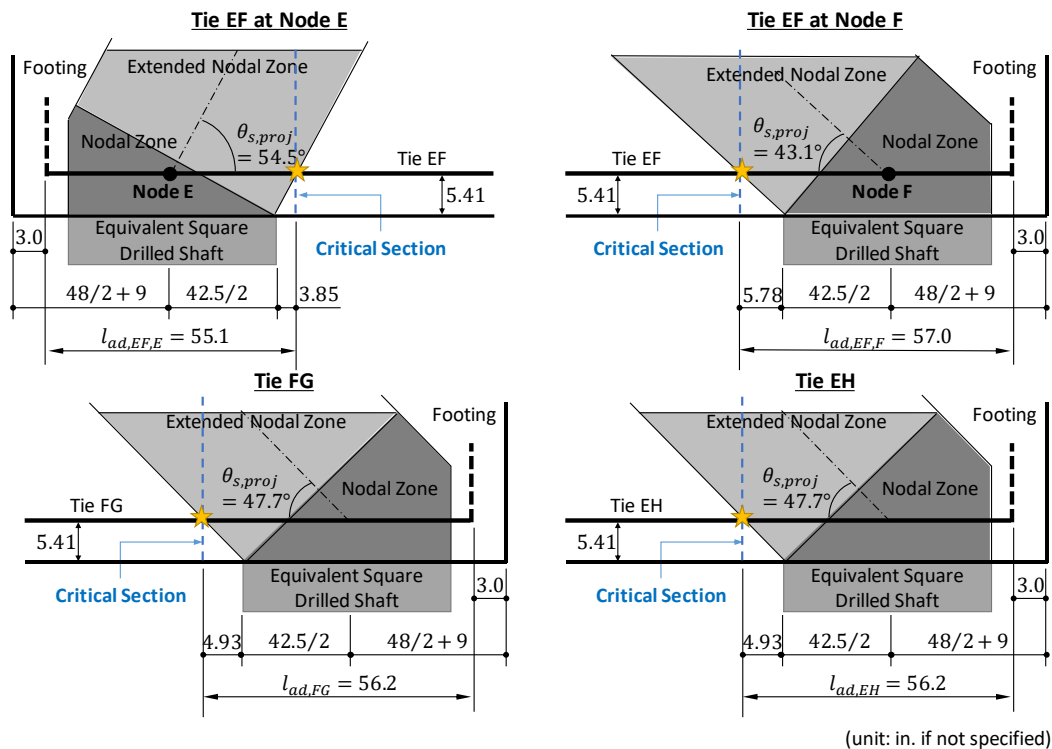


Figure 8.47 Critical sections for the development of ties: Load Case II

Straight bars for bottom mat reinforcement were recommended for Load Case I. Load Case II required a smaller steel area than did Load Case I, resulting in reduction of excess reinforcement factor; therefore, smaller development length would be required. To calculate the minimum required development length, reinforcement location factor, λ_{rl} , is 1.0; the reinforcement coating factor, λ_{cf} , is 1.0 for uncoated reinforcement; the reinforcement confinement factor, λ_{rc} , is 0.54 by given reinforcing details of the example; and the concrete density modification factor, λ , is 1.0 for normal weight concrete. The excess reinforcement factors, λ_{er} , for Tie EF, FG, and EH are 0.667, 0.569, and 0.853, respectively. According to Eq. (8.3), the required development length of a straight No. 11 bar is calculated as below:

$$l_{d,EF} = (2.4)(1.41 \text{ in.}) \frac{60}{\sqrt{3.6}} \frac{(1.0)(1.0)(0.54)(0.667)}{1.0} = 38.5 \text{ in.} < l_{ad,EF} (= 55.1 \text{ in.})$$

$$l_{d,FG} = (2.4)(1.41 \text{ in.}) \frac{60}{\sqrt{3.6}} \frac{(1.0)(1.0)(0.54)(0.569)}{1.0} = 32.9 \text{ in.} < l_{ad,FG} (= 56.2 \text{ in.})$$

$$l_{d,EH} = (2.4)(1.41 \text{ in.}) \frac{60}{\sqrt{3.6}} \frac{(1.0)(1.0)(0.54)(0.853)}{1.0} = 49.3 \text{ in.} < l_{ad,EH} (= 56.2 \text{ in.})$$

Therefore, straight bars are sufficient to develop yielding strength for bottom ties in Load Case II as well as Load Case I.

8.4.5. Design Calculations: Load Case III

Figure 8.24 shows the factored load case that the column is subjected to axial compressive force and moderate uniaxial flexural loading. The flexural loading results in tension at one face of the column, but all drilled shafts still remain in compression.

8.4.5.1. Step 1: Determine the Loads

Since the tensile column reinforcement starts to carry tensile stress due to the overturning moment applied to the column, the stress distribution of the column section considering the contribution of the tensile column reinforcement and nonlinear behavior of the concrete is developed based on the procedure specified in Figure 8.7.

Although the derived extreme compressive strain is in the elastic range (-6.4×10^{-4} in./in.), the equivalent stress block corresponding to the strain at the extreme compressive fiber can be developed from Eq. (8.6)-(a). The resultant force of the equivalent stress block is divided into two forces representing the resultant forces applied to the bearing face of the CCC node in the 3D STM. In addition, the depth of the block is considered as the depth of the bearing face of the CCC node. Under the factored load, the tensile column reinforcement is subjected to 19.8 ksi, about 33% of the yield stress. The derived stress distribution and positions of loading resultant forces on the column section are presented in Figure 8.48.

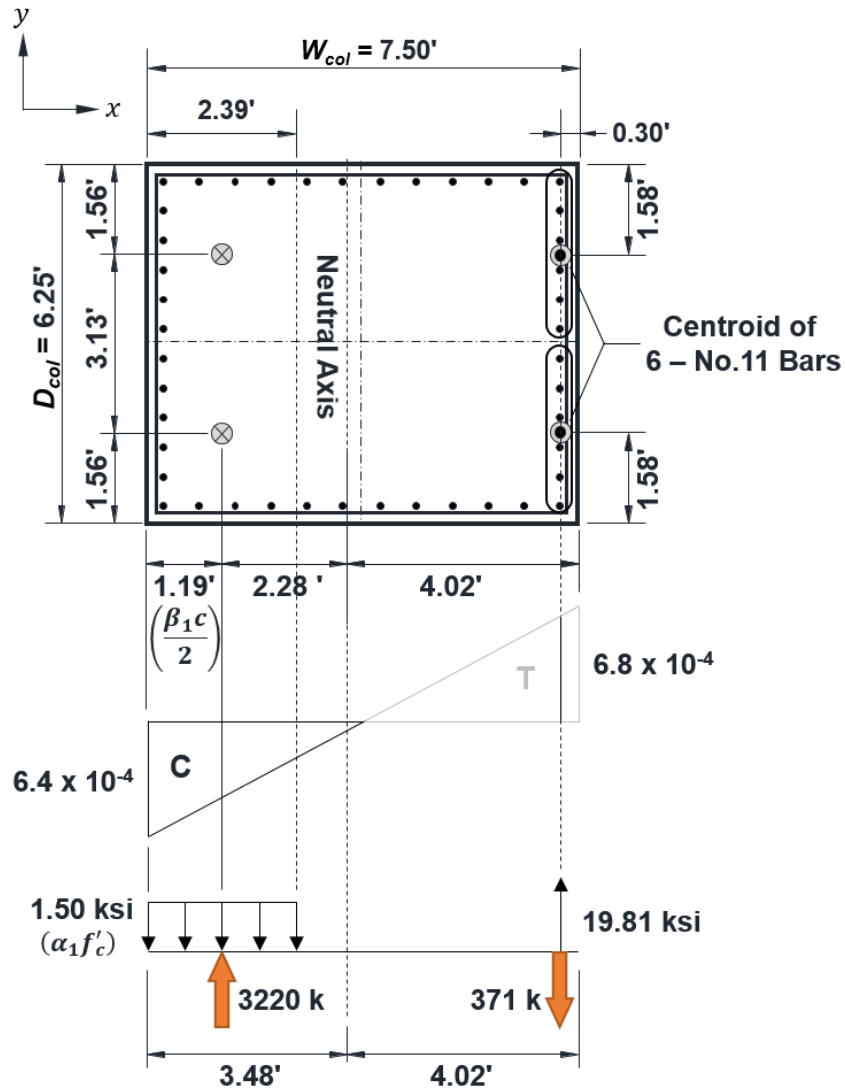


Figure 8.48 Stress distribution over the column section: Load Case III

8.4.5.2. Step 2: Analyze Structural Component

The reaction force of each drilled shaft can be calculated by the equilibrium conditions of the external loading and reactions at four shafts as described in Eq. (8.16). Figure 8.49 shows the result of the structural analysis.

$$R_1 = R_4 = \frac{P_u}{4} + \frac{1}{2} \left(\frac{M_{uyy}}{S_{DS,x}} \right) = \frac{2849 \text{ kip}}{4} + \frac{1}{2} \left(\frac{9507 \text{ k-ft}}{10.50 \text{ ft}} \right) = 1165.0 \text{ kip} \quad \text{(Compression)}$$

$$R_2 = R_3 = \frac{P_u}{4} - \frac{1}{2} \left(\frac{M_{uyy}}{S_{DS,x}} \right) = \frac{2849 \text{ kip}}{4} - \frac{1}{2} \left(\frac{9507 \text{ k-ft}}{10.50 \text{ ft}} \right) = 259.5 \text{ kip} \quad \text{(Compression)}$$

Eq. (8.16)

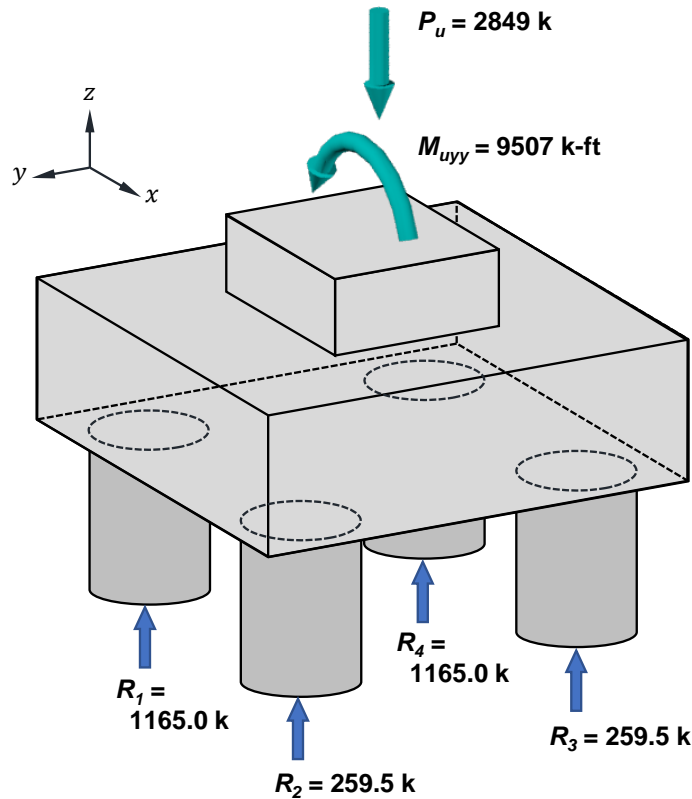


Figure 8.49 Applied loading and reaction forces: Load Case III

8.4.5.3. Step 3: Develop Strut-and-Tie Model

A 3D strut-and-tie model is developed following the basic principle of 3D STM specified in Section 8.3.1.1. The x- and y-axes of the vertical struts and ties are positioned at the centroid of the subdivided equivalent stress block and the centroids of the tensile reinforcement groups consisting of six No. 11 bars, respectively. The elevation of the nodes beneath the column is 0.6 ft (0.1h) below the top surface. The coordinates of nodes above shafts (Nodes E through H) are identical to Load Case I and II, and the vertical column tie elements extend down to the elevation of the nodes above the shafts. Tie forces and strut forces can be computed by the equilibrium of each axis at each node and the configuration of the model, as shown in Figure 8.50 and Figure 8.51.

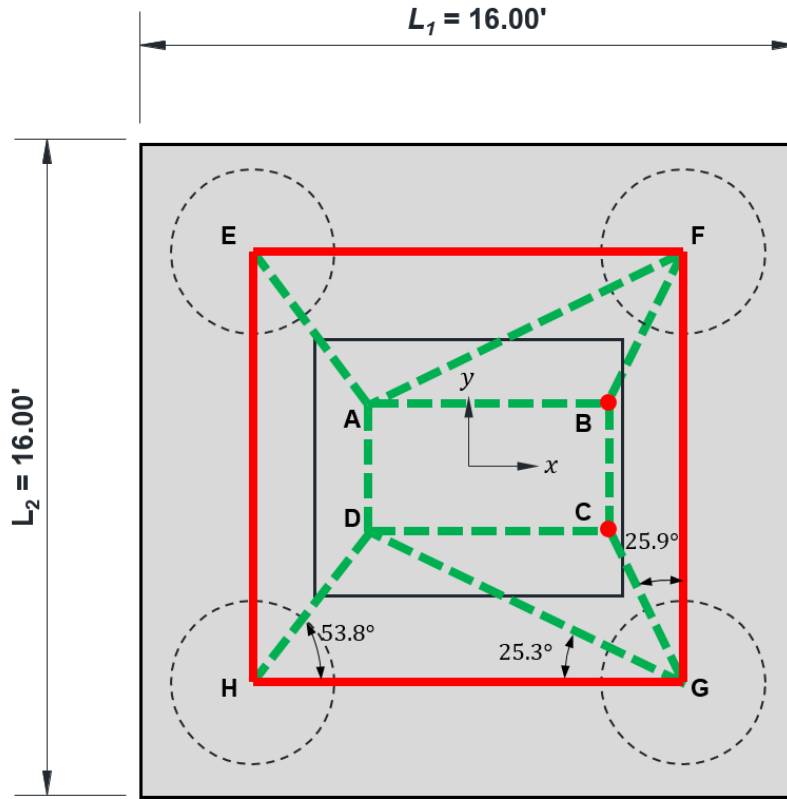


Figure 8.50 3D STM – plan view: Load Case III

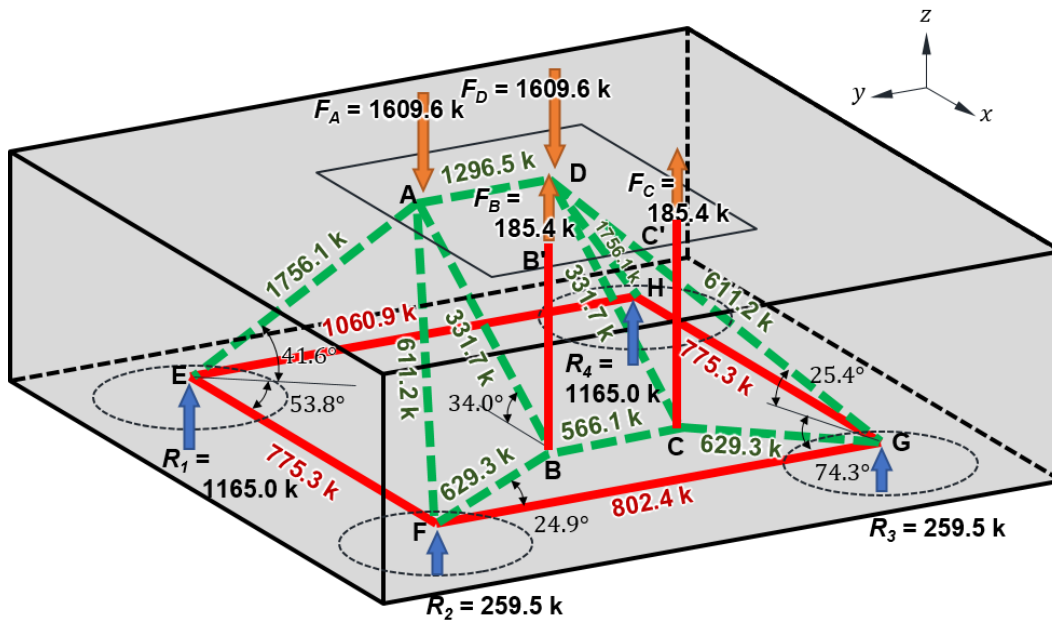


Figure 8.51 3D Strut-and-tie model: Load Case III

8.4.5.4. Step 4: Proportion Ties

As shown in Figure 8.51, tie EH carries the largest tension force among the tie elements. No. 11 bars are already assigned to the column reinforcement based on the column design. The bottom mat reinforcement will be designed with No. 11 bars, the same as the previous design example.

- Ties EF and HG (Bottom Mat Reinforcement)

Factored tie force: $F_{u,tie} = 775.3 \text{ kip}$

Tie capacity: $\phi \cdot f_y \cdot A_{st} = F_{u,tie}$
 $(0.9)(60 \text{ ksi})A_{st} = 775.3 \text{ kip}$
 $A_{st} = 14.36 \text{ in.}^2$

Number of No. 11 bars required: $14.36 \text{ in.}^2 / 1.56 \text{ in.}^2 = 10 \text{ bars}$

- Tie EH (Bottom Mat Reinforcement)

Factored tie force: $F_{u,tie} = 1060.9 \text{ kip}$

Tie capacity: $\phi \cdot f_y \cdot A_{st} = F_{u,tie}$
 $(0.9)(60 \text{ ksi})A_{st} = 1060.9 \text{ kip}$
 $A_{st} = 19.65 \text{ in.}^2$

Number of No. 11 bars required: $19.65 \text{ in.}^2 / 1.56 \text{ in.}^2 = 13 \text{ bars}$

- Tie FG (Bottom Mat Reinforcement)

Factored tie force: $F_{u,tie} = 802.4 \text{ kip}$

Tie capacity: $\phi \cdot f_y \cdot A_{st} = F_{u,tie}$
 $(0.9)(60 \text{ ksi})A_{st} = 802.4 \text{ kip}$
 $A_{st} = 14.86 \text{ in.}^2$

Number of No. 11 bars required: $14.86 \text{ in.}^2 / 1.56 \text{ in.}^2 = 11 \text{ bars}$

- Tie BB' and CC' (Column Reinforcement)

Factored tie force: $F_{u,tie} = 185.4 \text{ kip}$

Tie capacity: $\phi \cdot f_y \cdot A_{st} = F_{u,tie}$
 $(0.9)(60 \text{ ksi})A_{st} = 185.4 \text{ kip}$
 $A_{st} = 3.43 \text{ in.}^2$

Number of No. 11 bars required: $3.43 \text{ in.}^2 / 1.56 \text{ in.}^2 = 3 \text{ bars}$
(6 bars already provided)

In conclusion, the same number of bars (19 bars for each tie element) as used in Load Case I is provided in both orthogonal directions since the required amount of bottom mat reinforcement for Load Case I is greater than that of Load Case III. Furthermore, the provided tensile column reinforcement is enough to resist the force applied to the vertical tie element.

8.4.5.5. Step 5: Perform Strength Checks

A total of six nodes—Nodes A, D, E, F, G, and H—need to be checked for the nominal capacity at the bearing face, back face, and strut-to-node interface. The dimension of the nodal geometry of the CCC nodes—Node A and D—is determined based on the equivalent stress block depth derived in advance. All nodal strength checks are performed as follows:

- Nodes A and D (CCC node)

The bearing face of the nodes is defined by the depth of the equivalent stress block and half-width of the column section.

$$A_{cn,bearing} = (2.39 \text{ ft}) \left(\frac{6.25 \text{ ft}}{2} \right) = 7.47 \text{ ft}^2 = 1076 \text{ in.}^2$$

Nodes A and D are subjected to the forces of three diagonal struts in different directions and one horizontal strut. To simplify the nodal capacity check, three diagonal struts are resolved into a single diagonal strut, as shown in Figure 8.52. In accordance with the recommendation in Section 8.3.1.3, Figure 8.53 illustrates nodes A and D in three dimensions, including the forces at each face, so that nodal capacities at each face can be checked.

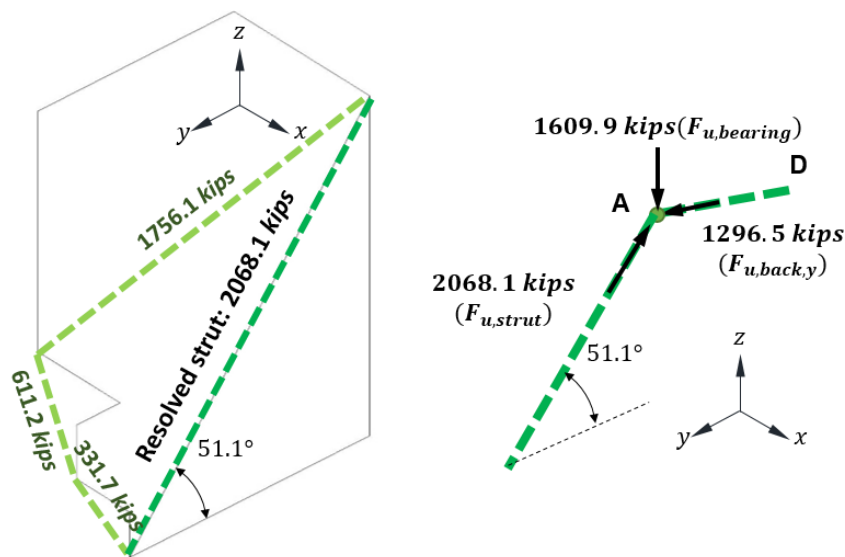
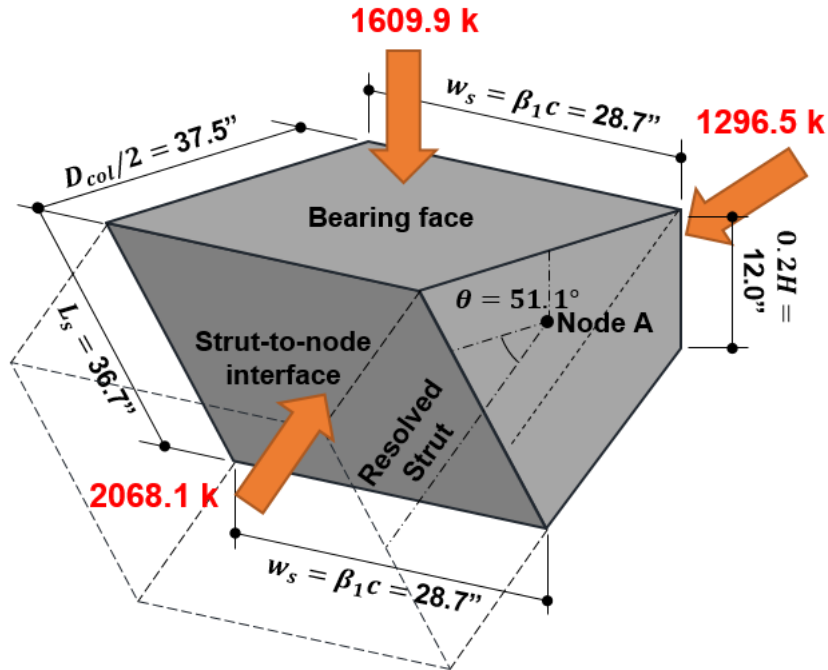


Figure 8.52 Resolving the force at Nodes A and D (CCC node)



$$\begin{aligned}
 L_s &= (D_{col}/2) \sin \theta + 0.2H \cos \theta \\
 &= 37.5" \sin 51.1^\circ + 0.2 \times 60" \cos 51.1^\circ \\
 &= 36.7"
 \end{aligned}$$

Figure 8.53 Details of 3D nodal geometry at Nodes A and D

The overall column section is no longer subjected to compression; therefore, the confinement factor needs to be defined based on the dimension of the bearing face on the column determined from the stress distribution. For consistency in design, the depth of the bearing area is assumed to be that of the equivalent stress block. The triaxial confinement factor is calculated as specified in Figure 8.54:

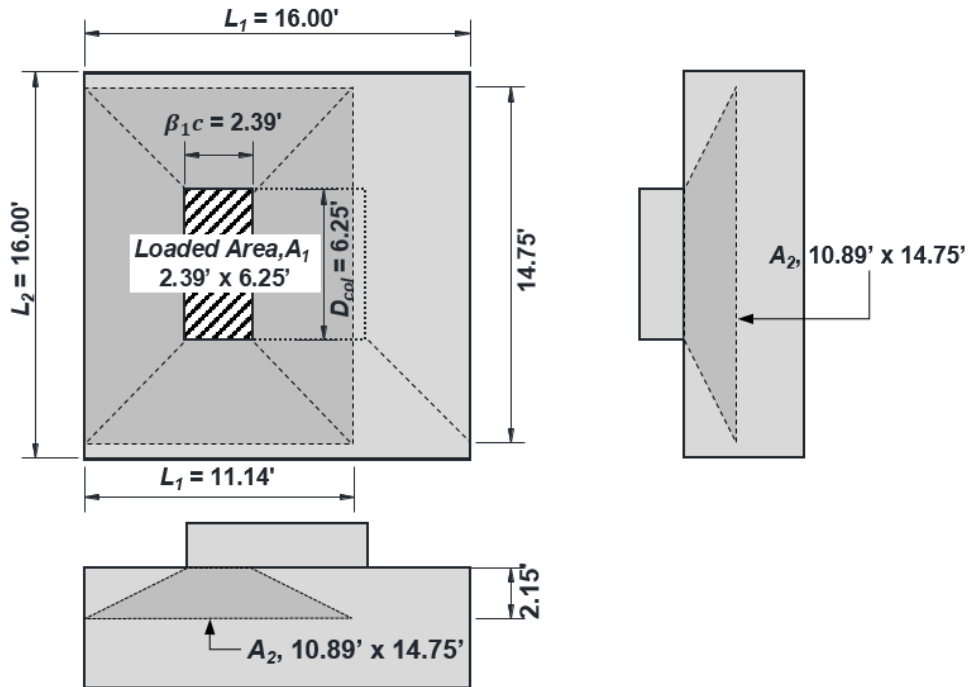


Figure 8.54 Determination of the confinement modification factor, m , for Nodes A and D

$$m = \sqrt{\frac{A_2}{A_1}} = \sqrt{\frac{14.75 \times 10.89}{6.25 \times 2.39}} = 3.28 \leq 3 \quad \therefore \text{se } m = 3.00$$

Concrete efficiency factor, ν , is determined in accordance with Table 5.8.2.5.3a-1 of AASHTO LRFD (2020). It should be noted that the concrete efficiency factor does not have to decrease to 0.45 because the side face reinforcement provided will be more than 0.18%.

o NODAL STRENGTH AT BEARING FACE

Factored load: $F_{u,bearing} = 1609.9 \text{ kip}$

Concrete efficiency factor: $\nu = 0.85$

Concrete capacity: $f_{cu} = m \cdot \nu \cdot f'_c = (3.00)(0.85)(3.6 \text{ ksi}) = 9.18 \text{ ksi}$

Nodal capacity: $\phi F_{n,bearing} = \phi f_{cu} A_{cn,bearing} = (0.7)(9.18 \text{ ksi})(1076 \text{ in.}^2) = 6914.4 \text{ kip} > 1609.9 \text{ kip} \quad \mathbf{OK}$

o NODAL STRENGTH AT BACK FACE

Factored load: $F_{u,back} = 1296.5 \text{ kip}$

Effective area: $A_{cn,back} = w_s \cdot 0.2H = (28.7 \text{ in.})(12.0 \text{ in.})$
 $= 344.2 \text{ in}^2$

Concrete efficiency factor: $\nu = 0.85$

Concrete capacity: $f_{cu} = m \cdot \nu \cdot f'_c = (3.00)(0.85)(3.6 \text{ ksi})$
 $= 9.18 \text{ ksi}$

Nodal capacity: $\phi F_{n,back} = \phi f_{cu} A_{cn,back}$
 $= (0.7)(9.18 \text{ ksi})(344.2 \text{ in.}^2)$
 $= 2211.8 \text{ kip} > 1296.5 \text{ kip} \quad \mathbf{OK}$

o NODAL STRENGTH AT STRUT-TO-NODE INTERFACE

Factored load: $F_{u,SNI} = 2068.1 \text{ kip}$

Effective area: $A_{cn,SNI} = w_s \cdot L_S = (28.7 \text{ in.})(36.7 \text{ in.})$
 $= 1053.3 \text{ in.}^2$

Concrete efficiency factor: $\nu = 0.85 - \frac{f'_c}{20 \text{ ksi}} = 0.85 - \frac{3.6 \text{ ksi}}{20 \text{ ksi}}$
 $= 0.67 > 0.65 \quad \therefore \text{se } \nu = 0.65$

Concrete capacity: $f_{cu} = m \cdot \nu \cdot f'_c = (3.00)(0.65)(3.6 \text{ ksi})$
 $= 7.02 \text{ ksi}$

Nodal capacity: $\phi F_n = \phi f_{cu} A_{cn,SNI}$
 $= (0.7)(7.02 \text{ ksi})(1053.3 \text{ in.}^2)$
 $= 5175.9 \text{ kip} > 2068.1 \text{ kip} \quad \mathbf{OK}$

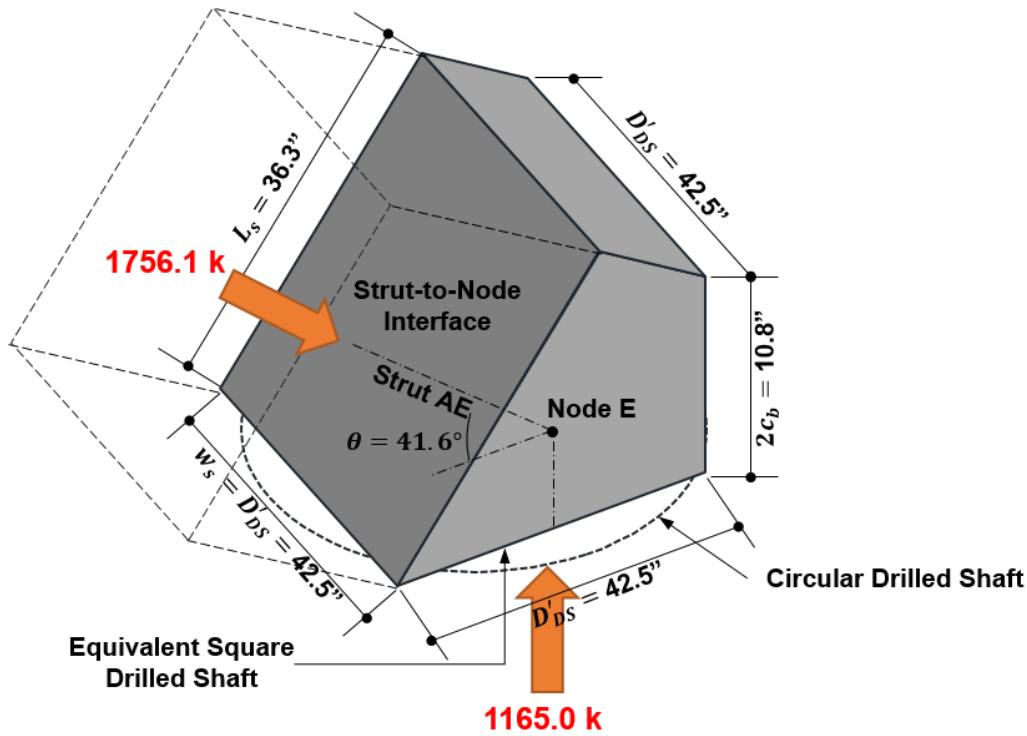
- Nodes E and H (CTT node)

Figure 8.55 illustrates the dimension and applying forces of nodes E and H in three dimensions based on this study's proposed recommendations. The confinement modification factors of Nodes E and H in Load Case III are the same as those in Load Case I ($m = 1.55$) as illustrated in Figure 8.33.

For the CTT node, the concrete efficiency factors at each face are identical to the following:

$$\nu = 0.85 - \frac{f'_c}{20 \text{ ksi}} = 0.85 - \frac{3.6 \text{ ksi}}{20 \text{ ksi}} = 0.67 > 0.65 \quad \therefore \text{se } \nu = 0.65$$

Note that the nodal strength check at back faces is not necessary since an adequate development length that satisfies the anchorage requirement is provided in this example.



$$\begin{aligned}
 L_s &= D'_{DS} \sin \theta + 2c_b \cos \theta \\
 &= 42.5'' \sin 41.6^\circ + 2 \times (4'' + 1.41'') \cos 41.6^\circ \\
 &= 36.3''
 \end{aligned}$$

Figure 8.55 Details of 3D nodal geometry at Nodes E and H

o NODAL STRENGTH AT BEARING FACE

Factored load: $F_{u,bearing} = 1165.0 \text{ kip}$

Concrete efficiency factor: $\nu = 0.65$

Concrete capacity: $f_{cu} = m \cdot \nu \cdot f'_c = (1.55)(0.65)(3.6 \text{ ksi}) = 3.63 \text{ ksi}$

Nodal capacity: $\phi F_{n,bearing} = \phi f_{cu} A_{cn,bearing} = (0.7)(3.63 \text{ ksi})(1809.6 \text{ in.}^2) = 4598.8 \text{ kip} > 1165.0 \text{ kip} \quad \mathbf{OK}$

o NODAL STRENGTH AT STRUT-TO-NODE INTERFACE

Factored load: $F_{u,SNI} = 1756.1 \text{ kip}$

Concrete efficiency factor: $\nu = 0.65$

Effective area: $A_{cn,SNI} = w_s \cdot L_s = (42.5 \text{ in.})(36.3 \text{ in.}) = 1544.9 \text{ in.}^2$

Concrete capacity: $f_{cu} = m \cdot \nu \cdot f'_c = (1.55)(0.65)(3.6 \text{ ksi}) = 3.63 \text{ ksi}$

Nodal capacity: $\phi F_{n,SNI} = \phi f_{cu} A_{cn,SNI}$
 $= (0.7)(3.63 \text{ ksi})(1544.9 \text{ in}^2)$
 $= 3925.6 \text{ kip} > 1756.1 \text{ kip} \quad \text{OK}$

- Nodes F and G (CTT node)

Nodes F and G have the same 3D nodal geometry, but length of the strut-to-node interface needs to be determined based on the axis of the resolved strut, as shown in Figure 8.56. As mentioned earlier, the confinement modification factors ($m = 1.55$) and concrete efficiency factor ($\nu = 0.65$) of Nodes F and G are the same as Nodes E and H.

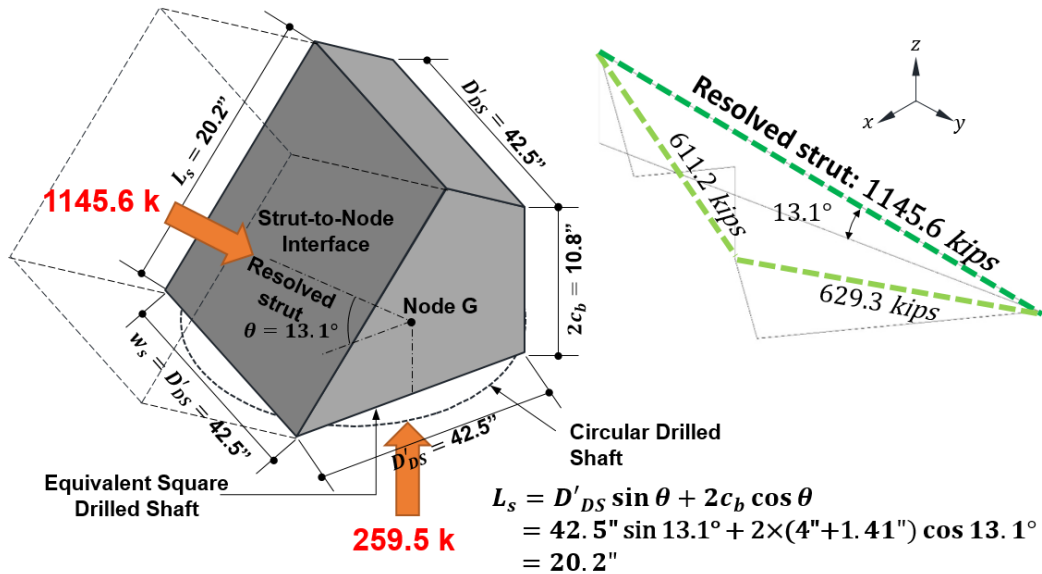


Figure 8.56 Details of 3D nodal geometry at Nodes F and G

o NODAL STRENGTH AT BEARING FACE

Factored load: $F_{u,bearing} = 259.5 \text{ kip}$

Concrete efficiency factor: $\nu = 0.65$

Concrete capacity: $f_{cu} = m \cdot \nu \cdot f'_c = (1.55)(0.65)(3.6 \text{ ksi})$
 $= 3.63 \text{ ksi}$

Nodal capacity: $\phi F_{n,bearing} = \phi f_{cu} A_{cn,bearing}$
 $= (0.7)(3.63 \text{ ksi})(1809.6 \text{ in.}^2)$
 $= 4598.8 \text{ kip} > 259.5 \text{ kip} \quad \mathbf{OK}$

o NODAL STRENGTH AT STRUT-TO-NODE INTERFACE

Factored load: $F_{u,SNI} = 1235.4 \text{ kip}$

Concrete efficiency factor: $\nu = 0.65$

Effective area: $A_{cn,SNI} = w_s \cdot L_s = (42.5 \text{ in.})(20.2 \text{ in.})$
 $= 858.5 \text{ in.}^2$

Concrete capacity: $f_{cu} = m \cdot \nu \cdot f'_c = (1.55)(0.65)(3.6 \text{ ksi})$
 $= 3.63 \text{ ksi}$

Nodal capacity: $\phi F_{n,SNI} = \phi f_{cu} A_{cn,SNI}$
 $= (0.7)(3.63 \text{ ksi})(858.5 \text{ in.}^2)$
 $= 2181.4 \text{ kip} > 1145.6 \text{ kip} \quad \mathbf{OK}$

Therefore, the nodal capacities of the CCC nodes and CTT nodes with defined nodal geometry are greater than factored loads.

8.4.5.6. Step 6: Proportion Shrinkage and Temperature Reinforcement

The necessary shrinkage and temperature reinforcement for the footing was specified in Section 8.4.3. On the side faces, No. 6 bars with 10 in. spacing ($A_s = 0.53 \text{ in.}^2/\text{ft.}$) are required in both horizontal and vertical directions. On the top face, No. 6 bars with 10 in. spacing A_s ($0.53 \text{ in.}^2/\text{ft.}$) are provided; however, the top mat reinforcement can be dependent on the other loading cases.

8.4.5.7. Step 7: Provide Necessary Anchorage for Ties

Figure 8.57 shows the available development length for the ties comprising the bottom tie ring in each direction. The research team suggests calculating the available development length at each node and checking the minimum length against the requirement. The resolved strut is also employed to compute the available lengths. According to Eq. (8.11), the available development lengths for each bottom tie are determined by the following calculations:

$$l_{ad,EF,E} = \frac{c_b}{\tan \theta_{s,proj,EF,E}} + D_{DS}'/2 + D_{DS}/2 + OH - c$$

$$= \frac{(5.41 \text{ in.})}{\tan 56.4^\circ} + (42.5 \text{ in.})/2 + (48.0 \text{ in.})/2 + 9 \text{ in.} - 3 \text{ in.} = 54.9 \text{ in.}$$

$$l_{ad,EF,F} = \frac{c_b}{\tan \theta_{s,proj,EF,F}} + D_{DS}'/2 + D_{DS}/2 + OH - c$$

$$= \frac{(5.41 \text{ in.})}{\tan 18.5^\circ} + (42.5 \text{ in.})/2 + (48.0 \text{ in.})/2 + 9 \text{ in.} - 3 \text{ in.} = 67.5 \text{ in.}$$

$$l_{ad,FG} = \frac{c_b}{\tan \theta_{s,proj,FG}} + D_{DS}'/2 + D_{DS}/2 + OH - c$$

$$= \frac{(5.41 \text{ in.})}{\tan 17.9^\circ} + (42.5 \text{ in.})/2 + (48.0 \text{ in.})/2 + 9 \text{ in.} - 3 \text{ in.} = 68.0 \text{ in.}$$

$$l_{ad,EH} = \frac{c_b}{\tan \theta_{s,proj,EH}} + D_{DS}'/2 + D_{DS}/2 + OH - c$$

$$= \frac{(5.41 \text{ in.})}{\tan 47.7^\circ} + (42.5 \text{ in.})/2 + (48.0 \text{ in.})/2 + 9 \text{ in.} - 3 \text{ in.} = 56.2 \text{ in.}$$

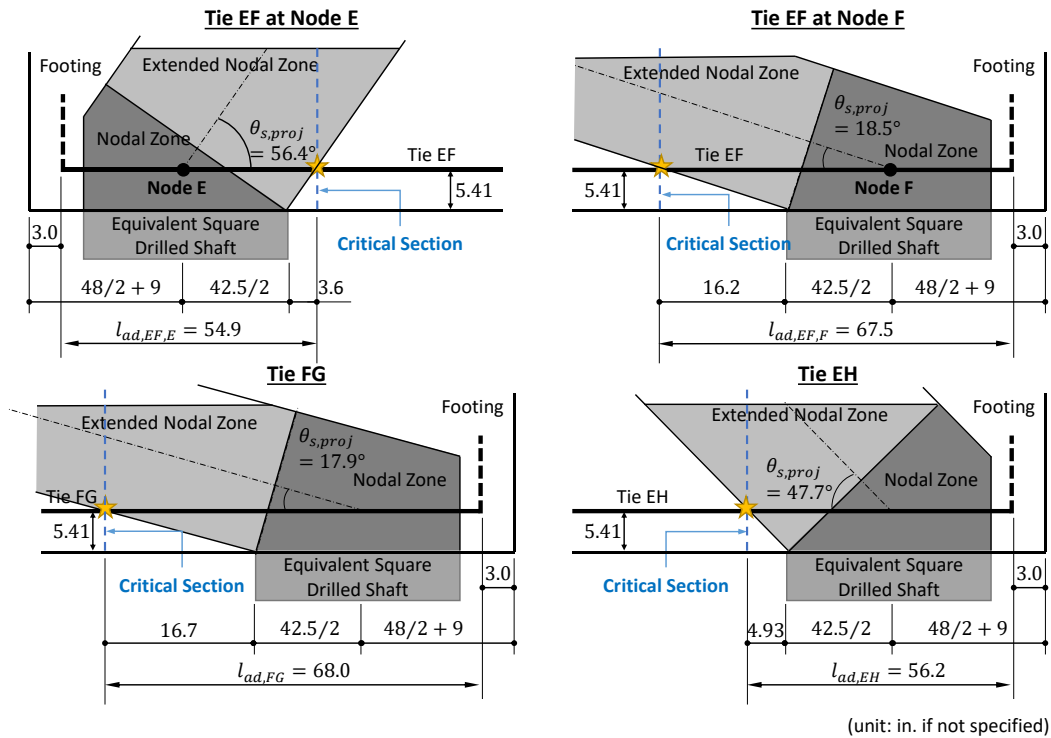


Figure 8.57 Critical sections for the development of ties: Load Case III

Straight bars for bottom mat reinforcement were recommended for Load Case I. Load Case III required a smaller steel area than did Load Case I, resulting in reduction of excess reinforcement factor; therefore, smaller development length would be required. To calculate the minimum required development length,

reinforcement location factor, λ_{rl} , is 1.0; the reinforcement coating factor, λ_{cf} , is 1.0 for uncoated reinforcement; the reinforcement confinement factor, λ_{rc} , is 0.54 by given reinforcing details of the example; and the concrete density modification factor, λ , is 1.0 for normal weight concrete. The excess reinforcement factors, λ_{er} , for Tie EF, FG, and EH are 0.484, 0.501, and 0.663, respectively. According to Eq. (8.4), the required development length of a straight No. 11 bar is calculated as below:

$$l_{d,EF} = (2.4)(1.41 \text{ in.}) \frac{60}{\sqrt{3.6}} \frac{(1.0)(1.0)(0.54)(0.484)}{1.0} = 28.0 \text{ in.} < l_{ad,EF} (= 54.9 \text{ in.})$$

$$l_{d,FG} = (2.4)(1.41 \text{ in.}) \frac{60}{\sqrt{3.6}} \frac{(1.0)(1.0)(0.54)(0.501)}{1.0} = 29.0 \text{ in.} < l_{ad,FG} (= 67.5 \text{ in.})$$

$$l_{d,EH} = (2.4)(1.41 \text{ in.}) \frac{60}{\sqrt{3.6}} \frac{(1.0)(1.0)(0.54)(0.663)}{1.0} = 38.3 \text{ in.} < l_{ad,EH} (= 56.2 \text{ in.})$$

Load Case III contains vertical tie elements (Ties BB' and CC') for the column reinforcement; therefore, the available length for the column reinforcement needs to be checked. Figure 8.58 depicts the available length for the column tie of the 3D STM for Load Case III, and the length can be computed as follow:

$$l_{ad.} = \left(\frac{L_t}{L_s}\right) (0.9H - c_b) - (d_{b,bu}) = \left(\frac{28.90}{93.66}\right) (0.9(60) - 5.41) - (1.41) = 13.6 \text{ in.}$$

To satisfy the anchorage requirement, hooked bars are employed for the column reinforcement, and the required development length of 90-degree and 180-degree hooked bars can be computed based on Eq. (8.5). The reinforcement confinement factor, λ_{rc} , is 0.8 by given reinforcing details of the example; the coating factor, λ_{cw} , is 1.0 for uncoated reinforcement; the excess reinforcement factor, λ_{er} , is 0.367 based on the designed column reinforcement; and the concrete density modification factor, λ , is 1.0 for normal weight concrete. The required development length of a hooked No. 11 bar is calculated as below:

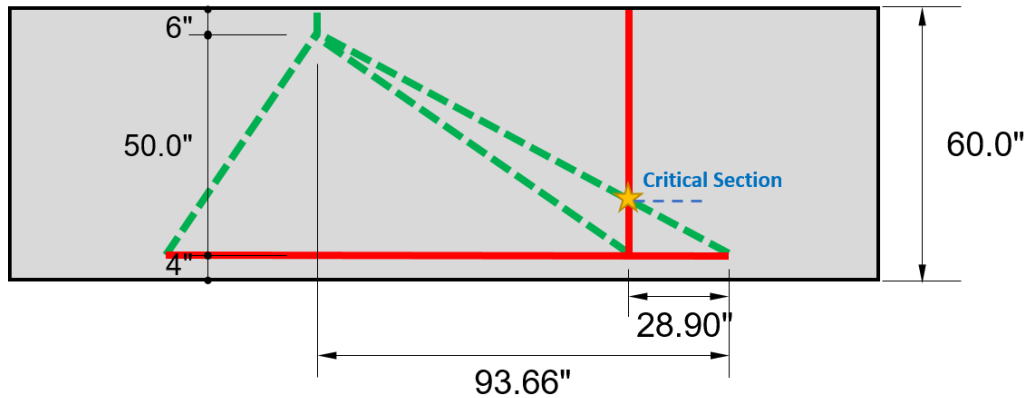


Figure 8.58 Critical section for the development of column ties

$$l_{dh} = \frac{38.0(1.41 \text{ in.})}{60.0} \cdot \frac{60 \text{ ksi}}{\sqrt{3.6 \text{ ksi}}} \times \left(\frac{0.8 \cdot 1.0 \cdot 0.367}{1.0} \right) = 8.2 \text{ in.} < l_{ad}, \quad (= 13.6 \text{ in.})$$

Therefore, the bottom mat straight bars and the column hooked bars all satisfy the anchorage requirement, and they can develop enough stress levels to be safe under Load Case III.

8.4.6. Design Calculations: Load Case IV

Figure 8.25 illustrates the factored load case that the column is subjected to axial compressive force and severe uniaxial flexural loading. Similar to Load Case III, one face of the column is subjected to tension. Furthermore, the severe overturning moment induces tension reaction at two of four drilled shafts whereas the others are in compression.

8.4.6.1. Step 1: Determine the Loads

Following the procedure presented in Figure 8.7, the stress distribution of the column section is developed. The nonlinear behavior of the concrete and the tensile reinforcement of the column are considered in the stress distribution to determine the resultant loads and their positions on the column section.

Similar to the stress distribution developed in Load Case III, the derived extreme compressive strain is also in the elastic range (-5.7×10^{-4} in./in.). However, the tensile column reinforcement stress is computed as 38.1 ksi, approximately 64% of the yield stress. The column stress of Load Case IV is greater than that of Load Case III due to the higher overturning moment applied to the column section.

In addition, the depth of the block is considered as the depth of the bearing face of the CCC node. The derived stress distribution and positions of loading resultant forces on the column section are presented in Figure 8.59.

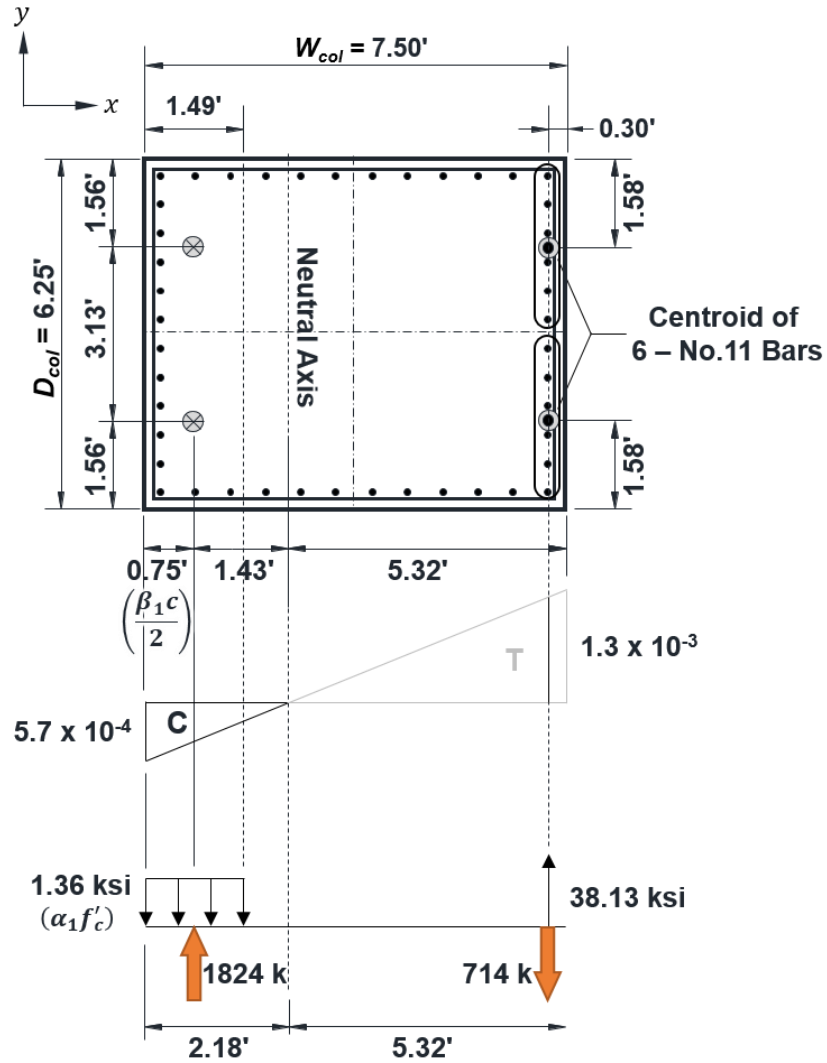


Figure 8.59 Stress distribution over the column section: Load Case IV

8.4.6.2. Step 2: Analyze Structural Component

The reaction force of each drilled shaft can be calculated by the equilibrium conditions of the external loading and reactions at four shafts as described in Eq. (8.17). Figure 8.60 shows the result of the structural analysis.

$$R_1 = R_4 = \frac{P_u}{4} + \frac{1}{2} \left(\frac{M_{uyy}}{S_{DS,x}} \right) = \frac{1100 \text{ kip}}{4} + \frac{1}{2} \left(\frac{7942 \text{ k-ft}}{10.50 \text{ ft}} \right) = 655.7 \text{ kip} \quad \text{(Compression)}$$

$$R_2 = R_3 = \frac{P_u}{4} - \frac{1}{2} \left(\frac{M_{uyy}}{S_{DS,x}} \right) = \frac{1100 \text{ kip}}{4} - \frac{1}{2} \left(\frac{7942 \text{ k-ft}}{10.50 \text{ ft}} \right) = 100.7 \text{ kip} \quad \text{(Tension)}$$

Eq. (8.17)

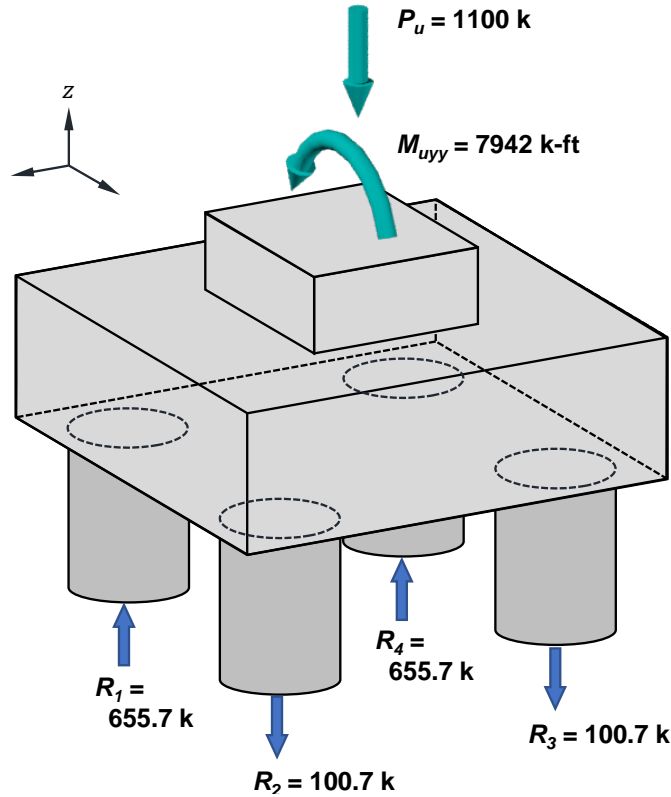


Figure 8.60 Applied loading and reaction forces: Load Case IV

8.4.6.3. Step 3: Develop Strut-and-Tie Model

A 3D strut-and-tie model is developed following the basic principle of 3D STM specified in Section 8.3.1.1. The x- and y-axes of the vertical struts and ties are positioned at the centroid of the subdivided equivalent stress block and the centroids of the tensile reinforcement groups consisting of six No. 11 bars, respectively. The coordinates of nodes above shafts (Nodes E through H) are identical to Load Case I and II, and the vertical column tie elements extend down to the elevation of the nodes above the shafts. In addition, the large overturning moment generates the tensile reaction at two drilled shafts, and it results in additional tie elements comprising another tie ring near the top surface of the footing. The top ties of the STM should correspond to the centroid of the top mat reinforcement that the tie represents. Therefore, the nodes beneath the column are also positioned at the same level of the top tie ring for the consistency of the STM model. The research team assumed to use two orthogonal layers of No. 6 bars for the top mat reinforcement of the footing designed for Load Case IV since the footings designed for previous loading cases provided No. 6 bars to the top mat reinforcement for the shrinkage and temperature reinforcement. A clear cover of 4 in. measured from the top surface of the footing is also provided. Tie forces and

strut forces can be computed by the equilibrium of each axis at each node and the configuration of the model, as shown in Figure 8.61 and Figure 8.62.

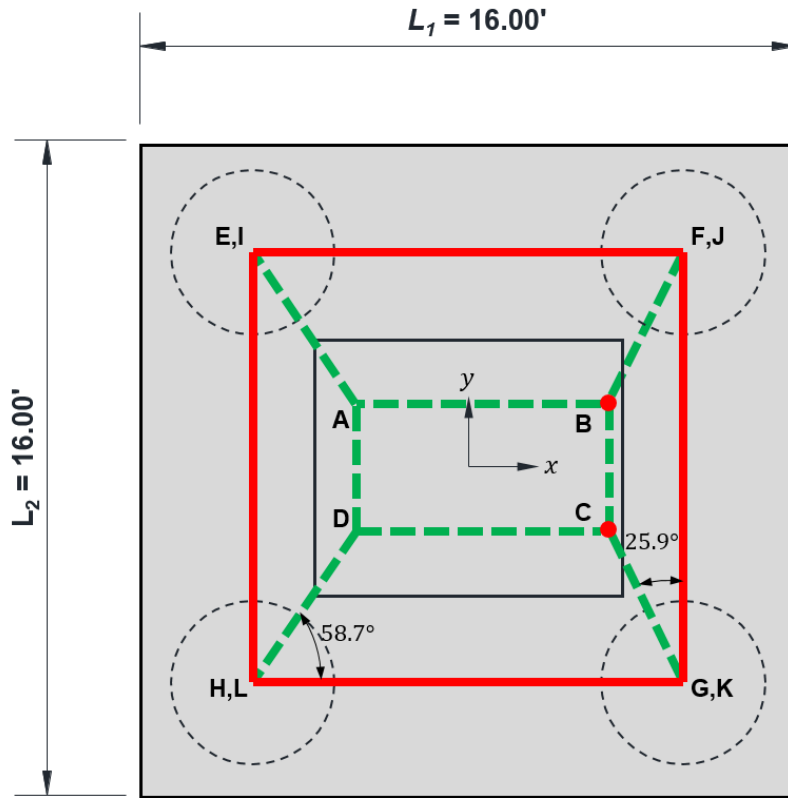


Figure 8.61 3D STM – plan view: Load Case IV

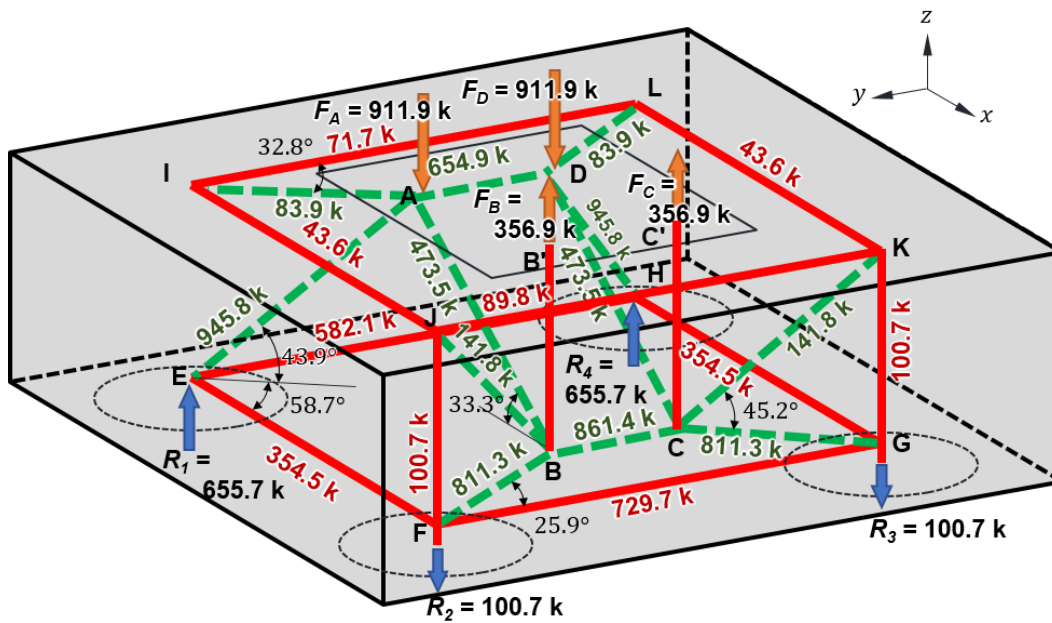


Figure 8.62 3D Strut-and-tie model: Load Case IV

8.4.6.4. Step 4: Proportion Ties

The top mat and bottom mat reinforcement will be designed with No. 6 and No. 11 bars, respectively. The same as Load Case III, No. 11 bars will be used for the column reinforcement since the column design is already provided with No. 11 bars. Drilled shafts commonly feature No. 9 bars as longitudinal reinforcement; therefore, No. 9 bars will be used to resist the force of the vertical tie elements for drilled shaft reinforcement.

- Ties EF and HG (Bottom Mat Reinforcement)

Factored tie force: $F_{u,tie} = 354.4 \text{ kip}$

Tie capacity: $\phi \cdot f_y \cdot A_{st} = F_{u,tie}$
 $(0.9)(60 \text{ ksi})A_{st} = 354.5 \text{ kip}$
 $A_{st} = 6.57 \text{ in.}^2$

Number of No. 11 bars required: $6.57 \text{ in.}^2 / 1.56 \text{ in.}^2 = 5 \text{ bars}$

- Tie EH (Bottom Mat Reinforcement)

Factored tie force: $F_{u,tie} = 582.1 \text{ kip}$

Tie capacity: $\phi \cdot f_y \cdot A_{st} = F_{u,tie}$
 $(0.9)(60 \text{ ksi})A_{st} = 582.1 \text{ kip}$
 $A_{st} = 10.78 \text{ in.}^2$

Number of No. 11 bars required: $10.78 \text{ in.}^2 / 1.56 \text{ in.}^2 = 7 \text{ bars}$

- Tie FG (Bottom Mat Reinforcement)

Factored tie force: $F_{u,tie} = 729.7 \text{ kip}$

Tie capacity: $\phi \cdot f_y \cdot A_{st} = F_{u,tie}$
 $(0.9)(60 \text{ ksi})A_{st} = 729.7 \text{ kip}$
 $A_{st} = 13.51 \text{ in.}^2$

Number of No. 11 bars required: $13.51 \text{ in.}^2 / 1.56 \text{ in.}^2 = 9 \text{ bars}$

- Ties IJ and LK (Top Mat Reinforcement)

Factored tie force: $F_{u,tie} = 43.6 \text{ kip}$

Tie capacity: $\phi \cdot f_y \cdot A_{st} = F_{u,tie}$
 $(0.9)(60 \text{ ksi})A_{st} = 43.6 \text{ kip}$
 $A_{st} = 0.81 \text{ in.}^2$

Number of No. 6 bars required: $0.81 \text{ in.}^2 / 0.44 \text{ in.}^2 = 2 \text{ bars}$

- Tie IL (Top Mat Reinforcement)

Factored tie force: $F_{u,tie} = 71.7 \text{ kip}$

Tie capacity: $\phi \cdot f_y \cdot A_{st} = F_{u,tie}$
 $(0.9)(60 \text{ ksi})A_{st} = 71.7 \text{ kip}$
 $A_{st} = 1.33 \text{ in.}^2$

Number of No. 6 bars required: $1.33 \text{ in.}^2 / 0.44 \text{ in.}^2 = 4 \text{ bars}$

- Tie JK (Top Mat Reinforcement)

Factored tie force: $F_{u,tie} = 89.8 \text{ kip}$

Tie capacity: $\phi \cdot f_y \cdot A_{st} = F_{u,tie}$
 $(0.9)(60 \text{ ksi})A_{st} = 89.8 \text{ kip}$
 $A_{st} = 1.66 \text{ in.}^2$

Number of No. 6 bars required: $1.66 \text{ in.}^2 / 0.44 \text{ in.}^2 = 4 \text{ bars}$

- Tie BB' and CC' (Column Reinforcement)

Factored tie force: $F_{u,tie} = 356.9 \text{ kip}$

Tie capacity: $\phi \cdot f_y \cdot A_{st} = F_{u,tie}$
 $(0.9)(60 \text{ ksi})A_{st} = 356.9 \text{ kip}$
 $A_{st} = 6.61 \text{ in.}^2$

Number of No. 11 bars required: $6.61 \text{ in.}^2 / 1.56 \text{ in.}^2 = 5 \text{ bars}$
 (6 bars already provided)

- Tie JF and KG (Drilled Shaft Reinforcement)

Factored tie force: $F_{u,tie} = 100.7 \text{ kip}$

Tie capacity: $\phi \cdot f_y \cdot A_{st} = F_{u,tie}$
 $(0.9)(60 \text{ ksi})A_{st} = 100.7 \text{ kip}$
 $A_{st} = 1.86 \text{ in.}^2$

Number of No. 9 bars required: $1.86 \text{ in.}^2 / 1.0 \text{ in.}^2 = 2 \text{ bars}$

In conclusion, the same number of bars (19 bars for each tie element) as used in Load Case I is provided in both orthogonal directions since the required amount of bottom mat reinforcement for Load Case I is greater than that of Load Case IV. Furthermore, a total of 20 bars of No. 6 are provided in both directions of the top mat reinforcement in previous load cases for the shrinkage and temperature reinforcement. The amount of the reinforcement is equivalent to 10 bars of No. 6 per each tie element in both orthogonal directions. Therefore, the shrinkage and

temperature reinforcement provided for the top mat reinforcement in previous load cases is sufficient to resist the tension forces applied in Load Case IV. The provided tensile column reinforcement is also enough to resist the force applied to the vertical tie element. At least two No. 9 bars are required to be provided per drilled shaft in tension.

8.4.6.5. Step 5: Perform Strength Checks

Since two of four drilled shafts are in tension, two nodes at drilled shafts in compression (Nodes E and H) and two nodes beneath the column (Nodes A and D) need to be checked for the nominal capacity at the bearing face, back face, and strut-to-node interface. The dimension of the nodal geometry of the CCC nodes—Nodes A and D—is determined based on the equivalent stress block depth. All nodal strength checks are performed as follows:

- Nodes A and D (CCC node)

The bearing face of the nodes is defined by the depth of the equivalent stress block and half-width of the column section.

$$A_{cn,bearing} = (1.49 \text{ ft}) \left(\frac{6.25 \text{ ft}}{2} \right) = 4.66 \text{ ft}^2 = 671 \text{ in.}^2$$

Nodes A and D are subjected to the forces of two diagonal struts in different directions and two horizontal struts. The resultant force in x-axis of two diagonal struts (Strut AE and AB for Node A; Strut DH and DC for Node D) and one horizontal strut (Strut AI for Node A; Strut DL for Node D) is zero; therefore, they are resolved into a single diagonal strut to simplify the nodal capacity check, as shown in Figure 8.63. In accordance with the recommendation in Section 8.3.1.3, Figure 8.64 illustrates nodes A and D in three dimensions, including the forces at each face, so that nodal capacities at each face can be checked.

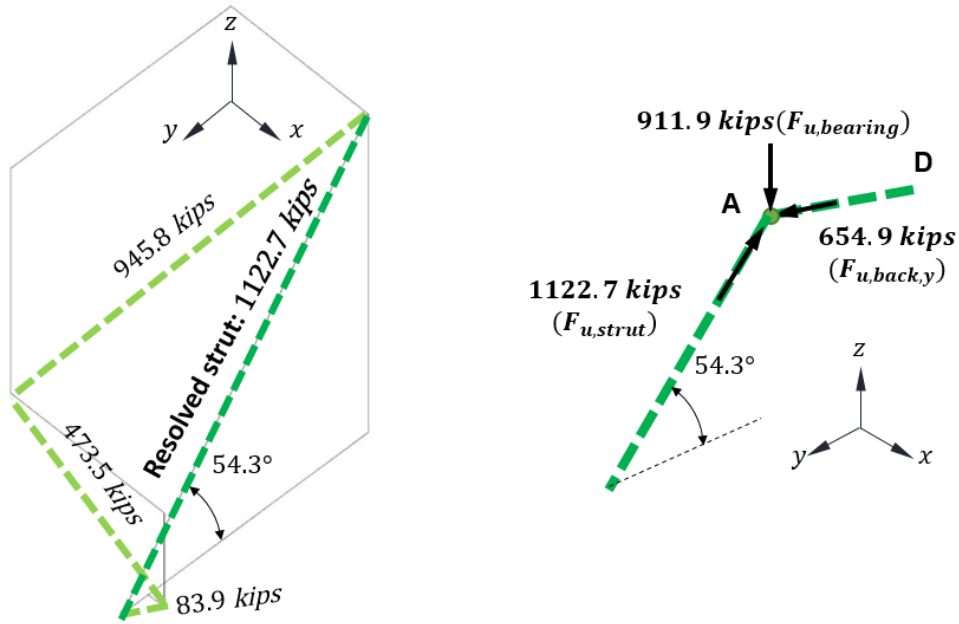
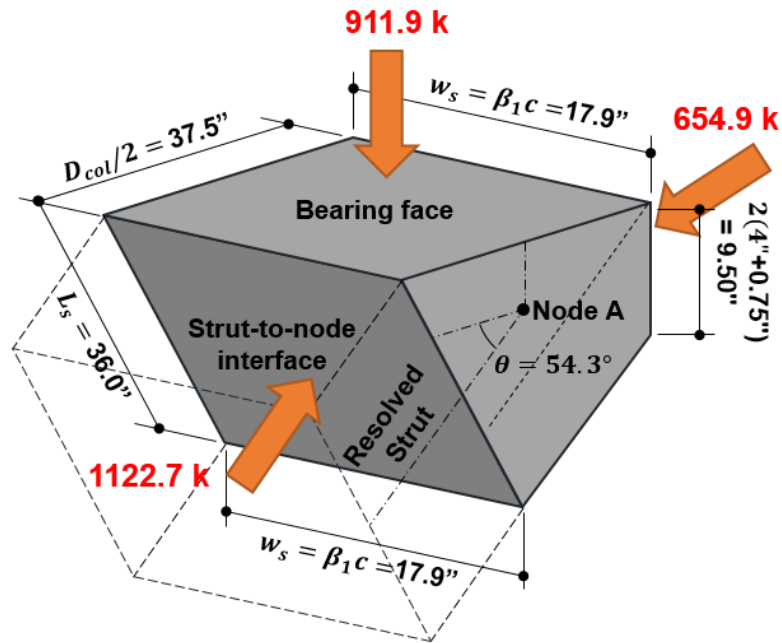


Figure 8.63 Resolving the force at Nodes A and D (CCC node)



$$\begin{aligned}
 L_s &= (D_{col}/2) \sin \theta + (9.50") \cos \theta \\
 &= 37.5" \sin 54.3^\circ + (9.50") \cos 54.3^\circ \\
 &= 36.0"
 \end{aligned}$$

Figure 8.64 Details of 3D nodal geometry at Nodes A and D

The overall column section is no longer subjected to compression; therefore, the confinement factor needs to be defined based on the dimension of the bearing face on the column determined from the stress distribution. For consistency in design,

the depth of the bearing area is assumed to be that of the equivalent stress block. The triaxial confinement factor is calculated as specified in Figure 8.65:

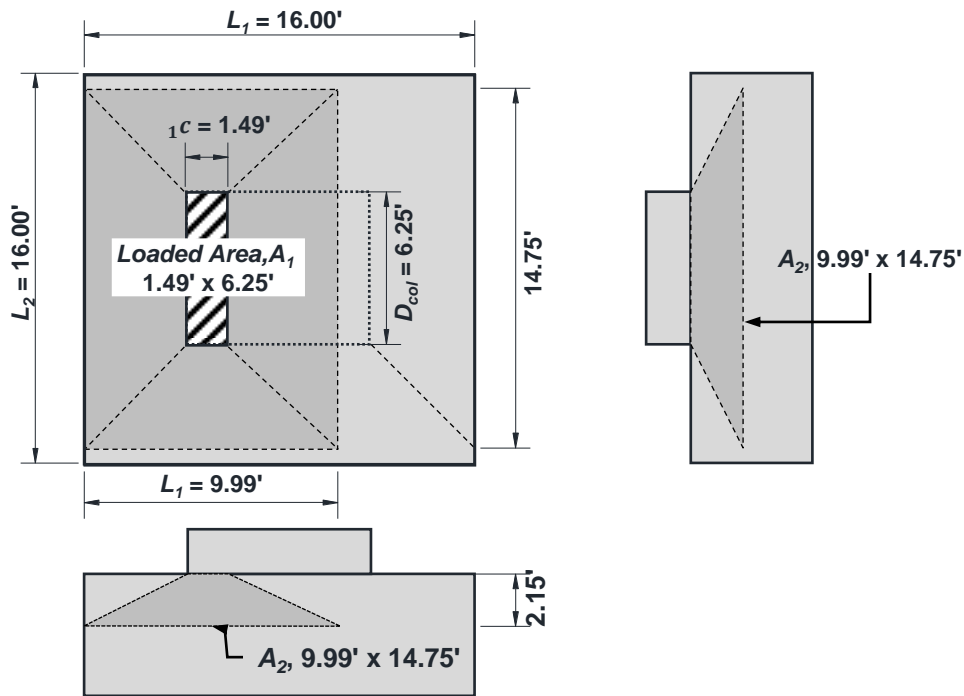


Figure 8.65 Determination of the confinement modification factor, m , for Nodes A and D

$$m = \sqrt{\frac{A_2}{A_1}} = \sqrt{\frac{14.75 \times 9.99}{6.25 \times 1.49}} = 3.97 \leq 3 \quad \therefore \text{se } m = 3.00$$

Concrete efficiency factor, ν , is determined in accordance with Table 5.8.2.5.3a-1 of AASHTO LRFD (2020). It should be noted that the concrete efficiency factor does not have to decrease to 0.45 because the side face reinforcement provided will be more than 0.18%.

o NODAL STRENGTH AT BEARING FACE

Factored load: $F_{u,bearing} = 911.9 \text{ kip}$

Concrete efficiency factor: $\nu = 0.85$

Concrete capacity: $f_{cu} = m \cdot \nu \cdot f'_c = (3.00)(0.85)(3.6 \text{ ksi}) = 9.18 \text{ ksi}$

Nodal capacity: $\phi F_{n,bearing} = \phi f_{cu} A_{cn,bearing} = (0.7)(9.18 \text{ ksi})(671 \text{ in.}^2) = 4311.8 \text{ kip} > 911.9 \text{ kip} \quad \mathbf{OK}$

o NODAL STRENGTH AT BACK FACE

Factored load: $F_{u,back} = 654.9 \text{ kip}$

Effective area: $A_{cn,back} = w_s \cdot (9.50 \text{ in.}) = 170.1 \text{ in.}^2$

Concrete efficiency factor: $\nu = 0.85$

Concrete capacity: $f_{cu} = m \cdot \nu \cdot f'_c = (3.00)(0.85)(3.6 \text{ ksi}) = 9.18 \text{ ksi}$

Nodal capacity: $\phi F_{n,back} = \phi f_{cu} A_{cn,back} = (0.7)(9.18 \text{ ksi})(170.1 \text{ in.}^2) = 1093.1 \text{ kip} > 654.9 \text{ kip} \quad \mathbf{OK}$

o NODAL STRENGTH AT STRUT-TO-NODE INTERFACE

Factored load: $F_{u,SNI} = 1122.7 \text{ kip}$

Effective area: $A_{cn,SNI} = w_s \cdot L_s = (17.9 \text{ in.})(36.0 \text{ in.}) = 644.4 \text{ in.}^2$

Concrete efficiency factor: $\nu = 0.85 - \frac{f'_c}{20 \text{ ksi}} = 0.85 - \frac{3.6 \text{ ksi}}{20 \text{ ksi}} = 0.67 > 0.65 \quad \therefore \text{se } \nu = 0.65$

Concrete capacity: $f_{cu} = m \cdot \nu \cdot f'_c = (3.00)(0.65)(3.6 \text{ ksi}) = 7.02 \text{ ksi}$

Nodal capacity: $\phi F_n = \phi f_{cu} A_{cn,SNI} = (0.7)(7.02 \text{ ksi})(644.4 \text{ in.}^2) = 3166.6 \text{ kip} > 1122.7 \text{ kip} \quad \mathbf{OK}$

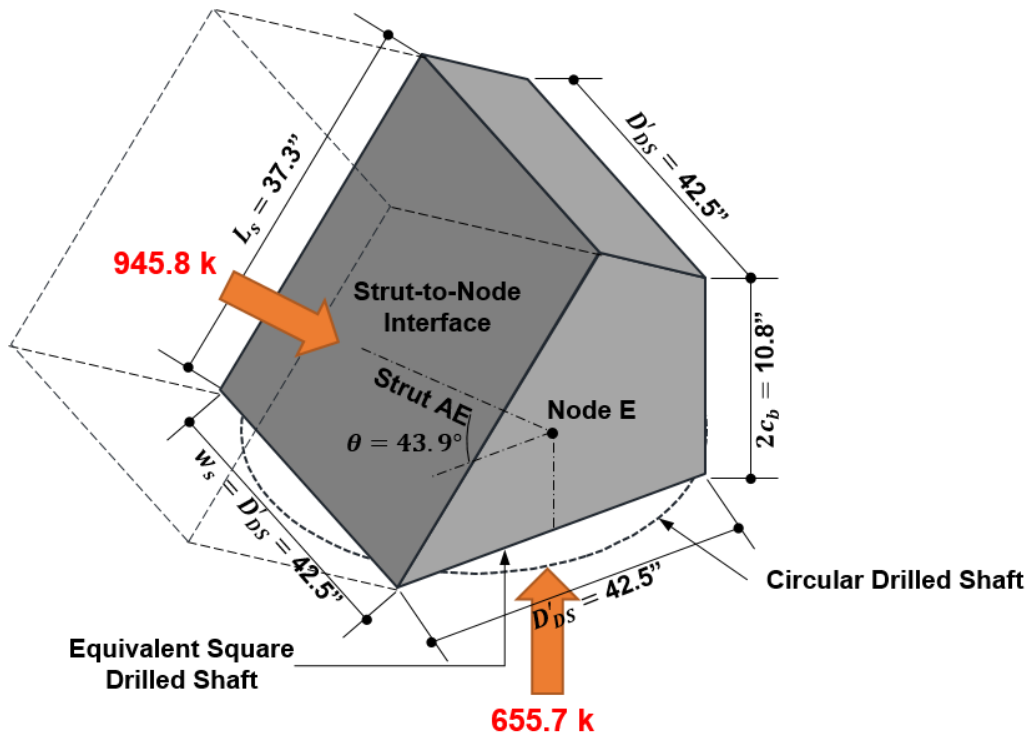
- Nodes E and H (CTT node)

Figure 8.66 illustrates the dimension and applying forces of nodes E and H in three dimensions based on this study's proposed recommendations. The confinement modification factors of Nodes E and H in Load Case IV are the same as those in Load Case I ($m = 1.55$) as illustrated in Figure 8.35.

For the CTT node, the concrete efficiency factors at each face are identical to the following:

$$\nu = 0.85 - \frac{f'_c}{20 \text{ ksi}} = 0.85 - \frac{3.6 \text{ ksi}}{20 \text{ ksi}} = 0.67 > 0.65 \quad \therefore \text{se } \nu = 0.65$$

Note that the nodal strength check at back faces is not necessary since an adequate development length that satisfies the anchorage requirement is provided in this example.



$$\begin{aligned}
 L_s &= D'_{DS} \sin \theta + 2c_b \cos \theta \\
 &= 42.5'' \sin 43.9^\circ + 2 \times (4'' + 1.41'') \cos 43.9^\circ \\
 &= 37.3''
 \end{aligned}$$

Figure 8.66 Details of 3D nodal geometry at Nodes E and H

o NODAL STRENGTH AT BEARING FACE

Factored load: $F_{u,bearing} = 655.7 \text{ kip}$

Concrete efficiency factor: $\nu = 0.65$

Concrete capacity: $f_{cu} = m \cdot \nu \cdot f'_c = (1.55)(0.65)(3.6 \text{ ksi}) = 3.63 \text{ ksi}$

Nodal capacity: $\phi F_{n,bearing} = \phi f_{cu} A_{cn,bearing} = (0.7)(3.63 \text{ ksi})(1809.6 \text{ in.}^2) = 4598.8 \text{ kip} > 655.7 \text{ kip} \quad \mathbf{OK}$

NODAL STRENGTH AT STRUT-TO-NODE INTERFACE

Factored load: $F_{u,SNI} = 945.8 \text{ kip}$

Effective area: $A_{cn,SNI} = w_s \cdot L_s = (42.5 \text{ in.})(37.3 \text{ in.}) = 1586.2 \text{ in.}^2$

Concrete capacity: $f_{cu} = m \cdot \nu \cdot f'_c = (1.55)(0.65)(3.6 \text{ ksi}) = 3.63 \text{ ksi}$

Nodal capacity: $\phi F_{n,SNI} = \phi f_{cu} A_{cn,SNI} = (0.7)(3.63 \text{ ksi})(1586.2 \text{ in.}^2) = 4030.5 \text{ kip} > 945.8 \text{ kip} \quad \mathbf{OK}$

Therefore, the nodal capacities of Nodes A, D, E, and H are greater than factored loads.

8.4.6.6. Step 6: Proportion Shrinkage and Temperature Reinforcement

The necessary shrinkage and temperature reinforcement for the footing was specified in Section 8.4.3. On the side faces, No. 6 bars with 10 in. spacing ($A_s = 0.53 \text{ in.}^2/\text{ft.}$) are required in both horizontal and vertical directions. No. 6 bars with 10 in. spacing as the top mat reinforcement is sufficient to the required strength as calculated in Section 8.4.6.4. Therefore, the original reinforcement plan (No. 6 bars with 10 in. spacing) will be used.

8.4.6.7. Step 7: Provide Necessary Anchorage for Ties

Figure 8.67 shows the available development length for the ties comprising the bottom and top tie rings in each direction. The research team suggests calculating the available development length at each node and checking the minimum length against the requirement. The nodes without defined nodal geometry (Nodes F, G, I, J, K, and L) cannot determine the critical section for the anchorage requirement based on the extended nodal zone. Therefore, the critical section of the tie bars at those nodes is assumed to be at the point directly above the interior edge of the equivalent square drilled shaft. This conservative way was proposed by Williams et al. (2012). The available development lengths for each tie are determined by the following calculations:

$$\begin{aligned} l_{ad,EF,E} &= \frac{c_b}{\tan \theta_{s,proj,EF,E}} + D_{DS}'/2 + D_{DS}/2 + OH - c \\ &= \frac{(5.41 \text{ in.})}{\tan 61.6^\circ} + (42.5 \text{ in.})/2 + (48.0 \text{ in.})/2 + 9 \text{ in.} - 3 \text{ in.} = 54.2 \text{ in.} \end{aligned}$$

$$\begin{aligned} l_{ad,EH} &= \frac{c_b}{\tan \theta_{s,proj,EH}} + D_{DS}'/2 + D_{DS}/2 + OH - c \\ &= \frac{(5.41 \text{ in.})}{\tan 47.7^\circ} + (42.5 \text{ in.})/2 + (48.0 \text{ in.})/2 + 9 \text{ in.} - 3 \text{ in.} = 56.2 \text{ in.} \end{aligned}$$

$$\begin{aligned} l_{ad,SM} &= D_{DS}'/2 + D_{DS}/2 + OH - c \\ &= (42.5 \text{ in.})/2 + (48.0 \text{ in.})/2 + 9 \text{ in.} - 3 \text{ in.} = 51.3 \text{ in.} \end{aligned}$$

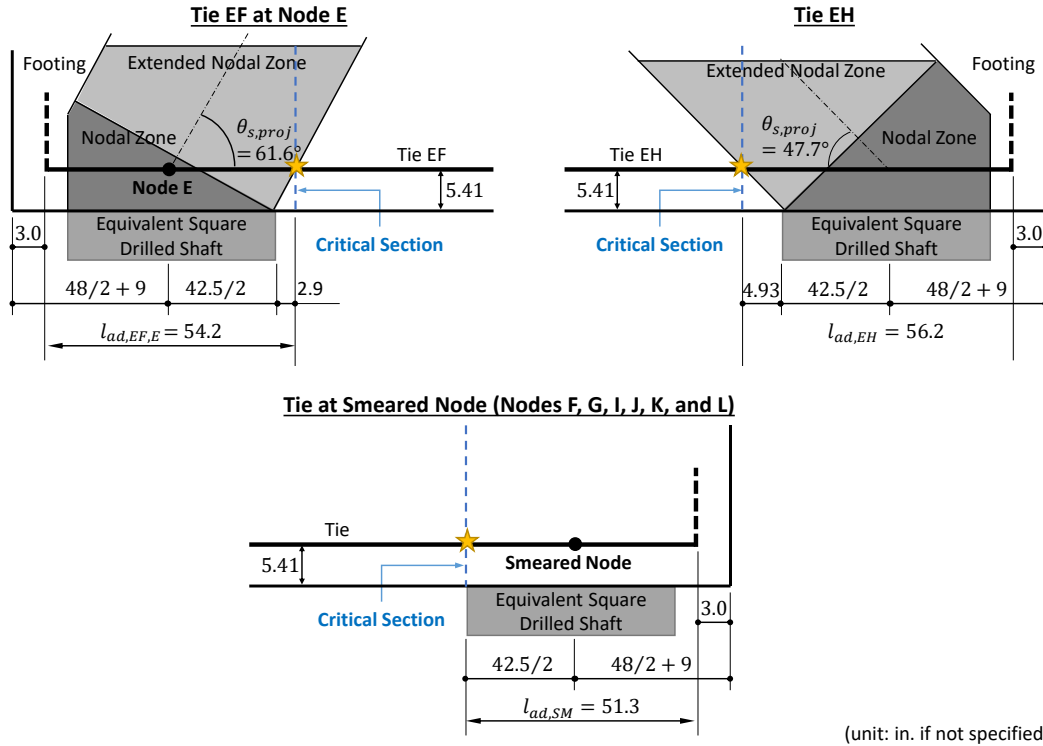


Figure 8.67 Critical sections for the development of ties: Load Case IV

Straight bars for bottom mat reinforcement were recommended for Load Case I. Load Case IV required a smaller steel area than did Load Case I, resulting in reduction of excess reinforcement factor; therefore, smaller development length would be required. To calculate the minimum required development length, reinforcement location factor, λ_{rl} , is 1.0; the reinforcement coating factor, λ_{cf} , is 1.0 for uncoated reinforcement; the reinforcement confinement factor, λ_{rc} , is 0.54 for No. 11 bars and 0.28 for No. 6 bars by given reinforcing details of the example; and the concrete density modification factor, λ , is 1.0 for normal weight concrete. The excess reinforcement factors, λ_{er} , for Tie EF, FG, and EH are 0.222, 0.456, and 0.364, respectively. According to Eq. (8.4), the required development length of a straight No. 11 bar is calculated as below:

$$l_{d,EF} = (2.4)(1.41 \text{ in.}) \frac{60 (1.0)(1.0)(0.54)(0.222)}{\sqrt{3.6} \cdot 1.0} = 12.8 \text{ in.} < l_{ad,SM} (= 51.4 \text{ in.})$$

$$l_{d,FG} = (2.4)(1.41 \text{ in.}) \frac{60 (1.0)(1.0)(0.54)(0.456)}{\sqrt{3.6} \cdot 1.0} = 26.3 \text{ in.} < l_{ad,SM} (= 51.4 \text{ in.})$$

$$l_{d,EH} = (2.4)(1.41 \text{ in.}) \frac{60 (1.0)(1.0)(0.54)(0.364)}{\sqrt{3.6} \cdot 1.0} = 21.0 \text{ in.} < l_{ad,EH} (= 56.2 \text{ in.})$$

To compute the required development length of a straight No. 6 bar, the same factors are used, and the reinforcement confinement factor, λ_{rc} , is 0.40 based on the diameter of a No. 6 bar. The excess reinforcement factors, λ_{er} is 1.0 to add conservatism. The required development length of a No. 6 bar is calculated as below:

$$l_{d,IJ} = (2.4)(0.75 \text{ in.}) \frac{60 (1.0)(1.0)(0.40)(1.0)}{\sqrt{3.6} \cdot 1.0} = 22.8 \text{ in.} < l_{ad,SM} (= 51.4 \text{ in.})$$

$$l_{d,JK} = (2.4)(0.75 \text{ in.}) \frac{60 (1.0)(1.0)(0.40)(1.0)}{\sqrt{3.6} \cdot 1.0} = 22.8 \text{ in.} < l_{ad,SM} (= 51.4 \text{ in.})$$

$$l_{d,IL} = (2.4)(0.75 \text{ in.}) \frac{60 (1.0)(1.0)(0.40)(1.0)}{\sqrt{3.6} \cdot 1.0} = 22.8 \text{ in.} < l_{ad,SM} (= 51.4 \text{ in.})$$

The Load Case IV also contains vertical tie elements for the column (Ties BB' and CC') and drilled shaft reinforcement (Ties FJ and GK); therefore, the available lengths for both types of reinforcement need to be checked. Figure 8.68 presents the available lengths for the column tie and drilled shaft tie of the 3D STM for Load Case IV, and the lengths can be computed as follow:

$$\begin{aligned} l_{ad} &= H - (c_b + c_t) - (d_{b,bu}) - z_s \tan 25^\circ \\ &= (60 \text{ in.}) - (5.41 \text{ in.} + 4.75 \text{ in.}) - (1.41 \text{ in.}) - (49.5 \text{ in.}) \tan 25^\circ \\ &= 25.3 \text{ in.} \end{aligned}$$

$$\begin{aligned} l_{ad,DS} &= H - (c_b + c_t) - (d_{b,tl}) - z_s \tan 25^\circ \\ &= (60 \text{ in.}) - (5.41 \text{ in.} + 4.75 \text{ in.}) - (0.75 \text{ in.}) - (49.5 \text{ in.}) \tan 25^\circ \\ &= 26.0 \text{ in.} \end{aligned}$$

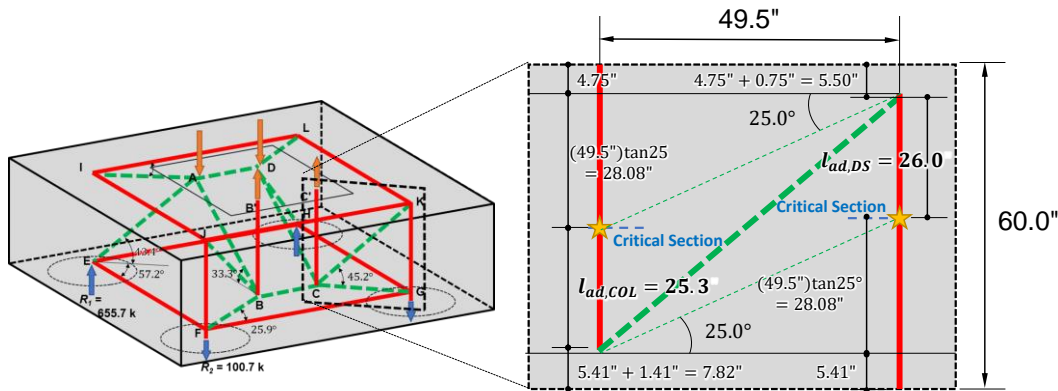


Figure 8.68 Critical section for the development of column ties and drilled shaft ties

To satisfy the anchorage requirement, hooked bars are employed for the column reinforcement, and the required development length of 90-degree and 180-degree hooked bars can be computed based on Eq. (8.5). The reinforcement confinement factor, λ_{rc} , is 0.8 by given reinforcing details of the example; the coating factor,

λ_{cw} , is 1.0 for uncoated reinforcement; the excess reinforcement factor, λ_{er} , is 0.706 based on the designed column reinforcement; and the concrete density modification factor, λ , is 1.0 for normal weight concrete. The required development length of a hooked No. 11 bar is calculated as below:

$$\begin{aligned} l_{dh} &= \frac{38.0(1.41 \text{ in.})}{60.0} \cdot \frac{60 \text{ ksi}}{\sqrt{3.6 \text{ ksi}}} \times \left(\frac{0.8 \cdot 1.0 \cdot 0.706}{1.0} \right) \\ &= 16.0 \text{ in.} < l_{ad}, \quad (= 25.3 \text{ in.}) \end{aligned}$$

The drilled shaft reinforcement also uses No.9 hooked bars to satisfy the anchorage requirement. The same equation is used to calculate the development length of a hooked No. 9 bar with the excess reinforcement factor, λ_{er} , is 0.932 based on the designed drilled shaft reinforcement as below:

$$\begin{aligned} l_{dh,DS} &= \frac{38.0(1.128 \text{ in.})}{60.0} \cdot \frac{60 \text{ ksi}}{\sqrt{3.6 \text{ ksi}}} \times \left(\frac{0.8 \cdot 1.0 \cdot 0.932}{1.0} \right) \\ &= 16.8 \text{ in.} < l_{ad,DS} (= 26.0 \text{ in.}) \end{aligned}$$

Therefore, all reinforcing bars comprising the footing are confirmed to be safe under Load Case IV by satisfying the anchorage requirement.

8.4.7. Design Calculations: Load Case V

Figure 8.26 depicts the factored load case that the column is subjected to axial compressive force with the combination of mild biaxial flexural loading. Despite the biaxial eccentric loading, the column section remains in compression with varied stress level in both x- and y-axes as illustrated in Figure 8.69. It should be noted that the stress distribution over the column is bilinear since the maximum compressive stress on the interface does not exceed the elastic limit state; half of the design strength of the concrete (1.80 ksi). If the maximum compressive stress on the column exceeds the elastic stress limit, nonlinear stress distribution should to be considered; however, it is not covered in this example. The loading was designed so that the maximum stress is the similar level to other load cases (around 1.3 ksi).

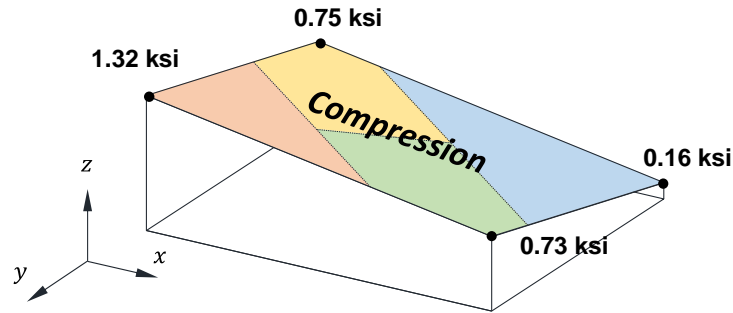


Figure 8.69 Stress distribution over the column section: Load Case V

Similar to other load cases, the load can be divided into four sets of loading, with resultant force components that are equal amounts with the reaction forces of adjacent drilled shafts so that only one diagonal strut at each top and bottom node would be developed. This constraint leads to the simple 3D strut-and-tie model, however, the calculation procedure of positions in bilinear stress distribution and forces of STM component is complicated; and results might be in slight disequilibrium. The recommended calculation procedure for positions of loading resultant forces and for 3D strut-and-tie model is based on the equilibrium on the column section as well as the equilibrium at nodes as the following steps:

- 1) Calculate reactions that satisfy the equilibrium conditions of the external loading
- 2) Determine the regions where resultant forces on the column section (Figure 8.70) were equal to the reactions adjacent drilled shafts (Figure 8.71)
- 3) Calculate positions of A and C, the centroid of forces in the triangular regions (Region A and C)
- 4) Develop 3D strut-and-tie model (Figure 8.72 and Figure 8.73) with the coordinates of A and C
- 5) Calculate the angles at F and H from the equilibrium at Nods F and H
- 6) Find coordinates of B and D from the geometric details of F and H

8.4.7.1. Step 1: Determine the Loads

The stress on the column section varied along the both x- and y-axes as shown in Figure 8.69. The maximum and the minimum compressive stress are 1321 psi and 160 psi respectively with the assumption of linear stress distribution. Figure 8.70 illustrates the coordinates of the positions of the loads comprising the equivalent force system based on the calculation procedure in the previous section. The detail calculation is provided Appendix I.

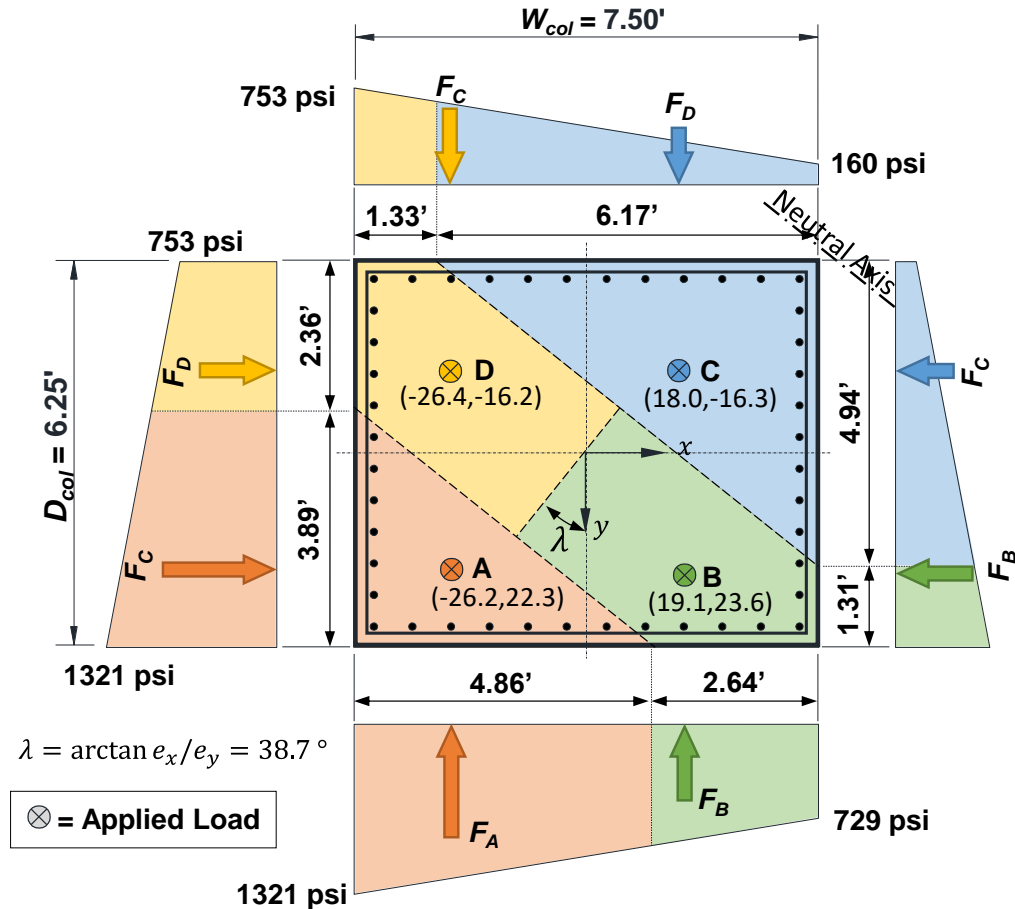


Figure 8.70 Positions of the subdivided loads in the equivalent force system: Load Case V

8.4.7.2. Step 2: Analyze Structural Component

The reaction force of each drilled shaft can be calculated by the equilibrium conditions of the external loading and reactions at four shafts as described in Eq. (8.18). Figure 8.71 shows the result of the structural analysis.

$$R_1 = \frac{P_u}{4} + \frac{1}{2} \left(\frac{M_{uyy}}{S_{DS,x}} \right) + \frac{1}{2} \left(\frac{M_{uxx}}{S_{DS,y}} \right) = \frac{5000 \text{ kip}}{4} + \frac{1}{2} \left(\frac{2500 \text{ k-ft}}{10.50 \text{ ft}} \right) + \frac{1}{2} \left(\frac{2000 \text{ k-ft}}{10.50 \text{ ft}} \right) \quad \text{Eq. (8.18)}$$

$$= 1464.3 \text{ kip (Compression)}$$

$$R_2 = \frac{P_u}{4} - \frac{1}{2} \left(\frac{M_{uyy}}{S_{DS,x}} \right) + \frac{1}{2} \left(\frac{M_{uxx}}{S_{DS,y}} \right) = \frac{5000 \text{ kip}}{4} - \frac{1}{2} \left(\frac{2500 \text{ k-ft}}{10.50 \text{ ft}} \right) + \frac{1}{2} \left(\frac{2000 \text{ k-ft}}{10.50 \text{ ft}} \right)$$

$$= 1226.2 \text{ kip (Compression)}$$

$$R_3 = \frac{P_u}{4} - \frac{1}{2} \left(\frac{M_{uyy}}{S_{DS,x}} \right) - \frac{1}{2} \left(\frac{M_{uxx}}{S_{DS,y}} \right) = \frac{5000 \text{ kip}}{4} - \frac{1}{2} \left(\frac{2500 \text{ k-ft}}{10.50 \text{ ft}} \right) - \frac{1}{2} \left(\frac{2000 \text{ k-ft}}{10.50 \text{ ft}} \right)$$

$$= 1035.7 \text{ kip (Compression)}$$

$$R_4 = \frac{P_u}{4} + \frac{1}{2} \left(\frac{M_{uyy}}{S_{DS,x}} \right) - \frac{1}{2} \left(\frac{M_{uxx}}{S_{DS,y}} \right) = \frac{5000 \text{ kip}}{4} + \frac{1}{2} \left(\frac{2500 \text{ k-ft}}{10.50 \text{ ft}} \right) - \frac{1}{2} \left(\frac{2000 \text{ k-ft}}{10.50 \text{ ft}} \right)$$

$$= 1273.8 \text{ kip (Compression)}$$

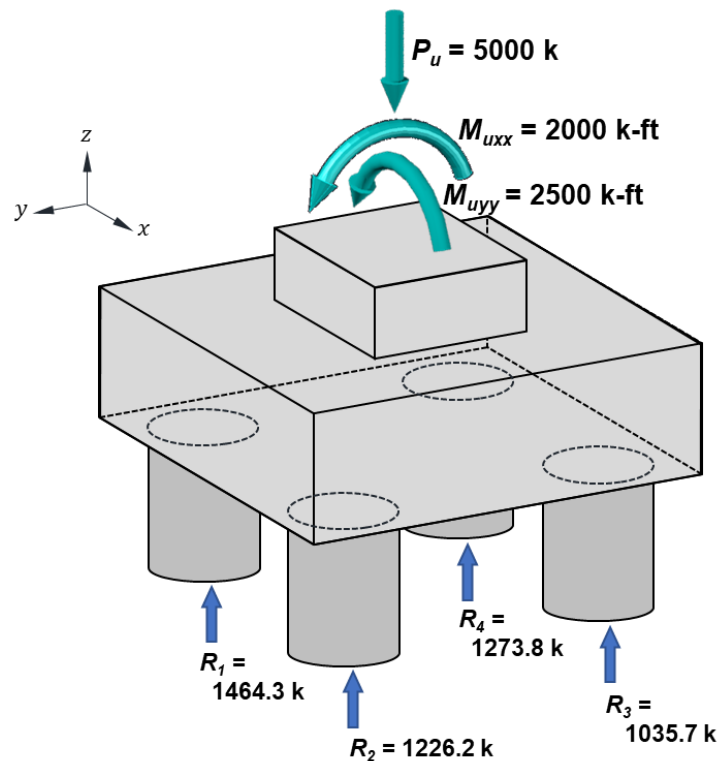


Figure 8.71 Applied loading and reaction forces: Load Case V

8.4.7.3. Step 3: Develop Strut-and-Tie Model

The research team developed the simplest 3D strut-and-tie model according to the principle of 3D STM specified in Section 8.3.1.1. The x-, y- and z-coordinates of the nodes below the column (Nodes A through D) comes from the results of previous subsection. The coordinates of nodes above shafts (Nodes E through H) are equal to those in Load Case I. Figure 8.72 and Figure 8.73 shows tie forces and strut forces from the equilibrium of each axis at each node and the geometric properties. As provided in Appendix I, even though slight force differences between both nodes of horizontal struts and ties occurred, the differences were less than 3% and 0.5%, respectively, which stems from the assumption that subdivided force components make equal amounts with the reaction forces of adjacent drilled shafts. If the forces at both ends were different, the greater values between both ends were used.

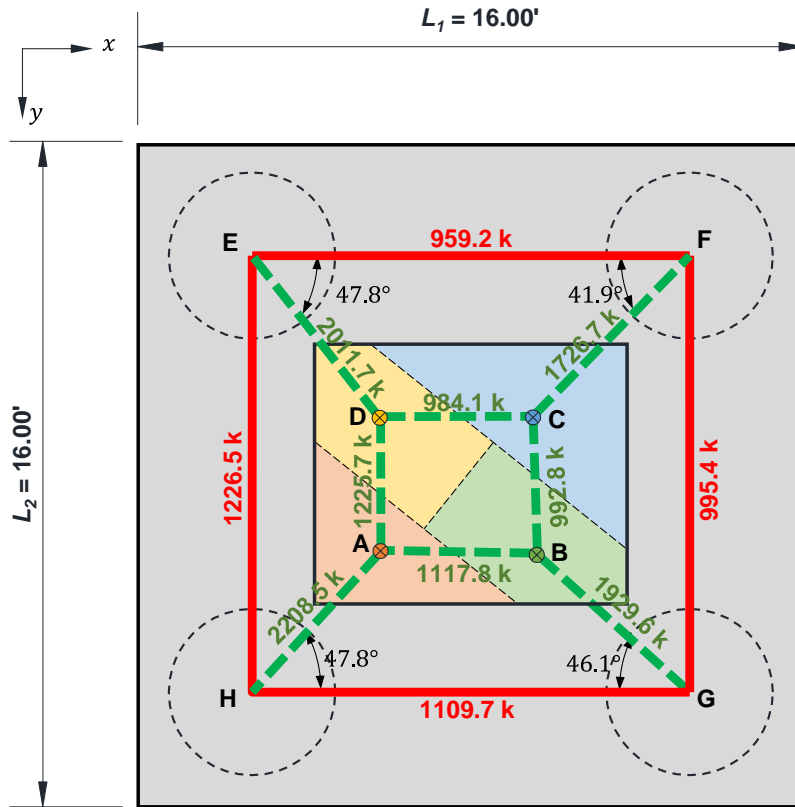


Figure 8.72 Strut-and-tie model – plan view: Load Case V

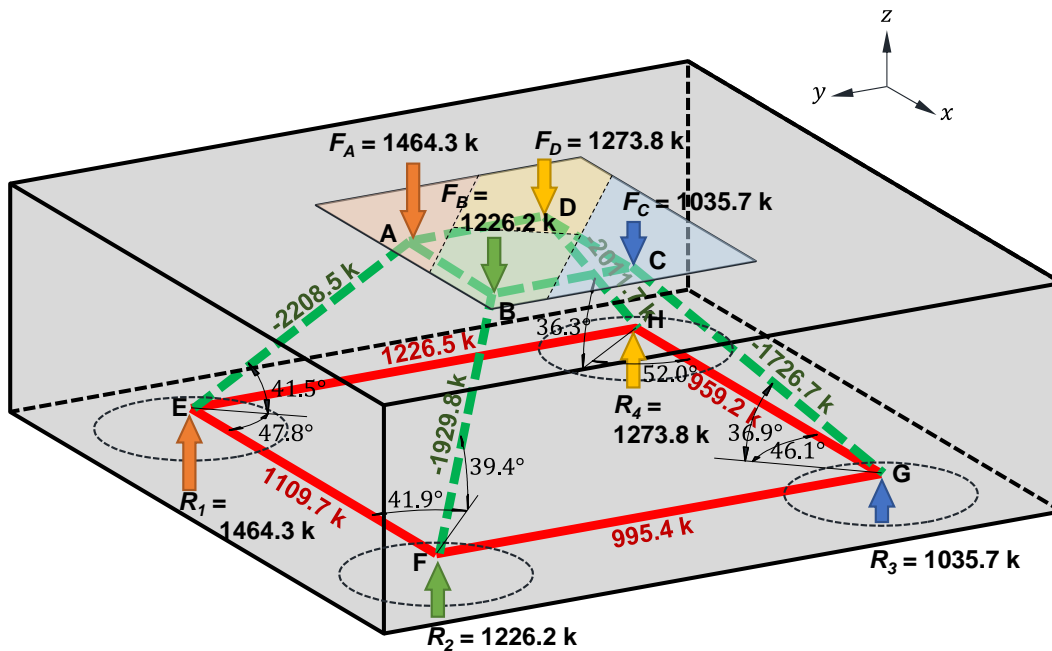


Figure 8.73 3D strut-and-tie model: Load Case V

8.4.7.4. Step 4: Proportion Ties

As shown in Figure 8.73, tie EH is the most critical to calculate the required amount of reinforcement. Similar to Load Case I, No. 11 bars will be used for the bottom mat reinforcement.

- Tie EF

Factored tie force: $F_{u,tie} = 1109.7 \text{ kip}$

Tie capacity: $\phi \cdot f_y \cdot A_{st} = F_{u,tie}$
 $(0.9)(60 \text{ ksi})A_{st} = 1109.7 \text{ kip}$
 $A_{st} = 20.55 \text{ in.}^2$

Number of No. 11 bars required: $20.55 \text{ in.}^2 / 1.56 \text{ in.}^2 = 14 \text{ bars}$

- Tie FG

Factored tie force: $F_{u,tie} = 995.4 \text{ kip}$

Tie capacity: $\phi \cdot f_y \cdot A_{st} = F_{u,tie}$
 $(0.9)(60 \text{ ksi})A_{st} = 995.4 \text{ kip}$
 $A_{st} = 18.43 \text{ in.}^2$

Number of No. 11 bars required: $18.43 \text{ in.}^2 / 1.56 \text{ in.}^2 = 12 \text{ bars}$

- Tie GH

Factored tie force: $F_{u,tie} = 959.2 \text{ kip}$

Tie capacity: $\phi \cdot f_y \cdot A_{st} = F_{u,tie}$
 $(0.9)(60 \text{ ksi})A_{st} = 959.2 \text{ kip}$
 $A_{st} = 17.76 \text{ in.}^2$

Number of No. 11 bars required: $17.76 \text{ in.}^2 / 1.56 \text{ in.}^2 = 12 \text{ bars}$

- Tie EH

Factored tie force: $F_{u,tie} = 1226.5 \text{ kip}$

Tie capacity: $\phi \cdot f_y \cdot A_{st} = F_{u,tie}$
 $(0.9)(60 \text{ ksi})A_{st} = 1226.5 \text{ kip}$
 $A_{st} = 22.71 \text{ in.}^2$

Number of No. 11 bars required: $22.71 \text{ in.}^2 / 1.56 \text{ in.}^2 = 15 \text{ bars}$

In conclusion, the same number of bars (19 bars) as used in Load Case I is provided in both orthogonal directions since the required amount of bottom mat reinforcement for Load Case I is greater than that of Load Case V.

8.4.7.5. Step 5: Perform Strength Checks

Checking the nominal capacity at the bearing face, back face, and strut-to-node interface is necessary at every node. Nodes A and E among CCC and CTT nodes, respectively, are critical for nodal strength checks since the force at the bearing face and strut force is the greatest; moreover, the node type is CTT node (Node E), which has the smallest concrete efficiency factor.

- Node A (CCC node)

Firstly, the area of bearing face at Node A is used to define the detailed 3D nodal geometry. The bearing area of the nodes, as indicated by the orange shaded region on the column section in Figure 8.69, is calculated thusly:

$$A_{cn,bearing} = \frac{1}{2}(4.86 \text{ ft})(3.89 \text{ ft}) = 9.45 \text{ ft}^2 = 1361.2 \text{ in.}^2$$

The length of the equivalent square bearing face, $L'_{cn,b}$, is:

$$L'_{cn,b} = \sqrt{A_{cn,bearing}} = 36.9 \text{ in.}$$

Figure 8.74 illustrates resolving the force at Node A from multiple loads at back faces. In accordance with the recommendation in Section 8.3.1.3, Figure 8.75 illustrates Node A in three dimensions, including the forces at each face, so that nodal capacities at each face can be checked.

The triaxial confinement factor is identical to the one used in Load Case I ($m = 2.34$) because the entire column section is in compression. The concrete efficiency factor, ν , is determined in accordance with Table 5.8.2.5.3a-1 of AASHTO LRFD (2020). It should be noted that the concrete efficiency factor does not have to decrease to 0.45 because the side face reinforcement provided will be more than 0.18%.

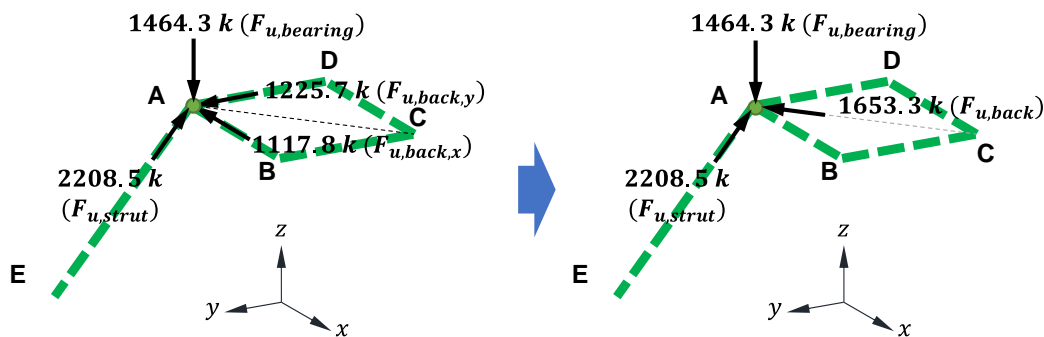


Figure 8.74 Resolving the force at Node A (CCC node)

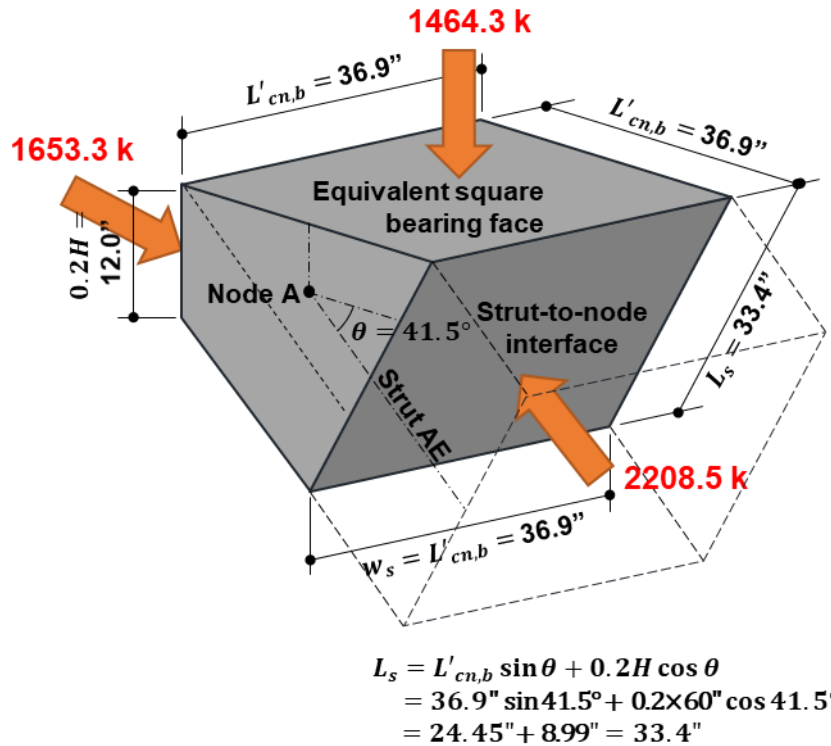


Figure 8.75 Details of 3D nodal geometry at Node A

o NODAL STRENGTH AT BEARING FACE

- Factored load: $F_{u,bearing} = 1464.3 \text{ kip}$
- Concrete efficiency factor: $\nu = 0.85$
- Concrete capacity: $f_{cu} = m \cdot \nu \cdot f'_c = (2.34)(0.85)(3.6 \text{ ksi}) = 7.16 \text{ ksi}$
- Nodal capacity: $\phi F_{n,bearing} = \phi f_{cu} A_{cn,bearing} = (0.7)(7.16 \text{ ksi})(1361.2 \text{ in.}^2) = 6822.3 \text{ kip} > 1464.3 \text{ kip} \quad \mathbf{OK}$

o NODAL STRENGTH AT BACK FACE

- Factored load: $F_{u,back} = \sqrt{1109.7^2 + 1225.5^2} = 1653.3 \text{ kip}$
- Effective area: $A_{cn,back} = L'_{cn,b} \cdot 0.2H = 442.8 \text{ in.}^2$
- Concrete efficiency factor: $\nu = 0.85$
- Concrete capacity: $f_{cu} = m \cdot \nu \cdot f'_c = (2.34)(0.85)(3.6 \text{ ksi}) = 7.16 \text{ ksi}$
- Nodal capacity: $\phi F_{n,back} = \phi f_{cu} A_{cn,back} = (0.7)(7.16 \text{ ksi})(442.8 \text{ in.}^2) = 2219.3 \text{ kip} > 1653.3 \text{ kip} \quad \mathbf{OK}$

o NODAL STRENGTH AT STRUT-TO-NODE INTERFACE

Factored load:	$F_{u,SNI} = 2208.5 \text{ kip}$
Effective area:	$A_{cn,SNI} = w_s \cdot L_S = (36.9 \text{ in.})(33.4 \text{ in.})$ $= 1232.5 \text{ in.}^2$
Concrete efficiency factor:	$v = 0.85 - \frac{f'_c}{20 \text{ ksi}} = 0.85 - \frac{3.6 \text{ ksi}}{20 \text{ ksi}}$ $= 0.67 > 0.65 \quad \therefore \text{se } v = 0.65$
Concrete capacity:	$f_{cu} = m \cdot v \cdot f'_c = (2.34)(0.65)(3.6 \text{ ksi})$ $= 5.48 \text{ ksi}$
Nodal capacity:	$\phi F_{n,SNI} = \phi f_{cu} A_{cn,SNI}$ $= (0.7)(5.48 \text{ ksi})(1232.5 \text{ in.}^2)$ $= 4727.9 \text{ kip} > 2208.5 \text{ kip} \quad \mathbf{OK}$

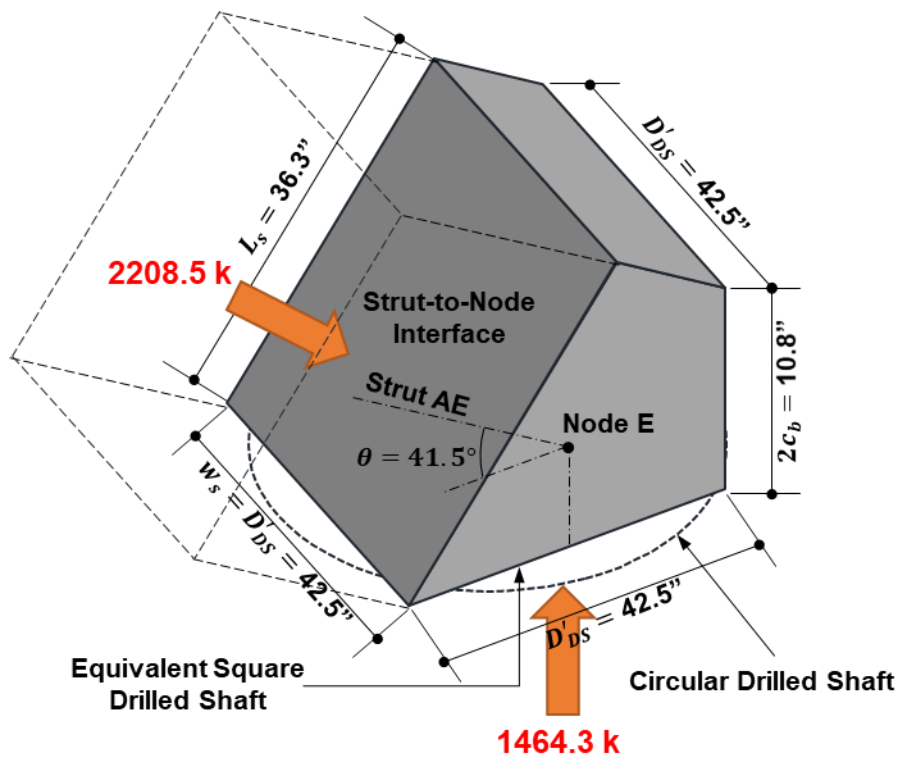
- Node E (CTT node)

Figure 8.76 shows the dimension and applying forces of nodes E and H in three dimensions based on this study's proposed recommendations. The confinement modification factors of Node E in Load Case V are the same as those in Load Case I ($m = 1.55$), as depicted in Figure 8.35. In addition, the length of the equivalent square bearing face ($D'_{DS} = 42.5 \text{ in.}$) is identical as well.

For the CTT node, the concrete efficiency factors at each face are identical to the following:

$$v = 0.85 - \frac{f'_c}{20 \text{ ksi}} = 0.85 - \frac{3.6 \text{ ksi}}{20 \text{ ksi}} = 0.67 > 0.65 \quad \therefore \text{se } v = 0.65$$

Note that the nodal strength check at back faces is not necessary since an adequate development length that satisfies the anchorage requirement is provided in this example.



$$\begin{aligned}
 L_s &= D'_{DS} \sin \theta + 2c_b \cos \theta \\
 &= 42.5'' \sin 41.5^\circ + 2 \times (4'' + 1.41'') \cos 41.5^\circ \\
 &= 28.16'' + 8.10'' = 36.3''
 \end{aligned}$$

Figure 8.76 Details of 3D nodal geometry at Node E

o NODAL STRENGTH AT BEARING FACE

Factored load: $F_{u,bearing} = 1464.3 \text{ kip}$

Concrete efficiency factor: $\nu = 0.65$

Concrete capacity: $f_{cu} = m \cdot \nu \cdot f'_c = (1.55)(0.65)(3.6 \text{ ksi}) = 3.63 \text{ ksi}$

Nodal capacity: $\phi F_{n,bearing} = \phi f_{cu} A_{cn,bearing} = (0.7)(3.63 \text{ ksi})(1809.6 \text{ in.}^2) = 4598.2 \text{ kip} > 1464.3 \text{ kip} \quad \mathbf{OK}$

o NODAL STRENGTH AT STRUT-TO-NODE INTERFACE

Factored load:	$F_{u,SNI} = 2208.5 \text{ kip}$
Concrete efficiency factor:	$\nu = 0.65$
Effective area:	$A_{cn,SNI} = w_s \cdot L_s = (42.5 \text{ in.})(36.3 \text{ in.})$ $= 1544.3 \text{ in.}^2$
Concrete capacity:	$f_{cu} = m \cdot \nu \cdot f'_c = (1.55)(0.65)(3.6 \text{ ksi})$ $= 3.63 \text{ ksi}$
Nodal capacity:	$\phi F_{n,SNI} = \phi f_{cu} A_{cn,SNI}$ $= (0.7)(3.63 \text{ ksi})(1544.3 \text{ in.}^2)$ $= 3924.1 \text{ kip} > 2208.5 \text{ kip} \quad \mathbf{OK}$

In conclusion, the nodal capacities of Nodes A through H are greater than factored loads.

8.4.7.6. Step 6: Proportion Shrinkage and Temperature Reinforcement

The necessary shrinkage and temperature reinforcement for the side faces of the footing was No. 6 bars with 10 in. spacing ($A_s = 0.53 \text{ in.}^2/\text{ft.}$) in both horizontal and vertical directions specified in Section 8.4.3. On the top face, the same amount (No. 6 bars with 10 in. spacing, $A_s = 0.53 \text{ in.}^2/\text{ft.}$) will be provided as introduced in Section 8.4.6.6.

8.4.7.7. Step 7: Provide Necessary Anchorage for Ties

Each tie has different available development length at both ends. The proposed available development length of each tie is the minimum when the projected strut angle at both end nodes is the greatest. As shown in Figure 8.77, Node E for Tie EF, Node F for Tie FG, Node G for Tie GH, and Node E for Tie EH are the critical locations. According to Eq. (8.11), the critical available development lengths for Ties EF, FG, GH, and HE are determined by the following calculations:

$$l_{ad,EF,E} = \frac{c_b}{\tan \theta_{s,proj,EF,E}} + D'_{DS}/2 + D_{DS}/2 + OH - c$$

$$= \frac{(5.41 \text{ in.})}{\tan 47.8^\circ} + (42.5 \text{ in.})/2 + (48.0 \text{ in.})/2 + 9 \text{ in.} - 3 \text{ in.} = 56.2 \text{ in.}$$

$$l_{ad,FG,F} = \frac{c_b}{\tan \theta_{s,proj,FG,F}} + D'_{DS}/2 + D_{DS}/2 + OH - c$$

$$= \frac{(5.41 \text{ in.})}{\tan 48.1^\circ} + (42.5 \text{ in.})/2 + (48.0 \text{ in.})/2 + 9 \text{ in.} - 3 \text{ in.} = 56.1 \text{ in.}$$

$$\begin{aligned}
 l_{ad,GH,H} &= \frac{c_b}{\tan \theta_{s,proj,GH,H}} + D'_{DS}/2 + D_{DS}/2 + OH - c \\
 &= \frac{(5.41 \text{ in.})}{\tan 52.0^\circ} + (42.5 \text{ in.})/2 + (48.0 \text{ in.})/2 + 9 \text{ in.} - 3 \text{ in.} = 55.5 \text{ in.}
 \end{aligned}$$

$$\begin{aligned}
 l_{ad,EH,E} &= \frac{c_b}{\tan \theta_{s,proj,EG,E}} + D'_{DS}/2 + D_{DS}/2 + OH - c \\
 &= \frac{(5.41 \text{ in.})}{\tan 42.2^\circ} + (42.5 \text{ in.})/2 + (48.0 \text{ in.})/2 + 9 \text{ in.} - 3 \text{ in.} = 57.2 \text{ in.}
 \end{aligned}$$

Straight bars for bottom mat reinforcement were recommended for Load Case I. Load Case V required a smaller steel area than did Load Case I, resulting in a reduction of excess reinforcement factor; therefore, smaller development length would be required that that in Load Case I. To calculate the minimum required development length, reinforcement location factor, λ_{rl} , is 1.0; the reinforcement coating factor, λ_{cf} , is 1.0 for uncoated reinforcement; the reinforcement confinement factor, λ_{rc} , is 0.54 by given reinforcing details of the example; and the concrete density modification factor, λ , is 1.0 for normal weight concrete. The excess reinforcement factors, λ_{er} , for Ties EF, FG, GH, and EH are 0.693, 0.622, 0.599, and 0.766, respectively. According to Eq. (8.4), the required development length of a straight No. 11 bar is calculated as below:

$$l_{d,EF} = (2.4)(1.41 \text{ in.}) \frac{60}{\sqrt{3.6}} \frac{(1.0)(1.0)(0.54)(0.693)}{1.0} = 40.0 \text{ in.} < l_{ad,EF} (= 56.2 \text{ in.})$$

$$l_{d,FG} = (2.4)(1.41 \text{ in.}) \frac{60}{\sqrt{3.6}} \frac{(1.0)(1.0)(0.54)(0.622)}{1.0} = 35.9 \text{ in.} < l_{ad,FG} (= 56.1 \text{ in.})$$

$$l_{d,GH} = (2.4)(1.41 \text{ in.}) \frac{60}{\sqrt{3.6}} \frac{(1.0)(1.0)(0.54)(0.599)}{1.0} = 34.6 \text{ in.} < l_{ad,GH} (= 56.5 \text{ in.})$$

$$l_{d,EH} = (2.4)(1.41 \text{ in.}) \frac{60}{\sqrt{3.6}} \frac{(1.0)(1.0)(0.54)(0.766)}{1.0} = 44.3 \text{ in.} < l_{ad,EH} (= 57.2 \text{ in.})$$

In conclusion, straight bars can reach sufficient yield strength for bottom ties in Load Case V.

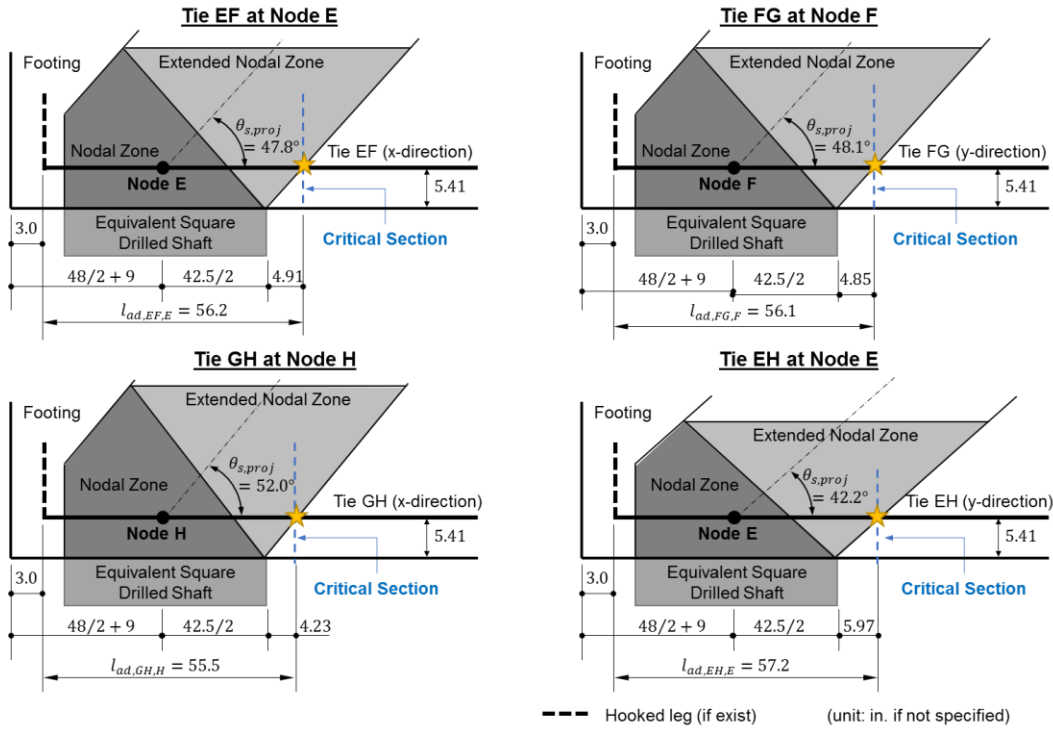


Figure 8.77 Critical sections for the development of ties: Load Case V

8.4.8. Reinforcement Layout

Figure 8.78 presents the anchorage detail of the designed footing. The 90-degree hooked column reinforcing bars are oriented in two directions. In the experimental program, the research team confirmed the effectiveness of the hooks oriented inward to the column. Therefore, the orientation of the hooks is placed inward to the column with respect to the direction of the moment that this study designed for, and the hooks placed on the other sides of the column are oriented outward to the column. This hybrid detail can provide optimized structural performance with acceptable constructability. The other designed reinforcement details are depicted in Figure 8.79 through Figure 8.82.

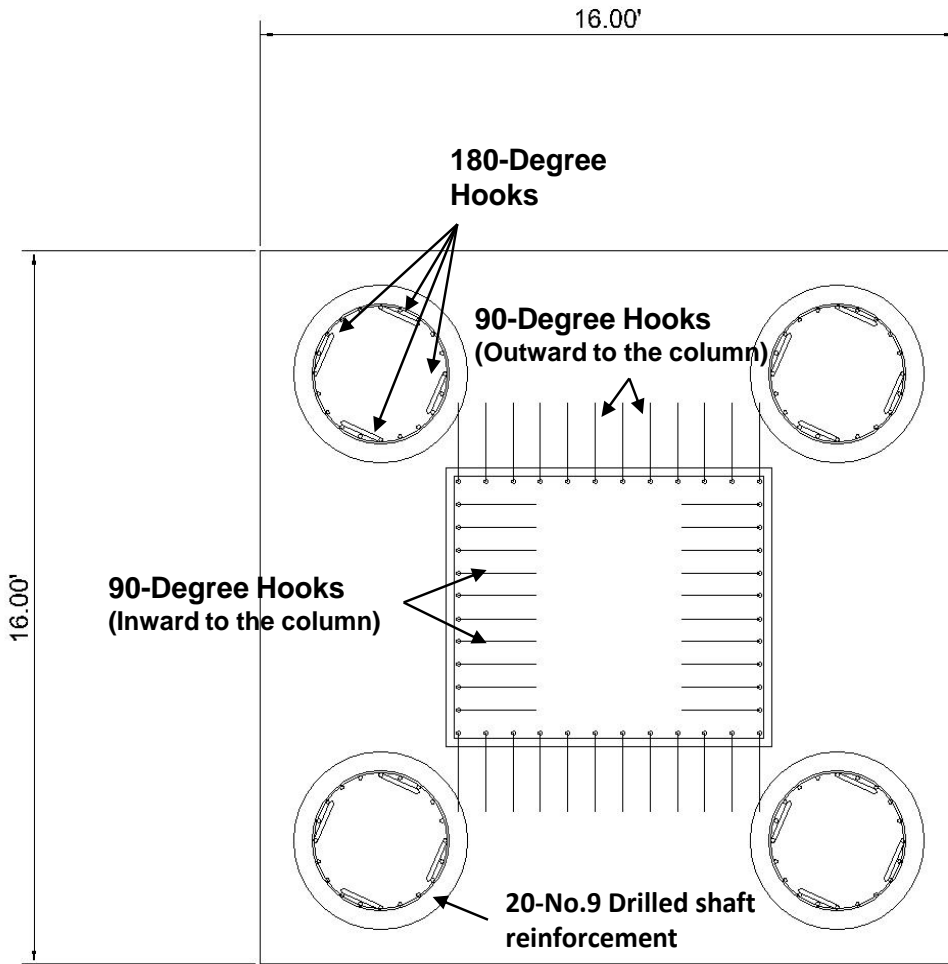


Figure 8.78 Reinforcement details for anchorage of vertical ties

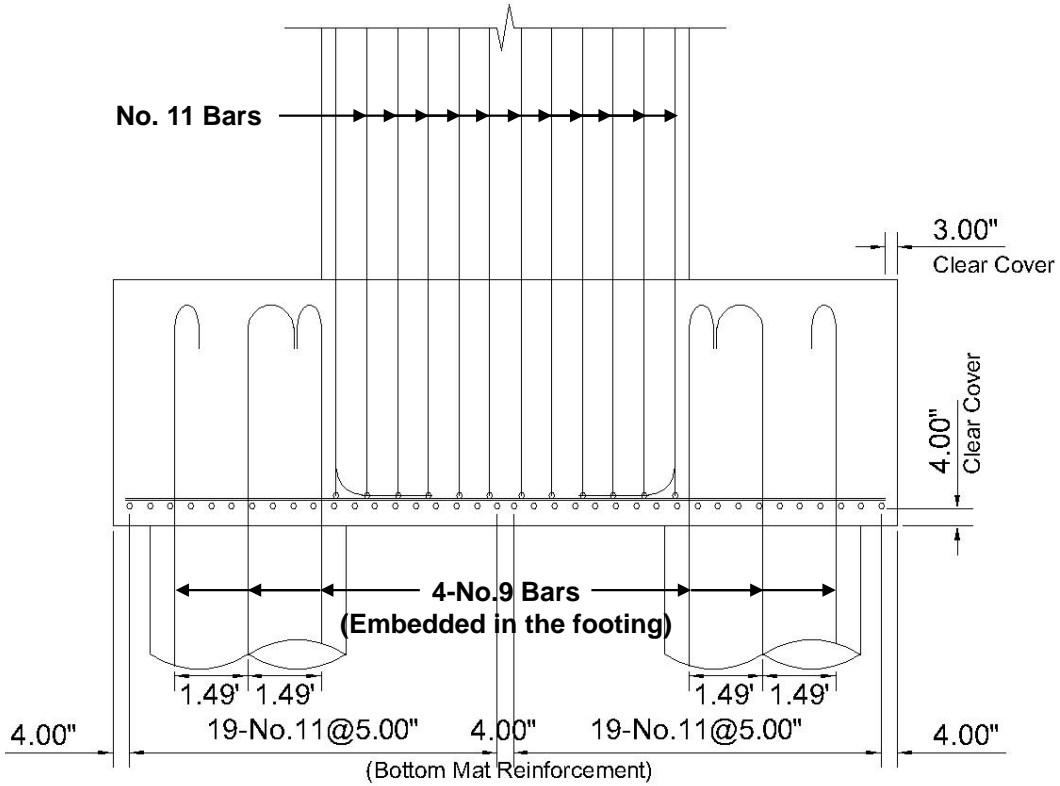


Figure 8.79 Reinforcement details for ties: elevation view

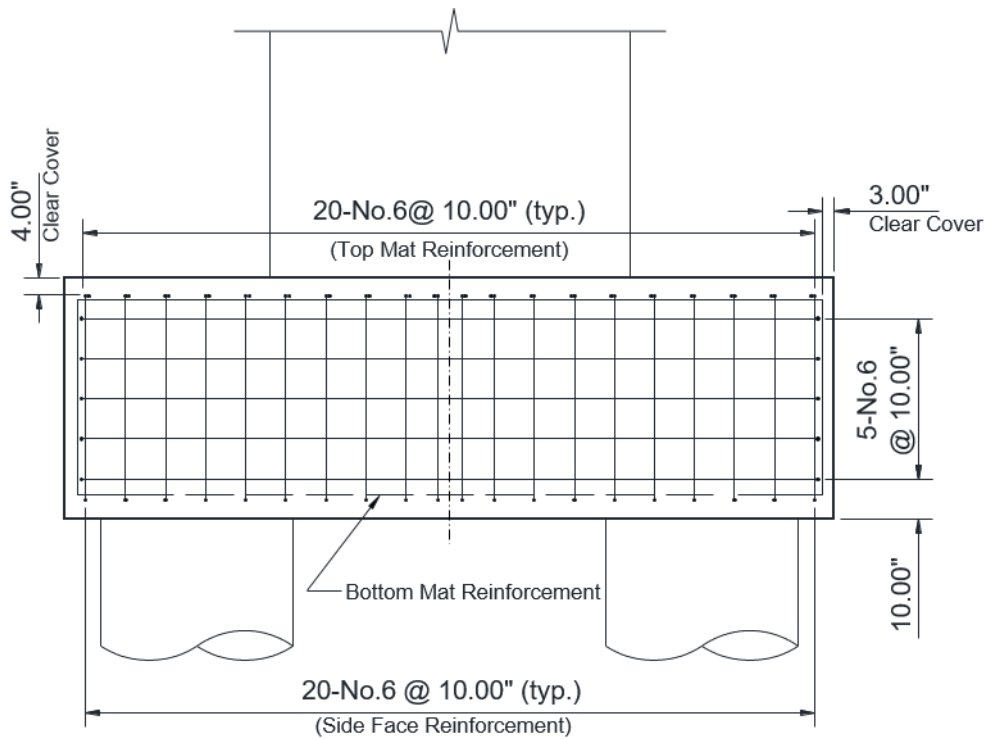


Figure 8.80 Reinforcement details for shrinkage and temperature reinforcement: elevation view

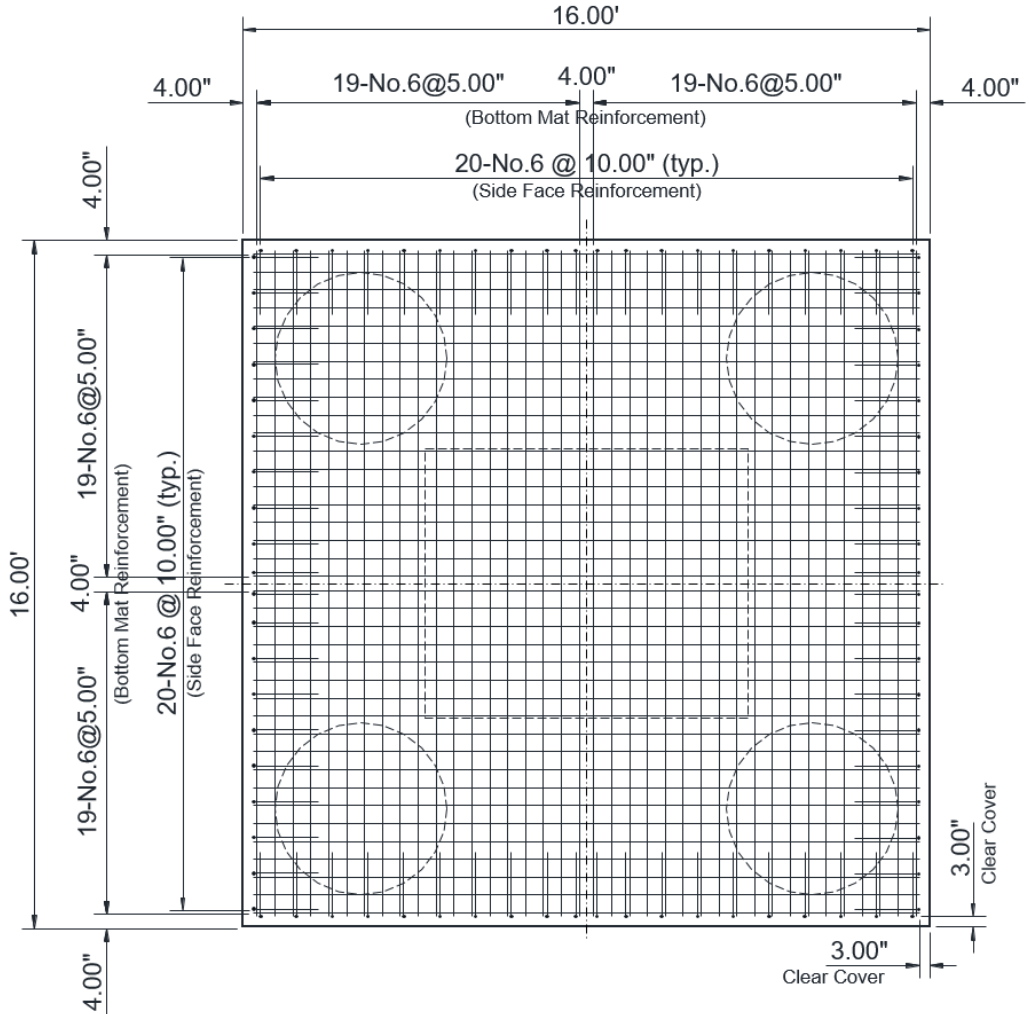


Figure 8.81 Reinforcement details for bottom mat reinforcement: plan view

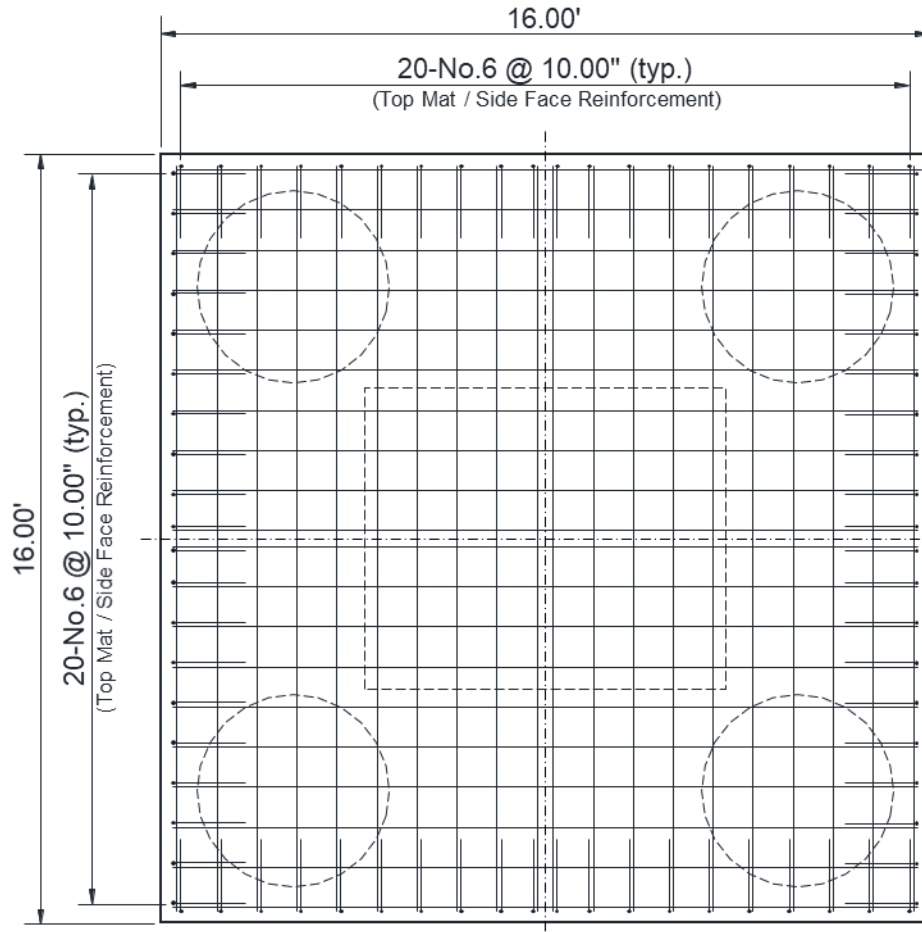


Figure 8.82 Reinforcement details for top mat reinforcement: plan view

8.5. Summary and Discussion

This chapter presents the 3D STM guidelines and the design example of the drilled shaft footing subjected to various load combinations based on the proposed 3D STM guidelines. Key modifications of 3D STM guidelines for drilled shaft footings are summarized as follows:

- Recommendations are provided to determine the 3D nodal geometry in footings, which can be used to determine the nodal capacities at each face.
- The nodal strength at the bearing face and strut-to-node interface can be calculated based on the 3D nodal geometry. Nodal strength at the back face does not need to be considered if the tie is properly anchored at the CTT node in accordance with AASHTO LRFD (2020).

- The confinement modification factor allows up to 3.0 for CCC, as in Eurocode 2 (2004) and fib Model Code 2010 (2013), and 2.0 for other node types, identical to AASHTO LRFD (2020).
- At least 0.18% of shrinkage and temperature reinforcement on the side face is suggested, identical to Article 5.10.6 of AASHTO LRFD (2020). If the requirement is not satisfied, the minimum concrete efficiency factor (0.45) should be considered.
- A procedure that determines available development lengths for horizontal ties and vertical column reinforcement is proposed based for the 3D STM based on compressive stress flow within a footing. The approach leads to a longer available development length compared.

The improvement of the accuracy of the ultimate capacities predicted by the proposed 3D STM guidelines compared to the recommendation by Williams et al. (2012) was validated using the *evaluation database*. The average ultimate capacity ratio (P_u/P_{STM}) used by the new proposed 3D STM guidelines decreased from 1.97 (Williams et al., 2012) to 1.44. No case was observed in which the ultimate capacity ratio is greater than 2 when using the new proposed 3D STM guidelines. When using the current recommendation, 27 out of 60 cases (45%) exhibited ultimate capacity ratios that exceeded 2, when using the current recommendation (Williams et al., 2012).

The design example of the drilled shaft footing with various loading conditions—1) axial compression, 2) axial compression with mild uniaxial flexure, 3) axial compression with moderate uniaxial flexure, 4) axial compression with severe uniaxial flexure, and 5) axial compression with biaxial flexure—were provided to familiarize designers with the 3D STM guidelines. The updated reinforcing layout designed using the new proposed 3D STM guidelines was presented.

Chapter 9. Summary and Conclusions

9.1. Summary

Strut-and-tie modeling, first introduced within AASHTO LRFD in 1994, is a practical design method for deep structural members based on an equivalent representation of the internal force flow. The implemented design method for deep and planar structural members such as deep beams is based on the two-dimensional (2D) strut-and-tie method (STM). However, drilled shaft footings are structural members that present a three-dimensional (3D) internal force flow, resulting in the need for 3D strut-and-tie models. A lack of experimental research conducted on the application of the 3D STM to the design of drilled shaft footings presented a challenge. Moreover, TxDOT attributed the variations of the design and detailing of drilled shaft footings to lacking specific guidance and standards. The primary objectives of this research were to resolve ambiguities in the application of the 3D STM to designing drilled shaft footings and to provide a safe, consistent method for designing and detailing drilled shaft footings.

The research team comprehensively planned and conducted a series of tasks to accomplish those objectives. Each chapter of this report organizes the outcomes attained from each task, and the outcomes of each task are presented at the end of each chapter. The summary and featured conclusions of each chapter are as follows:

- Chapter 2: The research team reviewed current STM-based provisions and previous research on drilled shaft footings to identify uncertainties of the application of the 3D STM in designing drilled shaft footings. A database of 147 drilled shaft footing tests was also compiled based on this effort.
- Chapter 3: Drawings from 35 drilled shaft footings designed and constructed by TxDOT in Texas were compiled for a database, which was analyzed to determine geometric properties and reinforcement details of the experimental program of this project.
- Chapter 4: The first phase of the experimental program (Phase I testing) included specimens of drilled shaft footings subjected to uniaxial compression only. Thirteen large-scale test specimens divided into five series with varying design parameters were constructed and tested. This experimental program tested the largest drilled shaft footings (V-13) ever. It was concluded from Series I testing (bottom mat reinforcement configuration) that the structural behaviors of drill-shaft footings would be comparable if reinforcing bars are developed with proper anchorage. Series II testing (strut inclination) exhibited a negative linear correlation between

the ultimate strength and the strut inclination. The research team concluded that non-existence of side face reinforcement adversely affects the ultimate strength and the serviceability from Series IV testing (side face reinforcement ratio). The ratio of side face reinforcement does not obviously cause difference of structural behaviors if higher than 0.18% of side face reinforcement is provided. The effects of the shaft diameter (Series III testing) and the footing height (Series V testing) on structural behaviors were not clearly found.

- Chapter 5: The second phase of the experimental program (Phase II testing) was conducted for drilled shaft footings subjected to uniaxial compression and moderate bending moment. Four drilled shaft footings presenting different anchorage types for the column reinforcement were constructed and tested to investigate behavior of the column reinforcement. It was found that the anchorage detail influences the stress profile of the column reinforcement. Moreover, the hooked column reinforcement oriented towards the side of the diagonal strut flowing from the compression-side of the column demonstrates the best structural performance among the investigated anchorage types. Furthermore, the research team proposed a critical section for the column reinforcement based on the large compression field crossing the vertical tie.
- Chapter 6: The third phase of the experimental program (Phase III testing) was conducted for the drilled shaft footings subjected to uniaxial compression and severe bending moment. An equivalent loading condition was proposed for large-scale structural testing. Four tests were conducted with different anchorage types of the drilled shaft reinforcement to investigate behavior of the drilled shaft reinforcement. It was found that drilled shaft reinforcement stress profiles obtained from the tests were comparable regardless of the anchorage type. The critical section of the drilled shaft reinforcement defined from the assumed boundary of the fan-shaped strut of the equivalent loading condition was conservative enough to ensure yielding of the drilled shaft reinforcement. Similarly, the research team also proposed a critical section for the drilled shaft reinforcement based on the assumed compression field forming at the non-contact lap splice between the column and drilled shaft reinforcement of the drilled shaft footings subjected to uniaxial compression and severe bending moment.
- Chapter 7: To supplement the results obtained from the experimental program, a series of parametric numerical studies were conducted for each

phase of the experimental program. The numerical analyses were conducted with finite element models that were validated using experimental data from footing tests from the current and previous studies. With respect to the parametric study for Phase I testing, numerous finite element models were developed with additional design parameters that could not be covered in the experimental program. The numerical parametric analysis confirmed that the geometric discrepancy between test specimens (a rectangular footing with a square column) and footings in current practice (a square footing with a rectangular column) does not affect the structural behaviors, which means test specimens can represent the constructed footings. In addition, the experimental findings from Phase I testing were successfully captured by the numerical analysis. Finite element parametric studies for Phase II and Phase III testing were also conducted to include more design parameters that could affect the position of the proposed critical sections for the column and drilled shaft reinforcement. The results of the parametric studies verified the conservativeness of the proposed critical sections for the column (Phase II) and the drilled shaft reinforcement (Phase III).

- Chapter 8: Based on the results and insights described in the previous chapters, 3D STM design guidelines were established. The guidelines were built on the recommendations of TxDOT Project 0-5253 and 5-5253-01 and proposed refinements in terms of 3D nodal geometry, nodal strength, and critical sections for tie elements. This project's test specimens and evaluation database (containing previous drilled shaft footing tests) were assessed by examining strengths calculated using both the proposed method of this project and that of TxDOT Project 5-5253-01. The results indicated that the newly proposed 3D STM guidelines improve the accuracy of the ultimate strength predictions, without generating unconservative predictions. In addition, the average and dispersion of the strength ratios using the proposed method were similar to methods employed in the current AASHTO LRFD. A design example of a drilled shaft footing under various loading conditions was also provided.

9.2. Concluding Remarks

The proposed 3D STM guidelines based on the comprehensive research work can provide a uniform and consistent design for drilled shaft footings. The recommendations comprising the guidelines can be employed for other structural members to be designed with the 3D STM. A set of revisions to the most recent edition of AASHTO LRFD was also created (Appendix A); implementation of the updated provision and the design examples will allow designers to design safe

drilled shaft footings throughout the United States. Moreover, the experimental program of this project provides an extensive experimental database of large-scale drilled shaft footings subjected to various loading scenarios. Employing large-scale test specimens in the experimental program would allow investigation of more realistic structural behavior of footings, more closely resembling the behavior of footings in the field. The database will be a valuable resource for future research on drilled shaft footings.

However, there is a limitation in that the experimental programs for the drilled shaft footings under the eccentric loads as Phase II and Phase III tests were conducted with a single design parameter (Phase II: anchorage type of the column reinforcement; Phase III: anchorage type of the drilled shaft reinforcement) per loading. The parametric studies were conducted to compensate for the limitation. Still, additional experimental research is required for the drilled shaft footings under loading scenarios with eccentric loads to cover more design parameters not tested in this research. Furthermore, the drilled shaft footing under biaxial eccentric loading covered in the design example section of this project needs to be validated with additional experimental studies.

References

- AASHTO (1996) *Standard Specifications for Highway Bridges 16th Edition Including interim revisions for 1997 through 2002*, American Association of State Highway and Transportation Officials Washington, D.C.
- AASHTO LRFD (2004) *Bridge Design Specifications, 3rd Edition, 2004*, American Association of State Highway and Transportation Officials, Washington, D.C.
- AASHTO LRFD (2004) *Bridge Design Specifications, 5th Edition, 2010*, American Association of State Highway and Transportation Officials, Washington, D.C.
- AASHTO LRFD (2020) *Bridge Design Specifications, 9th Edition, 2020*, American Association of State Highway and Transportation Officials, Washington, D.C.
- ACI Committee 318-77 (1977) *Building Code Requirements for Reinforced Concrete (ACI 318-77)*, American Concrete Institute, Detroit, MI.
- ACI Committee 318-83 (1983) *Building Code Requirements for Reinforced Concrete (ACI 318-83)*, American Concrete Institute, Detroit, MI.
- ACI Committee 318-02 (2002) *Building Code Requirements for Reinforced Concrete (ACI 318-02) and Commentary (318R-02)*, American Concrete Institute, Farmington Hills, MI.
- ACI Committee 318-08 (2008) *Building Code Requirements for Reinforced Concrete (ACI 318-08) and Commentary (318R-08)*, American Concrete Institute, Farmington Hills, MI.
- ACI Committee 318-19 (2019) *Building Code Requirements for Reinforced Concrete (ACI 318-19) and Commentary (318R-19)*, American Concrete Institute, Farmington Hills, MI.
- Adebar, P., Kuchma, D., and Collins, M (1990) “Strut-and-Tie Models for the Design of Pile Caps: An Experimental Study,” *ACI Structural Journal*, Vol. 87, No. 1, pp. 81-92.
- Adebar, P., and Zhou, Z. (1993) Bearing strength of compressive struts confined by plain concrete, *ACI Structural Journal*, Vol. 90, No. 5, pp. 535-535.
- Adebar, P., and Zhou, Z. (1996) Design of Deep Pile Caps by Strut-and-Tie Models, *ACI Structural Journal*, Vol. 93, No. 4, pp. 1-12.
- Araújo, J. M. de (2016) Design of Rigid Pile Caps through an Iterative Strut-and-Tie Model, *Journal of Advanced Concrete Technology*, Vol. 14, No.8, pp. 397-407.
- Bentz, E.C., Vechhio, F.J., and Collins, M.P., Simplified Modified Compression Field Theory for Calculating Shear Strength of Reinforced Concrete Elements, *ACI Structural Journal*, Vol. 103, No. 4, 2006, pp 614-624.

- Bentz, E. C., and Collins, M.P. (2017) Updating the ACI shear design provisions, *Concrete International*, Vol. 39, No. 9, pp. 33-38.
- Birrcher, D., Tuchscherer, R., Huizinga, M., Bayrak, O., Wood, S. L., and Jirsa, J. O. (2009) *Strength and Serviceability Design of Reinforced Concrete Deep Beams*, Report No. FHWA/TX-09/0-5253-1., Center of Transportation Research, The University of Texas at Austin.
- Blevot, J., and Frémy, R. (1967) Semelles sur Pieux, *Annales de l'Institut Technique du Batiment et des Travaux Publics*, Vol. 20, No. 230, pp. 223-295.
- BS 5400-4 (1990) *Steel, concrete and composite bridges — Part 4: Code of practice for design of concrete bridges*, British Standard Institution, London, United Kingdom.
- Canadian Standards Association (1984) *Design of Concrete Structures for Buildings (CAN3 A23.3-M84)*, Canadian Standards Association, Rexdale, Ontario, Canada
- Canadian Standards Association (2014) *Design of Concrete Structures (CSA-A23.3-14)*, Canadian Standards Association, Mississauga, Ontario, Canada.
- CEB-FIP (1990) *CEB-FIP Model Code 1990*, Thomas Telford Services, Ltd., London, UK.
- CEN EN 1992-1-1 (2004) Eurocode 2: Design of Concrete Structures. Part 1-1: General Rules and Rules for Buildings, European Committee for Standardization, Brussels, Belgium.
- Clarke, J. (1973) Behavior and Design of Pile Caps with Four Piles, *Technical Report* No. 42.489, Cement and Concrete Association, Wexham Springs, 1973.
- Collins, M. P., and Mitchell, D. (1991). *Prestressed concrete structures* (Vol. 9). Prentice Hall, Englewood Cliffs, NJ.
- Comisión Permanente del Hormigón (2008) *Instrucción de Hormigón Estructural EHE-2008*. Madrid: Ministerio de Fomento, Madrid, Spain.
- CRSI Handbook* (1992) Concrete Reinforcing Steel Institute, Chicago.
- Eligehausen, R., Popov, E., and Bertero, V. (1983) *Local Bond Stress-Slip Relationships of Deformed Bars under Generalized Excitations*, Rep. UCB/EERC 83-23, University of California, Berkeley, California.
- fib (2013) *fib Model Code for Concrete Structures 2010*, Wilhelm Ernst & Sohn, Germany.
- Gogate, A. B., and Sabnis, G. M. (1980) Design of Thick Pile Cap, *ACI Journal*, Vol. 77, No. 1, pp. 18-22

- Goh, C. Y. M., and Hrynyk, T. D. (2018) Numerical Investigation of the Punching Resistance of Reinforced Concrete Flat Plates. *Journal of Structural Engineering*, Vol. 144, No. 10, 04018166.
- Guo, H. (2015) Evaluation of Column Load for Generally Uniform Grid-Reinforced Pile Cap Failing in Punching, *ACI Structural Journal*, Vol. 112, No. 2, pp. 123-134.
- Hawkins, N. M., Kuchma, D. A., Mast, R. F., and Reineck, K. (2005), *Simplified Shear Design of Structural Concrete Members*, NCHRP Report 549, NCHRP, Washington, D.C.
- Klein, Gary J. (2002) Example 9: Pile Cap, *SP-208 Examples for the Design of Structural Concrete with Strut-and-Tie Models*. Ed. Karl-Heinz Reineck. Farmington Hills, Michigan: American Concrete Institute, 250 pp.
- Leu, L., Huang, C., Chen, C., and Liao, Y. (2006) Strut-and-Tie Design Methodology for Three-Dimensional Reinforced Concrete Structures, *Journal of Structural Engineering*, Vol. 132, No. 6, pp. 929–938.
- Mathern, A., Chantelot, G., Per-Ola Svahn, P. K., and Rasmus Rempling, B. E. (2017) “Enhanced strut-and-tie model for reinforced concrete pile caps”, in *39th IABSE Symposium, Vancouver 2017: Engineering the Future*, Vancouver, Canada: International Association for Bridge and Structural Engineering (IABSE), pp. 607-614.
- Miguel-Tortola, L., Pallarés, L., and Miguel, P. F. (2018). Punching shear failure in three-pile caps: Influence of the shear span-depth ratio and secondary reinforcement. *Engineering Structures*, Vol. 155, pp. 127-143.
- Mitchell, D., Collins, M., Bhide, S., and Rabbat, B. (2004) *AASHTO LRFD Strut-and-Tie Model Design Examples*, Skokie, Illinois: Portland Cement Association, 76 pp.
- Nakamura, E., Avendaño, A.R., and Bayrak. O. (2013) Shear Database for Prestressed Concrete Members, *ACI Structural Journal*, Vol. 110, No.6, pp.909-918.
- NBR 6118 (2014) *Design of concrete structures - Procedure (In Portuguese)*, Brazilian Association of Technical Standards, Rio de Janeiro City, Brazil.
- Ngo, D., and Scordelis, A.C. (1967) Finite Element Analysis of Reinforced Concrete Beams, *ACI Journal*, Vol. 64, No. 3, pp. 152-163.
- Nilsson, I. H., and Losberg, A. (1976) Reinforced Concrete Corners and Joints Subjected to Bending Moment, *Journal of the Structural Division*, Vol. 102, No. 6, pp. 1229-1254.
- Ottosen, N. S. (1977) A failure criterion for concrete, *Journal of Engineering Mechanics*, Vol.103, No.4, pp. 527–535.
- Park, J., Kuchma, D. and Souza, R. (2008) Strength predictions of pile caps by a strut-and-tie model approach, *Canadian Journal of Civil Engineering*, Vol. 35, No. 12, pp. 1399–1413.

- Paulay, T. and Priestley, M.J.N. (1992) *Seismic design of reinforced concrete and masonry buildings*. John Wiley and Sons, New York.
- Sabnis, G., and Gogate, A. (1984) Investigation of Thick Slab (Pile Cap) Behavior, *ACI Journal*, Vol. 81, No. 1, pp. 35-39.
- Sam, C., and Iyer, P. K. (1995) Nonlinear finite element analysis of reinforced concrete four-pile caps, *Computers & Structures*, Vol. 57, No. 4, pp. 605-622.
- Siao W. B. (1993) Strut-and-Tie Model for Shear Behavior in Deep Beams and Pile Caps Failing in Diagonal Splitting, *ACI Structural Journal*, Vol. 90, No. 4, pp.356-363.
- Schlaich, J., Schafer, K., and Jennewein, M. (1987) Toward a Consistent Design of Structural Concrete, *PCI Journal*, Vol.32, No. 3, pp.74-150.
- Souza, R. A., Kuchma, D. A., Park, J., and Bittencourt, T. N. (2007) Nonlinear finite element analysis of four-pile caps supporting columns subjected to generic loading, *Computers and Concrete*, Vol. 4, No. 5, pp. 363–376.
- Souza, R. A., Kuchma, D. A., Park, J., and Bittencourt, T. (2009) Adaptable Strut-and-Tie Model for Design and Verification of Four-Pile Caps, *ACI Structural Journal*, Vol. 106, No. 2, pp.142-150.
- Suzuki, K., Otsuki, K., and Tsubata, T. (1998) Influence of Bar Arrangement on Ultimate Strength of Four-Pile Caps, *Transactions of the Japan Concrete Institute*, Vol. 20, pp. 195-202.
- Suzuki, K., Otsuki, K., and Tsubata, T. (1999) Experimental Study on Four-Pile Caps with Taper, *Transactions of the Japan Concrete Institute*, Vol. 21, pp. 327-334.
- Suzuki, K., Otsuki, K., and Tsuchiya, T. (2000) Influence of Edge Distance on Failure Mechanism of Pile Caps, *Transactions of the Japan Concrete Institute*, Vol. 22, pp. 361-367.
- Suzuki, K., and Otsuki, K. (2002) Experimental Study on Corner Shear Failure of Pile Caps, *Transactions of the Japan Concrete Institute*, Vol. 23, pp. 303-310.
- TxDOT Bridge Division (2020) *Bridge Design Guide*, Texas Department of Transportation, Austin, Texas.
- Widianto, Bayrak, O. (2011) Example 11: Deep Pile Cap with Tension Piles, *SP-273 Further Examples for the Design of Structural Concrete with Strut-and-Tie Models*. Ed. Karl-Heinz Reineck. Farmington Hills, Michigan: American Concrete Institute.
- Willam, K. J., and Warnke, E. P. (1974) Constitutive Model for the Triaxial Behavior of Concrete, *Proceedings of the International Association of Bridge Structures*, Vol. 19, pp. 1-30.

- Williams, C., Deschenes, D., and Bayrak, O. (2012) *Strut-and-Tie Model Design Examples for Bridges*, Rep. FHWA/TX-12/5-5253-01-1. Center for Transportation Research, The University of Texas at Austin.
- Yun, Y. M., Kim, B. and Ramirez, J. A. (2018) Three-Dimensional Grid Strut-and-Tie Model Approach in Structural Concrete Design, *ACI Structural Journal*, Vol. 115, No. 1, pp. 15-26.

Appendix A. Proposed Modifications of AASHTO LRFD

5.8.2.10—Application to the Design of Drilled Shaft Footings

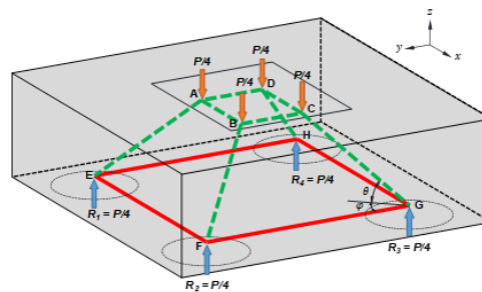
Refined three-dimensional STM should be considered for the design of three-dimensional deep structural members such as deep footings and pile caps in which the distance between the centers of applied load and the supporting reactions is less than two times the member depth.

5.8.2.10.1—General

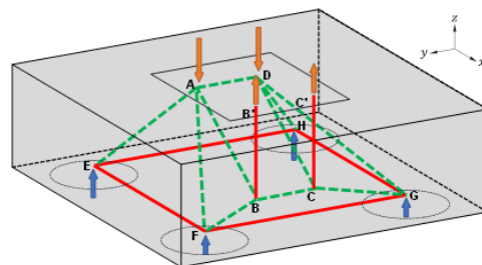
The flow of forces in drilled shaft footings may be approximated by the strut-and-tie method developed in three dimensions as illustrated in **Figure C5.8.2.10.1-1**. Details shall conform to Article 5.8.2 through 5.8.2.6 if not specified in this section.

C5.8.2.10.1

Figure C5.8.2.10.1-1 illustrates the application of strut-and-tie models to analysis of drilled shaft footings under various loading conditions

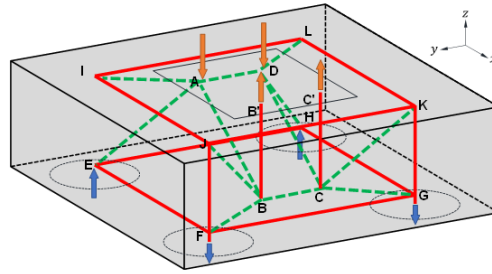


(a) Compression loading only
(uniform compression in shafts)



(b) Compression with the combination of uniaxial flexural loading
(non-uniform compression in shafts)

Figure C5.8.2.10.1-1—**Three-dimensional Strut-and-Tie Models (Cont'd)**



(c) Compression with the combination of uniaxial flexural loading (tension-compression in shafts)

Figure C5.8.2.10.1-1—**Three-dimensional Strut-and-Tie Models**

5.8.2.10.2—Structural Modeling

The nodes beneath the column are located 0.1 times the height in the gravity direction if top tie does not exist (**Figure C5.8.2.10.1-1a** and **b**). If top tie exists, the nodes beneath the column are positioned on the same horizontal plane of the top tie ring (**Figure C5.8.2.10.1-1c**). The horizontal plane coordinates of nodes beneath the column varied by the loading condition. If the entire column section is under compression the coordinates would be the centroids of resultant forces equal to reactions of adjacent shafts in the equivalent force system on the column as illustrated in **Figure C5.8.2.10.2-1a**. If the column section is under compression and tension due to eccentric loading, A sectional analysis at the interface shall be conducted as shown in **Figure C5.8.2.10.2-1b** to determine the equivalent force system on the column. The geometry and magnitude of the stress block is then used to determine the compressive resultant force and its position on the column section. An iterative procedure is needed to determine the values of ε_{ct} and c that will satisfy force and moment equilibrium.

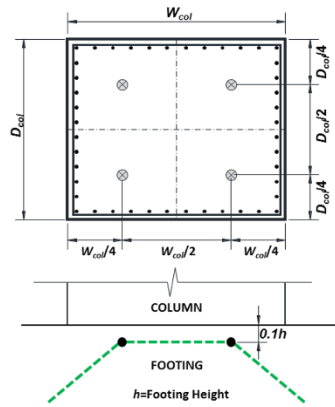
C5.8.2.10.2

For the sectional analysis to determine the equivalent force system on the column under eccentric loading, a simplified rectangular stress block is used for the concrete in compression. The equivalent stress block factors proposed by Collins and Mitchell (1991), α_1 and β_1 , shall be calculated by:

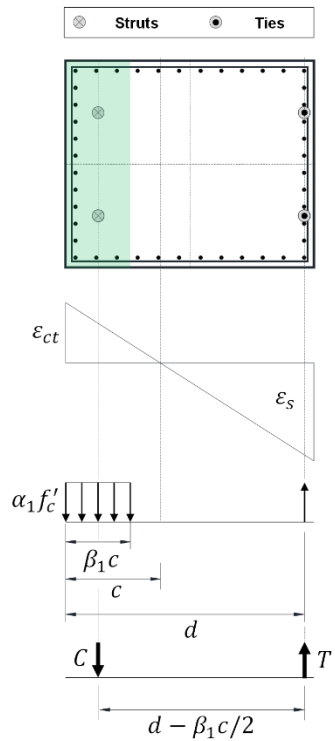
$$\alpha_1 = \frac{1}{\beta_1} \left[\left(\frac{\varepsilon_{ct}}{\varepsilon'_c} \right) - \frac{1}{3} \left(\frac{\varepsilon_{ct}}{\varepsilon'_c} \right)^2 \right] \quad (\text{C5.8.2.10.2a})$$

$$\beta_1 = \frac{4 - (\varepsilon_{ct}/\varepsilon'_c)}{6 - 2(\varepsilon_{ct}/\varepsilon'_c)} \quad (\text{C5.8.2.10.2b})$$

where ε_{ct} is the compressive strain at the extreme fiber of the column; ε'_c is the compressive strain at peak strength. Given the factored axial and moment applied on the section (P_u and M_u), the neutral axis depth, c , and the compressive strain at the extreme fiber of the column, ε_{ct} , can be found by force and moment equilibrium. The contribution of the tensile reinforcement of the column section should be considered for the sectional analysis based on strain compatibility. The geometry and magnitude of the stress block is then used to determine the compressive resultant force and its position on the column section.



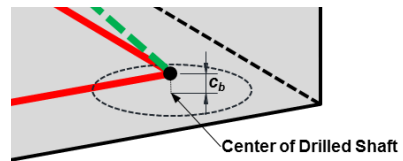
(a) Uniform Compression in the Column Section



(b) Compression and Tension in the Column Section

Figure C5.8.2.10.2-1—Top Nodal Position beneath the Column

The positions of the nodes above the drilled shafts are the projection of the center of the drilled shafts at the elevation of bottom mat reinforcement as shown in **Figure C5.8.2.10.2-2**.

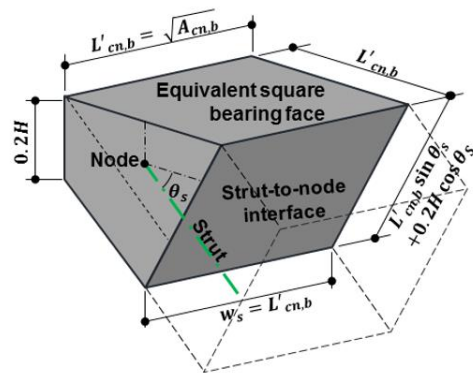


c_b : Centroid of Bottom Mat Reinforcement

Figure C5.8.2.10.2-2—Bottom Nodal Position above the Shafts

To define the 3D nodal geometry, the section of the diagonal struts is utilized as illustrated in **Figure C5.8.2.10.2-3** with assumptions described as follows: 1) non-hydrostatic nodes and prismatic struts with a rectangular cross-section are used; 2) the strut width at the node is taken as the width of the equivalent square bearing face; 3) multiple struts acting on each face the node are resolved with a single strut applied perpendicularly to the faces of the node, and the geometry of the node is determined based on the angle of the resolved strut; 4) the back face height of the CCC node is taken as twice the distance from the top surface to the CCC node. The elevation of the CCC node is assumed to be at $0.1h$ from the top surface if there are no tie elements on the plane of the top mat reinforcement. The elevation of the CCC node in the strut-and-tie model containing top tie elements on the plane of the top mat reinforcement shall be positioned at the same elevation as that of the top tie elements for consistency, and 5) the height of the back face is taken as twice the distance from the bottom surface to the centroid of the tie (c_b) for CTT nodes above the drilled shafts.

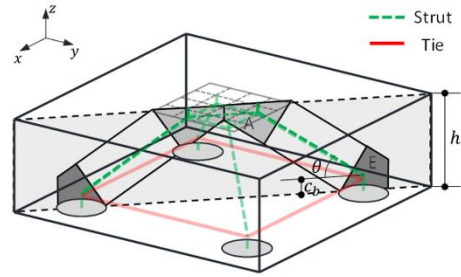
With the specified dimensions, the length of the strut-to-node interface can be derived from the generalized 3D nodal geometry, as illustrated in **Figure 5.8.2.10.2-1**.



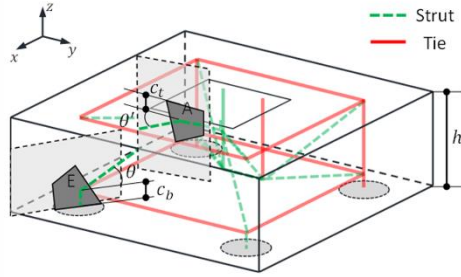
- θ_s = strut angle (degrees)
- H = footing height (in.)
- $A_{cn,b}$ = area of bearing face (in.²)
- $L'_{cn,b}$ = length of equivalent square bearing face (in.)
- w_s = width of strut (in.)

(a) Top Node

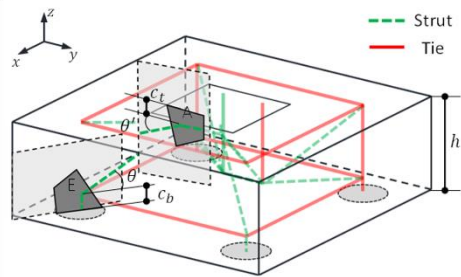
Figure 5.8.2.10.2-1—Detail of Three-dimensional Nodal Geometries (Cont'd)



(a) Compression loading only
(uniform compression in shafts)



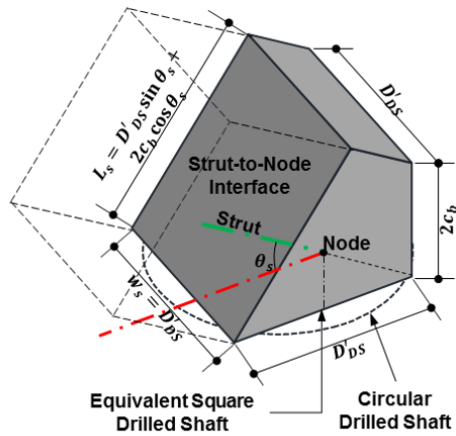
(b) Compression with the combination of uniaxial flexural loading
(non-uniform compression in shafts)



(c) Compression with the combination of uniaxial flexural loading
(tension-compression in shafts)

- α = angle between x-axis and projected strut to plane of bottom ties (degrees)
- θ = strut angle between strut and plane of bottom ties (degrees)
- θ', θ'' = angle between resolved strut and plane of bearing face (degrees)
- $A_{cn,b}$ = area of bearing face (in.²)
- D_{DS} = shaft diameter (in.)
- D'_{DS} = length of equivalent square shaft (in.)
- c_b = distance from bottom surface to centroid of bottom ties (in.)
- c_t = distance from top surface to centroid of top ties (in.)
- h = height of footing (in.)

Figure C5.8.2.10.2-3—Section of Diagonal Struts



- D_{DS} = shaft diameter (in.)
 - D'_{DS} = length of equivalent square shaft (in.)
 - c_b = distance from bottom surface to centroid of bottom ties (in.)
- (b) Bottom Node

Figure 5.8.2.10.2-1—Detail of Three-dimensional Nodal Geometries

5.8.2.10.3—Proportioning of Ties

5.8.2.10.3.1—Strength of Tie

C5.8.2.10.3-1

The nominal resistance of a tie in drilled shaft footing in kips shall be taken as:

$$P_{n,tie} = f_y A_{st} \quad (5.8.2.10.3.1-1)$$

where:

- $P_{n,tie}$ = nominal resistance of a tie (kip)
- f_y = yield strength of nonprestressed longitudinal reinforcement (ksi)
- A_{st} = area of nonprestressed longitudinal reinforcement engaged to take the tie force (in²)

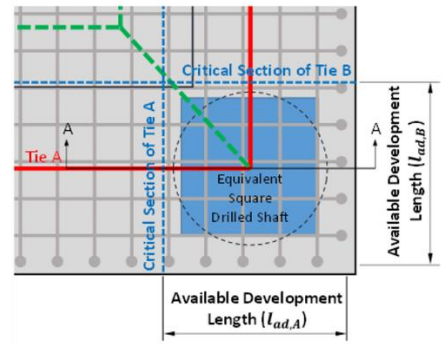
In drilled shaft footings, two horizontal bottom ties are placed in each direction. Therefore, A_{st} represents half the amount of bottom mat reinforcement in one direction when calculating the tie capacity.

5.8.2.10.3.2—*Anchorage of Tie*

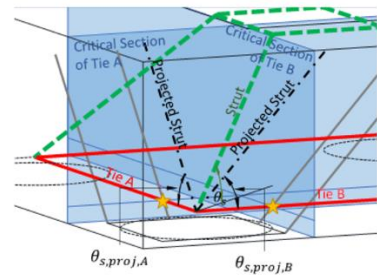
All tie elements shall be anchored properly to transfer the tension force therein to the node regions of the truss in accordance with the requirements for development of reinforcement as specified in Articles 5.9.4.3 and 5.10.8.2.

C5.8.2.10.3.2

The critical section of the bottom tie element anchored at a singular node is defined based on the geometry of the 3D nodal geometry, similar to **Figure C5.8.2.4.2-1**. The critical section on the plane of the strut can be defined as the point where the tie centroid intersects with the extended nodal zone as specified in **Figure C5.8.2.10.3.2-1**.

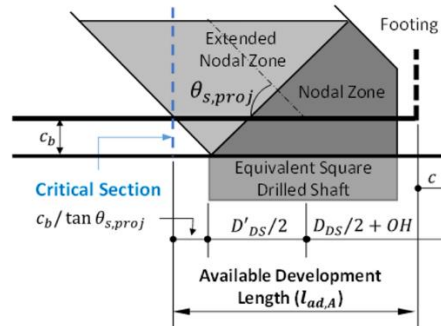


(a) Plan view



(b) Isometric view

Section A-A



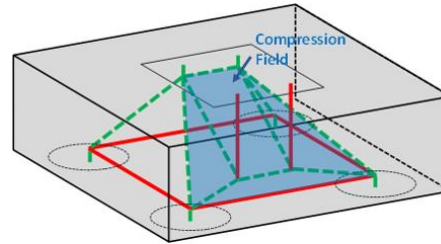
(c) Sectional view

- $\theta_{s,proj}$ = projected strut angle on plane parallel to ties (degrees)
- D_{DS} = shaft diameter (in.)
- D'_{DS} = length of equivalent square shaft (in.)
- c_b = distance from bottom surface to centroid of bottom ties (in.)
- OH = edge distance (the minimum distance from the edge of drilled shaft to the closest surface) (in.)
- c = clear cover between bottom mat reinforcement and the side face (in.)

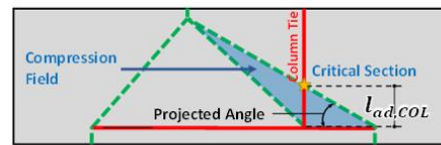
Figure C5.8.2.10.3.2-1—Available Development Length for Bottom Ties in 3D STM (at singular node)

C5.8.2.10.3.2b

As illustrated in Figure C5.8.2.10.3.2-2 and C5.8.2.10.3.2-3, the critical sections of the column and drilled shaft tie elements anchored at smeared nodes are defined based on the compression field representing the internal force flow vicinity of the smeared nodes.

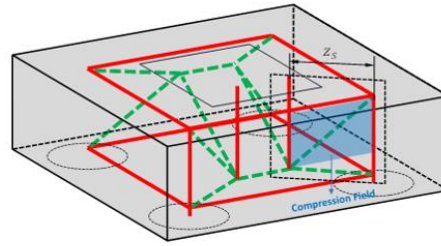


(a) Isometric view

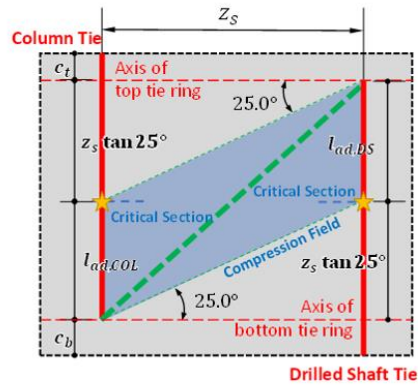


(b) Sectional view

Figure C5.8.2.10.3.2-2—Available Development Length for Column Ties in 3D STM (non-uniform compression in shafts)



(a) Isometric view



(b) Sectional view

Figure C5.8.2.10.3.2-3—Available Development Length for Column Ties and Drilled shaft Ties in 3D STM (tension-compression in shafts)

In the case where the bottom and top tie elements anchored at a smeared node, the critical section is assumed to be correspond with the interior edge of the equivalent square shafts as specified in Figure C5.8.2.10.3.2.3-4.

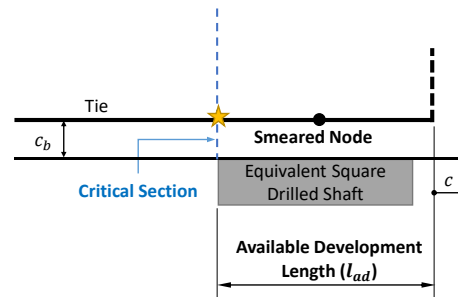


Figure C5.8.2.10.3.2-4—Available Development Length for Top and Bottom Ties in 3D STM (at smeared node)

5.8.2.10.4—Proportioning of Node Regions

5.8.2.10.4.1—Effective Cross-Sectional Area of the Node Face in Three Dimension

The nominal resistance of the node face shall be taken as Eq. 5.8.2.5.1-1.

5.8.2.10.4.2—Limiting Compressive Stress at the Node Face

Unless confinement reinforcement is provided and its effect is supported by analysis or experimentation, the limiting compressive stress at the node face, f_{cu} , shall be taken as:

$$f_{cu} = mvf'_c \quad (5.8.2.10.4.2-1)$$

where:

m = confinement modification factor, taken as $\sqrt{A_2/A_1} \leq 3.0$ for CCC node and 2.0 for other node types (CCT and CTT) as defined in Article 5.6.5

v = concrete efficiency factor

- 0.45 for footings that do not contain the shrinkage and temperature reinforcement on side faces as specified in Article 5.10.6
- as shown in Table 5.8.2.5.3a-1 for footings with shrinkage and temperature reinforcement on side faces as specified in Article 5.10.6

f'_c = compressive strength of concrete for use in design (ksi)

C5.8.2.10.4.2

Research has shown that any signs of the failure of CCC node was not observed in the experiments since the under triaxial compression condition at CCC node. Confinement factor is allowed for drilled shaft footings since nodes in a drilled shaft footing are significantly confined by massive surrounding concrete for all types of nodes. The maximum confinement factor of 3.0 for CCC node is based on Eurocode 2 (2004) and fib Model Code 2010 (2013).

Research has shown that the shrinkage and temperature reinforcement on side faces, side face reinforcement, improved the structural safety of drilled shaft footings, greater ultimate strength and less brittle failure. Consequently, the side face reinforcement plays a similar role in the crack control reinforcement. Even though the requirement of crack control reinforcement is exempted for footings, it is recommended that the side face reinforcement should satisfy the requirement as specified in Article 5.10.6.

Appendix B. Footing Research Database

Collection Database

Table B1. Details of Test Specimens: Blevot & Frémy (1967)

Spec ID	Length ^a [in.]	Height ^b [in.]	Pile spcg ^c [in.]	Column ^d [in.]	Pile dim ^d [in.]	<i>d</i> [in.]	<i>f_c'</i> [ksi]	Reinforcing Details			Length ^a [in.]	Height ^b [in.]	Failure Type
								Layout	Reinforcement	Area [in. ²]			
9	23.6	11.8	16.5	5.9	5.5	9.8	4.14	Banded ^e	4 x Φ8mm	0.31	62.5	187	Shear
14	23.6	11.8	16.5	5.9	5.5	11.0	4.64	Banded	4 x Φ10mm	0.49	40.3	165	Shear
19	23.6	7.9	16.5	5.9	5.5	7.1	4.56	Banded	4 x Φ8mm	0.31	66.7	105	Shear
24	23.6	11.8	16.5	5.9	5.5	10.6	3.78	Banded	2 x Φ10mm + 2 x Φ12mm	0.59	70.3	254	Shear
29	23.6	7.9	16.5	5.9	5.5	6.7	4.15	Banded ^f	2 x Φ10mm + 2 x Φ12mm	0.59	72.4	180	Shear
34	23.6	7.9	16.5	5.9	5.5	6.7	4.82	Grid	8 x Φ8mm	0.62	65.3	90	Shear
35	23.6	11.8	16.5	5.9	5.5	10.6	4.37	Grid	8 x Φ10mm	0.98	48.7	143	Shear
36	23.6	11.8	16.5	5.9	5.5	10.6	2.99	Grid	8 x Φ8mm	0.62	46.3	112	Shear
37	23.6	5.5	16.5	5.9	5.5	4.3	1.87	Banded	4 x Φ10mm	0.49	70.8	55	Shear
38	23.6	5.5	16.5	5.9	5.5	4.3	1.87	Banded	4 x Φ14mm	0.95	65.6	64	Shear
39	23.6	7.9	16.5	5.9	5.5	7.1	3.14	Banded	4 x Φ10mm	0.49	72.8	143	Shear
40	23.6	7.9	16.5	5.9	5.5	6.7	4.35	Banded	4 x Φ14mm	0.95	67.7	187	Shear
41	23.6	11.8	16.5	5.9	5.5	10.2	2.62	Banded	4 x Φ12mm	0.70	73.6	186	Shear
42	23.6	11.8	16.5	5.9	5.5	11.0	2.62	Banded	4 x Φ16mm	1.25	66.5	179	Shear
43	23.6	19.7	16.5	5.9	5.5	18.5	3.88	Banded Grid	4 x Φ12mm 8 x Φ12mm	0.70 1.40	65.3	265	Shear
44	23.6	19.7	16.5	5.9	5.5	18.5	5.80	Banded	4 x Φ16mm	1.25	66.4	419	Shear
45	23.6	19.7	16.5	5.9	5.5	18.5	4.89	Banded	4 x Φ12mm	0.70	64.0	375	Shear
46	23.6	9.8	16.5	5.9	5.5	9.1	4.92	Banded	4 x Φ12mm	0.70	63.4	187	Shear
48	23.6	9.8	16.5	5.9	5.5	8.7	4.82	Banded	4 x Φ12mm	0.70	64.5	165	Shear
52	23.6	11.8	16.5	5.9	5.5	10.6	3.82	Banded	4 x Φ12mm	0.70	44.2	124	Shear
53	23.6	11.8	16.5	5.9	5.5	10.6	2.77	Banded	4 x Φ12mm	0.70	44.2	109	Shear
54	23.6	11.8	16.5	5.9	5.5	11.0	4.39	Banded	4 x Φ10mm	0.49	63.2	123	Shear
55	23.6	11.8	16.5	5.9	5.5	10.6	4.27	Banded	4 x Φ10mm	0.49	62.7	129	Shear
56	23.6	7.9	16.5	5.9	5.5	6.7	2.95	Banded	4 x Φ12mm	0.70	45.3	185	Shear
57	23.6	7.9	16.5	5.9	5.5	6.7	3.11	Banded	4 x Φ12mm	0.70	45.3	153	Shear
58	23.6	7.9	16.5	5.9	5.5	6.7	4.61	Banded	4 x Φ10mm	0.49	62.0	165	Shear
59	23.6	7.9	16.5	5.9	5.5	6.7	3.71	Banded	4 x Φ10mm	0.49	61.4	141	Shear

a – Square specimens

d – Square column and square piles

b – Top surfaces tapered (height includes taper)

e – Reinforcement shown is per band

c – Center-on-center pile spacing in each direction

f – Each direction

Table B2. Details of Test Specimens: Clarke (1973)

Spec ID	Length ^a [in.]	Height [in.]	Pile spcg ^b [in.]	Column ^c [in.]	Pile dia ^d [in.]	<i>d</i> ^e [in.]	<i>f</i> _c ' cube ^f [ksi]	<i>f</i> _c ' cyl [ksi]	Reinforcement				<i>f</i> _y ⁱ [ksi]	<i>N</i> _{ult} [kip]	Failure Type
									Layout	Anchorage ^g	No. of 10mm bars each way	Area ^h [in. ²]			
A1	37.4	17.7	23.6	7.9	7.9	15.7	3.86	3.09	Grid	nominal	10	1.22	59.5	250	Shear
A2	37.4	17.7	23.6	7.9	7.9	15.7	4.93	3.94	Banded	nominal	10	0.61	59.5	319	Shear
A4	37.4	17.7	23.6	7.9	7.9	15.7	3.87	3.10	Grid	nil	10	1.22	59.5	277	Shear
A5	37.4	17.7	23.6	7.9	7.9	15.7	4.81	3.85	Banded	nil	10	0.61	59.5	315	Shear
A7	37.4	17.7	23.6	7.9	7.9	15.7	4.39	3.51	Grid	full	10	1.22	59.5	369	Shear
A8	37.4	17.7	23.6	7.9	7.9	15.7	4.93	3.94	Banded	nominal	10	0.61	59.5	339	Shear
A9	37.4	17.7	23.6	7.9	7.9	15.7	4.81	3.85	Grid	nominal	10	1.22	59.5	326	Shear
A10	37.4	17.7	23.6	7.9	7.9	15.7	3.41	2.73	Grid	full + bob	10	1.22	59.5	342	Shear
A11	37.4	17.7	23.6	7.9	7.9	15.7	3.26	2.61	Grid	full	10	1.22	59.5	369	Shear
A12	37.4	17.7	23.6	7.9	7.9	15.7	4.58	3.67	Grid	full + bob	10	1.22	59.5	369	Shear
B1	29.5	17.7	15.7	7.9	7.9	15.7	4.84	3.87	Grid	full	8	0.97	59.5	468	Shear
B2	29.5	17.7	15.7	7.9	7.9	15.7	4.47	3.57	Grid	full	10	1.22	59.5	420	Shear
B3	29.5	17.7	15.7	7.9	7.9	15.7	6.34	5.07	Grid	full	6	0.73	59.5	398	Shear

a – Square specimens
d – Circular piles
g – See reference for more info

b – Center-on-center pile spacing in both directions
e – Assumed effective depth (see reference)
h – For “grid,” total reinf area, for “banded,” reinf area per band

c – Square column (loading plate)
f – Specimen strengths are based on 150 mm cubes
i – Based on 0.2% offset, per the report

Table B3. Details of Test Specimens: Sabnis & Gogate (1984)

Spec ID	Length ^a [in.]	Height [in.]	Pile spcg ^b [in.]	Column ^c [in.]	Pile ^c [in.]	<i>d</i> [in.]	<i>f</i> _c ' [ksi]	<i>A</i> _s [in. ²]	<i>f</i> _y [ksi]	<i>N</i> _{ult} [kip]	Failure Type
SS1	13.0	6.0	8.0	3.0	3.0	4.4	4.54	0.12	72.4	56.3	Shear
SS2	13.0	6.0	8.0	3.0	3.0	4.4	4.54	0.08	100.5	55.0	Shear
SS3	13.0	6.0	8.0	3.0	3.0	4.4	4.54	0.10	128.5	55.8	Shear
SS4	13.0	6.0	8.0	3.0	3.0	4.4	4.54	0.15	66.0	50.8	Shear
SS5	13.0	6.0	8.0	3.0	3.0	4.3	5.95	0.30	71.0	59.3	Shear
SS6	13.0	6.0	8.0	3.0	3.0	4.3	5.95	0.44	72.4	63.0	Shear
SG2	13.0	6.0	8.0	3.0	3.0	4.6	2.60	0.33	72.4	39.0	Shear
SG3	13.0	6.0	8.0	3.0	3.0	4.6	2.60	1.50	72.4	39.8	Shear

a – Square specimens

b – Center-on-center pile spacing in each direction

c – Column and pile were 3” diameter steel

Table B4. Details of Test Specimens: Adebar et al. (1990)

Spec ID	Length ^a (Long) [in.]	Width ^a (Trans) [in.]	Height [in.]	Pile Spacing		Column dim ^b [in.]	Pile dia ^c [in.]	f_c' [ksi]	Reinf Layout	Longitudinal Reinforcement ^d			Transverse Reinforcement ^d			f_y [ksi]	N_{ult} [kip]
				Long [in.]	Trans [in.]					Description	Area [in. ²]	Depth ^e [in.]	Description	Area [in. ²]	Depth ^e [in.]		
A	92.9	66.9	23.6	61.4	35.4	11.8	7.9	3.60	Grid	15-No 10 at 100mm	2.33	17.7	9-No 10 at 260mm	1.40	17.3	69.5	400.4
B	92.9	66.9	23.6	61.4	35.4	11.8	7.9	3.60	Banded ^f	6-No 10 at 45mm	0.93	13.8	4-No 10 at 70mm	0.62	13.4	69.5	492.1
										8-No 10 at 45mm	1.24	15.7	4-No 10 at 70mm	0.62	15.4		
										8-No 10 at 45mm	1.24	17.7	4-No 10 at 70mm	0.62	17.3		
D	92.9	66.9	23.6	61.4	35.4	11.8	7.9	4.39	Banded	8-No 15 at 45mm	2.48	13.8	4-No 15 at 70mm	1.24	13.0	70.5	724.4
										8-No 15 at 45mm	2.48	15.7	4-No 15 at 70mm	1.24	15.0		
										8-No 15 at 45mm	2.48	17.7	4-No 15 at 70mm	1.24	16.9		
E	92.9	66.9	23.6	61.4	35.4	11.8	7.9	5.96	Banded	8-No 15 at 45mm	2.48	13.8	4-No 15 at 70mm	1.24	13.0	70.5	1058.7
										8-No 15 at 45mm	2.48	15.7	4-No 15 at 70mm	1.24	15.0		
										8-No 15 at 45mm	2.48	17.7	4-No 15 at 70mm	1.24	16.9		
									Grid	5-No 10 at 240mm	0.78	19.1	9-No 10 at 210mm	1.40	19.5	69.5	
F	92.9	66.9	23.6	61.4	35.4	11.8	7.9	4.39	Banded	8-No 15 at 45mm	2.48	13.8	4-No 15 at 70mm	1.24	13.0	70.5	680.3
										8-No 15 at 45mm	2.48	15.7	4-No 15 at 70mm	1.24	15.0		
										8-No 15 at 45mm	2.48	17.7	4-No 15 at 70mm	1.24	16.9		

a – Specimens A - E were diamond-shaped, specimen F was cruciform-shaped

c – Circular piles

e – From top of cap to centroid of reinforcement

b – Square columns

d – Long reinforcement runs in direction of length, transverse reinforcement runs in direction of width

f– All banded layouts had (3) layers of reinforcement

Table B5. Details of Test Specimens: Suzuki et al. (1998)

Test No.	Specimen ID	Length X [in.]	Length Y [in.]	Height [in.]	Pile spcg ^a [in.]	Column ^b [in.]	Pile dia [in.]	<i>d</i> [in.]	<i>f_c'</i> [ksi]	Reinf Layout	Reinforcement ^c		<i>f_y</i> [ksi]	<i>N_{ult}</i> [kip]	Failure Type ^d
											X-Direction	Y-Direction			
1	BP-20-1	35.4	35.4	7.9	21.3	11.8	5.9	5.9	3.09	Grid	8-D10 at 100	8-D10 at 100	59.9	117	B S
2	BP-20-2	35.4	35.4	7.9	21.3	11.8	5.9	5.9	2.96	Grid	8-D10 at 100	8-D10 at 100	59.9	108	B S
3	BPC-20-1	35.4	35.4	7.9	21.3	11.8	5.9	5.9	3.18	Banded	8-D10 at 40	8-D10 at 40	59.9	117	B P
4	BPC-20-2	35.4	35.4	7.9	21.3	11.8	5.9	5.9	2.89	Banded	8-D10 at 40	8-D10 at 40	59.9	119	B P
5	BP-25-1	35.4	35.4	9.8	21.3	11.8	5.9	7.9	3.28	Grid	10-D10 at 80	10-D10 at 80	59.9	165	S
6	BP-25-2	35.4	35.4	9.8	21.3	11.8	5.9	7.9	3.12	Grid	10-D10 at 80	10-D10 at 80	59.9	170	S
7	BPC-25-1	35.4	35.4	9.8	21.3	11.8	5.9	7.9	2.74	Banded	10-D10 at 40	10-D10 at 40	59.9	184	B S
8	BPC-25-2	35.4	35.4	9.8	21.3	11.8	5.9	7.9	3.19	Banded	10-D10 at 40	10-D10 at 40	59.9	183	B P
9	BP-20-30-1	31.5	31.5	7.9	19.7	11.8	5.9	5.9	4.22	Grid	6-D10 at 120	6-D10 at 120	58.7	109	B S
10	BP-20-30-2	31.5	31.5	7.9	19.7	11.8	5.9	5.9	4.32	Grid	6-D10 at 120	6-D10 at 120	58.7	108	B S
11	BPC-20-30-1	31.5	31.5	7.9	19.7	11.8	5.9	5.9	4.32	Banded	6-D10 at 40	6-D10 at 40	58.7	112	B
12	BPC-20-30-2	31.5	31.5	7.9	19.7	11.8	5.9	5.9	4.32	Banded	6-D10 at 40	6-D10 at 40	58.7	111	B
13	BP-30-30-1	31.5	31.5	11.8	19.7	11.8	5.9	9.8	3.96	Grid	8-D10 at 90	8-D10 at 90	58.7	206	S
14	BP-30-30-2	31.5	31.5	11.8	19.7	11.8	5.9	9.8	4.13	Grid	8-D10 at 90	8-D10 at 90	58.7	204	B S
15	BPC-30-30-1	31.5	31.5	11.8	19.7	11.8	5.9	9.8	4.19	Banded	8-D10 at 40	8-D10 at 40	58.7	234	B S
16	BPC-30-30-2	31.5	31.5	11.8	19.7	11.8	5.9	9.8	4.48	Banded	8-D10 at 40	8-D10 at 40	58.7	231	B S
17	BP-30-25-1	31.5	31.5	11.8	19.7	9.8	5.9	9.8	4.48	Grid	8-D10 at 90	8-D10 at 90	58.7	179	B S
18	BP-30-25-2	31.5	31.5	11.8	19.7	9.8	5.9	9.8	3.81	Grid	8-D10 at 90	8-D10 at 90	58.7	163	S
19	BPC-30-25-1	31.5	31.5	11.8	19.7	9.8	5.9	9.8	4.22	Banded	8-D10 at 40	8-D10 at 40	58.7	192	B S
20	BPC-30-25-2	31.5	31.5	11.8	19.7	9.8	5.9	9.8	4.23	Banded	8-D10 at 40	8-D10 at 40	58.7	196	B S
21	BDA-70x90-1	27.6	35.4	11.8	19.7	9.8	5.9	9.8	4.22	Grid	8-D10 at 90	7-D13 at 90	51.6/50.0 ^e	176	B S
22	BDA-70x90-2	27.6	35.4	11.8	19.7	9.8	5.9	9.8	4.38	Grid	8-D10 at 90	7-D13 at 90	51.6/50.0	170	B S
23	BDA-80x90-1	31.5	35.4	11.8	19.7	9.8	5.9	9.8	4.22	Grid	8-D10 at 90	8-D13 at 90	51.6/50.0	193	B S
24	BDA-80x90-2	31.5	35.4	11.8	19.7	9.8	5.9	9.8	4.25	Grid	8-D10 at 90	8-D13 at 90	51.6/50.0	192	B S
25	BDA-90x90-1	35.4	35.4	11.8	19.7	9.8	5.9	9.8	4.28	Grid	8-D10 at 90	9-D13 at 90	51.6/50.0	192	B D
26	BDA-90x90-2	35.4	35.4	11.8	19.7	9.8	5.9	9.8	4.57	Grid	8-D10 at 90	9-D13 at 90	51.6/50.0	207	B D
27	BDA-100x90-1	39.4	35.4	11.8	19.7	9.8	5.9	9.8	4.31	Grid	8-D10 at 90	10-D13 at 90	51.6/50.0	205	B D
28	BDA-100x90-2	39.4	35.4	11.8	19.7	9.8	5.9	9.8	4.54	Grid	8-D10 at 90	10-D13 at 90	51.6/50.0	209	B D

a – Square pile layout

c – *f_y* for D10/D13 bars

e – For banded layouts, reinforcing shown is both bands

b – Square columns

d – B: Flexural failure, S: Corner shear failure, P: Punching failure, D: One-way shear failure

Table B6. Details of Test Specimens: Suzuki et al. (1999)

Test No.	Specimen ID	Length ^a [in.]	Height ^b		Pile Spcg ^c [in.]	Column Width ^d [in.]	Pile Diam [in.]	Reinf Elev ^e [in.]	f_c' [ksi]	Reinf Layout	Reinforcement (Each Way)	f_y [ksi]	N_{ult} [kip]	Failure Type ^f
			Col Face [in.]	Edge [in.]										
1	TDL1-1	35.4	13.8	7.9	23.6	9.8	5.9	2.0	4.48	Grid	4-D10 at 220	51.6	88	B
2	TDL1-2	35.4	13.8	7.9	23.6	9.8	5.9	2.0	4.09	Grid	4-D10 at 220	51.6	88	B
3	TDL2-1	35.4	13.8	7.9	23.6	9.8	5.9	2.0	4.15	Grid	6-D10 at 130	51.6	117	B
4	TDL2-2	35.4	13.8	7.9	23.6	9.8	5.9	2.0	4.18	Grid	6-D10 at 130	51.6	106	B
5	TDL3-1	35.4	13.8	7.9	23.6	9.8	5.9	2.0	4.29	Grid	8-D10 at 100	51.6	137	B
6	TDL3-2	35.4	13.8	7.9	23.6	9.8	5.9	2.0	4.25	Grid	8-D10 at 100	51.6	141	B
7	TDS1-1	35.4	13.8	7.9	17.7	9.8	5.9	2.0	3.71	Grid	6 - D10 at 130	51.6	207	B
8	TDS1-2	35.4	13.8	7.9	17.7	9.8	5.9	2.0	3.92	Grid	6 - D10 at 130	51.6	187	B
9	TDS2-1	35.4	13.8	7.9	17.7	9.8	5.9	2.0	3.94	Grid	8-D10 at 100	51.6	226	B
10	TDS2-2	35.4	13.8	7.9	17.7	9.8	5.9	2.0	3.96	Grid	8-D10 at 100	51.6	237	B
11	TDS3-1	35.4	13.8	7.9	17.7	9.8	5.9	2.0	4.06	Grid	11-D10 at 75	51.6	292	B S
12	TDS3-2	35.4	13.8	7.9	17.7	9.8	5.9	2.0	4.07	Grid	11-D10 at 75	51.6	293	B S
13	TDM1-1	35.4	11.8	5.9	19.7	9.8	5.9	2.0	3.99	Grid	4-D10 at 220	55.5	110	B
14	TDM1-2	35.4	11.8	5.9	19.7	9.8	5.9	2.0	3.81	Grid	4-D10 at 220	55.5	104	B
15	TDM2-1	35.4	11.8	5.9	19.7	9.8	5.9	2.0	4.29	Grid	6-D10 at 130	55.5	148	B
16	TDM2-2	35.4	11.8	5.9	19.7	9.8	5.9	2.0	4.00	Grid	6-D10 at 130	55.5	148	B
17	TDM3-1	35.4	11.8	5.9	19.7	9.8	5.9	2.0	3.92	Grid	10-D13 at 80	53.7	280	S
18	TDM3-2	35.4	11.8	5.9	19.7	9.8	5.9	2.0	4.06	Grid	10-D13 at 80	53.7	272	S

a – Specimens were square
d – Square columns

b – Top of specimens tapered
e – Elevation of reinforcement, from bottom of cap to centroid of bar

c – Square pile layout
f – B: Flexural failure, S: Corner shear failure, f – B: Flexural failure, S: Corner shear failure,

Table B7. Details of Test Specimens: Suzuki et al. (2000)

Test No.	Specimen	Length ^a [in.]	Height [in.]	Pile spec ^b [in.]	Column ^c [in.]	Pile dia [in.]	<i>d</i> [in.]	<i>f_c'</i> [ksi]	Reinf Layout	Reinforcement (Each Way)	<i>f_y</i> [ksi]	<i>N_{ult}</i> [kip]	Failure Type ^d
1	BDA-20-25-70-1	27.6	7.9	17.7	9.8	5.9	5.9	3.78	Grid	4-D10 at 170	51.9	66	B
2	BDA-20-25-70-2	27.6	7.9	17.7	9.8	5.9	5.9	3.78	Grid	4-D10 at 170	51.9	68	B
3	BDA-20-25-80-1	31.5	7.9	17.7	9.8	5.9	5.9	3.68	Grid	4-D10 at 200	51.9	68	B
4	BDA-20-25-80-2	31.5	7.9	17.7	9.8	5.9	5.9	3.68	Grid	4-D10 at 200	51.9	68	B
5	BDA-20-25-90-1	35.4	7.9	17.7	9.8	5.9	5.9	3.74	Grid	4-D10 at 220	51.9	75	B
6	BDA-20-25-90-2	35.4	7.9	17.7	9.8	5.9	5.9	3.74	Grid	4-D10 at 220	51.9	75	B
7	BDA-30-20-70-1	27.6	11.8	17.7	7.9	5.9	9.8	3.65	Grid	6-D10 at 100	51.9	120	B
8	BDA-30-20-70-2	27.6	11.8	17.7	7.9	5.9	9.8	3.57	Grid	6-D10 at 100	51.9	123	B S
9	BDA-30-20-80-1	31.5	11.8	17.7	7.9	5.9	9.8	3.65	Grid	6-D10 at 120	51.9	128	B
10	BDA-30-20-80-2	31.5	11.8	17.7	7.9	5.9	9.8	3.86	Grid	6-D10 at 120	51.9	127	B
11	BDA-30-20-90-1	35.4	11.8	17.7	7.9	5.9	9.8	3.77	Grid	6-D10 at 130	51.9	131	B
12	BDA-30-20-90-2	35.4	11.8	17.7	7.9	5.9	9.8	3.78	Grid	6-D10 at 130	51.9	132	B
13	BDA-30-25-70-1	27.6	11.8	17.7	9.8	5.9	9.8	4.18	Grid	6-D10 at 100	55.5	149	B S
14	BDA-30-25-70-2	27.6	11.8	17.7	9.8	5.9	9.8	3.84	Grid	6-D10 at 100	55.5	152	B S
15	BDA-30-25-80-1	31.5	11.8	17.7	9.8	5.9	9.8	4.26	Grid	6-D10 at 120	55.5	156	B S
16	BDA-30-25-80-2	31.5	11.8	17.7	9.8	5.9	9.8	4.03	Grid	6-D10 at 120	55.5	163	B S
17	BDA-30-25-90-1	35.4	11.8	17.7	9.8	5.9	9.8	4.21	Grid	6-D10 at 130	55.5	172	B S
18	BDA-30-25-90-2	35.4	11.8	17.7	9.8	5.9	9.8	3.89	Grid	6-D10 at 130	55.5	172	B
19	BDA-30-30-70-1	27.6	11.8	17.7	11.8	5.9	9.8	3.89	Grid	6-D10 at 100	51.9	173	B S
20	BDA-30-30-70-2	27.6	11.8	17.7	11.8	5.9	9.8	3.76	Grid	6-D10 at 100	51.9	164	B S
21	BDA-30-30-80-1	31.5	11.8	17.7	11.8	5.9	9.8	3.97	Grid	6-D10 at 120	51.9	186	B S
22	BDA-30-30-80-2	31.5	11.8	17.7	11.8	5.9	9.8	3.97	Grid	6-D10 at 120	51.9	182	B S
23	BDA-30-30-90-1	35.4	11.8	17.7	11.8	5.9	9.8	3.94	Grid	6-D10 at 130	51.9	190	B S
24	BDA-30-30-90-2	35.4	11.8	17.7	11.8	5.9	9.8	3.55	Grid	6-D10 at 130	51.9	183	B S
25	BDA-40-25-70-1	27.6	15.7	17.7	9.8	5.9	13.8	3.76	Grid	8-D10 at 70	51.9	229	S
26	BDA-40-25-70-2	27.6	15.7	17.7	9.8	5.9	13.8	3.60	Grid	8-D10 at 70	51.9	240	B S
27	BDA-40-25-80-1	31.5	15.7	17.7	9.8	5.9	13.8	3.84	Grid	8-D10 at 90	51.9	251	B S
28	BDA-40-25-80-2	31.5	15.7	17.7	9.8	5.9	13.8	3.70	Grid	8-D10 at 90	51.9	251	B
29	BDA-40-25-90-1	35.4	15.7	17.7	9.8	5.9	13.8	3.73	Grid	8-D10 at 100	51.9	264	B
30	BDA-40-25-90-2	35.4	15.7	17.7	9.8	5.9	13.8	3.77	Grid	8-D10 at 100	51.9	266	B

a – Specimens were square
c – Square columns

b – Pile layout was square
d – B: Flexural failure, S: Corner shear failure, P: Punching failure, D: One-way shear failure

Table B8. Details of Test Specimens: Suzuki and Otsuki (2002)

Test No.	Specimen	Length ^a [in.]	Height [in.]	Pile Spcg ^a [in.]	Column ^b [in.]	Pile Diam [in.]	<i>d</i> [in.]	<i>f</i> _c ' [ksi]	Reinf Layout	Reinforcement (Each Way)	Anchorage	<i>f</i> _y [ksi]	<i>N</i> _{ult} [kip]	Failure Type ^c
1	BPL-35-30-1	31.5	13.8	19.7	9.8	5.9	11.8	3.49	Grid	9-D10 at 75	180-Deg Hook	51.2	216	S
2	BPL-35-30-2	31.5	13.8	19.7	9.8	5.9	11.8	3.71	Grid	9-D10 at 75	180-Deg Hook	51.2	212	S
3	BPB-35-30-1	31.5	13.8	19.7	9.8	5.9	11.8	3.44	Grid	9-D10 at 75	Bent-up	51.2	231	B S
4	BPB-35-30-2	31.5	13.8	19.7	9.8	5.9	11.8	3.41	Grid	9-D10 at 75	Bent-up	51.2	248	B S
5	BPH-35-30-1	31.5	13.8	19.7	9.8	5.9	11.8	4.57	Grid	9-D10 at 75	180-Deg Hook	51.2	220	S
6	BPH-35-30-2	31.5	13.8	19.7	9.8	5.9	11.8	4.74	Grid	9-D10 at 75	180-Deg Hook	51.2	245	B S
7	BPL-35-25-1	31.5	13.8	19.7	9.8	5.9	11.8	3.93	Grid	9-D10 at 75	180-Deg Hook	51.2	203	B S
8	BPL-35-25-2	31.5	13.8	19.7	9.8	5.9	11.8	3.71	Grid	9-D10 at 75	180-Deg Hook	51.2	196	S
9	BPB-35-25-1	31.5	13.8	19.7	9.8	5.9	11.8	3.36	Grid	9-D10 at 75	Bent-up	51.2	205	B S
10	BPB-35-25-2	31.5	13.8	19.7	9.8	5.9	11.8	3.44	Grid	9-D10 at 75	Bent-up	51.2	207	B S
11	BPH-35-25-1	31.5	13.8	19.7	9.8	5.9	11.8	5.31	Grid	9-D10 at 75	180-Deg Hook	51.2	198	S
12	BPH-35-25-2	31.5	13.8	19.7	9.8	5.9	11.8	5.50	Grid	9-D10 at 75	180-Deg Hook	51.2	214	S
13	BPL-35-20-1	31.5	13.8	19.7	9.8	5.9	11.8	3.26	Grid	9-D10 at 75	180-Deg Hook	51.2	170	S
14	BPL-35-20-2	31.5	13.8	19.7	9.8	5.9	11.8	3.12	Grid	9-D10 at 75	180-Deg Hook	51.2	165	S
15	BPB-35-20-1	31.5	13.8	19.7	9.8	5.9	11.8	2.96	Grid	9-D10 at 75	Bent-up	51.2	170	B P
16	BPB-35-20-2	31.5	13.8	19.7	9.8	5.9	11.8	2.93	Grid	9-D10 at 75	Bent-up	51.2	181	B S
17	BPH-35-20-1	31.5	13.8	19.7	9.8	5.9	11.8	4.55	Grid	9-D10 at 75	180-Deg Hook	51.2	183	S
18	BPH-35-20-2	31.5	13.8	19.7	9.8	5.9	11.8	4.47	Grid	9-D10 at 75	180-Deg Hook	51.2	179	S

a – Specimens and pile layouts were square

b – Columns were square

c – B: Flexural failure, S: Corner shear failure, P: Punching failure, D: One-way shear failure

Evaluation Database

Table B9. Details of Test Specimens in Evaluation Database

No.	Researcher	Specimen ID	Footing Dim. ^a [in.]	Footing Height ^b [in.]	Footing Depth ^c [in.]	Shaft Span ^d [in.]	z/d ^e	Column Dim. ^f [in.]	Shaft Dia. [in.]	f_c' [ksi]	Bottom mat Reinforcing Details (Layout) ^g	Reinf. Ratio [%]	f_y [ksi]	N_{ult} [kip]	Failure Type ^h
1	Suzuki et al. (1998)	BP-25-1	35.4 x 35.4	9.8	7.87	21.3	1.91	11.8	5.9	3.28	10-D10 at 80mm (G)	0.40	59.9	165	S
2		BP-25-2	35.4 x 35.4	9.8	7.87	21.3	1.91	11.8	5.9	3.12	10-D10 at 80mm (G)	0.40	59.9	170	S
3		BPC-25-1	35.4 x 35.4	9.8	7.87	21.3	1.91	11.8	5.9	2.74	10-D10 at 40mm (B)	0.40	59.9	184	B S
4		BPC-25-2	35.4 x 35.4	9.8	7.87	21.3	1.91	11.8	5.9	3.19	10-D10 at 40mm (B)	0.40	59.9	183	B P
5		BP-30-30-1	31.5 x 31.5	11.8	9.84	19.7	1.41	11.8	5.9	3.96	8-D10 at 90mm (G)	0.29	58.7	206	S
6		BP-30-30-2	31.5 x 31.5	11.8	9.84	19.7	1.41	11.8	5.9	4.13	8-D10 at 90mm (G)	0.29	58.7	204	B S
7		BPC-30-30-1	31.5 x 31.5	11.8	9.84	19.7	1.41	11.8	5.9	4.19	10-D10 at 40mm (B)	0.29	58.7	234	B S
8		BPC-30-30-2	31.5 x 31.5	11.8	9.84	19.7	1.41	11.8	5.9	4.48	10-D10 at 40mm (B)	0.29	58.7	231	B S
9		BP-30-25-1	31.5 x 31.5	11.8	9.84	19.7	1.41	9.8	5.9	4.48	8-D10 at 90mm (G)	0.29	58.7	179	B S
10		BP-30-25-2	31.5 x 31.5	11.8	9.84	19.7	1.41	9.8	5.9	3.81	8-D10 at 90mm (G)	0.29	58.7	163	S
11		BPC-30-25-1	31.5 x 31.5	11.8	9.84	19.7	1.41	9.8	5.9	4.22	10-D10 at 40mm (B)	0.29	58.7	192	B S
12		BPC-30-25-2	31.5 x 31.5	11.8	9.84	19.7	1.41	9.8	5.9	4.23	10-D10 at 40mm (B)	0.29	58.7	196	B S
13		BDA-70x90-1	27.6 x 35.4	11.8	9.84	19.7	1.41	9.8	5.9	4.22	8-D10 at 90mm (G)	0.29	51.6	176	B S
14		BDA-70x90-2	27.6 x 35.4	11.8	9.84	19.7	1.41	9.8	5.9	4.38	8-D10 at 90mm (G)	0.29	51.6	170	B S
15		BDA-80x90-1	31.5 x 35.4	11.8	9.84	19.7	1.41	9.8	5.9	4.22	8-D10 at 90mm (G)	0.27	51.6	193	B S
16		BDA-80x90-2	31.5 x 35.4	11.8	9.84	19.7	1.41	9.8	5.9	4.25	8-D10 at 90mm (G)	0.27	51.6	192	B S
17		BDA-90x90-1	35.4 x 35.4	11.8	9.84	19.7	1.41	9.8	5.9	4.28	8-D10 at 90mm (G)	0.25	51.6	192	B D
18		BDA-90x90-2	35.4 x 35.4	11.8	9.84	19.7	1.41	9.8	5.9	4.57	8-D10 at 90mm (G)	0.45	50.0	207	B D
19	Suzuki et al. (1998)	TDM3-1	35.4 x 35.4	11.8	9.84	19.7	1.41	9.8	5.9	3.92	10-D13 at 80mm (G)	0.56	53.7	280	S
20		TDM3-2	35.4 x 35.4	11.8	9.84	19.7	1.41	9.8	5.9	4.06	10-D13 at 80mm (G)	0.56	53.7	272	S
21	Suzuki et al. (2000)	BDA-30-20-70-2	27.6 x 27.6	11.8	9.84	17.7	1.27	7.9	5.9	3.57	6-D10 at 100mm (G)	0.24	51.9	123	B S
22		BDA-30-25-70-1	27.6 x 27.6	11.8	9.84	17.7	1.27	9.8	5.9	4.18	6-D10 at 100mm (G)	0.24	55.5	149	B S
23		BDA-30-25-70-2	27.6 x 27.6	11.8	9.84	17.7	1.27	9.8	5.9	3.84	6-D10 at 100mm (G)	0.24	55.5	152	B S
24		BDA-30-25-80-1	31.5 x 31.5	11.8	9.84	17.7	1.27	9.8	5.9	4.26	6-D10 at 120mm (G)	0.21	55.5	156	B S
25		BDA-30-25-80-2	31.5 x 31.5	11.8	9.84	17.7	1.27	9.8	5.9	4.03	6-D10 at 120mm (G)	0.21	55.5	163	B S
26		BDA-30-30-70-1	27.6 x 27.6	11.8	9.84	17.7	1.27	11.8	5.9	3.89	6-D10 at 100mm (G)	0.24	51.9	173	B S

No.	Researcher	Specimen ID	Footing Dim. ^a [in.]	Footing Height ^b [in.]	Footing Depth ^c [in.]	Shaft Span ^d [in.]	z/d^e	Column Dim. ^f [in.]	Shaft Dia. [in.]	f_c' [ksi]	Bottom mat Reinforcing Details (Layout) ^g	Reinf. Ratio [%]	f_p [ksi]	N_{ult} [kip]	Failure Type ^h
27	Suzuki et al. (2000)	BDA-30-30-70-2	27.6 x 27.6	11.8	9.84	17.7	1.27	11.8	5.9	3.76	6-D10 at 100mm (G)	0.24	51.9	164	B S
28		BDA-30-30-80-1	31.5 x 31.5	11.8	9.84	17.7	1.27	11.8	5.9	3.97	6-D10 at 120mm (G)	0.21	51.9	186	B S
29		BDA-30-30-80-2	31.5 x 31.5	11.8	9.84	17.7	1.27	11.8	5.9	3.97	6-D10 at 120mm (G)	0.21	51.9	182	B S
30		BDA-30-30-90-2	35.4 x 35.4	11.8	9.84	17.7	1.27	11.8	5.9	3.55	6-D10 at 130mm (G)	0.25	51.9	183	B S
31	Suzuki & Otsuki (2002)	BPL-35-30-1	31.5 x 31.5	13.8	11.81	19.7	1.18	9.8	5.9	3.49	9-D10 at 75mm (G)	0.27	51.2	216	S
32		BPL-35-30-2	31.5 x 31.5	13.8	11.81	19.7	1.18	9.8	5.9	3.71	9-D10 at 75mm (G)	0.27	51.2	212	S
33		BPB-35-30-1	31.5 x 31.5	13.8	11.81	19.7	1.18	9.8	5.9	3.44	9-D10 at 75mm (G)	0.27	51.2	231	B S
34		BPB-35-30-2	31.5 x 31.5	13.8	11.81	19.7	1.18	9.8	5.9	3.41	9-D10 at 75mm (G)	0.27	51.2	248	B S
35		BPH-35-30-1	31.5 x 31.5	13.8	11.81	19.7	1.18	9.8	5.9	4.57	9-D10 at 75mm (G)	0.27	51.2	220	S
36		BPH-35-30-2	31.5 x 31.5	13.8	11.81	19.7	1.18	9.8	5.9	4.74	9-D10 at 75mm (G)	0.27	51.2	245	B S
37		BPL-35-25-1	31.5 x 31.5	13.8	11.81	19.7	1.18	9.8	5.9	3.93	9-D10 at 75mm (G)	0.27	51.2	203	B S
38		BPL-35-25-2	31.5 x 31.5	13.8	11.81	19.7	1.18	9.8	5.9	3.71	9-D10 at 75mm (G)	0.27	51.2	196	S
39		BPB-35-25-1	31.5 x 31.5	13.8	11.81	19.7	1.18	9.8	5.9	3.36	9-D10 at 75mm (G)	0.27	51.2	205	B S
40		BPB-35-25-2	31.5 x 31.5	13.8	11.81	19.7	1.18	9.8	5.9	3.44	9-D10 at 75mm (G)	0.27	51.2	207	B S
41		BPH-35-25-1	31.5 x 31.5	13.8	11.81	19.7	1.18	9.8	5.9	5.31	9-D10 at 75mm (G)	0.27	51.2	198	S
42		BPH-35-25-2	31.5 x 31.5	13.8	11.81	19.7	1.18	9.8	5.9	5.50	9-D10 at 75mm (G)	0.27	51.2	214	S
43		BPL-35-20-1	31.5 x 31.5	13.8	11.81	19.7	1.18	9.8	5.9	3.26	9-D10 at 75mm (G)	0.27	51.2	170	S
44		BPL-35-20-2	31.5 x 31.5	13.8	11.81	19.7	1.18	9.8	5.9	3.12	9-D10 at 75mm (G)	0.27	51.2	165	S
45		BPB-35-20-1	31.5 x 31.5	13.8	11.81	19.7	1.18	9.8	5.9	2.96	9-D10 at 75mm (G)	0.27	51.2	170	B P
46		BPB-35-20-2	31.5 x 31.5	13.8	11.81	19.7	1.18	9.8	5.9	2.93	9-D10 at 75mm (G)	0.27	51.2	181	B S
47	BPH-35-20-1	31.5 x 31.5	13.8	11.81	19.7	1.18	9.8	5.9	4.55	9-D10 at 75mm (G)	0.27	51.2	183	S	
48	BPH-35-20-2	31.5 x 31.5	13.8	11.81	19.7	1.18	9.8	5.9	4.47	9-D10 at 75mm (G)	0.27	51.2	179	S	
49	Present Study	I-1	96.0 x 96.0	32.0	27.00	65.0	1.70	32.0	16.0	5.07	14-2xNo.8 at 6.00 in. (G)	0.85	71.9	2107	B S
50		I-2	96.0 x 96.0	32.0	27.00	65.0	1.70	32.0	16.0	5.22	14-2xNo.8 at 6.00 in. (G)	0.85	64.1	2775	B S
51		I-3	96.0 x 96.0	32.0	27.00	65.0	1.70	32.0	16.0	5.09	14-No.8 at 3.75 in. (B)	0.85	64.1	2703	B P
52		I-4	96.0 x 96.0	32.0	27.00	65.0	1.70	32.0	16.0	5.06	14-No.8 at 3.75 in. (B)	0.85	64.1	2884	B P
53		II-5	72.0 x 96.0	40.0	34.87	41.1/65.1	1.10	32.0	16.0	3.24	12-2xNo.9 at 5.00 in./ 16-2xNo.9 at 5.00 in. (G)	0.96	63.5	3273	S
54		II-6	96.0 x 96.0	40.0	34.87	66.8	1.35	32.0	16.0	4.62	16-2xNo.9 at 5.00 in. (G)	0.96	63.5	3648	S

No.	Researcher	Specimen ID	Footing Dim. ^a [in.]	Footing Height ^b [in.]	Footing Depth ^c [in.]	Shaft Span ^d [in.]	z/d^e	Column Dim. ^f [in.]	Shaft Dia. [in.]	f_c' [ksi]	Bottom mat Reinforcing Details (Layout) ^g	Reinf. Ratio [%]	f_y [ksi]	N_{ult} [kip]	Failure Type ^h
55	Present Study	II-7	132.0 x 96.0	40.0	34.87	100.25/ 64.0	1.71	32.0	16.0	5.86	22-2xNo.9 at 5.25 in./ 16-2xNo.9 at 5.00 in. (G)	0.96	62.8	3387	B S
56		III-8	132.0 x 96.0	40.0	34.87	100.25/ 64.0	1.71	32.0	12.0	4.66	22-2xNo.9 at 5.25 in./ 16-2xNo.9 at 5.00 in. (G)	0.96	67.5	2886	S
57		III-9	132.0 x 96.0	40.0	34.87	100.25/ 64.0	1.71	32.0	20.0	3.71	22-2xNo.9 at 5.25 in./ 16-2xNo.9 at 5.00 in. (G)	0.96	67.5	2902	S
58		IV-10	132.0 x 96.0	40.0	34.87	100.25/ 64.0	1.71	32.0	16.0	4.66	22-2xNo.9 at 5.25 in./ 16-2xNo.9 at 5.00 in. (G)	0.96	78.3	2523	S
59		IV-11	132.0 x 96.0	40.0	34.87	100.25/ 64.0	1.71	32.0	16.0	4.65	22-2xNo.9 at 5.25 in./ 16-2xNo.9 at 5.00 in. (G)	0.96	78.3	2990	S
60		V-12	96.0 x 96.0	32.0	27.00	65.0	1.70	32.0	16.0	3.52	16-2xNo.8 at 5.25 in. (G)	0.98	67.0	2239	S

a– Length x width

d– If not specified, the same spacing in length and width directions

g– If not specified, the same details in both orthogonal directions, G (grid layout), B(banded layout)

b– The maximum Height

e– Strut inclination (shear span divided by depth)

h– B (bending failure), S (shear failure), P (punching failure) categorized by Suzuki et al. (1998)

c– The maximum depth

f– Square shaped

Appendix C. TxDOT Footing Database


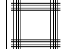

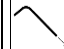

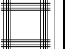

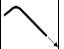

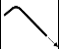


Table C1. Geometric Properties

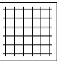
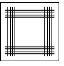
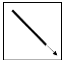

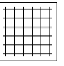
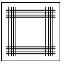
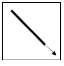

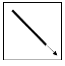

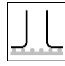

No.	City	Year	Length [in.]	Width [in.]	Depth [in.]	z/d	Con'c Strength [ksi]	Rebar Strength (Footing) [ksi]	Rebar Strength (Shafts) [ksi]	Column		Drilled Shaft			Footing-to- shaft edge distance [in.]
										Depth [in.]	Width [in.]	Shaft Diameter [in.]	Spacing (*L) [in.]	Spacing (*W) [in.]	
1	Austin	2002	252	228	60	2.03	3.6	60	40	120	60	60	168	144	12
2	Austin	2006	216	216	84	1.3	3.6	60	60	120	72	48	144	144	12
3	Austin	2010	192	192	48	1.85	3.6	60	60	84	48	48	120	120	12
4	Austin	2010	213	213	56	1.85	3.6	60	60	84	42	54	135	135	12
5	Austin	2010	213	213	56	1.82	3.6	60	60	84	54	54	135	135	12
6	Austin	2009	208	184	60	1.36	3.6	60	60	120	66	48	120	96	20
7	Bryan	2014	264	216	75	1.77	3.6	60	60	120	66	48	192	144	12
8	Dallas	2008	192	192	48	1.95	3.6	60	60	96	60	48	120	120	12
9	Fort Worth	2009	228	228	84	1.34	3.6	60	60	162	72	54	150	150	12
10	Houston	2007	216	216	48	2.29	3.6	60	60	72	54	48	144	144	12
11	Houston	2007	234	234	48	2.63	3.6	60	60	114	66	54	162	162	9
12	Houston	2010	186	186	54	1.8	3.6	60	60	78	60	36	126	126	12
13	Houston	2010	204	204	54	1.97	3.6	60	60	96	72	42	138	138	12
14	Houston	2010	240	240	60	2.03	3.6	60	60	120	72	54	162	162	12
15	Houston	2009	204	186	54	2.14	3.6	60	60	78	48	42	156	138	3
16	Houston	2009	132	132	48	1.49	3.6	60	60	32	32	30	90	90	6
17	Lubbock	2004	198	198	60	1.6	3.6	60	60	120	72	36	126	126	18
18	Lubbock	2005	228	228	68	1.44	3.6	60	60	120	72	48	144	144	18
19	Lubbock	2004	228	228	68	1.45	3.6	60	60	96	48	48	144	144	18

No.	City	Year	Length [in.]	Width [in.]	Depth [in.]	z/d	Con'c Strength [ksi]	Rebar Strength (Footing) [ksi]	Rebar Strength (Shafts) [ksi]	Column		Drilled Shaft			Footing-to- shaft edge distance [in.]
										Depth [in.]	Width [in.]	Shaft Diameter [in.]	Spacing (*L) [in.]	Spacing (**W) [in.]	
20	San Antonio	1999	240	240	60	2.03	3.6	60	60	102	60	54	162	162	12
21	San Antonio	1999	234	234	60	1.88	3.6	60	60	120	72	60	150	150	12
22	San Antonio	1999	276	276	72	1.86	3.6	60	60	144	72	72	180	180	12
23	San Antonio	1999	213	213	56	1.82	3.6	60	60	144	72	54	135	135	12
24	San Antonio	1999	294	294	60	2.70	3.6	60	60	102	60	60	210	210	12
25	San Antonio	1999	255	255	66	1.87	3.6	60	60	120	72	66	165	165	12
26	San Antonio	2002	234	234	56	2.10	3.6	60	60	102	60	54	156	156	12
27	San Antonio	2002	213	213	56	1.82	3.6	60	60	120	60	54	135	135	12
28	San Antonio	2002	213	213	56	1.82	3.6	60	60	102	60	54	135	135	12
29	San Antonio	2002	234	234	66	1.70	3.6	60	60	84	48	60	150	150	12
30	San Antonio	2002	255	255	66	1.87	3.6	60	60	120	72	66	165	165	12
31	San Antonio	2002	240	240	60	2.1	3.6	60	60	102	60	54	168	168	9
32	Waco	2010	192	192	60	1.59	3.6	60	40	96	54	48	126	126	9
33	Waco	2010	192	192	60	1.59	3.6	60	40	90	78	48	126	126	9
34	Waco	2010	204	204	66	1.37	3.6	60	40	108	78	60	120	120	12
35	Waco	2010	192	192	60	1.59	3.6	60	40	96	78	48	126	126	9

*L: Length direction / **W: Width direction

Table C2. Reinforcing Details

No.	City	Year	Footing										Drilled Shaft		Column			
			Bottom Reinforcement				Top Reinforcement				Face Reinforcement							
			Avg. Ratio [%]	Configuration		Anchorage		Avg. Ratio [%]	Configuration		Anchorage		Avg. Ratio (*L) [%]	Avg. Ratio (**T) [%]	Anchorage		Anchorage	
																		
1	Austin	2002	0.472					0.123					0.322	0.044				
2	Austin	2006	0.220					0.086					0.137	0.070				
3	Austin	2010	0.770					0.144					0.410	0.074				
4	Austin	2010	0.660					0.137					0.296	0.068				
5	Austin	2010	0.647					0.124					0.296	0.068				
6	Austin	2009	0.362					0.117					0.142	0.035				
7	Bryan	2014	0.432					0.095					0.242	0.111	†N/A			
8	Dallas	2008	0.478					0.149					0.158	0.027				
9	Fort Worth	2009	0.742					0.323					0.093	0.875				
10	Houston	2007	0.385					0.083					0.213	0.070				
11	Houston	2007	0.745					0.257					††-	††-				
12	Houston	2010	0.566					0.335					††-	††-				
13	Houston	2010	0.504					0.331					††-	††-				
14	Houston	2010	0.711					0.296					††-	††-				
15	Houston	2009	0.504					0.331					††-	††-				
16	Houston	2009	0.233					0.044					0.083	0.020				
17	Lubbock	2004	0.507					0.148					0.325	0.112				
18	Lubbock	2005	0.405					0.117					0.285	0.088				
19	Lubbock	2004	0.323					0.075					0.244	0.056				

No.	City	Year	Footing										Drilled Shaft	Column				
			Bottom Reinforcement				Top Reinforcement				Face Reinforcement							
			Avg. Ratio [%]	Configuration		Anchorage		Avg. Ratio [%]	Configuration		Anchorage		Avg. Ratio (*L) [%]	Avg. Ratio (**T) [%]	Anchorage			
																		
20	San Antonio	1999	0.240					0.090					0.252	0.033				
21	San Antonio	1999	0.246					0.092					0.254	0.035				
22	San Antonio	1999	0.261					0.074					0.216	0.028				
23	San Antonio	1999	0.257					0.109					0.296	0.042				
24	San Antonio	1999	0.289					0.092					0.243	0.028				
25	San Antonio	1999	0.237					0.076					0.259	0.029				
26	San Antonio	2002	0.202					0.125					0.467	0.044				
27	San Antonio	2002	0.245					0.131					0.296	0.050				
28	San Antonio	2002	0.245					0.131					0.296	0.050				
29	San Antonio	2002	0.365					0.100					0.211	0.042				
30	San Antonio	2002	0.253					0.107					0.259	0.041				
31	San Antonio	2002	0.298					0.125					0.316	0.046				
32	Waco	2010	0.546					0.386					0.157	0.032				
33	Waco	2010	0.546					0.386					0.157	0.032				
34	Waco	2010	0.592					0.278					0.151	0.035				
35	Waco	2010	0.546					0.386					0.157	0.032				

*L: Longitudinal direction / **T: Transverse direction

†N/A: Insufficient information about dowel bars coming from shafts

††-: No face reinforcement in footing plans

Appendix D. Drawings of Specimens

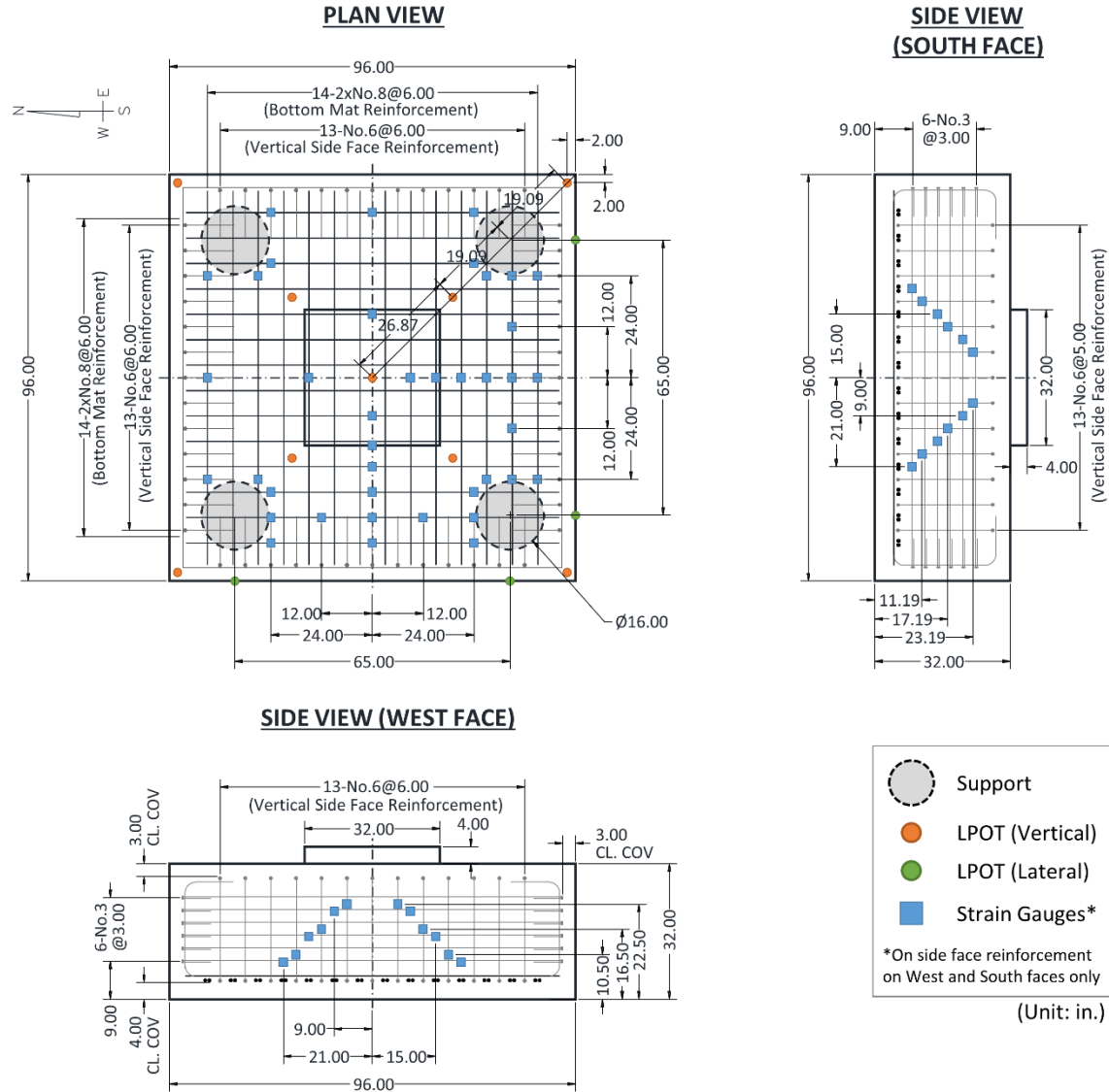


Figure D.1 Drawing of I-1: Phase I

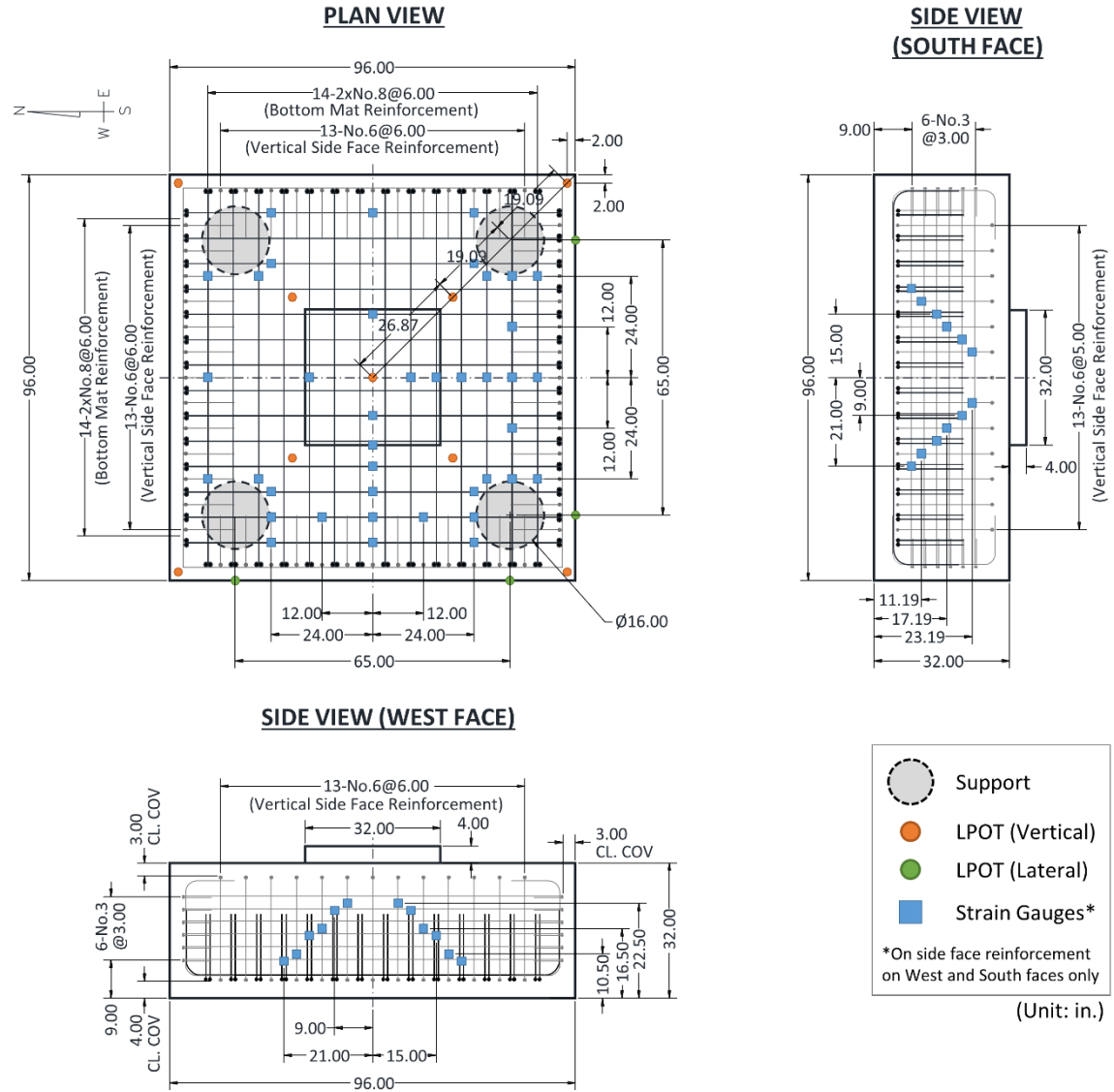


Figure D.2 Drawing of I-2: Phase I

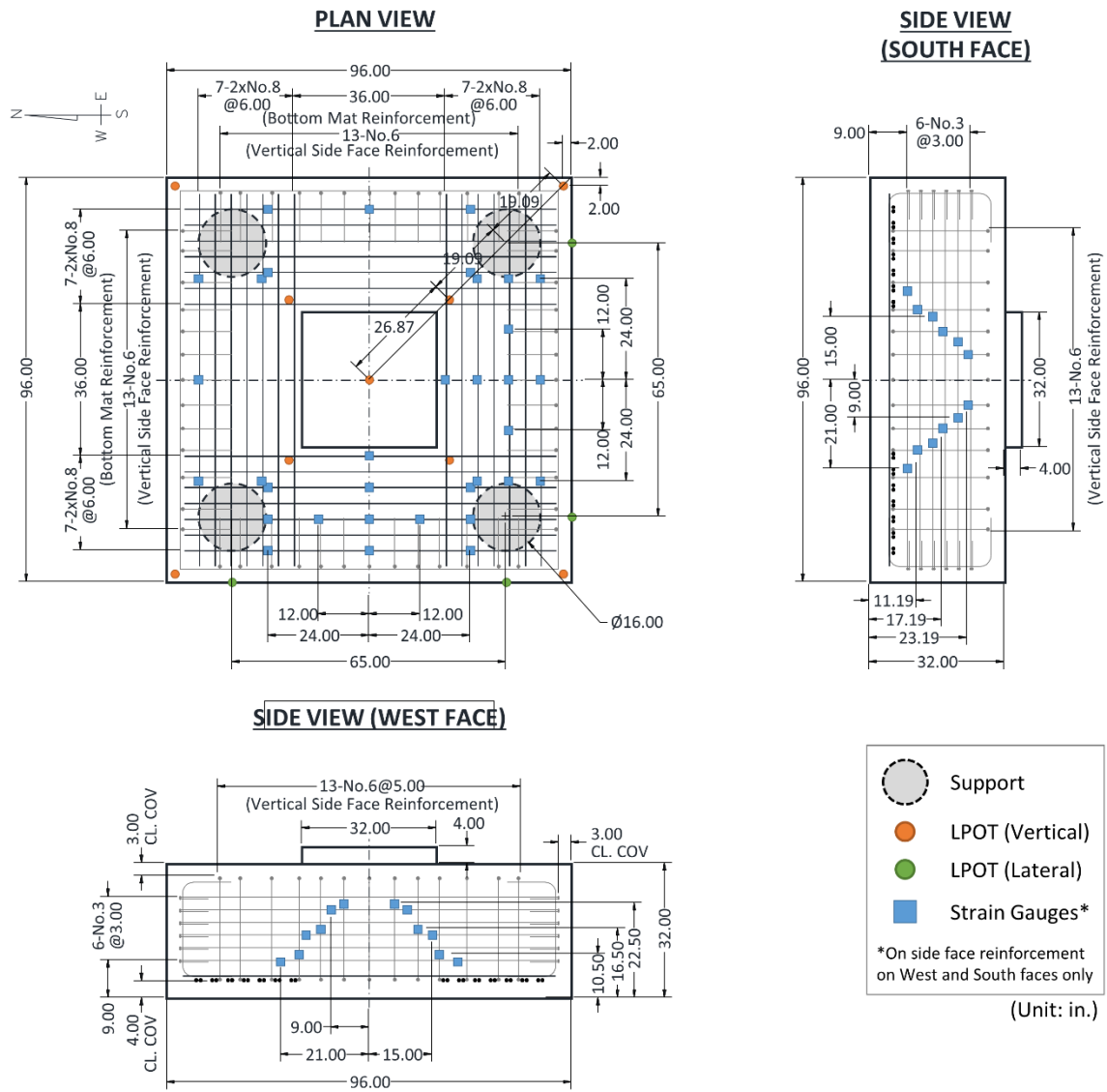


Figure D.3 Drawing of I-3: Phase I

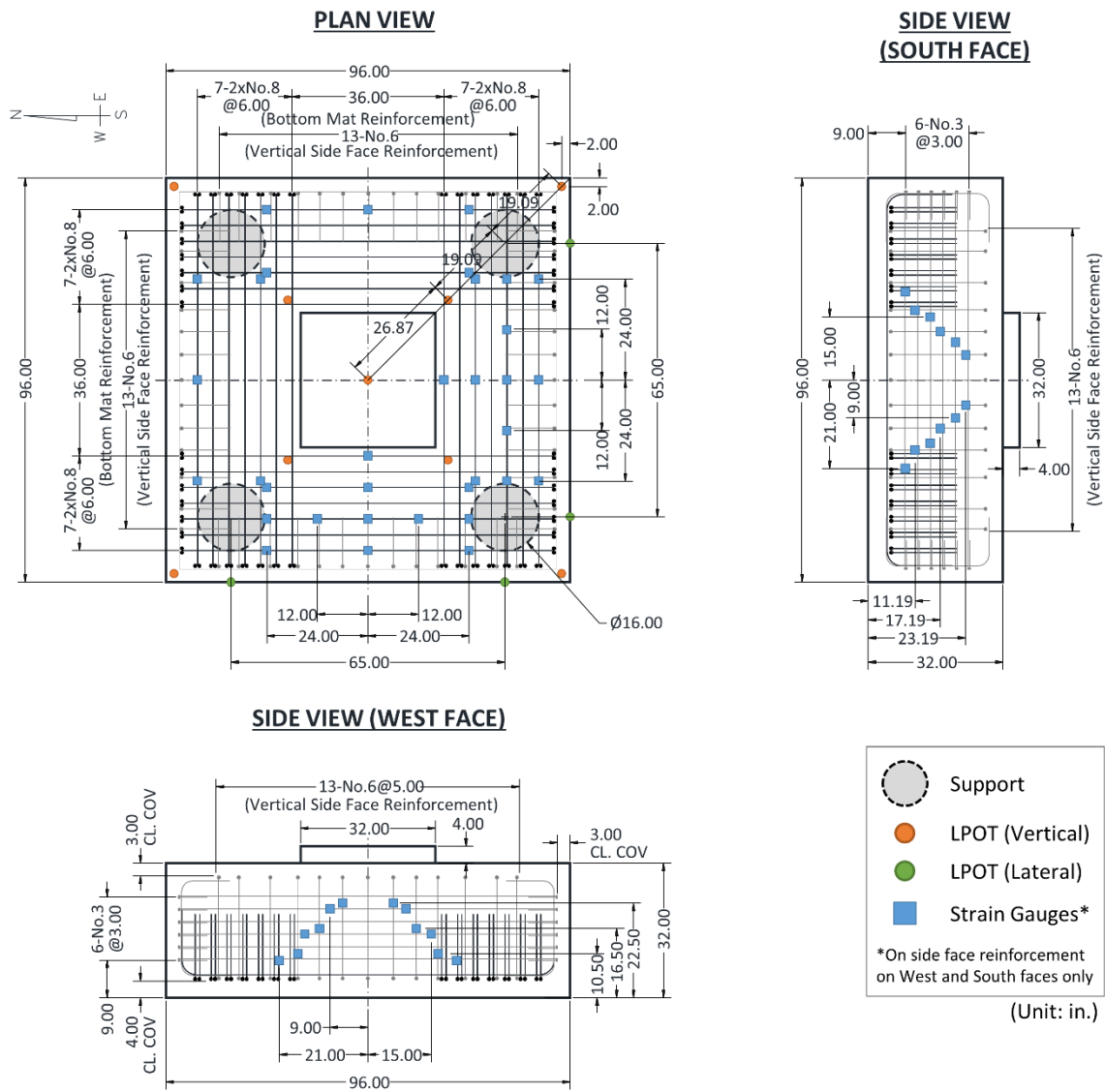


Figure D.4 Drawing of I-4: Phase I

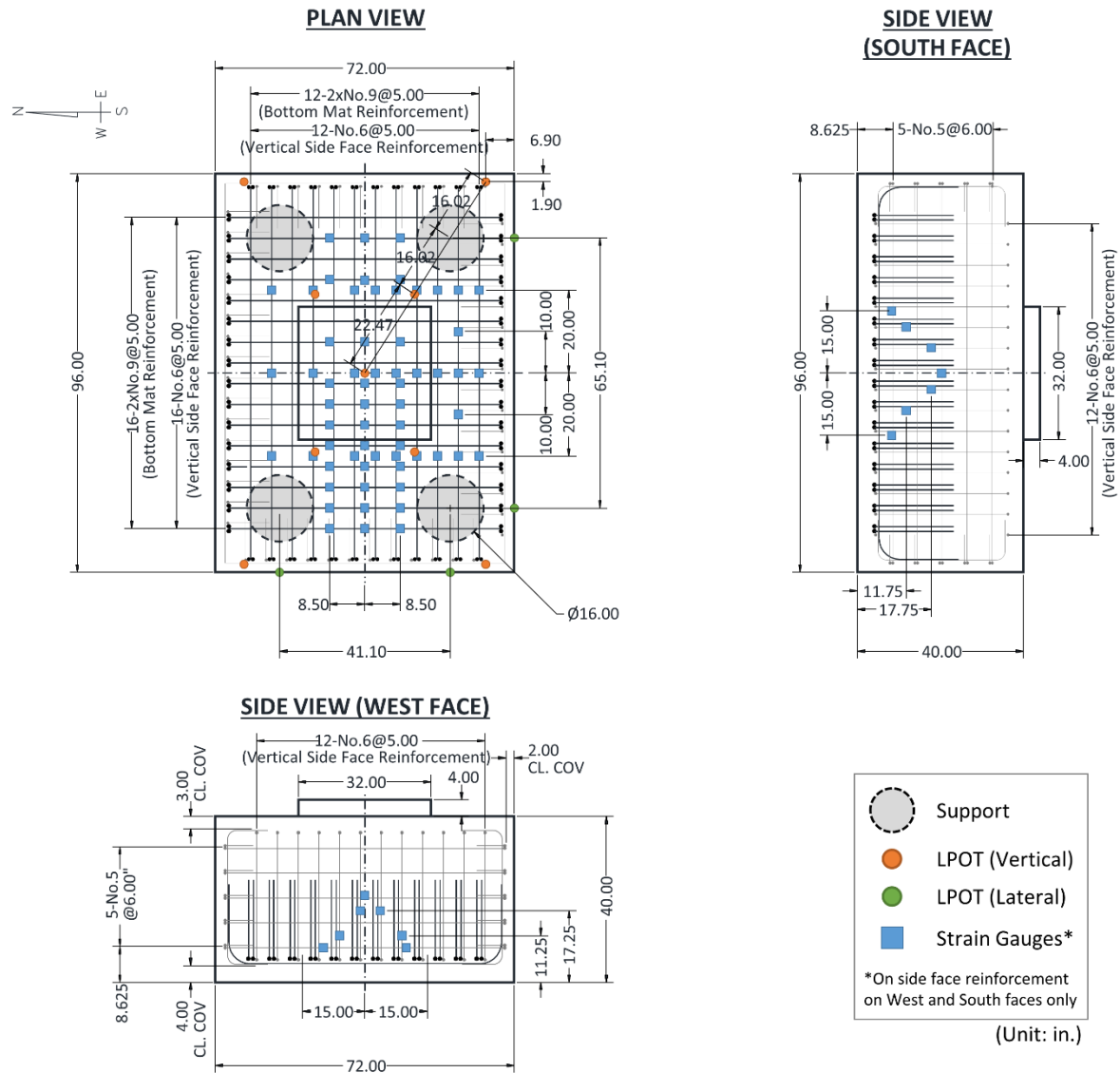


Figure D.5 Drawing of II-5: Phase I

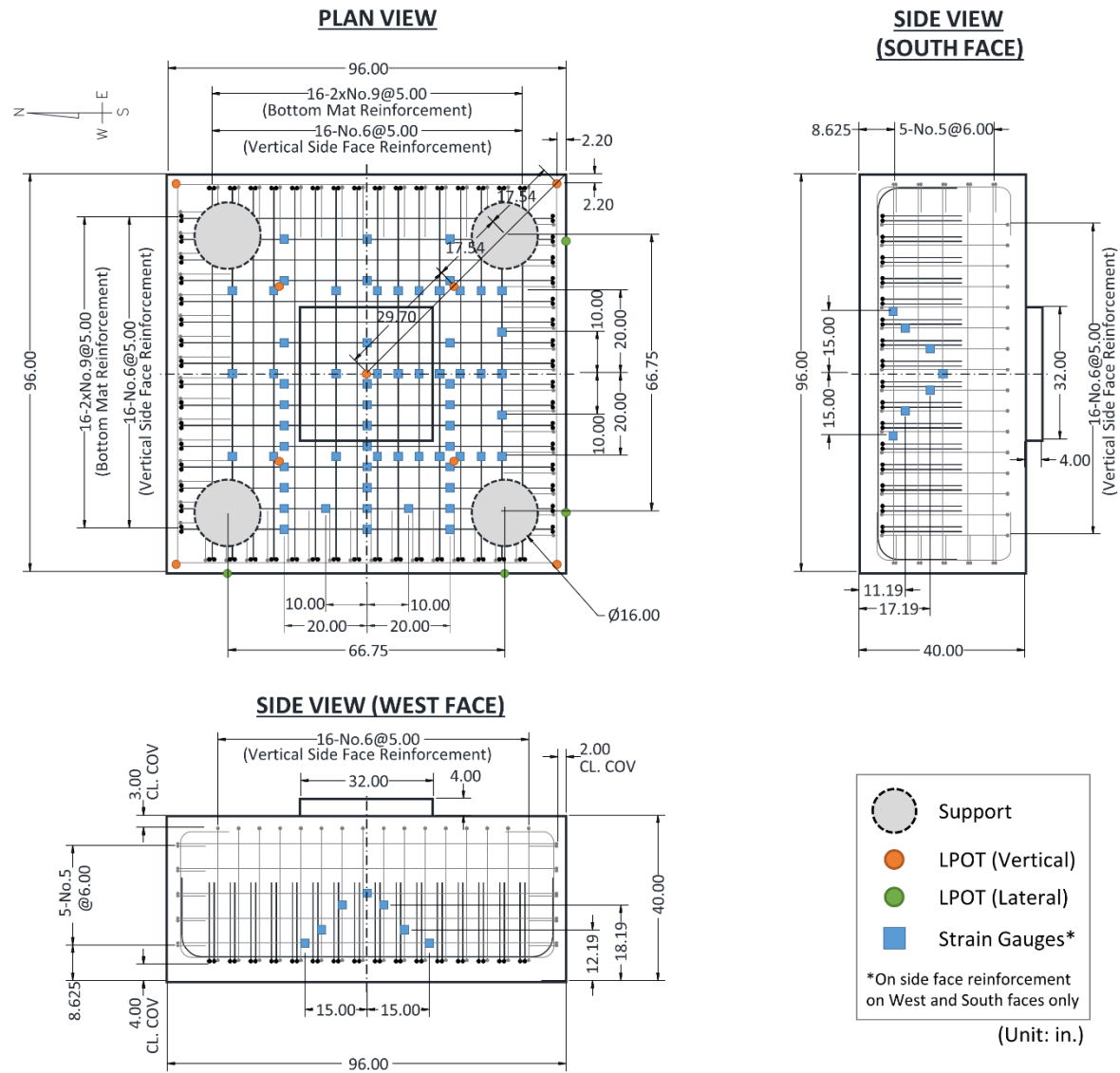


Figure D.6 Drawing of II-6: Phase I

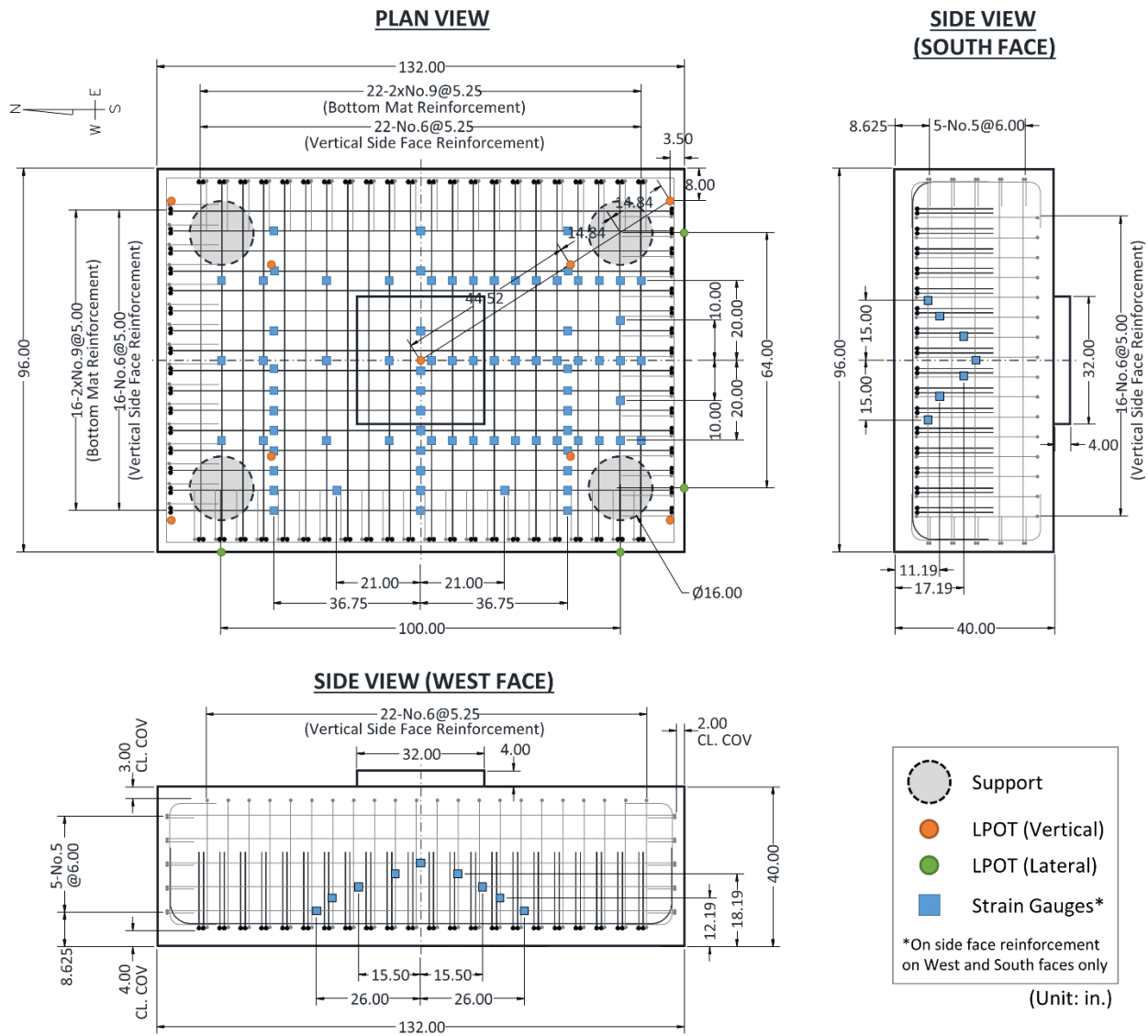


Figure D.7 Drawing of II-7: Phase I

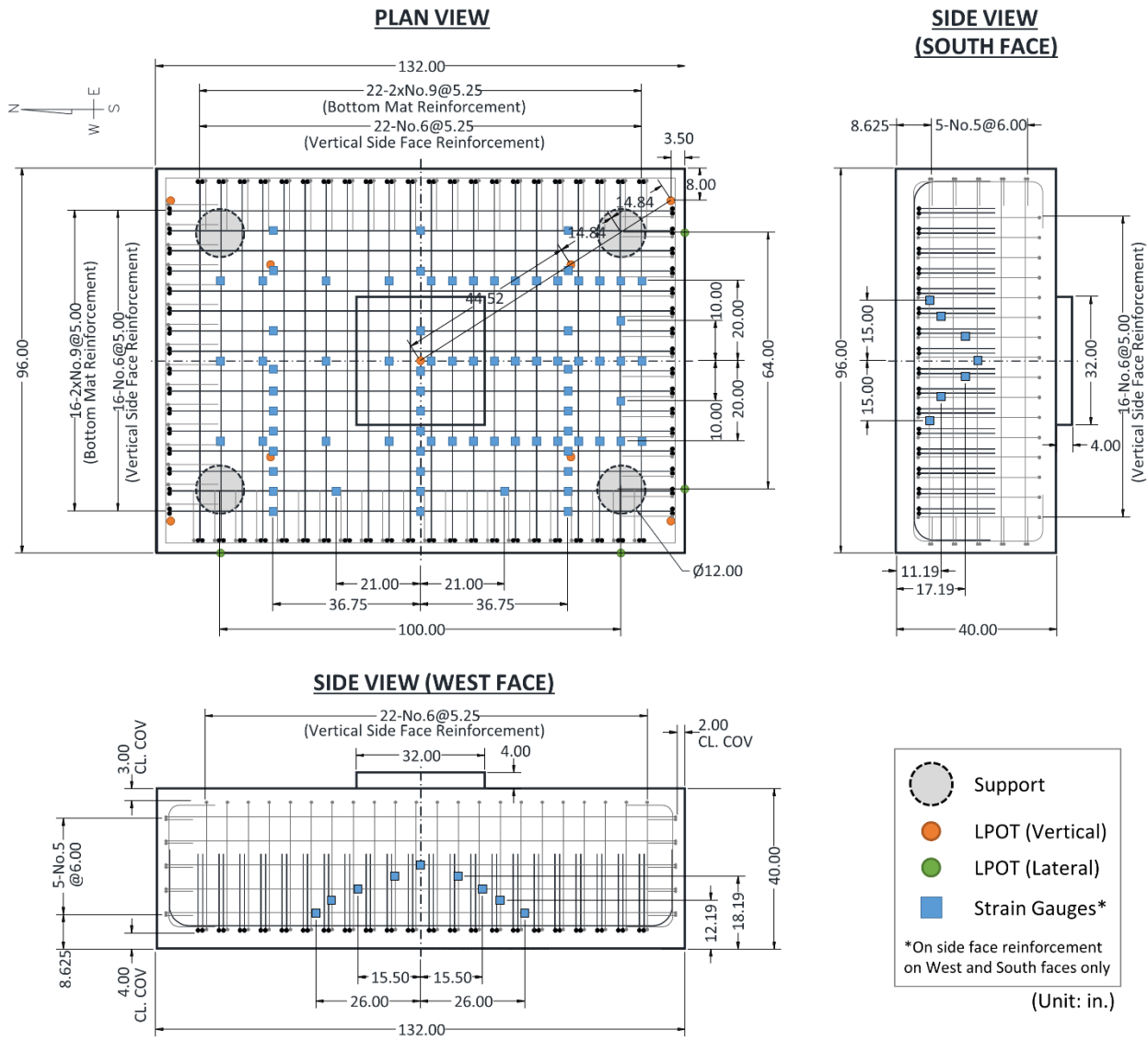


Figure D.8 Drawing of III-8: Phase I

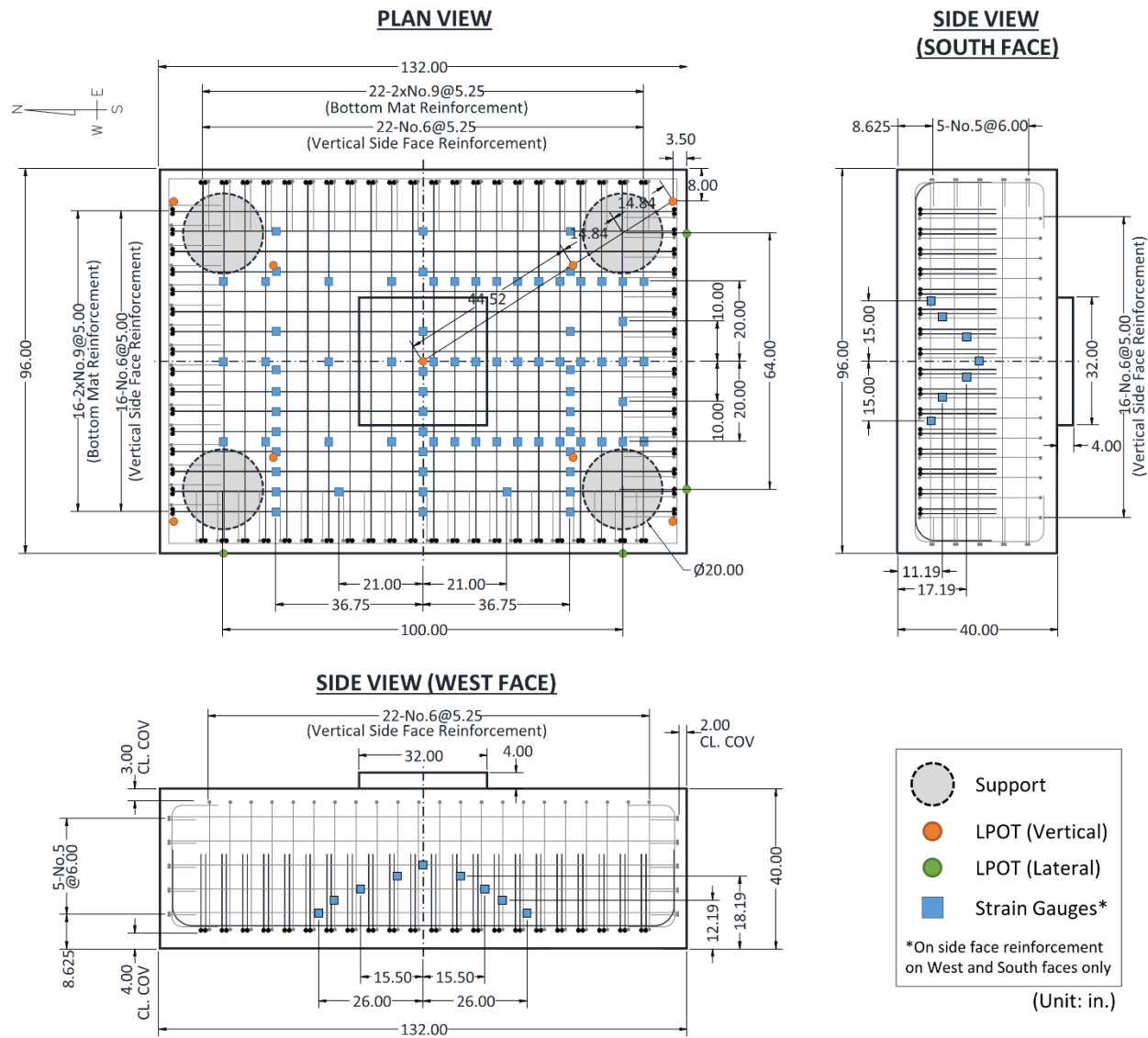


Figure D.9 Drawing of III-9: Phase I

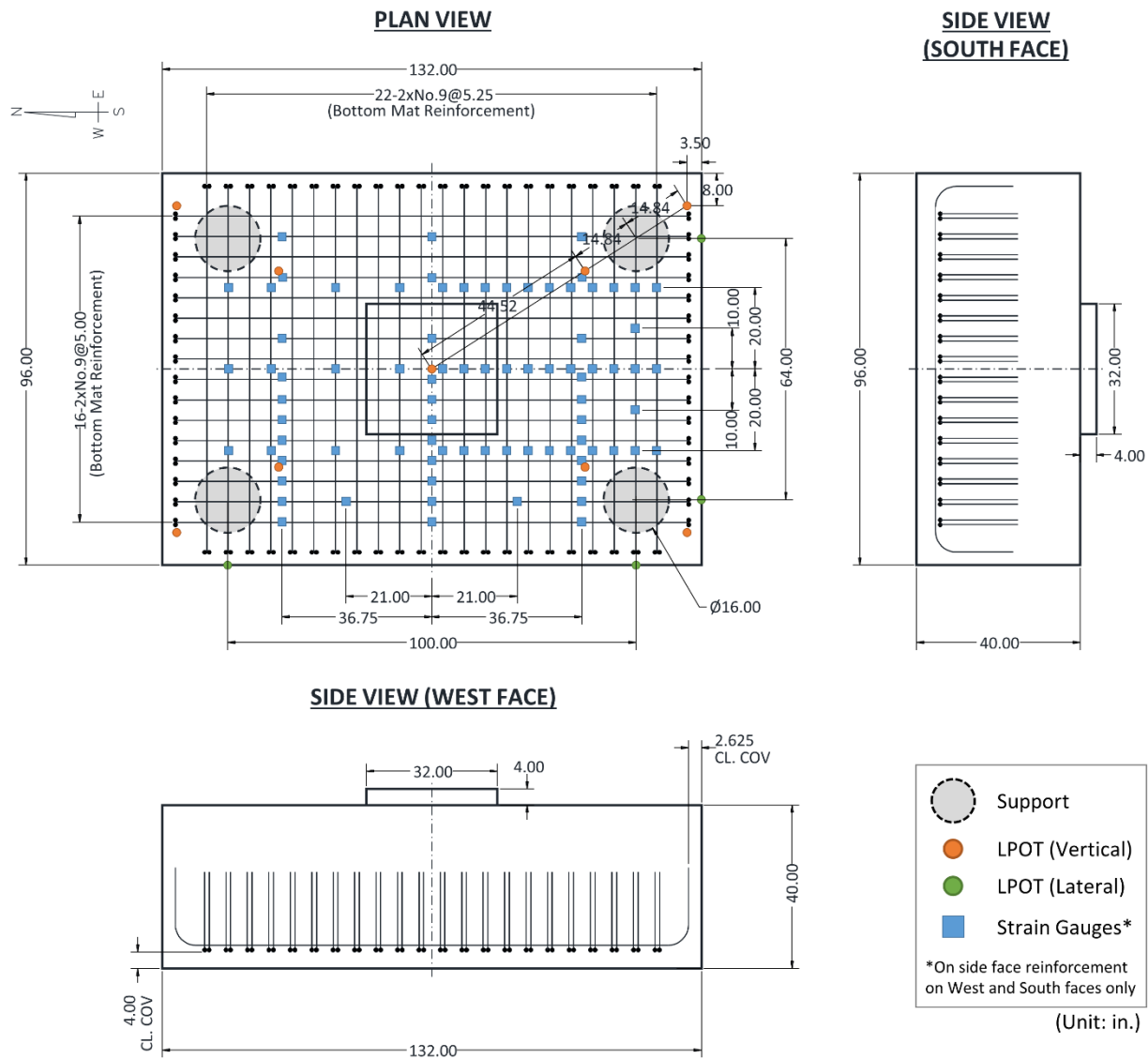


Figure D.10 Drawing of IV-10: Phase I

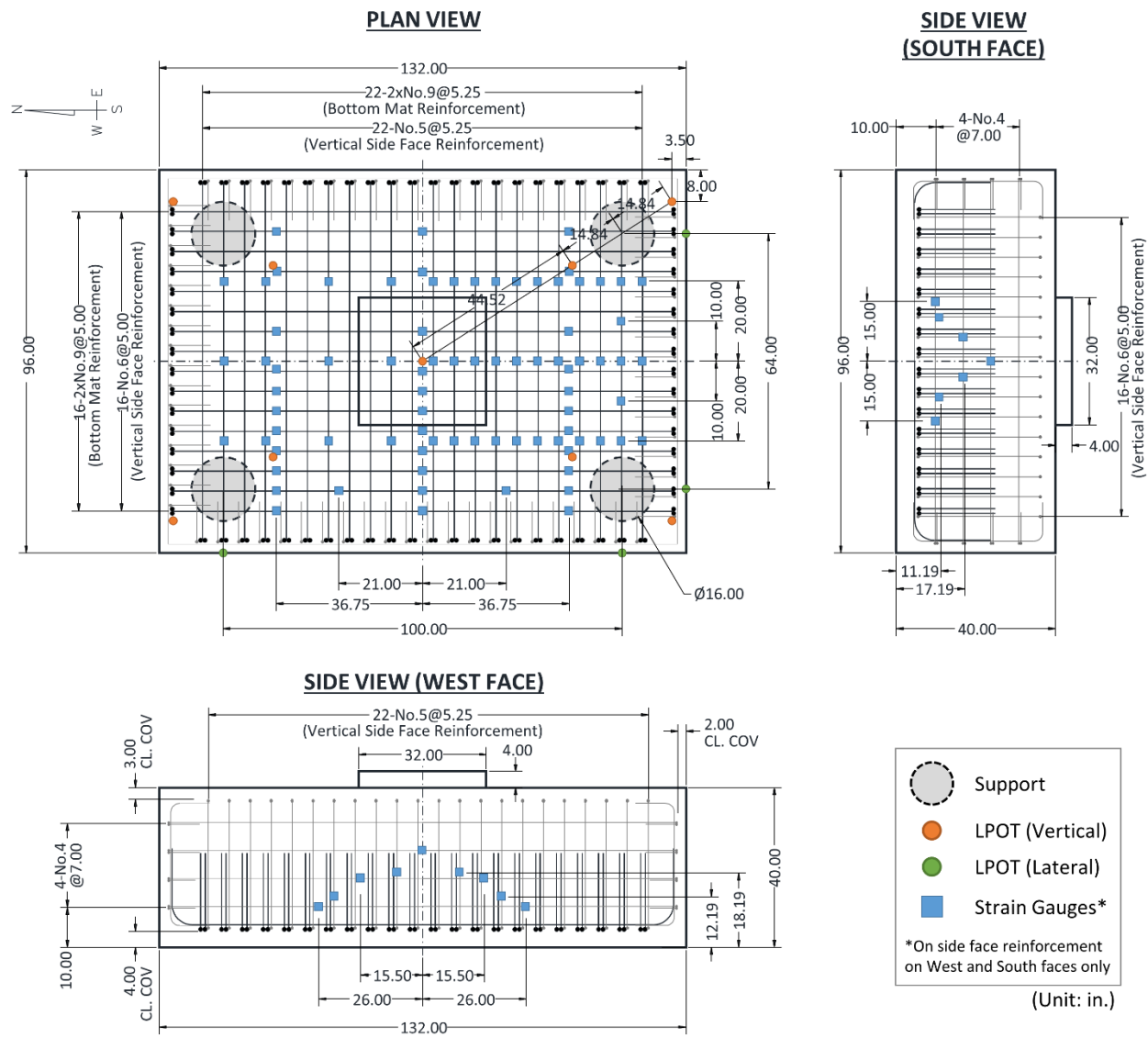


Figure D.11 Drawing of IV-11: Phase I

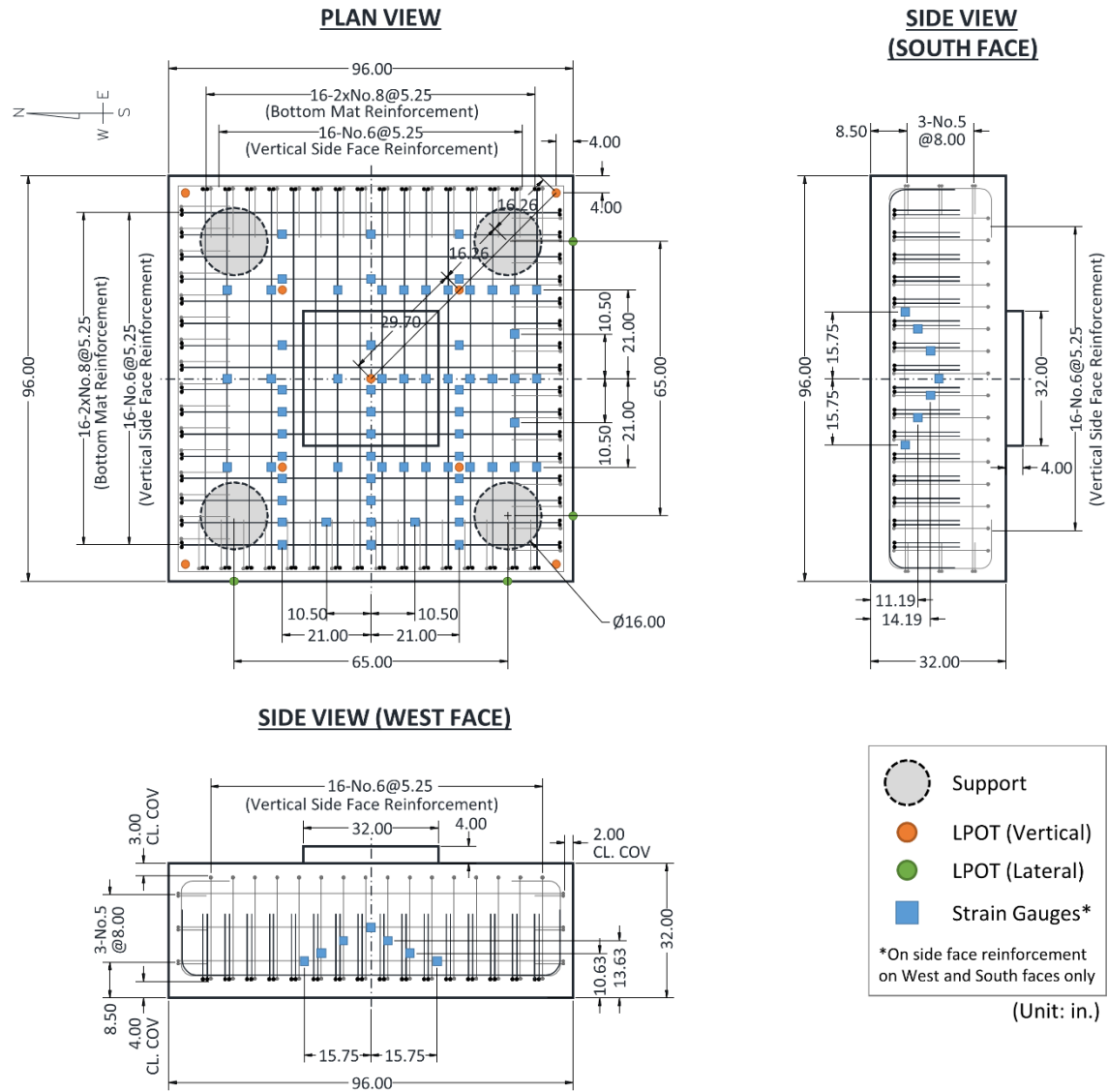


Figure D.12 Drawing of V-12: Phase I

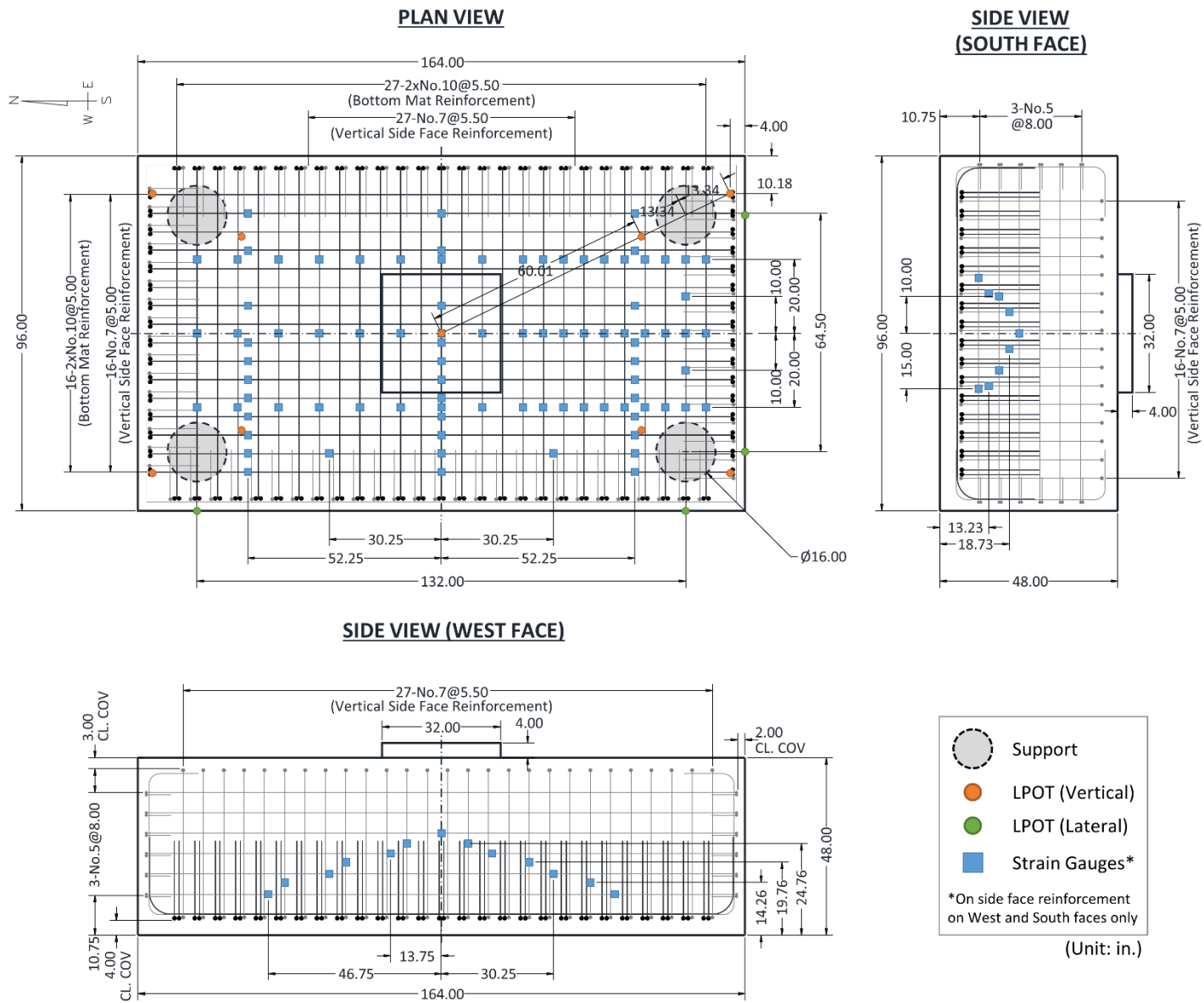


Figure D.13 Drawing of V-13: Phase I

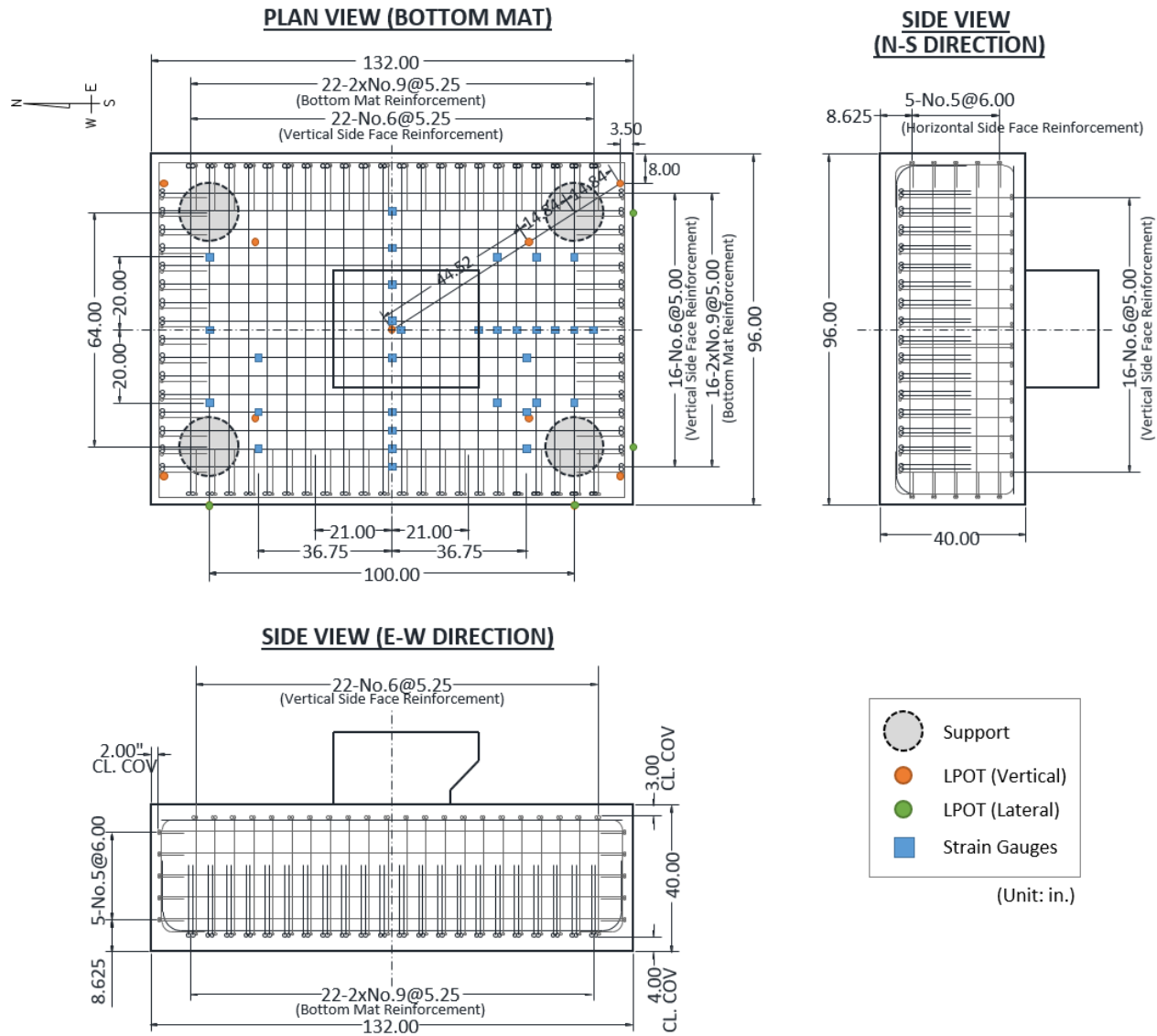


Figure D.14 Drawing of VI-ST (bottom mat & side face reinforcement): Phase II

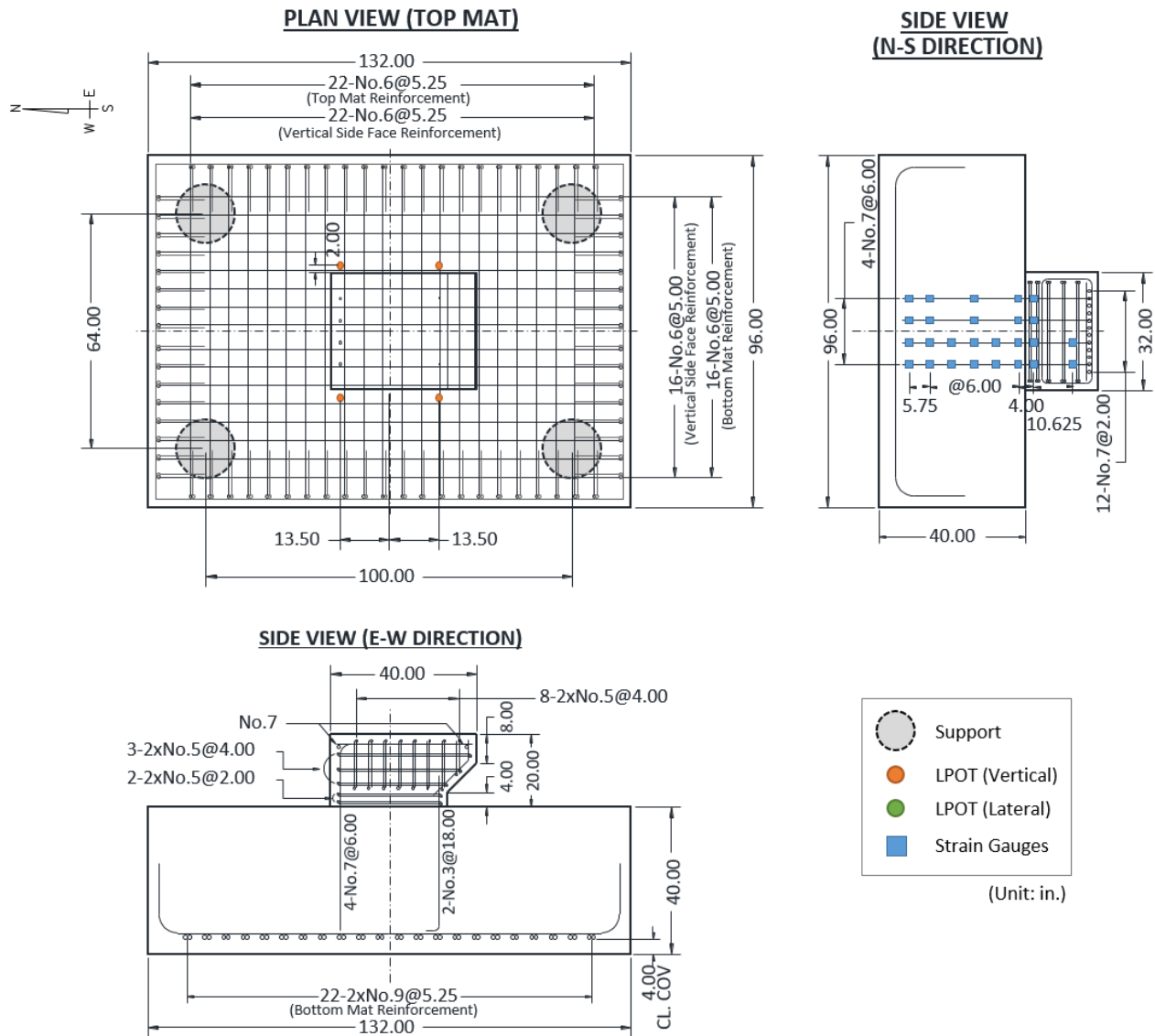


Figure D.15 Drawing of VI-ST (top mat & column reinforcement): Phase II

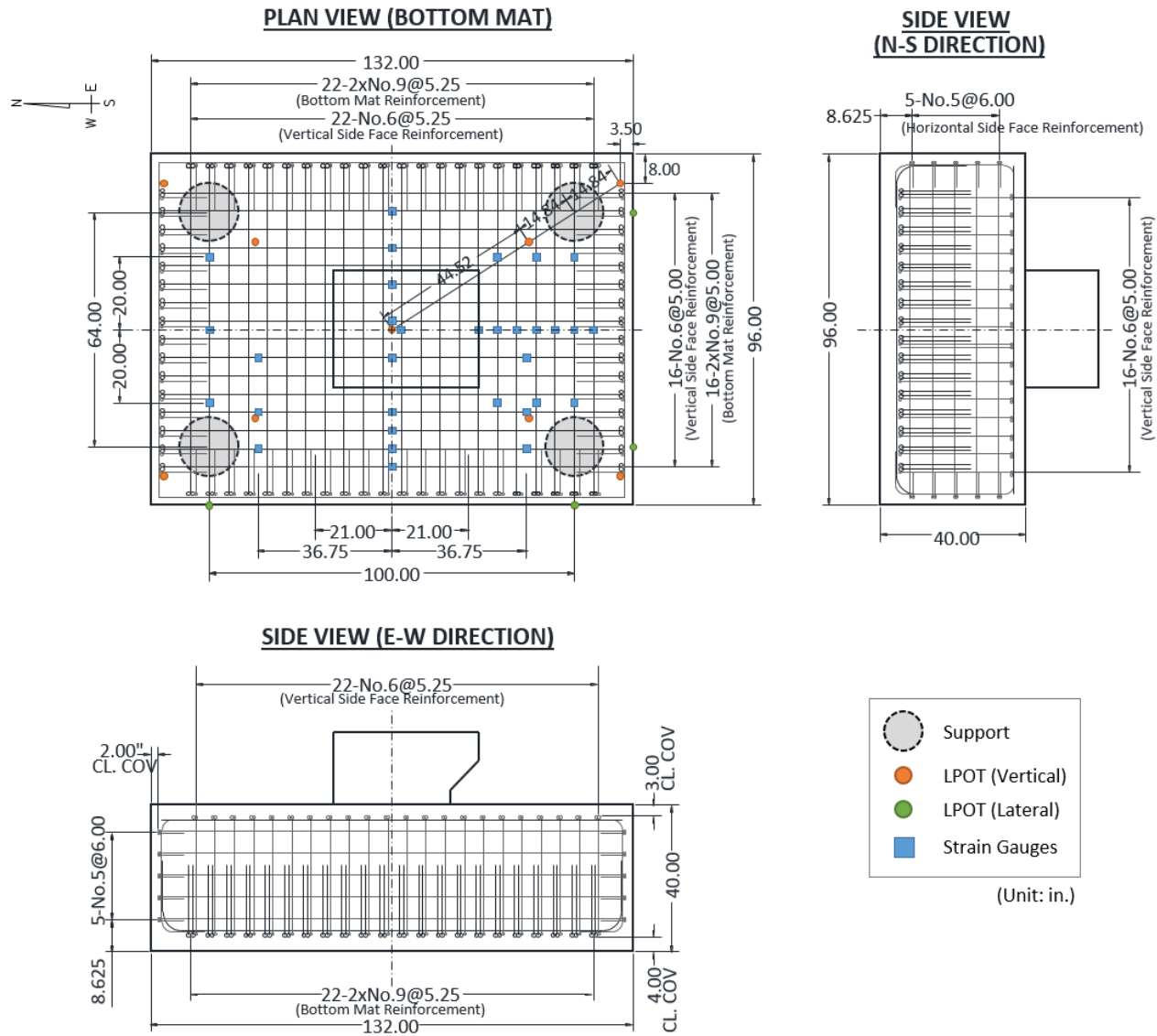


Figure D.16 Drawing of VI-HD (bottom mat & side face reinforcement): Phase II

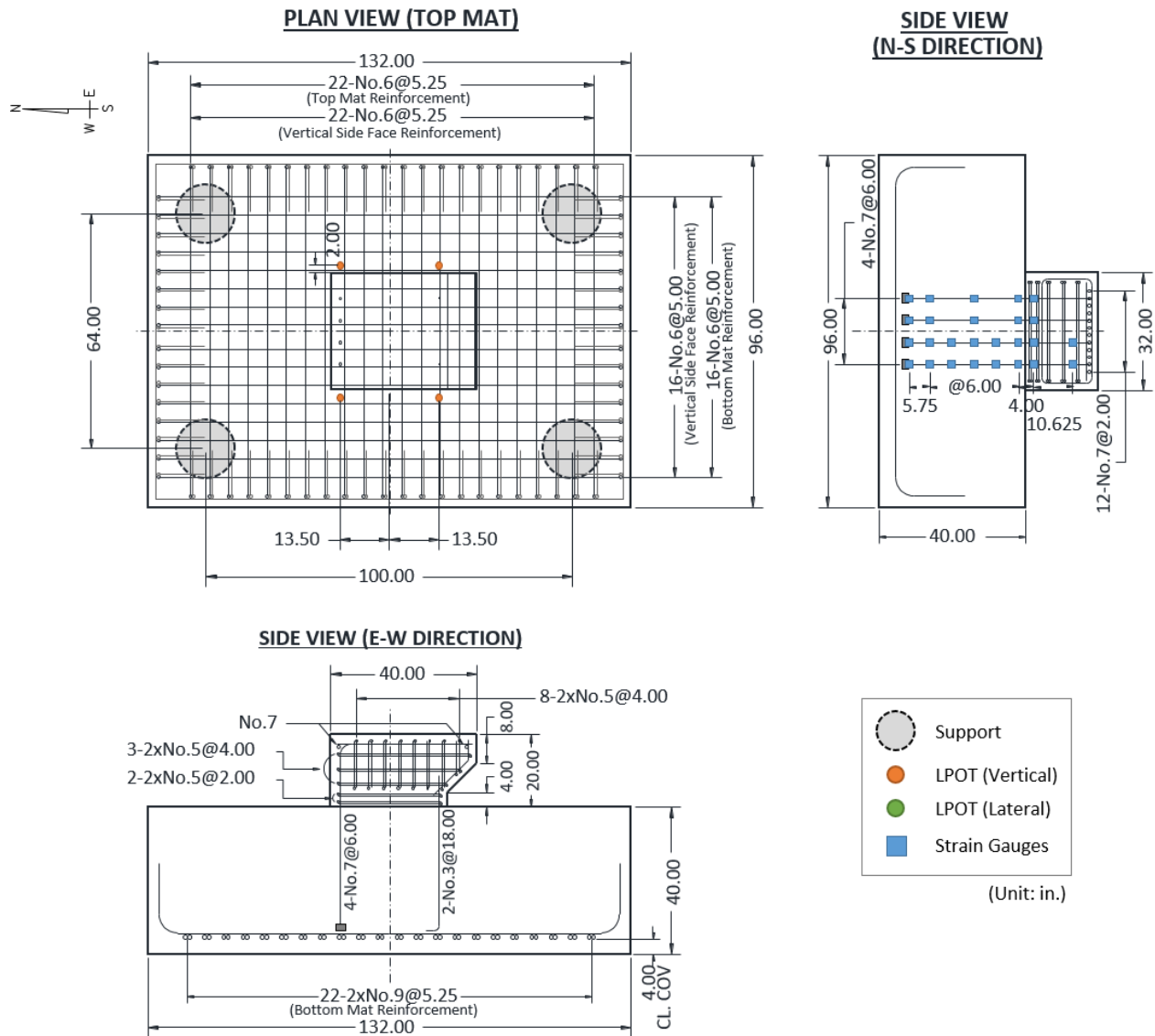


Figure D.17 Drawing of VI-HD (top mat & column reinforcement): Phase II

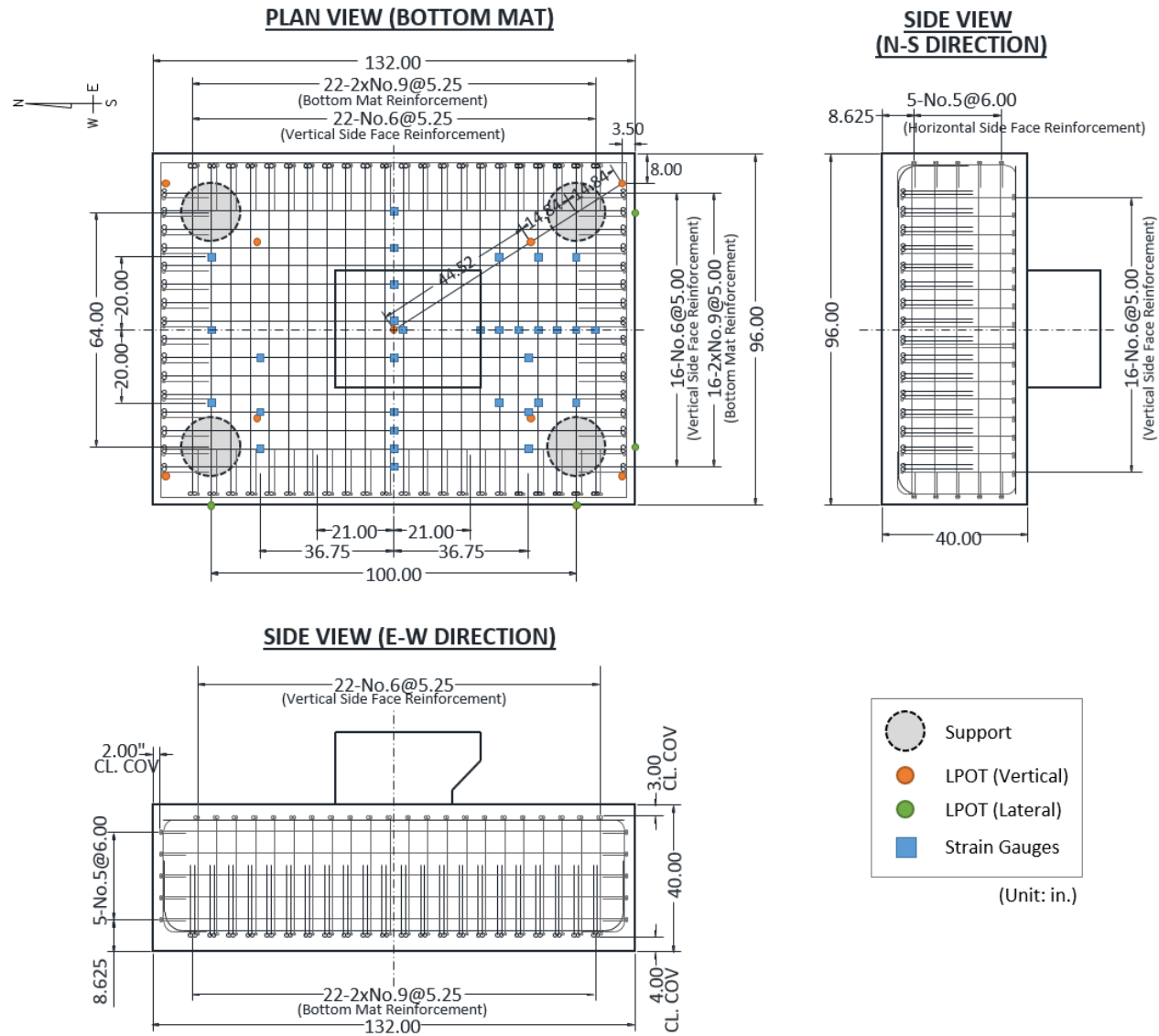


Figure D.18 Drawing of VI-HKO (bottom mat & side face reinforcement): Phase II

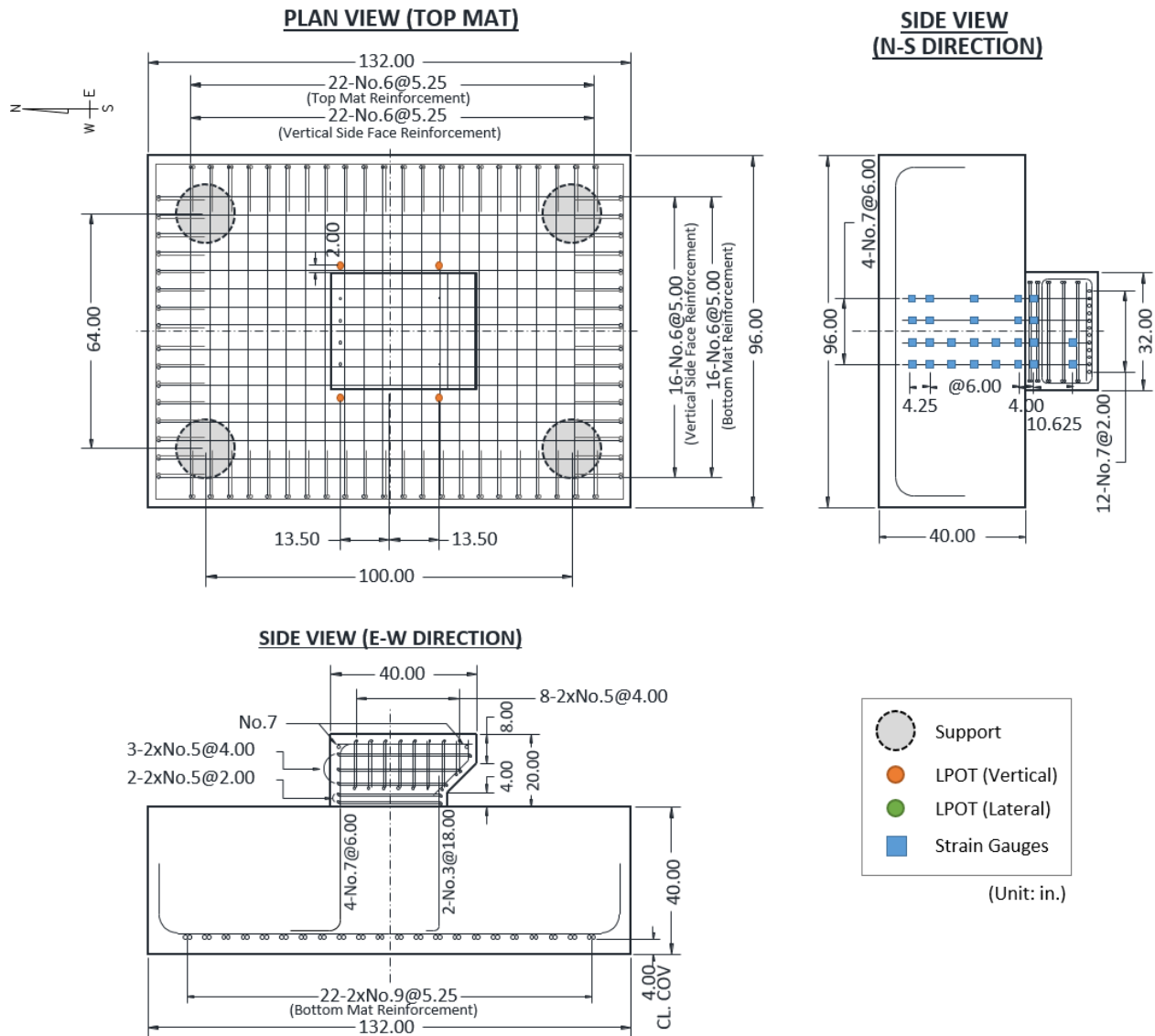


Figure D.19 Drawing of VI-HKO (top mat & column reinforcement): Phase II

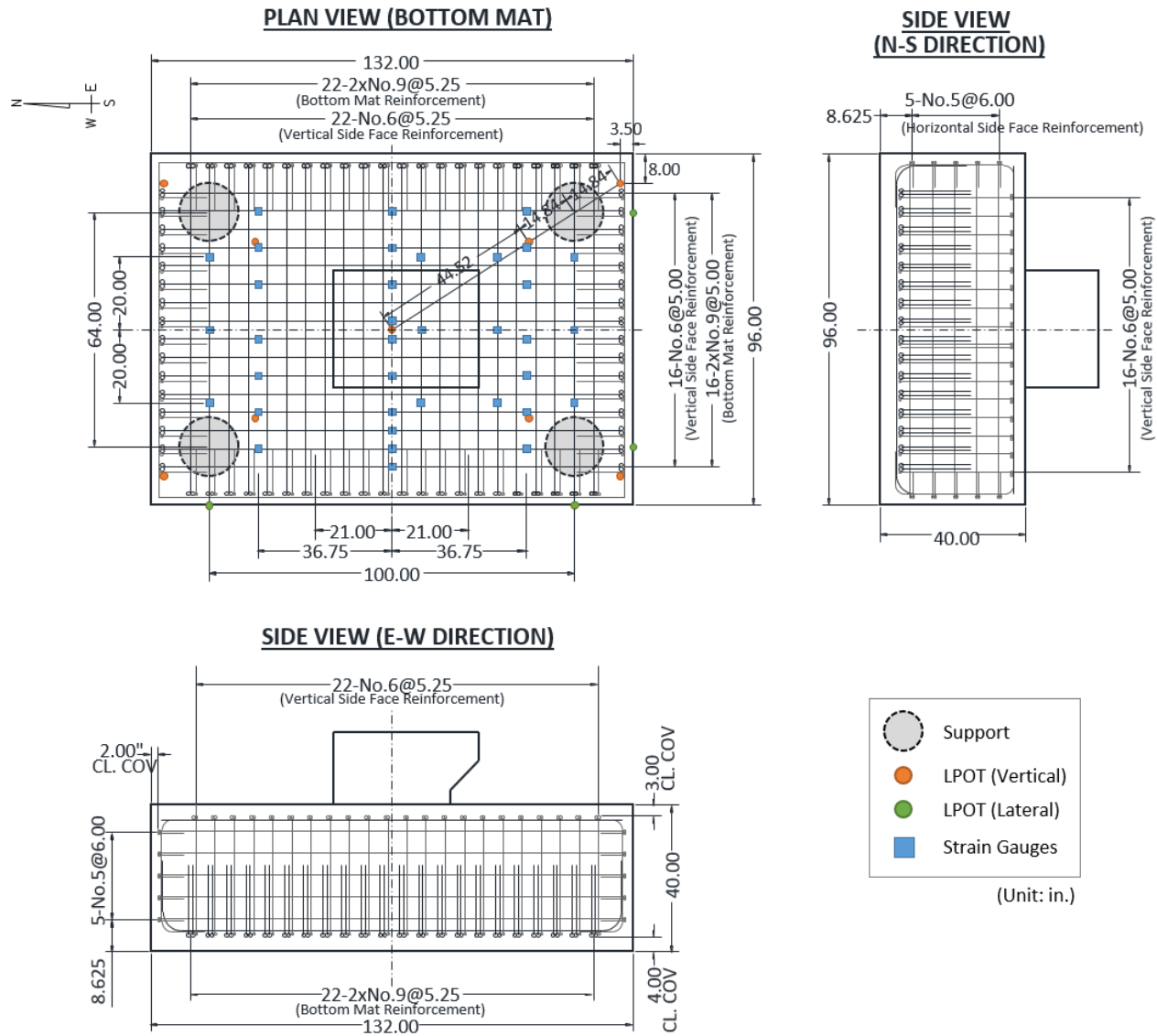


Figure D.20 Drawing of VI-HKI (bottom mat & side face reinforcement): Phase II

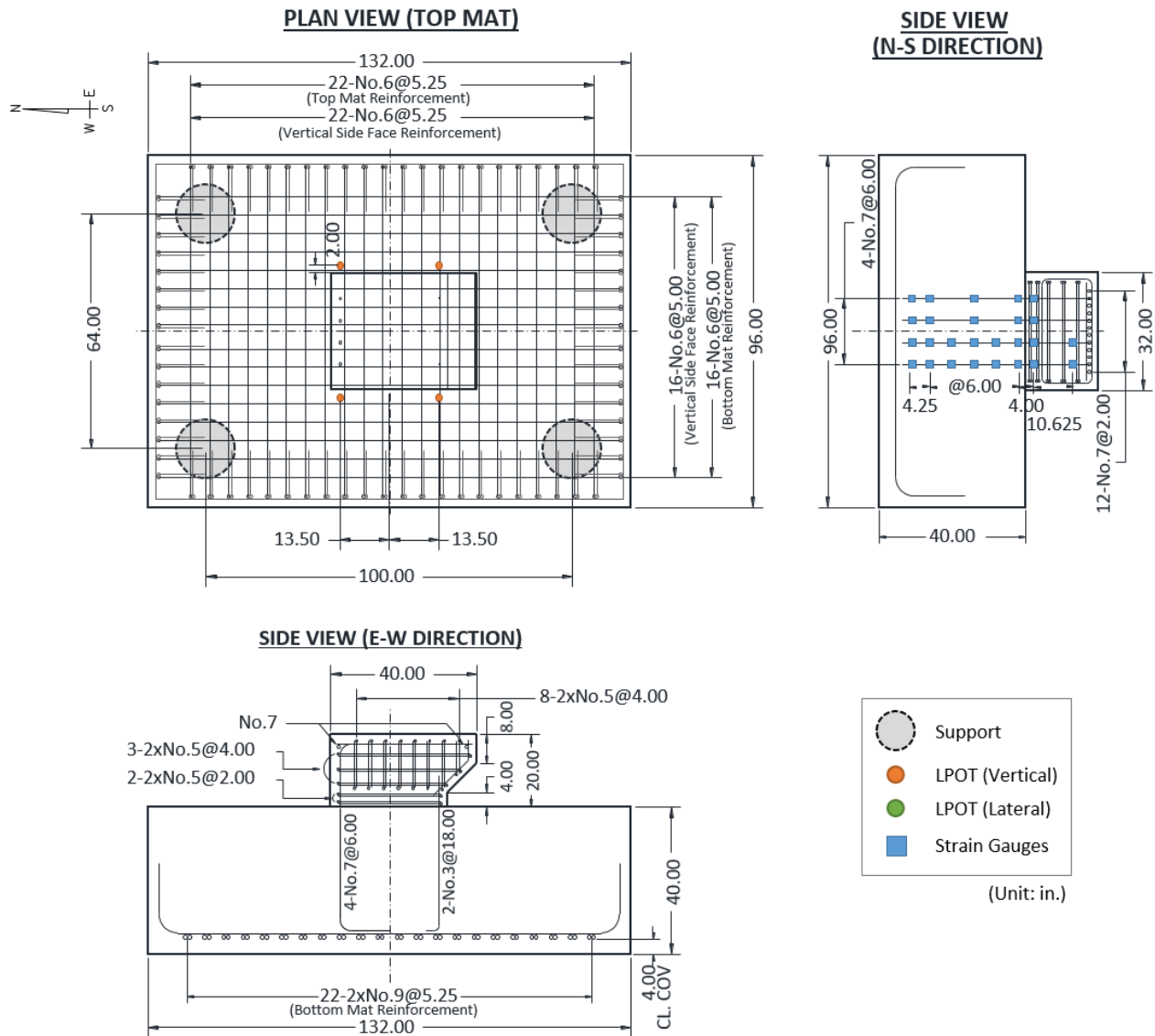


Figure D.21 Drawing of VI-HKI (top mat & column reinforcement): Phase II

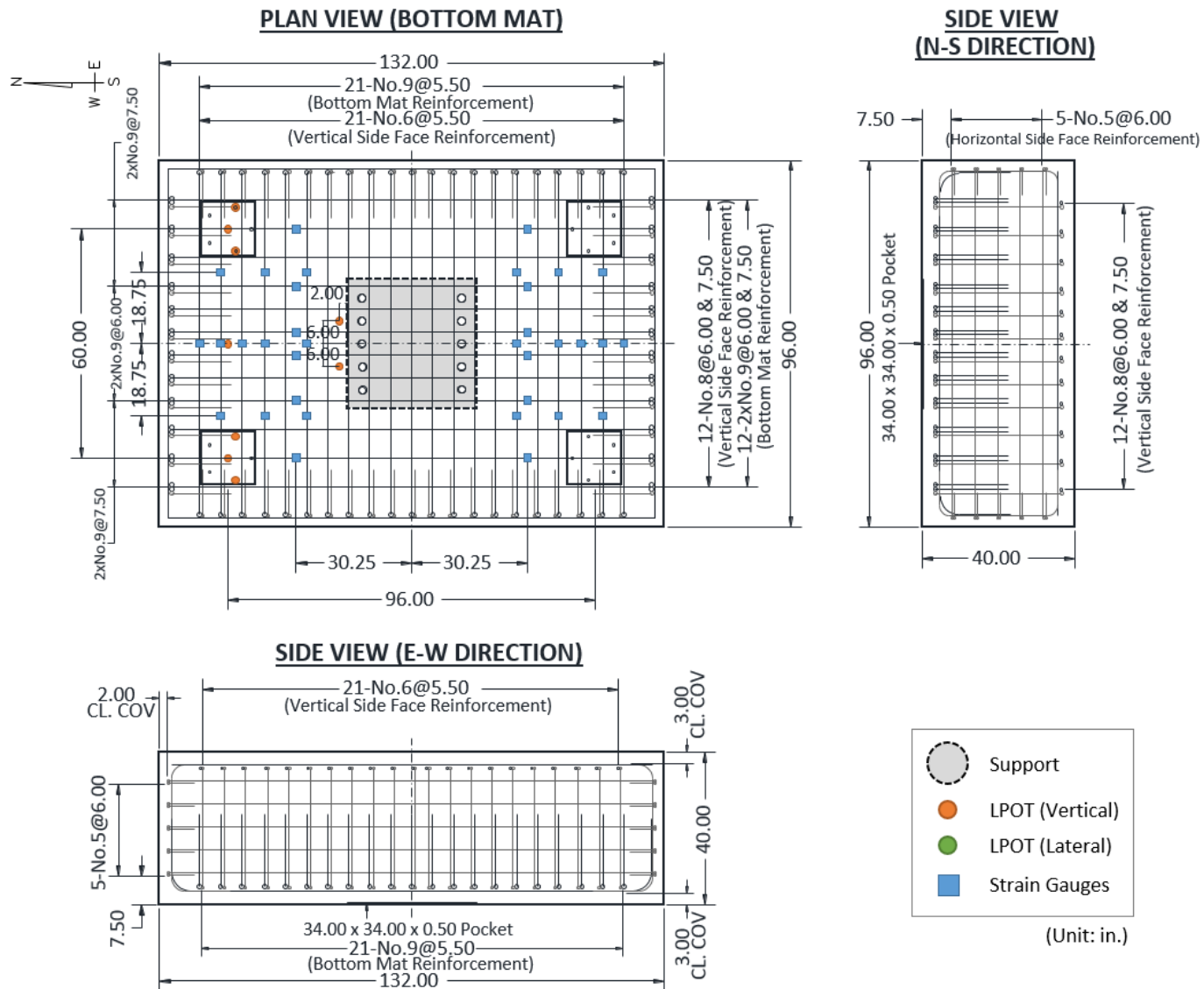


Figure D.22 Drawing of VII-TD (bottom mat & side face reinforcement): Phase III

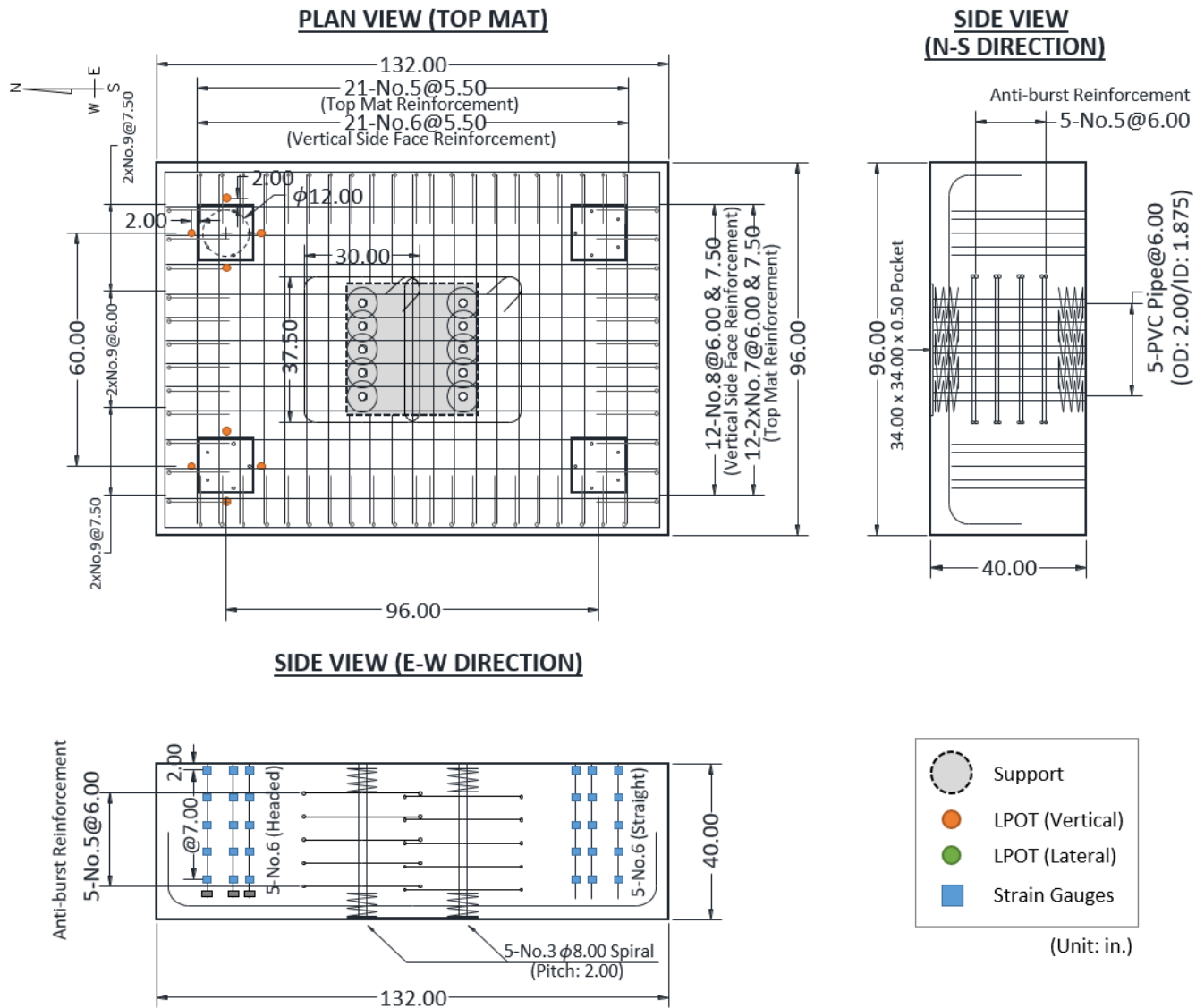


Figure D.23 Drawing of VII-TD (top mat & anti-burst & drilled shaft reinforcement): Phase III

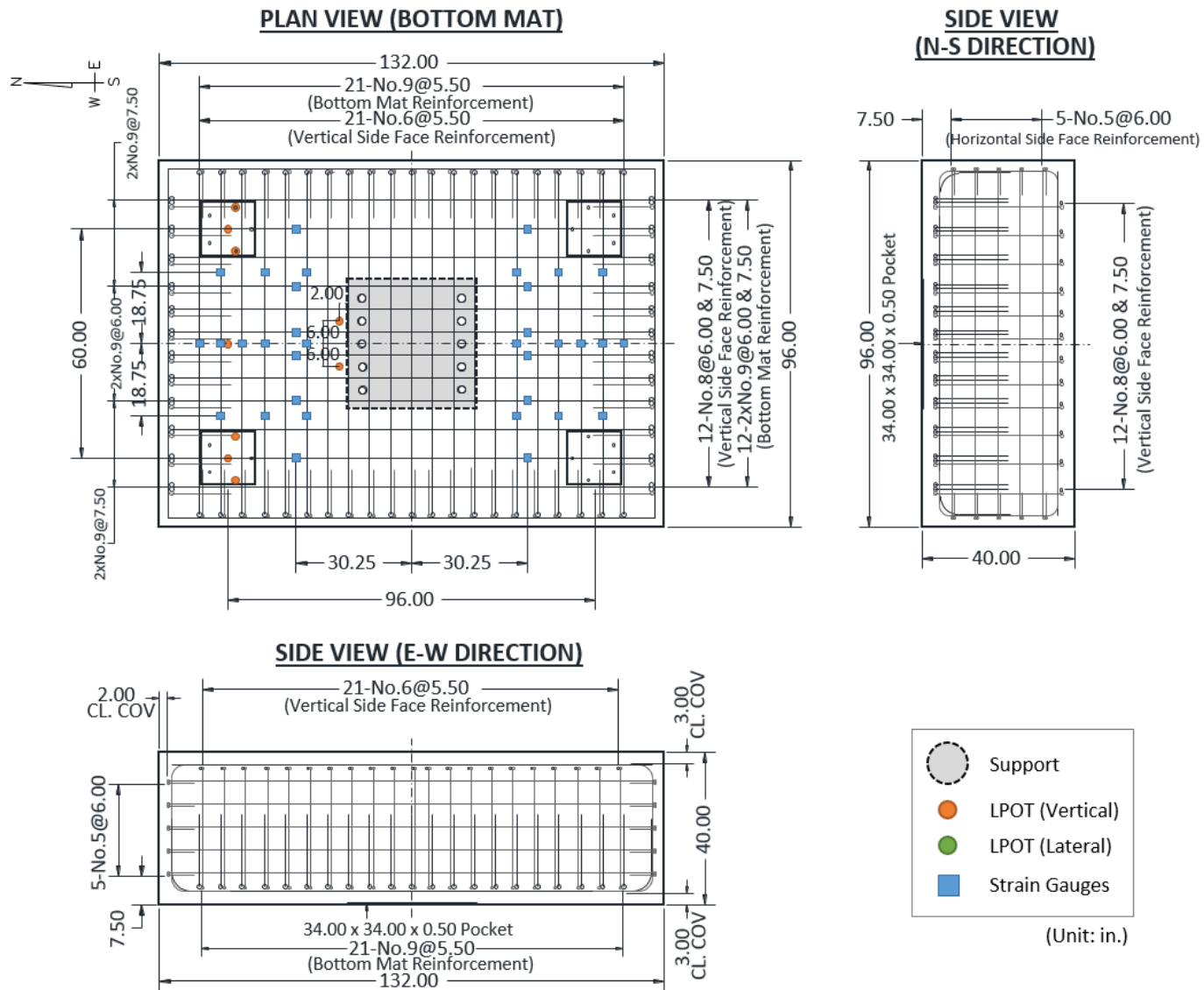


Figure D.24 Drawing of VII-TK (bottom mat & side face reinforcement): Phase III

Appendix E. Material Test Results

Reinforcing Bars

Table E1. Mechanical properties of bottom mat reinforcement

Specimen ID	Bar Size	Yield Strength (f_y) [ksi]	Tensile Strength (f_u) [ksi]	Curve Type
I-1	#8	71.9	106.4	2
I-2, I-3, & I-4	#8	64.1	107.6	2
II-5, II-6, & II-7	#9	62.8	105.8	2
III-8 & III-9	#9	67.5	108.2	2
IV-10 & IV-11	#9	78.3	113.2	1
V-12	#8	67.0	109.5	2
V-13	#10	68.2	103.7	2

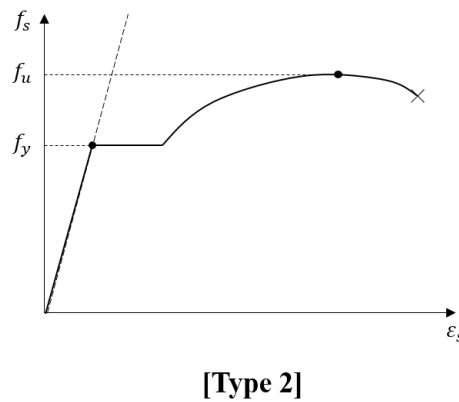
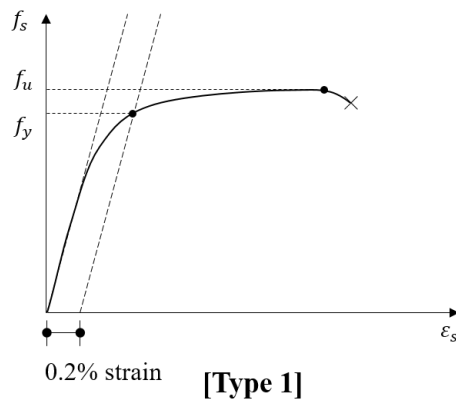
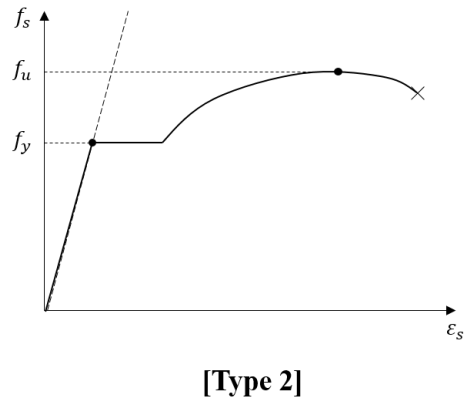
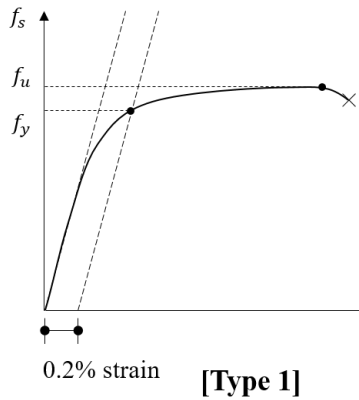


Table E2. Mechanical properties of side face reinforcement

Specimen ID	Bar Size	Yield Strength (f_y) [ksi]	Tensile Strength (f_u) [ksi]	Curve Type
I-1 & I-2	#6	68.8	111.5	2
	#3	66.9	104.8	2
I-3 & I-4	#6	60.8	99.7	2
	#3	82.3	108.6	1
II-5, II-6, & II-7	#6	62.2	103.9	2
	#5	63.6	103.0	2
III-8 & III-9	#6	62.6	100.2	2
	#5	61.8	99.4	2
IV-10 & IV-11	#5	63.6	101.8	2
	#4	65.6	104.5	2
V-12 & V-13	#7	65.0	105.5	2
	#6	64.5	105.1	2
	#5	62.4	104.0	2



Appendix F. Test Results: Phase I

I-1

- Load-Deflection Response

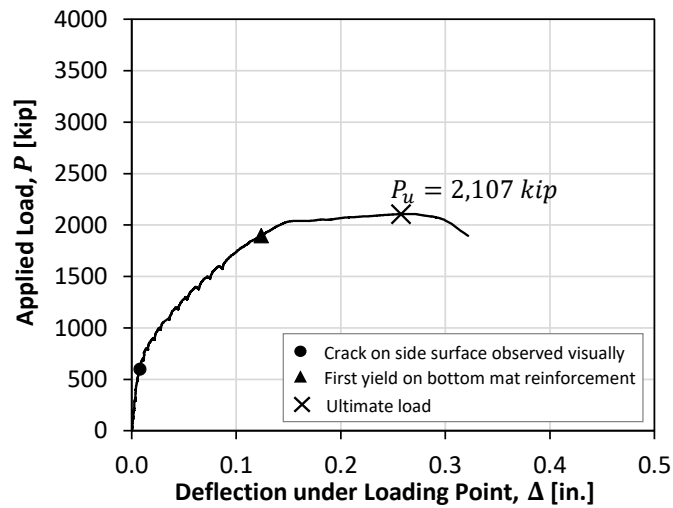


Figure F.1 Plot of the applied load versus the measured deflection: I-1

- Stresses in Main Reinforcement

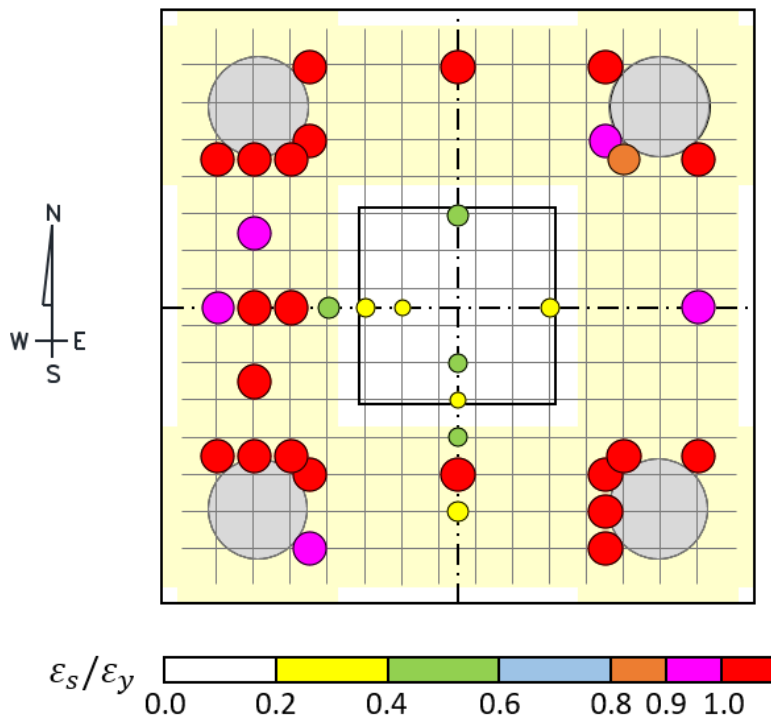


Figure F.2 Stress distribution in main reinforcements at ultimate load: I-1

- Post-failure Conditions

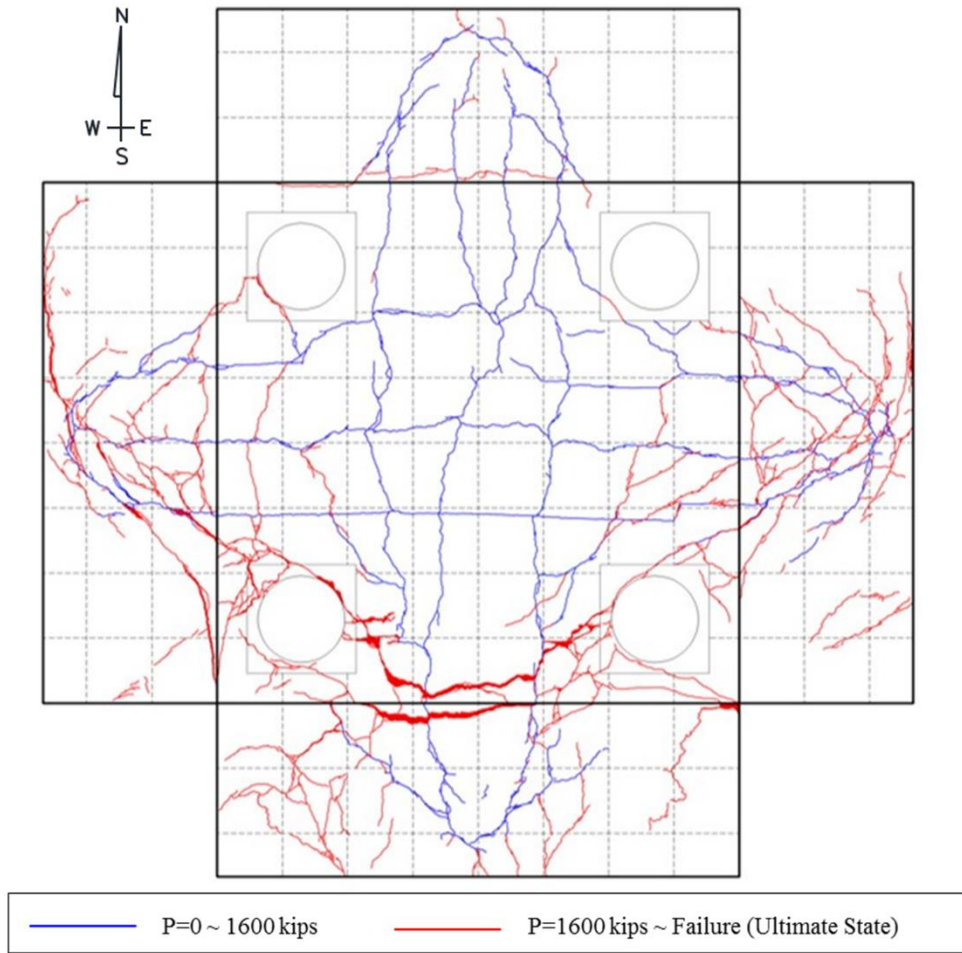


Figure F.3 Post-failure crack map: I-1

I-2

- Load-Deflection Response

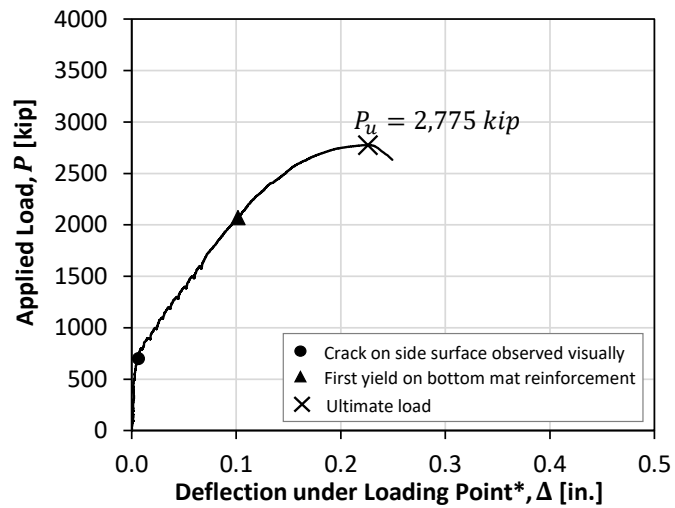


Figure F.4 Plot of the applied load versus the measured deflection: I-2

- Stresses in Main Reinforcement

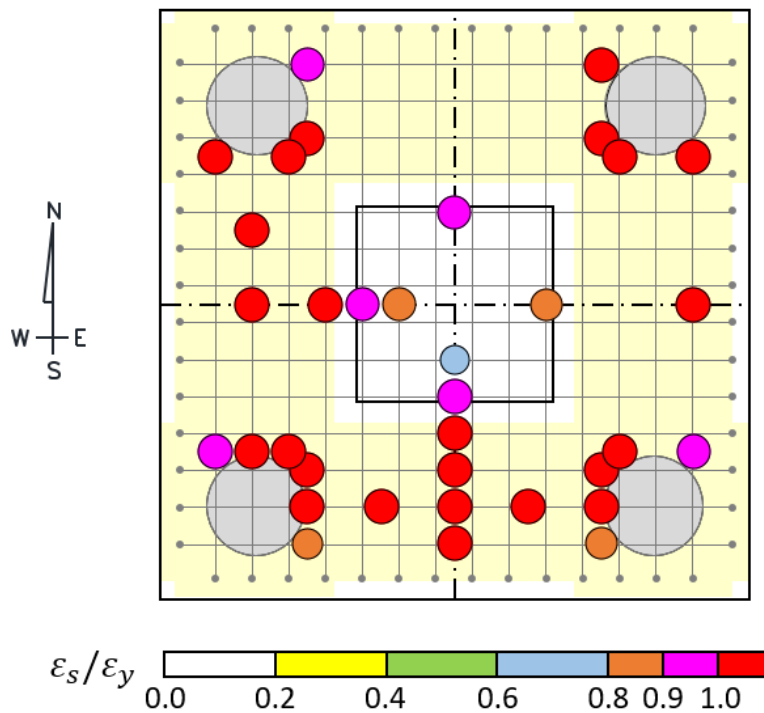


Figure F.5 Stress distribution in main reinforcements at ultimate load: I-2

- Post-failure Conditions

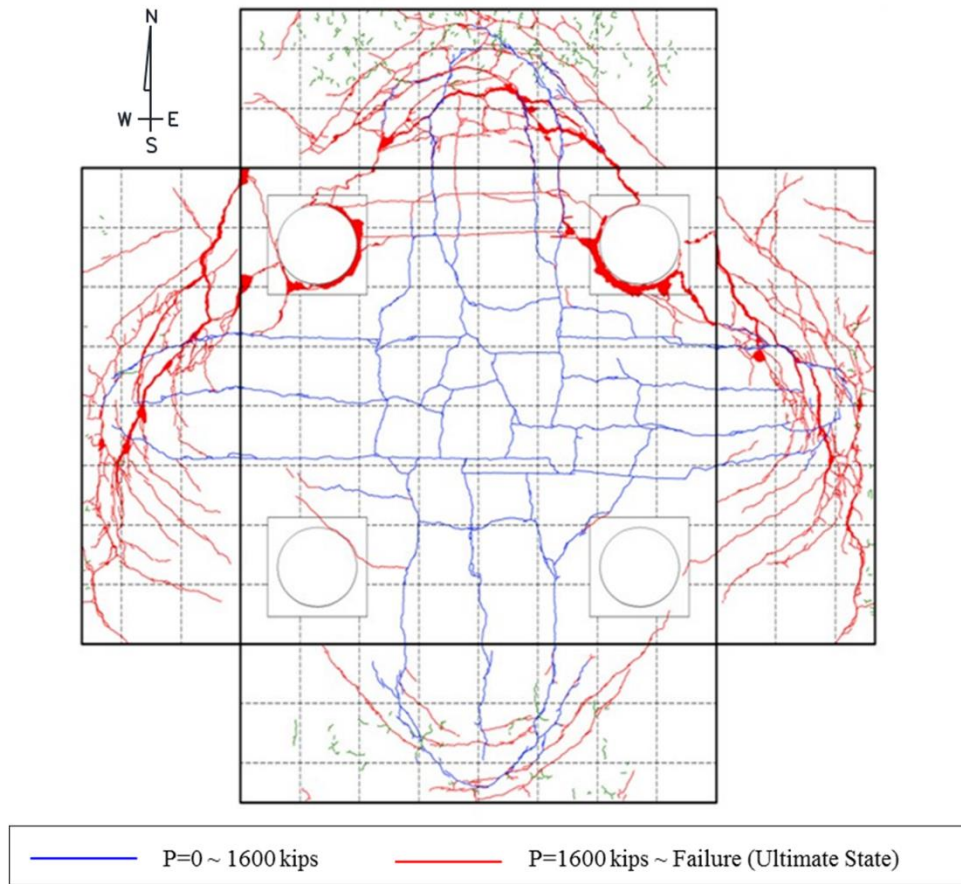


Figure F.6 Post-failure crack map: I-2

I-3

- Load-Deflection Response

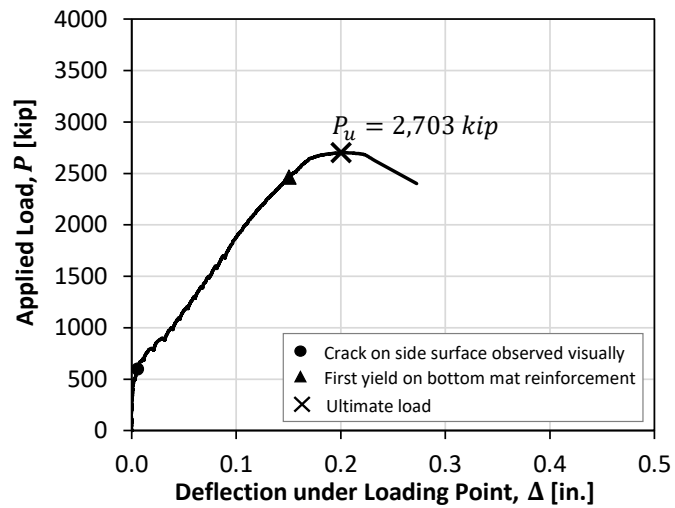


Figure F.7 Plot of the applied load versus the measured deflection: I-3

- Stresses in Main Reinforcement

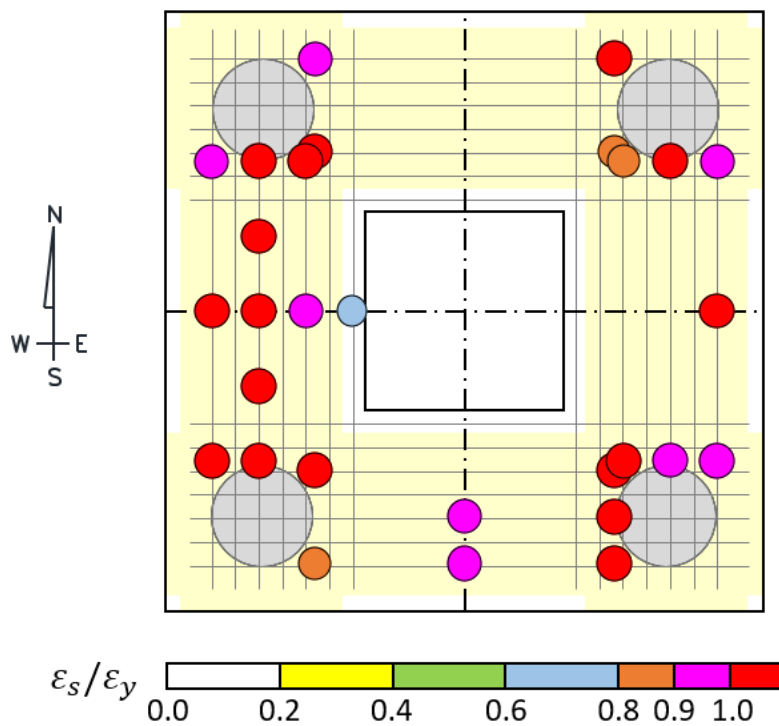


Figure F.8 Stress distribution in main reinforcements at ultimate load: I-3

- Post-failure Conditions

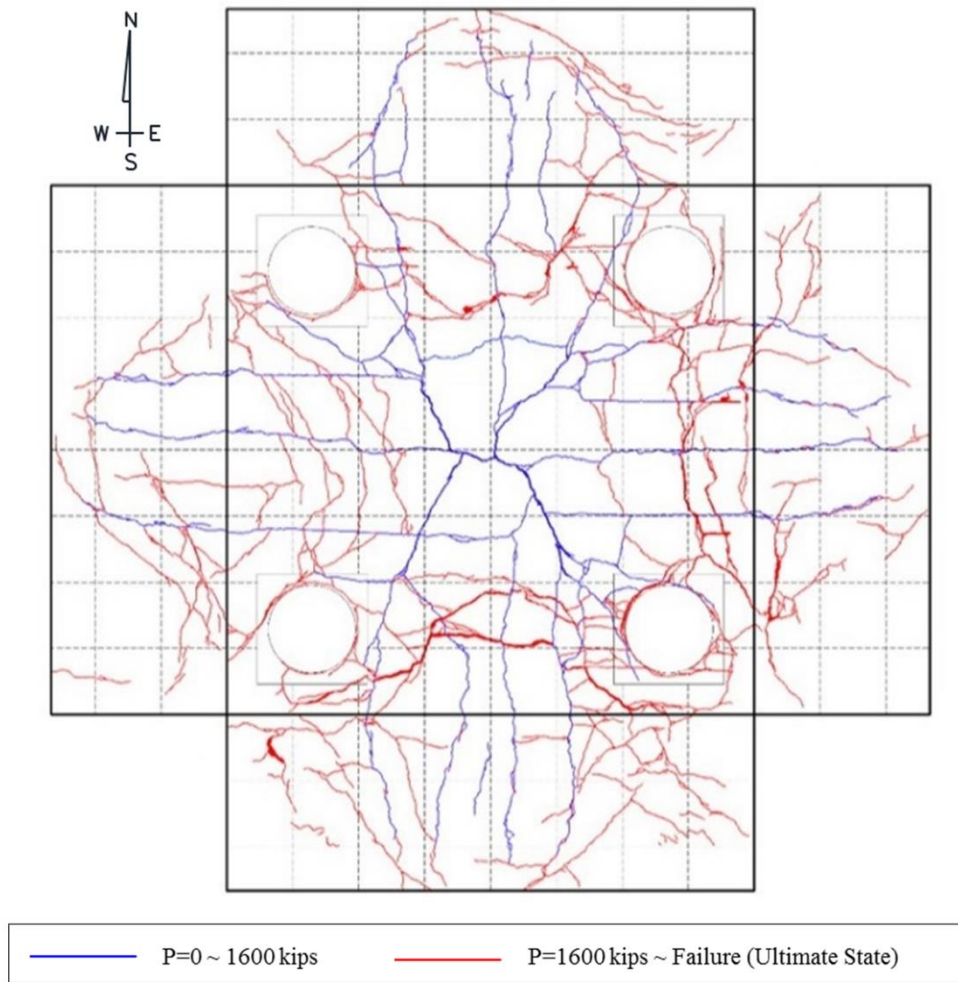


Figure F.9 Post-failure crack map: I-3

I-4

- Load-Deflection Response

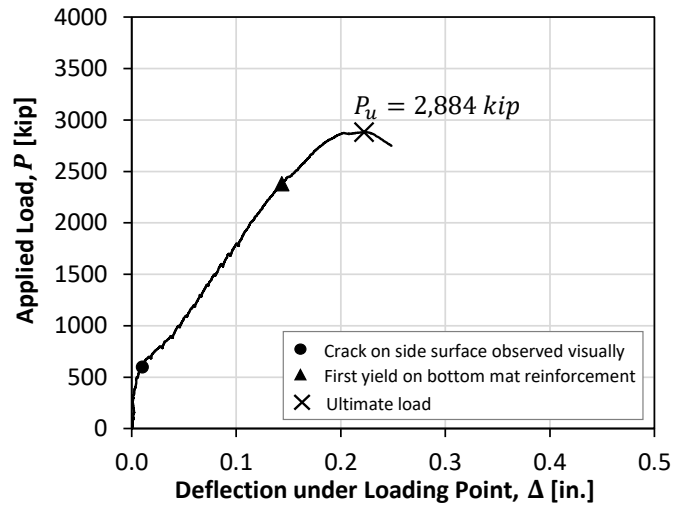


Figure F.10 Plot of the applied load versus the measured deflection: I-4

- Stresses in Main Reinforcement

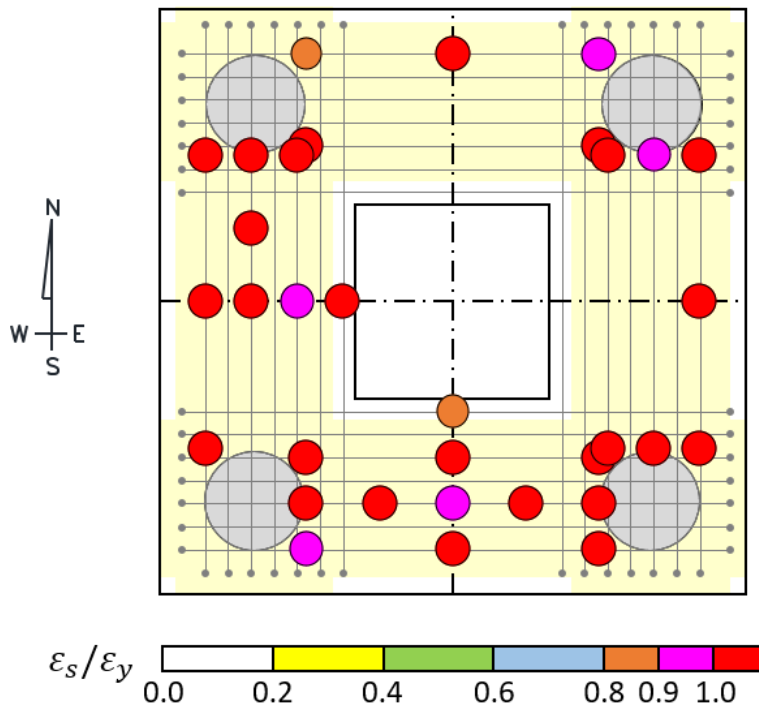


Figure F.11 Stress distribution in main reinforcements at ultimate load: I-4

- Post-failure Conditions

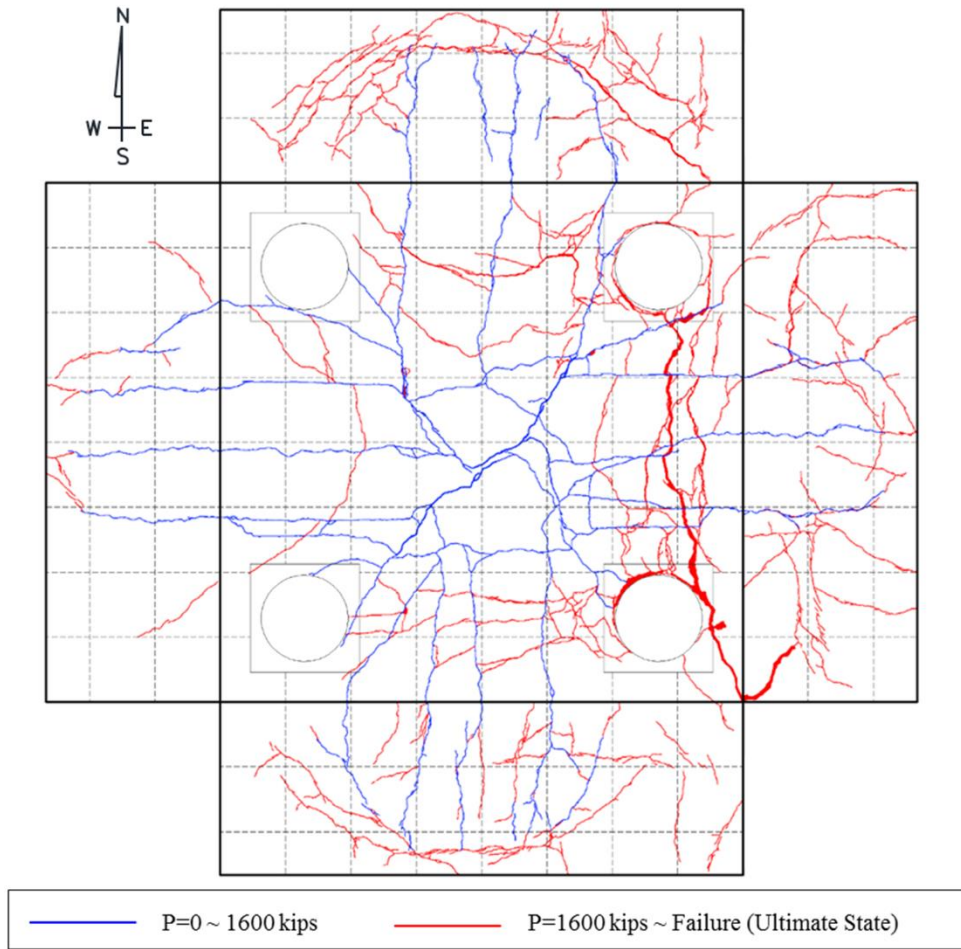


Figure F.12 Post-failure crack map: I-4

II-5

- Load-Deflection Response

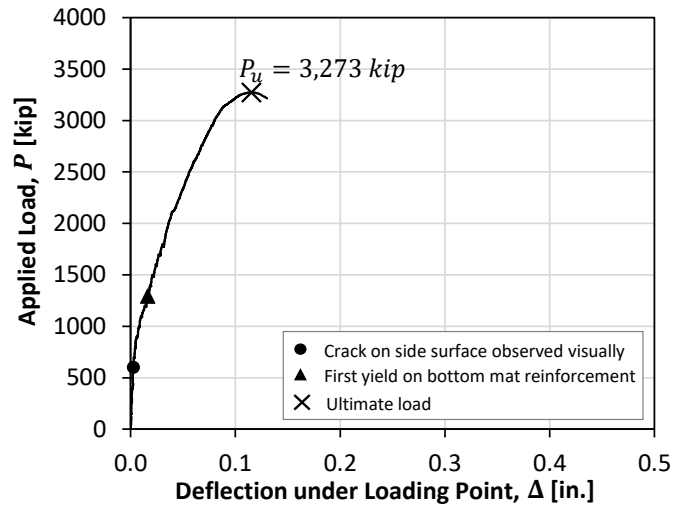


Figure F.13 Plot of the applied load versus the measured deflection: II-5

- Stresses in Main Reinforcement

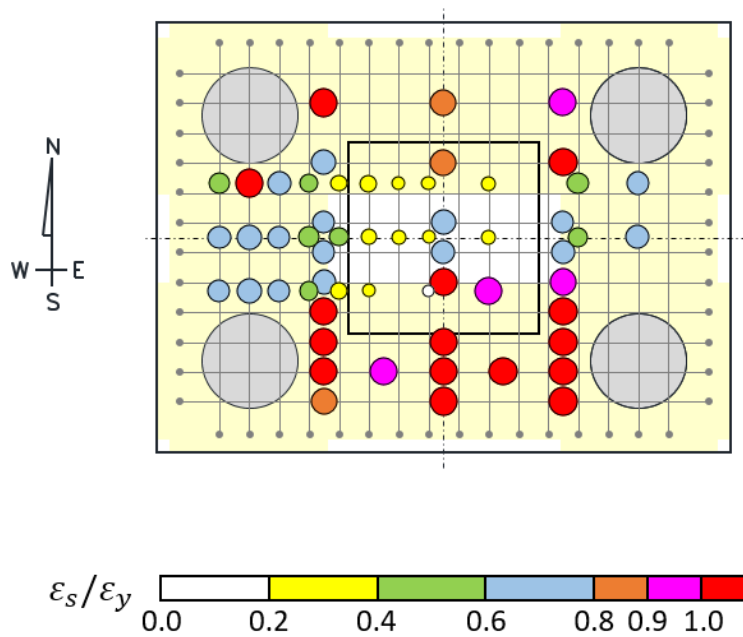


Figure F.14 Stress distribution in main reinforcements at ultimate load: II-5

- Post-failure Conditions

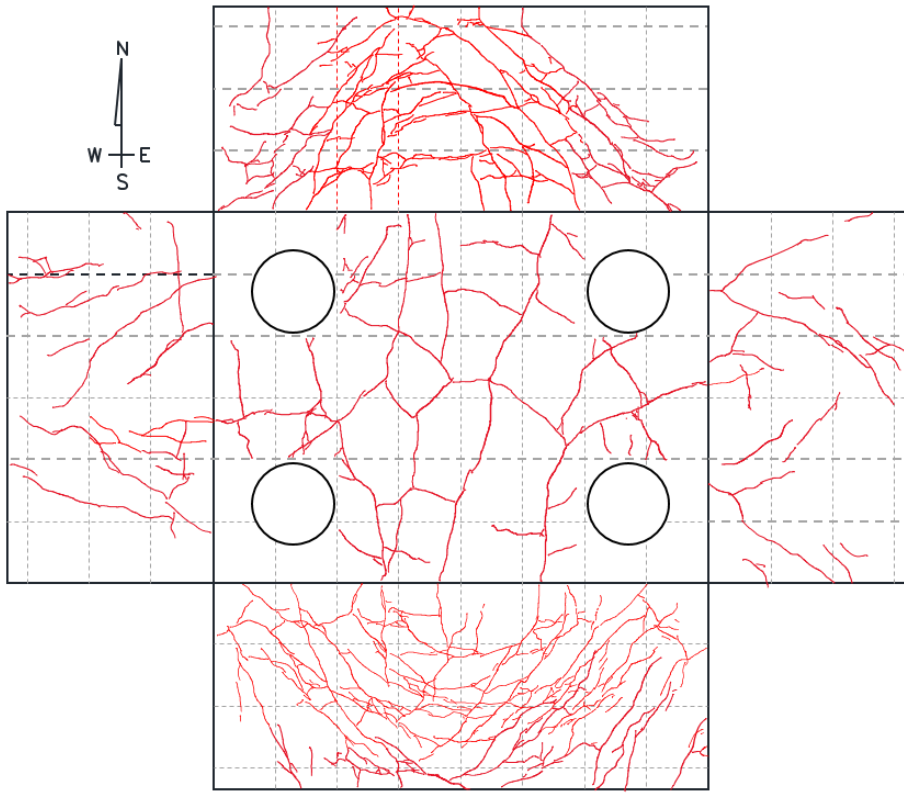


Figure F.15 Post-failure crack map: II-5

II-6

- Load-Deflection Response

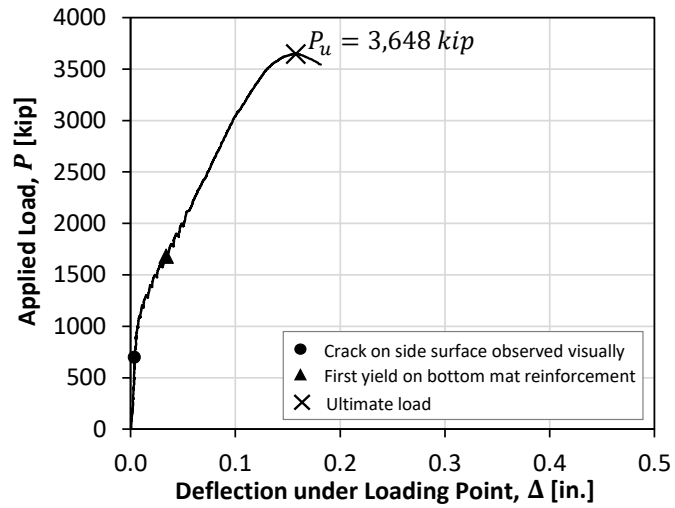


Figure F.16 Plot of the applied load versus the measured deflection: II-6

- Stresses in Main Reinforcement

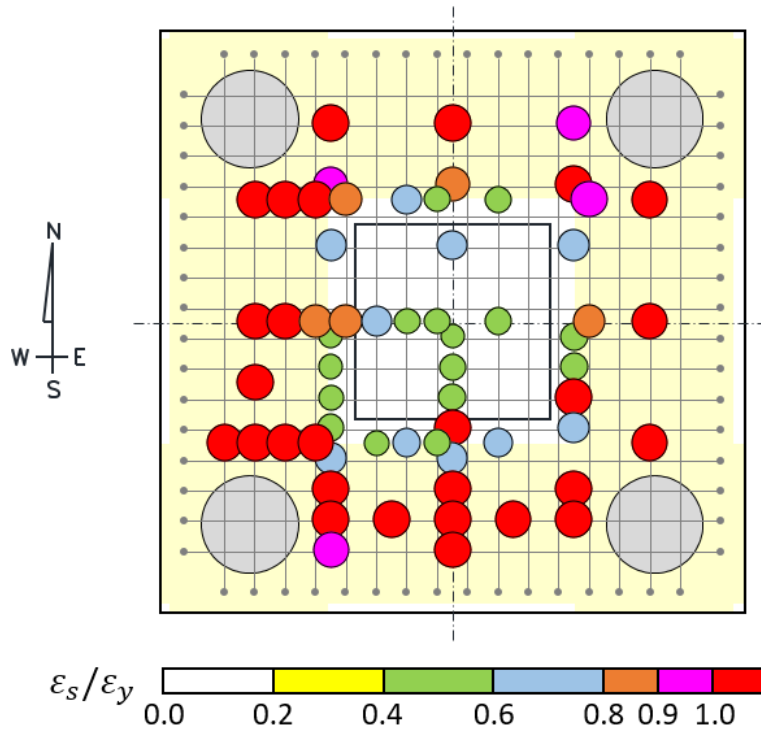


Figure F.17 Stress distribution in main reinforcements at ultimate load: II-6

- Post-failure Conditions

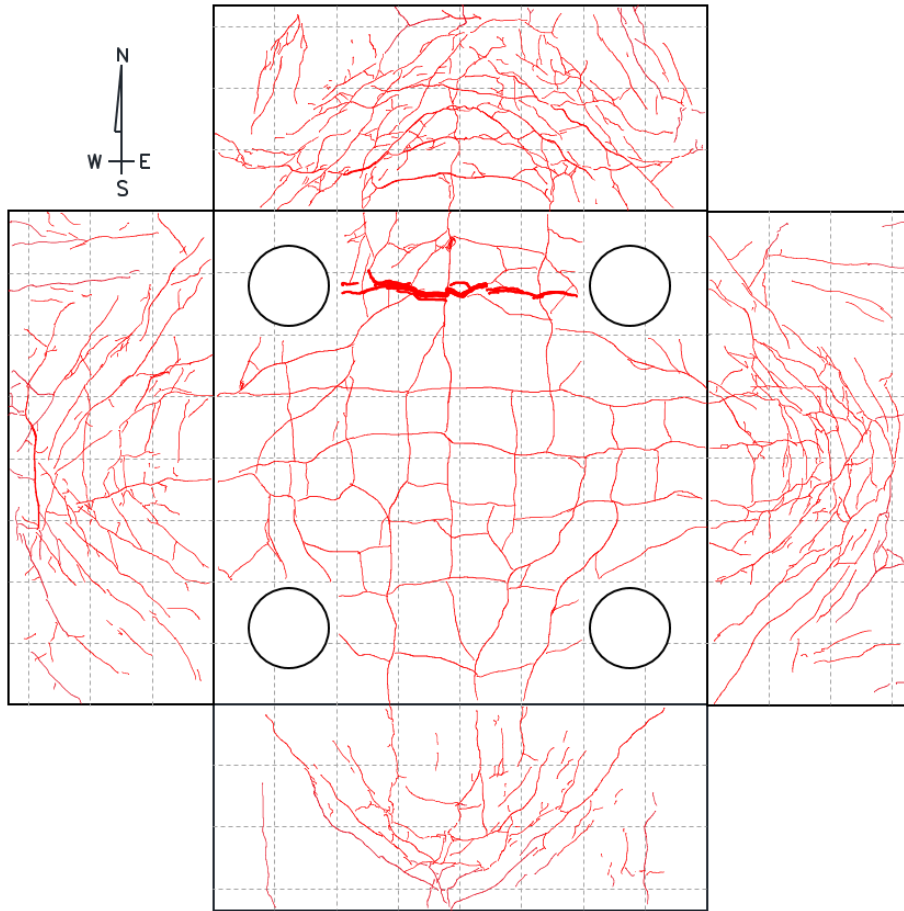


Figure F.18 Post-failure crack map: II-6

II-7

- Load-Deflection Response

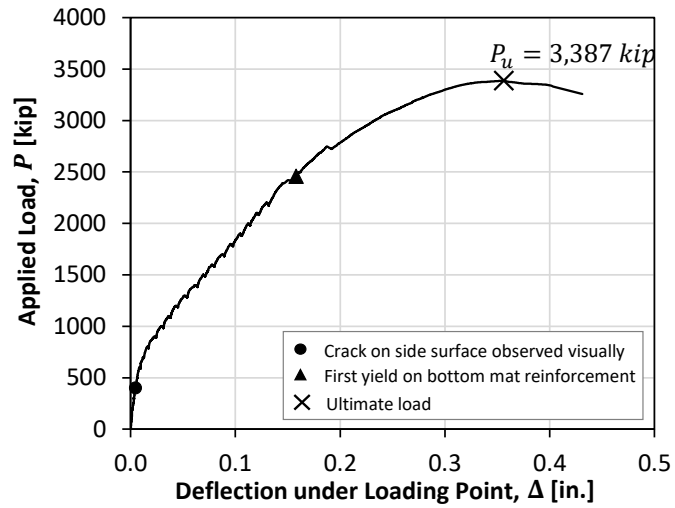


Figure F.19 Plot of the applied load versus the measured deflection: II-7

- Stresses in Main Reinforcement

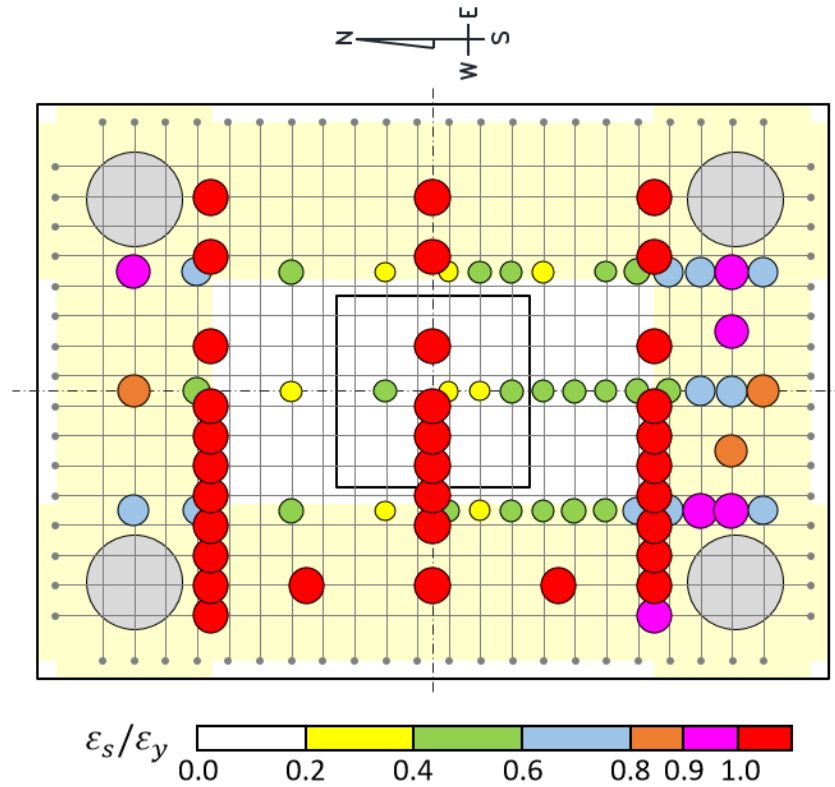


Figure F.20 Stress distribution in main reinforcements at ultimate load: II-7

- Post-failure Conditions

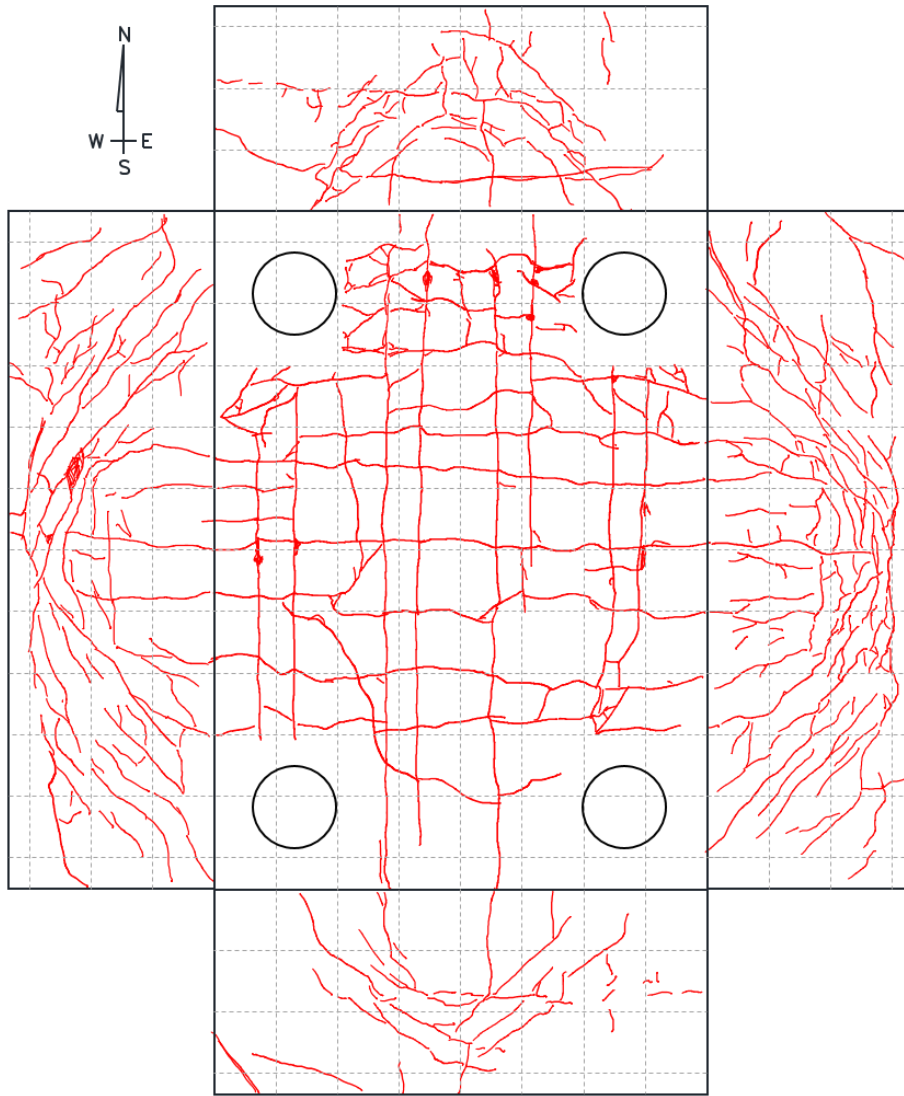


Figure F.21 Post-failure crack map: II-7

III-8

- Load-Deflection Response

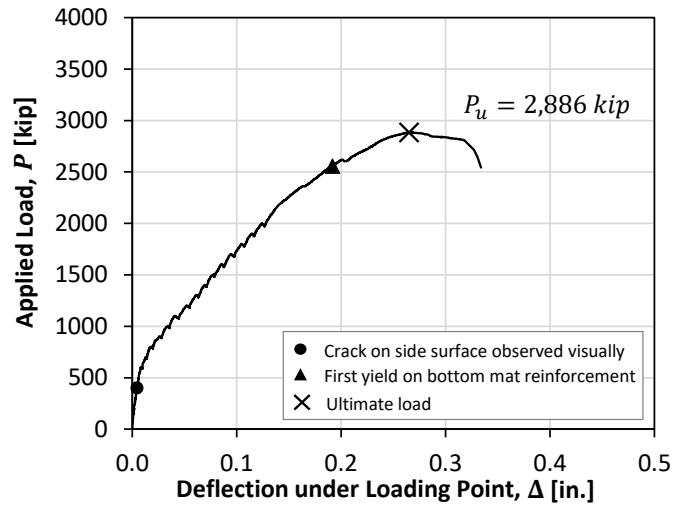


Figure F.22 Plot of the applied load versus the measured deflection: III-8

- Stresses in Main Reinforcement

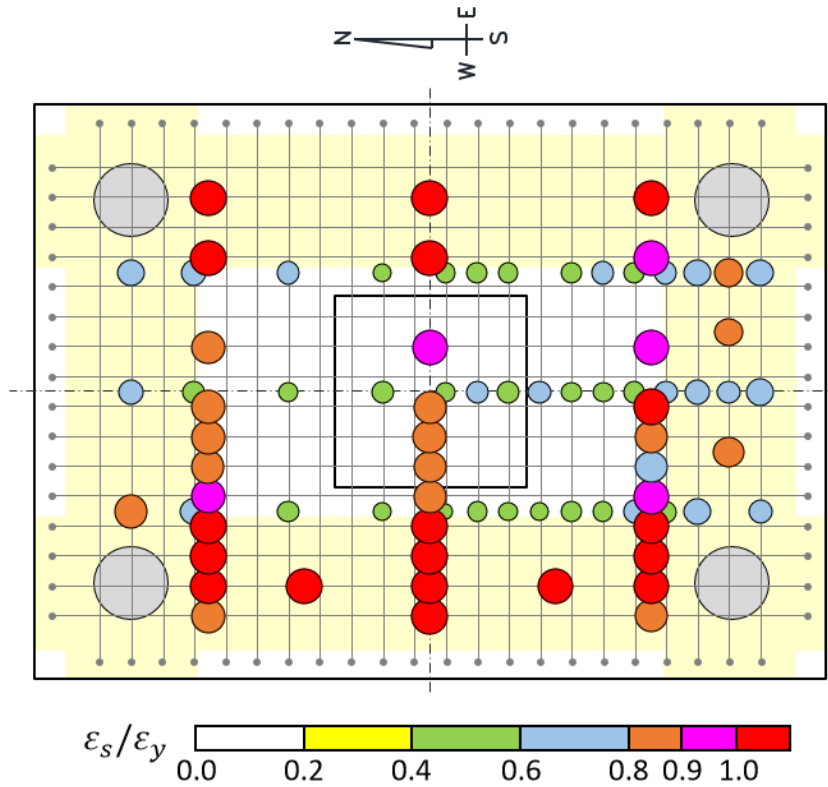


Figure F.23 Stress distribution in main reinforcements at ultimate load: III-8

- Post-failure Conditions

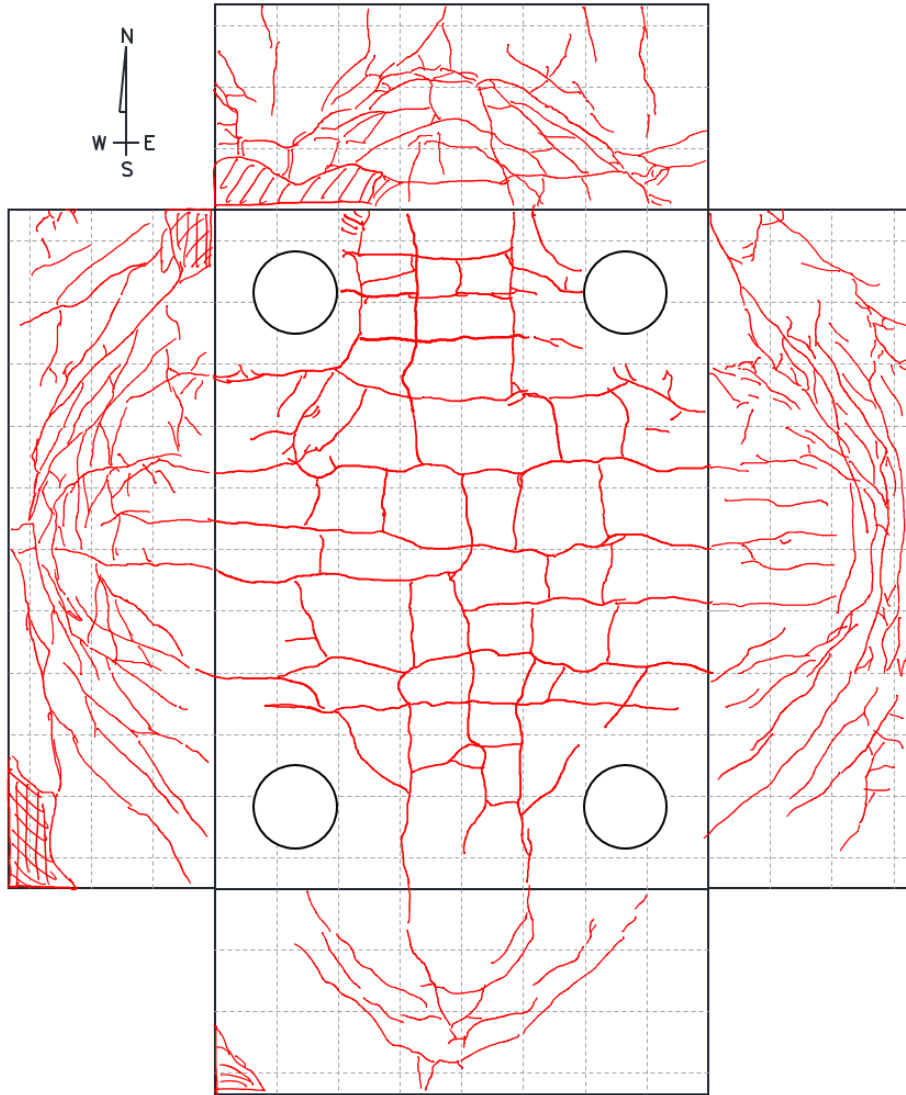


Figure F.24 Post-failure crack map: III-8

III-9

- Load-Deflection Response

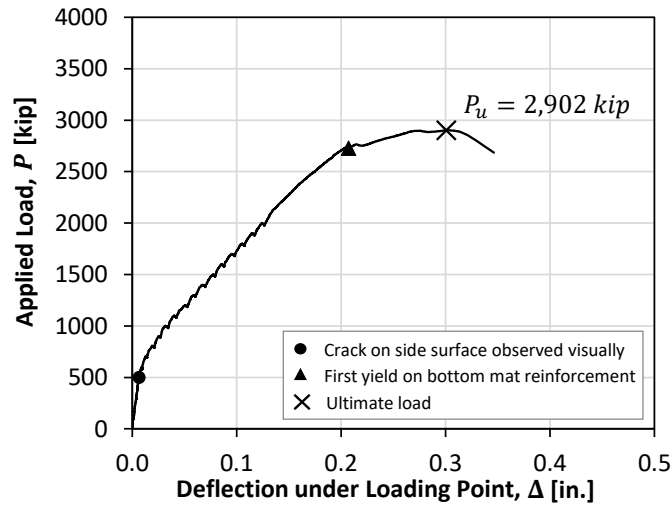


Figure F.25 Plot of the applied load versus the measured deflection: III-9

- Stresses in Main Reinforcement

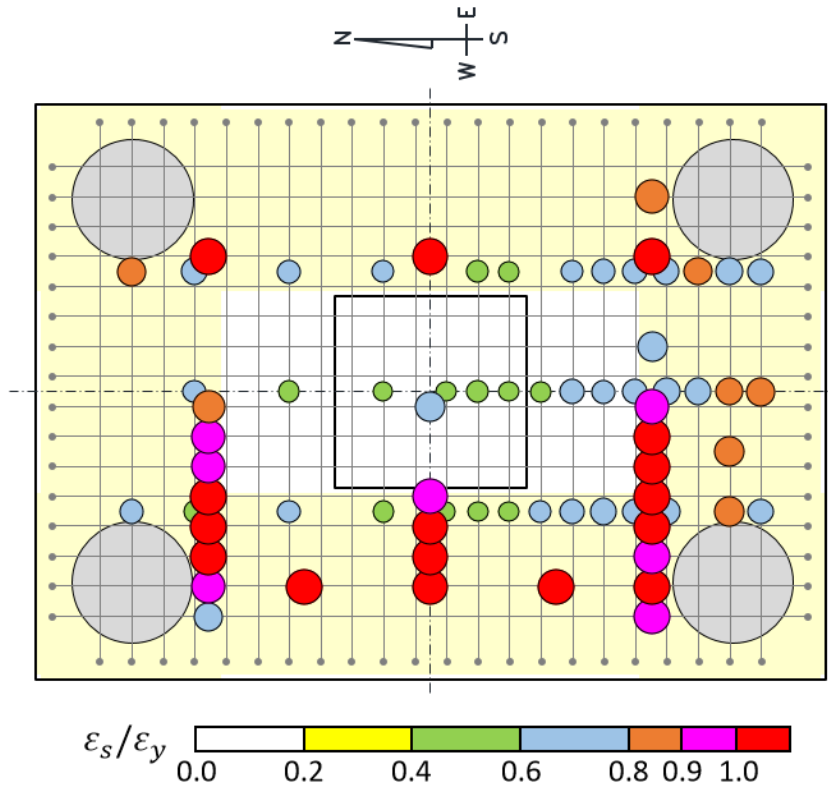


Figure F.26 Stress distribution in main reinforcements at ultimate load: III-9

- Post-failure Conditions

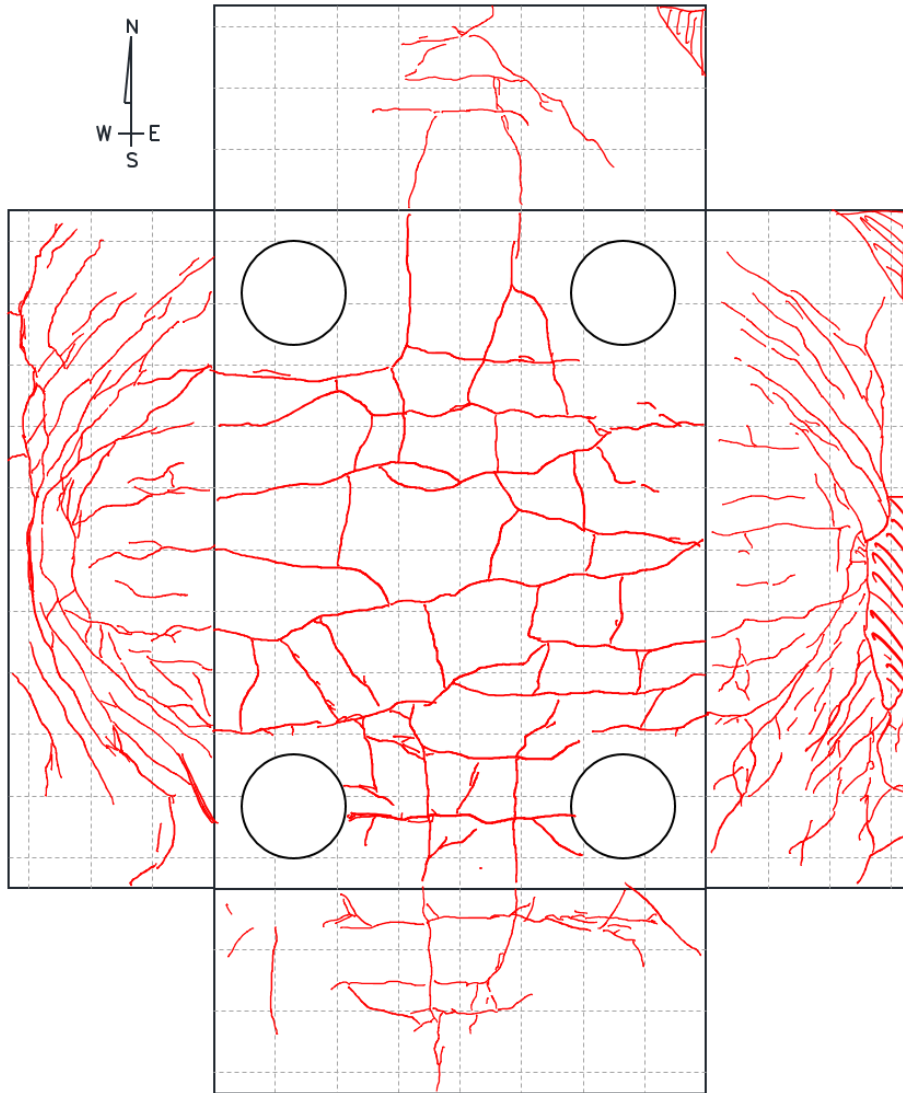


Figure F.27 Post-failure crack map: III-9

IV-10

- Load-Deflection Response

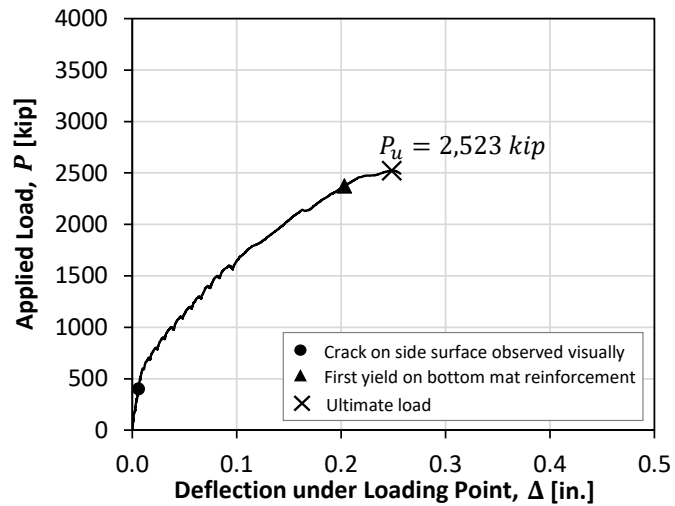


Figure F.28 Plot of the applied load versus the measured deflection: IV-10

- Stresses in Main Reinforcement

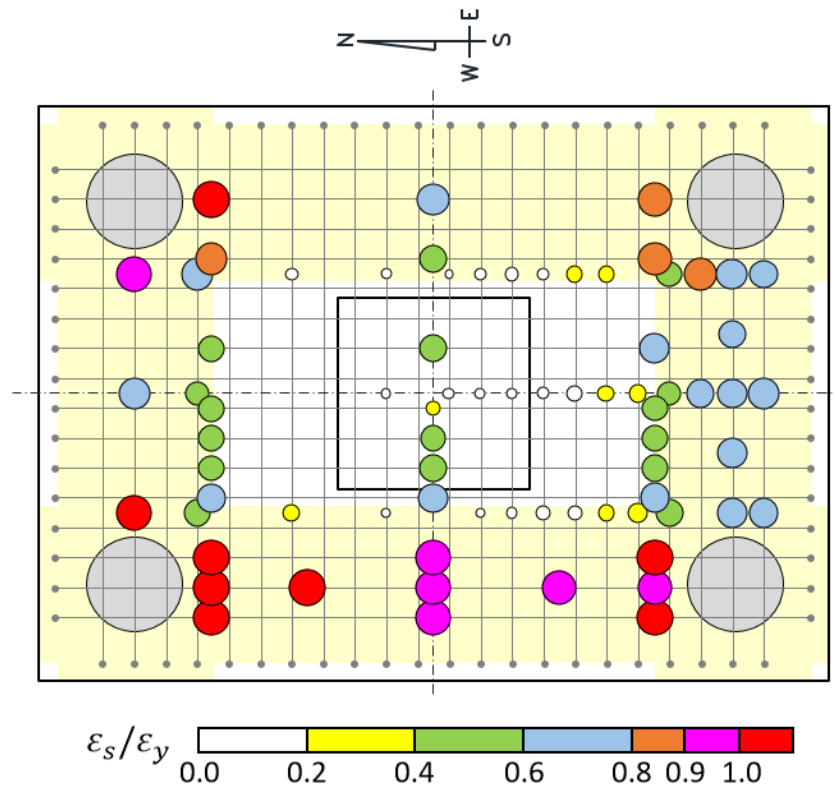


Figure F.29 Stress distribution in main reinforcements at ultimate load: IV-10

- Post-failure Conditions

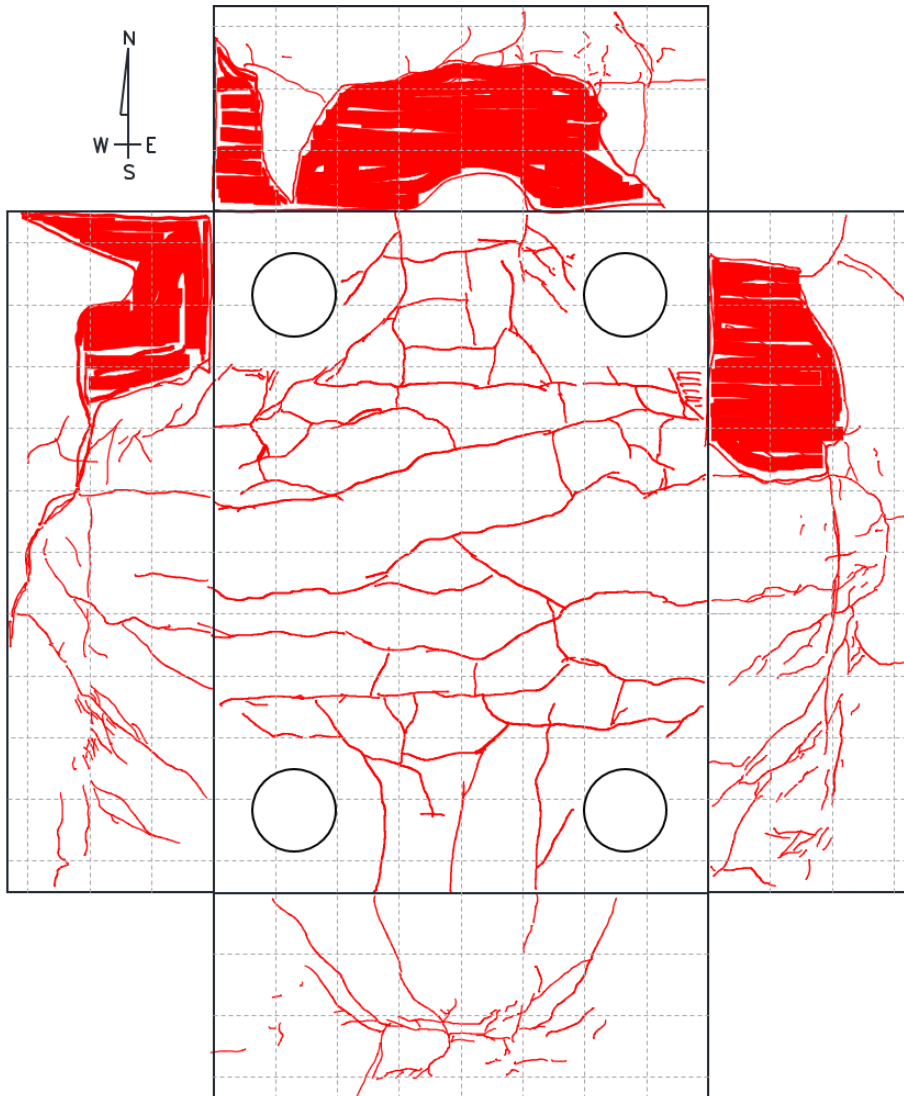


Figure F.30 Post-failure crack map: IV-10

IV-11

- Load-Deflection Response

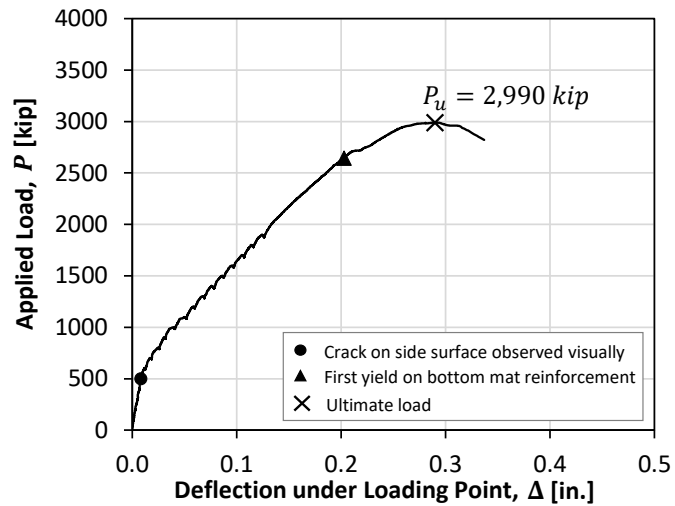


Figure F.31 Plot of the applied load versus the measured deflection: IV-11

- Stresses in Main Reinforcement

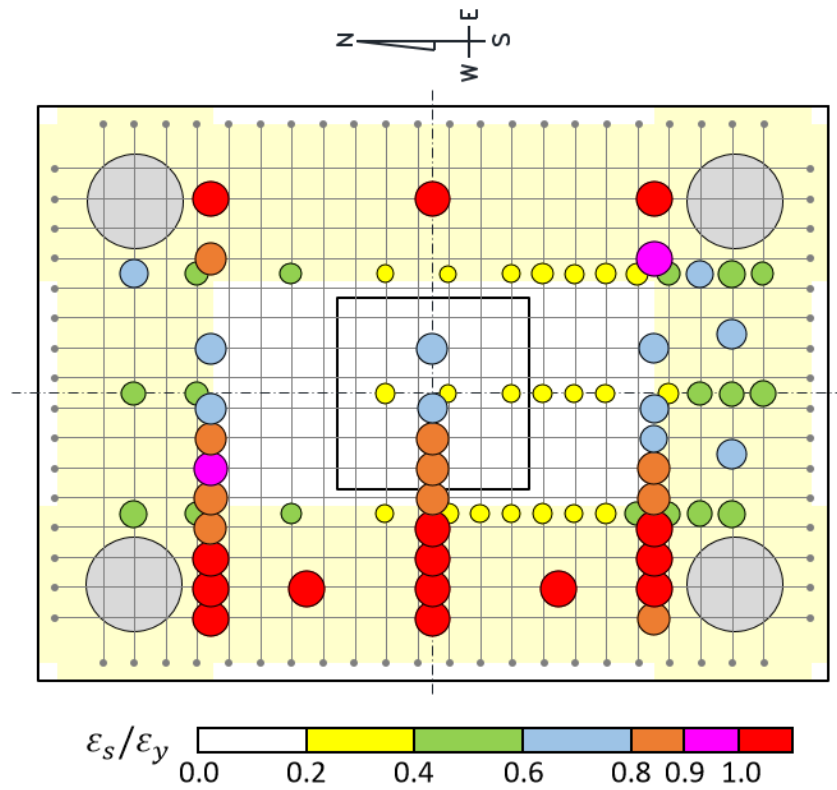


Figure F.32 Stress distribution in main reinforcements at ultimate load: IV-11

- Post-failure Conditions

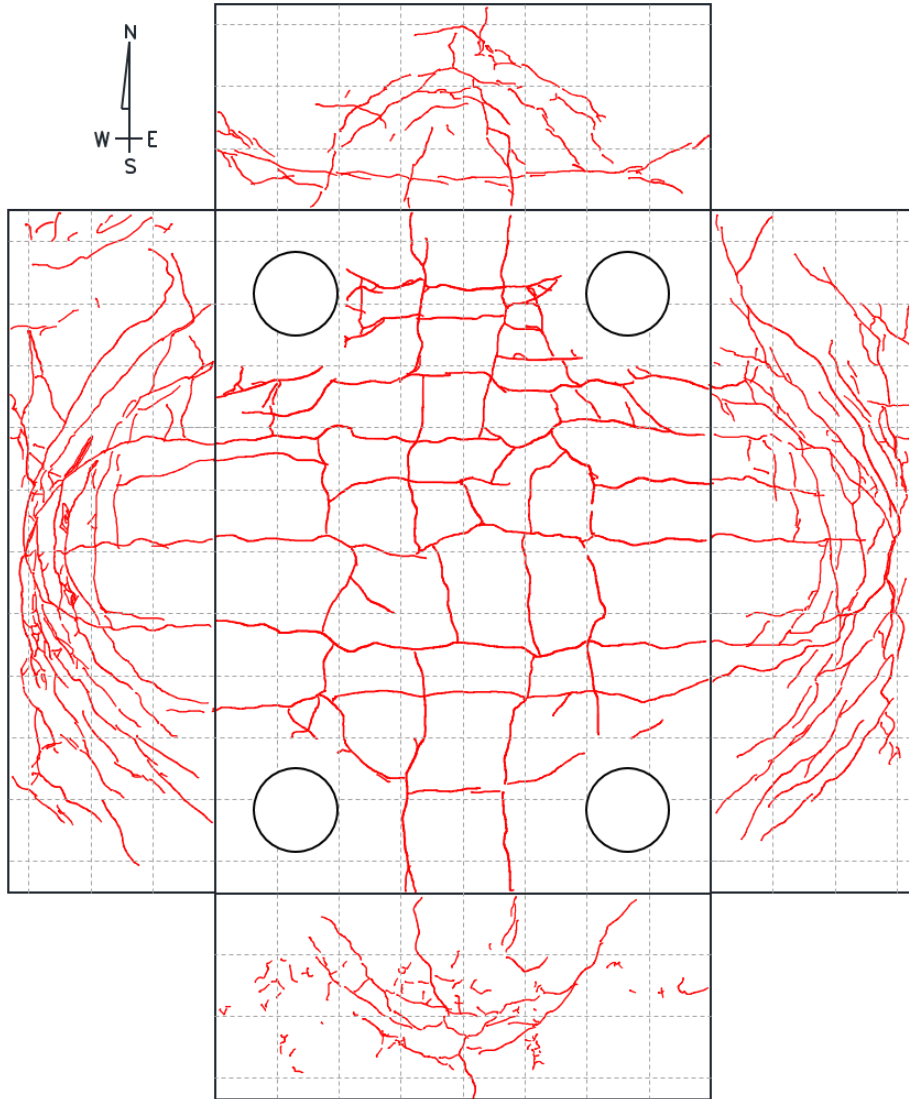


Figure F.33 Post-failure crack map: IV-11

V-12

- Load-Deflection Response

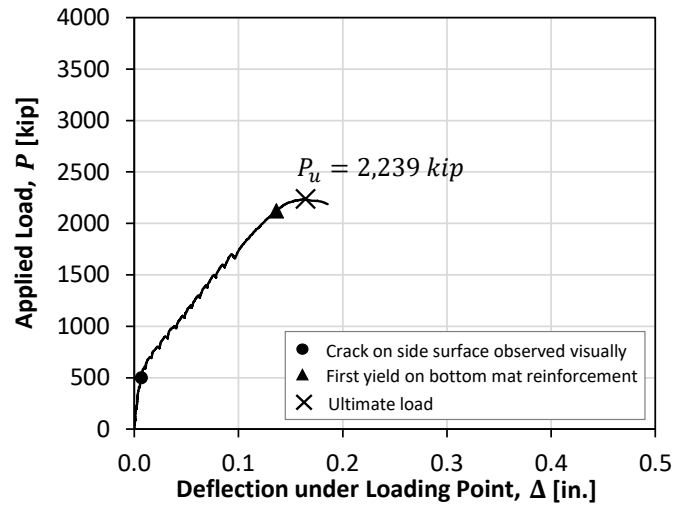


Figure F.34 Plot of the applied load versus the measured deflection: V-12

- Stresses in Main Reinforcement

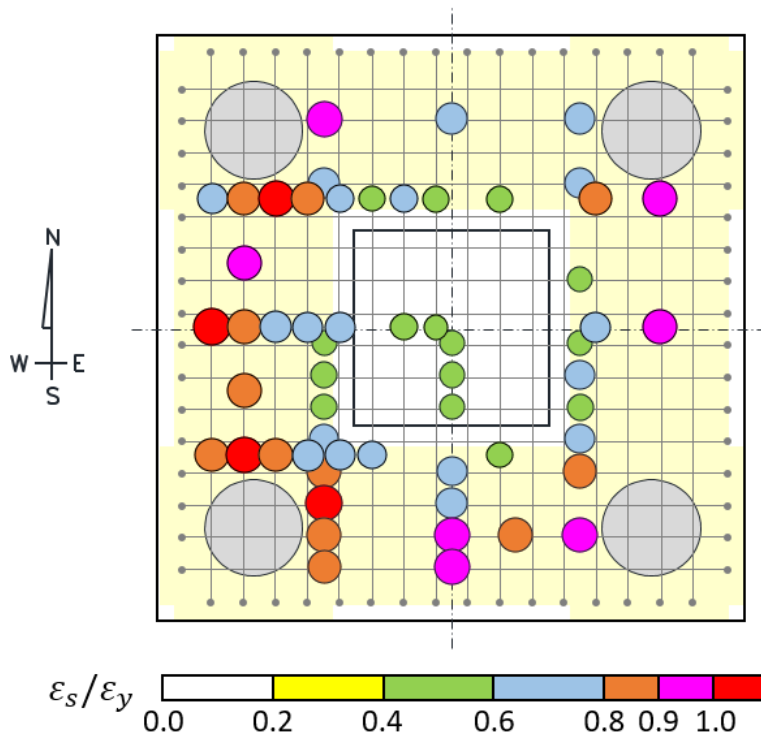


Figure F.35 Stress distribution in main reinforcements at ultimate load: V-12

- Post-failure Conditions

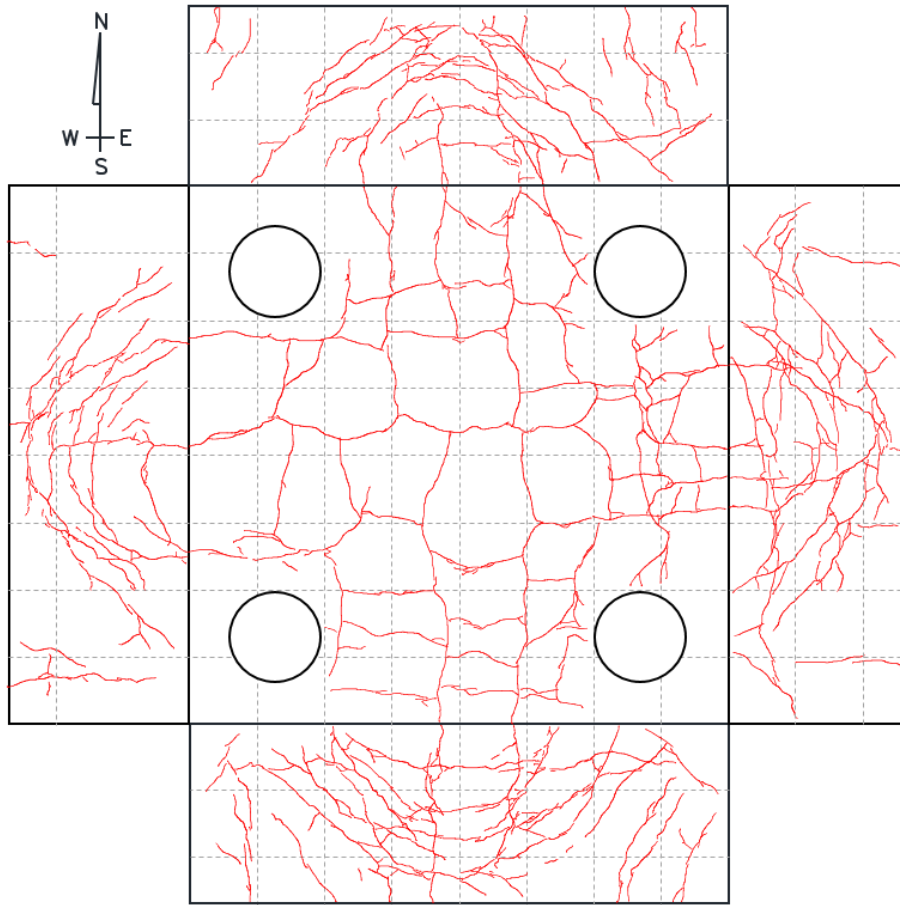


Figure F.36 Post-failure crack map: V-12

V-13

- Load-Deflection Response

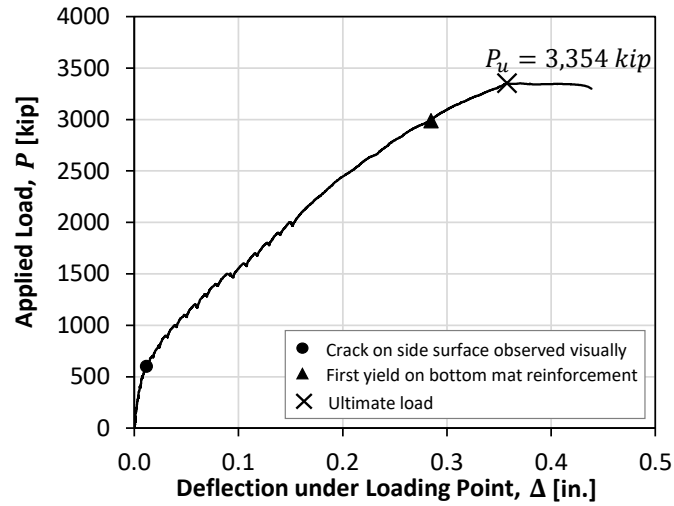


Figure F.37 Plot of the applied load versus the measured deflection: V-13

- Stresses in Main Reinforcement

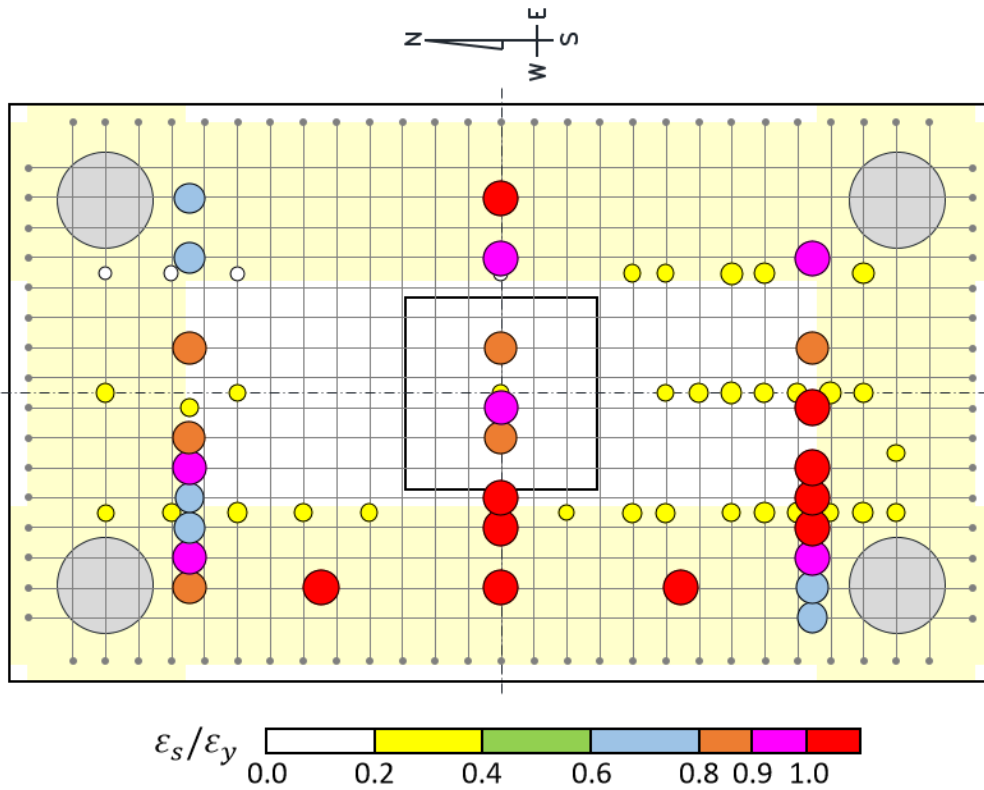


Figure F.38 Stress distribution in main reinforcements at ultimate load: V-13

- Post-failure Conditions

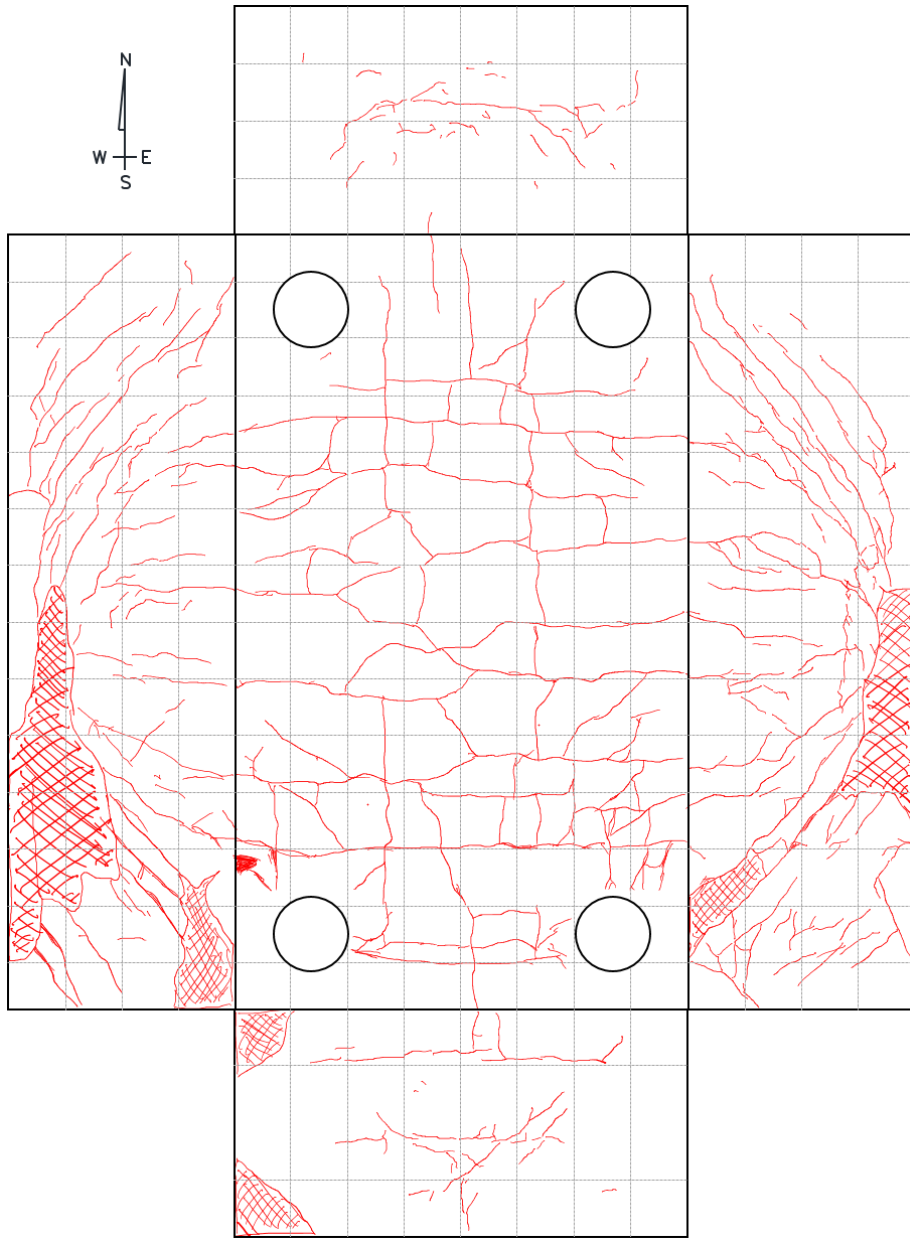


Figure F.39 Post-failure crack map: V-13

Appendix G. 3D STM Predictions (Williams et al., 2012)

Calculation Outlines

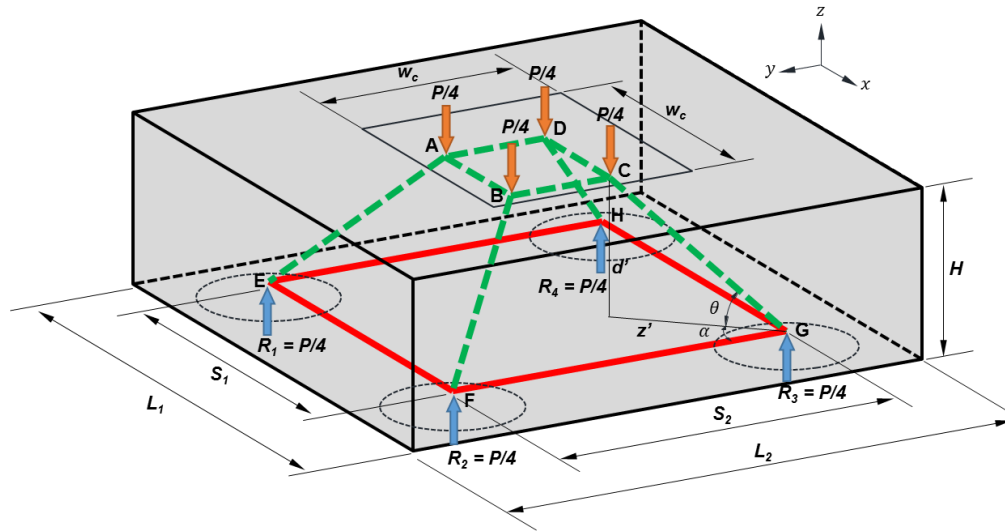


Figure G.1 Dimension of a drilled shaft footing for 3D STM calculation

II-7 (Present study)

$$f'_c = 5.86 \text{ ksi}, f_{yb} = 62.83 \text{ ksi}$$

$$L_1 = 96 \text{ in.}, L_2 = 132 \text{ in.}, H = 40 \text{ in.}$$

$$D_{DS} = 16 \text{ in.}, S_1 = 64 \text{ in.}, S_2 = 100.25 \text{ in.}$$

$$d' = H - 0.1H - (c_b + d_b) = 30.87 \text{ in.}$$

$$z' = \sqrt{(S_1/2 - w_c/4)^2 + (S_2/2 - w_c/4)^2} = 48.48 \text{ in.}$$

$$\theta = \tan^{-1}(d'/z') = 32.49^\circ$$

$$\alpha = \tan^{-1}\left(\frac{S_1/2 - w_c/4}{S_2/2 - w_c/4}\right) = 29.67^\circ$$

Ultimate capacity by tie yielding

Tie in x-direction

- Tie capacity:

$$T_x = A_{s,x} f_{yb} = 4(2 \cdot 1.00 \text{ in.}^2)(62.83 \text{ ksi}) = 502.64 \text{ kip}$$

$$\frac{P_{tie,x}}{4} \cdot \frac{1}{\tan \theta} = \frac{T_x}{\sin \alpha}$$

$$P_{tie,x} = \frac{4T \tan \theta}{\sin \alpha} = 2586.5 \text{ kip}$$

Tie in y-direction

- Tie capacity:

$$T_y = A_{s,y} f_{yb} = 4(2 \cdot 1.00 \text{ in.}^2)(62.83 \text{ ksi}) = 502.64 \text{ kip}$$

$$\frac{P_{tie,y}}{4} \cdot \frac{1}{\tan \theta} = \frac{T_y}{\cos \alpha}$$

$$P_{tie,y} = \frac{4T_y \tan \theta}{\cos \alpha} = 1473.4 \text{ kip}$$

Ultimate capacity by nodal capacity

Node A through D (CCC Node)

- Bearing Area (Quadrant of Column)

$$A_{b,col} = \left(\frac{32}{2} \text{ in.}\right)^2 = 256 \text{ in.}^2$$

- Maximum Bearing Stress: $f_{cu} = mvf'_c$

$$m = 1.0, v = 0.85 \text{ (CCC)}$$

$$f_{cu} = mvf'_c = (1.00)(0.85)(5.86) = 4.98 \text{ ksi}$$

- Nodal capacity at bearing face:

$$F_{b,CCC} = A_{b,col}f_{cu} = (256)(4.98) = 1275.14 \text{ kip}$$

$$\frac{P_{b,CCC}}{4} = F_{b,CCC} \rightarrow P_{b,CCC} = 4F_{b,CCC} = 5100.5 \text{ kip}$$

Node E through F (CTT Node)

- Bearing Area (Drilled Shaft)

$$A_{b,DS} = \frac{\pi}{4} \cdot (16 \text{ in.})^2 = 201.06 \text{ in}^2$$

- Maximum Bearing Stress: $f_{cu} = mvf'_c$

$$m = 1.0, v = 0.85 - \frac{f'_c}{20 \text{ ksi}} = 0.557 \leq 0.65 \text{ (CTT)}$$

$$f_{cu} = mvf'_c = (1.00)(0.557)(5.86) = 3.26 \text{ ksi}$$

- Nodal capacity at bearing face:

$$F_{b,CTT} = A_{b,DS}f_{cu} = (201.06)(3.26) = 656.27 \text{ kip}$$

$$\frac{P_{b,CTT}}{4} = F_{b,CTT} \rightarrow P_{b,CTT} = 4F_{b,CTT} = 2625.1 \text{ kip}$$

Predicted Ultimate Capacity

$$\begin{aligned} P_{STM} &= \min(P_{tie,x}, P_{tie,y}, P_{b,CCC}, P_{b,CTT}) \\ &= P_{tie,y} = \mathbf{1473.4 \text{ kip}} \end{aligned}$$

Evaluation Database

Table G1. Summary of 3D STM Predictions based on the recommendation by Williams et al. (2012)

No.	Researcher	Specimen ID	Geometric Properties			STM Prediction by Controlled Failure Mechanism				3D STM Prediction Result		
			θ^a [deg.]	α^b [deg.]	$\frac{l_{ad}}{l_{d,req'd}}$	Tie Length-Dir. [kip]	Tie Width-Dir. [kip]	CCC ^c Bearing [kip]	CTT ^d Bearing [kip]	P_u^e [kip]	P_{STM}^f [kip]	$\frac{P_u}{P_{STM}}$
1	Suzuki et al. (1998)	BP-25-1	32.4	45.0	1.00	<u>71</u>	<u>71</u>	389	233	165	71	2.32
2		BP-25-2	32.4	45.0	1.00	<u>71</u>	<u>71</u>	370	222	170	71	2.38
3		BPC-25-1	32.4	45.0	1.00	<u>119</u>	<u>119</u>	325	195	184	119	1.55
4		BPC-25-2	32.4	45.0	1.00	<u>119</u>	<u>119</u>	378	227	183	119	1.54
5		BP-30-30-1	41.6	45.0	1.00	<u>98</u>	<u>98</u>	469	282	206	98	2.10
6		BP-30-30-2	41.6	45.0	1.00	<u>98</u>	<u>98</u>	490	291	204	98	2.08
7		BPC-30-30-1	41.6	45.0	1.00	<u>131</u>	<u>131</u>	497	294	234	131	1.79
8		BPC-30-30-2	41.6	45.0	1.00	<u>131</u>	<u>131</u>	531	307	231	131	1.77
9		BP-30-25-1	39.7	45.0	1.00	<u>91</u>	<u>91</u>	369	307	179	91	1.95
10		BP-30-25-2	39.7	45.0	1.00	<u>91</u>	<u>91</u>	314	272	163	91	1.78
11		BPC-30-25-1	39.7	45.0	1.00	<u>122</u>	<u>122</u>	347	295	192	122	1.57
12		BPC-30-25-2	39.7	45.0	1.00	<u>122</u>	<u>122</u>	349	296	196	122	1.61
13		BDA-70x90-1	39.7	45.0	1.00	<u>80</u>	95	347	295	176	80	2.19
14		BDA-70x90-2	39.7	45.0	1.00	<u>80</u>	95	361	303	170	80	2.11
15		BDA-80x90-1	39.7	45.0	1.00	<u>80</u>	143	347	295	193	80	2.40
16		BDA-80x90-2	39.7	45.0	1.00	<u>80</u>	143	350	297	192	80	2.39
17		BDA-90x90-1	39.7	45.0	1.00	80	<u>71</u>	352	298	192	71	2.69
18		BDA-90x90-2	39.7	45.0	1.00	139	<u>123</u>	376	311	207	123	1.68

No.	Researcher	Specimen ID	Geometric Properties			STM Prediction by Controlled Failure Mechanism				3D STM Prediction Result		
			θ^a [deg.]	α^b [deg.]	$\frac{l_{ad}}{l_{d,req'd}}$	Tie Length-Dir. [kip]	Tie Width-Dir. [kip]	CCC ^c Bearing [kip]	CTT ^d Bearing [kip]	P_u^e [kip]	P_{STM}^f [kip]	$\frac{P_u}{P_{STM}}$
19	Suzuki et al. (1998)	TDM3-1	39.7	45.0	1.00	<u>198</u>	<u>198</u>	322	279	280	198	1.41
20		TDM3-2	39.7	45.0	1.00	<u>198</u>	<u>198</u>	334	288	272	198	1.37
21	Suzuki et al. (2000)	BDA-30-20-70-2	41.6	45.0	1.00	<u>58</u>	<u>58</u>	188	254	123	58	2.14
22		BDA-30-25-70-1	43.8	45.0	1.00	<u>66</u>	<u>66</u>	344	293	149	66	2.24
23		BDA-30-25-70-2	43.8	45.0	1.00	<u>66</u>	<u>66</u>	316	274	152	66	2.29
24		BDA-30-25-80-1	43.8	45.0	1.00	<u>66</u>	<u>66</u>	351	297	156	66	2.36
25		BDA-30-25-80-2	43.8	45.0	1.00	<u>66</u>	<u>66</u>	332	286	163	66	2.45
26		BDA-30-30-70-1	46.0	45.0	1.00	<u>67</u>	<u>67</u>	461	277	173	67	2.57
27		BDA-30-30-70-2	46.0	45.0	1.00	<u>67</u>	<u>67</u>	445	267	164	67	2.44
28		BDA-30-30-80-1	46.0	45.0	1.00	<u>67</u>	<u>67</u>	471	283	186	67	2.77
29		BDA-30-30-80-2	46.0	45.0	1.00	<u>67</u>	<u>67</u>	471	283	182	67	2.70
30		BDA-30-30-90-2	46.0	45.0	1.00	<u>90</u>	<u>90</u>	421	253	183	90	2.04
31		Suzuki & Otsuki (2002)	BPL-35-30-1	45.0	45.0	1.00	<u>108</u>	<u>108</u>	288	249	216	108
32	BPL-35-30-2		45.0	45.0	1.00	<u>108</u>	<u>108</u>	306	264	212	108	1.96
33	BPB-35-30-1		45.0	45.0	1.00	<u>108</u>	<u>108</u>	283	245	231	108	2.14
34	BPB-35-30-2		45.0	45.0	1.00	<u>108</u>	<u>108</u>	281	243	248	108	2.30
35	BPH-35-30-1		45.0	45.0	1.00	<u>108</u>	<u>108</u>	376	311	220	108	2.04
36	BPH-35-30-2		45.0	45.0	1.00	<u>108</u>	<u>108</u>	390	318	245	108	2.27
37	BPL-35-25-1		45.0	45.0	1.00	<u>108</u>	<u>108</u>	324	280	203	108	1.88
38	BPL-35-25-2		45.0	45.0	1.00	<u>108</u>	<u>108</u>	306	264	196	108	1.82
39	BPB-35-25-1		45.0	45.0	1.00	<u>108</u>	<u>108</u>	277	240	205	108	1.90
40	BPB-35-25-2		45.0	45.0	1.00	<u>108</u>	<u>108</u>	283	245	207	108	1.92

No.	Researcher	Specimen ID	Geometric Properties			STM Prediction by Controlled Failure Mechanism				3D STM Prediction Result		
			θ^a [deg.]	α^b [deg.]	$\frac{l_{ad}}{l_{d,req'd}}$	Tie Length-Dir. [kip]	Tie Width-Dir. [kip]	CCC ^c Bearing [kip]	CTT ^d Bearing [kip]	P_u^e [kip]	P_{STM}^f [kip]	$\frac{P_u}{P_{STM}}$
41	Suzuki & Otsuki (2002)	BPH-35-25-1	45.0	45.0	1.00	<u>108</u>	<u>108</u>	437	340	198	108	1.84
42		BPH-35-25-2	45.0	45.0	1.00	<u>108</u>	<u>108</u>	453	346	214	108	1.98
43		BPL-35-20-1	45.0	45.0	1.00	<u>108</u>	<u>108</u>	269	232	170	108	1.57
44		BPL-35-20-2	45.0	45.0	1.00	<u>108</u>	<u>108</u>	257	222	165	108	1.53
45		BPB-35-20-1	45.0	45.0	1.00	<u>108</u>	<u>108</u>	244	211	170	108	1.57
46		BPB-35-20-2	45.0	45.0	1.00	<u>108</u>	<u>108</u>	241	209	181	108	1.67
47		BPH-35-20-1	45.0	45.0	1.00	<u>108</u>	<u>108</u>	375	310	183	108	1.69
48		BPH-35-20-2	45.0	45.0	1.00	<u>108</u>	<u>108</u>	368	307	179	108	1.65
49	Present Study	I-1	34.5	45.0	0.57	<u>1002</u>	<u>1002</u>	4413	2432	2107	1002	2.10
50		I-2	34.5	45.0	1.00	<u>1574</u>	<u>1574</u>	4543	2473	2775	1574	1.76
51		I-3	34.5	45.0	0.41	<u>978</u>	<u>978</u>	4430	2438	2703	978	2.76
52		I-4	34.5	45.0	1.00	2361	2361	4404	2429	2884	2361	1.22
53		II-5	48.2	27.1	1.00	4999	2555	2820	<u>1694</u>	3273	1694	1.93
54		II-6	40.7	45.0	1.00	2472	2472	4021	<u>2300</u>	3648	2300	1.59
55		II-7	32.5	29.7	1.00	2585	<u>1473</u>	5101	2625	3387	1473	2.30
56		III-8	32.5	29.7	1.00	2778	<u>1583</u>	4056	1301	2886	1301	2.22
57		III-9	32.5	29.7	1.00	3468	1976	3229	3030	2902	1976	1.47
58		IV-10	32.5	29.7	0.99	3180	<u>1812</u>	4056	2312	2523	1812	1.39
59		IV-11	32.5	29.7	0.99	3178	<u>1811</u>	4047	2309	2990	1811	1.65
60		V-12	34.5	45.0	1.00	<u>1645</u>	<u>1645</u>	3064	1840	2239	1645	1.36

a: strut angle as shown in Figure G.1, b: angle between tie and strut in plan view as shown in Figure G.1, c: Node beneath the column (CCC node, d: Node above the shaft (CTT node), e: Ultimate load by the structural testing, f: Minimum load depending on controlled failure mode, underline: controlled failure mechanism

Ultimate capacity by nodal capacity

Node A through D (CCC Node)

- Bearing Area (Quadrant of Column)

$$A_{b,col} = \left(\frac{32}{2} \text{ in.}\right)^2 = 256 \text{ in.}^2$$

- Confinement Modification Factor

$$m = \sqrt{\frac{A_2}{A_1}} = \sqrt{\frac{96 \cdot 96}{32 \cdot 32}} = 3.0$$

- Nodal capacity at bearing face:

$$v = 0.85 \text{ (Bearing face of CCC node)}$$

$$f_{cu} = mvf'_c = (3.00)(0.85)(5.86) = 14.94 \text{ ksi}$$

$$F_{b,CCC} = A_{b,col}f_{cu} = (256)(14.94) = 3824.6 \text{ kip}$$

$$\frac{P_{b,CCC}}{4} = F_{b,CCC} \rightarrow P_{b,CCC} = 4F_{b,CCC} = 15298.6 \text{ kip}$$

- Nodal capacity at back face:

$$v = 0.85 \text{ (Back face of CCC node)}$$

$$f_{cu} = mvf'_c = (3.00)(0.85)(5.86) = 14.94 \text{ ksi}$$

$$A_{bk,col} = \sqrt{A_{b,col}} \cdot 0.2H = (16)(0.2 \cdot 40) = 128 \text{ in.}^2$$

$$F_{bk,CCC} = A_{bk,col}f_{cu} = (128)(14.94) = 1912.3 \text{ kip}$$

$$\frac{P_{bk,CCC}}{4} = F_{bk,CCC} \tan \theta$$

$$P_{bk,CCC} = 4F_{bk,CCC} \tan \theta = 4870.8 \text{ kip}$$

Node E through F (CTT Node)

- Bearing Area (Drilled Shaft):

$$A_{b,DS} = \frac{\pi}{4} \cdot (16 \text{ in.})^2 = 201.06 \text{ in.}^2$$

- Confinement Modification Factor

$$m = \sqrt{\frac{A_2}{A_1}} = \sqrt{\frac{32 \cdot 32}{A_{b,DS}}} = 2.26 > 2.0 \rightarrow m = 2.0$$

- Nodal capacity at bearing face:

$$v = 0.85 - \frac{f'_c}{20 \text{ ksi}} = 0.557 \leq 0.65 \text{ (CTT Node)}$$

$$f_{cu} = mvf'_c = (2.00)(0.557)(5.86) = 6.53 \text{ ksi}$$

$$F_{b,CTT} = A_{b,DS}f_{cu} = (201.06)(6.53) = 1312.9 \text{ kip}$$

$$\frac{P_{b,CTT}}{4} = F_{b,CTT} \rightarrow P_{b,CTT} = 4F_{b,CTT} = 5250.2 \text{ kip}$$

- Nodal capacity at back face: Not necessary if proper anchorage provided

- Nodal capacity at strut-to-node interface:

$$v = 0.85 - \frac{f'_c}{20} = 0.557 \text{ (Strut-to-node interface of CCC node)}$$

$$f_{cu} = mvf'_c = (3.00)(0.557)(5.86) = 9.79 \text{ ksi}$$

$$A_{SNI,col} = \sqrt{A_{b,col}} \cdot (\sqrt{A_{b,col}} \sin \theta + 0.2H \cos \theta) \\ = (16)(16 \sin \theta + 0.2 \cdot 40 \cos \theta) = 245.48 \text{ in.}^2$$

$$F_{SNI,CCC} = A_{SNI,col} f_{cu} = (245.48)(9.79) = 2403.2 \text{ kip}$$

$$\frac{P_{SNI,CCC}}{4} = F_{SNI,CCC} \sin \theta$$

$$P_{SNI,CCC} = 4F_{SNI,CCC} \sin \theta = 5163.2 \text{ kip}$$

Predicted Ultimate Capacity

$$P_{STM} = \min(P_{tie,x}, P_{tie,y}, P_{b,CCC}, P_{bk,CCC}, P_{SNI,CCC}, P_{b,CTT}, P_{SNI,CTT}) \\ = P_{tie,y} = \mathbf{2945.5 \text{ kip}}$$

- Nodal capacity at strut-to-node interface:

$$v = 0.85 - \frac{f'_c}{20 \text{ ksi}} = 0.557 \leq 0.65 \text{ (CTT Node)}$$

$$f_{cu} = mvf'_c = (2.00)(0.557)(5.86) = 6.53 \text{ ksi}$$

$$A_{SNI,col} = \sqrt{A_{b,DS}} \cdot (\sqrt{A_{b,DS}} \sin \theta + 2c_b \cos \theta) \\ = (14.18)(14.18 \sin \theta + 2 \cdot 5.128 \cos \theta) = 230.7 \text{ in.}^2$$

$$F_{SNI,CCC} = A_{SNI,col} f_{cu} = (230.7)(6.53) = 1506.2 \text{ kip}$$

$$\frac{P_{SNI,CCC}}{4} = F_{SNI,CCC} \sin \theta$$

$$P_{SNI,CCC} = 4F_{SNI,CCC} \sin \theta = 3236.0 \text{ kip}$$

Evaluation Database

Table H1. Summary of 3D STM Predictions based on the proposal by present study

No.	Researcher	Specimen ID	Geometric Properties			STM Prediction by Controlled Failure Mechanism						3D STM Result			
			θ^a [deg]	α^b [deg.]	$\frac{l_{ad}}{l_{d,req'd}}$	Tie Length-Dir. [kip]	Tie Width-Dir. [kip]	CCC ^c Bearing [kip]	CCC ^c Back [kip]	CCC ^c SNI ^d [kip]	CTT ^e Bearing [kip]	CTT SNI ^d [kip]	P_u^f [kip]	P_{STM}^g [kip]	$\frac{P_u}{P_{STM}}$
1	Suzuki et al. (1998)	BP-25-1	32.4	45.0	1.00	<u>119</u>	<u>119</u>	617	130	504	323	378	165	119	1.39
2		BP-25-2	32.4	45.0	1.00	<u>119</u>	<u>119</u>	587	124	480	308	360	170	119	1.43
3		BPC-25-1	32.4	45.0	1.00	119	119	516	<u>109</u>	422	271	317	184	109	1.68
4		BPC-25-2	32.4	45.0	1.00	<u>119</u>	<u>119</u>	601	127	491	314	368	183	119	1.54
5		BP-30-30-1	41.6	45.0	1.00	<u>131</u>	<u>131</u>	663	236	638	390	478	206	131	1.58
6		BP-30-30-2	41.6	45.0	1.00	<u>131</u>	<u>131</u>	692	246	666	408	500	204	131	1.56
7		BP-25-1	41.6	45.0	1.00	<u>131</u>	<u>131</u>	702	250	676	413	507	234	131	1.79
8		BPC-30-30-2	41.6	45.0	1.00	<u>131</u>	<u>131</u>	751	267	723	442	542	231	131	1.77
9		BP-30-25-1	39.7	45.0	1.00	<u>122</u>	<u>122</u>	586	233	591	442	538	179	122	1.47
10		BP-30-25-2	39.7	45.0	1.00	<u>122</u>	<u>122</u>	499	199	503	376	458	163	122	1.34
11		BPC-30-25-1	39.7	45.0	1.00	<u>122</u>	<u>122</u>	552	220	556	416	507	192	122	1.57
12		BPC-30-25-2	39.7	45.0	1.00	<u>122</u>	<u>122</u>	554	221	558	418	508	196	122	1.61
13		BDA-70x90-1	39.7	45.0	1.00	<u>107</u>	167	515	205	520	416	507	176	107	1.65
14		BDA-70x90-2	39.7	45.0	1.00	<u>107</u>	167	535	213	539	432	526	170	107	1.58
15		BDA-80x90-1	39.7	45.0	1.00	<u>107</u>	191	552	220	556	416	507	193	107	1.80
16		BDA-80x90-2	39.7	45.0	1.00	<u>107</u>	191	556	221	560	418	510	192	107	1.79
17		BDA-90x90-1	39.7	45.0	1.00	<u>107</u>	107	559	223	564	422	514	192	107	1.79
18		BDA-90x90-2	39.7	45.0	1.00	<u>185</u>	185	598	238	602	450	548	207	185	1.12
19	Suzuki et al. (1998)	TDM3-1	39.7	45.0	1.00	248	248	513	<u>204</u>	516	386	470	280	204	1.37
20		TDM3-2	39.7	45.0	1.00	248	248	531	<u>211</u>	535	400	487	272	211	1.29

No.	Researcher	Specimen ID	Geometric Properties			STM Prediction by Controlled Failure Mechanism							3D STM Result		
			θ^a [deg]	α^b [deg.]	$\frac{l_{ad}}{l_{d,req'd}}$	Tie Length-Dir. [kip]	Tie Width-Dir. [kip]	CCC ^c Bearing [kip]	CCC ^c Back [kip]	CCC ^c SNI ^d [kip]	CTT ^e Bearing [kip]	CTT SNI ^d [kip]	P_u^f [kip]	P_{STM}^g [kip]	$\frac{P_u}{P_{STM}}$
21	Suzuki et al. (2000)	BDA-30-20-70-2	41.6	45.0	1.00	<u>87</u>	<u>87</u>	299	159	332	331	406	123	87	1.43
22		BDA-30-25-70-1	43.8	45.0	1.00	<u>100</u>	<u>100</u>	510	234	529	387	478	149	100	1.49
23		BDA-30-25-70-2	43.8	45.0	1.00	<u>100</u>	<u>100</u>	469	216	487	356	440	152	100	1.53
24		BDA-30-25-80-1	43.8	45.0	1.00	<u>100</u>	<u>100</u>	558	257	579	421	520	156	100	1.57
25		BDA-30-25-80-2	43.8	45.0	1.00	<u>100</u>	<u>100</u>	527	242	547	398	491	163	100	1.64
26		BDA-30-30-70-1	46.0	45.0	1.00	<u>101</u>	<u>101</u>	569	236	568	360	448	173	101	1.71
27		BDA-30-30-70-2	46.0	45.0	1.00	<u>101</u>	<u>101</u>	550	228	548	348	433	164	101	1.63
28		BDA-30-30-80-1	46.0	45.0	1.00	<u>101</u>	<u>101</u>	665	276	664	392	487	186	101	1.84
29		BDA-30-30-80-2	46.0	45.0	1.00	<u>101</u>	<u>101</u>	665	276	664	392	487	182	101	1.80
30		BDA-30-30-90-2	46.0	45.0	1.00	<u>135</u>	<u>135</u>	670	278	668	351	436	183	135	1.36
31	Suzuki & Otsuki (2002)	BPL-35-30-1	45.0	45.0	1.00	<u>144</u>	<u>144</u>	457	256	504	345	428	216	144	1.50
32		BPL-35-30-2	45.0	45.0	1.00	<u>144</u>	<u>144</u>	485	271	535	366	453	212	144	1.47
33		BPB-35-30-1	45.0	45.0	1.00	<u>144</u>	<u>144</u>	450	251	496	338	420	231	144	1.61
34		BPB-35-30-2	45.0	45.0	1.00	<u>144</u>	<u>144</u>	446	249	492	336	417	248	144	1.72
35		BPH-35-30-1	45.0	45.0	1.00	<u>144</u>	<u>144</u>	598	335	659	450	558	220	144	1.53
36		BPH-35-30-2	45.0	45.0	1.00	<u>144</u>	<u>144</u>	620	347	684	468	580	245	144	1.70
37		BPL-35-25-1	45.0	45.0	1.00	<u>144</u>	<u>144</u>	513	287	566	388	480	203	144	1.41
38		BPL-35-25-2	45.0	45.0	1.00	<u>144</u>	<u>144</u>	485	271	535	366	453	196	144	1.36
39		BPB-35-25-1	45.0	45.0	1.00	<u>144</u>	<u>144</u>	440	246	485	332	411	205	144	1.42
40		BPB-35-25-2	45.0	45.0	1.00	<u>144</u>	<u>144</u>	450	251	496	338	420	207	144	1.44
41		BPH-35-25-1	45.0	45.0	1.00	<u>144</u>	<u>144</u>	694	388	765	524	649	198	144	1.38
42		BPH-35-25-2	45.0	45.0	1.00	<u>144</u>	<u>144</u>	719	402	793	542	672	214	144	1.49

No.	Researcher	Specimen ID	Geometric Properties			STM Prediction by Controlled Failure Mechanism							3D STM Result		
			θ^a [deg]	α^b [deg.]	$\frac{l_{ad}}{l_{d,req'd}}$	Tie Length-Dir. [kip]	Tie Width-Dir. [kip]	CCC ^c Bearing [kip]	CCC ^c Back [kip]	CCC ^c SNI ^d [kip]	CTT ^e Bearing [kip]	CTT SNI ^d [kip]	P_u^f [kip]	P_{STM}^g [kip]	$\frac{P_u}{P_{STM}}$
43	Suzuki & Otsuki (2002)	BPL-35-20-1	45.0	45.0	1.00	<u>144</u>	<u>144</u>	426	239	470	322	399	170	144	1.18
44		BPL-35-20-2	45.0	45.0	1.00	<u>144</u>	<u>144</u>	408	228	450	308	382	165	144	1.15
45		BPB-35-20-1	45.0	45.0	1.00	<u>144</u>	<u>144</u>	387	216	426	292	361	170	144	1.18
46		BPB-35-20-2	45.0	45.0	1.00	<u>144</u>	<u>144</u>	383	214	422	289	358	181	144	1.26
47		BPH-35-20-1	45.0	45.0	1.00	<u>144</u>	<u>144</u>	596	333	657	449	556	183	144	1.27
48		BPH-35-20-2	45.0	45.0	1.00	<u>144</u>	<u>144</u>	584	327	644	440	386	179	144	1.24
49	Present Study	I-1	34.5	45.0	0.74	<u>2287</u>	<u>2287</u>	13240	3638	4711	4712	3161	2107	2287	0.92
50		I-2	34.5	45.0	1.00	<u>2755</u>	<u>2755</u>	13629	3745	4789	4791	3213	2775	2755	1.01
51		I-3	34.5	45.0	0.54	<u>1488</u>	<u>1488</u>	13292	3652	4722	4723	3167	2703	1488	1.82
52		I-4	34.5	45.0	1.00	<u>2755</u>	<u>2755</u>	13210	3630	4706	4707	3156	2884	2755	1.05
53		II-5	48.2	27.1	1.00	3833	9997	6349	3554	3906	3271	<u>3100</u>	3273	3100	1.06
54		II-6	40.7	45.0	1.00	4944	4944	12063	5189	5909	4205	<u>3602</u>	3648	3602	1.01
55		II-7	32.5	29.7	1.00	<u>2946</u>	7109	15299	4871	5163	5250	3236	3387	2946	1.15
56		III-8	32.5	29.7	1.00	3166	7641	12165	3873	4551	2601	<u>1887</u>	2886	1887	1.53
57		III-9	32.5	29.7	1.00	3161	7630	9687	3084	3813	4849	<u>3003</u>	2902	3003	0.97
58		IV-10	32.5	29.7	1.00	3673	8863	6441	<u>2051</u>	3317	4625	2077	2523	2051	1.23
59		IV-11	32.5	29.7	1.00	3673	8863	12145	3867	4541	3366	<u>2845</u>	2990	2845	1.05
60		V-12	34.5	45.0	1.00	3291	3291	9196	2527	3563	3565	<u>2393</u>	2239	2393	0.94

a: strut angle as shown in Figure G.1, b: angle between tie and strut in plan view as shown in Figure G.1, c: Node beneath the column (CCC node), d: Sturt-to-Node Interface, e: Node above the shaft (CTT node), f: Ultimate load by the structural testing, g: Minimum load depending on controlled failure mode, underline: controlled failure mechanism

Appendix I. Equivalent Force System of Design Example: Load Case V

1. Calculate reactions that satisfy the equilibrium conditions of the external loading

$$R_1 = \frac{P_u}{4} + \frac{1}{2} \left(\frac{M_{uyy}}{S_{DS,x}} \right) + \frac{1}{2} \left(\frac{M_{uxx}}{S_{DS,y}} \right) = \frac{5000 \text{ kip}}{4} + \frac{1}{2} \left(\frac{2500 \text{ k-ft}}{10.50 \text{ ft}} \right) + \frac{1}{2} \left(\frac{2000 \text{ k-ft}}{10.50 \text{ ft}} \right) = 1464.3 \text{ kip (Compression)}$$

$$R_2 = \frac{P_u}{4} - \frac{1}{2} \left(\frac{M_{uyy}}{S_{DS,x}} \right) + \frac{1}{2} \left(\frac{M_{uxx}}{S_{DS,y}} \right) = \frac{5000 \text{ kip}}{4} - \frac{1}{2} \left(\frac{2500 \text{ k-ft}}{10.50 \text{ ft}} \right) + \frac{1}{2} \left(\frac{2000 \text{ k-ft}}{10.50 \text{ ft}} \right) = 1226.2 \text{ kip (Compression)}$$

$$R_3 = \frac{P_u}{4} - \frac{1}{2} \left(\frac{M_{uyy}}{S_{DS,x}} \right) - \frac{1}{2} \left(\frac{M_{uxx}}{S_{DS,y}} \right) = \frac{5000 \text{ kip}}{4} - \frac{1}{2} \left(\frac{2500 \text{ k-ft}}{10.50 \text{ ft}} \right) - \frac{1}{2} \left(\frac{2000 \text{ k-ft}}{10.50 \text{ ft}} \right) = 1035.7 \text{ kip (Compression)}$$

$$R_4 = \frac{P_u}{4} + \frac{1}{2} \left(\frac{M_{uyy}}{S_{DS,x}} \right) - \frac{1}{2} \left(\frac{M_{uxx}}{S_{DS,y}} \right) = \frac{5000 \text{ kip}}{4} + \frac{1}{2} \left(\frac{2500 \text{ k-ft}}{10.50 \text{ ft}} \right) - \frac{1}{2} \left(\frac{2000 \text{ k-ft}}{10.50 \text{ ft}} \right) = 1273.8 \text{ kip (Compression)}$$

2. Determine the regions where resultant forces on the column section (Figure 8.70) were equal to the reactions adjacent drilled shaft footings (Figure 8.71)

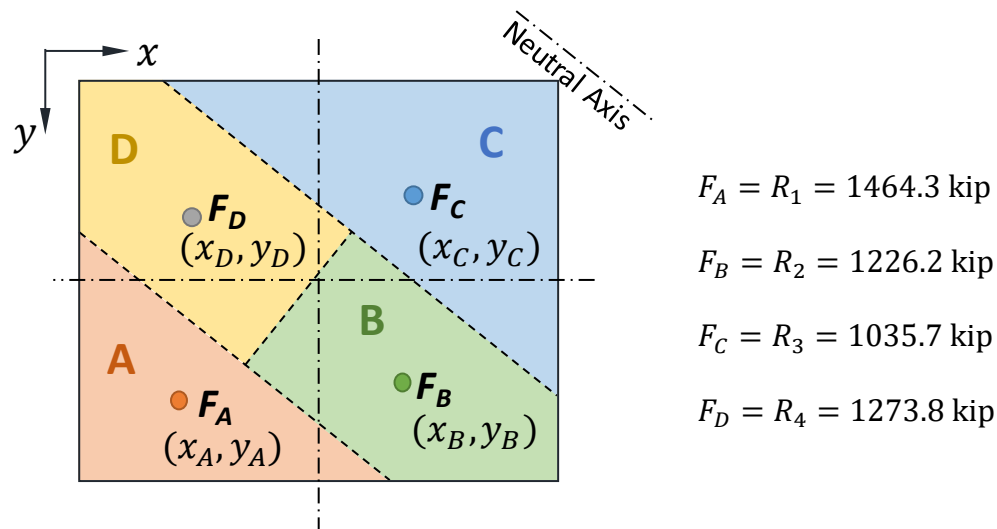
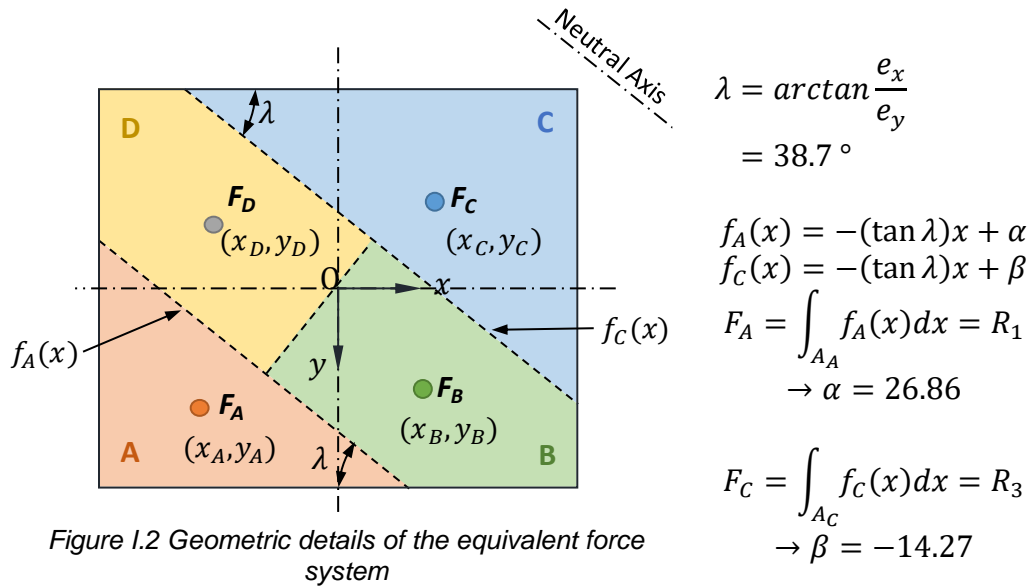


Figure I.1 Position and reaction for the equivalent force system

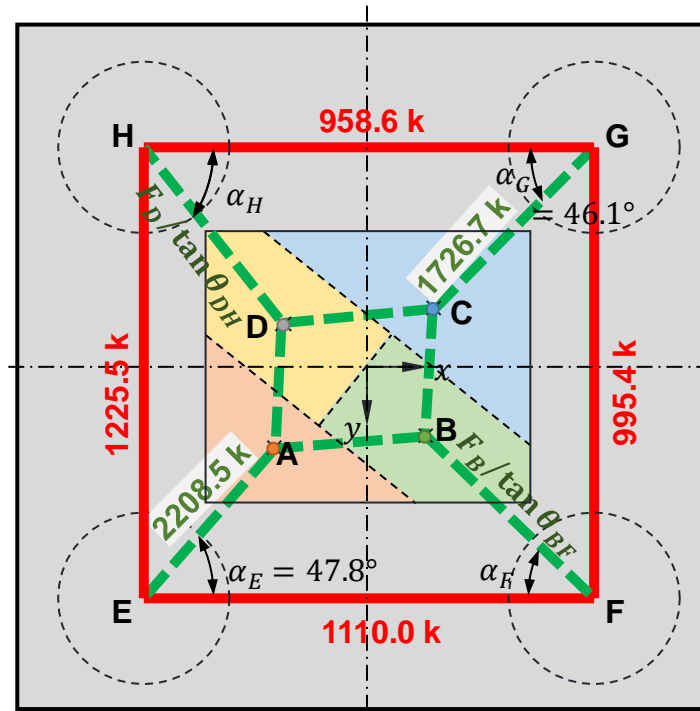
3. Calculate positions of A and C, the centroid of forces in the triangular regions (Region A and C)



$$x_A = \int_{A_A} x \cdot f_A(x) dx / F_A = -26.2 \text{ in.}, y_A = \int_{A_A} y \cdot f_A(x) dx / F_A = 22.3 \text{ in.}$$

$$x_C = \int_{A_C} x \cdot f_C(x) dx / F_C = 18.0 \text{ in.}, y_C = \int_{A_C} y \cdot f_C(x) dx / F_C = -16.3 \text{ in.}$$

4. Develop 3D strut-and-tie model (Figure 8.72 and Figure 8.73) with the coordinates of A and C



Strut Angles: $\theta_{AE} = 41.5^\circ$, $\theta_{CG} = 36.9^\circ$

Figure 1.3 3D strut-and-tie model based on the coordinates of nodes A and C

5. Calculate the angles at F and H from the equilibrium at Nodes F and H

- 1) Equilibrium conditions at Nodes F and H

$$F_{F,x} = -F_{E,x}, F_{F,y} = -F_{G,y}, F_{H,x} = -F_{G,x}, F_{H,y} = -F_{E,y}$$

- 2) Calculate angles at F and H

$$\theta_F = 39.5^\circ, \alpha_F = 41.9^\circ, \theta_H = 39.3^\circ, \alpha_H = 52.0^\circ$$

6. Find coordinates of B and D from the geometric details of F and H

$$\mathbf{B}: (19.1, 23.6, 54.0), \mathbf{D}: (-26.4, -16.2, 54.0)$$

7. Check the equilibrium on the column section

$$M_x = \sum_A^D F_i y_i = 2003.5 \text{ kip} - \text{ft} \cong M_{uxx} (0.2\% \text{ diff.})$$

$$M_y = \sum_A^D F_i x_i = 2494.5 \text{ kip} - \text{ft} \cong M_{uyy} (0.2\% \text{ diff.})$$

8. Horizontal strut forces

- 1) Equilibrium at Nodes A through D

$$\begin{array}{rcl}
F_{A,x} = F_{AB} \cos \beta_{AB} + F_{AD} \sin \beta_{AD} & \rightarrow & F_{AB} = 1117.8 \text{ kip} \\
F_{A,y} = F_{AB} \sin \beta_{AB} + F_{AD} \cos \beta_{AD} & & F_{AD} = 1255.7 \text{ kip} \\
F_{B,x} = F_{BA} \cos \beta_{BA} + F_{BC} \sin \beta_{BC} & \rightarrow & F_{BA} = 1084.5 \text{ kip} \\
F_{B,y} = F_{BA} \sin \beta_{BA} + F_{BC} \cos \beta_{BC} & & F_{BC} = 966.4 \text{ kip} \\
F_{C,x} = F_{CD} \cos \beta_{CD} + F_{CB} \sin \beta_{CB} & \rightarrow & F_{CB} = 992.8 \text{ kip} \\
F_{C,y} = F_{CD} \sin \beta_{CD} + F_{CB} \cos \beta_{CB} & & F_{CD} = 984.1 \text{ kip} \\
F_{D,x} = F_{DC} \cos \beta_{DC} + F_{DA} \sin \beta_{DA} & \rightarrow & F_{DC} = 951.7 \text{ kip} \\
F_{D,y} = F_{DC} \sin \beta_{DC} + F_{DA} \cos \beta_{DC} & & F_{DA} = 1228.9 \text{ kip}
\end{array}$$

* β_{ij} : Angle of strut from i-node to j-node with respect to x- or y-axes

2) Check the equilibrium

$$\begin{array}{l}
F_{AB} \cong F_{BA} \text{ (3.0\% diff.)}, F_{BC} \cong F_{CB} \text{ (2.7\% diff.)} \\
F_{CD} \cong F_{DC} \text{ (3.3\% diff.)}, F_{DA} \cong F_{AD} \text{ (2.1\% diff.)}
\end{array}$$